inventions

Special Issue Reprint

Innovative Research and Applications in Hydrodynamics and Flow Control, 2nd Edition

Edited by
Peng Du, Haibao Hu and Xiaopeng Chen

mdpi.com/journal/inventions

MDPI

Innovative Research and Applications in Hydrodynamics and Flow Control, 2nd Edition

Innovative Research and Applications in Hydrodynamics and Flow Control, 2nd Edition

Guest Editors

Peng Du
Haibao Hu
Xiaopeng Chen

MDPI

Basel • Beijing • Wuhan • Barcelona • Belgrade • Novi Sad • Cluj • Manchester

Guest Editors

Peng Du
School of Marine Science and Technology
Northwestern Polytechnical University
Xi'an
China

Haibao Hu
School of Marine Science and Technology
Northwestern Polytechnical University
Xi'an
China

Xiaopeng Chen
School of Marine Science and Technology
Northwestern Polytechnical University
Xi'an
China

Editorial Office
MDPI AG
Grosspeteranlage 5
4052 Basel, Switzerland

This is a reprint of the Special Issue, published open access by the journal *Inventions* (ISSN 2411-5134), freely accessible at: https://www.mdpi.com/journal/inventions/special_issues/6JPUU4302Z.

For citation purposes, cite each article independently as indicated on the article page online and as indicated below:

Lastname, A.A.; Lastname, B.B. Article Title. *Journal Name* **Year**, *Volume Number*, Page Range.

ISBN 978-3-7258-8717-0 (Hbk)
ISBN 978-3-7258-8718-7 (PDF)
https://doi.org/10.3390/books978-3-7258-8718-7

© 2026 by the authors. Articles in this reprint are Open Access and distributed under the Creative Commons Attribution (CC BY) license. The reprint as a whole is distributed by MDPI under the terms and conditions of the Creative Commons Attribution-NonCommercial-NoDerivs (CC BY-NC-ND) license (https://creativecommons.org/licenses/by-nc-nd/4.0/).

Contents

About the Editors . . . . . **vii**

Preface . . . . . **ix**

Ping-Chen Wu, Tzu-Chi Yeh and Yu-Cheng Wang
Stern Duct with NACA Foil Section Designed by Resistance and Self-Propulsion Simulation for Japan Bulk Carrier
Reprinted from: *Inventions* **2025**, *10*, 32, https://doi.org/10.3390/inventions10020032 . . . . . **1**

Adrian Clenci, Bogdan Cioc, Julien Berquez, Victor Iorga-Simăn, Robert Stoica and Rodica Niculescu
Results on the Use of an Original Burner for Reducing the Three-Way Catalyst Light-Off Time
Reprinted from: *Inventions* **2024**, *9*, 112, https://doi.org/10.3390/inventions9060112 . . . . . **24**

J. J. H. Brouwers
Anisotropic k-ϵ Model Based on General Principles of Statistical Turbulence
Reprinted from: *Inventions* **2024**, *9*, 95, https://doi.org/10.3390/inventions9050095 . . . . . **40**

Chunyun Wei, Hongjia Xie, Zixuan Liu, Xinfeng Zhai, Hongna Zhang and Xiaobin Li
Control on Flow Separation over a Cylinder by a Ferrofluid Film Adsorbed by a Magnet
Reprinted from: *Inventions* **2024**, *9*, 65, https://doi.org/10.3390/inventions9030065 . . . . . **50**

Jian Tiong Lim, Eddie Yin-Kwee Ng, Hamid Saeedipour and Hiang Kwee Lee
Numerical Simulation of Effective Heat Recapture Ammonia Pyrolysis System for Hydrogen Energy
Reprinted from: *Inventions* **2024**, *9*, 56, https://doi.org/10.3390/inventions9030056 . . . . . **67**

Przemysław Toczek, Rafał Wiśniowski, Albert Złotkowski and Wojciech Teper
Hydraulic Drilling Nozzle Design and Research
Reprinted from: *Inventions* **2024**, *9*, 51, https://doi.org/10.3390/inventions9030051 . . . . . **89**

José Azevedo, Violeta Carvalho, Tiago Bartolomeu, Ana Arieira, Senhorinha F. Teixeira and José C. Teixeira
Improving the Hydrodynamic Performance of Underwater Tags for Blue Shark Monitoring
Reprinted from: *Inventions* **2024**, *9*, 48, https://doi.org/10.3390/inventions9030048 . . . . . **98**

Alina Beatrice Răileanu, Liliana Rusu, Andra Marcu and Eugen Rusu
The Expected Dynamics for the Extreme Wind and Wave Conditions at the Mouths of the Danube River in Connection with the Navigation Hazards
Reprinted from: *Inventions* **2024**, *9*, 41, https://doi.org/10.3390/inventions9020041 . . . . . **113**

J. J. H. Brouwers
The Basic k-ϵ Model and a New Model Based on General Statistical Descriptions of Anisotropic Inhomogeneous Turbulence Compared with DNS of Channel Flow at High Reynolds Number
Reprinted from: *Inventions* **2024**, *9*, 38, https://doi.org/10.3390/inventions9020038 . . . . . **140**

Yanqin Mao, Roman Chertovskih and Liang Cai
Numerical Study of the Gas–Solid Separation Performance of Axial Flow Cyclone Separators
Reprinted from: *Inventions* **2024**, *9*, 34, https://doi.org/10.3390/inventions9020034 . . . . . **160**

Haixia Gong, Zhuoran Ping, Fance Meng and Shuping Hou
Modeling and Optimization of Interior Ballistics within Pneumatic Underwater Launchers
Reprinted from: *Inventions* **2024**, *9*, 30, https://doi.org/10.3390/inventions9020030 . . . . . **179**

Filippos Sofos, George Sofiadis, Efstathios Chatzoglou, Apostolos Palasis, Theodoros E. Karakasidis and Antonios Liakopoulos
From Sparse to Dense Representations in Open Channel Flow Images with Convolutional Neural Networks
Reprinted from: *Inventions* **2024**, *9*, 27, https://doi.org/10.3390/inventions9020027 . . . . . **199**

About the Editors

Peng Du

Peng Du is currently a professor and doctoral supervisor at the School of Marine Science and Technology, Northwestern Polytechnical University. He also serves as the deputy director of the Shaanxi Provincial Key Laboratory. Prof. Peng Du's research focuses on the environmental hydrodynamics of marine structures. He has published over 80 journal papers, applied for more than 40 invention patents, and registered over 30 software copyrights. He serves as an editorial board member for the *Journal of Hydrodynamics* and *Chinese Journal of Ship Research*, as a young editorial board member for *Engineering Reports* and *Marine Engineering*, and as a reviewer for more than 30 journals. He has been invited to give plenary/keynote speeches at numerous academic conferences and has led several national and provincial-level projects.

Haibao Hu

Haibao Hu is a professor and doctoral supervisor at the School of Marine Science and Technology, Northwestern Polytechnical University. He is a national leading talent and a recipient of the Shaanxi Provincial Distinguished Youth Award. He serves as the director of the Shaanxi Key Laboratory of Marine Engineering Hydrodynamics and Underwater Power Technology. He has long been dedicated to the overall design of underwater vehicles, complex hydrodynamics, and research and engineering applications of underwater drag reduction and energy-saving technologies. He has published more than 110 academic papers in journals such as *Science Advances*, *Journal of Fluid Mechanics*, *Physics of Fluids*, and *Ocean Engineering*.

Xiaopeng Chen

Xiaopeng Chen is a Professor at the School of Marine Science and Technology, Northwestern Polytechnical University. His research focuses on multiphase flow, bubble dynamics, the lattice Boltzmann method, and computational fluid mechanics. He has conducted extensive research on bubble dynamics and multiphase flow applications in ocean engineering. He has served as a Guest Editor for multiple special issues related to hydrodynamics and CFD.

Preface

This Reprint compiles papers from the Special Issue "Innovative Research and Applications in Hydrodynamics and Flow Control, 2nd Edition" published in *Inventions* (MDPI). Hydrodynamics and flow control represent core disciplines that underpin the performance, safety, and energy efficiency of ships, underwater vehicles, marine structures, energy equipment, and various industrial fluid systems. In recent years, rapid progress in computational simulation, experimental measurement, intelligent algorithms, and multiphase flow dynamics has greatly promoted breakthroughs in flow control strategies, drag reduction technologies, hydrodynamic optimization, and intelligent flow perception.

This second edition of the Special Issue continues to gather high-quality original research, numerical studies, and experimental investigations that bridge fundamental fluid mechanics and industrial applications. It emphasizes innovative methodologies, practical engineering solutions, and emerging interdisciplinary approaches such as machine learning for fluids and data-driven flow analysis. The works included in this volume reflect the latest developments and future trends in hydrodynamics and flow control, providing new insights for both academic research and engineering implementation.

We sincerely thank all authors for their high-quality contributions, the anonymous reviewers for their rigorous and constructive comments, and the editorial team of Inventions for their efficient support throughout the publication process. We hope this Reprint will facilitate academic communication, inspire further research, and promote technological innovation in hydrodynamics and flow control worldwide.

Peng Du, Haibao Hu, and Xiaopeng Chen
Guest Editors

inventions

MDPI

Article

Stern Duct with NACA Foil Section Designed by Resistance and Self-Propulsion Simulation for Japan Bulk Carrier

Ping-Chen Wu *, Tzu-Chi Yeh and Yu-Cheng Wang

Department of Systems and Naval Mechatronic Engineering, National Cheng Kung University, Tainan City 70101, Taiwan; p16104190@gs.ncku.edu.tw (T.-C.Y.); p16091135@gs.ncku.edu.tw (Y.-C.W.)
* Correspondence: z10702010@email.ncku.edu.tw

Abstract: The objective of the presented work is the stern duct design for the JBC (Japan Bulk Carrier) hull form. Since the original duct only provides a 0.6% resistance reduction, an innovative duct will be proposed to improve the ship resistance and propulsion performance. The duct section geometry is based on the NACA (National Advisory Committee for Aeronautics) 4-digit foil series. First, we analyze whether the wake flow field and total resistance of the ship are improved, and then we investigate the self-propulsion performance for the selected ones. The research tool is the CFD (Computational Fluid Dynamics) software OpenFOAM 9 with the viscous free surface flow field modelled by the VOF (Volume of Fluid) method and the SST (Shear Stress Transport) k–ω turbulence model. The propeller effect is implemented by the MRF (Multi-Reference Frame). Compared to the original duct, two ducts, namely, NACA 7908 and NACA 6.3914, show the best (2.8%) resistance reduction in the bare hull condition. By installing both ducts, the propeller thrust decreases 6 and 5% to reach the self-propulsion point, and the behind-hull efficiency increases 7 and 6%. Both ducts save the energy, i.e., effective horsepower, by 4.3%, and produce obvious flow acceleration, achieving around 10% higher effective wake factor $(1 - w)$. The nominal and propeller wakes are improved as well.

Keywords: energy saving duct; ship resistance; self-propulsion

1. Introduction

Against the growing threat of global warming, extreme weather, and climate change mitigation, countries and international organizations have long and constantly paid attention to environmental issues. Progressively strict regulations have been imposed on marine transportation such as carbon emission reduction. The sea shipping industry emitted one billion tons of CO_2 globally in 2018. The Emissions Trading System (ETS) had just taken effect on the very first day of 2024, and the ships berthing in EU (European Union) ports will face the carbon tax bill reaching USD 3.6 billion. The next stage of ETS will cover 100% carbon emission. The research and development of energy saving technology is crucial to pursue low, even zero, carbon emissions as the primary goal for ship design.

Based on the installation location of the energy saving devices (ESDs), there are several types of ESD. They can be installed: (1) on the ship's stern in front of the propeller, or (2) on the propeller, or (3) behind the propeller on the rudder or even behind the rudder, or (4) a combination of the above-mentioned methods. ESDs have been practically used on newly designed ships or refurbished old ships.

Our study objective: The JBC (Japan Bulk Carrier) ship model and its type (1) ESDs, i.e., a stern duct (pre-duct, energy saving duct) in front of the propeller, were proposed by

the T2015 (Tokyo 2015 Workshop on CFD in Ship Hydrodynamics; CFD = Computational Fluid Dynamics) [1] along with the experimental data of resistance and propulsion. The original duct is axisymmetric, with the NACA (National Advisory Committee for Aeronautics) 4420 section providing only a 0.6% reduction for the calm water bare hull resistance. Therefore, the presented work aims to further improve resistance reduction and achieve a better self-propulsion performance.

The ESDs of type (1) are the main concern of this study, which commonly consist of a duct, vortex generators, spoilers, fins, stators, or their combination. The WED (Wake Equalization Duct) developed by Schneekluth Hydrodynamik GmbH [2] claimed a fuel saving of up to 12%, and 50% lower vibration. On a container ship model measurement, the inward flow angle along the ship's longitudinal axis on the propeller plane behind the duct is reduced to 7° from 20°. Sanoyas shipbuilding Co., Ltd., Osaka, Japan [3] deployed STF (Sanoyas Tandem Fin) in front of their ACE (Advanced flow Controlling and Energy saving) duct. The fuel consumption decreased by 8%. One STF is above the shaft tube, and another one is placed more upstream around shaft axis height. The ACE is an upper half circle with a port and starboard horizontal strut. A pre-swirl stator (PSS) proposed by DSME (Daewoo Shipbuilding & Marine Engineering) was mentioned in [4], saving energy by 4−6%. Lee et al. [5] applied a potential theory and experiment to design axisymmetric PSS to obtain a 3% increase of propulsive efficiency. Park et al. [6] used the CFD software Star-CCM+ to design a PSS, and suggested a method to estimate the full-scale wake behind ESDs. The so-called pre-swirl duct (PSD) combined a PSS and duct, e.g., the Becker Mewis Duct®, which lowered power output by 6.3%, based on the ship's model test database [7]. In the earlier design, the stators were trimmed with different angles inside the duct, and later the Becker twisted fins were extended outside the duct [8]. Andersson et al. [9] proposed a PSD for a KVLCC2 (KRISO Very Large Crude Carrier 2) tanker for a full-scale CFD benchmark. Among the total of 22 CFD results collected, the power reduction was ±4% on average, with a standard deviation of 1.6%.

The S-PIV (Stereoscopic Particle Image Velocimetry) measurement for the wake field behind a PSD or PSS mounted on a C259 bulk carrier was conducted by Falchi and Aloisio [10]. Three PSDs and one PSS were tested. Great insight into the fluid mechanism of the ESDs was gleaned. The objective ship was that the nominal and propeller wakes were measured on the propeller plane, and 41.4 mm behind the plane, respectively. In the nominal wakes, the fins inside the PSDs eliminated the portside bilge vortex with two vertically located vortices induced underneath the shaft tube. The flow acceleration of the propeller wake remained as the velocity distribution without ESDs. However, in the case of the PSS, the bilge vortices on the starboard and port sides only move their position. In addition, two vortices under the shaft tube and starboard outer region were generated. Corresponding to the propeller wake, the high velocity profile deforms, and another high velocity region was formed in the upper portside.

Schuiling and van Terwisga [11] reviewed the commercial duct designs chronologically, such as the MIDP (Mitsui Integrated Duct, 1981) [12], the HZN (Hitachi Zosen Nozzle, 1982) [13], the Schneekluth WED (1986) [14], the SILD (Sumitomo Integrated Lammeren Duct, 1997) [15], the IHIMU semi-circular duct (2007) [16], the Becker Mewis Duct (2009) [17], and the Kawasaki SDS-F (Semi-Duct System with contra-Fins, 2012) [18]. In their work, a BSD (Blade efficiency improving Stator Duct) [19] mounted on a chemical tanker was investigated by using the CFD code ReFRESCO for the model and full scale. The 94-m-long, 7000 DWT tanker was named STREAMLINE with a *CB* (block coefficient) = 0.762, and a four-bladed propeller and rudder. The turbulence model was SST (shear stress transport) k–ω, i.e., SST-2003 [20]. The double-body model was used with the sliding mesh for the propeller rotating 2 deg per time step. The total grid number

N_G was 14.3 M (million) and 5.8 M for the model and full scale, respectively, with 1.8 M around the propeller. The average $y+$ (non-dimensional wall distance) was 0.1 and 355 on the model and full-scale ship, respectively. The power was reduced by 4.1% in the model and 3.4% at full scale. The propeller rotation rate decreased 4.1% to reach self-propulsion with a less asymmetrical propeller loading through blade circumferential positions. The propeller efficiency increased by around 6%. However, it caused 0.8% higher ship resistance because the lower pressure induced by the lift device, i.e., pre-swirl stator, led to a pressure resistance increase.

Nicorelli et al. [21] applied the CFD software StarCCM+ to study a PSD, PSS, or WED equipped on a DTC (Duisburg Test Case) hull which belonged to a typical 14000 TEU container ship. The turbulence model was realizable k–ε. The ship model was appended with a five-bladed propeller and a twisted rudder featuring a Costa bulb. RANS (Reynolds-averaged Navier–Stokes equations) simulations were performed for ship resistance and self-propulsion, and an open-water test (OPT). The sinkage and trim were predicted in RANS CFD. In addition, the OPT was also analyzed by the BEM (Boundary Element Method). The propeller was modelled by the MRF (moving reference frame) in the OPT, and by the sliding mesh for the self-propulsion. The free surface was considered by the VOF (volume of fluid) in the resistance test but neglected by the double body model in the self-propulsion test. For the model and full-scale propeller simulation, N_G = 1.2 M and 1.5 M, $y+$ = 15 and 60. The grid sensitivity and uncertainty analyses were conducted for ship resistance with N_G = 0.5~6.3 M, with 4% over-prediction. The reference grid was N_G = 1.3 M, the average $y+$ = 30 and 160 in the model and full-scale, and 2% uncertainty. For self-propulsion, the error of the wake factor $(1 - w)$ and thrust deduction $(1 - t)$ against the experimental value was 3~5%. To estimate self-propulsion performance for the duct and fin designs in simulation-based design optimization (SBDO), another RANS/BEM coupling method was proposed to exchange the wake data from the RANS actuator disk and to subtract propeller-induced velocity in BEM. In SBDO, 14 parameters were considered for the three fins of PSD and PSS, and four (diameter, chord, angle of attack, and maximum sectional camber) for WED. A total of 160 PSDs or PSSs, and 70 WEDs, were generated by the Uniform Latin Hypercube method. Targeting the minimal propeller delivered horsepower (DHP) with 10 evolutions for every geometry, and the optimal geometry was found among 1600 PSDs, 1600 PSSs, and 700 WEDs, individually. A 4% DHP reduction was achieved. The PSD was suggested as the most suitable device, and the full-scale RANS showed the reduction was lowered by 2.4%. The PSS performed close to the PSD or was ineffective. The WED tended to increase ship resistance.

For a Panamax bulk carrier, a stern duct and stern bluntness were designed in a study by Sakamoto et al. [22]. The duct parameter included angles of attack (AOA), chord length, and tailing edge diameter. The $(1 - w)$ was improved by 2~3%. The hull efficiency was improved for the model and full scale by 1~3%.

Intelligent optimization algorithms have been applied in ship design, such as the MOGA (Multi-Objective Genetic Algorithm), the NSGA-II (Non-dominating Sorting Genetic Algorithm-II), and the ANN (Artificial Neural Network), etc. For instance, MOGA for a destroyer hull form [23,24] and ANN for flow control fins (FCFs) on a small container ship [25]. NSGA-II has been widely used in many aspects of ship engineering, e.g., for a destroyer hull form [26,27], a trimaran [28], FCFs on KVLCC2 [29], marine propeller [30,31], and the duct for a rim-driven thruster [32]. For the stern duct, a reduced order model-based optimization [33] and global convergence optimization [34] were proposed.

Nguyen and Chandar [33] designed the stern duct for the JBC ship model using a double body model simulation in OpenFOAM with MRF for propeller effect. The SST k–ω turbulence model was utilized. The independent grid block of duct was attached

to the hull-propeller grid system by the overset method. The CFD method was verified and validated first for the self-propulsion test with 1.7 M, 3.2 M, 7.6 M grids without duct, and then a 3.2 M grid was selected for oversetting the duct. The design goal was maximum propeller propulsive efficiency η_D. Based on the four-digit NACA foil profile with fixed chord length, the design parameter included the thickness (0.05~0.25), camber (0~10%), AOA (0~25 deg), and ratio (0.45~0.85) between the propeller radius r and duct radius r_D. The reference point of r_D and AOA is the duct trailing edge. The reduced order model-based optimization consisted of off- and online stages. The proper orthogonal decomposition (POD) was executed in the offline stage. In the online stage, a surrogate model using a Gaussian process regression was then built to evaluate the objective function approximately in the loop between the POD with parametric interpolation and optimizer. The optimizer was gradient-free global optimization. Consequently, η_D was improved by 10%. The optimal duct was characterized by 4.5% of camber, 10.2% of thickness, 8.7 deg of AOA, and r/r_D = 0.68.

Furcas et al. [34] utilized a global convergence optimization algorithm and Star-CCM+ with a k–ε turbulence model to maximize the delivered power for JBC. The error of the open water propeller simulation was less than 1% to 4% for thrust, and the torque was over-predicted by 4~8%. The resistance simulation was performed by the double body and free surface model to obtain the wave resistance for the self-propulsion simulation in the optimization process. The iterative and grid sensitivity were investigated for the double body and free surface model (N_G = 0.25 M, 0.73 M, 9.5 M), respectively. In the self-propulsion test, the body force propeller disk or sliding mesh with the realistic propeller was used. Three runs of design were performed with different parameter limits. The chord length c = 0.147~0.440D (propeller diameter), AOA: 5~35 deg, longitudinal position x = 0.016~0.75L_{PP} (length between particulars), and duct radius r = 0.147~0.63D. The NACA digit for camber m = 0~7, position of maximal m: p = 0~6, and thickness t = 0.15~0.25c. In run 1, the NACA4420 section remained by changing (c, AOA, x, r). In run 2, the variation of (c, AOA, x, r, m, p, t) was considered. In run 3, the duct geometric parameters were described by the B-Spline control polygon of the generator curve with (c, x, m, p) varying. The result of (c/D, r/D, AOA) of run 1 is (0.325, 0.320, 9 deg). Run 2 generated NACA 5715 with (c/D, r/D, AOA) = (0.345, 0.359, 9 deg). The product of run 3 is a non-symmetric, trapezoid-like nozzle with a longer upper base with NACA 6716 and (c/D, r/D, AOA) = (0.443, 0.404, 10.45 deg). Consequently, the delivery power was reduced by 5.9%, 6.4%, 7.2% in runs 1, 2, 3, respectively, compared to 4.9% in the original ducts. The overall propulsive efficiency was significantly improved by considering the actual ship wake profile.

In our work, the parameter of the NACA's four digits covers the whole range for m and p, with c fixed as the original duct. AOA = 7.06 deg had been found as in our previous work [35], comparable to the 8.7 deg of [33] and 9 deg of runs 1 and 2 in [34]. t = 0.4~0.24c.

The presented work is divided into three stages to enhance the energy-saving effect of the JBC stern duct in ship resistance and self-propulsion in calm water by using CFD:

1. V and V (Verification and Validation) analysis.
    a. Resistance simulation without the original duct;
    b. Resistance simulation with the original duct;
    c. Open-water propeller test (OPT) simulation;
    d. Self-propulsion simulation with the original duct.
2. Resistance simulation with various duct designs with a NACA four-digit series foil section.
3. Self-propulsion simulation with the optimized duct selected from the stage 2 result.

The results of stages 1,2,3 are presented in the following Section 3.1, 3.2, and 3.3, respectively. In stage 1, the V and V (Verification and Validation) analysis is conducted to ensure our CFD method is reliable before further application to the design procedure: stages 2 and 3. The V and V theory used here is based on the ITTC (International Towing Tank Conference) 75-03-01-01 guideline [36]. The simulations for V and V were conducted based on the experimental conditions of the test cases suggested by T2015 [1]. The simulation results are compared to the experimental data provided by T2015 [1], including OPT. Stages 1a, 1b, and 1d correspond to the T2015 test cases 1.1, 1.2, and 1.6, respectively. In stage 2, the lowest resistance reduction, i.e., the total ship resistance difference between the original duct and other design, is pursued. In stage 3, the self-propulsion point is simulated and found by CFD simulation for the ship with the appended optimal duct from stage 2. The improvement of self-propulsion performance compared with the original duct is discussed.

2. Methods

2.1. Numerical Schemes

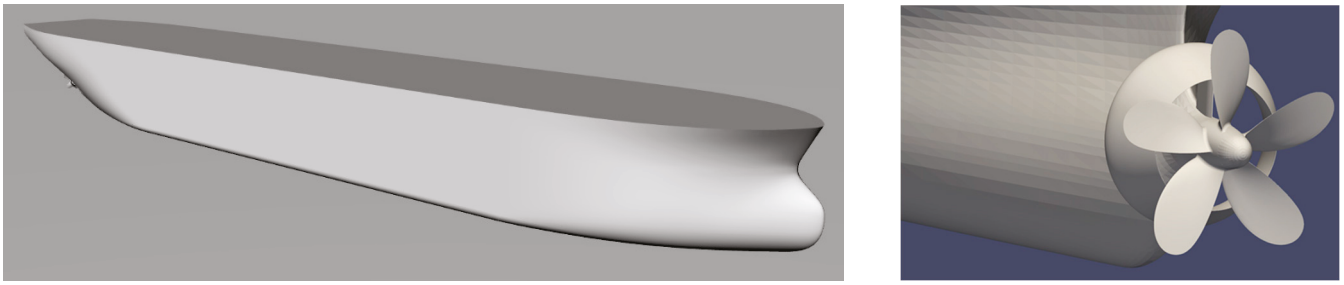
The analysis and simulation tool in the presented work is the open source CFD software OpenFOAM (open-source field and manipulation) version 9 for the viscous flow simulation considering the free surface. An incompressible two-phase flow model VOF [37], i.e., interFoam solver, was applied with the SST-2003 turbulence model [20] to solve the flow field around the ship, including velocity, pressure field, and free surface elevation. The velocity and pressure coupling algorithm is PIMPLE [38], which was exclusively developed by OpenFOAM since version 2 to combine PISO (pressure implicit with splitting of operator) and SIMPLE (semi-implicit method for pressure linked equations).

The numerical schemes selected to discretize the steady Reynolds-averaged Navier–Stokes equations (RANS) and the above-mentioned flow field model are briefed as below. The temporal discretization method was the first-order Euler implicit with local time stepping. The gradient term was calculated by the first-order central difference. The second-order upwind method was used mainly for the divergence term. The Laplacian term was computed by a linear interpolation. The gradient of surface normal direction was obtained by a second-order explicit scheme with non-orthogonal corrections. The control point value of a volume or surface was also interpolated linearly. The steady propeller effect is achieved by the MRF with the realistic geometry discretization through the Coriolis term added in RANS. The ship motions, i.e., sinkage and trim, are not considered, and the ship is fixed with even keel and the uniform inflow velocity corresponding to the ship speed.

2.2. Geomtry and Test Conditions

The geometry of the JBC (Japan Bulk Carrier) ship model with and without an axisymmetric stern duct, i.e., energy saving duct, was proposed by T2015 (National Maritime Research Institute, Tokyo, Japan) [1], along with its propeller (MP. 687). The experimental data including ship resistance, self-propulsion in calm water, and open-water propeller test were provided. The ship length, beam, and draft for the 1/40 scale model are $L = L_{PP} = 7$ m (length between particulars), $B_{WL} = 1.125$ m (waterline beam), and $t = 0.4125$ m, respectively. The block coefficient $CB = 0.8580$ indicates the JBC is a full hull form. Figure 1a shows the 3D geometry of the JBC hull form generated by Rhinoceros 3D using the IGES file provided by [1]. The towing tank test condition is Froude number $Fr = 0.142$, corresponding to the design speed 14.5 knots in full scale and $U = 1.179$ m/s for the model. The Reynolds number in the model scale is $Re = 7.44 \times 10^6$. The original duct was appended through an upward and vertical strut on the JBC stern in front of the propeller, see Figure 1b, with a

20° AOA (Angles of Attack) and a NACA 4420 section. The duct design parameters are explained at the beginning of Section 3.2.



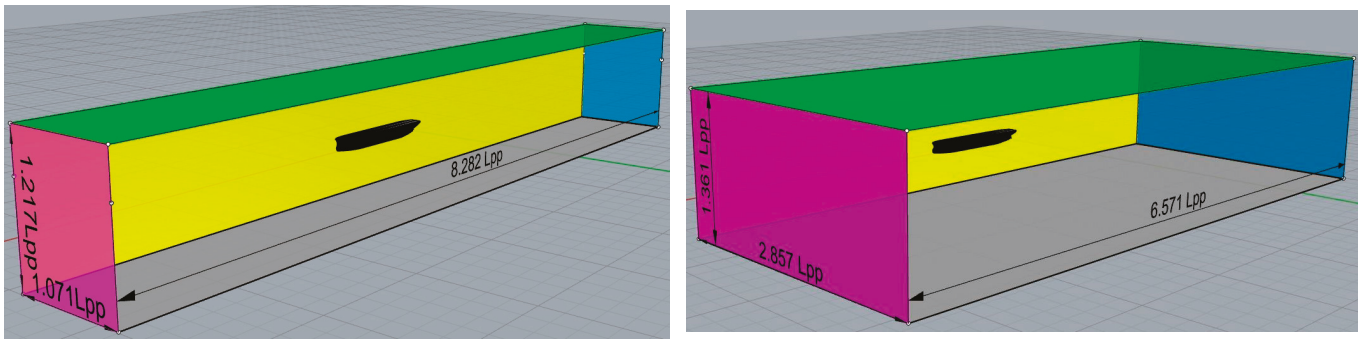
(**a**) (**b**)

Figure 1. Ship and propeller model [1]: (**a**) the hull with bulbous bow; (**b**) propeller and stern duct.

For the 5-bladed right-rotating MP. 687 propeller, its main particulars are: diameter D = 0.203 m, pitch ratio P/D = 0.75, blade thickness ratio t/D = 0.050, hub ratio is 0.180, rake angle is 5 deg. The propeller center is at x/L_{PP} = 0.9854 for FP (Front Particulars) at x = 0, and $z = 0.0185L_{PP}$ above the keel (baseline) or $-0.0404L_{PP}$ below the waterline.

2.3. Domain and Boundary Conditions

The computational domain size is described in Figure 2, where the proper distance from the study object, i.e., the JBC hull, to the boundaries ensures the external flow fully developed and prevents the numerical bounce and truncation error. Since the ship geometry and flow filed are symmetric, the resistance simulation only solves the starboard flow field, i.e., half domain, as shown in Figure 2a. The domain length in front of ship FP $L_{upstream}$, the length behind ship AP (Aft Perpendicular) $L_{downstream}$, the distance L_{side} to the side from y = 0 plane, the height H_{air} of the air part, and the depth D_{water} of the water part are 2.157, 5.125, 1.971, 0.848, $0.369L_{PP}$, respectively.



(**a**) (**b**)

Figure 2. Computational domain size: (**a**) resistance simulation; (**b**) self-propulsion simulation.

Exactly the same CFD and grid method and setup are adopted for the OPT and self-propulsion simulation. The effort is to satisfy the V and V requirement of the OPT and self-propulsion test by using the same propeller modeling method. Thus, both domain sizes are identical as shown in Figure 2b which is a full domain due to the right-rotating propeller. Since the flow field is no longer symmetric, both port and starboard domains should be considered. For the OPT, the propeller is located in the same position as in Figure 2b, but the hull and duct are removed. $(L_{upstream}, L_{downstream}, L_{side}, H_{air}, D_{water}) = (1.5714, 4.0, 1.4285, 0.5267, 0.8348)L_{PP}$.

Each domain in Figure 2 consists of seven boundary faces which are identified by colors. The black, purple, blue, green, yellow, and grey faces correspond to the solid surface, inlet, outlet, top, side (starboard), and bottom boundaries, respectively. In Figure 2a, the

transparent face is the mid-plane boundary laying on $y = 0$, i.e., the ship's center plane. In Figure 2b, the transparent face is another side boundary (portside). The boundary conditions shown in Table 1 are specified on the above-mentioned boundaries. Those condition names are the standard defaults in OpenFOAM.

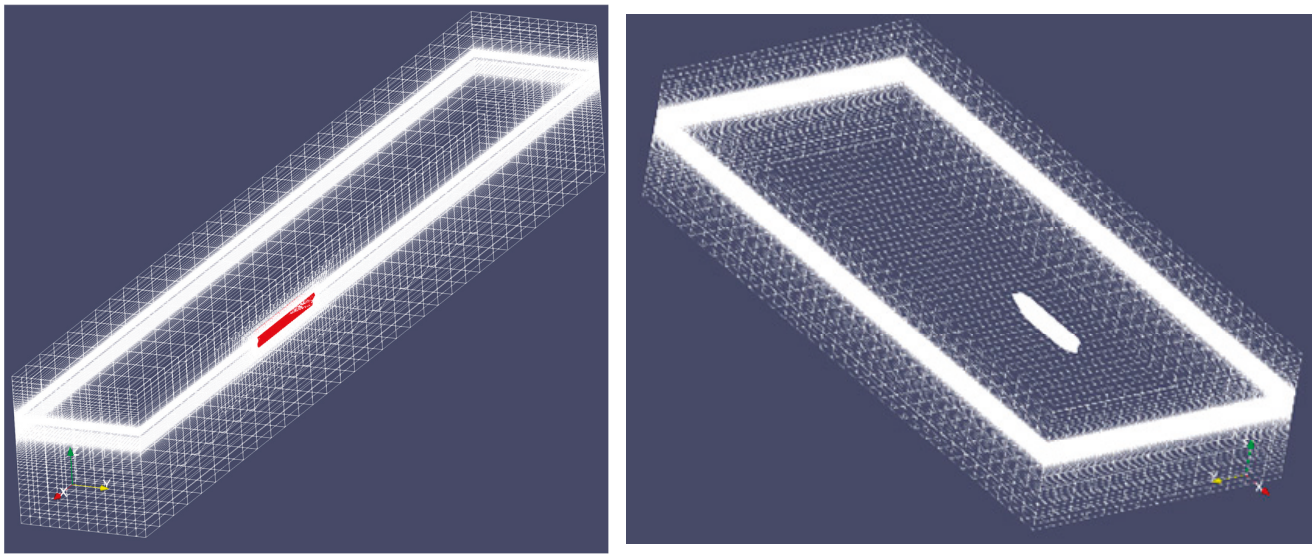
Table 1. Boundary conditions.

	U = (*u*,*v*,*w*)	***p***	μ_t	***k***	ω	α
Hull	movingWallVelocity	fixedFluxPressure	nutkWallFunction	kqRWallFunction	omegaWallFunction	zeroGradient
Propeller Duct	movingWallVelocity	fixedFluxPressure	nutLowReWallFunction	kLowReWallFunction	omegaWallFunction	zeroGradient
Inlet	fixedValue	fixedFluxPressure	fixedValue	fixedValue	fixedValue	fixedValue
Outlet	outletPhaseMeanVelocity	zeroGradient	zeroGradient	inletOutlet	inletOutlet	variableHeightFlow Rate
Top	pressureInletOutlet Velocity	prghEntrainment Pressure	zeroGradient	inletOutlet	inletOutlet	inletOutlet
Bottom Mid-plane Sides	SymmetryPlane					

On the inlet, the uniform inflow velocity (fixedValue) was imposed as $-U$. The non-slip is applied on the solid surface including the hull, duct, and propeller, i.e., movingWallVelocity is forced to be 0. The near-wall treatment, i.e., wall function, for the smooth wall is specified on the boundary values of viscous turbulence μ_t (nutkWallFunction), turbulent kinematic energy k (kqRWallFunction), and the specific turbulent dissipation rate ω (omegaWallFunction). Because the propeller and duct are inside the ship's wake, the μ_t and k wall functions for low Re (nutLowReWallFunction, kLowReWallFunction) are applied on their surfaces. The initial μ_t, k, ω, and total pressure p_0 of the inlet are estimated based on the far field freestream values (fixedValue). The volume fraction $\alpha = 0.5$ is set at $z = t$ (ship draft) as the initial water surface (fixedValue of α on the inlet). Zero total pressure with pseudo-hydrostatic pressure (prghEntrainmentPressure) is used on the top. The gradient normal to the surface of the domain's side and bottom (and $y = 0$ plane in resistance simulation) is zero, i.e., SymmetryPlane. The static pressure p and α on the hull surface, p on the outlet face, and μ_t on the outlet and top face are zero-gradient conditions (zeroGradient). The rest of the boundary conditions are a variation of zero-gradient condition. The backward flow is avoided by inletOutlet and pressureInletOutletVelocity. The water height as the inlet input is maintained by outletPhaseMeanVelocity and variableHeight-FlowRate. The pressure gradient is regulated by fixedFluxPressure based on the flux.

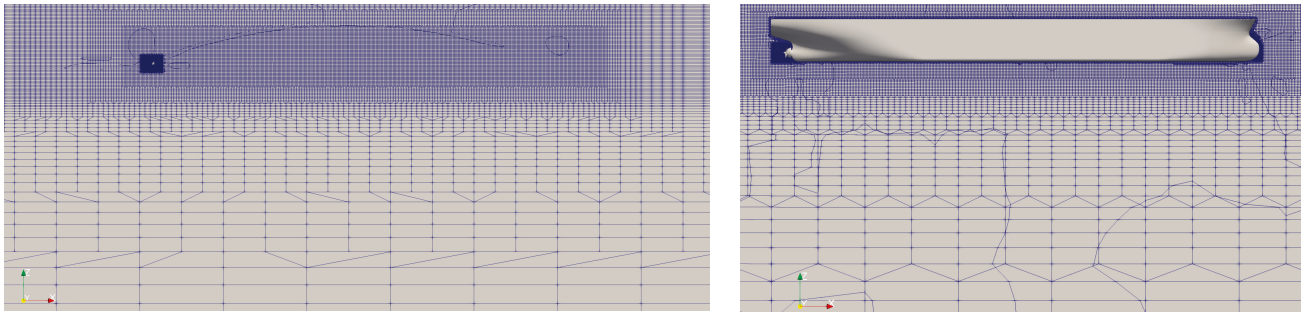
2.4. Unstructured Grid Generation

Constant grid spacing along x–y plane on far field boundaries is applied (Figure 3). A denser grid is allocated toward the free surface vertically based on the geometric distribution. Figure 4 indicates that the Cartesian grid generates finer and finer grids around the ship's body by six levels from the far field. As mentioned in the previous Section 2.3, the OPT grid in Figure 4a is built by removing the ship hull and duct from the self-propulsion grid in Figures 3b and 4b. The body-fitted grid is constructed as the zoom-in view around the ship stern and bow in Figure 5 as an example. Figure 5 also lists the grid building result of the coarse, medium, and coarse grids for the self-propulsion requested by the V and V analysis. The result is in Section 3.1. Finally, the unstructured grid is built by a polyhedral element with arbitrary polygonal faces. The face number, the edge number, and the alignment of the face are unlimited in OpenFOAM. The element majority is hexahedron. The other polygon is split or degenerated from hexahedra, e.g., the face becomes line, or the line becomes points. Those polygonal elements include tetrahedral wedges, two kinds of pentahedron: prism and pyramid, and two kinds of tet: tetrahedron and tetrahedral wedge.



(**a**) (**b**)

Figure 3. Grid distribution on far field boundaries: (**a**) resistance (the hull surface is in red color); (**b**) self-propulsion test.



(**a**) (**b**)

Figure 4. Grid refinement levels: (**a**) open-water propeller; (**b**) self-propulsion.

The layered grids attached on the solid surface to resolve the boundary layer flow can be observed in Figure 6. The layer number of layered grids is 3 on the hull, 4~5 on the duct, and 4 on the propeller. To form a good quality body-fitted (surface) grid and layered grid, an additional grid refinement is added for self-propulsion (Figure 5 left column) in the stern region. As a result, the complicated and delicate geometry details of the stern shape, duct, and propeller are captured in Figure 6a. Those appendages are, relatively, much smaller than the hull body. The stern is characterized by a blunt and curvy lower bottom and sharp upper part toward the centerline plane. A series of grid refinement is also arranged along the bulbous bow (see Figure 5, right column, and Figure 6b). This is required because the propeller has very different feature edges compared with the other parts of the ship. The layered grid generation is influenced by the propeller appearance, and results in low coverage. This bow refinement is unnecessary in the resistance test. The stern refinement is excluded in the resistance test without the duct. In the OPT, the Cartesian meshing method and (stern) grid refinement are inherited from the self-propulsion test. Consequently, the grid generation result around the propeller is shown in Figure 7.

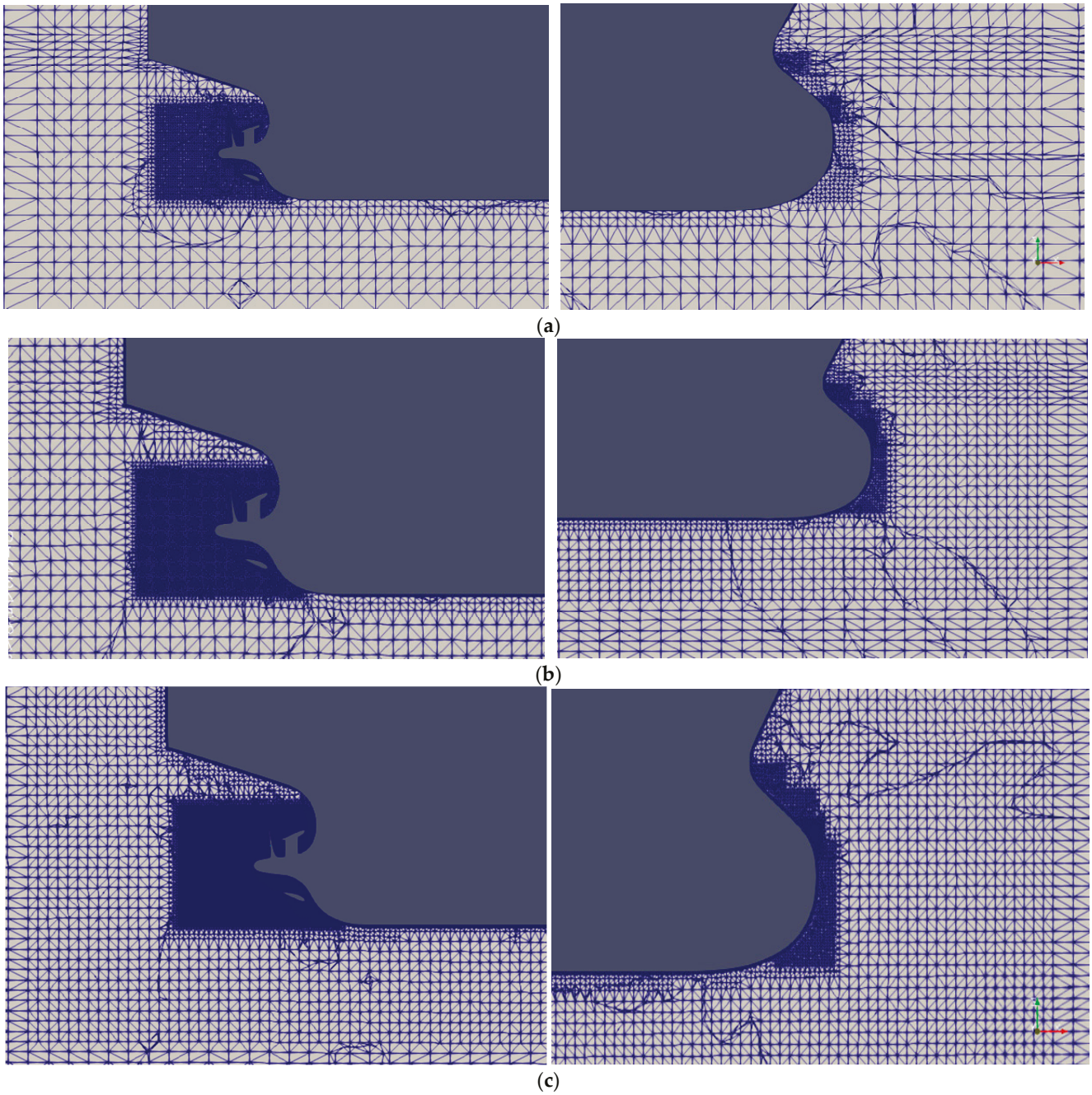
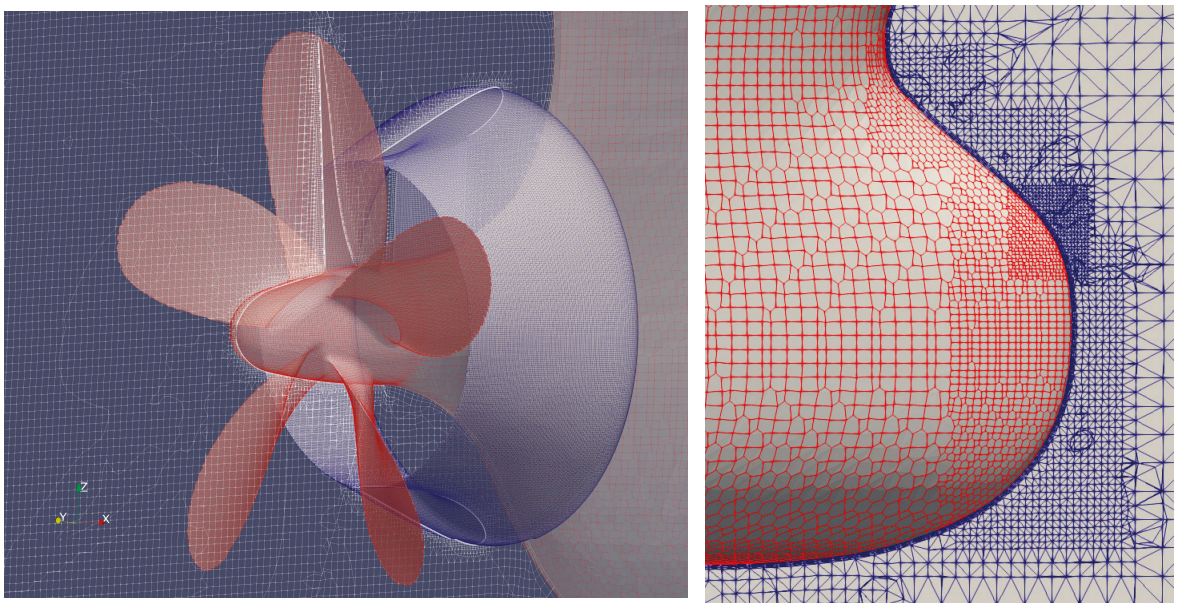


Figure 5. The unstructured grid topology around the ship bow (**right**) and stern (**left**) for self-propulsion simulation: (**a**) coarse grid; (**b**) medium grid; (**c**) fine grid.

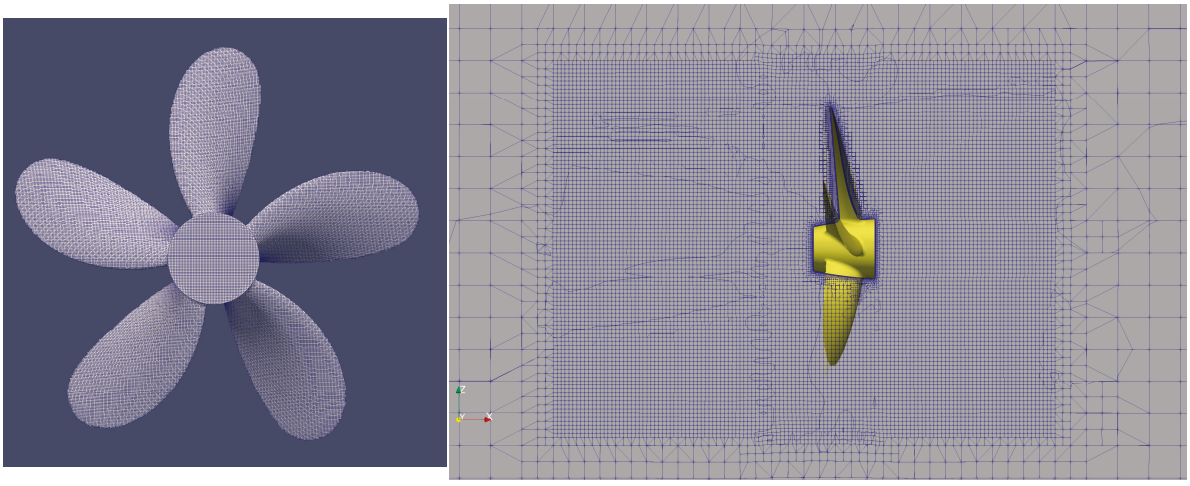
Between two nearby different grid densities, i.e., coarse to medium, and medium to fine grids, the refinement ratio $\sqrt{2}$ is recommended by ITTC 75-03-01-01 [36] along the x, y, and z directions, respectively. Due to the unstructured grid, the increase ratio of the total grid number N_{total} as close as possible to $\sqrt{8}$ ($= \sqrt{2} \times \sqrt{2} \times \sqrt{2}$) is attempted. Tables 2 and 3 list the N_{total} of the main cases in this work. In the resistance test, N_{total} for coarse, medium, and fine grids = 0.32 M (million), 1.2 M, and 2.3 M without duct (T2015 case 1.1); 0.58 M, 1.5 M, and 4.0 M with the original duct (T2015 case 1.2). For the OPT, N_{total} = 4.9 M, 1.4 M, and 3.7 M. In the self-propulsion test with the original duct (T2015 case 1.6), N_{total} = 0.79 M, 2.1 M, and 5.2 M with the average $y+$ = 11.5 on the hull, 1.54 on the duct, and 4.42 on the propeller. Since there is no experiment for our optimal ducts, the grid sensitivity, i.e., only the verification of V and V, is analyzed in Section 3.6. The geometry difference between

two optimal ducts is subtle, so that their N_{total} are close to each other. For the resistance test, N_{total} = 0.55 M, 1.5 M, 3.9 M; 0.76 M, 2.1 M, 5.1 M for self-propulsion.



(**a**) (**b**)

Figure 6. Layered and surface grids (fine grid for self-propulsion simulation): (**a**) around the stern, propeller and duct; (**b**) on the bow.



(**a**) (**b**)

Figure 7. Grids around the open-water propeller (fine grid): (**a**) back surface; (**b**) y = 0 plane.

Table 2. Total grid number for T2015 cases.

	Case 1.1	**Case 1.2**	**OPT**	**Case 1.6**
Coarse grid	321,463	581,168	493,679	790,082
Medium grid	1,245,900	1,547,393	1,422,479	2,125,520
Fine grid	2,263,181	3,989,685	3,733,057	5,192,505

Table 3. Total grid number for optimal duct simulations.

	Resistance		**Self-Propulsion**	
	NACA 7908	**NACA 6.3914**	**NACA 7908**	**NACA 6.3914**
Coarse grid	551,138	551,677	765,272	763,202
Medium grid	1,481,464	1,488,405	2,071,378	2,073,981
Fine grid	3,886,754	3,886,754	5,073,662	5,083,935

3. Results

3.1. V and V (Verification and Validation)

The resistance, OPT, and self-propulsion simulations for the T2015 cases are verified and validated, as shown in Table 4. *CT*, *KT*, and *KQ* are the hull resistance with or without duct, propeller thrust, and torque coefficient. *D*, the experimental value, and its uncertainty, *Ud*, are provided by T2015 [1]. *Si* with *i* = 1, 2, 3 is the simulation value for the fine, medium, coarse grid. The error *E%D* is defined as

$$E\%D = (D - S1)/D \quad (1)$$

$$R_G = \varepsilon_{21}/\varepsilon_{32} = (S2 - S1)/(S3 - S2) \quad (2)$$

Table 4. V and V results.

	Case 1.1	**Case 1.2**	**OPT (*J* = 0.4)**		**Case 1.6**		
	1000*CT*	**1000*CT***	***KT***	***KQ***	**1000*CT***	***KT***	***KQ***
S1	4.3642	4.3272	0.2160	0.03079	5.0053	0.2375	0.02762
S2	4.4031	4.3989	0.2108	0.02976	5.0474	0.2344	0.02759
S3	4.6327	4.6671	0.2022	0.02870	5.5656	0.2131	0.02587
D	4.289	4.263	0.2214	0.02871	4.762	0.233	0.0295
ε_{21}	0.03884	0.07164	−0.0052	−0.0103	0.04211	−0.00313	−0.000023
ε_{32}	0.22967	0.26818	−0.0087	−0.0106	0.51815	−0.02132	−0.001727
R_G	0.16912	0.26713	0.5982	0.9679	0.08128	0.1471	0.01361
E%D	−1.76%	−1.51%	2.43%	−7.25%	−5.11%	−1.96%	6.37%
Ug	0.05562	0.05801	0.04351	135%	0.12496	0.09756	0.07219
Ud	1%	1%	Not provided	Not provided	1%	Not provided	Not provided
Ui	0.00046	0.00108	7.8×10^{-5}	6.01×10^{-5}	0.0026	0.0108	0.00738
Uv	5.6516%	5.8877%	4.4199%	135%	12.5385%	9.8163%	7.2567%

The grid convergence is estimated by Equation (2), in which $0 < R_G < 1$ indicates that the grid independence is verified for all cases with the monotonic convergence in Table 4. This means that, as the grid number increases, the difference between the results of two nearby grid sizes tends to decrease. Grid uncertainty *Ug* is evaluated by the V and V theory suggested in ITTC 75-03-01-01 [36]. The iterative uncertainty *Ui* is calculated by the difference between the maximal and minimal values of the *S1* iteration oscillation divided by the mean value of *S1*. Since all $Uv = \sqrt{Ug^2 + Ud^2 + Ui^2} > |E\%D|$, the validation is achieved conclusively. The fine grids are used in the following analysis.

The OPT experimental data of the JBC propeller are also provided by T2015 along with case 1.6 [1], but U_D is not provided, so assume $U_D = 0$ here. The OPT V and V analysis is only conducted for the advance coefficient *J* = 0.4 close to the value determined by the thrust identity method referring to the *KT* of case 1.6.

In Table 4, the K_T and *CT* errors are around 2%. The propeller behind the hull increasing the hull resistance also increases the over-predicted *CT* error to 5%. However, the K_Q error is larger (6~7%), and OPT U_V is more than 100% in particular. This is because the coarse grid (*S3*) results in a very small K_Q error, almost zero, but as the grid number increases, the error magnitude increases, i.e., deviates from the experimental data, and it turns from the over-prediction (*S3*, *S2*) to under-prediction (*S1*). In fact, ε_{21}~ε_{32}~−0.01 (almost zero) and R_G~1 provide insight into the K_Q being almost completely converged, i.e., the K_Q barely changes as the grid number increases.

For different J values, the OPT simulation result including K_T, K_Q, and propeller efficiency η are listed in Table 5 with the error against the experimental data. From the open water curves plotted in Figure 8, the experimental and numerical curves share a similar trend, and both point out the highest η at J = 0.65. Basically, the error appears the lowest, less than 2% at J = 0.45 for K_T, which is also a switch point from (lower J) over- to (higher J) under-prediction. On the contrary, all K_Q is over-predicted, and the error increases from about 6% to 30% as J increases. As also listed in Table 5, the average $y+$ increases, corresponding to a thicker boundary layer, as J increases. This implies that, on the propeller foil section, the lift is predicted well but poorly for the drag related to the wall function not suitable for propeller rotational flow in high J. All η errors are less than 10%, with an increasing trend following the J increment.

Table 5. OPT result.

J	K_T	$10K_Q$	η	*E%D of* K_T	*E%D of* $10K_Q$	*E%D of* η	Average $y+$
0.15	0.3023	0.3839	0.1880	2.87%	−5.78%	8.19%	4.98
0.25	0.2675	0.3526	0.3019	3.67%	−4.90%	8.17%	5.00
0.35	0.2337	0.3238	0.4020	3.01%	−6.28%	8.75%	5.03
0.4	0.2160	0.3078	0.4466	2.45%	−7.22%	9.02%	5.07
0.45	0.1975	0.2905	0.4869	1.74%	−8.32%	9.29%	5.12
0.55	0.1588	0.2506	0.5549	−0.72%	−10.83%	9.12%	5.23
0.65	0.1177	0.2072	0.5877	−5.85%	−16.59%	9.21%	5.32
0.75	0.0711	0.1571	0.5405	−15.86%	−28.36%	9.74%	5.42

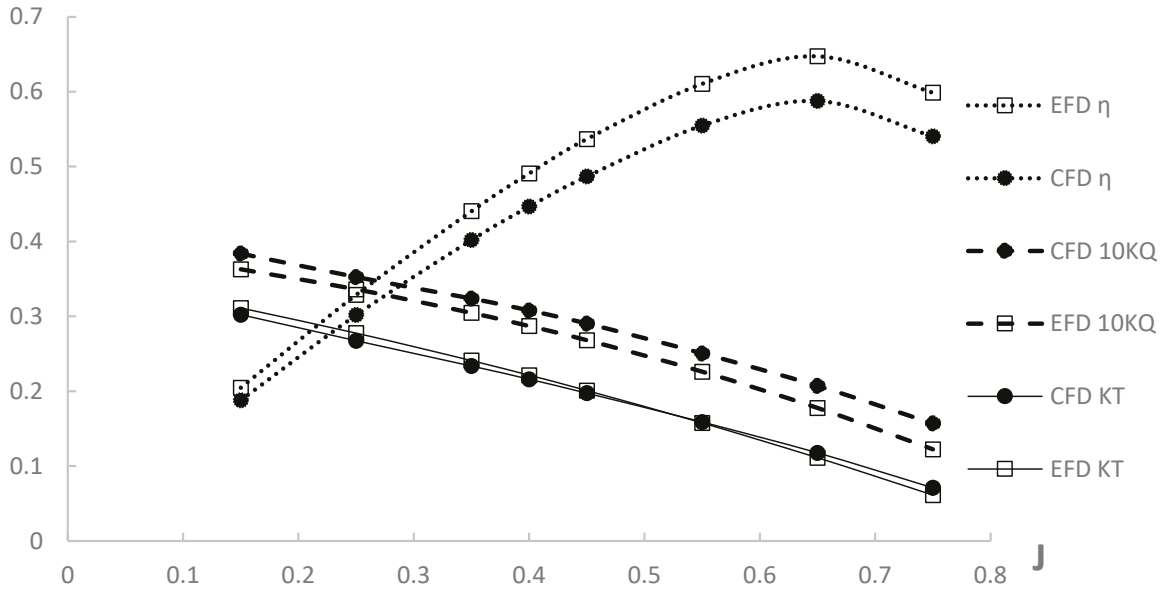


Figure 8. Propeller open water curves (EFD = Experimental Fluid Dynamics).

3.2. Duct Design by Resistance Test

The resistance reduction *Rd* is defined as:

$$Rd\ (\%) = \frac{1000CT_{with\ duct} - 4.3642}{4.3642} \times 100\%, \tag{3}$$

where 4.3642 is the *S1* value of case 1.1 in Table 4.

The foil section of the axisymmetric duct is designed by the NACA 4-digits series. The optimal AOA for NACA 4420 (the original section) was found to be 7.06 deg in [35] from 20.06 deg proposed by T2015 [1] for the original duct. Our AOA is defined from

the propeller shaft axis with the fixed foil trailing edge, i.e., the duct exit radius does not change. Thus, the 7.06 deg AOA is fixed in this study. In this design stage, the foil section is adjusted from NACA 4420 targeting the maximum *Rd*, i.e., minimum total resistance, and the optimization step follows as below:

1. Maximum camber, e.g., NACA m420 series. Test m = 1~9 and found NACA 6.320 and NACA7420 the best;
2. Location of the maximum camber. Test NACA6.3p20 and 7p20 with p = 1~9 and found p = 9 the best for both;
3. Maximum thickness. Test NACA 6.39xx with xx = 8~23 and 79xx with xx = 4~24.

Consequently, the NACA 6.3914 and 7908 are concluded as the optimal ducts. Compared to the original duct, both ducts provide 2.8% resistance reduction. Figure 9 shows the history of each optimization step. Figure 10 plots the geometry of the NACA 6.3914 and 7908 ducts, and compared their sections with the original duct. Next, the self-propulsion performance affected by both ducts will be analyzed and investigated.

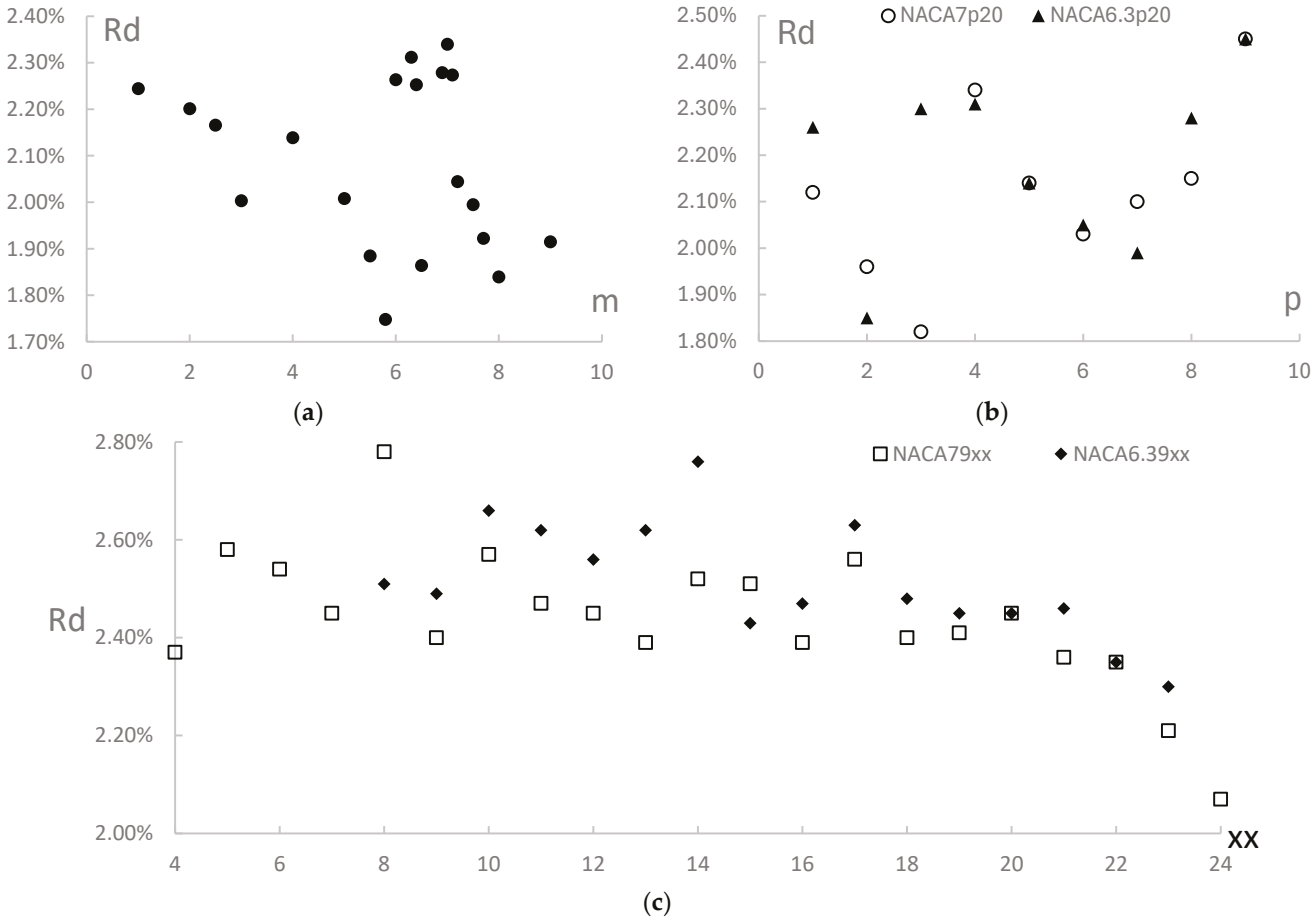


Figure 9. NACA 4-digits design for the duct section: (**a**) NACA m420 series; (**b**) NACA6.3p20 and 7p20; (**c**) NACA6.39xx and 79xx.

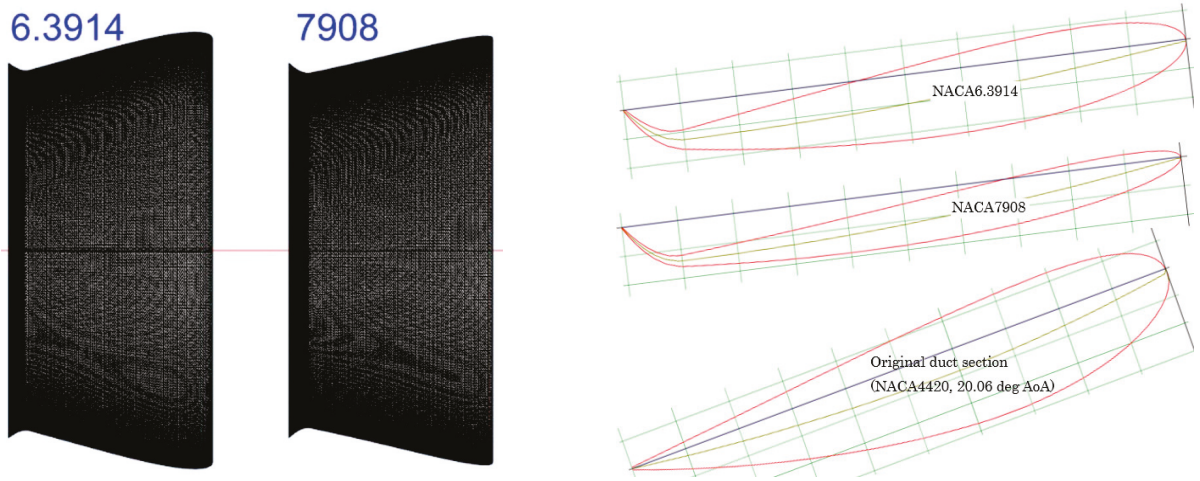


Figure 10. NACA6.3914 and NACA7908 ducts, and their sections compared with the original duct.

3.3. Self-Propulsion Simulation

For self-propulsion performance, the original duct result in Table 6 is computed from the case 1.6 *S1* result in Table 4. The propeller rotational rate n = 7.5 rps (revolution per sec) is provided by T2015 [1]. The self-propulsion point is searched for the NACA 6.3914 and 7908 ducts individually targeting the SFC (Skin Friction Correction) = 19.9551 N.

Table 6. CFD self-propulsion performance.

	Original Duct	NACA 7908 Duct	Diff. from Orig.	NACA 6.3914 Duct	Diff. from Orig.
n (rps)	7.5	7.62542	−1.67%	7.5735	−0.98%
$10KQ$	0.276	0.267604	3.12%	0.267699	3.08%
KT	0.238	0.223	6.30%	0.225	5.46%
$1000CT$	5.005	4.925	1.60%	4.918	1.74%
$1-w$	0.464	0.520	−12.07%	0.509	−9.70%
$1-t$	0.740	0.730	1.35%	0.732	1.08%
Va	0.546	0.614	−12.45%	0.600	−9.89%
EHP [1] (W)	19.754	18.911	4.27%	18.902	4.31%
DHP [2] (W)	25.194	25.654	−1.83%	25.143	0.20%
THP [3] (W)	12.379	13.479	−8.89%	13.144	−6.18%
η_H	1.596	1.403	12.09%	1.438	9.90%
η_o	0.449	0.487	−8.46%	0.481	−7.13%
η_D	0.784	0.737	5.99%	0.752	4.08%
η_R	1.094	1.079	1.37%	1.087	0.64%
η_B	0.491	0.525	−6.92%	0.523	−6.52%

[1] EHP = effective horsepower; [2] DHP = delivered horsepower; [3] THP = thrust horsepower.

When the resistance (R) including ship hull and stern duct, minus the propeller thrust (T), is approximately close to the SFC value, the ship self-propulsion point is achieved. The searching history of finding self-propulsion point is shown in Figure 11. The convergence trend is clear for NACA 7908 duct, instead the $R-T$ of NACA 6.3914 duct with more curvy and thicker section (see Figure 10) oscillates within a band of approximate 0.08N.

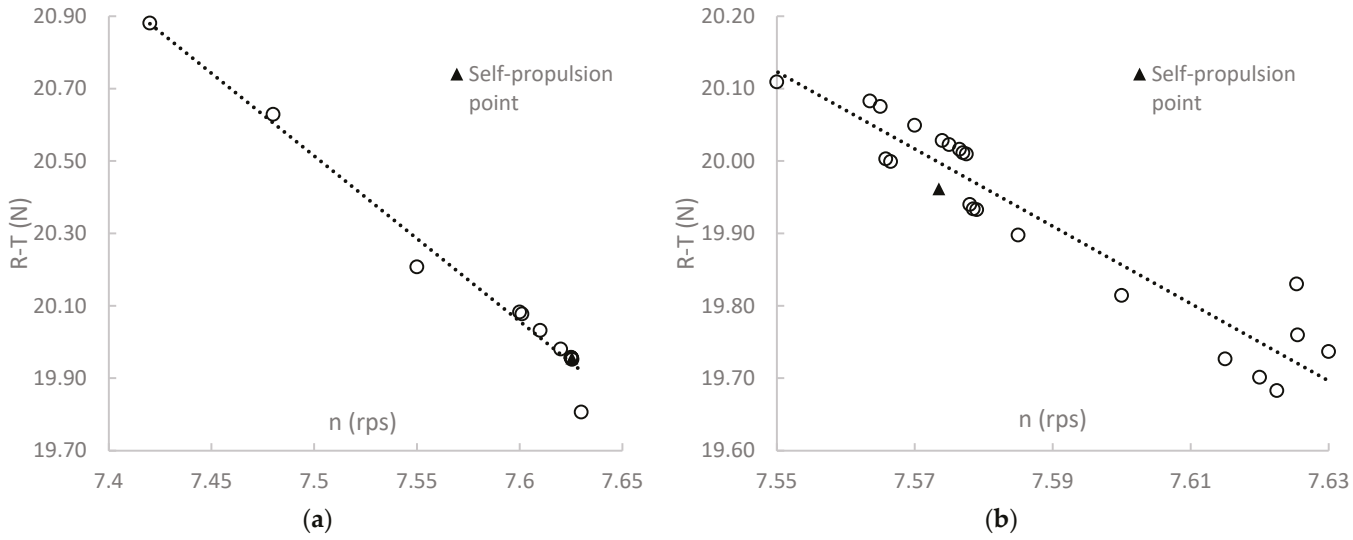


Figure 11. Self-propulsion point searching history: (**a**) NACA 7908 duct; (**b**) NACA6.3914.

The self-propulsion performance parameters in Table 6 are calculated based on the *KT* and *KQ* curves fitted from the OPT experimental data provided by T2015 [1]:

$$KT = -0.1633{*}{J_a}^2 - 0.2694 * J_a + 0.3553, \tag{4}$$

$$10KQ = -0.0956{*}{J_a}^3 - 0.1549{*}{J_a}^2 - 0.1947 * J_a + 0.3959, \tag{5}$$

where $J_a = U/(n{*}D)$ is the advance coefficient with propeller diameter D and n (rps).

In Table 6, the difference from the original duct is calculated as:

$$\text{Diff. from Orig. } (\%) = \frac{(\text{Orignal duct value}) - (\text{Optimal duct value})}{(\text{Orignal duct value})} \times 100\%. \tag{6}$$

Table 6 shows some and similar improvements for self-propulsion performance are provided by installing NACA 7908 and 6.3914. The hull resistance (*CT*) decreases by 1.6 and 1.7%. The propeller thrust coefficient decreases by 6 and 5% to reach a higher self-propulsion point near 7.6 rps (1% higher than 7.5 rps for the original duct). The 3% lower torque indicates the propeller rotates easier behind two ducts. In particular, the NACA 6.3914 requires slightly less delivered horsepower. Basically, the lower effective horsepower and higher thrust horsepower correspond to the lower hull resistance (*CT*) and higher propeller rps, respectively. The propeller behind-hull efficiency η_B increases by around 7%. Both ducts produce obvious flow acceleration, achieving around a 10% higher effective wake factor $(1-w)$ corresponding to faster propeller advance velocity *Va*.

The main efficiency improvement of the optimal ducts is propeller-related, such as η_B and η_o (open water efficiency). The hull efficiency η_H, quasi-propulsive efficiency η_D, relative rotative efficiency η_R, and thrust deduction factor $(1-t)$ are not improved. Since the ship hull and propeller geometry are not modified, the traditional ship propulsion efficiency definition might not be fair for an energy saving device [11].

3.4. Nominal and Propeller Wake Field

For nominal wake, Figure 12a,b show the large flow separation, i.e., u/U (non-dimensional axial flow velocity) < 0, behind the lower half part of the original duct presented in both experiments and our fine grid simulation. Figure 12c,d reveal that both optimal ducts effectively reduce the flow separation area. In fact, their u/U would not be less than 0 in this region, explaining the resistance reduction. Although both optimal

ducts provide the same resistance reduction (2.8%, see Section 3.2), their velocity profile patterns are slightly different. For the NACA 6.3914 duct, the width of the u/U = 0~0.1 region around (y/L_{PP}, z/L_{PP}) = ($\pm$0.0065, 0.008~0.014) is thinner in y direction, but a small branch of the u/U = 0.2~0.3 region extends from ($\pm$0.008, 0.013) to ($\pm$0.01, 0.015) which does not exist for the NACA 7908 duct. However, the small flow separation is caused behind the upper half of both ducts, i.e., the wake becomes slightly worse in this part of the flow field.

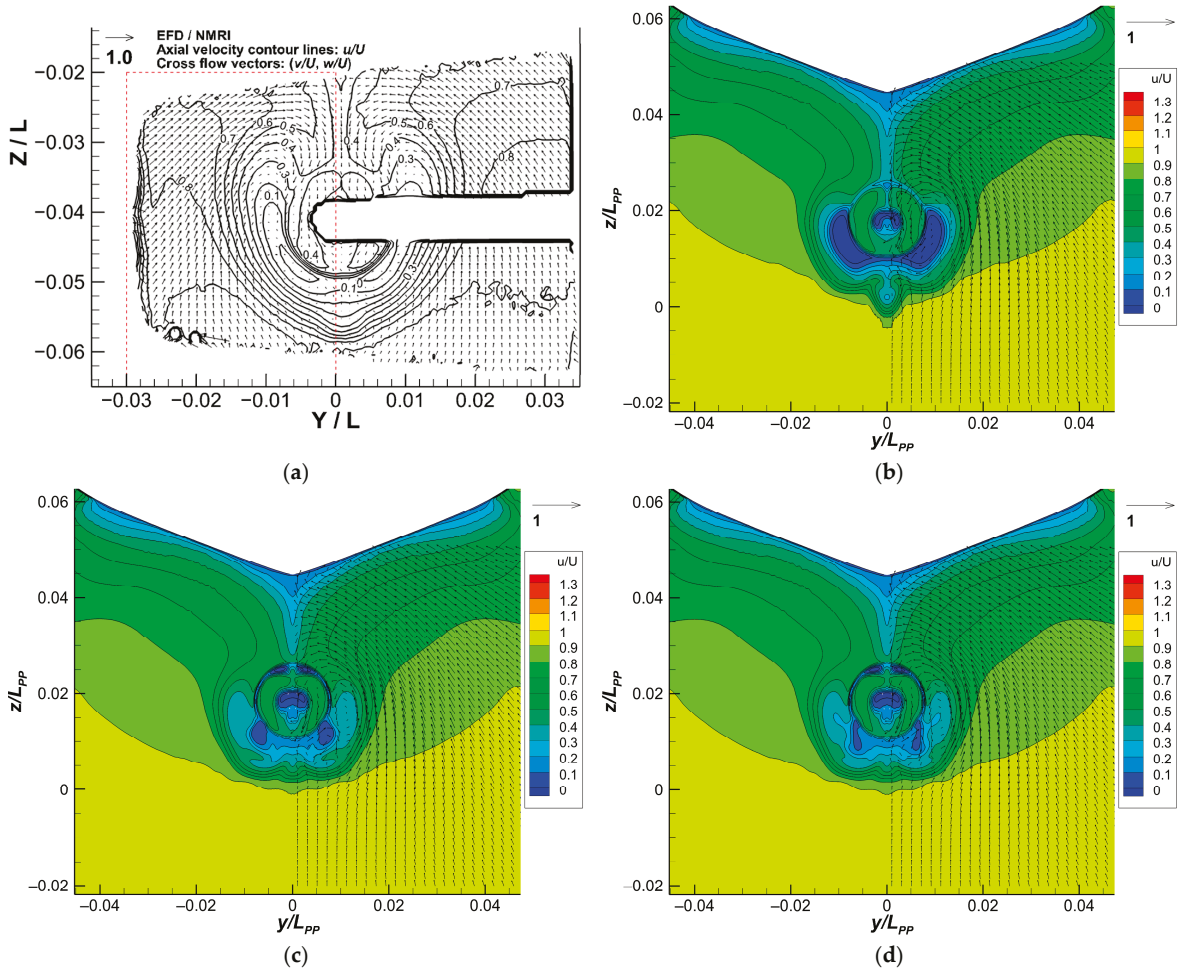


Figure 12. Nominal wake velocity field (u/U, v/U, w/U) at x/L_{pp} = 0.9843 (between duct and propeller): (**a**) experimental data [1] for the original duct; (**b**) original duct; (**c**) NACA7908 duct; (**d**) NACA6.3914 duct. The fine grid result (S1) is shown for the CFD results.

The high axial velocity ($u/U > 1.2$) distributed in the upper and starboard sides of the propeller wake behind the hull are measured by the experiment in Figure 13a and captured by our fine grid simulation in Figure 13b. The starboard portion corresponds to the interaction of the right rotating propeller and stern upward flow causing a higher relative velocity and leading to a higher propeller inflow velocity. The upper port side portion is induced by the right rotating propeller and bilge vortex downward flow, e.g., the vectors around (y/L, z/L) = (-0.006, -0.034) in Figure 12a. The larger area of the $u/U > 1.3$ distribution for CFD results corresponds to the over-predicted propeller KT (case 1.6 *S1* in Table 4). This reflects the ship's stern wake as not being well equalized or uniformed for the propeller inflow. By contrast, for the optimal ducts, a small portion of the $u/U > 1.2$ can be observed in Figure 13c,d in the port-side lower part of the propeller wake. In other words, the propeller loading, i.e., propeller wake distribution or output, is more circumferentially even. This confirms that the more uniform wake and better wake equalization are produced by the two optimal ducts. The lower torque in Table 6 also

supports this observation. Two ducts result in the slight difference here. For the NACA 6.3914 duct, the $u/U > 1.2$ is more scattered, e.g., (y/L_{PP}, z/L_{PP}) in the lower port side around (-0.05~-0.01, 0.015), and upper starboard side around (0.01, 0.02).

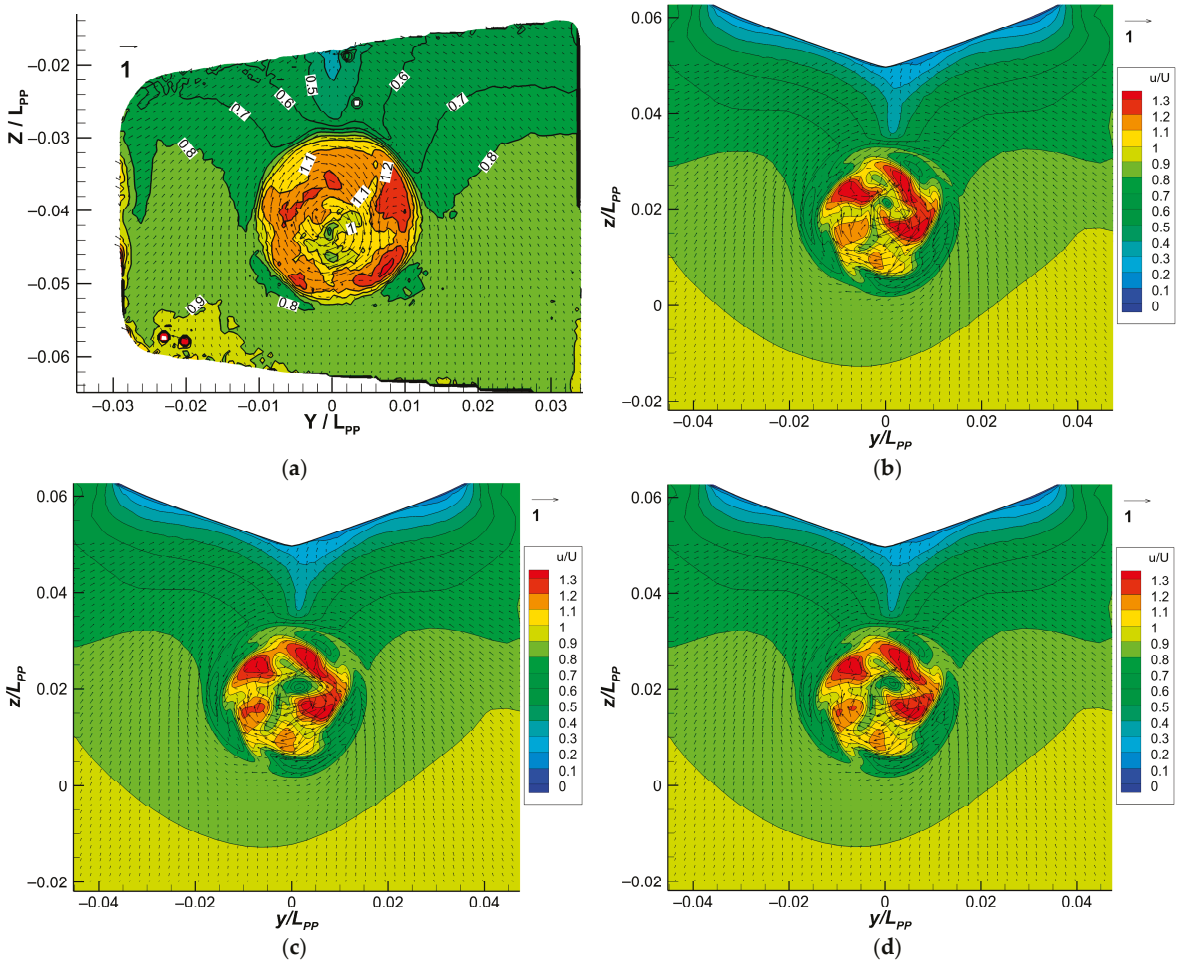


Figure 13. Axial velocity distribution (u/U) and cross flow vectors (v/U, w/U) of propeller wake behind the hull at ship AP (x/L_{pp} = 1.0): (**a**) experimental data [1] for the original duct; (**b**) original duct; (**c**) NACA 7908 duct; (**d**) NACA 6.3914 duct. The fine grid result (*S1*) is shown for the CFD results.

3.5. Pressure Coefficient Distribution

Figure 14 plots the pressure coefficient (C_P) distribution on the ship stern, propeller, and duct, including the original and two optimal ducts: the NACA7908 and 6.3914 ducts. The benefit of the optimal ducts for energy saving and propulsion performance is explored in detail in the figure. On the outer surface of the original duct (the pressure/back side), the low and negative C_P (in blue) occurs near the leading edge. The high and positive C_P (in red) appears near the leading edge of the inner surface of the original duct (the suction/face side). It turns out that the pressure difference on the original duct causes resistance, i.e., the resultant force pointing backward against the propeller's thrust direction or ship's advancing direction. Instead, on both optimal ducts, the high and positive C_P (in red) is located near the leading edge of the outer surface (the pressure/back side). Also, the low and negative C_P (in blue) is observed near the trailing edge of the inner surface (the suction/face side), i.e., the bending outward exit. As a result, the pressure difference on the optimal ducts yields the additional thrust. In other words, the foil lift contributes to a forward component.

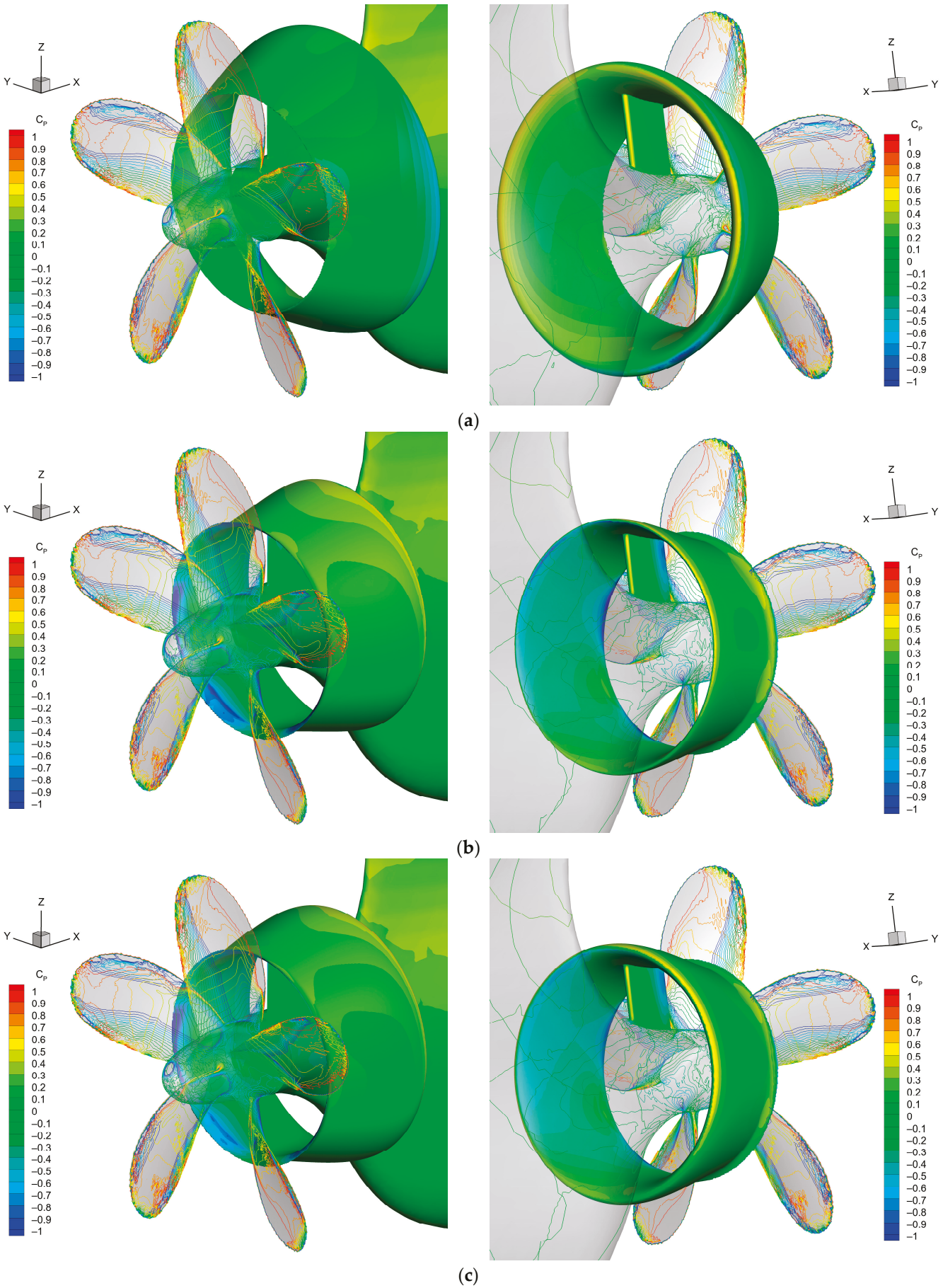


Figure 14. Pressure coefficient distribution on stern, duct, and propeller surface: (**a**) original duct; (**b**) NACA7908 duct; (**c**) NACA6.3914 duct. The fine grid result (S1) is shown here.

The propeller thrust is produced by the high and positive C_P (in red) on the propeller face and the low and negative C_P (in blue) on the propeller back.

Some sight deterioration of C_P is found locally for two optimal ducts in comparison of the original duct. The C_P around the trailing edge of the strut is negative and lower (in blue) for both optimal ducts, but for the original duct, the C_P is about zero (in green). The core of the low and negative C_P (in blue) on the propeller hub surface is larger for the NACA7908 duct.

3.6. Grid Sensitivity for Optimal Ducts

In this section, the grid sensitivity is examined since the experiment is unavailable currently for the optimal ducts. The fine grid result (*S1*) is assumed to be close enough to the experimental value in order to estimate the grid uncertainty, *Ug*. The results for the resistance and self-propulsion simulations are presented in Table 7. All R_G = 0~1 indicates the grid convergence is confirmed as monotonic convergence. Compared to the *Uv* of cases 1.1 and 1.6 in Section 3.1 (Table 4), the *Uv* values show the same level of uncertainty. For resistance simulation, *Uv* is 5~6%. In the self-propulsion simulation, *Uv* is 12~13% for the resistance, 8~10% for the propeller thrust, and 6~7% for the propeller torque.

Table 7. Grid sensitivity for the optimal ducts.

	NACA7908 Duct				**NACA6.3914 Duct**			
	Resistance Test	**Self-Propulsion Test (Propeller Rotational Rate = 7.5 rps)**			**Resistance Test**	**Self-Propulsion Test (Propeller Rotational Rate = 7.5 rps)**		
	1000*CT*	**1000*CT***	***KT***	***KQ***	**1000*CT***	**1000*CT***	***KT***	***KQ***
S1 = D *	4.2431	4.9098	0.2232	0.0265	4.2429	4.9193	0.2250	0.0266
S2	4.3130	4.9327	0.2192	0.0262	4.3083	4.9311	0.2191	0.0262
S3	4.5724	5.4231	0.1974	0.0243	4.5282	5.4413	0.1988	0.0244
ε_{21}	0.06993	0.04657	−0.00403	−0.00033	0.06535	0.01176	−0.00591	−0.00045
ε_{32}	0.25934	0.02284	−0.02183	−0.00189	0.21991	0.51024	−0.02028	−0.00174
R_G	0.26966	0.04657	0.18471	0.17502	0.29715	0.02305	0.29179	0.25990
Ug	0.05620	0.11907	0.10008	0.07425	0.04621	0.12667	0.08078	0.06089
Ui	0.00120	0.00173	0.00887	0.01054	0.00119	0.00142	0.00026	0.00025
Uv	5.6206%	11.905%	10.008%	7.425%	4.6211%	12.667%	8.078%	6.089%

* It is assumed, since the experiment is unavailable currently.

4. Discussion

The CFD method for resistance, open water propeller, and self-propulsion simulation is verified and validated in the presented work and then is extended to design the JBC's stern duct. The duct section is designed by using the NACA 4-digits foil series profile. The optimal duct with the NACA 7908 or 6.3914 sections is found with a 2.8% reduction for bare hull resistance. In the self-propulsion point, the propeller thrust decreases by 6 and 5% to achieve the 1.6 and 1.7% lower hull resistance. Eventually, the 7 and 6% higher propeller behind-hull efficiency and 10% higher effective wake factor are obtained. Both ducts achieve energy saving by decreasing effective horsepower by 4.3%. In other words, by installing one of the ducts, less power output is required to propel the ship in the design speed. Other than slightly less delivered power is required, the NACA 6.3914 duct also performs slightly better for the local flow field phenomena. Since the flow separation in the nominal wake is improved, the more uniform propeller wake is caused by the better wake equalization presenting a more uniform propeller inflow.

In the presented work, the stern duct was optimized for a particular ship model, JBC, in a calm water condition. Since the JBC is a bulk carrier, the optimal duct and design outcome might be only suitable for or recommended for a similar hull form, i.e., full hull form. For

slimmer ship types, e.g., container ships, the stern duct needs another optimization. Also, a ship sailing in the sea encounters waves and requires it to perform turning or zig-zags. In addition, the surface roughness of a ship's hull changes continuously along its service life due to fouling, corrosion, deformation, etc. However, a smooth surface is assumed in this study. Therefore, the seakeeping and maneuvering performance, and proper roughness of the ship with ESDs, should be considered and designed accordingly. The above-mentioned challenges and limitations are our future work.

Author Contributions: Conceptualization, P.-C.W.; methodology, P.-C.W.; software, Y.-C.W.; validation, T.-C.Y.; formal analysis, T.-C.Y.; investigation, T.-C.Y.; resources, P.-C.W.; data curation, Y.-C.W.; writing—original draft preparation, Y.-C.W.; writing—review and editing, T.-C.Y.; visualization, T.-C.Y.; supervision, P.-C.W.; project administration, P.-C.W.; funding acquisition, P.-C.W. All authors have read and agreed to the published version of the manuscript.

Funding: This research was funded by the National Science and Technology Council (NSTC) with the project [113-2221-E-006-196-].

Data Availability Statement: The original contributions presented in this study are included in the article. Further inquiries can be directed to the corresponding author(s).

Acknowledgments: The authors would like to thank the National Science and Technology Council (NSTC), for their support of the project [113-2221-E-006-196-]. It was thanks to the generous patronage of the NSTC that this study was smoothly performed.

Conflicts of Interest: The funders had no role in the design of the study; in the collection, analyses, or interpretation of data; in the writing of the manuscript; or in the decision to publish the results.

Abbreviations

The following abbreviations are used in this manuscript:

$1-t$	thrust deduction
$1-w$	wake factor
ANN	Artificial Neural Network
AOA	angle of attack
AP	Aft Particulars
BEM	Boundary Element Method
BSD	Blade efficiency improving Stator Duct
B_{WL}	waterline beam, ship beam
c	Foil chord length
CB	block coefficient
CFD	Computational Fluid Dynamics
C_P	Pressure coefficient
CT	Total ship resistance coefficient with or without duct
D	Propeller diameter, experimental value or data
DHP	delivered horsepower
DTC	Duisburg Test Case
D_{water}	Domain water depth
DWT	Deadweight Tonnage
$E\%D$	error
EHP	effective horsepower
EFD	Experimental Fluid Dynamics
ETS	Emissions Trading System
EU	European Union
FCFs	flow control fins
FP	Front Particulars
Fr	Froude number

H_{air}	Domain air par height
HZN	Hitachi Zosen Nozzle
IGES	Initial Graphics Exchange Specification
IHIMU	Ishikawajima-Harima Heavy Industries & Marine United Inc.
ITTC	International Towing Tank Conference
Ja	advance coefficient
JBC	Japan Bulk Carrier
k	turbulent kinematic energy
KQ	propeller torque coefficient
KT	propeller thrust coefficient
L, L_{PP}	length between particulars
$L_{downstram}$	Domain length after ship AP
L_{side}	Domain length to the side
$L_{upstram}$	Domain length before ship FP
m	Foil camber
MIDP	Mitsui Integrated Duct
MOGA	Multi-Objective Genetic Algorithm
MRF	Multi-Reference Frame
n	propeller rotation rate
NACA	National Advisory Committee for Aeronautics
N_G, N_{total}	total grid number
NSGA-II	Non-Dominating Sorting Genetic Algorithm-II
OpenFOAM	open-source field and manipulation
OPT	Openwater Propeller Test
p	static pressure, position of maximal camber
P/D	pitch ratio
p_0	total pressure
PIMPLE	PISO + SIMPLE
PISO	pressure implicit with splitting of operator
POD	proper orthogonal decomposition
PSD	pre-swirl ducts
PSS	pre-swirl stators
r	propeller radius
R	Ship resistance
RANS	Reynolds-averaged Navier–Stokes equations
r_D	duct radius
Re	Reynolds number
R_G	grid convergence indicator
rps	revolutions per sec
SBDO	Simulation-based design optimization
SDS-F	Semi-Duct System with contra-Fins
SFC	Skin Friction Correction
Si	simulation value for i = 1, 2, 3
SILD	Sumitomo Integrated Lammeren Duct
SIMPLE	semi-implicit method for pressure linked equations
SST	Shear Stress Transport
t	ship draft, foil thickness
T	Propeller Thrust
T2015	Tokyo 2015 Workshop on CFD in Ship Hydrodynamics
TEU	Twenty-foot Equivalent Unit (container size and cargo capacity)
THP	thrust horsepower
U	Model ship speed
u/U	Non-dimensional axial flow velocity
Ud	Experimental uncertainty
Ug	Grid uncertainty

Ui	Iterative uncertainty
Uv	Validation uncertainty
V and V	Verification and Validation
VOF	Volume of Fluid
WED	Wake Equalizing Duct
x	Longitudinal position
$y+$	non-dimensional wall distance
η, η_o	Efficiency, propeller open water efficiency
η_B	propeller behind-hull efficiency
η_D	quasi-propulsive, propeller propulsive efficiency
η_H	hull efficiency
η_R	relative rotative efficiency
μ_t	viscous turbulence
ω	Specific turbulent dissipation rate

References

1. JAPAN Bulk Carrier (JBC), Tokyo 2015 a Workshop on CFD in Ship Hydrodynamics. Available online: https://t2015.nmri.go.jp/jbc_gc.html (accessed on 28 February 2025).
2. Schneekluth Hydrodynamik GmbH. Available online: https://www.schneekluth.com/en/ (accessed on 4 April 2025).
3. Sanoyas Shipbuilding Co., Ltd. Available online: https://www.sanoyas.skdy.co.jp/technology (accessed on 4 April 2025).
4. Gougoulidis, G.; Vasileiadis, N. An Overview of Hydrodynamic Energy Efficiency Improvement Measures. In Proceedings of the 5th International Symposium on Ship Operations, Athens, Greece, 28–29 May 2015.
5. Lee, J.-T.; Kim, M.-C.; Suh, J.-C.; Kim, S.-H.; Choi, J.-K. Development of a preswirl stator-propeller system for improvement of propulsion efficiency: A symmetric stator propulsion system. *J. Soc. Nav. Archit. Korea* **1992**, *29*, 132–145.
6. Park, S.; Oh, G.; Rhee, S.H.; Koo, B.Y.; Lee, H. Full scale wake prediction of an energy saving device by using computational fluid dynamics. *Ocean Eng.* **2015**, *101*, 254–263. [CrossRef]
7. Guiard, T.; Leonard, S. The Becker Mewis Duct®-Challenges in Full-Scale Design and new Developments for Fast Ships. In Proceedings of the 3rd International Symposium on Marine Propulsors, Launceston, Australia, 5–8 May 2013.
8. Elangovan, M. Hydrodynamic Energy Devices to Improve the Efficiency of Propulsion System in AUVs. *Int. Res. J. Adv. Sci. Hub* **2020**, *2*, 18–22. [CrossRef]
9. Andersson, J.; Shiri, A.A.; Bensow, R.E.; Yixing, J.; Chengsheng, W.; Gengyao, Q.; Deng, G.; Queutey, P.; Xing-Kaeding, Y.; Horn, P.; et al. Ship-scale CFD benchmark study of a pre-swirl duct on KVLCC2. *Appl. Ocean Res.* **2022**, *123*, 103134. [CrossRef]
10. Falchi, M.; Aloisio, G. On the Effect of Energy Saving Devices on the Wake Hydrodynamics of a Bulk Carrier Model. In Proceedings of the Thirty-First International Ocean and Polar Engineering Conference, Rhodes, Greece, 20–25 June 2021.
11. Schuiling, B.; van Terwisga, T. Hydrodynamic working principles of Energy Saving Devices in ship propulsion systems. *Int. Shipbuild. Prog.* **2017**, *63*, 255–290. [CrossRef]
12. Narita, H.; Yagi, H.; Johnson, H.D.; Breves, L.R. Development and full scale experiences of a novel integrated duct propeller. *SNAME Trans.* **1981**, *89*, 319–346.
13. Kitazawa, T.; Hukino, M.; Fujimoto, T.; Ueda, K. Increase in the propulsive efficiency of a ship with the installation of a nozzle immediately forward of the propeller. *J. Kansai Soc. Nav. Archit. Jpn.* **1982**, *184*, 73–78.
14. Schneekluth, H. Wake equalizing duct. *Nav. Archit.* **1986**, *103*, 147–150.
15. Sasaki, N.; Aono, T. Energy saving device "SILD". *J. Shipbuild. Jpn.* **1997**, *45*, 47–50.
16. Inukai, Y.; Itabashi, M.; Sudo, Y.; Takeda, T.; Ochi, F. Energy saving device for ship IHIMU semicircular duct. *IHI Eng. Rev.* **2007**, *40*, 59–63.
17. Mewis, F. A novel power saving device for full form vessels. In Proceedings of the First International Symposium on Marine Propulsors (SMP'09), Trondheim, Norway, 22–24 June 2009.
18. Energy-Saving Technology. Available online: https://global.kawasaki.com/en/mobility/marine/technology/energy_saving.html (accessed on 28 February 2025).
19. Schuiling, B. The design and numerical demonstration of a new energy saving device. In Proceedings of the 16th Numerical Towing Tank Symposium (NUTTS 2013), Mulheim, Germany, 2–4 September 2013.
20. Menter, F.; Kuntz, M.; Langtry, R. Ten years of industrial experience with the SST turbulence model, in: Turbulence, Heat and Mass Transfer. In Proceedings of the 4th International Symposium on Turbulence, Heat and Mass Transfer, Antalya, Turkey, 12–17 October 2003; pp. 625–632.

21. Nicorelli, G.; Villa, D.; Gaggero, S. Pre-swirl ducts, pre-swirl fins and wake-equalizing ducts for the DTC hull: Design and scale effects. *J. Mar. Sci. Eng.* **2023**, *11*, 1032. [CrossRef]
22. Sakamoto, N.; Kawanami, Y.; Hinatsu, M.; Uto, S. Viscous CFD analysis of stern duct installed on panamax bulk carrier in model and full scale. In Proceedings of the 15th International Conference on Computer and IT Applications in the Maritime Industries, Lecce, Italy, 9–11 May 2016.
23. Tahara, Y.; Peri, D.; Campana, E.F.; Stern, F. Computational fluid dynamics-based multiobjective optimization of a surface combatant using a global optimization method. *J. Mar. Sci. Technol.* **2008**, *13*, 95–116. [CrossRef]
24. Tahara, Y.; Norisada, K.; Yamane, M.; Takai, T. Development and demonstration of CAD/CFD/optimizer integrated simulation-based design framework by using high-fidelity viscous free-surface RANS equation solver. *J. Jpn. Soc. Nav. Archit. Ocean Eng.* **2008**, *7*, 171–184. [CrossRef]
25. Lee, M.-K.; Lee, I. Optimal Design of Flow Control Fins for a Small Container Ship Based on Machine Learning. *J. Mar. Sci. Eng.* **2023**, *11*, 1149. [CrossRef]
26. Diez, M.; Serani, A.; Campana, E.F.; Goren, O.; Sarioz, K.; Danisman, D.B.; Grigoropoulos, G.; Aloniati, E.; Visonneau, M.; Queutey, P.; et al. Multi-objective hydrodynamic optimization of the DTMB 5415 for resistance and seakeeping. In Proceedings of the 13th International Conference on Fast Sea Transportation (FAST 2015), Washington, DC, USA, 1–4 September 2015.
27. Grigoropoulos, G.; Campana, E.; Diez, M.; Serani, A.; Goren, O.; Sariöz, K.; Danisman, D.B.; Visonneau, M.; Queutey, P.; Abdel-Maksoud, M.; et al. Mission-based hull-form and propeller optimization of a transom stern destroyer for best performance in the sea environment. In Proceedings of the VII International Conference on Computational Methods in Marine Engineering (MARINE2017), Nantes, France, 15–17 May 2017.
28. Guo, J.; Zhang, Y.; Chen, Z.; Feng, Y. CFD-based multi-objective optimization of a waterjet-propelled trimaran. *Ocean Eng.* **2020**, *195*, 106755. [CrossRef]
29. Wie, D.-E.; Kim, D.-J. The Design Optimization of a Flow Control Fin Using CFD. *J. Soc. Nav. Archit. Korea* **2012**, *49*, 174–181. [CrossRef]
30. Vesting, F.; Bensow, R. Propeller Optimisation Considering Sheet Cavitation and Hull Interaction. In Proceedings of the Second International Symposium on Marine Propulsors (SMP'11), Hamburg, Germany, 15–17 June 2011.
31. Vázquez-Santos, A.; Camacho-Zamora, N.; Hernández-Hernández, J.; Herrera-May, A.L.; Santos-Cortes, L.d.C.; Tejeda-del-Cueto, M.E. Numerical Analysis and Validation of an Optimized B-Series Marine Propeller Based on NSGA-II Constrained by Cavitation. *J. Mar. Sci. Eng.* **2024**, *12*, 205. [CrossRef]
32. Zhai, S.; Jin, S.; Chen, J.; Liu, Z.; Song, X. CFD-based multi-objective optimization of the duct for a rim-driven thruster. *Ocean Eng.* **2022**, *264*, 112467. [CrossRef]
33. Nguyen, V.T.; Chandar, D. Ship specific optimization of pre-duct energy saving devices using reduced order models. *Appl. Ocean Res.* **2023**, *131*, 103449. [CrossRef]
34. Furcas, F.; Vernengo, G.; Villa, D.; Gaggero, S. Design of wake equalizing ducts using RANSE-based SBDO. *Appl. Ocean Res.* **2020**, *97*, 102087. [CrossRef]
35. Wu, P.-C.; Chang, C.-W.; Huang, Y.-C. Design of Energy-Saving Duct for JBC to Reduce Ship Resistance by CFD Method. *Energies* **2022**, *15*, 6484. [CrossRef]
36. ITTC Recommended Procedures and Guidelines 7.5-03-01-01: Uncertainty Analysis in CFD Verification and Validation Methodology and Procedures. Available online: https://ittc.info/media/4184/75-03-01-01.pdf (accessed on 20 September 2008).
37. Rusche, H. Computational Fluid Dynamics of Dispersed Two-Phase Flows at High Phase Fractions. Ph.D. Thesis, Imperial College London, London, UK, 2002.
38. Holzmann, T. The numerical algorithms: SIMPLE, PISO and PIMPLE. In *Mathematics, Numerics, Derivations and OpenFOAM®*; Holzmann CFD: Loeben, Germany, 2006; pp. 93–121.

Disclaimer/Publisher's Note: The statements, opinions and data contained in all publications are solely those of the individual author(s) and contributor(s) and not of MDPI and/or the editor(s). MDPI and/or the editor(s) disclaim responsibility for any injury to people or property resulting from any ideas, methods, instructions or products referred to in the content.

inventions

MDPI

Article

Results on the Use of an Original Burner for Reducing the Three-Way Catalyst Light-Off Time

Adrian Clenci [1,*], Bogdan Cioc [1], Julien Berquez [2], Victor Iorga-Simăn [1], Robert Stoica [1] and Rodica Niculescu [1]

[1] National University of Science and Technology POLITEHNICA Bucharest, Pitești University Centre, 110040 Pitești, Romania; bogdan.cioc@upit.ro (B.C.); victor.iorga@upit.ro (V.I.-S.); robert.stoica@upit.ro (R.S.); rodica.niculescu@upit.ro (R.N.)

[2] Horse Romania, 115400 Mioveni, Romania; julien-michel-roger.berquez@renault.com

* Correspondence: adrian.clenci@upb.ro

Abstract: Individual road mobility comes with two major challenges: greenhouse gas emissions related to global warming and chemical pollution. For the pollution reduction in the spark ignition engine vehicle, the standard and reliable aftertreatment technology is the three-way catalytic converter (TWC). However, the TWC starts to convert once an optimal temperature, usually known as the light-off temperature, is reached. There are many methods to reduce the warm-up period of the TWC, among which is using a burner. The initial question underlying this study was to see if the use of a relatively straightforward extra-combustion device mounted upstream the TWC, without complex elements, was able to serve the purpose of reducing the light-off time. Consequently, an original burner was designed and investigated numerically via the CFD method and experimentally via measurements of the temperature evolution within a TWC, along with the emissions specific to the burner's operation. The main findings of this study are: (1) the CFD-based examination is a good way to decide on how to achieve the so-called fit-for-purpose internal aerodynamics of the burner (i.e., to obtain a homogeneous mixture) and (2) to reach the light-off temperature, conventionally taken as 500 K, the burner was operated for 5.2 s, i.e., 3.6 g of gasoline injected, 2.7 g of CO_2 and 1.351 g of CO, respectively, emitted. Moreover, this study identified measures for improving the burner's design as well as an enhanced procedure for the burner's operating control both aiming to produce a cleaner combustion during the TWC pre-heating.

Keywords: pollution reduction; three-way catalyst; light-off; burner; CFD

1. Introduction

Individual road mobility is paramount for human society. The passenger car became not only a means of ensuring door-to-door mobility, but also the very expression of the freedom of movement, hence its importance. However, the passenger car is also one of the major contributors to environmental degradation, as is well known. Pollution (unburnt hydrocarbon—UHC, carbon monoxide—CO, nitrogen oxides—NO_x, particulate matter—PM) and carbon dioxide (CO_2), emitted by their internal combustion (IC) engines, have become a growing global concern. A solution to this problem was to replace the thermal propulsion ensured by the IC engine with the electric propulsion ensured by the battery electric vehicles (BEVs). Some parts of the world even issued regulations to favor BEVs, as is the case in Europe—for instance, see the Green Deal's Fit-for-55 package, which "makes reaching the EU's climate goal of reducing EU emission by at least 55% by 2030 a legal obligation" [1]. This regulation also sets a target of 100% carbon emission reduction for 2035, meaning that "all new cars and vans placed on the market in the EU from 2035 should be zero-emission vehicles (ZEV)" [2], based on a tank-to-wheel approach, which also means BEVs. Nonetheless, the worldwide electrification of individual road mobility via BEVs is challenging and will not happen overnight. Thus, for the time being, the internal

combustion (IC) engine will continue to be used worldwide for individual road mobility either as standalone powerplants (ICEV—internal combustion engine vehicle) or as part of hybrid electric vehicles (HEVs). Obviously, the discussions are about the IC engine as a solution for sustainable road mobility, and consequently the IC engine should be as efficient and as ecologic as possible—an engine with "zero impact emissions", as defined in [3,4]: (1) its pollutants are reduced to such a low level that it does not have a negative impact on air quality anymore and (2) its net CO_2 emissions are zero (all local CO_2 are compensated by CO_2 capture elsewhere). To address this environmental challenge related to the ICEV, researchers are expected to develop even more efficient and cleaner technologies.

For the pollution reduction in the spark ignition engine vehicle (SIEV), the classic and reliable aftertreatment technology is the closed loop controlled three-way catalytic converter (*TWC*), which uses noble metal catalysts such as platinum (Pt), palladium (Pd) and rhodium (Rh) to facilitate the conversion of the aforementioned pollutants into harmless substances, such as CO_2, H_2O, N_2 and O_2. The conversion efficiency or the effectiveness of the catalytic converters for a given pollutant (x) is shown below:

$$\eta_{TWC_x} = 1 - \frac{Exhaust\_out_x}{Engine\_out_x}, \tag{1}$$

where x may be any of the regulated gaseous pollutants, e.g., UHC, CO, NO, NO_2; *Exhaust_out* and *Engine_out* are the pollutants at the tailpipe and produced by the engine (i.e., downstream and upstream the catalytic converter).

There are many studies focusing on the main parameters influencing the effectiveness of the catalytic converters [5–9]: oxygen storage capacity (OSC) of the converter (i.e., adsorption and release of oxygen from the converter's wash coat), air–fuel ratio (AFR), and catalyst temperature (T_{TWC}) as the bulk temperature of the converter's monolith. On this theme, the authors of papers [6,7] agreed that OSC is "not prevalent during the warm-up" and, consequently T_{TWC} and AFR would be the main factors to influence conversion efficiency. Hence, as discussed in [5], the effectiveness of the catalytic converter for a given pollutant (x) is the product of two efficiencies, as shown below:

$$\eta_{TWC_x} = \eta_{TWC_x}(AFR) \cdot \eta_{TWC_x}(T_{TWC}) \tag{2}$$

According to [7], both efficiencies introduced in relation (2) can be modelled with Wiebe mathematical functions, typically known as S-shaped curves.

The thermal behavior of the catalytic converter is well described in the paper [5], which is actually based on the papers [6,7]:

- Forced convection between the exhaust gas and the monolith, $\dot{Q}_{gas\_in}$,
- Forced convection between the converter's outer wall and the ambient air, $\dot{Q}_{out}$, and
- Exothermic and endothermic catalytic reactions to convert the pollutants, $\dot{Q}_{reaction}$.

So, during the TWC warm-up, Equation (3) gives the rate of T_{TWC}:

$$\dot{T}_{TWC} = \frac{\left(\dot{Q}_{gas\_in} + \dot{Q}_{reaction} - \dot{Q}_{out}\right)}{m_{TWC} \cdot C_p} \tag{3}$$

where $\dot{Q}$ [W] designates rates of heat flow, m_{TWC} [kg] is the TWC mass, and C_p [J/kg] is the TWC heat capacity at constant pressure.

However, the TWC starts to convert once an optimal operating temperature is reached. This is widely known as the light-off temperature, which based on the considerations presented above, varies with the gaseous pollutants. In the literature, most frequently, this temperature is referred to in a generic way, as the temperature corresponding to a catalyst effectiveness of 50% (T50); this temperature would be approximately 500 K, according to [5,10–14]. Obviously, one may consider any conversion efficiency for this light-off

temperature, e.g., T90, meaning the temperature at which 90% conversion is reached for any chemical species, as used in paper [15], which, among other findings, shows that T90 for CO is nearly insensitive to lambda (i.e., AFR made dimensionless by stoichiometric conditions) between 0.977 and 1.005, while "T90 for NO is constant for lambda inferior to 0.995 but increases by more than 200 °C for lambda values between 0.995 and 1.001, and 90% conversion is not achieved at any temperature for lambda higher than 1.001".

The above considerations convey the idea that the main problem with the TWC is the warm-up phase, i.e., the period after the engine's cold start, until the TWC reaches this temperature threshold called light-off. It is therefore vital to have the TWC light off as quickly as possible and this is harder as the ambient temperature decreases. This problem has been well known from the beginning of the pollution reduction via the TWC and, consequently various measures are used to address it, some of them already introduced in mass production.

Back in 1994, paper [12] argued that although TWC "has already achieved a high level of development, further improvements are still required in order to reliably fulfil the future standards". At present, this statement is still valid, especially because of the extreme tightening of the automotive pollution regulation. For instance, the objective of the future Euro7, as declared in the papers [4,16,17], is to be able to label the IC engine "zero impact emissions" to avoid banning it out of the European cities. Among the improvements proposed in [12], one may also find measures to reduce the warm-up period of the TWC:

- Thermally insulated exhaust pipes (not currently used in mass production).
- Converters installed as near to the engine as possible (today, this is called closed-coupled TWC and it is used in mass production).
- Injection of air upstream the TWC relying on fuel post-oxidation (this was and is still used in some mass production applications).
- Electrically heated catalytic converter, EHC (nowadays, it seems to be a potential solution for the HEV considering the frequent stop-and-start sequences of the IC engine and especially the on-board source of electricity; however, the reliability of the electrical metallic structure of the heated disc, which is in continuous contact with very hot exhaust gas from the IC engine is a potential blocking point).
- Fuel afterburner chamber and burner (the last two never entered the production phase).

Fuel post-oxidation benefits in terms of light-off time were assessed by a CFD investigation in paper [18]. The authors explored the effects of air injection into the exhaust on the light-off time, while each cylinder was operated with rich mixture, showing that "the observed temperature increase is obtained at the expenses of about 10% in terms of fuel consumption". The increased fuel consumption while using air injection for the enhancement of fuel post-oxidation generated by the engine operation in the rich mode was also reported in paper [19].

According to Langen et al. [12], the difference between the "fuel afterburner chamber" and the "burner" is that the former is burning fuel coming out from the engine, which has to be ran richer (hence, the term after-burner), while the latter has its own fuel supply. Obviously, both require an ignition source and a blower/air pump to provide the oxygen supply. Chan et al. [13] listed the same measures aiming to expedite the reaching of light-off temperature but discussed the solutions generated by different strategies used while calibrating the engine.

Returning to the heating time of the TWC, as discussed in [4], complying with Euro7 may require having the TWC already heated up even before the IC engine starts (i.e., pre-heating). If so, the only solutions able to provide this standard are burner technology and EHC, the latter, however, being reserved for the HEV (due to the need for sufficient onboard electric power, e.g., 2.0 kW, 4.0 kW or even 8.6 kW, coupled with a 45 kg/h mass air flow rate, as explored in [20]).

As regards the burner technology for TWCs, as already mentioned, it is not a new idea. Nonetheless, further to our literature survey, this technology is mainly cited in SAE papers from the 1990s, e.g., [12,21,22]. In more recent years, in the main scientific stream,

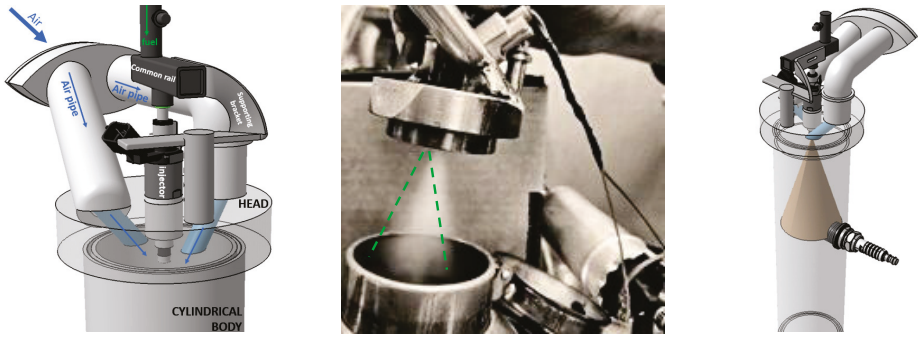
this solution is rather mentioned in review papers, such as [10], which do not provide many details about it and also quote SAE papers from the 1990s. Our extensive search on this particular subject revealed two recent papers [23,24] dealing with the numerical assessment of an aftertreatment system equipped with a burner, another article [4] presenting, among other details, clear results of using a so-called "additional fuel burner" in the attempt to achieve the "zero-impact emissions" engine and only one work [25] dedicated to a burner development for light-off speed-up of an aftertreatment system in gasoline engine (like the older paper [21]).

This paper also focuses on presenting an original burner designed to reduce the TWC light-off time. Previously, as presented in [26], our focus was on experimentally investigating the effect of a burner on the light-off performance of a TWC by using a retrofitted commercial Webasto^{TM} water heater to warm the vehicle cabin, to de-ice the vehicle windows and to pre-heat water-cooled vehicle engines. The findings of this research were valid; however, the retrofitted heater was not able to heat-up the pre-catalyst in reasonable time because of the insufficient air mass flow ensured by the heater's fan. Consequently, the original burner presented in this paper was designed to ensure a sufficient air mass flow and thus, a rapid heat-up of the pre-catalytic converter, in order to ensure a high aftertreatment effectiveness once the SI engine is turned on, without using the different penalizing strategies used while calibrating the engine (i.e., spark retardation, lambda-split or mixture leaning, etc., as presented in [13]). More precisely, the scope of this work was to develop an original extra-combustion device mounted upstream the TWC (i.e., a burner) characterized by the so-called fit-for-purpose internal aerodynamics able to quickly generate a homogeneous and ignitable mixture only relying on a simple design not using relatively complex elements imported from the aeronautical burner application, such as the ones presented in paper [25].

Accordingly, the remainder of this paper is structured as follows: first, the design of the burner's combustion chamber is presented, with a description of the internal aerodynamics of the burner based on CFD results; then, the investigation of the burner's operation, i.e., (1) the burner's control oriented to quickly achieve an ignitable mixture in the combustion chamber and (2) measurements of the temperature evolution within a two-part TWC (a smaller pre-catalytic converter and a main catalytic converter), along with the emissions specific to the burner's operation.

2. Burner Design and CFD Investigation

As mentioned before, when designing the burner's combustion chamber the focus was on how to obtain a homogeneous and ignitable mixture mainly relying on the airstream inside the burner's body. As shown in Figure 1a, the burner comprises two parts, which are welded together: (1) the head containing the injector with its fueling parts, two air pipes with their corresponding ducts through the head and (2) the body, which has a constant cylindrical section (purely for reasons of simplicity).



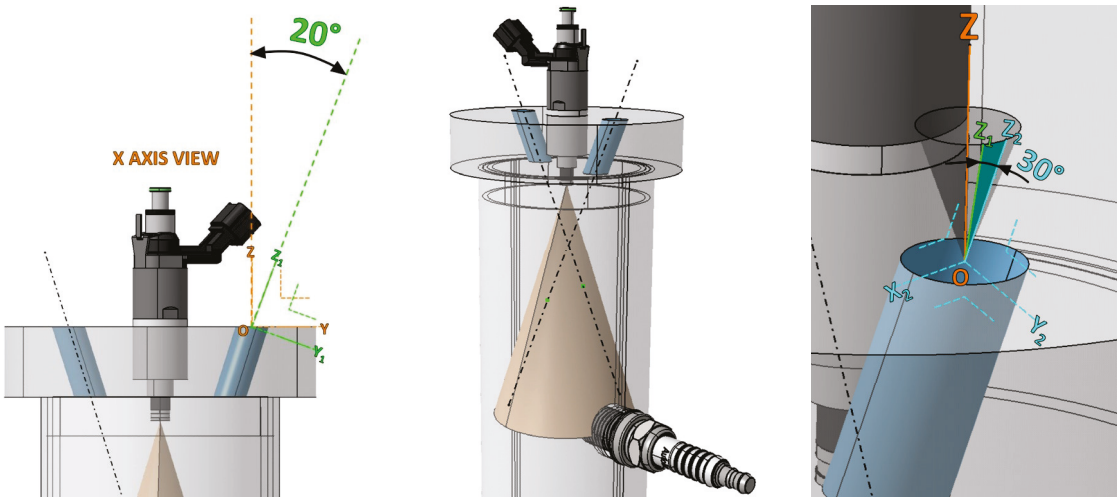
(**a**) (**b**) (**c**)

Figure 1. Burner's design: (**a**) main parts; (**b**) cone angle of injected fuel from the experiment; (**c**) positioning of the spark plug.

As seen in Figure 1c, the positioning of the spark plug was set based on the experimentally estimated cone angle of the injected fuel (34°—see the green dashed line in Figure 1b); thus, its vertical location on the cylindrical body was decided to be right where this cone touches the inner cylindrical surface. The hypothesis is that it is in this way that the flame occurrence is maximized. Evidently, the experimentally estimated injected fuel cone was necessary since the technical specifications of the injector were not provided by its manufacturer.

In order to obtain a homogeneous mixture, as mentioned before, the focus was on how to achieve the so-called fit-for-purpose internal aerodynamics.

Thus, the directions of the two ducts through the burner's head were designed, first, to conveniently intersect the injected fuel cone (see the arbitrary 20° angle in Figure 2a and, hence the two green dots in Figure 2b, which are the intersection points) and, second, to generate an air swirl motion (i.e., a rotation of the air around a vertical axis—see the arbitrary 30° angle in Figure 2c). On the latter, as there are two ducts through the head, two swirls were planned, both in the same direction, one following the other.



(**a**) (**b**) (**c**)

Figure 2. Burner's initial design for homogeneous mixture: (**a**) ducts inclination to achieve air intersection with the fuel cone; (**b**) intersection between air and fuel cone; (**c**) ducts inclination to achieve the swirl motions.

This is the first design iteration and the physical prototype was manufactured as such (see Section 3). Furthermore, to draw conclusions regarding the aerodynamics inside the burner, generated by the design explained above, a CFD simulation was performed.

The CFD simulation is ran in AVL FIRE^{TM} 2022 R1 software (Graz, Austria), which is based on the finite volume approach and is a 3D RANS-based (Reynolds-average Navier–Stokes) cold simulation of the air flow at 40 kg/h (boundary condition imposed at the inlet faces of the two air ducts) for 5 s with a time step of 0.05 s, using the *k*-ζ-*f* model. According to [27,28], this turbulence model produces reasonable results with good accuracy in resolving the dominant structures of the turbulent flow and gives a better prediction of flow separation and reattachment. The simulation is called cold because the burner is not fired.

The selection of the mesh size is the result of several simulations aiming to achieve the independence of the numerical solution with respect to the grid. Subsequently, to analyze the influence of the mesh/grid on the numerical solution, different values for the maximum cell size were used (0.7, 0.8, 0.9, 1.0 mm). Evidently, the finer the mesh, the higher the computational time. Table 1 shows the values of some physical parameters, calculated after the 5 s of simulation with a step of 0.05 s, as well as the CPU time specific to the workstation used (2.3 GHz, Intel Xeon 36 cores, 128 GB RAM).

Table 1. Influence of the mesh on the numerical solution for the *k-ζ-f* turbulence model.

Max. Cell Size [mm]	1.0	0.9	0.8	0.7
Number of cells	2,486,864	4,904,501	7,091,093	8,978,120
Simulation time [hours]	5.60	12.40	17.40	18.95
Number of CPU cores	20	10	11	34
Mean TKE [m^2/s^2] @ 5s	30.5	32.3	34.3	36.4
Max. 2D flow velocity [m/s] @ 5s	133.5	134.5	136.2	136.9
Mean 2D flow velocity [m/s] @ 5s	12.9	13.0	12.9	12.5

Since at this stage, the focus was mainly on predicting the large-scale air structures and because decreasing the maximum cell size from 1.0 to 0.7 did not result in significant changes in these structures, Figure 3, the maximum cell size used for this CFD RANS-based study was 0.7 mm.

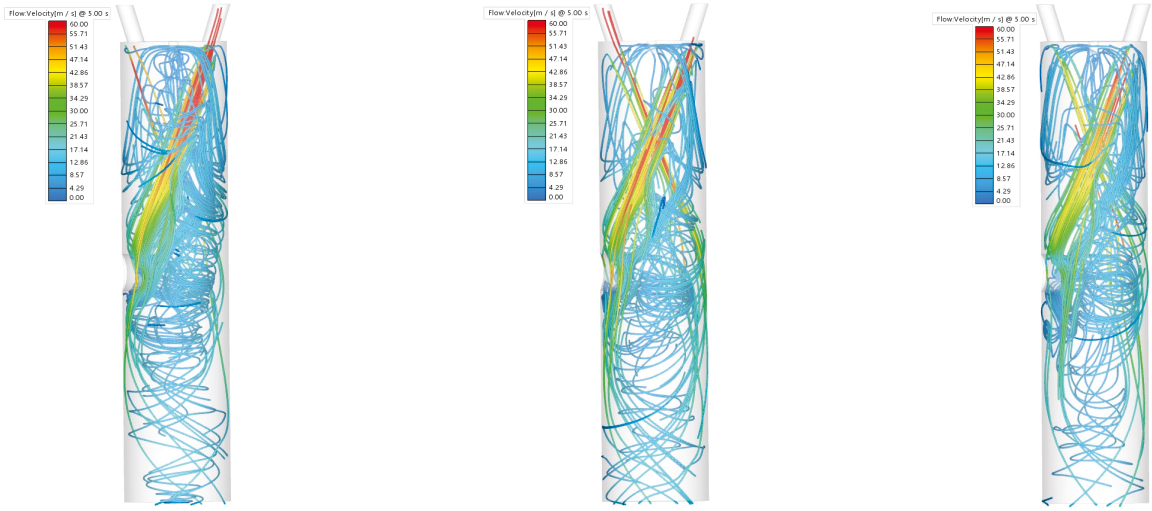


Figure 3. Burner's internal aerodynamics at 5s via the *k-ζ-f* model: (**a**) max. cell size: 0.9; (**b**) max. cell size: 0.8; (**c**) max. cell size: 0.7. NB. Spark plug location is visible at the left.

Choosing a suitable turbulence model is always a challenging task for the scientific community. As per [29], the scientific community argued that most turbulence models are validated for specific well-defined test cases, but it is not certain whether they are also valid for other type of flows generated by complex geometries where the flow might be different. In terms of the turbulence models that can be used with the RANS approach, each has advantages and disadvantages. For instance, according to [30], the *k-ε* model is "relatively simple to implement, leads to stable calculations that converge relatively easily and makes reasonable predictions for many flows, but is valid just for fully turbulent flows, and predicts the swirling and rotating flows rather poorly".

Based on the above considerations, another simulation was conducted, this time using the *k-ε* turbulence model. Thus, we were able to analyze comparatively the CFD results (i.e., using the same software, mesh size, initial and boundary conditions, based on the same RANS approach, only changing the turbulence models: *k-ζ-f* vs. *k-ε*). Table 2 shows the figures resulted from this *k-ε* simulation. When comparing with the data from Table 1, one may see that (1) when using the *k-ζ-f* model, the computing time was higher and (2) while the maximum and mean 2D flow velocities are within the same order for both models, the mean TKE is significantly higher in the *k-ε* case.

Table 2. Influence of the *k*-ε model on the simulation.

Turbulence Model	*k*-ε
Simulation time [hours] with 34 CPU cores	17.7
Mean TKE [m^2/s^2] @ 5s	40.8
Max. 2D flow velocity [m/s] @ 5s	136.3
Mean 2D flow velocity [m/s] @ 5s	11.3

Figure 4a–d shows the flow velocity fields obtained with both turbulence models in the vertical and horizontal planes containing the spark plug. While the maximum cell size was 0.7 mm, the area around the spark plug was refined and the smallest cell size reached 0.0437 mm between the two electrodes. The vectors displayed in Figure 4c,d are projected in plane.

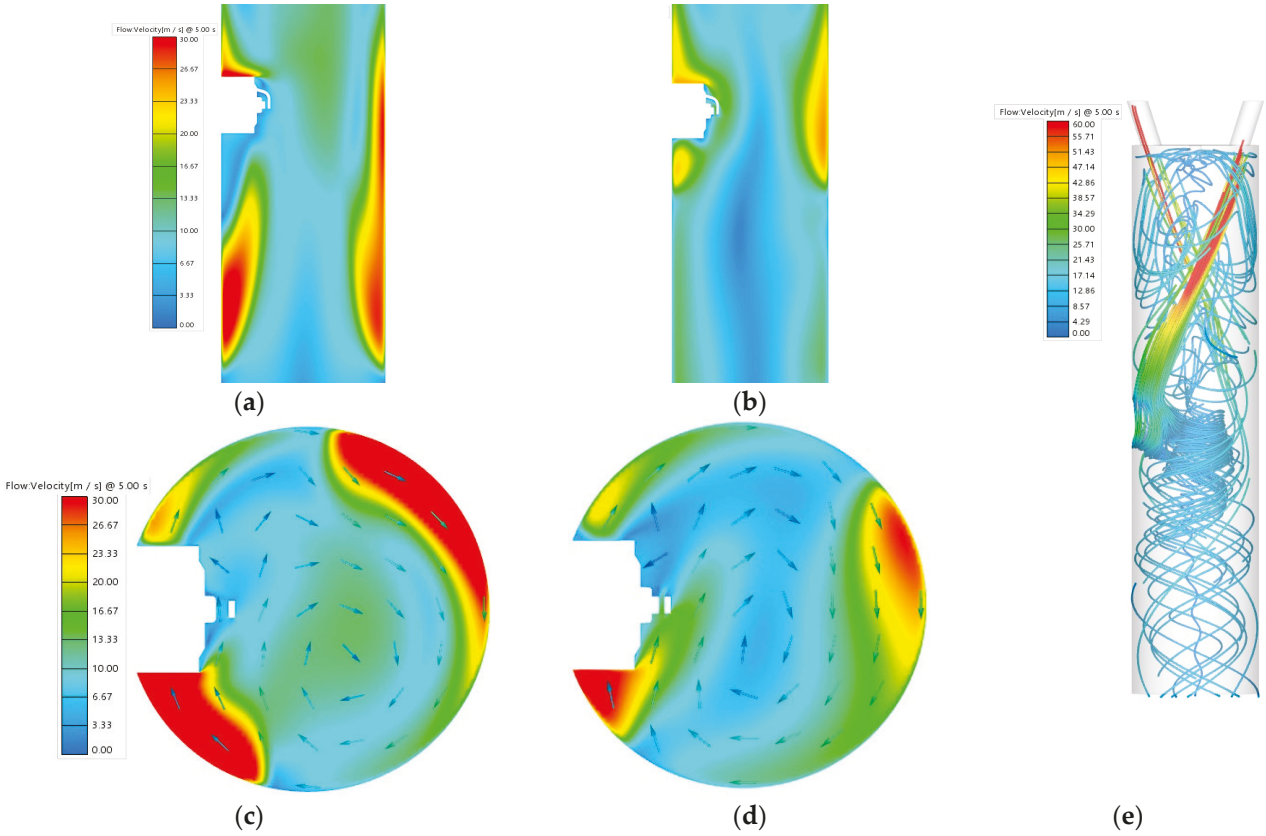


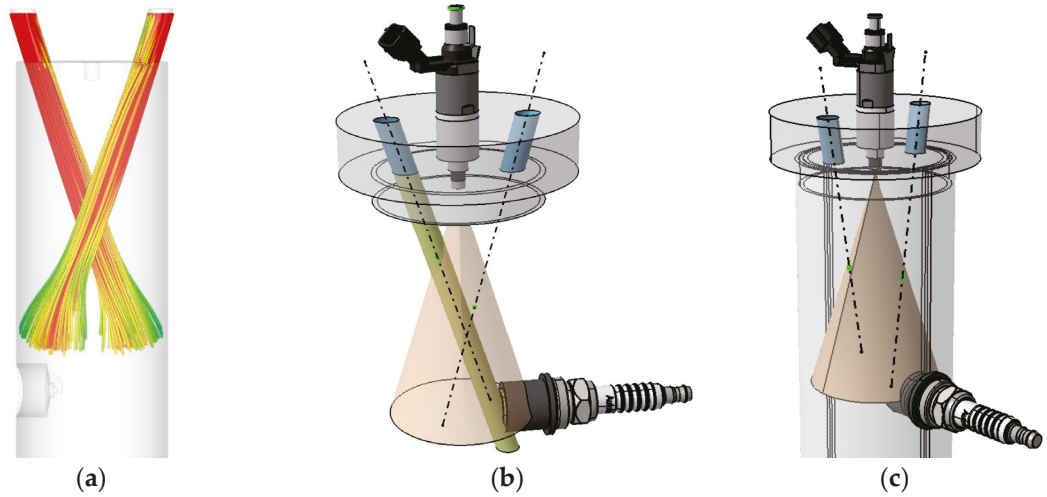
Figure 4. Burner's internal aerodynamics at 5s: (**a**) vertical plane with *k*-ζ-*f* model; (**b**) vertical plane with *k*-ε; (**c**) horizontal plane with *k*-ζ-*f* model; (**d**) horizontal plane with *k*-ε; (**e**) streamlines generated by the *k*-ε model.

As seen in Tables 1 and 2, the maximum 2D flow velocities are over 130 m/s, while Figure 4 shows values up to 30 m/s. Since Figure 4 was focused on the flow in the spark plug region, where the velocities are much lower than the maximum value, the color mapping range was conveniently chosen to discern more efficiently between different velocities in this area. The same was performed for Figures 3 and 4e, which presents the streamlines generated by the flow at 5 s, because the maximum flow velocities occur in the two entering air ducts from the burner's head.

When analyzing comparatively the results of the two turbulence models, Figure 4a–d, one may see that (1) both models predict horizontal large-scale vortexes rotating in the same direction (clockwise) and (2) the predicted velocities are globally lower for the *k*-ε model. This analysis of the flow around the spark plug is of interest because the flame

kernel development initiated by the spark produced between the electrodes is influenced by the flow: either the flow is too intense and the kernel may be extinguished or the flow is too low, the kernel develops poorly and affects negatively the combustion performance. In the situations presented in Figure 4a–d, the following velocities were obtained between the two electrodes: 14.9 m/s for the *k*-*ε* model and 5.7 m/s for the *k*-*ζ*-*f* model. Thus, noticeable difference between the results provided by the two models and somehow, unexpectedly higher for the *k*-*ε* model as globally, this model predicts lower velocities (Figure 4 and Tables 1 and 2). Nonetheless, as seen in Figure 4e, the *k*-*ε* model predicts intense rotating flows in the spark plug area, even though, globally, the large-scale structures seem like those presented in Figure 3.

Finally, the conclusion drawn from this CFD investigation is rather of a qualitative kind, meaning that the simulations predict comparable/similar large-scale air structures. As previously discussed, when first designing the air ducts through the burner's head, the idea was to direct one of the air flows towards the spark plug after hitting the fuel injected cone, Figure 2b, aiming to help flame propagation. As seen in Figure 4a,b, with the current 20° inclination, there is an impact between one of the two main airstreams and the cylindrical wall just above the spark plug, Figure 5a, which lowers the air velocities between the electrodes of the spark plug.



(**a**) (**b**) (**c**)

Figure 5. Burner's design evolution: (**a**) exclusive visualization of two main airstreams generated by the initial air ducts—results obtained with *k*-*ζ*-*f* model; (**b**) different inclination of the ducts; (**c**) 90° rotation around the burner's vertical axis of symmetry of the initial air ducts assembly.

The improving ideas that emerged from this study are: (1) to incline the duct responsible for directing the air towards the electrodes so as to achieve this specific goal and to maintain the other duct with the inclinations given in Figure 2 in order to generate a swirl, Figure 5b; (2) to rotate the initial air ducts assembly around the burner's vertical axis of symmetry in order to avoid blowing towards the electrodes, Figure 5c, in case the conclusion is that the flow at the electrodes' level is too intense and might extinguish the flame kernel.

To be able to draw more pertinent conclusions, all the design iterations should be complemented with CFD studies aiming to see the air–fuel interaction and the combustion process. The conclusions reached during this CFD investigation may be validated experimentally based on the measured starting delay of the burner, which may be an indication of the right choice for the two air ducts inclinations: the lower the starting delay, the better. This is part of the future works and based on the conclusions of this next CFD study, another prototype will be built.

3. Experimental Setup and Testing Methodology

When designing the burner, the focus was on obtaining a relatively affordable and straightforward extra-combustion device mounted upstream the TWC by relying on existing components on mass-production ICEV, such as the following: an air pump from a SI engine featuring air injection into the exhaust, a standard hot-wire mass air flowmeter (HW MAF), a gasoline injector taken rather from a port-fuel injection (PFI) system than from a gasoline direct injection (GDI) system, a usual spark plug together with its coil and a wide-band lambda probe. Moreover, this investigation's purpose was also to see if a simple design not using relatively complex elements such as the ones mentioned in [25] (e.g., an injector and a coil able to support high control frequencies, e.g., 200 and, respectively, 250 Hz, "a swirler containing a tiny slot with an optimized shape and location to promote a fast mixture preparation at the spark plug", a "prefilmer" taken from aeronautical burner applications and "a flame holder", the second one needing "optimization in relation to the swirler shape") is able to serve the purpose of rapidly reaching the light-off temperature.

The schema of the experimental setup for laboratory testing is presented in Figure 6.

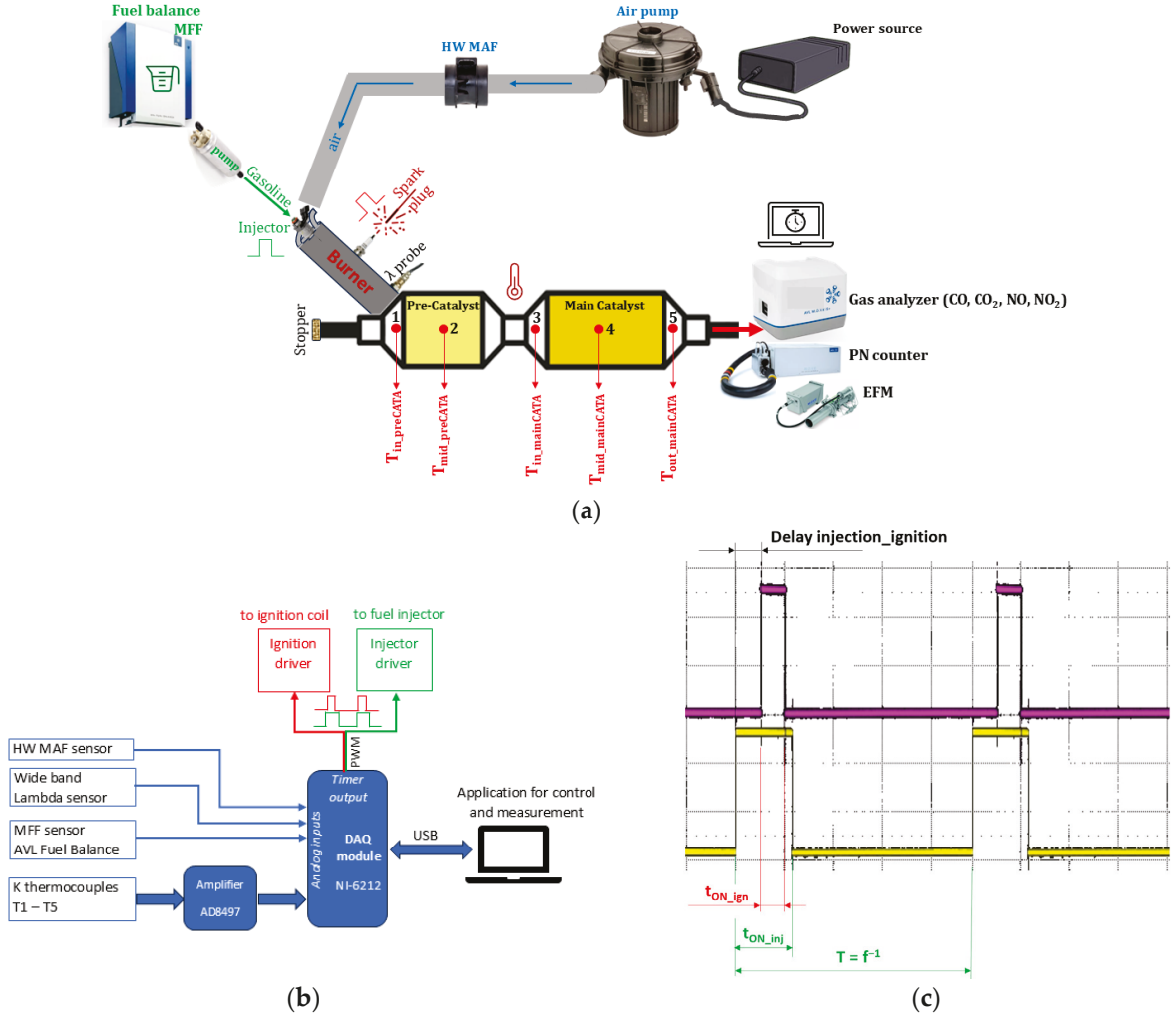


Figure 6. Schematic of the burner's lab testing: (**a**) components and instrumentation; (**b**) control and measurement; (**c**) oscilloscope acquired signals of ignition (magenta) and injection (yellow).

The testing methodology first aims to find how quickly the burner starts and then its effect on the heating of a two-part TWC (a smaller pre-catalytic converter and a main catalytic converter), along with the emissions specific to the burner's operation. Thus, it is about what is usually called "catalyst pre-heating", i.e., the burner operates before the

engine starts—as shown in Figure 6a, where there is no SI engine upstream the TWC and, consequently a stopper is used at the left side of the exhaust line.

To serve this purpose, first, the air pump was activated and operated at its maximum capacity of 40 kg/h steady flow, and then, the gasoline injection and the spark were activated via pulse-width modulation (PWM), Figure 6c, whereas the quality of the mixture (rich/stoichiometric/lean) was monitored via a wide-band lambda probe. The gasoline was pressurized by a usual electrically actuated pump at 5 bar. The fuel flow rate was adjusted to serve the need to control the mixture quality: rich in the beginning, to facilitate the starting of the burner, then, gradually and manually leaning the mixture (the lambda probe providing the feedback signal). The mass fuel flow rate (MFF) was measured with a usual AVL^{TM} 733S fuel balance (AVL, Graz, Austria). The TWC was instrumented with five K type thermocouples, as shown in Figure 6a. All these signals are controlled by a dedicated LabView^{TM} (National Instruments, USA) application, communicating with a data acquisition module from National Instruments^{TM}—Figure 6b. The software application interface showing how the burner's operational parameters are controlled is presented in Figure 7. The spark delay time related to the injection time is controlled by an Arduino^{TM} Uno module, in charge of the ignition coil command.

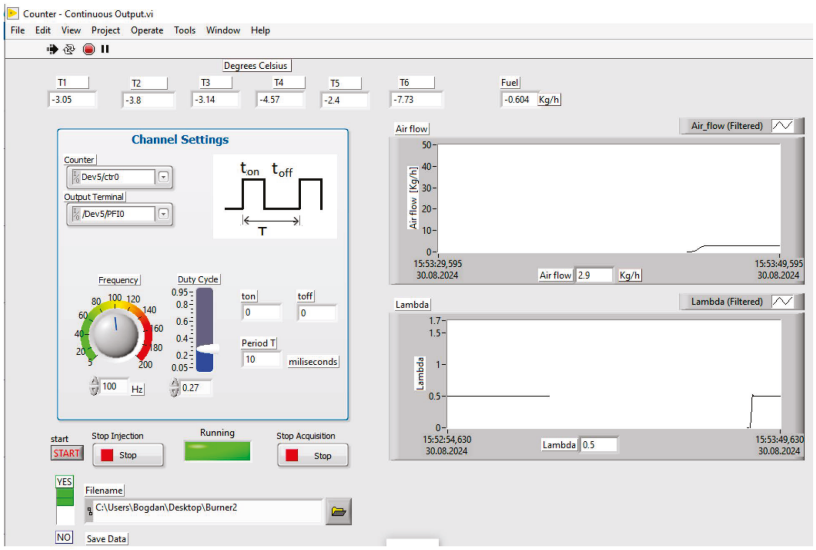


Figure 7. The software application interface: injection and ignition PWM specific parameters.

As Figure 6a shows, the exhaust emissions related to burner's operation are measured with an AVL^{TM} PEMS (Portable Emission Measurement System) containing a gas analyzer for CO, CO_2, NO and NO_2, a particle number (PN) counter able to detect particles with diameters higher than 23 nm and an exhaust flow mass rate (EFM) to express the chemical species in [kg/h] and by integration, in mass over a certain period of time.

4. Experimental Results and Discussion

After several attempts to achieve the optimal burner's starting, finally, the burner's injection and ignition were actuated as follows: 100 Hz actuating frequency for both signals; 3.7 ms injection duration at the beginning to achieve a rich and ignitable mixture and then, after the starting of the burner, gradually and manually decreasing it to 1.7 ms (thus, leaning the mixture); 3.5 ms actuation duration of the spark plug coil and 0 ms delay between the injection and ignition signals, aiming to produce the spark in a favorable environment (i.e., an ignitable mixture), Figure 6c. A picture with the flame produced by operating the burner as discussed above is presented in Figure 8.



Figure 8. The burner while operating.

Figure 9 is focused on the period corresponding to the starting delay of the burner: 2.19 s between the moment corresponding to the first positive value of the MFF and the moment when the inlet temperature of the pre-catalytic converter (T_1) increases. This period also corresponds to the endothermic phase of the injection, i.e., gasoline absorbs heat for the vaporization, as T_1 drops from 34.8 °C to 30.8 °C.

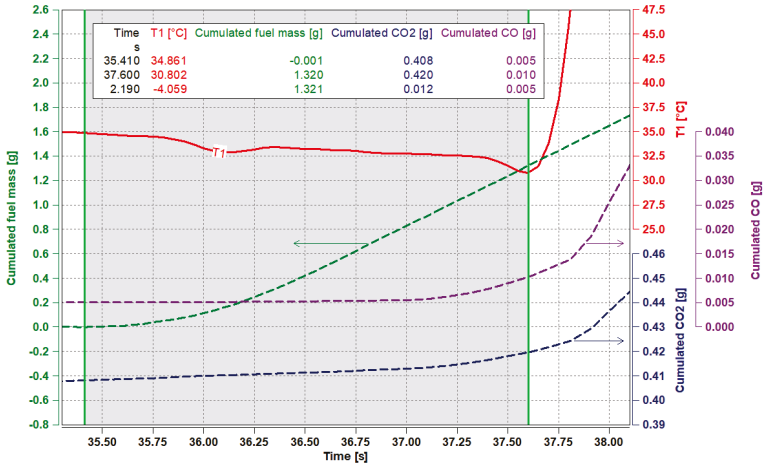


Figure 9. Starting delay of the burner (see the grey area).

Figure 9 also shows the cumulated values for fuel, CO, and CO_2 masses, obtained by integrating their corresponding evolutions in the period of the starting delay of the burner.

Thus, it is about 1.321 g of gasoline injected in this period, which during the events occurring before the start of combustion (SoC) generates 12 mg of CO_2 and 5 mg of CO. Regarding the nitric oxides (NO + NO_2), a technical problem occurred during the tests and the analyzer was unable to acquire data. However, they should be zero in this phase since the combustion did not start. The presence of CO_2 and CO in the exhaust species of the burner during these 2.19 s (regardless of their small amounts) means that some initiations of flames did occur.

After the starting of the burner (SoB), the focus was on how long it took the pre-catalytic converter to reach the light-off temperature, which in this study was conventionally considered as being 500 K, as discussed in the Introduction section. As seen in Figure 10, T_2 (i.e., the temperature in the mid-part of the pre-catalytic converter, Figure 6a) reached this temperature (227 °C) after 5.2 s. At this point, T_1 was at 1032 °C and the lambda coefficient arrived at 0.91 (still rich mixture favoring the formation of UHC and CO). According to [26], when not using a burner, i.e., when betting only on the engine to heat up the catalytic converter, with the penalizing measures related to the engine calibration (e.g., increase in the idle speed, lambda-split, spark retardation, as discussed in [13]), it took 21.4 s to reach T_2 = 500 K, while the exhaust temperatures measured at the outlet of the cylinder head achieved 700 °C, T_1 was at 340 °C, the engine idle speed at this moment was 1306 rpm and the cumulated CO_2 during this period was 20.5 g.

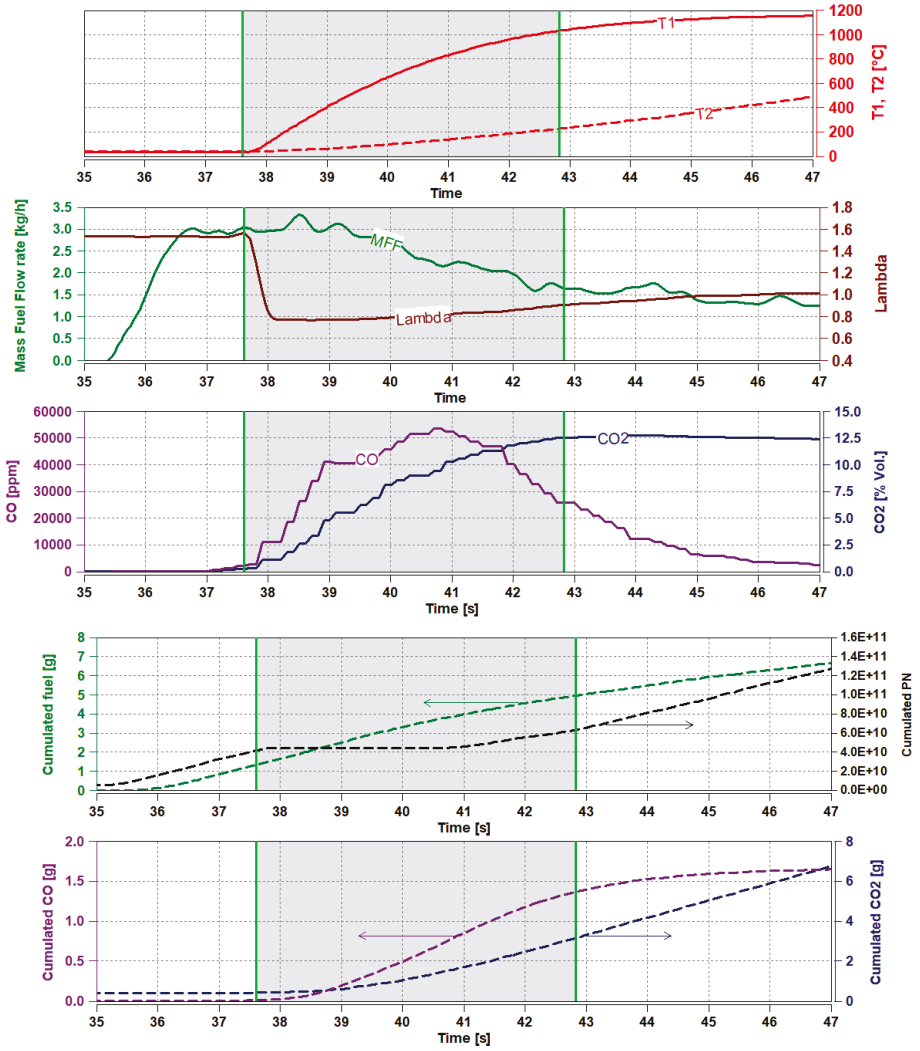


Figure 10. Experimental results illustrating the TWC light-off period (see the grey area).

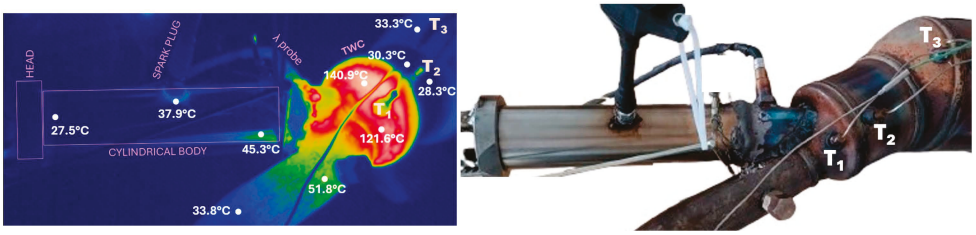
Returning to the present analysis, as regards the CO concentration, the same figure shows its instantaneous evolution, as well as the CO_2 concentration. By integrating the signals over the light-off period (the grey area illustrated in Figure 10), the following data were obtained: 3.6 g of gasoline injected, which via combustion produced 2.7 g of CO_2 and 1.351 g of CO. The lower value of CO_2 with respect to the gasoline mass injected and the high mass of CO are an indication of an incomplete combustion occurring in this light-off period, i.e., part of the fuel remaining unburnt. With a UHC gas analyzer, this hypothesis would have been confirmed. The incomplete combustion occurring during the TWC light-off period is also a result of the rich mixtures used ($0.78 < \text{lambda} < 0.91$), as seen in Figure 10. The control system used did not include an automatic regulation of the injection time after T_1 started to increase (the sign of SoB or SoC), i.e., automatically adjusting the injection time from the condition to reach lambda 1 or even higher (e.g., 1.2, as seen in [25]), so as to ensure lower CO and UHC. Only to have a measure of comparison, lambda 1 or the stoichiometric mixture is the theoretical condition for complete combustion, meaning that 1 g of octane generates 3.1 g of CO_2.

Regarding the air pump, it consumed 360.6 W, while the thermal power of the burner calculated for the complete combustion of the gasoline injected during the light-off period was 12.8 kW (with a specific heat capacity for gasoline of 2.22 kJ/kg/K and a specific heat ratio of 1.35).

On the PN subject, as illustrated in the same figure, before SoB, there are particles (4.1×10^{10}) displaced from upstream the PN counter by the air stream generated by the

burner's air pump. Then, first, there is a stagnation as if there are no more particles generated, followed by an increase in the cumulated PN. In total, the light-off period is characterized by a 2.15×10^{10} PN. The experimental setup used, Figure 6a, did not include a particulate filter (PF), which nowadays is a standard in the current SI engines for the passenger cars.

The skin temperatures at 5.2 s after SoB are presented in Figure 11. The slightly higher temperature from the lower part of the burner's cylindrical body (45.3 °C) could be an indication of a weak combustion occurring inside, in this area, as if some liquid gasoline arriving here was ignited somehow (as seen in Figure 8, the burner was inclined, having the head in a position that is higher than its body outlet, thus favoring the flow of a gasoline film on the lower wall of the cylindrical body). The highest skin temperatures (>100 °C) were in the area where the burner's flame occurred.



(**a**) (**b**)

Figure 11. Skin temperatures at 5.2 s after SoB: (**a**) picture taken with the thermal camera; (**b**) real picture of the assembly.

5. Conclusions and Future Works

As previously discussed, the initial question at the origin of this study was to see if a relatively affordable and straightforward extra-combustion device (i.e., a burner) can serve the purpose of reducing the TWC light-off time. The relevance of such a device related to the future development of more ecologic and efficient SIEV was substantiated in this paper with precise data obtained via numerical and experimental investigation, allowing others to replicate and build on the obtained results.

The main findings of this investigation are twofold:

1. Based on the CFD study,
    - This kind of examination is a good way to decide how to achieve a so-called fit-for-purpose internal aerodynamics of the burner (i.e., to quickly obtain a homogeneous and ignitable mixture) by relying only on a simple design, not using relatively complex elements such as the ones imported from the aeronautical burner application, i.e., relying only on conveniently orienting the two air inlets from the burner's head;
    - Two design improving ideas emerged from this numerical study; however, to be able to draw more pertinent conclusions, all the design iterations should be complemented with CFD studies aiming to see the air–fuel interaction and the combustion process;
    - The starting delay of the burner was identified as the parameter to be assessed experimentally to see the effects of the design decisions.
2. Based on the experimentation,
    - To reach the pre-catalytic converter light-off temperature, conventionally taken as 500 K, the burner was operated at a calculated thermal power of 12.8 kW for 5.2 s and consumed 3.6 g of gasoline, while T_1 attained 1032 °C, and the cumulated emissions were: 2.7 g of CO_2, 1.351 g of CO and 2.15×10^{10} particles, respectively;
    - To have a comparison measure, when not using a burner, i.e., when betting solely on the engine to heat-up the TWC, with the penalizing measures related to the engine calibration, it took 21.4 s to reach T_2 = 500 K, while the exhaust

temperatures measured at the outlet of the cylinder head attained 700 °C, T_1 was at 340 °C, the engine idle speed at this moment was 1306 rpm and the cumulated CO_2 during this period was 20.5 g.

- An enhanced procedure for the burner's operating control aiming to produce a cleaner combustion during the TWC pre-heating was identified: automatic control of the injection time after SoB from the condition to reach lambda 1 or even higher (if considered suitable).

As for the future works, based on the findings summarized above, another prototype is planned for manufacturing aiming to achieve a lower starting delay of the burner, an improved repeatability of the burner starting and a faster light-off period. Using the burner beyond the TWC pre-heating, i.e., using it in parallel with the engine's operation when needed (e.g., the operation of the hybridized vehicles, which involves repeating sequences of engine off/on for purely electric drive), is also planned.

Author Contributions: Conceptualization, A.C., B.C. and J.B.; methodology, A.C. and J.B.; data acquisition software and control system, B.C., A.C. and J.B.; CAD and CFD simulation, R.S., A.C. and V.I.-S.; experimental investigation, A.C., B.C., J.B. and R.S.; formal analysis, A.C., R.N. and V.I.-S.; writing—original draft preparation, A.C., B.C. and R.N. All authors have read and agreed to the published version of this manuscript.

Funding: In 2022, this research received funding from our institution gained through the "CIPCS" competition: grant title—"Dezvoltarea unui sistem de amorsare rapidă a convertoarelor catalitice pentru adaptarea autoturismelor la viitoarea normă de depoluare EURO7/Development of a fast TWC light-off system for the adaptation of cars to the future EURO7 norm".

Data Availability Statement: The raw data supporting the conclusions of this article will be made available by the authors on request.

Acknowledgments: The authors want to thank the following technicians who contributed with the manufacture of the burner prototype: Gheorghe Leașu and Ion Nițescu. We also acknowledge our institution for partially funding our project. Our gratitude goes also to AVL List Gmbh for providing freely the software we used (FIRE and CONCERTO).

Conflicts of Interest: Author Julien Berquez was employed by the company Horse Romania. The remaining authors declare that the re-search was conducted in the absence of any commercial or financial relationships that could be construed as a potential conflict of interest.

Nomenclature

2D, 3D	Two, three dimensional
AFR	Air–fuel ratio
BEVs	Battery Electric Vehicle(s)
CFD	Computational Fluid Dynamics
CPU	Central Processing Unit
CO	Carbon monoxide
CO_2	Carbon dioxide
DAQ	Data acquisition system
EFM	Exhaust flow mass(meter)
EHC	Electrically heated catalyst
EU	European Union
GB	Gigabyte
GDI	Gasoline direct injection
GHz	Gigahertz
HEV	Hybrid electric vehicle(s)
HW	Hot wire
IC	Internal combustion
ICEV	Internal combustion engine vehicle(s)

Lambda	Air excess coefficient (AFR made dimensionless by stoichiometric conditions)
MAF	Mass air flow(meter)
MFF	Mass fuel flow(meter)
ms	Milliseconds
nm	Nanometers
NO	Nitric monoxide
NO_2	Nitric dioxide
NO_x	Nitric oxides (NO + NO_2)
OSC	Oxygen storage capacity
PEMS	Portable Emission Measurement System
PF	Particulate Filter
PFI	Port-fuel injection
PN	Particle number
PWM	Pulse Width Modulation
RAM	Random access memory
RANS	Reynolds-average Navier–Stokes
SAE	Society of Automotive Engineers
SI	Spark ignition
SIEV	Spark ignition engine vehicle(s)
SoB	Start of burner
SoC	Start of combustion
T50, T90	Temperatures corresponding to a catalyst effectiveness of 50%/90%
TKE, k[$m^2 \cdot s^{-2}$]	Turbulent kinetic energy
TM	Trademark
TWC	Three-ways-catalytic converter
UHC	Unburnt hydrocarbon
USB	Universal Serial Bus
ZEVs	Zero-emission vehicle(s)
ζ	Eddy viscosity
ε	Rate of dissipation
f	Relaxation function
η_{TWCx}	Conversion efficiency or the effectiveness of the catalytic converters for a given pollutant (x)

References

1. Fit for 55. 2024. Available online: https://www.consilium.europa.eu/en/policies/green-deal/fit-for-55/ (accessed on 23 August 2024).
2. Fit for 55: Why the EU Is Toughening CO2 Emission Standards for Cars and Vans. 2024. Available online: https://www.consilium.europa.eu/en/infographics/fit-for-55-emissions-cars-and-vans/ (accessed on 23 August 2024).
3. Kapus, P. Passenger Car Powertrain 4.x—Fuel Consumption, Emissions and Cost. 2020. Available online: https://www.linkedin.com/pulse/webinar-passenger-car-powertrain-4x-fuel-consumption-emissions-kapus (accessed on 18 July 2024).
4. Maurer, R.; Kossioris, T.; Sterlepper, S.; Günther, M.; Pischinger, S. Achieving Zero-Impact Emissions with a Gasoline Passenger Car. *Atmosphere* **2023**, *14*, 313. [CrossRef]
5. Buttes, A.G.D.; Jeanneret, B.; Kéromnès, A.; Le Moyne, L.; Pélissier, S. Energy management strategy to reduce pollutant emissions during the catalyst light-off of parallel hybrid vehicles. *Appl. Energy* **2020**, *266*, 114866. [CrossRef]
6. Sanketi, P.R.; Zavala, J.C.; Hedrick, J.K.; Wilcutts, M.; Kaga, T. A Simplified Catalytic Converter Model for Automotive Coldstart Applications with Adaptive Parameter Fitting. In Proceedings of the the 8th International Symposium on Advanced Vehicle Control, Taipei, Taiwan, 20–24 August 2006.
7. Shaw, B.T.; Fischer, G.D.; Hedrick, J.K. A simplified coldstart catalyst thermal model to reduce hydrocarbon emissions. *IFAC Proc. Vol.* **2002**, *35*, 307–312. [CrossRef]
8. Zaccardi, J.-M.; Escudie, D. Overview of the main mechanisms triggering low-speed pre-ignition in spark-ignition engines. *Int. J. Engine Res.* **2014**, *16*, 152–165. [CrossRef]
9. Bratan, V.; Vasile, A.; Chesler, P.; Hornoiu, C. Insights into the Redox and Structural Properties of CoOx and MnOx: Fundamental Factors Affecting the Catalytic Performance in the Oxidation Process of VOCs. *Catalysts* **2022**, *12*, 1134. [CrossRef]
10. Gao, J.; Tian, G.; Sorniotti, A.; Karci, A.E.; Di Palo, R. Review of thermal management of catalytic converters to decrease engine emissions during cold start and warm up. *Appl. Therm. Eng.* **2019**, *147*, 177–187. [CrossRef]

11. Steiner, T.; Neurauter, D.; Moewius, P.; Pfeifer, C.; Schallhart, V.; Moeltner, L. Heat-Up Performance of Catalyst Carriers—A Parameter Studyand Thermodynamic Analysis. *Energies* **2021**, *14*, 964. [CrossRef]
12. Langen, P.; Theissen, M.; Mallog, J.; Zielinski, R. Heated Catalytic Converter Competing Technologies to Meet LEV Emissions Standards. *SAE J. Fuels Lubr.* **1994**, *103*, 141–150.
13. Chan, S.H. A practical approach for rapid catalyst light-off by means of strategic engine control. *Proc. Inst. Mech. Eng. Part D J. Automob. Eng.* **2001**, *215*, 545–555. [CrossRef]
14. Real, M.; Hedinger, R.; Pla, B.; Onder, C. Modelling three-way catalytic converter oriented to engine cold-start conditions. *Int. J. Engine Res.* **2021**, *22*, 640–651. [CrossRef]
15. Getsoian, A.B.; Theis, J.R.; Lambert, C.K. Sensitivity of Three-Way Catalyst Light-Off Temperature to Air-Fuel Ratio. *Emiss. Control Sci. Technol.* **2018**, *4*, 136–142. [CrossRef]
16. Samaras, Z.; Hausberger, S.; Mellios, E. Preliminary Findings on Possible Euro7 Emission Limits for LD and HD Vehicles, Brussels. 2020. Available online: https://www.heise.de/downloads/18/3/0/8/5/7/1/4/AGVES-2021-04-08-LDV_Exhaust.pdf (accessed on 10 December 2023).
17. Menne, C. Near Zero Impact Pollutant Emissions And Zero CO2—Is There a Future for Combustion Engine Powertrains? Aachen. 2021. Available online: http://siar.ro/wp-content/uploads/2021/05/Christoph-Menne-Near-zero-impact-pollutant-emissions-and-zero-CO2-%E2%80%93-is-there-a-future-for-combustion-engine-powertrains.pdf (accessed on 8 May 2021).
18. Barillari, L.; Pipolo, M.; Della Torre, A.; Montenegro, G.; Onorati, A.; Vacca, A.; Chiodi, M.; Kulzer, A. *Post-Oxidation Phenomena as a Thermal Management Strategy for Automotive After-Treatment Systems: Assessment by Means of 3D-CFD Virtual Development*; SAE Technical Paper; SAE International: Warrendale, PA, USA, 2024; pp. 1–16. [CrossRef]
19. Kumar, M.; Moriyoshi, Y.; Kuboyama, T. Post-oxidation phenomena enhancement with scavenging and secondary air injection in exhaust manifold of a turbocharged GDI engine. *Int. J. Engine Res.* **2023**, *24*, 2388–2409. [CrossRef]
20. Barillari, L.; Della Torre, A.; Montenegro, G.; Onorati, A.; Rossi, V.; Paltrinieri, S.; Gullino, F. CFD Assessment of an After-Treatment System Equipped with Electrical Heating for the Reduction of the Catalyst Light-Off Time. *SAE Int.* **2024**, *6*, 613–627. [CrossRef]
21. Oser, P.; Mueller, E.; Hartel, G.; Schurfeld, A. *Novel Emission Technologies with Emphasis on Catalyst Cold Start Improvements Status Report on VW-Pierburg Burner/Catalyst Systems*; SAE Technical Paper 940474; SAE International: Warrendale, PA, USA, 1994; p. 16. [CrossRef]
22. Kollmann, K.; Abthoff, J.; Zahn, W. *Concepts for Ultra Low Emission Vehicles*; SAE Technical Paper; SAE International: Warrendale, PA, USA, 1994. [CrossRef]
23. Della Torre, A.; Barillari, L.; Montenegro, G.; Onorati, A.; Rulli, F.; Paltrinieri, S.; Rossi, V.; Pulvirenti, F. *Numerical Assessment of an After-Treatment System Equipped with a Burner to Speed-Up the Light-Off During Engine Cold Start*; SAE Technical Paper; SAE International: Warrendale, PA, USA, 2021. [CrossRef]
24. Montenegro, G.; Torre, A.D.; Barillari, L.; Onorati, A. CFD Investigation of a Burner-base Heating Strategy to Speed up the cold Start Transient of ICEs. In *22. Internationales Stuttgarter Symposium. Proceedings*; Springer: Wiesbaden, Germany, 2022. [CrossRef]
25. Battistoni, M.; Zembi, J.; Casadei, D.; Ricci, F.; Al, E. *Burner Development for Light-Off Speed-Up of Aftertreatment Systems in Gasoline SI Engines*; SAE Technical Paper 2022-37-0033; SAE International: Warrendale, PA, USA, 2022. [CrossRef]
26. Clenci, A.; Berquez, J.; Stoica, R.; Niculescu, R.; Cioc, B.; Zaharia, C.; Iorga-Simăn, V. Experimental investigation of the effect of an afterburner on the light-off performance of an exhaust after-treatment system. *Energy Rep.* **2022**, *8*, 406–418. [CrossRef]
27. Hanjalić, K.; Popovac, M.; Hadžiabdić, M. A robust near-wall elliptic-relaxation eddy-viscosity turbulence model for CFD. *Int. J. Heat Fluid Flow* **2004**, *25*, 1047–1051. [CrossRef]
28. Karbon, M.; Sleiti, A.K. Turbulence modeling using Z-F, RSM, LES and WMLES for flow analysis in Z-Shape ducts. In Proceedings of the ASME 2020 Fluids Engineering Division Summer Meeting collocated with the ASME 2020 Heat Transfer Summer Conference and the ASME 2020 18th International Conference on Nanochannels, Microchannels, and Minichannels, Virtual, 13–15 July 2020; p. 3. [CrossRef]
29. Perceau, M.; Guibert, P.; Clenci, A.; Iorga-Simăn, V.; Niculae, M.; Guilain, S. Investigation of the Aerodynamic Performance of the Miller Cycle from Transparent Engine Experiments and CFD Simulations. *Machines* **2022**, *10*, 467. [CrossRef]
30. Bakker, A. Lectures on Applied CFD. 2008. Available online: https://www.bakker.org/Lectures-Applied-CFD.pdf (accessed on 1 July 2024).

Disclaimer/Publisher's Note: The statements, opinions and data contained in all publications are solely those of the individual author(s) and contributor(s) and not of MDPI and/or the editor(s). MDPI and/or the editor(s) disclaim responsibility for any injury to people or property resulting from any ideas, methods, instructions or products referred to in the content.

inventions

MDPI

Article

Anisotropic k-ϵ Model Based on General Principles of Statistical Turbulence

J. J. H. Brouwers

Romico Hold.VBA, 6226 GV Maastricht, The Netherlands; j.j.h.brouwers@gmail.com

Abstract: An upgrade is presented of a recently published model for the calculation of statistical averages of turbulent flow variables. Instead of empirical constructions, important parts of the model are based on general principles of statistical turbulence and physics. The upgrade concerns transparent and simplified descriptions of turbulent diffusion and Reynolds stresses which express their dependency of mean flow gradients in a direct manner. As before, prediction comparisons are satisfactory in relation to the results of DNS of channel flow. Implementation in a CFD code is straightforward and its application provides a significant improvement to the results of the widely used empirical basic k-ϵ model.

Keywords: turbulent flow; new k-ϵ model

1. Introduction

Models of computational fluid dynamics (CFD) are generally based on semi-empirical descriptions of diffusion by turbulent fluctuations [1,2]. This includes the basic k-ϵ model widely used in engineering and environmental analysis and offered in software packages [3,4]. Recently, a new model was presented [5]. Instead of empiricism, it rested on the application of general principles and properties of statistical turbulence. Predictions of the new model compared favourably with the results of direct numerical simulations (DNS) of channel flow at a large Reynolds number [6–8]. This contrasted with the predictions of the basic k-ϵ model which showed remarkable differences.

In the present paper, an upgrade and generalisation of the new model is given. As before, it is tested against DNS of channel flow. Equations are presented in a form which enable straightforward implementation in CFD codes.

2. Averaged Conservation Equations

Equations are presented for the calculation of the average values of fluctuating variables in turbulent flows. The flow is that of a fluid with constant or almost constant density ρ, e.g., a liquid or a gas at subsonic speed. Turbulent fluctuations measured at a fixed point in space are treated as a statistical process which is stationary or almost stationary in time compared to the time of velocity fluctuations. Statistical averages follow from time averaging over sufficiently long time intervals. The time averaged representation of the Navier–Stokes equations is given by

Conservation of mass:

$$\frac{\partial u_i}{\partial x_i} = 0 \tag{1}$$

Conservation of momentum:

$$\frac{\partial u_i}{\partial t} + u_j \frac{\partial u_i}{\partial x_j} + \frac{\partial < u_i' u_j' >}{\partial x_j} = -\frac{\partial p}{\partial x_i} \tag{2}$$

Conservation of energy:

$$\frac{\partial \theta}{\partial t} + u_j \frac{\partial \theta}{\partial x_j} + \frac{\partial < u_j' \theta' >}{\partial x_j} = 0 \tag{3}$$

where angled brackets represent statistical averaging, t and x are time and space coordinate, u, p, and θ are mean or time-averaged values of fluid velocity, pressure, and temperature, respectively, and u' and θ represent fluctuations of velocity and temperature, respectively, that is, the velocity and temperature minus their mean value. Throughout this paper, repeated indices imply summation unless otherwise stated. As we were concerned with flow at a high Reynolds number, the contributions of the viscous forces and heat conductivity present in the Navier–Stokes equations were dropped. Their effect can be disregarded when considering the main flow governed by the instability of inviscid flow outside small boundary layers. The average temperature in energy within Equation (3) can also be used to describe the average distribution of passive or almost passive admixture in the fluid.

3. Diffusion Representations of Turbulent Fluxes

The appearance of turbulent fluxes in the convection terms of the averaged conservation equations results in an unclosed set of equations for mean flow variables. To resolve this issue, descriptions of the turbulent flux terms were derived, which are based on general principles of statistical turbulence at a large Reynolds number [5,9]. The derivation starts from the formulation of a Langevin or fluctuation equation and the associated Fokker Planck or diffusion equation for the velocity and position of a marked fluid particle [10–13]. The approach is known from molecular dynamics and related stochastic problems [14–17] yielding the descriptions of the transport coefficients of viscosity, thermal conductivity, and diffusion of dilute gases [17,18]. Challenges in the case of turbulence are the inhomogeneous and anisotropic nature of turbulence, dissipation of energy, and general specification of the coefficients of the equations by Eulerian statistical values of flow.

The following principles and properties were invoked:

- The formulation of a Langevin equation for fluid particle velocity is in accordance with the property that autocorrelations of particle accelerations are vanishingly short compared to those of velocities in the limit of a large Reynolds number [19].
- Kolmogorov's similarity theory holds for the small viscous scales of turbulence [19]; it is an inertial subrange representation that specifies the white noise term in the Langevin equation.
- Solutions of the Langevin and diffusion equation are presented by a perturbation expansion in powers of the inverse of the Kolmogorov constant C_0 [8–11]. Matching predictions with data of measurements and DNS reveal values of C_0 around 6–7 [10–13,20,21]. In the present analysis, $C_0 = 7$.
- The time scale of velocity fluctuations and its decorrelation scales as C_0^{-1} compared to the time scale of energy dissipation. It enables us to treat the first term of the solution as a Hamiltonian process and to apply the fluctuation–dissipation theorem and Onsager symmetry [14–17].
- The well-mixing principle of Lagrangian and Eulerian velocities [22] enables to specify the second term in the expansion of the diffusion result.
- Particle displacement during velocity correlation scales as C_0^{-1} compared to the scale of inhomogeneity, enabling the Lagrangian formulation to be converted in an Eulerian one [9,13].

Results for turbulent fluxes of momentum and conservative scalars are as follows [5,9,13]:

Momentum flux

$$< u_j' u_i' >= \frac{2}{3} k_0 \delta_{ij} - D_{ik} \frac{\partial u_j}{\partial x_k} - D_{jk} \frac{\partial u_i}{\partial x_k} \tag{4}$$

Temperature flux (and flux of any conservative scalar)

$$< u_j' \theta' >= -D_{jk} \frac{\partial \theta}{\partial x_k} \tag{5}$$

In Equation (4), δ_{ij} is Kronecker delta and k_0 is the kinetic energy of the isotropic state. It is the analogue of the kinetic energy of translating gas molecules [23]. The value of k_0 follows from the equation for kinetic energy presented in the next section.

The diffusion coefficient D_{ij} in Equations (4) and (5) is specified by [5,9,13]

$$D_{ij} = 2C_0^{-1}\epsilon^{-1}\sigma_{in}\sigma_{nj} + 2C_0^{-2}\epsilon^{-2}\sigma_{li}\sigma_{jk}u_n\frac{\partial \sigma_{lk}}{\partial x_n} - 4C_0^{-2}\epsilon^{-1}\sigma_{kj}u_n\frac{\partial}{\partial x_n}(\epsilon^{-1}\sigma_{im}\sigma_{mk}) \tag{6}$$

where

$$\sigma_{ij} =< u_i' u_j' > \tag{7}$$

ϵ is the energy dissipation rate whose governing equation is presented in Section 5, and $C_0 = 7$ is the Kolmogorov constant.

Implementing the above expressions in Equation (4) results in a set of algebraic relations of the covariance tensor σ_{ij} in terms of k_0 and mean velocity gradients. Solving these non-linear coupled equations for given k_0 and mean velocity gradients can pose some problems due to multi-valued dependencies between variables in specific areas of the flow field [5]. An alternative formulation which circumvents such problems is obtained by the following procedure. The diffusion coefficients on the right-hand side of Equation (4) represent a certain state which is altered by the gradients of the mean flow, leading to a new state of covariance values described by the left-hand side of Equation (4). This principle can be applied to any state. It can be applied to a basic isotropic state $\sigma_{ij} = \frac{2}{3}k_0\delta_{ij}$. The thus-determined new state can serve as the basis for the calculation of the next state. This process can be continued up to and including terms of $O(C_0^{-2})$. The result inhibits the same truncation error as the original formulation, cf. Equation (6). For the diffusion coefficient D_{ik}, we obtain

$$D_{ik} = \frac{8}{9}\frac{k_0^2}{C_0\epsilon}\delta_{ik} - \frac{4k_0}{3}(\frac{4}{3}\frac{k_0}{C_0\epsilon})^2(\frac{\partial u_k}{\partial x_i} + \frac{\partial u_i}{\partial x_k}) + \frac{16k_0^6}{27C_0^2\epsilon^4}(u_n\frac{\partial}{\partial x_n}(\frac{\epsilon^2}{k_0^3}))\delta_{ik} \tag{8}$$

while the covariance tensor σ_{ij} is given by Equation (4) with the diffusion coefficients according to Equation (8). For kinetic energy $k = \frac{\sigma_{ii}}{2}$, we can write

$$k = k_0(1 + \frac{1}{3}(\frac{4k_0}{3C_0\epsilon})^2(\frac{\partial u_i}{\partial x_j} + \frac{\partial u_j}{\partial x_i})^2) \tag{9}$$

which relates k to the isotropic value of kinetic energy k_0. The second term on the RHS of this equation describes the increase in kinetic energy associated with the anisotropy of turbulent fluctuations. The expression is obtained upon implementing the description for σ_{ii} according to Equations (4) and (8) and making use of the equation of continuity Equation (1).

The last term of the RHS of Equation (8) originates from the $O(C_0^{-2})$ terms in Formulation (6). The term complies with the decaying part of kinetic energy and dissipation of homogeneous isotropic turbulence behind a grid [11–13]. The second term on the RHS of Equations (8) and (9) describes contributions, which are associated with the anisotropy caused by main flow gradients.

The presented descriptions are valid up to a truncation error of $O(C_0^{-3})$. They are the result of applying general principles and do not involve empiricism nor calibration factors.

4. Equation for Kinetic Energy

A closed set of equations is obtained upon formulating equations for k connected to k_0 through Equation (9), as well as ϵ. For both variables, equations can be derived from the Navier–Stokes equations. For k, we can write [7,8]

$$\frac{\partial k}{\partial t} + u_i \frac{\partial k}{\partial x_i} + \frac{\partial < u_i' k' >}{\partial x_i} + \rho^{-1} \frac{\partial < u_i' p' >}{\partial x_i} = P - \epsilon \tag{10}$$

where P is the mean production of energy via turbulent fluctuations defined by

$$P = \sigma_{ij} \frac{\partial u_i}{\partial x_j} \tag{11}$$

and where k' and p' are the fluctuating parts of kinetic energy and pressure, respectively, that is, the kinetic energy and dissipation rates minus their time-averaged values. There are two turbulent flux terms in Equation (10), i.e., the third and fourth term on the LHS of Equation (10), which need to be modelled. Equation (5) is valid for a conservative scalar, while kinetic energy and pressure are non-conservative variables. An approximate approach is to treat the sum of the two flux terms as a conservative scalar proceeded by a calibration constant c_k, which corrects for non-conservative behaviour [5].

$$< u_i' k' > + \rho^{-1} < u_i' p' >= -c_k D_{ij} \frac{\partial k}{\partial x_j} \tag{12}$$

Comparison with DNS of channel flow reveals $c_k = 1.3$; the dependency on distance from the channel wall is found to be well described by D_{ij} [5].

Substituting for σ_{ij} in Equation (11), as well as using Equations (4), (7) and (8) and making use of the equation of continuity Equation (1) yields the following:

$$P = (\frac{9 C_0 T^2}{8 k_0^2}) \epsilon \tag{13}$$

where T^2 is determined by shear stresses:

$$T^2 = \sigma_{12}^2 + \sigma_{23}^2 + \sigma_{13}^2 \tag{14}$$

which are specified by Equations (4) and (8). Thus, the following equation for kinetic energy is obtained:

$$\frac{\partial k}{\partial t} + u_i \frac{\partial k}{\partial x_i} = c_k \frac{\partial}{\partial x_i} (D_{ij} \frac{\partial k}{\partial x_j}) + (\frac{9 C_0 T^2}{8 k_0^2} - 1) \epsilon \tag{15}$$

where k can be replaced by k_0 using Equation (9), resulting in an equation specifying k_0. The equation describes the change of k_0 due to energy production and dissipation (the last term on RHS), diffusion of energy (the first term on the RHS), and energy convection (the term on the LHS). In case of the random motion of gasmolecules, k_0 is a constant depending on temperature. In case of turbulence, k_0 changes in value according to Equation (15).

5. Equation for Energy Dissipation

The basic form of the equation for energy dissipation obtained from the Navier–Stokes equations contains a number of terms which are governed by the small viscous scales of turbulence [1,2]. The terms can be replaced by expressions that meet the criteria of matching the results of decaying grid turbulence and the log layer of wall-induced turbulence [1,2].

$$\frac{\partial \epsilon}{\partial t} + \frac{\partial u_i \epsilon}{\partial x_i} = \frac{\partial}{\partial x_i} (\frac{D_{ij}}{\sigma_\epsilon^*} \frac{\partial \epsilon}{\partial x_j}) + (c_{\epsilon 1} P - c_{\epsilon 2} \epsilon) \frac{\epsilon}{k} \tag{16}$$

where the turbulent flux of energy dissipation is modelled as a conservative scalar proceeded by the calibration factor σ_ϵ^*. A comparison with DNS of channel flow revealed $\sigma_\epsilon^* = 0.3$. To match the decaying grid turbulence, the appropriate value for $c_{\epsilon 2}$ was set to 1.9, while the value of $c_{\epsilon 1}$ followed from the relation

$$c_{\epsilon 1} = c_{\epsilon 2} - \frac{\kappa^2}{\sigma_\epsilon^*}\sqrt{\frac{9C_0}{8}}(1 + \frac{8}{3C_0}) \tag{17}$$

The relation follows from Equation (16) by considering the behaviour of the equation near a wall where the log layer solution applies and where production equals dissipation.

6. Boundary Conditions

Equations (1)–(5), (7)–(9), (11) and (13)–(17) constitute a closed set of equations for the variables u_i, p, $< u_i' u_j' >$, $< u_i' \theta' >$, D_{ij}, k, ϵ, and k_0. Boundary conditions to be applied to the differential equations will vary from case to case, depending on the configuration under consideration. In many cases, they will be similar to those used in the basic k-ϵ model [1,2]. Along walls, thin boundary layers are present where the present formulae that are entirely devoted to large-scale turbulence at a high Reynolds number do not apply. In case of the equations for kinetic energy and energy dissipation, the area of the boundary layers can be surpassed by making use of the solutions of the log layer, which are valid just outside the boundary layer [1,2]. In the next section, this will be demonstrated for the case of channel flow.

7. Test Case: Channel Flow

We considered the flow between parallel plates with distance $2H$ between them. Mean flow is parallel to the plates in direction x_1. Statistical averages vary with distance x_2 from the wall. From the conservation Equations (1)–(3), analytical solutions can be derived [9,24]. This includes the solution for the turbulent shear stress outside the thin viscous layer at the wall.

$$< u_1' u_2' >= -u_\tau^2 (1 - \frac{x_2}{H}) \tag{18}$$

where u_τ is shear velocity. Its value follows from the solutions of the boundary layer at the wall [1,2,24]. It can also be obtained from the pressure drop over the channel [24]. Another expression for shear velocity is provided by the diffusion description for turbulent shear, which, in the case of channel flow, was obtained from Equations (4) and (8) as

$$< u_1' u_2' >= -D_{22}\frac{du_1}{dx_2} \tag{19}$$

$$D_{22} = \frac{8}{9}\frac{k_0^2}{C_0 \epsilon} \tag{20}$$

where D_{22} is the diffusion coefficient of turbulent shear flow or turbulent viscosity. Equating the RHS's of Equations (18) and (19) and implementing Equation (20) yields an expression for $\frac{du_1}{dx_2}$, which, upon substituting into the RHS's of Equations (4), (8) and (9), yields the following expressions for the mean squares of fluctuating velocities and mean kinetic energy:

$$< u_2' u_2' >=< u_3' u_3' >= \frac{2}{3}k_0 \tag{21}$$

$$< u_1' u_1' >= \frac{2}{3}k_0 + \frac{6}{k_0}u_\tau^4 (1 - \frac{x_2}{H})^2 \tag{22}$$

$$k = k_0 + \frac{3}{k_0}u_\tau^4 (1 - \frac{x_2}{H})^2 \tag{23}$$

The differential equations for k_0 with k specified by Equation (23) and ϵ with k, again specified by Equation (23), are given by

$$\frac{8c_k}{9C_0}\frac{d}{dx_2}(\frac{k_0^2}{\epsilon}\frac{dk}{dx_2}) + \left(\frac{9C_0u_\tau^4(1-\frac{x_2}{H})^2}{8k_0^2} - 1\right)\epsilon = 0 \tag{24}$$

$$\frac{8k}{9\sigma_\epsilon^* C_0}\frac{d}{dx_2}(\frac{k_0^2}{\epsilon}\frac{d\epsilon}{dx_2}) + \left(c_{\epsilon 1}\frac{9C_0u_\tau^4\left(1-\frac{x_2}{H}\right)^2}{8k_0^2} - c_{\epsilon 2}\right)\epsilon^2 = 0 \tag{25}$$

At the outer edge of the thin viscous laminar and buffer layer at the wall, the solutions for the log layer apply: $\frac{du_1}{dx_2} = -\frac{u_\tau}{\kappa x_2}$ and $\epsilon = \frac{u_\tau^3}{\kappa x_2}$ which pertains to the production being equal to dissipation and where κ is the Von Karman constant: $\kappa = 0.4$. Using Equations (19) and (20), we then obtain the following boundary conditions:

$$k_0 = \sqrt{\frac{9C_0}{8}}u_\tau^2; \quad \epsilon x_2 = \frac{u_\tau^3}{\kappa} \quad at \quad x_2 = \frac{100H}{Re_\tau} \tag{26}$$

where Re_τ is friction Reynolds number $Re_\tau = \frac{u_\tau H}{\nu}$ that is large, such that $\frac{100}{Re_\tau} << 1$. At the symmetry axis of the channel, we have

$$\frac{dk_0}{dx_2} = 0; \quad \frac{d\epsilon}{dx_2} = 0; \quad at \;\; x_2 = H \tag{27}$$

The boundary value for k_0 in Equation (26) also follows from the term between brackets in energy within Equation (24). The term originates from the difference between production and dissipation. Setting to zero results in the value for k_0 given by Equation (26).

Asymptotic analysis of the boundary layer [24], (pp. 279–281), reveals unspecified values for covariances at the outer edge of the layer. Normalised with shear velocity u_τ, these values and the distributions of $\frac{\sigma_{ij}}{u_\tau^2}$ with respect to $\frac{x_2}{H}$ are entirely determined by the statistics of the large scales, which are governed by mean flow gradients. This is reflected in the solutions from Equations (21)–(23).

Values for k_0 and ϵ were derived by obtaining the numerical solutions of Equations (24) and (25) that were subject to the boundary conditions of Equations (26) and (27). These values were used to determine the diffusion coefficient of turbulent shear stress or viscosity D_{22}, according to Equation (20); of the Reynolds stresses, according to Equations (21) and (22); and of the kinetic energy k according to Equation (23). Predictions were compared with the DNS results for $Re_\tau = 10^4$ [7]. In Figures 1 and 2, kinetic energy k and the energy dissipation rate represented by $G = \kappa\epsilon x_2$ are presented as a function of distance from the wall $\frac{x_2}{H}$. In Figure 3, plots are presented of the diffusion constant according to Equation (20) and turbulent viscosity $\nu_t = -\frac{<u_1'u_2'>}{\frac{du_1}{dx_2}}$ according to the DNS. Figure 4 shows the distributions of the standard deviations of the three velocity fluctuations, both according to the model and the DNS. In Figure 5, mean velocities u_1 obtained through the integration of Equation (19) and obtained from the DNS are shown. Integration starts at $x_2 = \frac{100H}{Re_\tau}$ with a value of u_1 in accordance with its value for the boundary layer at this point. In all figures, the viscous layer at $0 < \frac{x_2}{H} < 0.01$ is omitted.

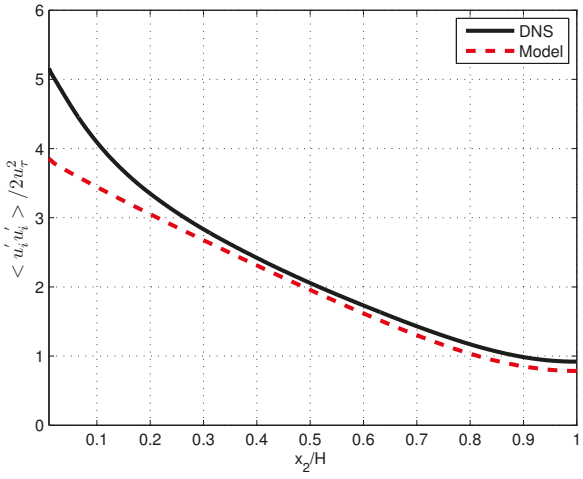


Figure 1. Dimensionless kinetic energy of fluctuations versus dimensionless distance from the channel wall $(0.01 \leq \frac{x_2}{H} \leq 1)$ according to DNS at $Re_\tau = 10^4$ and the anisotropic model.

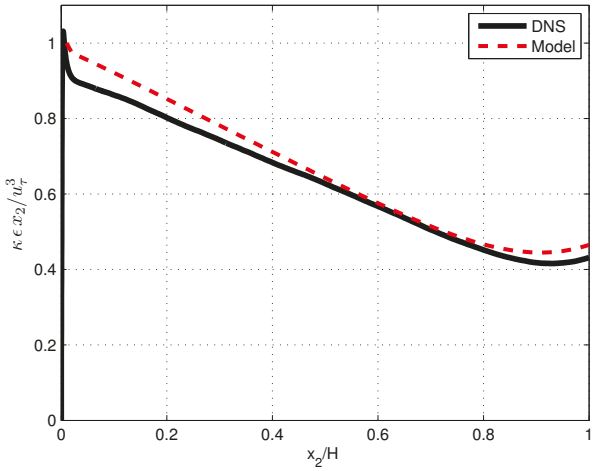


Figure 2. Dimensionless and normalised energy dissipation rate versus dimensionless distance from the channel wall $(0.01 \leq \frac{x_2}{H} \leq 1)$ according to DNS at $Re_\tau = 10^4$ and the anisotropic model.

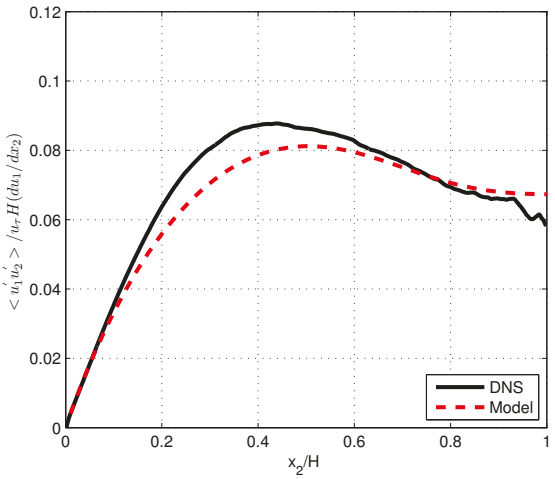


Figure 3. Dimensionless turbulent diffusion constant versus dimensionless distance from the channel wall $(0.01 \leq \frac{x_2}{H} \leq 1)$ according to DNS at $Re_\tau = 10^4$ and the anisotropic model.

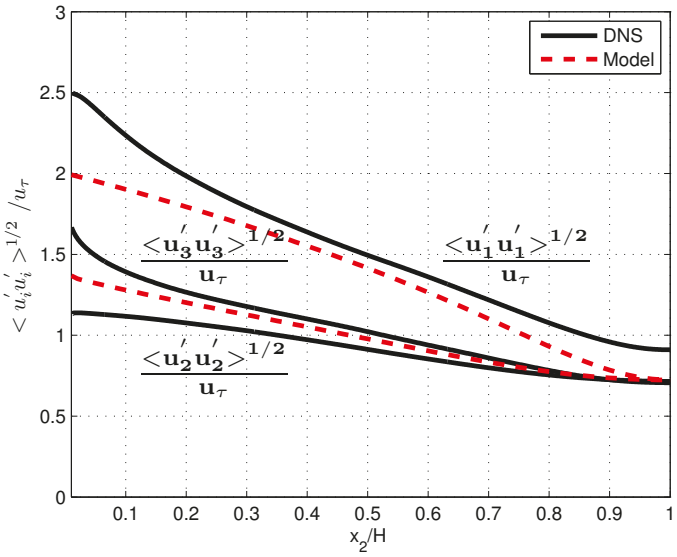


Figure 4. Dimensionless standard deviations of fluctuating velocities versus dimensionless distance from the channel wall ($0.01 \leq \frac{x_2}{H} \leq 1$) according to DNS at $Re_\tau = 10^4$ and the anisotropic model.

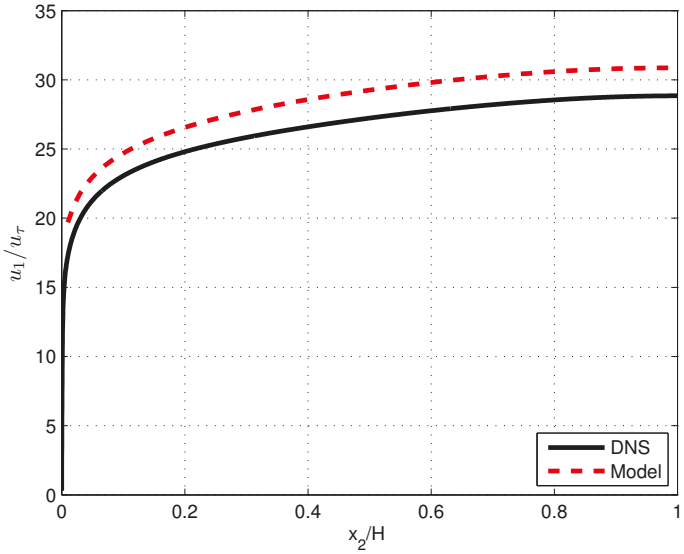


Figure 5. Dimensionless mean velocity versus dimensionless distance from the channel wall ($0.01 \leq \frac{x_2}{H} \leq 1$) according to DNS at $Re_\tau = 10^4$ and the anisotropic model.

8. Discussion of Results

Analytical expressions were given for turbulent diffusion and Reynolds stresses, describing their dependency on the gradients of mean flow. They are the result of further expanding previously published descriptions of these quantities [5] in powers of the inverse of the Kolmogorov constant C_0 while retaining the same truncation error (Section 3). Differences between the previously presented results for channel flow [5] and those of the upgraded model are limited. They are due to the direct or implicit inclusion of terms of an order higher than C_0^{-2} when using original Formulation (6), as was carried out in [5]; in the present upgraded model, such terms were dropped. Differences are indicative for the inaccuracy of truncation for both approaches. The advantage of the present model is that it provides a direct insight into the effect of mean flow gradients on parameters of turbulence. Moreover, implementation in a numerical code is much more easy as it circumvents the solution of complicated algebraic equations for covariances.

Predicted values of turbulent viscosity, turbulent diffusion of conservative scalars (temperature, passive admixture), and of mean velocity compare quite well with those of DNS of channel flow (Figures 3 and 5 and the results of ref. [8]). This contrasts with the predictions of the empirical basic k-ϵ model, revealing remarkable differences [5]. In the basic k-ϵ model, the turbulent diffusion coefficient is modelled by the following relation:

$$D_{ij} = c_\mu \frac{k^2}{\epsilon} \delta_{ij} \tag{28}$$

where c_μ is a calibration constant whose value is usually set to 0.09 [1–4]. Using DNS data for $\frac{k^2}{\epsilon}$, the value of the diffusion coefficient according to Equation (28) is seen to differ significantly from that of the DNS (Figures 1 and 2 of ref. [5]). Differences vary strongly with the distance from the wall, which indicates that the functional relationship according to Equation (28) is not a good representation of the turbulent diffusion of momentum [5]. It contrasts with the results of the present model. In case of channel flow, the second and third terms on the RHS of Equation (8) become zero when determining D_{22}, as is seen in Equation (20). Only the isotropic part of the general expression for diffusion remains in case of D_{22}. However, this isentropic representation differs from the semi-empirical model according to Equation (28). Firstly, Equation (20) does not contain a calibration factor, but it is specified by the universal Kolmogorov constant. Secondly, the value of the diffusion constant is determined by the kinetic energy associated with the isotropic state k_0. This parameter is smaller than the kinetic energy of anisotropic flow, as follows from Equation (9), and its dependency on distance from the wall is different as well. The result supports a favourable comparison of the present model with DNS (Figure 3).

Model results for kinetic energy and energy dissipation shown in Figures 1 and 2 are in satisfactory agreement with DNS. Results for the root mean squares of velocity fluctuations reveal basic trends of anisotropy (Figure 4). Deviations from DNS may be attributed to the omission of higher-order terms in the Langevin and diffusion equation, which were the origin of the present results.

The only fit factors in the model are c_k and σ_ϵ^*, which calibrate the magnitudes of the diffusion terms in the k-ϵ equations. Their effect on statistical predictions is limited to areas where turbulent shear stresses are small, e.g., in the core of channel flow [5].

9. Conclusions

The predictions of mean values of turbulence quantities using the anisotropic k-ϵ model show good to satisfactory agreement with the results of DNS of inhomogeneous anisotropic channel flow. Since important parts of the model are general, its application to other cases of turbulence has the potential of yielding good predictions as well. The equations underlying the model enable a straightforward implementation in a CFD code, starting from the code of the basic k-ϵ model.

Funding: This research received no external funding.

Informed Consent Statement: Not applicable.

Data Availability Statement: Data are contained within the article.

Acknowledgments: H.S. Janssen is acknowledged for performing numerical calculations; G.M. Janssen is acknowledged for preparing the manuscript.

Conflicts of Interest: Author J. J. H. Brouwers was employed by the company Romico Hold.VBA. The author declares that the research was conducted in the absence of any commercial or financial relationships that could be construed as a potential conflict of interest.

References

1. Hanjalić, K.; Launder, B. *Modelling Turbulence in Engineering and the Environment: Second-Moment Routes to Closure*; Cambridge University Press: Cambridge, UK, 2011.
2. Bernard, P.S.; Wallace, J.K. *Turbulent Flow: Analysis, Measurement and Prediction*; Wiley: New Jersey, NJ, USA, 2002.
3. Ansys Fluent 12.0, Theory Guide, Section 4 Turbulence, 4.4.1 Standard k-ϵ Model. Available online: https://www.afs.enea.it/ (accessed on 23 January 2009).
4. Comsol Multiphysics, The k-ϵ Turbulence Model. Available online: https://doc.comsol.com (accessed on 16 August 2024).
5. Brouwers, J.J.H. The Basic k-ϵ Model and a New Model Based on General Statistical Descriptions of Anisotropic Inhomogeneous Turbulence Compared with DNS of Channel Flow at High Reynolds Number. *Inventions* **2024**, *9*, 38. [CrossRef]
6. Hoyas, S.; Jiménez, J. Scaling of the velocity fluctuations in turbulent channels up to $Re\_\tau = 2003$. *Phys. Fluids* **2006**, *18*, 011702. [CrossRef]
7. Hoyas, S.; Oberlack, M.; Alcántara-Ávila, F.; Kraheberger, S.V.; Laux, J. Wall turbulence at high friction Reynolds numbers. *Phys. Rev. Fluids* **2022**, *7*, 014602. [CrossRef]
8. Kuerten, J.; Brouwers, J.J.H. Lagrangian statistics of turbulent channel flow at $Re\_\tau = 950$ calculated with direct numerical simulation and Langevin models. *Phys. Fluids* **2013**, *25*, 105108. [CrossRef]
9. Brouwers, J.J.H. Statistical Descriptions of Inhomogeneous Anisotropic Turbulence. *Mathematics* **2022**, *10*, 4619. [CrossRef]
10. Brouwers, J.J.H. Langevin equation of a fluid particle in wall-induced turbulence. *Theor. Math. Phys.* **2010**, *163*, 677–695.
11. Brouwers, J.J.H. Langevin and diffusion equation of turbulent fluid flow. *Phys. Fluids* **2010**, *22*, 085102. [CrossRef]
12. Brouwers, J.J.H. Statistical description of turbulent dispersion. *Phys. Rev. E Stat. Nonlinear Soft Matter Phys.* **2012**, *86*, 066309. [CrossRef] [PubMed]
13. Brouwers, J.J.H. Statistical Models of Large Scale Turbulent Flow. *Flow Turbul. Combust.* **2016**, *97*, 369–399. [CrossRef]
14. van Kampen, N.G. *Stochastic Processes in Physics and Chemistry*, 3rd ed.; Elsevier: New York, NY, USA, 2007.
15. Stratonovich, R.L. *Topics in the Theory of Random Noise*; Gordon and Breach: New York, NY, USA, 1967; Volume 1.
16. Landau, L.D.; Lifshitz, E.M. *Statistical Physics*; Elsevier: Amsterdam, The Netherlands, 2007.
17. Reichl, L.E. *A Modern Course in Statistical Physics*, 1st ed.; Wiley-VCH: New York, NY, USA, 2009.
18. Fertziger, J.H.; Kaper, H.G. *Mathematical Theory of Transport Processes in Gases*; North-Holland Publishing Company: Amsterdam, The Netherlands; London, UK, 1972.
19. Monin, A.S.; Yaglom, A.M. *Statistical Fluid Mechanics*; Dover: New York, NY, USA, 2007; Volume II, Chapter 8.
20. Sawford, B.L.; Yeung, P.K. Lagrangian statistics in uniform shear flow: Direct numerical simulation and Lagrangian stochastic models. *Phys. Fluids* **2001**, *13*, 2627. [CrossRef]
21. Pope, S.B. *Turbulent Flows*; Cambridge University Press: Cambride, UK, 2000.
22. Thomson, D.J. Criteria for the selection of stochastic models of particle trajectories in turbulent flows. *J. Fluid Mech.* **1987**, *180*, 529. [CrossRef]
23. Batchelor, G.K. *An Introduction to Fluid Dynamics*; Cambridge University Press: New York, NY, USA, 2006.
24. Monin, A.S.; Yaglom, A.M. *Statistical Fluid Mechanics*; Dover: New York, NY, USA, 2007; Volume I.

Disclaimer/Publisher's Note: The statements, opinions and data contained in all publications are solely those of the individual author(s) and contributor(s) and not of MDPI and/or the editor(s). MDPI and/or the editor(s) disclaim responsibility for any injury to people or property resulting from any ideas, methods, instructions or products referred to in the content.

inventions

MDPI

Article

Control on Flow Separation over a Cylinder by a Ferrofluid Film Adsorbed by a Magnet

Chunyun Wei [1,2], Hongjia Xie [1], Zixuan Liu [1], Xinfeng Zhai [1,*], Hongna Zhang [1,*] and Xiaobin Li [1]

[1] State Key Laboratory of Engines, School of Mechanical Engineering, Tianjin University, Tianjin 300350, China; weichunyun@tju.edu.cn (C.W.); xiehongjia@tju.edu.cn (H.X.); liu_zixuan@tju.edu.cn (Z.L.); in@tju.edu.cn (X.L.)

[2] School of Chemical Engineering and Technology, Tianjin University, Tianjin 300350, China

* Correspondence: zxf20pt@163.com (X.Z.); hongna@tju.edu.cn (H.Z.)

Abstract: Flow separation can lead to increased resistance and vibration generation, which is a difficult problem that cannot be ignored in engineering. In this paper, we propose a method of controlling flow separation by adsorbing ferrofluid onto the surface of a magnetized cylinder, taking the common flow around a cylinder as an example. Parametric effects of the ferrofluid film, including its viscosity and thickness, on the flow behavior were investigated in terms of the vortex shedding process, velocity distribution, dominant frequency, pressure distribution, and the flow motion inside the ferrofluid film. The results indicate that the ferrofluid film can suppress the generation of flow separation and achieve effective control, which is mainly caused by wall slip and the internal movement of the ferrofluid film. Furthermore, the flow separation control effect of ferrofluid thin films with different parameters varies, with low-viscosity ferrofluid exhibiting a superior control effect.

Keywords: flow separation; ferrofluid film; slip effect

1. Introduction

When fluid moves relative to a solid surface, a boundary layer forms and viscous forces act on the fluid near the surface. Flow separation from the solid surface often induces significant drag resistance, fluctuating lift force, structure vibration, and severe energy loss. Efficient control or elimination techniques of flow separation have long been the pursued target of engineers in various fields, such as chemical engineering, construction, water conservancy, marine engineering, and so forth [1–4]. So far, numerous techniques have been proposed to control or suppress flow separation, which can be generally divided into active and passive control techniques according to whether the external forces are exerted [5].

A passive flow control technique is mainly carried out by modulating the surface structure and geometry, such as applying surface grooving, attachment mounting, bionic structures, and so forth. For instance, Lee et al. achieved a 10% drag reduction in the vortex region by using a V-shaped notch on the surface of a cylinder, and they pointed out that the enhancement of a viscous-free fluid into the wake region is responsible for the achieved drag reduction [6,7]. Later, they found that spiral grooves are more effective in reducing the amplitude of vortex-induced microflow vibrations, which can reach 64% under proper conditions [8]. Wang et al. adopted slits to suppress the flow separation and found slits can destroy the extensive large-scale disordered vorticity induced by the pressure-side smooth airfoil to small-scale vortices induced by the coupled airfoil, which reduces the turbulence kinetic energy (TKE) generated during the flow separation [9]. In addition, the attachment mounting method can also suppress vortex generation as the interaction of the top and bottom sides of the shear layer. Gao et al. discovered that by mounting the attachment in a way that moves the interaction of vortex tails downstream, the vortex sheet elongates, and the TKE is significantly reduced [10]. In addition to the grooves and the

attachment, inspired by the silent flight and furry surfaces of birds, flow control methods for soft surfaces and furry brush-like structures are beginning to receive attention. Deng et al. designed a soft wake band that alters the vortex structure by separating the lower shear layer [11]. Brücker et al. found that furry surfaces reduce turbulent drag [12], and Hasegawa found that microfiber coatings delay flow separation [13]. Lin et al. proposed an adaptive furry microfiber surface drag reduction based on these experiences and found that nylon threads with appropriate lengths completely inhibit the trailing vortex shedding mode of the Kármen vortex street [14]. This passive control mechanism operates by utilizing nylon wires to elongate the unstable shear layer on both sides of the cylindrical model, thereby augmenting the length of vortex formation and propelling the vortex structure further downstream. The wake vortex shedding pattern of the Kárman vortex street is then suppressed.

The passive control techniques described above, although characterized by simplicity of operation and energy savings, are highly susceptible to vandalism and have the disadvantage of being extremely inflexible. They need to be designed specifically to cope with different surfaces. Active control, on the other hand, can actively change the flow by consuming external energy and controlling the system, which is adjustable and adaptable, responding and adjusting in real time as needed. It can be optimized for specific needs and provide more precise flow control. Nowadays, active flow control can be achieved by external energy input, such as rotating circular cylinders, surfactant release, microbubble method, magnetic fluid coating [15,16], and so forth. For example, the rotation of a circular cylinder changes the flow characteristics drastically, especially at high rotation rates. Tokumaru and Dimotakis achieved flow control by using a high-speed rotating cylinder. They discovered that the cylinder's rotation disrupted the symmetry of the wake flow, effectively controlling the process of vortex shedding [17]. Lam et al. found that as the rotational speed of the cylinder increases, the wake becomes narrower and deflected to the side, and the length of the vortex becomes smaller [18]. This leads to a slight increase in the frequency of vortex shedding. However, their efficiency is not particularly high. Releasing viscoelastic fluids near the turbulent boundary layer is also an active control method. In 1949, Toms reported the turbulence-damping effect of dilute solutions of polymers [19]. In the 1970s, surfactants with non-Newtonian fluid properties (later called viscoelastic fluids) were also found to reduce turbulent drag. This method provides high economic and environmental benefits in reducing drag and increasing transport in pipelines such as heating and cooling pipelines [20]. The active drag reduction by viscoelastic fluid can be achieved by continuously injecting viscoelastic fluid from both sides of the wall [21]. The microbubble method is another type of active control technique where drag reduction is achieved by somehow generating microbubbles and distributing them on the cylindrical surface to change the flow in the boundary layer. A large number of experiments have verified the drag-reduction performance of microbubbles. Bubble sizes in the tens of microns have a better drag-reduction effect [22,23]. A significant drag-reduction effect can be achieved by generating a large number of bubbles and making them stably attached within the turbulent boundary layer. The generation of microbubbles can be obtained by electrolysis, coating, and air jet methods, but all these microbubble generation methods require the installation of specific equipment.

However, it is notable that the above active control techniques consume a large amount of external energy. Drag reducers are difficult to maintain on the surface, which requires the constant release of liquid to form a liquid film and a dedicated space within the wall to store them. If applied to a navigational body, it would result in a significant reduction in space utilization, offsetting the economic benefits of drag reduction, and would be prone to impacts on the surrounding environment. Different from the above−mentioned methods, Krakov proposed the concept of magnetic fluid coating in 1984 and found that this method has a positive effect on the free flow structure [24]. Moreover, Krakov and Kamiyama systematically studied the changes in the flow field structure and the drag-reduction effect when a circle cylinder was coated with the magnetic fluid. The results showed that the

magnetic fluid layer could effectively prevent flow separation and the drag-reduction effect determined by the viscosity ratio between the magnetic fluid and the outer fluid [25]. Stancanelli et al. reported a drag-reduction technique involving a ferrofluid drag-reduction method using a permanent magnet-adsorbed ferrofluid to form a liquid film as a smooth surface to achieve wall slip, which reduced the drag in the inner pipe by more than 80% [26]. However, the stability of the magnetic fluid layer around the solid wall is a key factor in limiting the application of magnetic fluid coating. Krakov et al. experimentally investigated the stability of kerosene-based magnetic fluid in a glass tube. The results showed that the magnetic fluid layer waves became greater and even broke off as flow rates increased [27].

Above all, most scholars paid more attention to the qualitative analysis and the explanation of the flow control mechanism and less to the analysis of quantitative parameters. In this paper, we investigate the flow control effect of ferrofluid in external flow. To this end, the control performance of ferrofluid film for the flow separation over a cylinder is evaluated. A thin film of ferrofluid is absorbed on a cylinder magnet to alter the flow characteristics. This paper mainly examines the parametric effect including the viscosity and the thickness of the ferrofluid film on the flow performance such as pressure distribution, vortex shedding frequency, and so forth. Additionally, the flow motion inside the ferrofluid film is also investigated to understand the ferrofluid effect on flow separation.

2. Materials and Methods

2.1. Flow Configuration

Figure 1 illustrates the flow configuration, which consisted of three domains: a permanent magnet cylinder, a ferrofluid wrapped around the cylinder with a certain thickness, and a domain of water flow. In this case, the radius of the cylinder with magnetism was set to 2.0 mm; the thickness of the ferrofluid wrapped around the cylinder was set to 0.05 mm, 0.10 mm, and 0.15 mm, respectively; the length of the water basin was 100 mm, and the width was 30 mm. To ensure simplicity and validity, we made the following assumptions during the numerical simulations: (1) the flow was assumed to be incompressible; (2) there was no mass transfer between the ferrofluid and water; (3) changes in fluid properties due to temperature were not considered; and (4) the gravitational force was neglected.

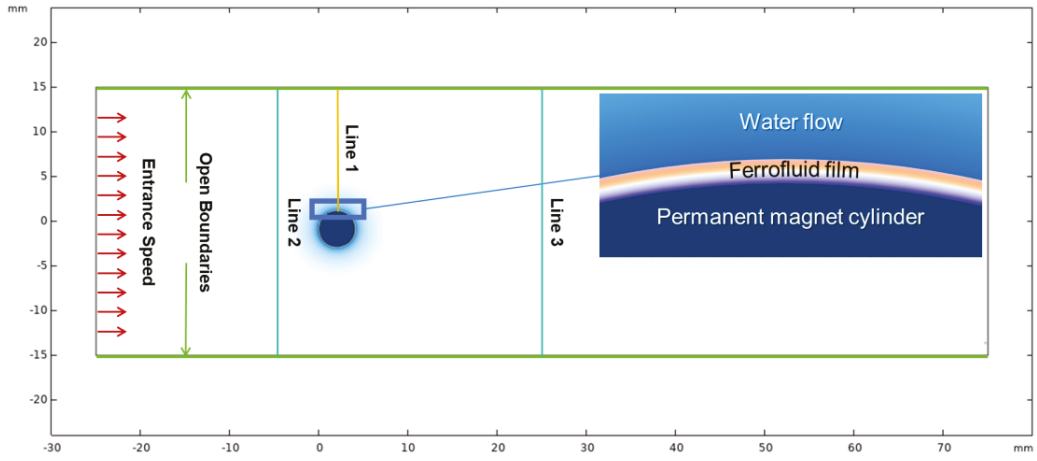


Figure 1. Schematic of the flow configuration.

Table 1 shows the detailed properties of ferrofluid. In this study, we chose the ferrofluid to be an oil phase liquid immiscible with water, and the surface tension between the ferrofluid and water was set to be 0.18 N/m. The cylinder was set to be a nonslip wall. In addition, the left boundary was the inlet with constant entrance velocity, the right boundary was the outlet with the atmosphere pressure, and the upper and lower boundaries were open boundaries. Table 2 displays the flow conditions applied in the simulation. The Reynolds number (Re) is defined by $Re = \rho u D/\mu$, where ρ is the fluid density, u is the

incoming velocity, D is the cylinder diameter, and μ is the fluid viscosity; Δ represents the thickness of the ferrofluid film.

Table 1. Material properties.

Material	ρ (kg/m^3)	μ (Pa·s)	Δ (mm)
Water	1000	0.001	/
Ferrofluid	1200	0.006, 0.06, 0.6	0.05, 0.1, 0.15

Table 2. Flow conditions.

u (m/s)	Re
0.075	300
0.1	400
0.125	500

2.2. Numerical Method

To track the interface movement and the phase distributions in two fluids, we used the level-set method in this study. The level-set method is known for its ability to capture interface curvature accurately and good conversation, which is crucial in analyzing thin ferrofluid films [28,29]. In this method, the phase field ϕ is used to denote the volume ratio of the ferrofluid, assuming two distinct values, namely $\phi = 1$ to characterize the water phase and $\phi = 0$ for the ferrofluid phase. The interface between the two mediums is represented by $\phi = 0.5$. The level-set equation is as follows:

$$\frac{\partial \phi}{\partial t} + u \cdot \nabla \phi = \gamma \nabla \cdot \left(\varepsilon_{ls} \nabla \phi - \phi(1-\phi) \frac{\nabla \phi}{|\nabla \phi|} \right) \tag{1}$$

where ε_{ls} is the thickness of the interface. Here, we set ε_{ls} to be equal to half of the largest mesh size in the computational domain to ensure simulation accuracy and make sure it is much smaller than the thickness of the ferrofluid film [30]. Additionally, γ represents the reinitialization parameter. Large values of the γ lead to calculation errors, while small values of γ create interface instability. Consequently, in this study, γ was determined by the maximum fluid velocity in the fluid field [28].

The two-phase flow can be described by the incompressible Navier–Stokes equation, which incorporates supplementary force terms in addition to the body force resulting from the magnetic field and surface tension. The governing equation is as follows:

$$\begin{array}{l} \rho_i \frac{\partial \boldsymbol{u}}{\partial t} + \rho_i (\boldsymbol{u} \cdot \nabla) \boldsymbol{u} = \nabla \cdot [-p\boldsymbol{I} + \boldsymbol{\sigma}] + \boldsymbol{f_s} + \boldsymbol{f_k} \\ \rho_i \nabla \cdot \boldsymbol{u} = 0 \end{array} \tag{2}$$

where $\boldsymbol{u}$ represents the velocity of the fluid, p represents the pressure exerted on the fluid, and $\boldsymbol{\sigma} = \boldsymbol{\mu_i}\left(\nabla \boldsymbol{u} + (\nabla \boldsymbol{u})^{\boldsymbol{T}}\right)$ represents the viscous shear stress. The effective density ρ_i and dynamic viscosity μ_i are, respectively, defined as follows:

$$\rho_i = \rho_m + (\rho_w - \rho_m)\phi \tag{3}$$

$$\mu_i = \mu_m + (\mu_w - \mu_m)\phi \tag{4}$$

where w represents the water field, and m represents the ferrofluid field. In addition, $\boldsymbol{f_s}$ is the surface tension exerted on the interface between the ferrofluid phase and the water phase, and magnetic stress is in the form of the volume force, namely $\boldsymbol{f_k}$, which is calculated using the following equation:

$$\boldsymbol{f_K} = \mu_0 (\boldsymbol{M} \cdot \nabla) \boldsymbol{H} + \frac{\mu_0}{2} \nabla \times (\boldsymbol{M} \times \boldsymbol{H}) \tag{5}$$

where $\boldsymbol{M}$ is the fluid magnetization, and $\boldsymbol{H}$ represents the magnetic field strength. The fluid magnetization $\boldsymbol{M}$ can be solved as follows:

$$\boldsymbol{M} = \chi \boldsymbol{H} \tag{6}$$

where χ represents the magnetic susceptibility of the fluid. In natural and thermomagnetic convection, the fluid velocity is low, and a steady-state magnetic field is applied. Therefore, it can be assumed that the magnetic moment is always aligned with the external magnetic field, and there is no magnetic dissipation in the fluid. Consequently, the last term in Equation (5) can be neglected [31]. The process of ferrofluid adsorption was simulated using the volume force in the magnetic field-coupled laminar flow. The magnet used in this case, like most magnets, was nonconductive. Maxwell's system of equations can be simplified as follows:

$$\begin{cases} \nabla \times \boldsymbol{H} = 0 \\ \nabla \cdot \boldsymbol{B} = 0 \end{cases} \tag{7}$$

where $\boldsymbol{B}$ represents the strength of the magnetic induction. In the ferrofluid field, magnetic induction and magnetic field can be calculated as follows:

$$\boldsymbol{B} = \mu_0(1 + \chi)\boldsymbol{H} \tag{8}$$

where μ_0 is the vacuum permeability and has the value $4\pi \times 10^{-7}$ H/m. In this study, the cylinder was assumed to be a permanent magnet, with the constitutive relation defined by its remanent flux density, expressed as follows:

$$\boldsymbol{B} = \mu_0(1 + \chi)\boldsymbol{H} + \boldsymbol{B_r} \tag{9}$$

where $\boldsymbol{B_r}$ is the remanent flux density of the permanent magnet after the removal of an external magnetic field, and it is defined as follows:

$$\boldsymbol{B_r} = ||\boldsymbol{B_r}|| \frac{\boldsymbol{e}}{||\boldsymbol{e}||} \tag{10}$$

where $\boldsymbol{e}$ represents the direction of the magnetic field. The influence of ferrofluid on the magnetic field was ignored [28].

2.3. Numerical Procedures

The numerical models were solved using COMSOL Multiphysics 6.1, involving two main steps: phase initialization and transient calculation. Phase initialization utilizes steady-state equations for laminar flow, magnetic field, and level-set function, while transient calculation employs their respective transient equations. To manage the fluid flow and the two-phase interface movement, we utilized the coupling of the laminar flow field and the level-set method. In this study, the permanent magnet cylinder employed the remanent flux density constitutive relation as depicted in Equation (9). The value of $\boldsymbol{B_r}$ was set to 250 mT, oriented along the y-axis. The resulting magnetic field distribution is illustrated in Figure 2.

To guarantee the convergence and the accuracy of transient numerical simulations, a fine mesh was used to capture the phase interface, which was refined at the phase interfaces of ferrofluid and water. The grid independence validation was first performed. Considering a ferrofluid with μ = 0.6 Pa·s and Δ = 0.1 mm, the mesh with 53,750 domain cells and 864 boundary cells was used. Moreover, a small time step of 0.001 s was used during the transient simulation, and a tolerance of 10^{-6} was set to ensure convergence of the numerical results. To verify the reliability of the current numerical simulation, we calculated the Strouhal number (St) for the case of *Re* = 300 and compared it with the ones obtained using the empirical formula proposed by Norberg [32]. The comparison results are shown in Table 3. It can be concluded that the error is just 0.79%, indicating that the chosen numerical model and simulation method are reliable.

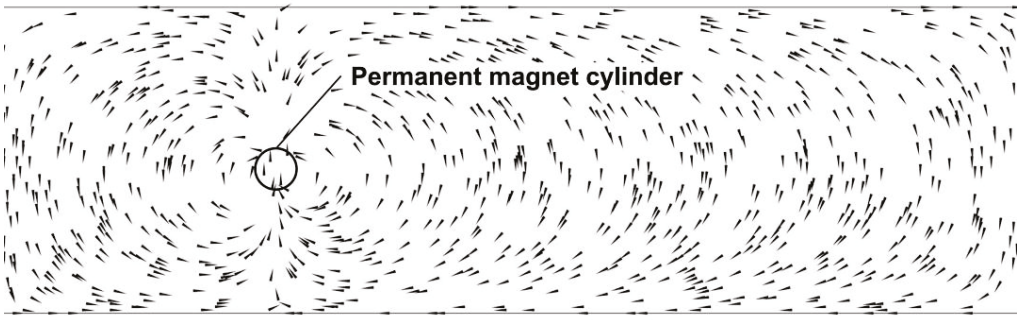


Figure 2. The distribution of the magnetic field for the cylinder magnetic strength at 250 mT.

Table 3. The comparison of the St number between numerical simulation and empirical function.

Re = 300	St	Error
Numerical simulation	0.2000	0.79%
Empirical function	0.2016 [32]	

3. Result and Analysis

3.1. Vortex Shedding Process

Firstly, to have an intuitive image of the ferrofluid film effect on the flow, we analyzed the vortex shedding process for the clean cylinder (clean case) and the cylinder wrapped with ferrofluid film (CF case), as illustrated in Figures 3 and 4. Here, the case with Δ = 0.1 mm at *Re* = 500 is chosen as an example. This process begins by observing the formation of two symmetric vortices in the wake of the cylinder. The edge length of these vortices increases with time. Subsequently, a vortex is formed in the center of the wake and is gradually elongated and compressed as the tail flow swings downward. Then, the vortex detaches from the wake during its upward swings. This entire process takes approximately 0.68 s for the clean cylinder. The process of vortex shedding in the presence of ferrofluid film is similar to that in the clean cylinder case, as shown in Figure 4. However, given the same initial condition, the width and the length of the wake increase significantly, leading to a larger vortex area and longer vortex shedding time by about 0.05 s delayed compared to the clean case cylinder.

Two factors, i.e., slightly larger cylinder diameter and the slip effect induced by the ferrofluid film, could be responsible for the different behaviors of the vortex shedding. To clarify whether the formation of ferrofluid-induced vortices is due to a slight increase in diameter, we conducted a control test using a clean cylinder with a diameter of 2.1 mm (named Cylinder B), which was equal to the diameter of the ferrofluid-wrapped cylinder. Figure 5 compares the vortex behavior for the clean cylinder cases with different diameters and the case of a ferrofluid-wrapped cylinder. It can be observed that in spite of the same overall diameter, the wake size of Cylinder B is still significantly smaller than that of the ferrofluid-wrapped cylinder case in Figure 5a. Little difference can be found in the first vortex shedding time between the cylinder with a diameter of 2.1 mm and the smaller cylinder with a diameter of 2.0 mm, as shown in Figure 5b. Therefore, we argue that the different behaviors of vortex shedding do not originate from the increase in the cylinder diameter but from the additional effect induced by the ferrofluid film.

Furthermore, to quantify the ferrofluid film effect on the vortex shedding, Figure 6 illustrates the energy spectrum in the frequency domain by fast Fourier transform (FFT) of the velocity signal at different locations and flow conditions. Here, six locations correspond to the points at (2, 4), (12, 4), (22, 4), (32, 4), (32, 0), and (32, −4). Figure 7a–c focus on the comparison between the ferrofluid-wrapped case of μ = 0.06 Pa·s and Δ = 0.1 mm and the clean case for different *Re* at the location of (32, 0). As can be seen, the existence of ferrofluid film leads to a significant reduction in the dominant frequency at all six locations compared with those of the clean cases at all *Re*, and this effect is stronger for ferrofluid films with viscosities of 0.006 Pa·s and 0.6 Pa·s. To more intuitively characterize

the effect of the ferrofluid film on the lift fluctuations, we collected data on the lift coefficient C_L of the cylinder for different cases and calculated its dominant frequency. Here, the dominant frequency is the frequency with the largest amplitude in the energy spectrum of the lift coefficient.

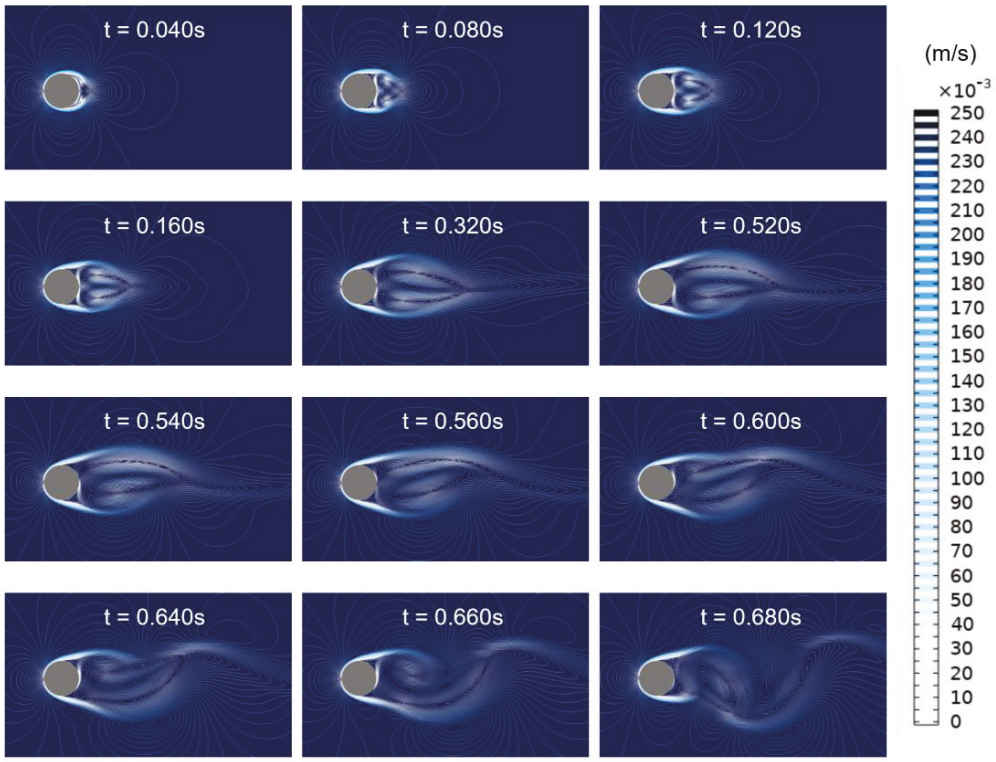


Figure 3. The process of vortex shedding for the case of the clean cylinder at Re = 500.

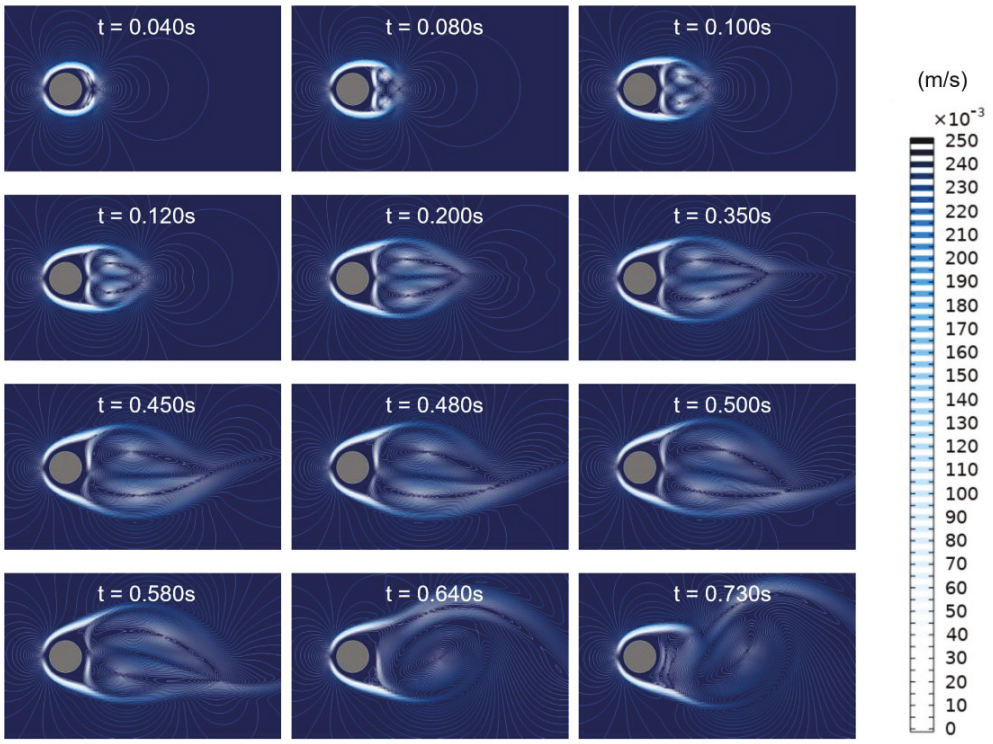


Figure 4. The process of vortex shedding for the case of the ferrofluid−wrapped cylinder at Re = 500, where μ = 0.06 Pa·s and Δ = 0.1 mm, respectively.

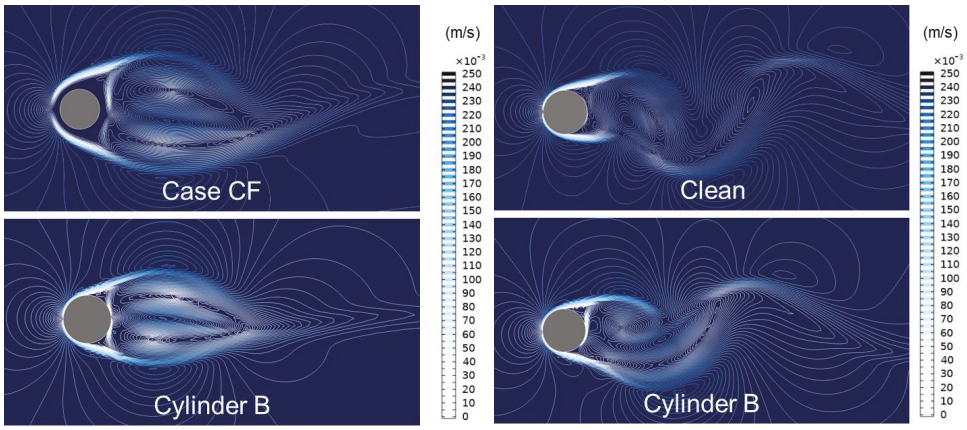


Figure 5. The effects of cylinder thickness on flow field at *Re* = 500: (**a**) t = 0.48 s, (**b**) t = 0.68 s.

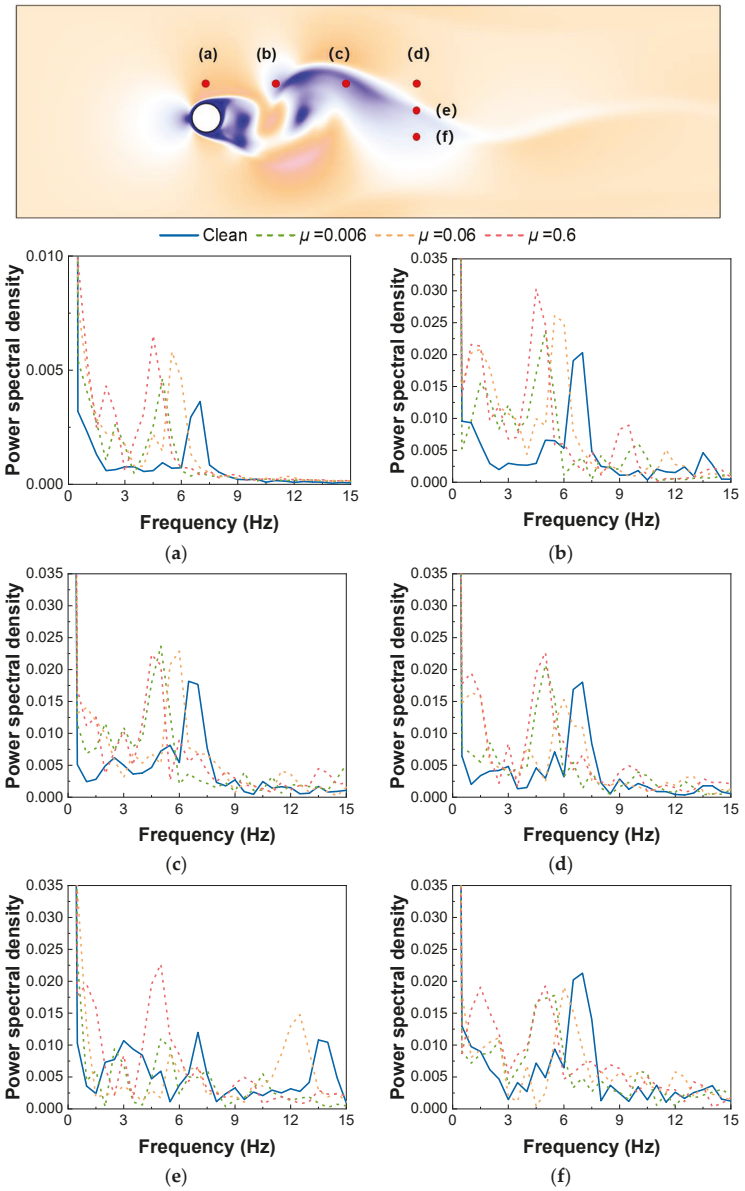


Figure 6. Comparisons of the energy spectrum in the frequency domain of the velocity at different locations and flow conditions: (**a**) (2, 4), (**b**) (12, 4), (**c**) (22, 4), (**d**) (32, 4), (**e**) (32, 0), (**f**) (32, −4).

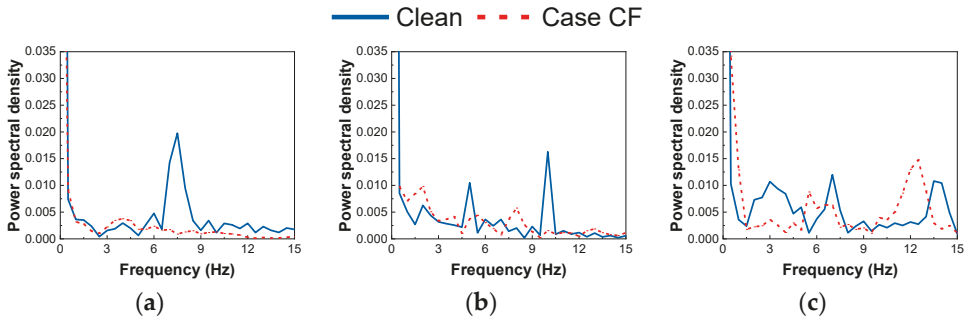


Figure 7. Comparison of clean case and ferrofluid-wrapped case with μ = 0.06 Pa·s and Δ = 0.10 mm different *Re* at the location of (32, 0): (**a**) *Re* = 300, (**b**) *Re* = 400, (**c**) *Re* = 500.

Figure 8 analyzes the thickness effect of ferrofluidic film on the suppression of vortex shedding under different conditions. It can be observed that as the ferrofluid thickness increases, the dominant frequency distribution of vortex shedding becomes more focused, with a tendency for the dominant frequency to decrease. Among them, the thickness of 0.15 mm demonstrates the most effective suppression of vortex shedding. Figure 9 further demonstrates the effects of ferrofluid viscosity on the dominant frequency of the lift coefficient. An apparent decrease in dominant frequency can be observed. After further calculations, we observed about 15.38% to 46.81% of the lift coefficient's dominant frequency attenuation effect.

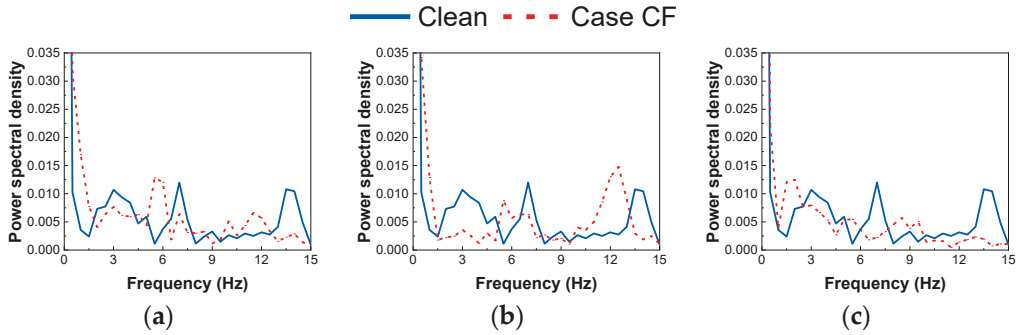


Figure 8. Thickness effect of the ferrofluid film on the energy spectrum of the velocity at *Re* = 500 with μ = 0.06 Pa·s: (**a**) Δ = 0.05 mm, (**b**) Δ = 0.10 mm, (**c**) Δ = 0.15 mm.

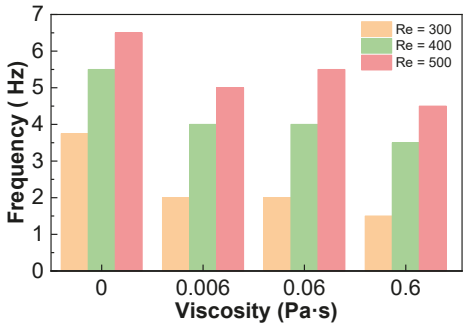


Figure 9. Viscosity effect of ferrofluid film with Δ = 0.1 mm on the dominant frequency of lift coefficient at different *Re*.

3.2. Velocity Distribution

We then evaluated the ferrofluidic film effect on the wake size. Figure 10 illustrates the ferrofluidic film on the temporally averaged velocity field $\overline{v}$ at *Re* =300. Here, $\overline{v} = \int_0^T v dt/T$, where T is the integrated time. It can be observed that in the clean case, a recirculation region is formed on the lee side of the flow field due to the flow separation on both sides of the cylinder and an upward shift of the vortex separation point. Furthermore, within this region, a pair of

vortices is distributed symmetrically around the centerline, and this vortex pair is the main cause of the uneven pressure distribution around the cylinder [14]. Similar flow characteristics appear in the case of a ferrofluid-wrapped cylinder. However, unlike those of clean cases, the length and width of the wake significantly enlarge. The vortices in the wake of the clean case both appear to be squeezed and move downstream. Consequently, the streamline between the wake and the cylinder becomes more regular in the case of ferrofluid-wrapped cylinder. In other words, the existence of the ferrofluid film changes the structure of the flow field and makes the streamline distribution more stable, which suppresses the flow separation. Furthermore, Figure 11 shows the parametric effects, including the viscosities and thickness of ferrofluidic film, on the mean velocity distribution at different *Re*. As can be seen, the ferrofluid film with lower viscosity and larger thickness is more effective in reducing vortex strength and enlarging the wake region. This is further demonstrated by the viscosity and thickness effect on the wake length, as shown in Figure 12.

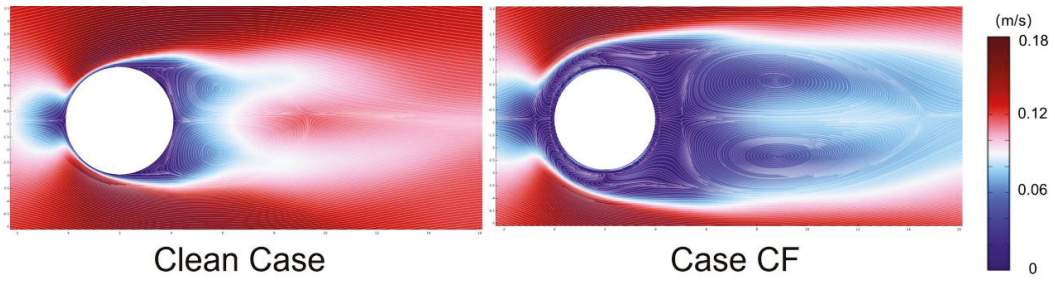


Figure 10. Comparison of the mean velocity distribution between the clean case and the ferrofluid−wrapped case with μ = 0.06 Pa·s and Δ = 0.10 mm at *Re* = 300.

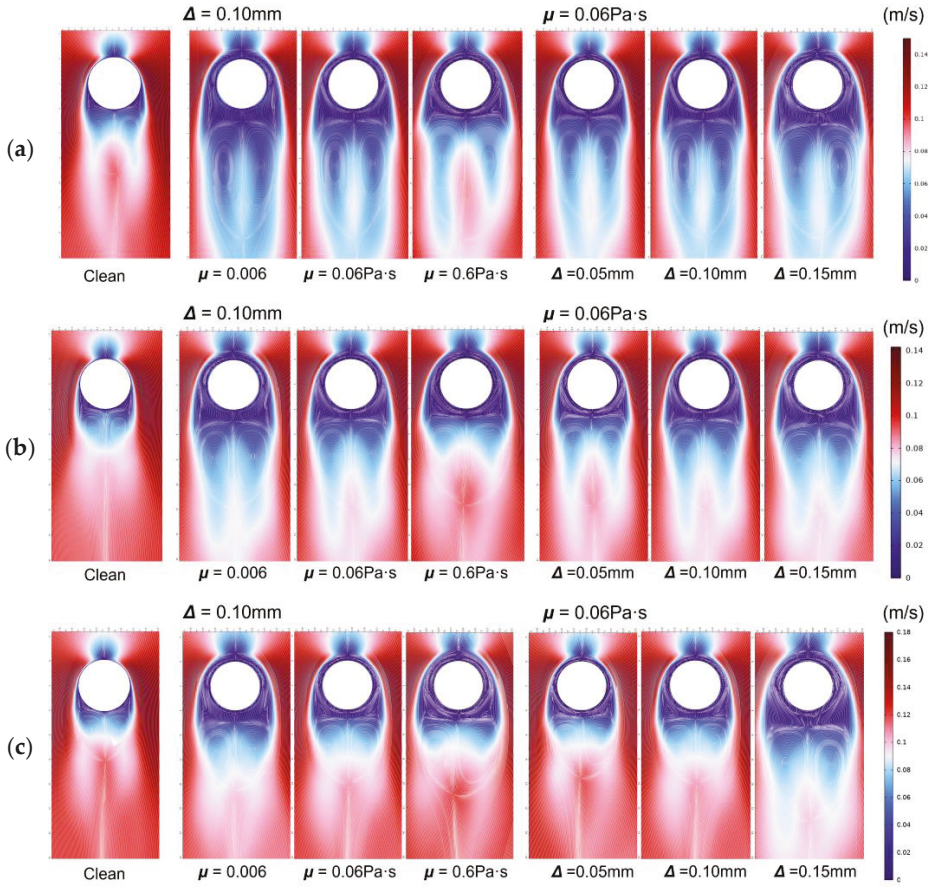


Figure 11. Ferrofluid viscosity and thickness effect on the mean velocity distribution under different situations: (**a**) *Re* = 300; (**b**) *Re* = 400; (**c**) *Re* = 500.

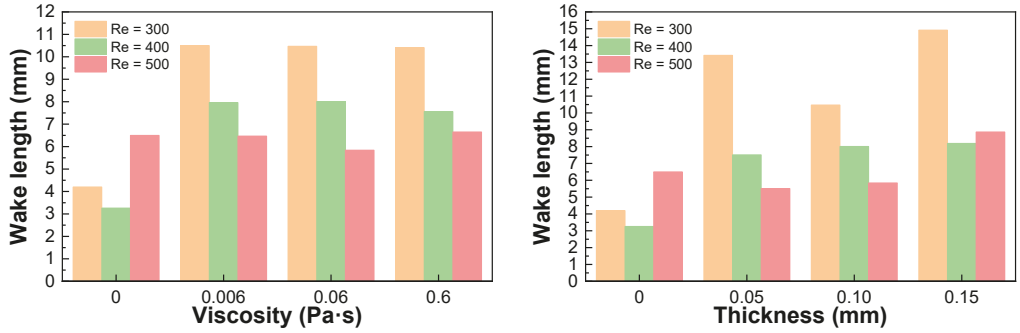


Figure 12. The effects of ferrofluid viscosity and thickness on the wake length under different situations: (**a**) Viscosity effect, (**b**) Thickness effect.

Figure 13 further illustrates the temporally averaged velocity profile $\overline{v}$ on the vertical line above the cylinder at different *Re* and ferrofluid properties. As is clearly shown, the $\overline{v}$ curve shows a smooth rise in the clean case, whereas in the case of the ferrofluid-wrapped cylinder, the $\overline{v}$ curve is divided into two phases: First, $\overline{v}$ in the region of the ferrofluid shows an approximation to 0, and then, starting from the interface of the ferrofluid, $\overline{v}$ rises sharply, and finally in the case of the ferrofluid-wrapped cylinder, it exceeds the clean case. This means that in the clean case, the fluid shows nonslip behavior on the cylinder wall, whereas in the case of the ferrofluid-wrapped cylinder, a velocity slip exists. The above results are consistent with those reported by Stancanelli et al. [26]. Ferrofluidic films can reduce the shear rate near the wall during fluid flow by introducing velocity slips. To further investigate the effect of the viscosity of the ferrofluid film on the slip phenomenon, we selected ferrofluids with different viscosities to observe the slip phenomenon. Figure 14 shows the slip phenomenon of ferrofluid with different viscosities, and we can observe that the lower the viscosity of the ferrofluid film, the larger the slip effect. Therefore, we argue that the wall slip widens the wake of the flow separation, which slows down the vortex formation and shedding.

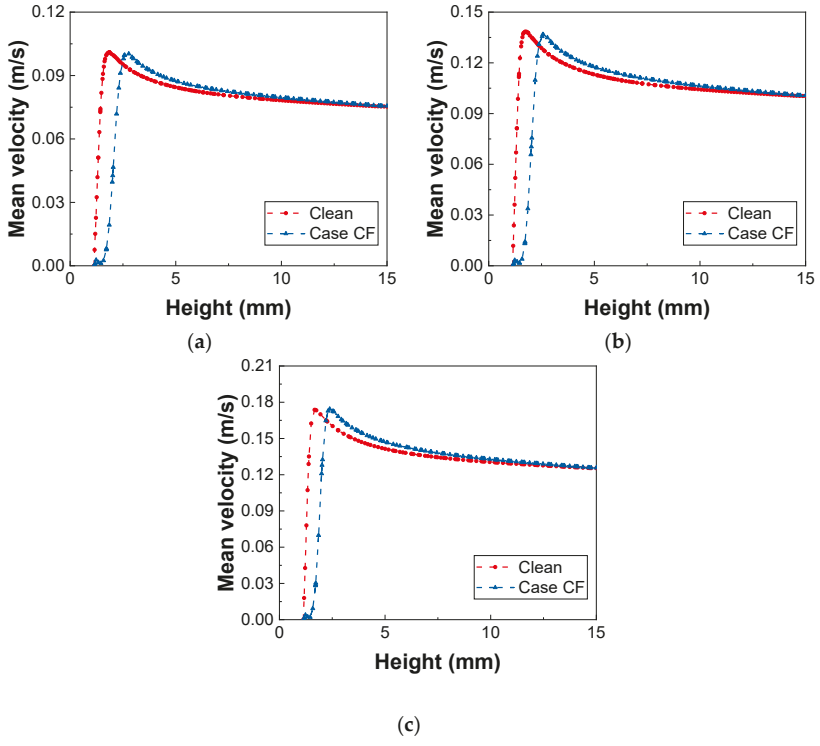


Figure 13. Slip phenomena on ferrofluid surfaces with different *Re*: (**a**) *Re* = 300, (**b**) *Re* = 400, (**c**) *Re* = 500.

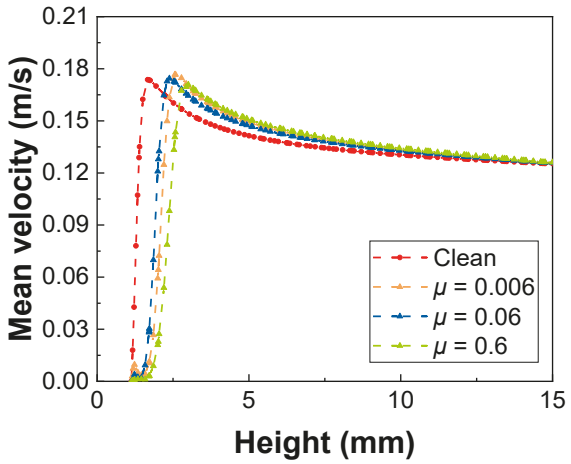


Figure 14. Slip phenomena on ferrofluid surfaces with different viscosities.

3.3. Pressure Distribution

Figure 15 illustrates the effect of ferrofluid film on the pressure distribution of the flow filed under different *Re* values. Similar to the mean velocity, the time-averaged pressure field $\overline{p}$ is calculated by $\overline{p} = \int_0^T pdt/T$, with p the pressure at each point. It can be observed that the mean pressure on the windward and leeward sides of the cylinder are reversed and that in some areas of the wake, the mean pressure is opposite to the mean pressure on the leeward side. This inversion becomes more pronounced as *Re* increases. In the case of a cylinder wrapped with ferrofluid, a widening range of color changes can be observed compared with the clean case on both the windward and leeward sides, suggesting that the pressure gradient decreases. To quantify the ferrofluid film effects on the pressure distribution, the mean pressure rates on two vertical lines on the windward and leeward sides are given in Figure 16 under different *Re* values. As can be seen, on the windward side, the depression of the pressure line in the case of the ferrofluid-wrapped cylinder is significantly deeper than that in the clean case, and the mitigating effect becomes more pronounced as *Re* increases. An opposite situation occurs on the leeward side, where the fluctuation of the pressure line in the case of the ferrofluid-wrapped cylinder is significantly lower than that in the clean case. The fluctuation of the leeward side pressure plateau is significantly slowed down under the control of the ferrofluid-wrapped cylinder, which suppresses the generation and fluctuation of lift. Figure 17 further demonstrates the parametric effect of ferrofluidic films on the mean pressure distribution on both the windward and leeward sides. It indicates that all ferrofluid films of different viscosities change the distribution of pressure on the windward side. Moreover, ferrofluids of different viscosities all slow down the pressure fluctuations on the leeward side, and unlike the windward side, this slowing effect becomes more pronounced as the viscosity of the ferrofluid film decreases. Based on the control effect of ferrofluid films with different viscosities, we suggest that low-viscosity ferrofluid films are more beneficial in slowing down the main frequency of the lift coefficient, as demonstrated above.

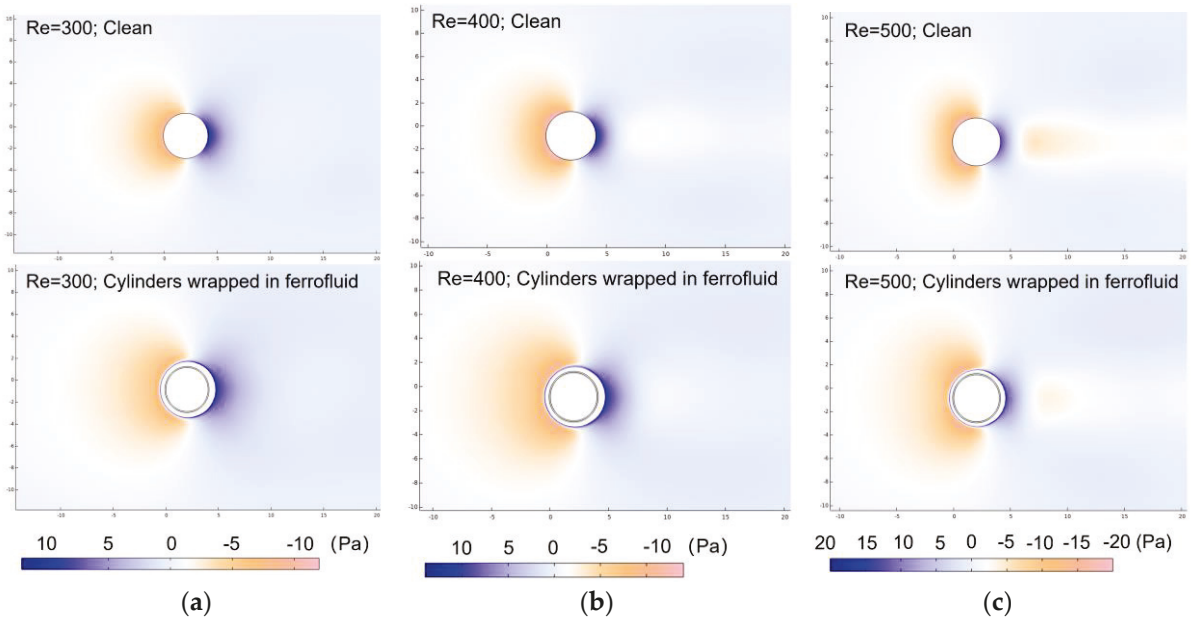


Figure 15. Comparison of pressure distribution between the clean case and the ferrofluid-wrapped case with μ = 0.06 Pa·s and Δ = 0.10 mm: (**a**) *Re* = 300, (**b**) *Re* = 400, (**c**) *Re* = 500.

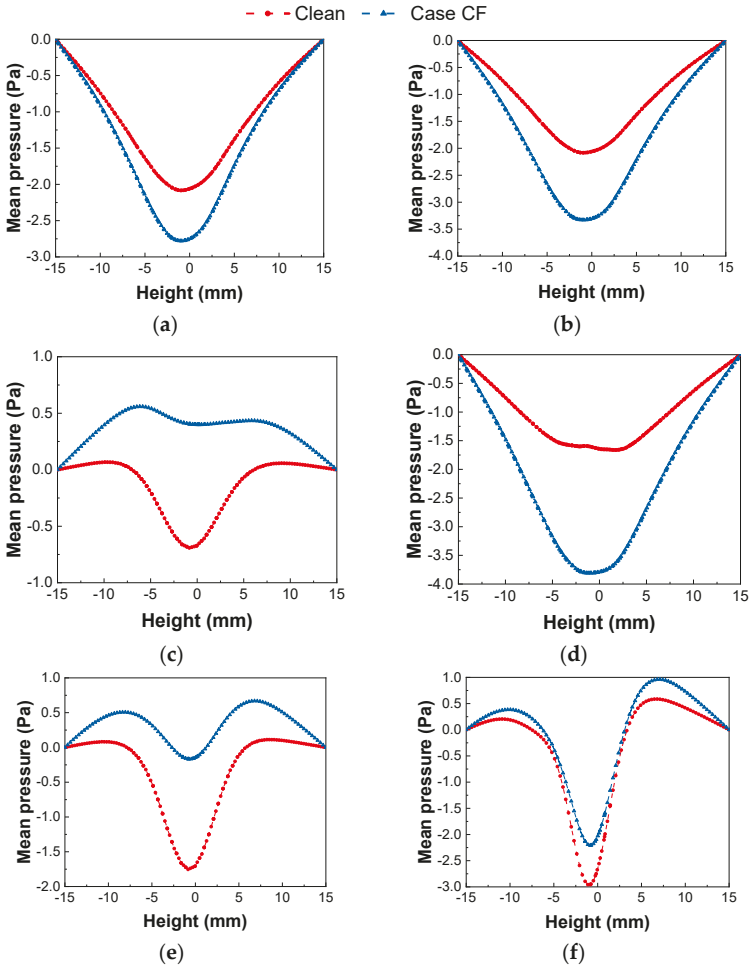


Figure 16. Comparison of pressure distribution between the clean case and the ferrofluid-wrapped case with μ = 0.06 Pa·s and Δ = 0.10 mm along Line 2 ((**a**) *Re* = 300, (**b**) *Re* = 400, and (**c**) *Re* = 500) and along Line 3 ((**d**) *Re* = 300, (**e**) *Re* = 400, and (**f**) *Re* = 500).

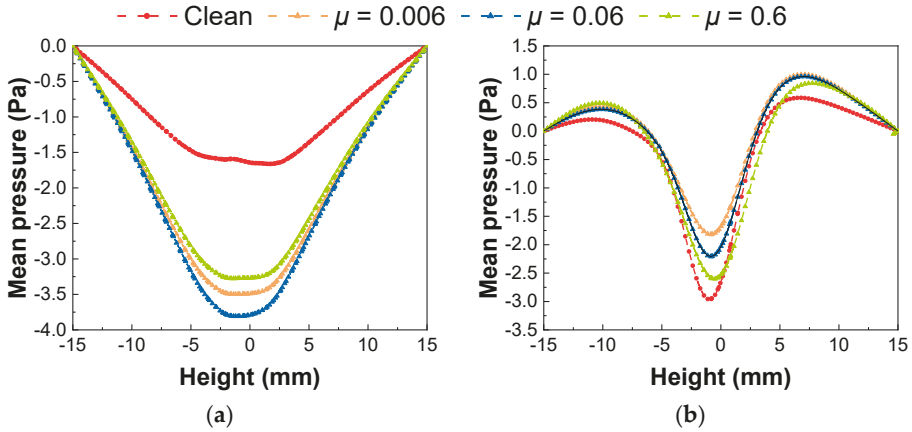


Figure 17. Ferrofluid viscosity effect on the mean velocity distribution under different situations on the windward and leeward sides: (**a**) Line 2 and (**b**) Line 3.

3.4. Flow Motion inside the Ferrofluid

Finally, to understand the ferrofluid film effect obtained above, we illustrate the flow motion inside the ferrofluid film. Here, the case of a ferrofluid with μ = 0.06 Pa·s and Δ = 0.10 mm and Re = 500 is selected as an example. Figures 18 and 19 show the flow evolution at different stages. Generally, the flow motion inside the ferrofluid film can be divided into three stages. At first, a closed recirculation loop is formed. Meanwhile, the surface of the ferrofluid becomes fluctuating. The change in the direction of the velocity inside the ferrofluid film may be related to the increase in wall slip, as this change is more pronounced as the viscosity decreases (as shown in Figure 19). This induces wall slip. Then, with the flow of water, the velocity direction of the outer surface of the ferrofluid remains essentially the same as that of water, while the internal velocity direction forms a closed loop. During the third stage, vortices are generated, causing periodic fluctuations in the velocity direction of the ferrofluid due to the vortex shedding. The period of fluctuation in the velocity direction is approximately the same for the three viscous ferrofluids, and no linear relationship is found. The streamline in the upper and lower parts of the closed loop exhibits approximate symmetry. Therefore, it can be inferred that the magnetic liquid creates a recirculation area where it comes into horizontal contact with the water flow, as confirmed by Stancanelli [26,33]. The detailed flow motion inside the ferrofluid film is shown on the right of Figure 20. It can be observed that the surface of the magnetic liquid fluctuates. In combination with the aforementioned slip, it can be assumed that the flow field generates a drag-reduction effect at this interface.

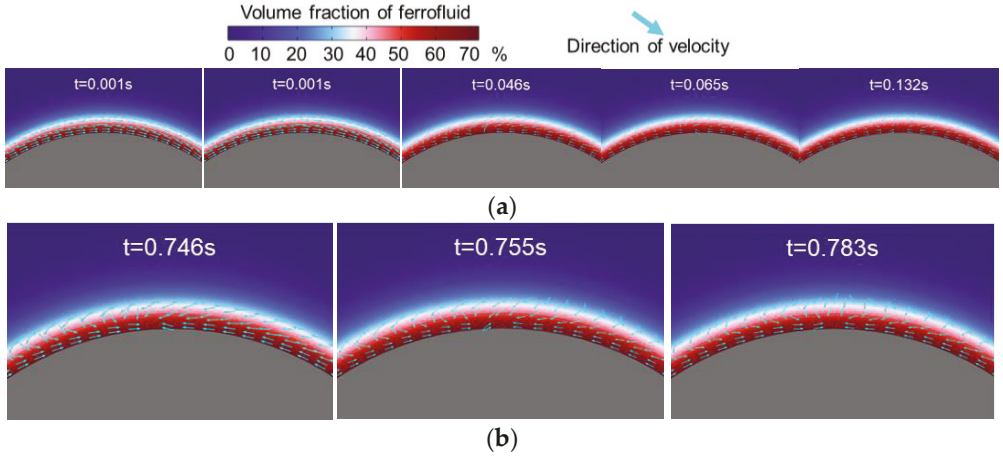


Figure 18. The flow behavior inside the ferrofluid film at different stages: (**a**) the stage without vortex shedding, (**b**) when vortex shedding begins to occur.

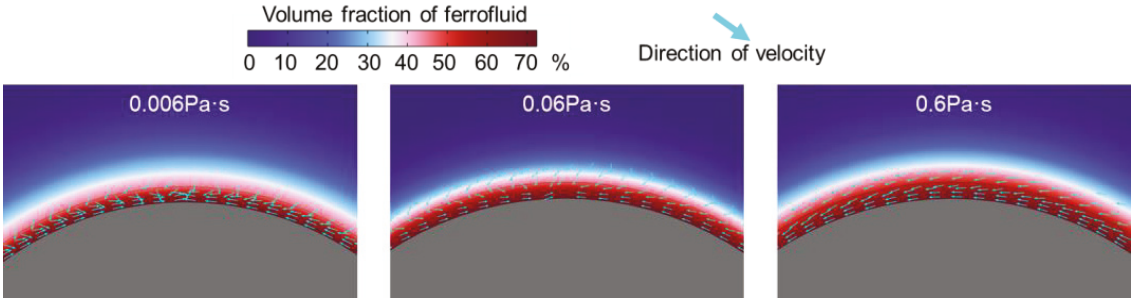


Figure 19. Flow behaviors of ferrofluids with different viscosities at t = 0.132 s.

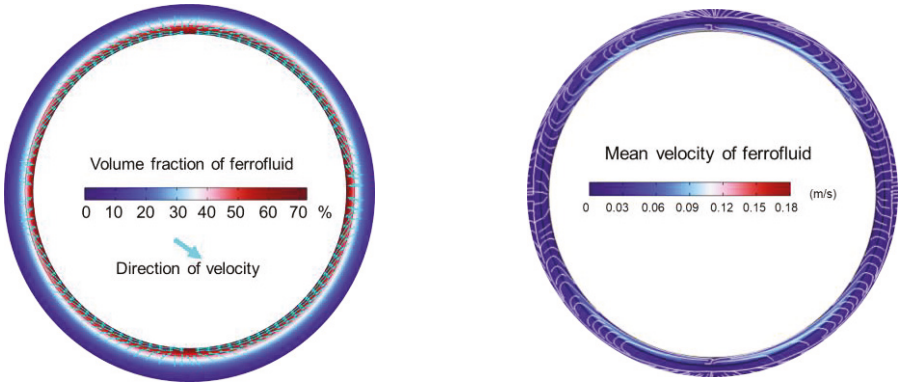


Figure 20. The flow motion inside the ferrofluid film with μ = 0.06 Pa·s and Δ = 0.10 mm at Re = 500: (**a**) the instantaneous flow motion at t = 0.783 s, (**b**) the mean flow motion.

4. Conclusions and Outlook

In summary, this article introduces a method of applying ferrofluid films for the control of flow separation in the external flow field. Numerical simulations were carried out to investigate the control performance of ferrofluid films as well as their parametric effects. The main conclusions are as follows:

(1) Ferrofluid films can prevent flow separation and stabilize the flow field in the wake. The cylinders wrapped with ferrofluid film have a larger vortex area and delay the first vortex shedding time. The maximum attenuation of the lift coefficient's dominant frequency is up to over 45%.

(2) A lower viscosity ferrofluid film has a more pronounced effect in reducing the frequency of lift coefficient, the frequency of vortex shedding in the flow field, and wall slip. In addition, a thicker ferrofluid film has a more pronounced effect in reducing the frequency of vortex shedding, enlarging the wake region, and decreasing the mean velocity of the wake flow.

(3) The control effect of ferrofluid film is primarily due to wall slip and surface fluctuations. Wall slip increases the width and length of the wake and makes the flow field more stable. The surface fluctuations of the ferrofluid film appear to suppress the interaction of the upper and lower lift forces, thus reducing the frequency of vortex shedding. Furthermore, a recirculation region with an approximate mean velocity of 0 is formed within the ferrofluidic film. The flow angle at the outer surface of this region is positively correlated with wall slip.

In fact, through our research and that of related researchers, we found that ferrofluid films have a very high potential for application in the field of flow control and drag reduction. However, it is undeniable that ferrofluid films are still a long way from practical application, and the stability at high flow rates and the homogeneity of the ferrofluid films are the key problems that need to be solved urgently. In addition, the specific relationship

between the internal motion of the ferrofluid films and the flow separation control will be further explored in the future.

Author Contributions: Conceptualization, H.Z.; methodology, C.W.; software, C.W.; validation, C.W., H.X. and Z.L.; formal analysis, C.W., H.X. and Z.L.; investigation, C.W. and H.X.; resources, C.W. and H.Z.; data curation, C.W.; writing—original draft preparation, C.W., H.X. and Z.L.; writing—review and editing, C.W., X.L., X.Z. and H.Z.; visualization, C.W., H.X. and Z.L.; supervision, X.L., X.Z. and H.Z.; project administration, X.L., X.Z. and H.Z.; funding acquisition, X.L. and H.Z. All authors have read and agreed to the published version of the manuscript.

Funding: This work was supported by the National Natural Science Foundation of China (52176160, 51976238, 12202308).

Data Availability Statement: The data that were used are confidential. The original contributions presented in the study are included in the article, further inquiries can be directed to the corresponding authors.

Acknowledgments: L. Yao is acknowledged for his instrumental role in the construction of the initial numerical simulation model.

Conflicts of Interest: The authors declare that they have no known competing financial interests or personal relationships that could have appeared to influence the work reported in this paper.

References

1. Chen, W.-L.; Huang, Y.; Chen, C.; Yu, H.; Gao, D. Review of active control of circular cylinder flow. *Ocean Eng.* **2022**, *258*, 111840. [CrossRef]
2. Jiang, H.; Cheng, L. Flow separation around a square cylinder at low to moderate Reynolds numbers. *Phys. Fluids* **2020**, *32*, 044103. [CrossRef]
3. Heil, M.; Rosso, J.; Hazel, A.L.; Brøns, M. Topological fluid mechanics of the formation of the Kármán-vortex street. *J. Fluid Mech.* **2017**, *812*, 199–221. [CrossRef]
4. Sohankar, A.; Norberg, C.; Davidson, L. Simulation of three-dimensional flow around a square cylinder at moderate Reynolds numbers. *Phys. Fluids* **1999**, *11*, 288–360. [CrossRef]
5. Choi, H. Control of flow over a bluff body. In *Fifth International Symposium on Turbulence and Shear Flow Phenomena*; Begel House Inc.: Danbury, CT, USA, 2007. [CrossRef]
6. Lee, S.J.; Lim, H.C.; Han, M.; Lee, S.S. Flow control of circular cylinder with a V-grooved micro-riblet film. *Fluid Dyn. Res.* **2005**, *37*, 246. [CrossRef]
7. Lim, H.C.; Lee, S.J. Flow control of circular cylinders with longitudinal grooved surfaces. *AIAA J.* **2002**, *40*, 2027–2036. [CrossRef]
8. Huang, S. VIV suppression of a two-degree-of-freedom circular cylinder and drag reduction of a fixed circular cylinder by the use of helical grooves. *J. Fluids Struct.* **2011**, *27*, 1124–1133. [CrossRef]
9. Wang, L.; Liu, X. Aeroacoustic investigation of asymmetric oblique trailing-edge serrations enlighted by owl wings. *Phys. Fluids* **2022**, *34*, 015113. [CrossRef]
10. Gao, D.; Huang, Y.; Chen, W.L.; Chen, G.; Li, H. Control of circular cylinder flow via bilateral splitter plates. *Phys. Fluids* **2019**, *31*, 057105. [CrossRef]
11. Deng, Z.; Chen, W.L.; Yang, Z.F. The control mechanism of the soft trailing fringe on the flow characteristics over an airfoil. *Phys. Fluids* **2022**, *34*, 95112. [CrossRef]
12. Brücker, C. Interaction of flexible surface hairs with near-wall turbulence. *J. Phys. Condens. Matter* **2011**, *23*, 184120. [CrossRef] [PubMed]
13. Hasegawa, M.; Sakaue, H. Microfibers coating for drag reduction by flocking technology. *Coatings* **2018**, *8*, 464. [CrossRef]
14. Lin, L.; Deng, Z.; Chen, W.; Li, H.; Gao, D. Flow control of a circular cylinder by self-adaptive furry microfibers. *Phys. Fluids* **2022**, *34*, 105128. [CrossRef]
15. Bashtovoi, V.G.; Krakov, M.S.; Taits, E.M. Intensification of heat transfer and reduction of the resistance under conditions of flow in channels with a magnetic-fluid coating. 1. Planar coating. *J. Eng. Phys.* **1990**, *58*, 435–439. [CrossRef]
16. Krakov, M.S. Experiments involving a cylindrical magnet coated with a magnetic fluid in a transverse flow. *Magnetohydrodynamics* **1989**, *1*, 61–64.
17. Jin, X.; Dai, M.; Zou, X.; Laima, S. Suppression of flow separation around a finite wall-mounted square cylinder by suction at the side leading edge. *Phys. Fluids* **2024**, *36*, 017120. [CrossRef]
18. Lam, K.M. Vortex shedding flow behind a slowly rotating circular cylinder. *J. Fluids Struct.* **2009**, *25*, 245–262. [CrossRef]
19. Toms, B.A. Observation on the flow of linear polymer solutions through straight tubes at large Reynolds numbers. *Proc. Int. Rheol. Congr.* **1948**, *2*, 131–141.
20. Li, F.; Bo, Y.; Wei, J.; Kawaguchi, Y. *Surfactant Turbulence Reduction*; Higher Education Publishing House: Beijing, China, 2012; p. 220, ISBN 9787040343151.

21. Solomon, B.R.; Khalil, K.S.; Varanasi, K.K. Correction to Drag Reduction using Lubricant-Impregnated Surfaces in Viscous Laminar Flow. *Langmuir* **2016**, *32*, 8287. [CrossRef]
22. Deutsch, S.; Castano, J. Microbubble skin friction reduction on an axisymmetric body. *Phys. Fluids* **1986**, *29*, 3590–3596. [CrossRef]
23. Madavan, N.K.; Detusch, S.; Merkle, C.L. Measurements of local skin friction in a microbubble–modified turbulent boundary layer. *Fluid. Mech.* **1985**, *156*, 37–256. [CrossRef]
24. Krakov, M.S. Flow separation control by means of magnetic fluid. *Izv. Akad. Nauk. SSSR Mekh. Zhidk. Gaza* **1984**, *39*, 119–122. [CrossRef]
25. Krakov, M.S.; Kamiyama, S. Steady flow past a circular cylinder coated with magnetic fluid: Flow structure, drag reduction and coating deformation. *J. Fluid Mech.* **1995**, *295*, 1–22. [CrossRef]
26. Stancanelli, L.M.; Secchi, E.; Holzner, M. Magnetic fluid film enables almost complete drag reduction across laminar and turbulent flow regimes. *Commun. Phys.* **2024**, *7*, 30. [CrossRef]
27. Krakov, M.S.; Maskalik, E.S.; Medvedev, V.F. Hydrodynamic resistance of pipelines with a magnetic fluid coating. *Fluid Dynam.* **1989**, *24*, 715–720. [CrossRef]
28. Outokesh, M.; Amiri, H.A.; Miansari, M. Numerical insights into magnetic particle enrichment and separation in an integrated droplet microfluidic system. *Chem. Eng. Process.-Process Intensif.* **2022**, *170*, 108696. [CrossRef]
29. Olsson, E.; Kreiss, G. A conservative level set method for two phase flow. *J. Comput. Phys.* **2005**, *210*, 225–246. [CrossRef]
30. Kholardi, M.D.; Farhadi, M. Understanding droplet formation in T-shaped channels with magnetic field influence: A computational investigation. *Phys. Fluids* **2024**, *36*, 053302. [CrossRef]
31. Ganguly, R.; Sen, S.; Puri, I.K. Thermomagnetic convection in a square enclosure using a line dipole. *Phys. Fluids* **2004**, *16*, 2228–2236. [CrossRef]
32. Norberg, C. Fluctuating lift on a circular cylinder: Review and new measurements. *J. Fluids Struct.* **2003**, *17*, 57–96. [CrossRef]
33. Dunne, P.; Adachi, T.; Dev, A.A.; Sorrenti, A.; Giacchetti, L.; Bonnin, A.; Bourdon, C.; Mangin, P.H.; Coey, J.M.D.; Doudin, B.; et al. Liquid flow and control without solid walls. *Nature* **2020**, *581*, 58–62. [CrossRef]

Disclaimer/Publisher's Note: The statements, opinions and data contained in all publications are solely those of the individual author(s) and contributor(s) and not of MDPI and/or the editor(s). MDPI and/or the editor(s) disclaim responsibility for any injury to people or property resulting from any ideas, methods, instructions or products referred to in the content.

inventions

MDPI

Article

Numerical Simulation of Effective Heat Recapture Ammonia Pyrolysis System for Hydrogen Energy

Jian Tiong Lim [1], Eddie Yin-Kwee Ng [1,*], Hamid Saeedipour [2,*] and Hiang Kwee Lee [3,*]

[1] School of Mechanical and Aerospace Engineering, College of Engineering, Nanyang Technological University, Singapore 639798, Singapore; jiantion001@e.ntu.edu.sg
[2] School of Engineering, Republic Polytechnic, Singapore 738964, Singapore
[3] Division of Chemistry and Biological Chemistry, School of Physical and Mathematical Sciences, Nanyang Technological University, Singapore 637371, Singapore
* Correspondence: mykng@ntu.edu.sg (E.Y.-K.N.); hamid_saeedipour@rp.edu.sg (H.S.); hiangkwee@ntu.edu.sg (H.K.L.)

Abstract: This paper proposes a solution to address the challenges of high storage and transport costs associated with using hydrogen (H_2) as an energy source. It suggests utilizing ammonia (NH_3) as a hydrogen carrier to produce H_2 onsite for hydrogen gas turbines. NH_3 offers higher volumetric hydrogen density compared to liquid H_2, potentially reducing shipping costs by 40%. The process involves NH_3 pyrolysis, which utilizes the heat waste from exhaust gas generated by gas turbines to produce H_2 and nitrogen (N_2). Numerical simulations were conducted to design and understand the behaviour of the heat recapture NH_3 decomposition system. The design considerations included the concept of the number of transfer units and heat exchanger efficiency, achieving a heat recapture system efficiency of up to 91%. The simulation of NH_3 decomposition was performed using ANSYS, a commercial simulation software, considering wall surface reactions, turbulent flow, and chemical reaction. Parameters such as activation energy and pre-exponential factor were provided by a study utilizing a nickel wire for NH_3 decomposition experiments. The conversion of NH_3 reached up to 94% via a nickel-based catalyst within a temperature range of 823 K to 923 K which is the exhaust gas temperature range. Various factors were considered to compare the efficiency of the system, including the mass flow of NH_3, operating gauge pressure, mass flow of exhaust gas, among others. Result showed that pressure would not affect the conversion of NH_3 at temperatures above 800 K, thus a lower amount of energy is required for a compression purpose in this approach. The conversion is maintained at 94% to 97% when lower activation energy is applied via a ruthenium-based catalyst. Overall, this study showed the feasibility of utilizing convective heat transfer from exhaust gas in hydrogen production by NH_3 pyrolysis, and this will further enhance the development of NH_3 as the potential H_2 carrier for onsite production in hydrogen power generation.

Keywords: ammonia; hydrogen; power generation; pyrolysis; simulation; gas turbine

1. Introduction

Industrial gas turbine engines are deployed in many of today's power plants for power generation due to high thermal efficiency. To respond to the initiative of decarbonization in the power industry and beyond, new gas turbines are being developed that will be completely fuelled by H_2 or blend with other carbon-free fuels as an attempt to significantly reduce carbon emissions, since the combustion of H_2 releases almost zero carbon and sulphur oxides [1–3]. Countries worldwide are increasingly focusing on the development and implementation of hydrogen-powered gas turbine technology [4–6]. This involves the research and development of new turbine designs and the conversion of existing gas turbine power plants to run on hydrogen or hydrogen blends.

With the increasing demand of H_2, total H_2 carrier demand is expected to reach 600 million to 660 million tons by 2050, abating more than 20% of global emissions [7]. The

challenges associated with H_2 storage and transportation are indeed significant barriers to its widespread adoption despite its potential as a clean energy carrier. H_2 is an ultralight gas with 0.08375 kgm^{-3} and a low boiling point of -252.9 °C. H_2 gas is widely stored under compressed gas at 35,000,000 Pa to 70,000,000 Pa or cryogenically stored at -252.9 °C. Hence, it would be very energy-intensive and challenging to store H_2. Beside this, H_2 pipeline has the risk of metal embrittlement that will weaken the strength of the material in the hydrogen environment, and it would result in leakage [8]. This would build up the electricity cost with the sophisticated tanks and hydrogen pipelines. The cost of shipping H_2 is estimated eight times higher compared with shipping NH_3 [9]. Therefore, an alternative H_2 carrier gas like NH_3 has been highly recommended. NH_3 decomposition into H_2 and N_2 can be performed via a catalytic pyrolysis process as described in Equation (1).

$$2NH_3 \leftrightarrow 3H_2 + N_2 \Delta H_{25^\circ C} = 92\ kJmol^{-1} \quad (1)$$

NH_3 is the second-most produced chemical globally [10]. Therefore, infrastructure like pipelines and storage tanks are available at a large scale for implementation of onsite H_2 generation. The use of NH_3 as a H_2 carrier gas is hence a promising method to transport H_2.

However, catalytic ammonia pyrolysis is an endothermic reaction that happens at a high temperature. A typical heavy-duty gas turbine used in the power industry has a maximum of 60% efficiency of the combined cycle, which means 40% of energy input is wasted in the whole cycle. This waste energy, which accounts for the inefficiency in the turbine's operation, can be harnessed to drive the decomposition of NH_3 into H_2, which can then be directed into the combustion chamber for power generation. This integration aims to improve the overall thermal efficiency and sustainability of the gas turbine system. This energy waste can be utilized in cracking NH_3 to produce H_2 fuel and can be directed into the combustion chamber. Therefore, the gas turbine is upgraded to a self-sustaining system. As a comparison, the current NH_3 cracker in the market is utilizing an external heat source for NH_3 decomposition.

In this research study, numerical simulation has been performed on a newly designed heat recapture NH_3 pyrolysis system to understand the behaviour of the system and optimize the conversion of NH_3. In contrast to existing NH_3 cracking methods that rely on external heat sources, the proposed approach integrates heat recapture mechanisms within the gas turbine system itself.

2. Literature Review

Research on the catalytic decomposition of NH_3 has indeed been extensive due to its significance in various industrial processes, such as the production of fertilizers and hydrogen fuel cells. The rate-determining step in this reaction on metal catalysts like iron (Fe), cobalt (Co), or nickel (Ni) is often the desorption of N_2. This means that the formation of N_2 molecules from adsorbed species on the catalyst surface is the slowest step in the overall reaction process.

Duan et al. showed that the desorption of the nitrogen atom on the Fe surface is harder compared with that on the Co or Ni surface [11]. The nitrogen atom is present at the interstitial site and energy for N_2 desorption is critical here for H_2 generation. Hence, N_2 desorption is the rate-determining step in NH_3 decomposition [11,12]. The study explained that the ease of NH_3 decomposition is improved on a Ni or Co surface than on an Fe surface. Maleki et al. have modelled a flat plate microreactor to generate hydrogen by using the decomposition of NH_3 on a CoCeAlO mixed oxide catalyst [13]. The numerical simulations that used two different kinetic rates of reaction models showed accuracy results that were validated by experiment data [13]. The experiment revealed that the conversion of NH_3 hit 100% at the temperature of 550 °C. However, a Ni-based catalyst is used in this research project due to material available and cost. Beside this, Robert showed that the rate of decomposition of NH_3 is independent of pressure at the temperature lower than 1000 K under the application of a Ni-catalyst [14]. The study also found that the reaction

activated at the energy of 211 ± 20 kJmol^{-1}. Different support material on the Ni catalyst have different reaction rates. Ni supported by La_2O_3 have a comparable conversion of NH_3 with Ni supported by Al_2O_3 as the basic components in the catalyst will promote the NH_3 decomposition [15]. The study also indicated that the Ni-La_2O_3 catalyst allowed a higher decomposition activity with a lower weightage of Ni compared with higher weightage. Kaname et al. showed that the conversion of NH_3 reached 65% with a Ni-based catalyst supported by Al_2O_3 at a temperature of 500 °C [16]. Next, Chellapa et al. have introduced a suitable kinetic rate of reaction equation to be used for NH_3 decomposition at a temperature higher than 520 °C and a pressure above 13,332.2 Pa while using a Ni catalyst [17]. The result from their study showed that the rate of reaction is first-order dependent over the entire temperature and pressure range which is different compared to other studies [14]. Realpe et al. determined that the optimization of hydrogen production cannot rely upon only one factor, such as the catalyst, by developing a dimensionless model of the membrane reactor [18]. The approach to improve the conversion of NH_3 needs to be all-rounded yet not only focused on the catalyst, as the conversion of NH_3 is also affected by the presence of a hydrogen-selective membrane. The above studies mainly focused on the development of the catalyst in NH_3 decomposition. The research in the energy efficiency of NH_3 decomposition has received little attention, yet the process is high energy-intensive due to the endothermic reaction. In a recent study, Jaewon et al. introduced an efficiency reactor which used induction heating for green hydrogen production with an assumption of electricity generated from renewable energy [19]. However, the energy required for heating purposes would increase the usage of electricity of the plant for onsite hydrogen generation. Beside this, Yazhou et al. recently conducted a thermodynamic analysis on a heat recuperator of NH_3 in a humidified gas turbine that showed a net electrical efficiency of 56.7% exceeded the NH_3-fueled Brayton cycle by 20.6% points [20]. Hence, this suggested that a chemical recuperator of NH_3 in a gas turbine plant can further reduce the cost and carbon footprint in the future. Thus, a novel green hydrogen generation process that utilizes heat wastage from gas turbines is proposed in this study. The proposed process is applicable to onsite hydrogen usage for small or big gas turbine power. In this study, a numerical simulation model is used to investigate the feasibility of the process in terms of the conversion of NH_3 at different pressures and temperatures.

3. Methodology

The key technology development described here includes NH_3 cracking system at 100,000 Pa and at a lower temperature than 500 °C–650 °C with a suitable catalyst material. Research indicates that 100,000 Pa is the optimum condition to decompose NH_3 [21]. In this computational experiment, the activation energy by using Ni-based alumina catalyst will be used in the numerical design. Studies have showed that nickel alumina can obtain high conversion of NH_3 at around 650 °C [22]. While studies revealed that Ru-based catalyst can achieve 100% conversion at lower temperature of 350 °C [23], the rarity of ruthenium and its associated higher cost make it less suitable for large-scale projects in term of commercialization. Choosing a nickel-based catalyst also addresses the issue of nitride formation, as nickel does not tend to form nitrides during the thermal decomposition of NH_3 [24]. This choice contributes to the feasibility and cost-effectiveness of the proposed technology for larger-scale applications.

4. Heat Recapture System

This study aimed at designing a high-efficiency heat recapture system using the Number of Transfer Units (NTU) method and heat exchanger efficiency. Typically, in the context of the NTU method, the heat capacity rates of the hot and cold fluids are determined based on their mass flow rates and specific heat capacities. The NTU method is a common approach used to analyze and design heat exchangers for maximizing thermal efficiency. In addition, the NTU method is used to calculate the rate of heat transfer in heat exchangers, especially parallel flow, counter current, and crossflow exchangers. This method began

with determining the heat capacity rates of the hot and cold fluids (in $J^{\circ}C^{-1}s^{-1}$) by using the Equations (2) and (3) [25]:

$$C_h = \dot{m}_h c_{ph} \tag{2}$$

$$C_c = \dot{m}_c c_{pc} \tag{3}$$

$\dot{m}_h, \dot{m}_c$: mass flow rate of the hot and cold fluid $\left(kgs^{-1}\right)$

c_{ph}, c_{pc} : specific heat capacity of the hot and cold fluid $\left(Jkg^{-1\circ}C^{-1}\right)$

After the heat capacity rates of the hot and cold fluids have been determined, it is necessary to proceed with calculating the NTU and heat exchanger efficiency to design the heat recapture system for achieving high thermal efficiency.

Capacity ratio c is calculated by using Equation (4) after the maximum and minimum heat capacity rates have been identified from Equations (2) and (3):

$$c = \frac{C_{min}}{C_{max}} \tag{4}$$

The dimensionless group called as number of transfer units (NTU) is expressed as Equation (5):

$$NTU = \frac{UA_s}{C_{min}} \tag{5}$$

U : overall heat transfer coefficienct $\left(Wm^{-2}K^{-1}\right)$

A_s : heat trasnfer surface area of the heat exchanger $\left(m^2\right)$

Table 1 shows that the value of overall heat transfer coefficient can be assumed at 25 $Wm^{-2}K^{-1}$ with a practical number of tubes; this value will be cross-checked on the numerical simulation. This leads to the calculation of effectiveness of a heat exchanger which is a function of NTU and the capacity ratio, c. Different types of heat exchangers have different effectiveness calculation equations. The heat exchange type in this research is crossflow with both fluids unmixed and the effectiveness is calculated by Equation (6):

$$\text{effectiveness} = 1 - e^{\left\{\frac{NTU^{0.22}}{c}\left[e^{(-cNTU^{0.78})} - 1\right]\right\}} \tag{6}$$

Table 1. Overall heat transfer coefficient and number of tubes.

Overall Heat Transfer Coefficient	Number of Tubes
10	49
25	19
50	9
75	6
100	4

The effectiveness values and NTU values are obtained from ([25], pp. 705–706) to identify the effectiveness and the length of the tubes in the heat exchanger [25]. The thermal efficiency of the design is calculated by Equation (7):

$$\text{thermal efficiency} = \frac{T_{NH_{3ave}} - T_{NH_{3in}}}{T_{hotgas_{in}} - T_{NH_{3in}}} \times 100\% \tag{7}$$

$T_{NH_{3ave}}$: NH_3 volumetric average temperature(K)

$T_{NH_{3in}}$: NH_3 inlet temperature(K)

$T_{\text{hot gas}_{in}}$: Hot gas inlet temperature (K)

Design of the heat recapture system as shown in Figure 1 has been developed by using NTU and effectiveness method. It had a dimension of 320 mm long with 120 mm diameter. It had 19 tubes with 12 mm external diameter and thickness of 1 mm. NH_3 inlet and NH_3 outlet are set at 5 mm diameter.

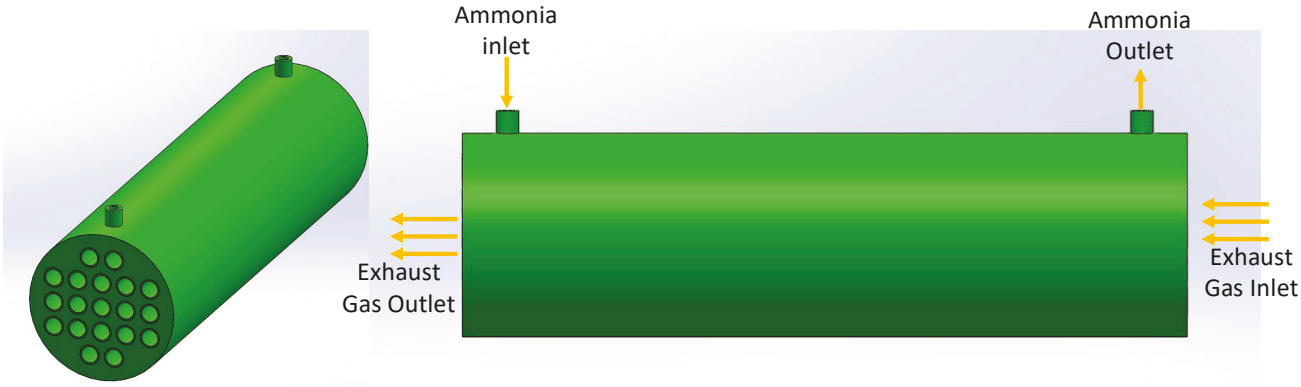


Figure 1. Design of heat recapture system.

ANSYS Fluent 2019 R1 software from Ansys, Canonsburg, US has been used for numerical simulation to validate theoretical calculations and perform a mesh independence analysis to ensure accurate results with low computational resources [26]. The computational analysis of the heat recapture system has been performed by using ANSYS Fluent to verify the theory calculation with the boundary conditions in Table 2. A grid-independent analysis is performed on the 3D geometry that could provide an accurate result with low computational time and cost. A table of mesh element size vs. other parameters is shown in Table 3. The mesh selected size is 8 mm with mesh node of 655,819 and mesh element of 1,206,553. Realizable $k-\varepsilon$ model, standard $k-\omega$ model and shear stress transport (SST) $k-\omega$ model are applied and their performance on this flow simulation is compared. Realizable $k-\varepsilon$ model is selected to determine the overall thermal efficiency of the entire system as $k-\omega$ model consumed lower computational cost compared with $k-\varepsilon$ model [27]. All the governing equations were solved using the commercial simulation software ANSYS Fluent 2019 R1.

Table 2. Values of each parameter.

Parameter	Value/Description
Exhaust Gas Inlet Temperature	650 °C
Exhaust Gas Inlet Velocity	12 m/s
NH_3 Inlet Temperature	30 °C
NH_3 Inlet Velocity	4 m/s
Material	Stainless Steel (SS316)

Table 3. Grid-independence test result for thermal simulation.

Mesh Element Size (mm)	Number of Mesh Node	Number of Mesh Elements	NH_3 Average Temperature (K)	NH_3 Average Turbulent Kinetic Energy (J/kg)	NH_3 Effective Prandtl Number
20	655,461	1,204,453	865.1	0.0161	0.8908
10	655,399	1,203,915	865.7	0.0161	0.8909
8	**655,819**	**1,206,553**	**867.5**	**0.0161**	**0.8909**
5	654,496	1,202,314	865.4	0.0161	0.8908

5. NH_3 Decomposition

A kinetic model that could express the rate of NH_3 decomposition reaction can be defined as Equation (8):

$$R_{NH_3} = k_{NH_3}\left[\left(\frac{C^2_{NH_3}}{C^3_{H2}}\right)^{\beta}\right] \tag{8}$$

where C_{NH_3} is the concentration of NH_3, C_{H_2} is the concentration of hydrogen, β is a fit parameter, k_{NH_3} is the rate constant of NH_3 decomposition [13]. This equation is based on the Temkin–Pyzhev model. Hence, beside the rate constant, the value of β has great impact on the rate of decomposition. Studies showed that the value of β approached unity with lower ΔH and approached zero at higher ΔH. β is set at 0.5 in this study as learned from [12].

A study conducted by Robert et al. on decomposition of NH_3 on nickel wire has been used as a reference for validation purposes in this study [14]. The study suggested that the rate constant for NH_3 pyrolysis under 1000 K is approximated by Equation (9):

$$k_{NH_3} = k^0 e^{-\frac{E}{RT}} \tag{9}$$

$k^0 = 1 \times 10^{13}\ s^{-1}$
$E = 211\ kJmol^{-1}$
$R = 8.314\ Jmol^{-1}K^{-1}$
$T = NH_3$ temperature (K)

The above values will be set in the ANSYS Chemkin Pro 2019 R1 software. For comparison purposes, 105 $kJmol^{-1}$ and 89.11 $kJmol^{-1}$ are set as the activation energy, respectively, as study suggested that the activation energy for NH_3 decomposition has a range of 211 $kJmol^{-1}$ to 25 $kJmol^{-1}$ [14,28]. The rate constant k used in ANSYS Chemkin Pro 2019 R1 software is described as Equation (10):

$$k = AT^B e^{-\frac{E}{RT}} \tag{10}$$

where B is temperature exponent (dimensionless), A is pre-exponential factor, and E is activation energy $\left(kJmol^{-1}\right)$. The rate of reaction R in ANSYS Chemkin Pro 2019 R1 software is described as Equation (11):

$$R = k\left(\prod_{i=1}^{N_g} C_i^{n_i}\right) \tag{11}$$

where N_g is the total number of gas species, C_i is the concentration of each species ith as reactant in the reaction $(moldm^{-3})$, and n_i is the rate exponent for the ith each species. The conversion of NH_3 obtained from this simulation will be calculated by using the following equation:

$$NH_3\ \text{conversion}\% = \frac{2\gamma_{N_2}}{2\gamma_{N_2} + \gamma_{NH_3}} \times 100\% \tag{12}$$

where γ_i is the mole fraction of the species i.

Other equations involved in mass transfer effect can be referred in [29]. A numerical simulation has been conducted to verify the study conducted by Robert et al. so that it verified that this simulation setup in this study is accurate [14]. This study investigated the reaction rate of NH_3 decomposition at 4 different operating gauge (or barometric) pressures which are 5.3 Pa, 13.3 Pa, 53 Pa, and 133 Pa. The simulation setup for validation is a 2D simulation represented in Figure 2. Grid-independent test has been conducted shown in Figure 3; the average rate of reaction reached the lowest after the mesh size reduced to

5 mm and a mesh element size of 5 mm with 1728 mesh nodes, and 1643 mesh elements have been selected as tetrahedral meshing method is used.

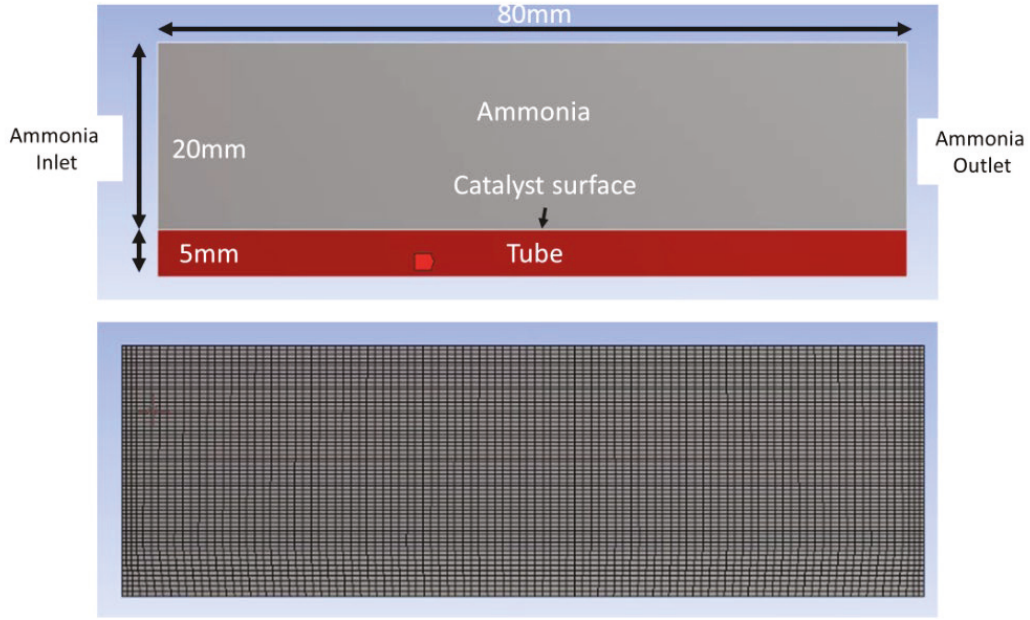


Figure 2. 2D Simulation setup for study validation.

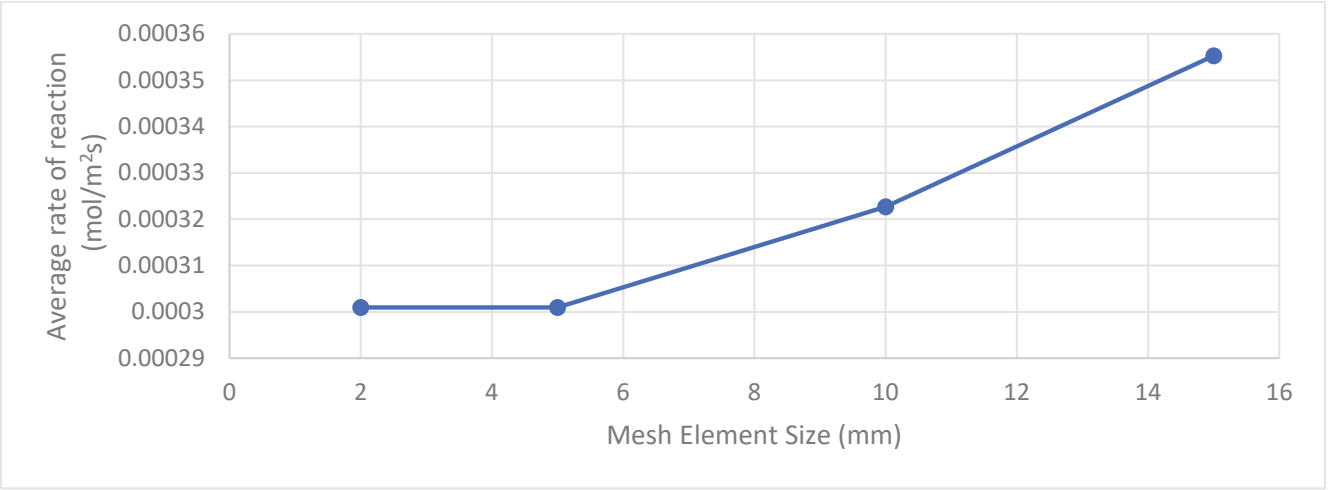


Figure 3. Grid-independent test: mesh element size vs. average rate of reaction graph.

The results suggest that the rate of reaction exhibits different dependencies on temperature and pressure within distinct temperature ranges at NH_3 inlet velocity of 5 m/s in Figure 4. Below 723 K, the reaction rate demonstrates a first-order dependence on temperature, while exhibiting zero-order dependence on pressure. However, at temperatures exceeding 723 K, the reaction rate becomes first-order dependent on pressure.

Moreover, the results indicate that at temperatures above 923 K, the reaction rate increases with higher pressure. Specifically, as shown in Figure 4, at 133 Pa, the rate of reaction is approximately 1.3 times higher compared to the rate at 53 Pa. Similarly, at 13.3 Pa, the rate is approximately 1.4 times higher than at 5.3 Pa. These findings are consistent with those reported in [14], reinforcing the validity of the numerical simulation in this study. It shows that numerical simulation can be used to investigate the chemical reaction in NH_3 decomposition.

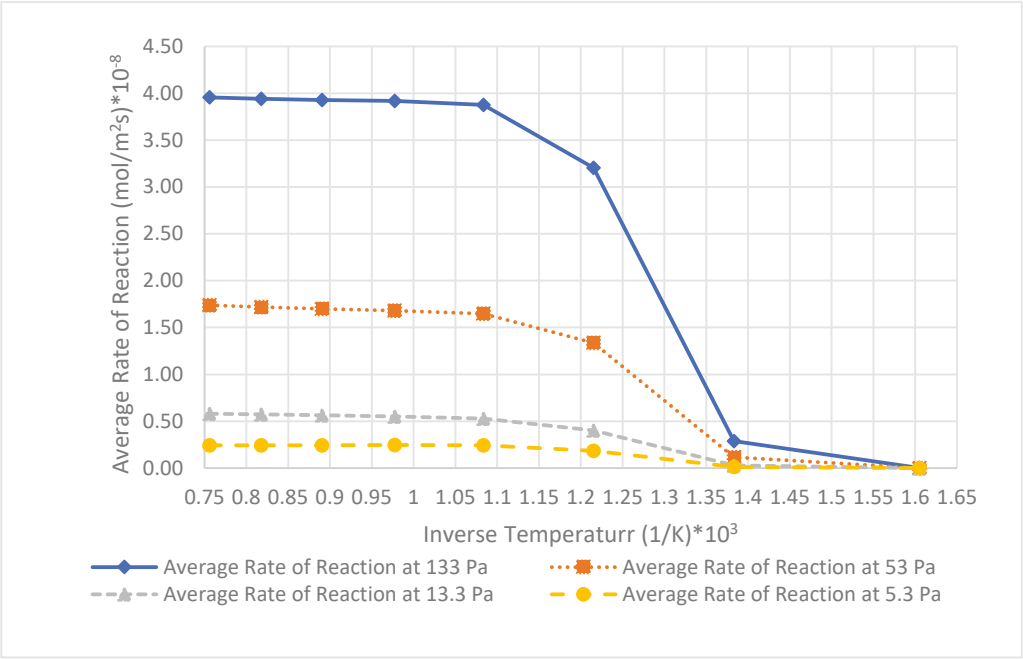


Figure 4. Inverse temperature vs. average rate of reaction graph at different pressure.

Moreover, the results indicate that at temperatures above 923 K, the reaction rate increases with higher pressure. Specifically, as shown in Figure 4, at 133 Pa, the rate of reaction is approximately 1.3 times higher compared to the rate at 53 Pa. Similarly, at 13.3 Pa, the rate is approximately 1.4 times higher than at 5.3 Pa. These findings are consistent with those reported in [14], reinforcing the validity of the numerical simulation in this study. It shows that numerical simulation can be used to investigate the chemical reaction in NH_3 decomposition.

In this study, numerical simulation has been applied to investigate the performance of the heat recapture NH_3 pyrolysis system under different operating conditions via convective heat transfer, while making necessary simplifications to manage computational resources effectively.

The grid-independence test has been applied in these numerical simulations where the mesh size was varied to ensure that the results of the simulation do not significantly change with different mesh sizes. It is important to establish grid independence to ensure the accuracy of the numerical simulation results.

It is assumed that the catalyst temperature remains constant across all surfaces. While this simplifies the simulation, it is important to note that the catalyst temperature may vary across different parts of the system. To reduce computational cost and time, it was decided not to simulate the flow of hot gas in the system. This simplification is common in simulations where the focus is on specific aspects of the system, such as the reaction kinetics or heat transfer within the catalyst bed. The performance of the system under different catalyst temperature conditions has been compared, ranging from 623 K to 923 K to study how changes in catalyst temperature affect the behaviour of the system and its efficiency in NH_3 pyrolysis.

In the numerical simulation of the newly designed heat recapture NH_3 pyrolysis system, grid-independent test has been conducted on this design shown in Figure 5. The 0.01 m mesh element size is chosen with a total of 842,165 elements and 185,873 mesh nodes as shown in Figure 6.

Planes at three sections, inlet, mid-length, and outlet shown in Figure 7, are used to simulate NH_3 gas temperature, NH_3 gas velocity, and mass fraction of each species. ZY plane in Figure 8 is used to simulate NH_3 temperature contour and mass fraction of H_2 at different NH_3 inlet velocity.

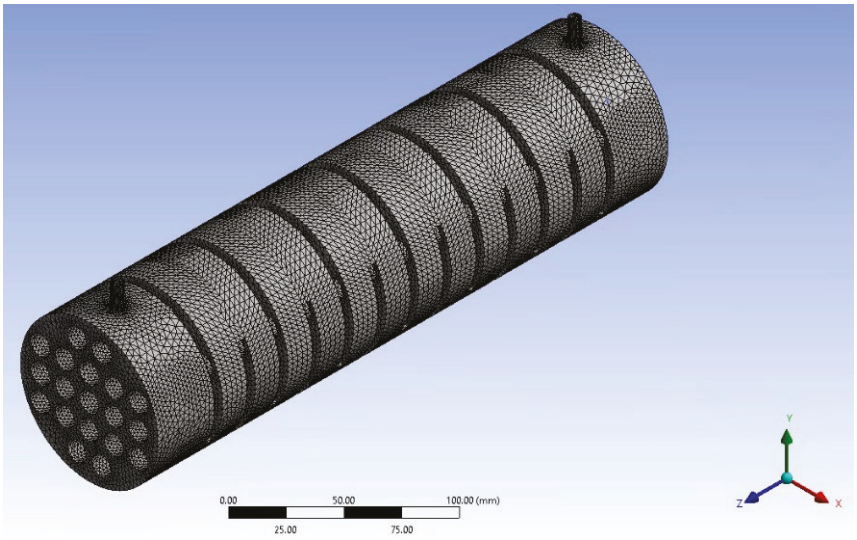


Figure 5. 3D simulation of NH_3 pyrolysis system.

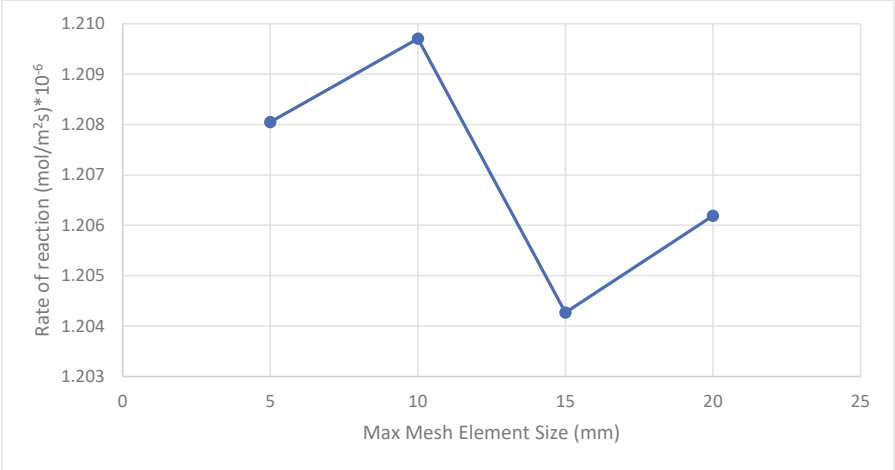


Figure 6. Grid-independent test result for 3D NH_3 decomposition simulation.

Planes at three sections, inlet, mid-length, and outlet shown in Figure 7, are used to simulate NH_3 gas temperature, NH_3 gas velocity, and mass fraction of each species. ZY plane in Figure 8 is used to simulate NH_3 temperature contour and mass fraction of H_2 at different NH_3 inlet velocity.

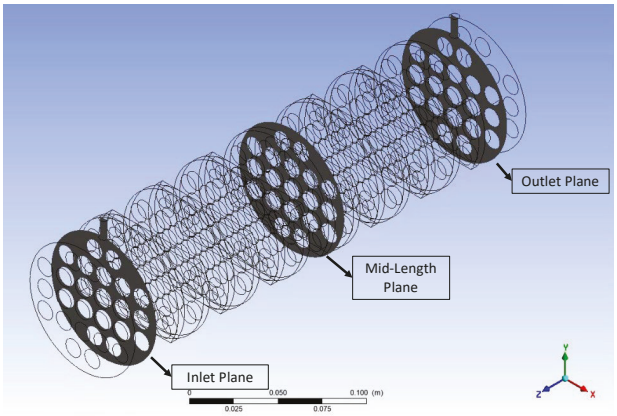


Figure 7. 3 Different section planes of the NH_3 pyrolysis system.

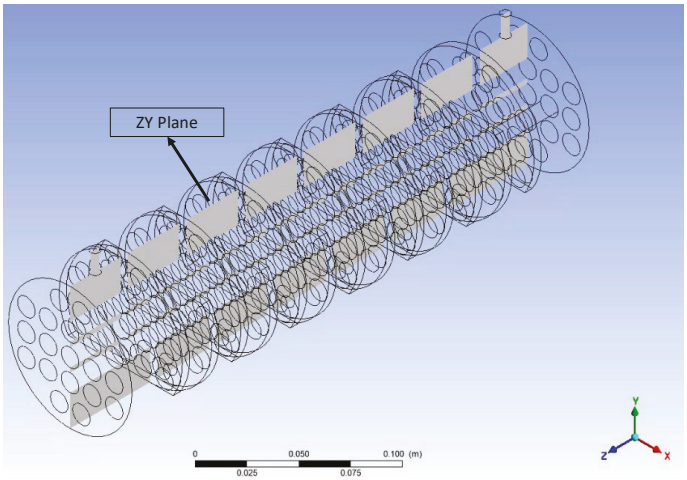


Figure 8. ZY plane of the NH_3 pyrolysis system.

6. Results and Discussion

6.1. Heat Recapture System

The realizable k − ε model, SST k − ω model, and standard k − ω model have been used in the thermal simulation for the heat recapture NH_3 pyrolysis system. Three of the models gave closed results as shown in Figure 9. The NH_3 average temperature that is taken from the volumetric average of the NH_3 temperature in the system is used as the comparison parameter. So, for a more efficient and conservative result, a realizable k − ε model has been selected as it has lower computational cost and time compared with the other two models.

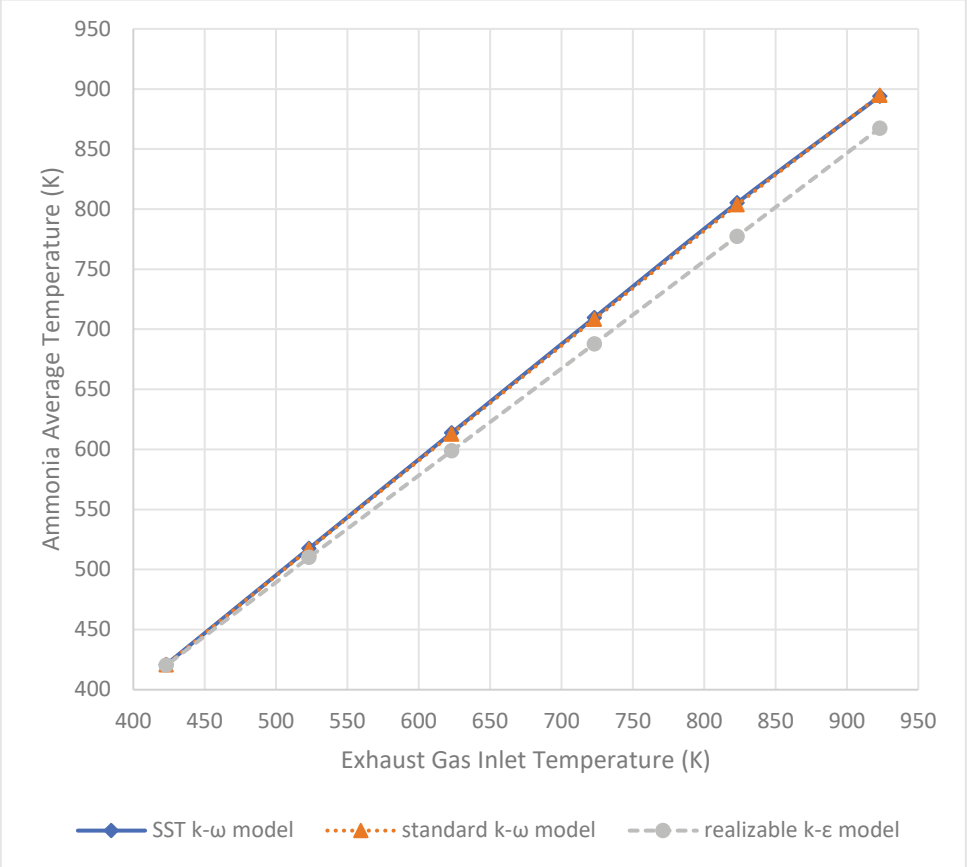


Figure 9. Exhaust gas inlet temperature vs. average NH_3 temperature graph.

Based on the designed system, a numerical simulation showed that the higher the exhaust gas velocity, the better the efficiency. Our calculation that was based on the NTU method revealed that the system could achieve 83.87% but the simulation indicated near to 91% at 4 ms^{-1} of NH_3 velocity plotted in Figure 10. This is due to the assumption of laminar flow in the NTU method; likewise, the realizable $k - \varepsilon$ model in the simulation took turbulent flow into consideration, hence efficiency could be higher due to turbulent enhancement on heat transfer and lesser pressure loss.

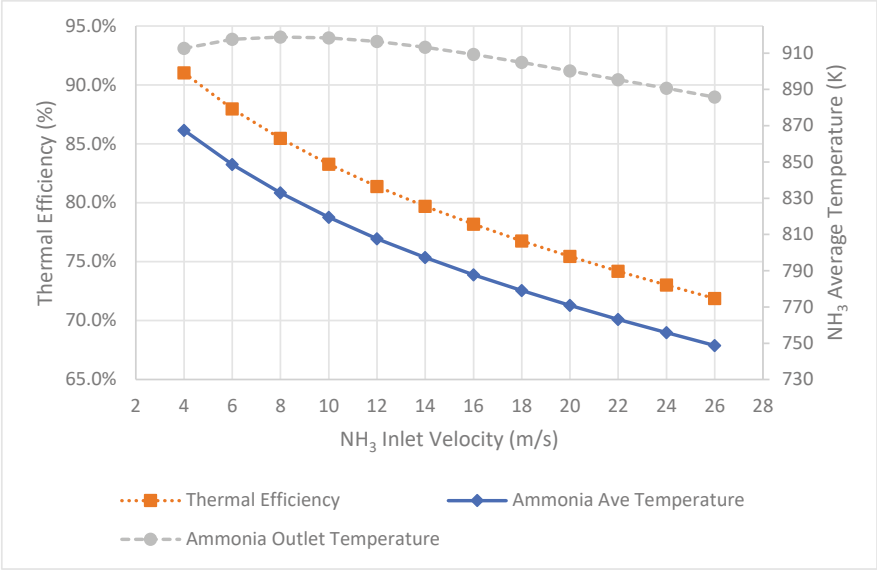


Figure 10. NH_3 Inlet velocity vs. thermal efficiency and NH_3 average temperature.

High exhaust gas inlet velocity resulted in high thermal efficiency in the system as presented in Figure 11 since high mass flow of high temperature will enhance the convective heat transfer from exhaust gas to NH_3 gas. This could further reduce the temperature of the exhaust gas if there is a surge in the gas turbine after the heat recapture system and release to the surrounding area. Hence, it eliminates the need of a cooling system downstream from the gas turbine before the release of the exhaust gas.

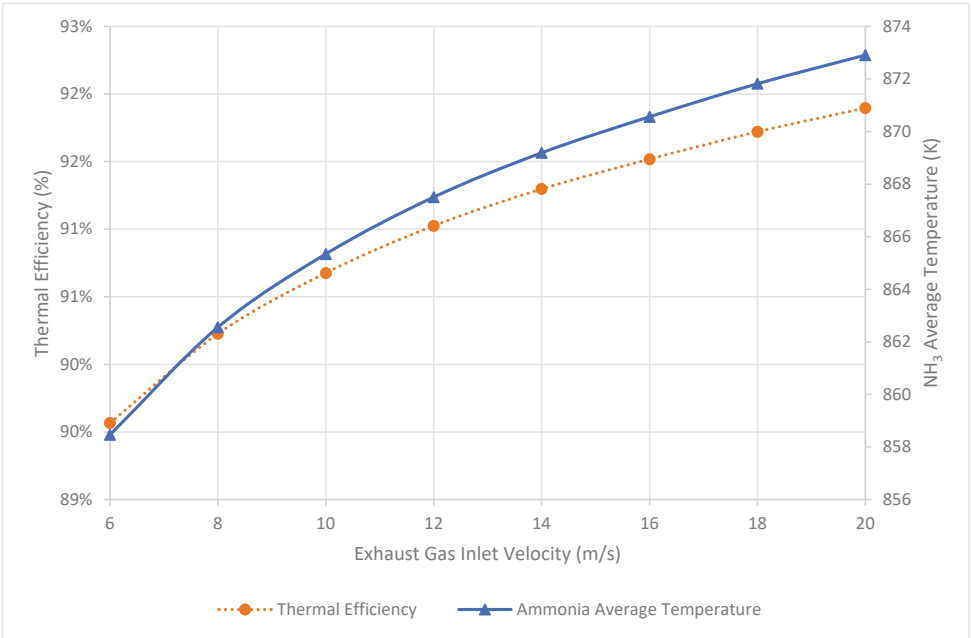


Figure 11. Exhaust gas inlet velocity vs. thermal efficiency and NH_3 average temperature.

Turbulent kinetic energy is high at the inlet section presented in Figure 12 as swirl flows occur at the inlet section when NH_3 gas is pumping in. It is observed that turbulent intensity is higher at the area where swirl flows occurred as shown in Figure 13, and swirl flows are distributed more closely at the gap between tubes. Hence, the mixture of NH_3 flow at the swirl flows could increase the thermal efficiency of NH_3 by enhancing the convective heat transfer [30] as swirl flows will increase the efficiency of the heat transfer of NH_3 and the catalyst tubes. Temperature contour in Figure 14 shows that more than half of the NH_3 volume at temperature of 904 K and this resulted in high total enthalpy gained by NH_3 plotted in Figure 15. NH_3 gained a maximum of 1.66×10^6 Jkg^{-1} total enthalpy. By assuming the activation energy is 211 $kJmol^{-1}$ for NH_3 decomposition, this enthalpy could convert 0.1 mol of NH_3 to 0.15 mol of hydrogen and 0.05 mol of nitrogen or 0.18 mass fraction of hydrogen and 0.92 mass fraction of nitrogen for complete conversion of NH_3. This result will be validated by the simulation result for NH_3 decomposition in the next section.

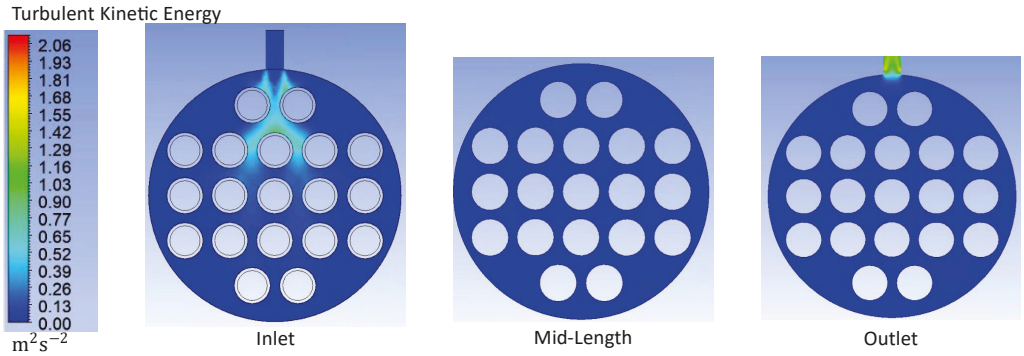


Figure 12. Turbulent kinetic energy contour of NH_3 gas at 3 different sections.

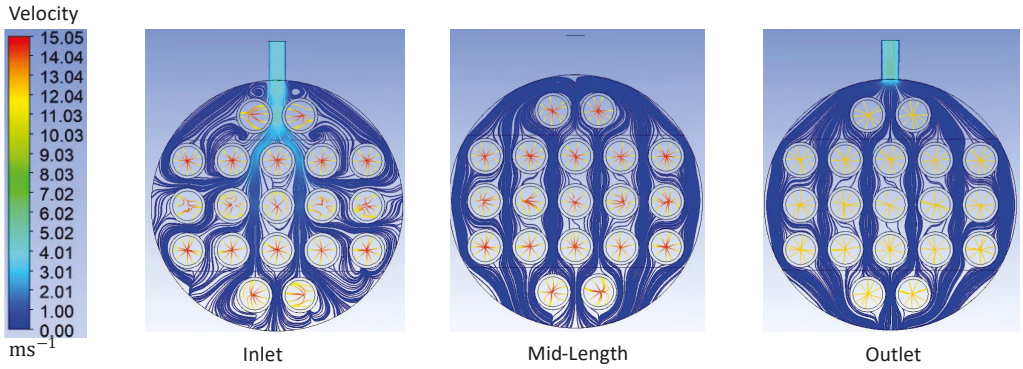


Figure 13. Velocity contour of NH_3 gas at 3 different sections.

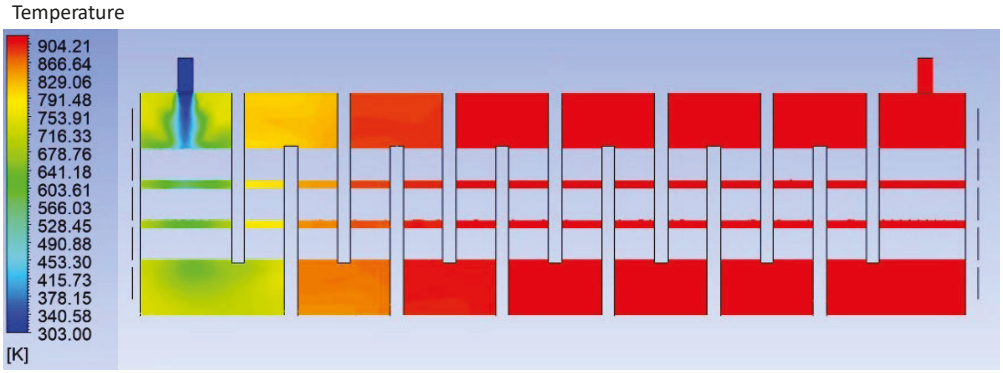


Figure 14. Temperature contour of NH_3 gas of ZY plane.

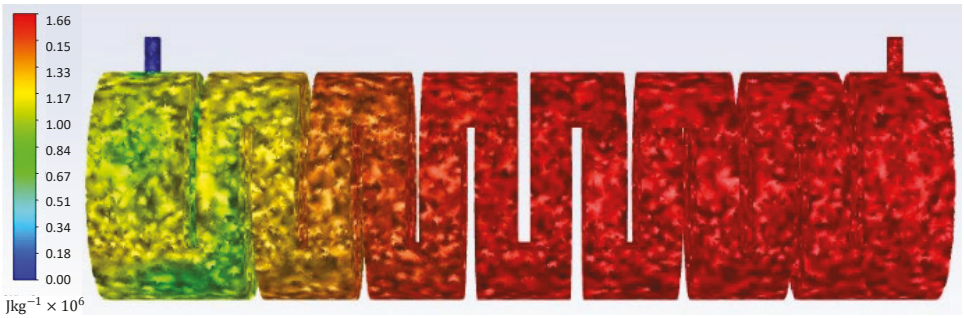


Figure 15. Total enthalpy contour of NH_3 gas in the system.

6.2. Heat Recapture NH_3 Pyrolysis System

Numerical simulation suggested that the rate of reaction of NH_3 pyrolysis is at first-order temperature dependent at temperature lower than 723 K and it changed from zero-order to first-order pressure dependent at temperature above 723 K as shown in Figures 16–18. The finding from this study is different from the observation made by [14] as the pressure dependent changed from zero to first order at temperature above 1000 K. Therefore, the heat capture NH_3 pyrolysis system has lowered the temperature for the pressure dependent and achieved a higher rate of reaction at a lower temperature. Our designed system has the highest rate of reaction at 823.15 K with a pressure of 300,000 Pa and NH_3 inlet velocity of 8 ms^{-1}. This could simply be explained by the effect of mass flow of the NH_3 on the rate of NH_3 decomposition. The rate of reaction seemed to reach the peak at 300,000 Pa between temperatures of 723 K and 923 K. This range of temperature is considered as the working temperature for NH_3 pyrolysis in this system as exhaust gas from a typical power plant gas turbine is released at temperatures between 823.15 K and 895.15 K.

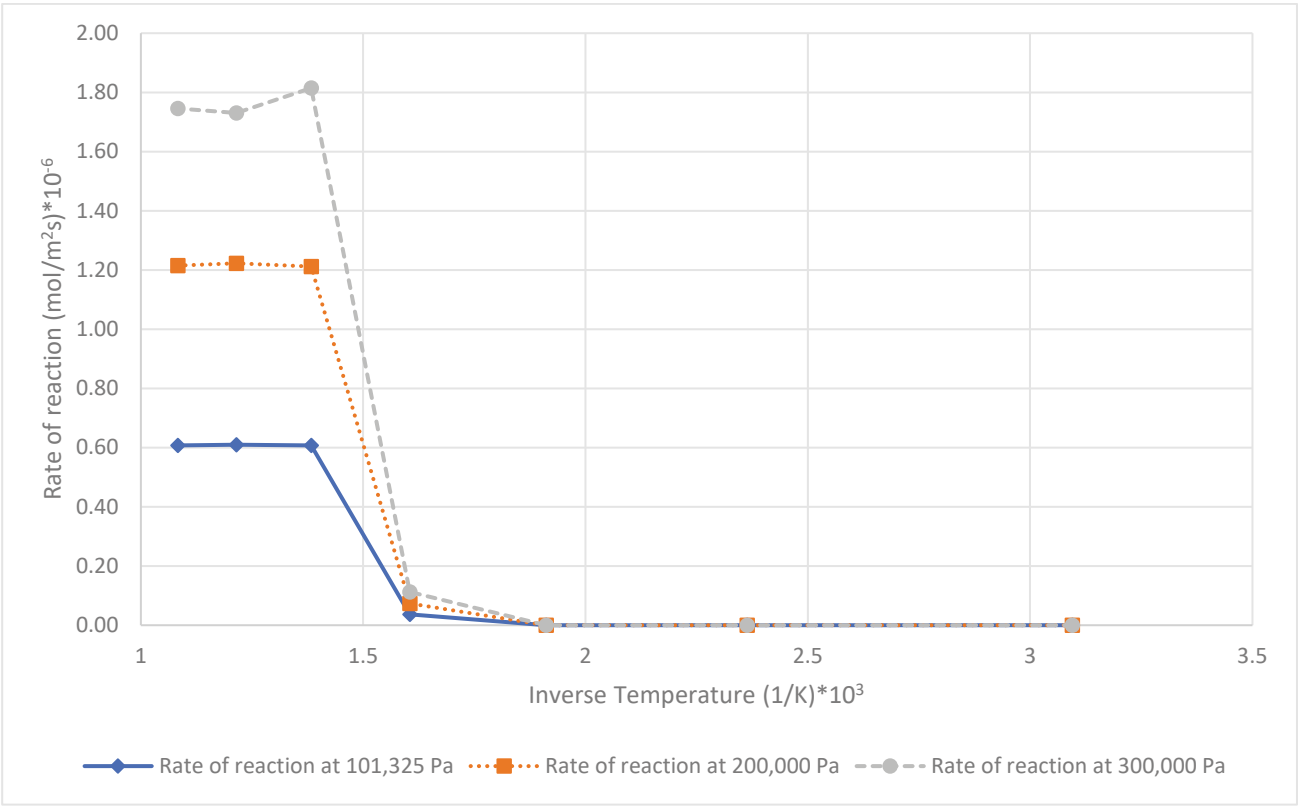


Figure 16. Inverse temperature vs. rate of reaction at NH_3 inlet velocity of 2 ms^{-1}.

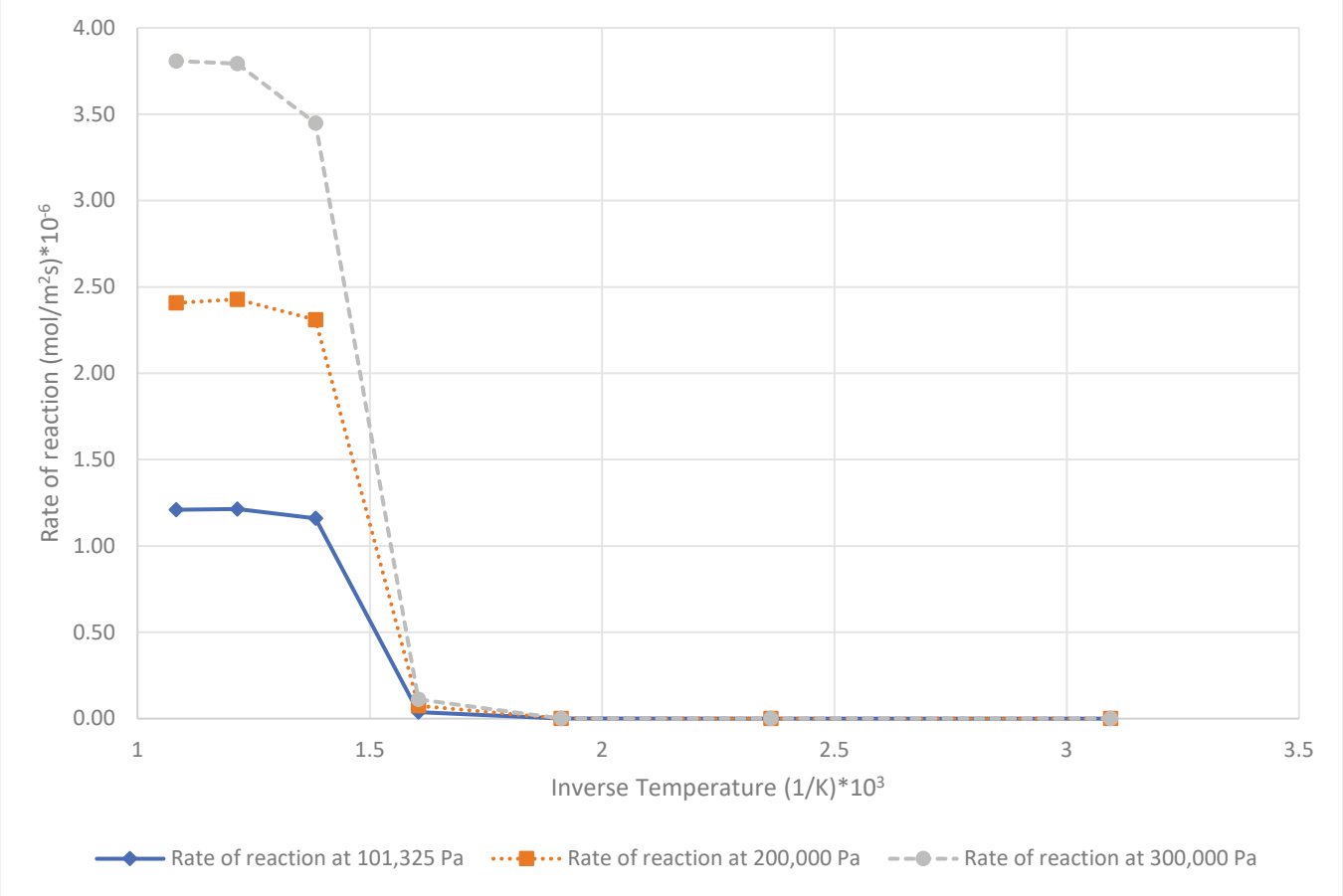


Figure 17. Inverse temperature vs. rate of reaction at NH_3 inlet velocity of 4 ms^{-1}.

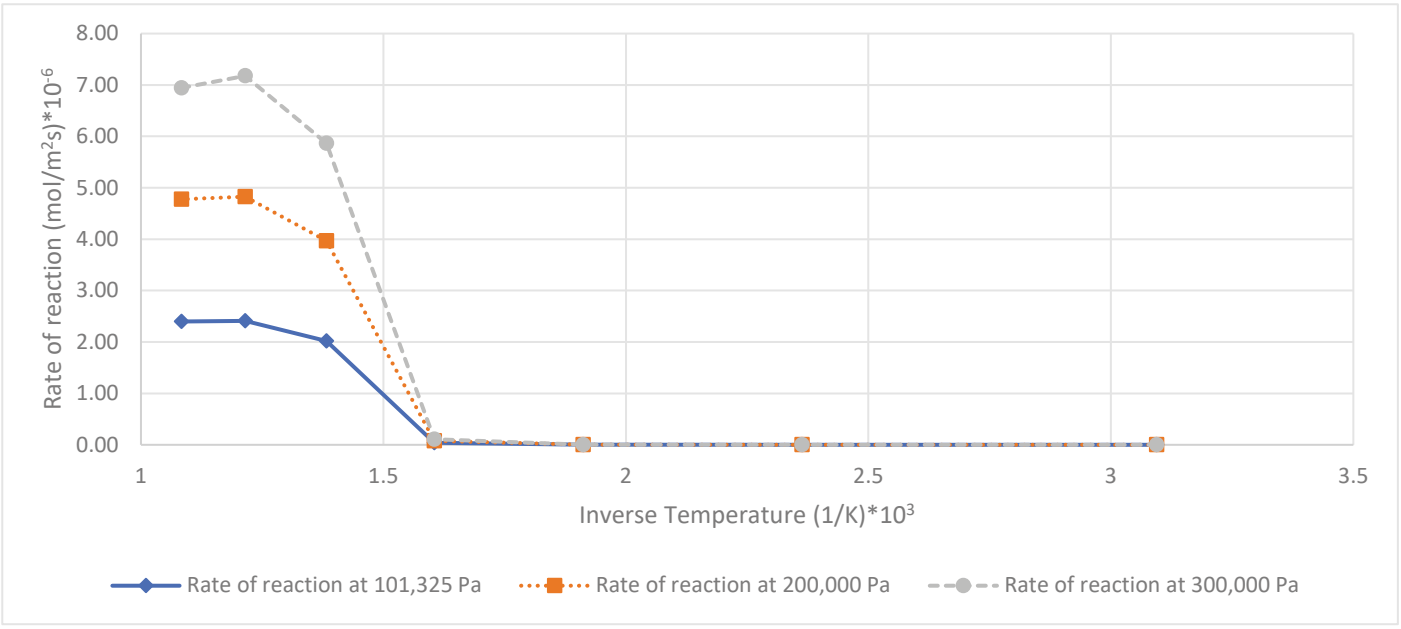


Figure 18. Inverse temperature vs. rate of reaction at NH_3 inlet velocity of 8 ms^{-1}.

Figures 16–18 outline the behaviour of the conversion of NH_3 under varying conditions of temperature and pressure, as well as the performance of a designed system within specific temperature ranges. The trends in these graphs show the influence of pressure

and temperature on the conversion of NH_3, as well as the successful performance of a designed system within a specific temperature range. The rate of reaction in this study is 1st order dependent of temperature but zero order dependent of pressure below 623.15K. Dependent of pressure changed to 1st order above temperature of 623.15K. The conversion of NH_3 decreased at a constant temperature with increasing pressure at temperature below 823 K and this is supported by study [31]. There is no conversion of NH_3 at temperature below 623 K where a reaction failed to take place as shown in Figure 19. Conversion of NH_3 remained the same at temperature above 800 K at different pressures. Thus, this could reduce the energy required from compression purposes. The designed system achieved near to 94% conversion of NH_3 at the temperature ranges from 823 K to 923 K which is the working temperature of the system. One of the possible reasons that the system failed to reach 99% conversion could be the assumption made at the NH_3 outlet condition. The NH_3 outlet is assumed to allow the backflow of non-decomposed NH_3. Beside this, it is important to note that the calculation of the conversion of NH_3 is taken with the average mole fraction of each species.

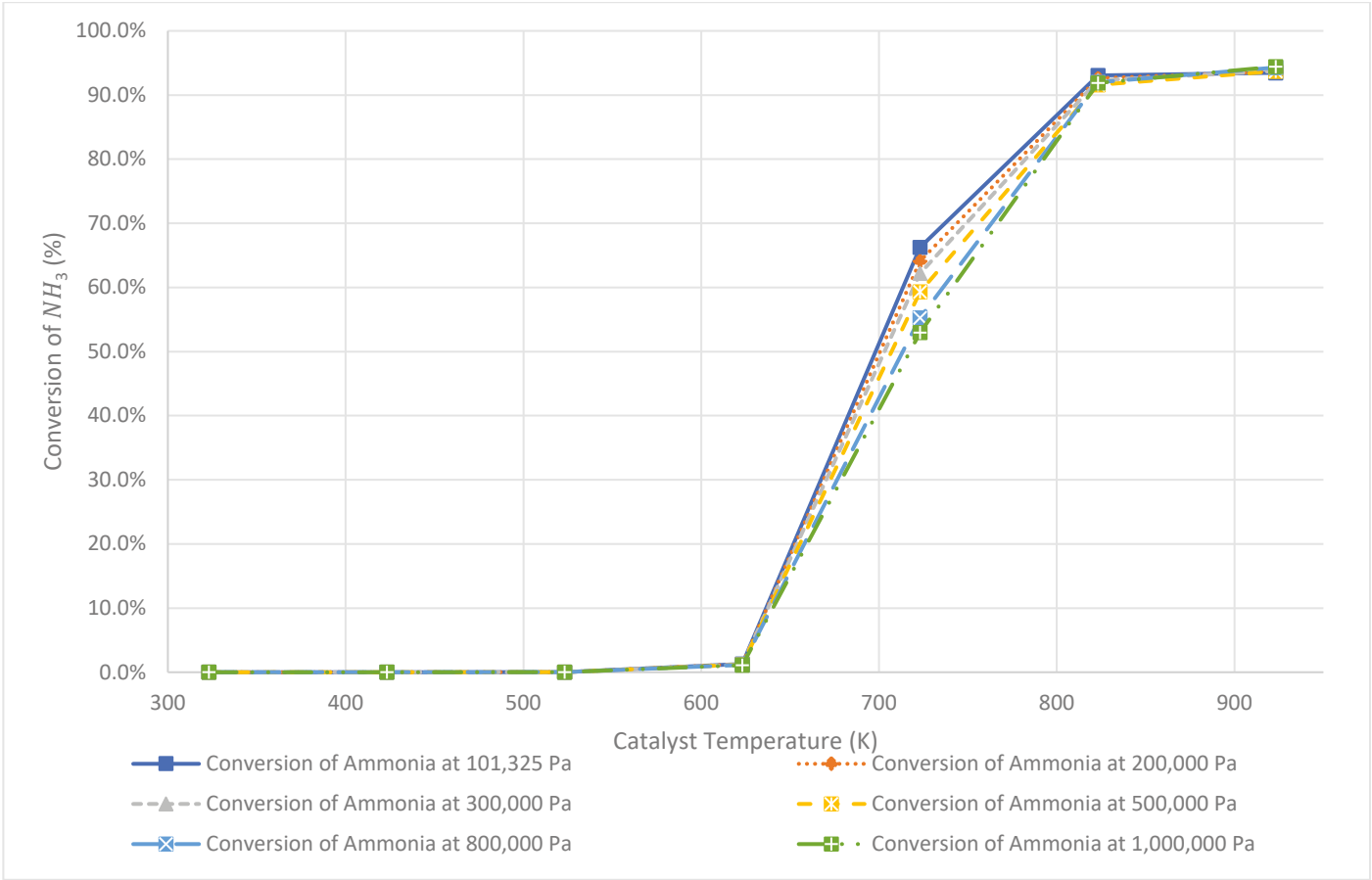


Figure 19. Catalyst temperature vs. conversion of NH_3.

At NH_3 inlet velocity of 4 ms^{-1}, NH_3 begins to be decomposed at the inlet section as seen in Figure 20. NH_3 gas gained enough energy near the catalyst tubes and hence, NH_3 started to decompose into hydrogen and nitrogen around the tubes' surfaces as catalyst NH_3 pyrolysis is a wall surface reaction [32]. The mass fraction of H_2 reaches up to 0.18 at the mid-plane and outlet plane shown in Figures 21 and 22 which are consistent with the mole concept calculation based on the total enthalpy gained by the NH_3 gas and the activation energy of 211 $kJmol^{-1}$. The theoretical calculation involved is explained in Appendix A to verify the validity of the result obtained from numerical simulation.

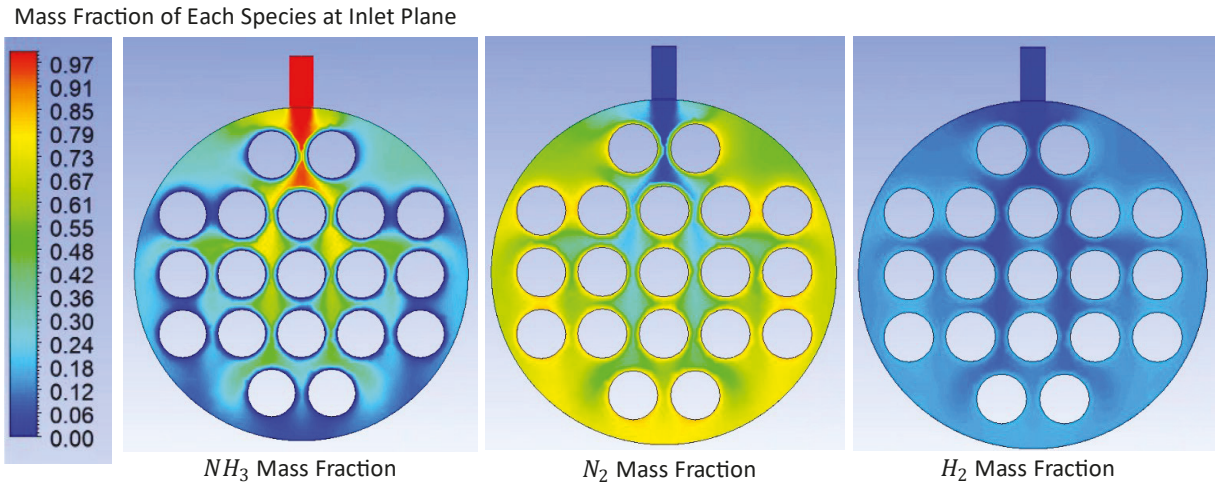


Figure 20. Mass fraction of each species at inlet plane.

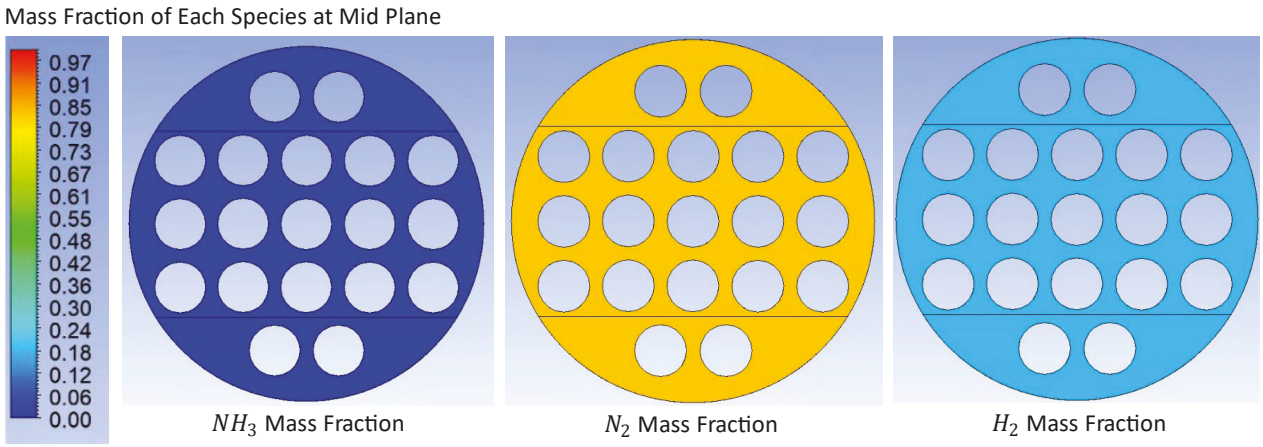


Figure 21. Mass fraction of each species at mid-length.

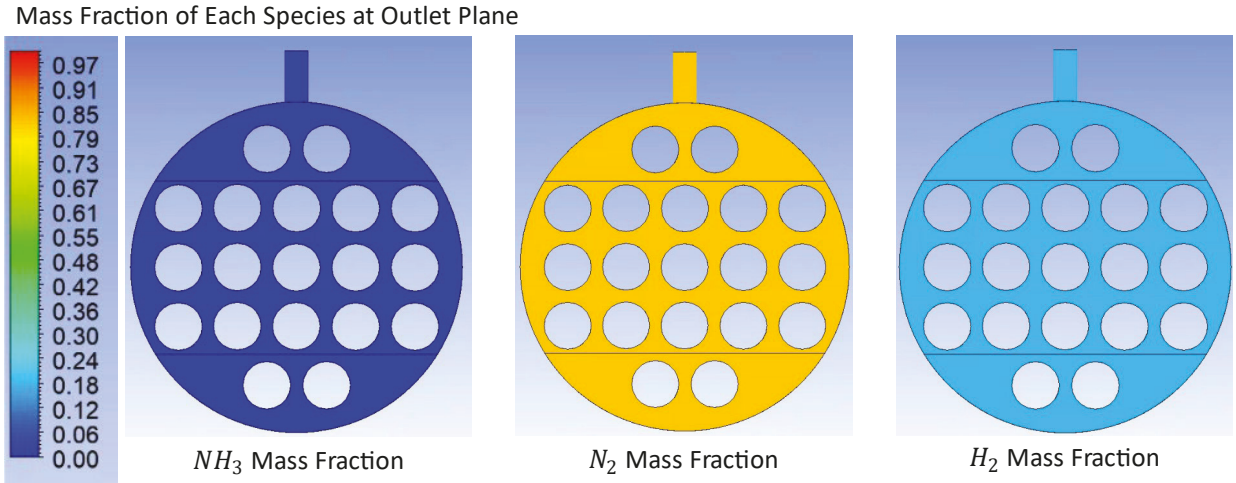


Figure 22. Mass fraction of each species at outlet plane.

NH_3 mass flow is required for high hydrogen generation in the system. However, the higher the NH_3 inlet velocity, the lower the conversion of NH_3 as shown in Figures 23 and 24. The contour area for 0.18 mass fraction of H_2 is reducing with the increase of NH_3 inlet velocity. NH_3 gas escaped from the system before it gained enough energy for

decomposition to take place. The maximum velocity of the NH_3 inlet as it provided the maximum thermal efficiency is 4 ms^{-1} in this study and the highest conversion of NH_3 when the exhaust gas inlet velocity is 12 ms^{-1}. The possible way to increase the effective mass flow of NH_3 is to increase the exhaust gas inlet velocity as this will certainly improve the convective heat transfer from Figure 11. The exhaust gas inlet velocity is reduced by a diffuser downstream the gas turbine to slow down the exhaust gas velocity. The design of the diffuser would thus be one of the critical parts in system integration of heat recapture NH_3 pyrolysis with a gas turbine.

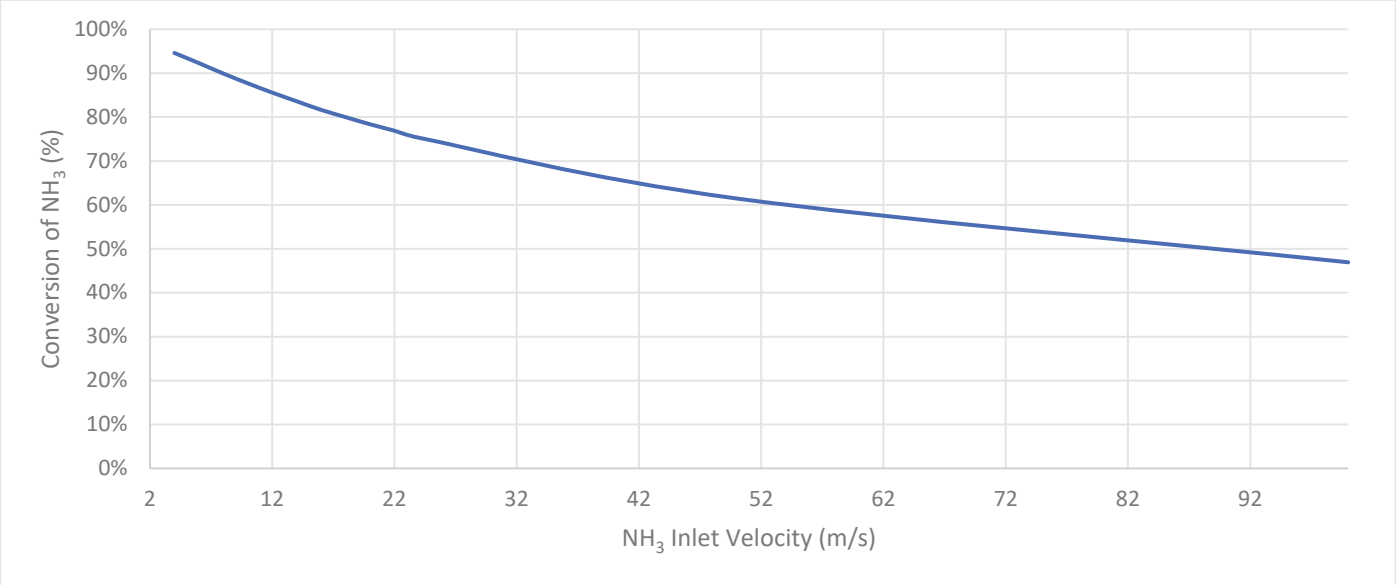


Figure 23. NH_3 Inlet velocity vs. conversion of NH_3.

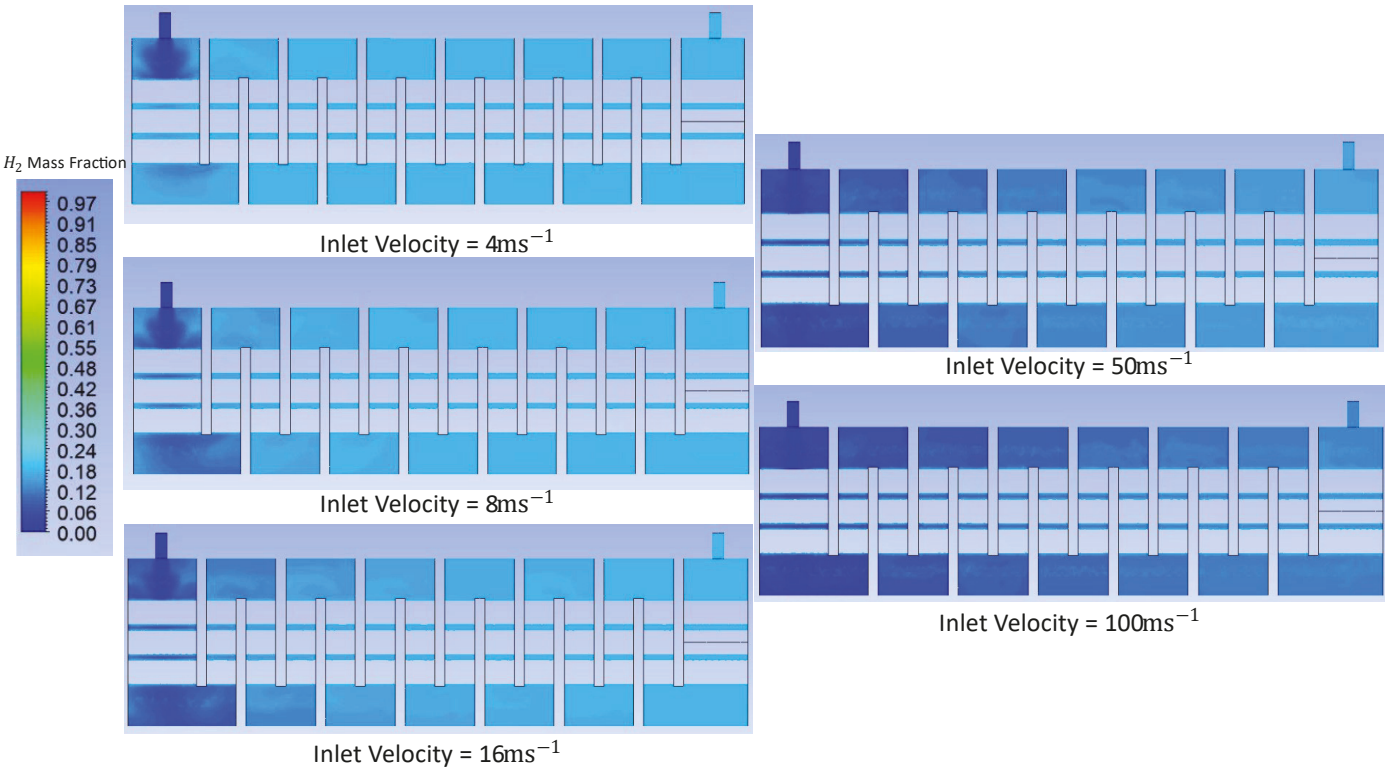


Figure 24. Contour of mass fraction of H_2 at different NH_3 inlet velocity.

Three different activation energies are used in the numerical simulation and the conversion of NH_3 on these energies is plotted in Figure 25. The graph suggests that the lower the activation energy, the higher the conversion of NH_3. A lower activation energy also allowed NH_3 to be decomposed at a lower temperature. Hence, the coatings of the catalyst and the catalyst material are important factors here. The coating of the catalyst can affect the surface binding and heat transfer of the tubes and the catalyst. Catalysts like a Ni-based catalyst will give a higher activation energy. Catalysts like a ruthenium-based catalyst and a platinum-based catalyst will give a lower activation energy [33].

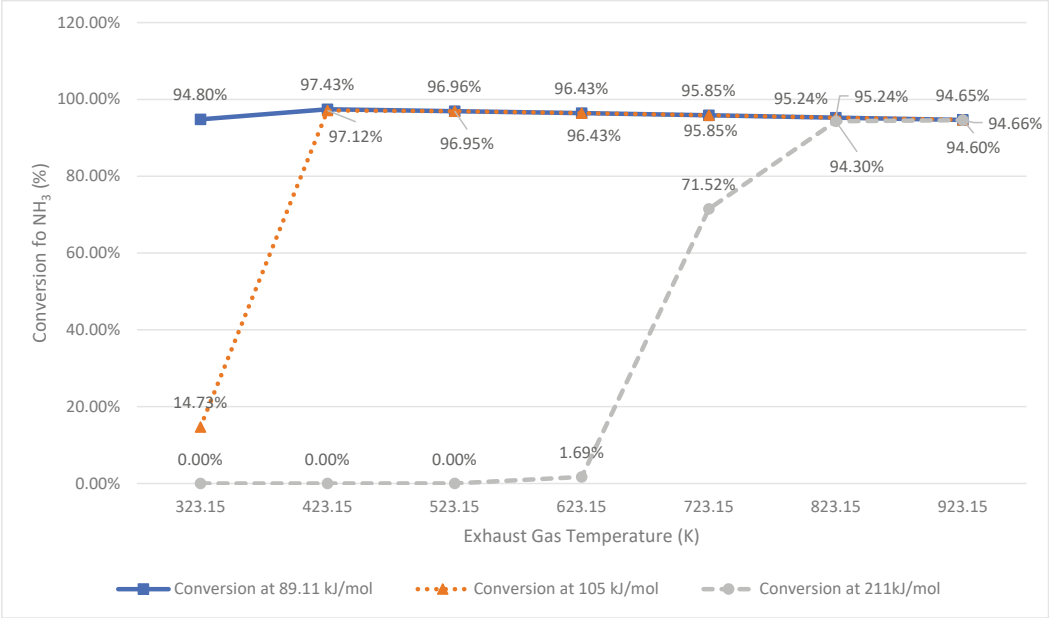


Figure 25. Exhaust gas temperature vs. conversion of NH_3 at different activation energies.

Last but not least, the temperature exponent, B, is one of the important dimensionless parameters in the rate of reaction equation. However, no study has been conducted to determine the suitable value of the temperature exponent for the NH_3 decomposition rate of reaction but the temperature exponent could certainly affect the rate of reaction shown in Figure 26. The shift is from a near 0 rate of reaction to the peak of the rate of reaction at 1.2×10^{-6} $m^{-2}s^{-1}$mol at the temperature of 623 K. Hence, the temperature exponent could be one of the parameters to be tuned in an NH_3 pyrolysis system design either via electrolysis or heat recapture.

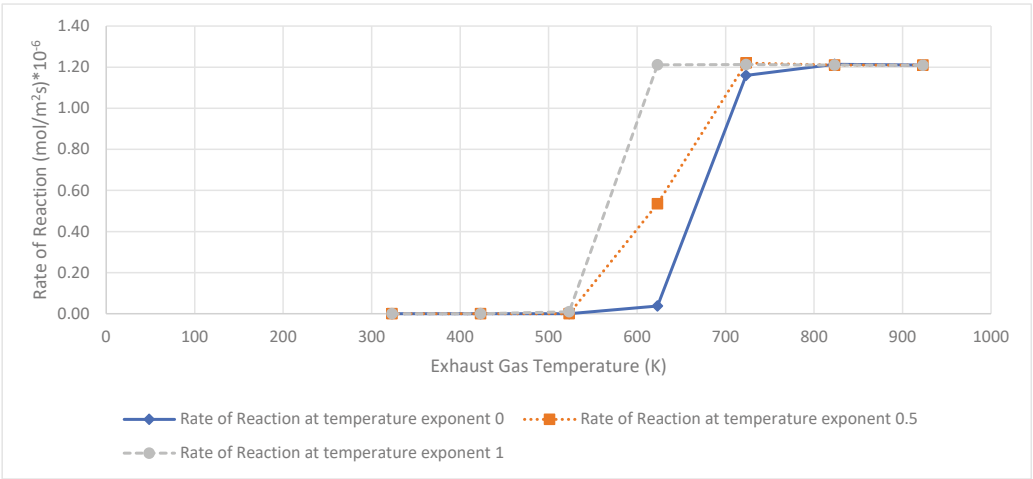


Figure 26. Exhaust gas temperature vs. rate of reaction at different temperature exponents.

7. Conclusions

NH_3 pyrolysis presents a promising avenue for sustainable hydrogen production, but its efficiency can be significantly enhanced through the integration of heat recapture systems. In this study, we present a numerical simulation of a heat recapture NH_3 pyrolysis system, aiming to evaluate its performance and potential for industrial application. The simulation framework encompasses thermodynamic modelling of the pyrolysis reactor, heat exchangers, and associated components. Utilizing advanced computational fluid dynamics techniques, we analyzed the heat transfer mechanisms and optimized system parameters to maximize energy efficiency. Our results demonstrate the effectiveness of heat recapture strategies in improving overall process efficiency and reducing environmental impact. This research contributes to the advancement of sustainable hydrogen production technologies and offers insights for the design and operation of NH_3 pyrolysis systems in real-world applications.

The shift towards hydrogen-powered gas turbines is crucial for decarbonizing the power industry and mitigating climate change. Despite its environmental benefits, challenges in storage and transportation hinder widespread adoption. This paper explores using NH_3 as a hydrogen carrier, leveraging its higher energy density and existing infrastructure. NH_3 decomposition, utilizing waste heat from gas turbines, offers a promising solution. The conversion process involves technical and logistical challenges but promises significant emission reductions. The global demand for H_2 carriers is rising, emphasizing the need for alternative solutions. This paper proposes integrating NH_3 decomposition within gas turbine systems to enhance efficiency and sustainability.

An extensive literature survey has been conducted on catalytic NH_3 decomposition, highlighting its importance in various industrial processes. Studies demonstrate the significance of catalysts like nickel in achieving high conversion rates. Various factors, including catalyst composition and temperature, influence NH_3 decomposition kinetics. Numerical simulations and experimental validations provide insights into reaction mechanisms and system performance. Previous research emphasizes the potential of NH_3 as a hydrogen carrier and its integration within gas turbine systems to improve efficiency.

The transition to H_2 as an energy source faces challenges related to high storage and transportation costs. This paper proposes a solution using NH_3 as a hydrogen carrier, offering higher volumetric hydrogen density and potential shipping cost reduction by 40%. This study focuses on designing a high-efficiency NH_3 cracking system using a nickel-based catalyst. Numerical simulations and theoretical calculations are performed to optimize system design and understand reaction kinetics. The heat recapture system is designed using the NTU method and heat exchanger efficiency considerations. ANSYS simulations validate theoretical calculations and analyze system behaviour under different operating conditions. The NH_3 decomposition kinetics are modelled based on experimental data, considering factors such as temperature and pressure dependencies. NH_3 pyrolysis, utilizing waste heat from gas turbines, can produce H_2 onsite.

Numerical simulations were conducted to design a high-efficiency NH_3 decomposition system. The system achieved up to 91% thermal efficiency, validated through ANSYS simulations considering wall surface reactions and turbulent flow. Factors such as NH_3 mass flow, operating gauge pressure, and exhaust gas flow were analyzed. The proposed solution aims to address challenges in hydrogen storage and transportation, offering a promising approach for energy applications. Numerical simulations demonstrate the effectiveness of the designed heat recapture NH_3 pyrolysis system, achieving up to 94% conversion of NH_3 with the use of a nickel catalyst. The rate of NH_3 decomposition shows temperature and pressure dependencies, with optimal conditions identified for enhanced reaction rates. Conversion of NH_3 remains high within 823 K to 923 K, highlighting the system's efficiency. Comparison between theoretical predictions and simulation results underscores the importance of considering turbulent flow effects in system design.

The proposed solution offers a promising approach to address challenges in hydrogen storage and transportation in the power plant industry. It offers an insight into convective

heat transfer for NH_3 pyrolysis. By utilizing NH_3 as a hydrogen carrier and integrating its decomposition within gas turbine systems, significant efficiency improvements can be achieved. Further research is needed to optimize system parameters and validate experimental results. Last but not least, the design of a catalyst tube could be one of the approaches to enhance the conversion of NH_3 in terms of fluid flow mechanics. One potential approach could be to use swirl tubes to increase the surface area for better convective heat transfer. These findings contribute to advancing clean energy technologies and promoting sustainable power generation.

Author Contributions: Conceptualization, methodology, software, analysis, validation, investigation, formal analysis, draft preparation and data curation, J.T.L.; Conceptualization, methodology, investigation, writing—review and editing, supervision and project administration, E.Y.-K.N.; software, writing—review and editing, visualization, and supervision, H.S.; Methodology, supervision and writing—review and editing, H.K.L. All authors have read and agreed to the published version of the manuscript.

Funding: This research received no external funding.

Data Availability Statement: The datasets presented in this article are not readily available because the data are part of an ongoing study. Requests to access the datasets should be directed to the authors on request.

Acknowledgments: The author would like to first express his gratitude to Nanyang Technological University (NTU), Singapore, for the opportunity to study this topic. The author would also like to extend his sincere appreciation to other co-authors for their support.

Conflicts of Interest: The authors declare no conflicts of interest.

Appendix A

The total enthalpy gained by NH_3 reported from the numerical simulation is 1.66×10^6 Jkg^{-1}. With the activation energy of 211 $kJmol^{-1}$ or 12,411 $kJkg^{-1}$, the design could convert 0.134 kg of NH_3. The mole ratio of $NH_3 : H_2 : N_2$ obtained from Equation (1) is 2:3:1.

Product mass is calculated by Equation (A1) based on an assumption of full conversion of NH_3.

$$\text{Product mass} = \text{mole} \times \text{relative molecular mass} \tag{A1}$$

Product mass fraction is calculated by Equation (A2):

$$\text{Product mass fraction}_i = \frac{\text{mass of product}_i}{\text{total mass of products}} \tag{A2}$$

i : product i.

Percentage difference is calculated to compare between the results obtained in the numerical simulation and the theoretical calculation.

$$\text{Percentage difference} = \left| \frac{\text{RPMF} - \text{CPMF}}{\text{RPMF}} \right| \times 100 \tag{A3}$$

The result obtained from the theoretical calculation is tabulated in Table A1. The percentage differences of H_2 mass and N_2 mass obtained from the numerical simulation and theoretical calculations are 2.22% and 0.49%, respectively. This could validate the results obtained from the numerical simulation in this study.

Table A1. Theoretical Calculation for Mass Fraction of H_2 and NH_3.

	Reactant	**Product**	
	NH_3	H_2	N_2
Mole ratio	2	3	1
Relative molecular mass ($gmol^{-1}$)	17	2	28
Reactant Mass (g)	134	-	-
Mole (mol)	7.88	11.82	3.94
Product Mass (g)	-	23.64	110.32
Calculated Product Mass Fraction (CPMF)	-	0.176	0.824
Reported Product Mass Fraction (RPMF)	-	0.18	0.82
Percentage Difference	-	2.22%	0.49%

References

1. Power, M. Mitsubishi Power | Mitsubishi Power Commences Development of World's First Ammonia-fired 40 MW Class Gas Turbine System—Targets to Expand Lineup of Carbon-free Power Generation Options, with Commercialization around 2025. 2021. Available online: https://power.mhi.com/news/20210301.html#:~:text=YOKOHAMA,%20JAPAN%20(March%201,,increasing%20global%20focus%20on%20decarbonization (accessed on 21 February 2024).
2. Goldmeer, D.J. *Ammonia as a Gas Turbine Fuel*; GE Gas Power: Atlanta, GA, USA, 2021.
3. Conti, J.; Holtberg, P.; Diefenderfer, J.; LaRose, A.; Turnure, J.T.; Westfall, L. *International Energy Outlook 2016 with Projections to 2040*; USDOE Energy Information Administration (EIA): Washington, DC, USA, 2016.
4. Africa's First Hydrogen Power Plant to Produce Electricity by 2024. 2022. Available online: https://www.reuters.com/business/energy/africas-first-hydrogen-power-plant-seen-producing-electricity-2024-2022-09-12/#:~:text=CAPE%20TOWN,%20Sept%2012%20(Reuters,company%20executive%20said%20on%20Monday (accessed on 21 February 2024).
5. Aresi, L. *EnergyAustralia Modernizes Tallawarra A Power Plant to Support Energy Transition in Australia*; GE VERNOVA: Cambridge, MA, USA, 2023.
6. Qing, A. First hydrogen power plant in S'pore expected by first half of 2026. In *The Straits Times*; The Straits Times: Singapore, 2022.
7. Hydrogen for Net Zero-A Critical Cost-Competitive Energy Vector. Hydrogen Council. 2021. Available online: https://hydrogencouncil.com/wp-content/uploads/2021/11/Hydrogen-for-Net-Zero.pdf (accessed on 21 February 2024).
8. Dwivedi, S.K.; Vishwakarma, M. Hydrogen embrittlement in different materials: A review. *Int. J. Hydrogen Energy* **2018**, *43*, 21603–21616. [CrossRef]
9. Ammonia: Zero-Carbon Fertiliser, Fuel and Energy Store. The Royal Society. 2020. Available online: https://royalsociety.org/green-ammonia (accessed on 21 February 2024).
10. Cheddie, D. *Ammonia as a Hydrogen Source for Fuel Cells: A Review*; InTech: London, UK, 2012. [CrossRef]
11. Duan, X.; Ji, J.; Qian, G.; Fan, C.; Zhu, Y.; Zhou, X.; Chen, D.; Yuan, W. Ammonia decomposition on Fe (1 1 0), Co (1 1 1) and Ni (1 1 1) surfaces: A density functional theory study. *J. Mol. Catal. A Chem.* **2012**, *357*, 81–86. [CrossRef]
12. Tamaru, K.; Tanaka, K.-i.; Fukasaku, S.; Ishida, S. Decomposition of ammonia on a nickel catalyst. *Trans. Faraday Soc.* **1965**, *61*, 765–772. [CrossRef]
13. Maleki, H.; Fulton, M.; Bertola, V. Kinetic assessment of H_2 production from NH_3 decomposition over CoCeAlO catalyst in a microreactor: Experiments and CFD modelling. *Chem. Eng. J.* **2021**, *411*, 128595. [CrossRef]
14. McCabe, R.W. Kinetics of ammonia decomposition on nickel. *J. Catal.* **1983**, *79*, 445–450. [CrossRef]
15. Muroyama, H.; Saburi, C.; Matsui, T.; Eguchi, K. Ammonia decomposition over Ni/La_2O_3 catalyst for on-site generation of hydrogen. *Appl. Catal. A Gen.* **2012**, *443*, 119–124. [CrossRef]
16. Okura, K.; Miyazaki, K.; Muroyama, H.; Matsui, T.; Eguchi, K. Ammonia decomposition over Ni catalysts supported on perovskite-type oxides for the on-site generation of hydrogen. *RSC Adv.* **2018**, *8*, 32102–32110. [CrossRef] [PubMed]
17. Chellappa, A.; Fischer, C.; Thomson, W. Ammonia decomposition kinetics over $Ni\text{-}Pt/Al_2O_3$ for PEM fuel cell applications. *Appl. Catal. A Gen.* **2002**, *227*, 231–240. [CrossRef]
18. Realpe, N.; Kulkarni, S.R.; Cerrillo, J.L.; Morlanés, N.; Lezcano, G.; Katikaneni, S.P.; Paglieri, S.N.; Rakib, M.; Solami, B.; Gascon, J. Modeling-aided coupling of catalysts, conditions, membranes, and reactors for efficient hydrogen production from ammonia. *React. Chem. Eng.* **2023**, *8*, 989–1004. [CrossRef]
19. Lee, J.; Ga, S.; Lim, D.; Lee, S.; Cho, H.; Kim, J. Carbon-free green hydrogen production process with induction heating-based ammonia decomposition reactor. *Chem. Eng. J.* **2023**, *457*, 141203. [CrossRef]
20. Shen, Y.; Nazir, S.M.; Zhang, K.; Duwig, C. Waste heat recovery optimization in ammonia-based gas turbine applications. *Energy* **2023**, *280*, 128079. [CrossRef]
21. Badescu, V. Optimal design and operation of ammonia decomposition reactors. *Int. J. Energy Res.* **2020**, *44*, 5360–5384. [CrossRef]

22. Liang, C.; Li, W.; Wei, Z.; Xin, Q.; Li, C. Catalytic decomposition of ammonia over nitrided MoNx/α-Al_2O_3 and NiMoNy/α-Al2O3 catalysts. *Ind. Eng. Chem. Res.* **2000**, *39*, 3694–3697. [CrossRef]
23. Hu, X.-C.; Fu, X.-P.; Wang, W.-W.; Wang, X.; Wu, K.; Si, R.; Ma, C.; Jia, C.-J.; Yan, C.-H. Ceria-supported ruthenium clusters transforming from isolated single atoms for hydrogen production via decomposition of ammonia. *Appl. Catal. B Environ.* **2020**, *268*, 118424. [CrossRef]
24. Logan, S.R.; Kemball, C. The catalytic decomposition of ammonia on evaporated metal films. *Trans. Faraday Soc.* **1960**, *56*, 144–153. [CrossRef]
25. Yunus, A.; Cengel, A.J.G. *Heat and Mass Transfer: Fundamentals & Applications*, 6th ed.; McGraw Hill Education: New York, NY, USA, 2020.
26. Ansys®. *Workbench*; 2019 R1; Ansys, Inc.: Canonsburg, PA, USA, 2019.
27. Adanta, D.; Fattah, I.R.; Muhammad, N.M. Comparison of standard k-epsilon and sst k-omega turbulence model for breastshot waterwheel simulation. *J. Mech. Sci. Eng.* **2020**, *7*, 39–44. [CrossRef]
28. Tsai, W.; Vajo, J.; Weinberg, W. Inhibition by hydrogen of the heterogeneous decomposition of ammonia on platinum. *J. Phys. Chem.* **1985**, *89*, 4926–4932. [CrossRef]
29. ANSYS. ANSYS FLUENT 12.0 Theory Guide. 23 January 2009. Available online: https://www.afs.enea.it/project/neptunius/docs/fluent/html/th/main_pre.htm (accessed on 8 April 2024).
30. Sheikholeslami, M.; Gorji-Bandpy, M.; Ganji, D.D. Review of heat transfer enhancement methods: Focus on passive methods using swirl flow devices. *Renew. Sustain. Energy Rev.* **2015**, *49*, 444–469. [CrossRef]
31. Ojelade, O.A.; Zaman, S.F. Ammonia decomposition for hydrogen production: A thermodynamic study. *Chem. Pap.* **2021**, *75*, 57–65. [CrossRef]
32. Feng, P.; Lee, M.; Wang, D.; Suzuki, Y. Ammonia thermal decomposition on quartz and stainless steel walls. *Int. J. Hydrogen Energy* **2023**, *48*, 29209–29219. [CrossRef]
33. Lucentini, I.; Garcia, X.; Vendrell, X.; Llorca, J. Review of the decomposition of ammonia to generate hydrogen. *Ind. Eng. Chem. Res.* **2021**, *60*, 18560–18611. [CrossRef]

Disclaimer/Publisher's Note: The statements, opinions and data contained in all publications are solely those of the individual author(s) and contributor(s) and not of MDPI and/or the editor(s). MDPI and/or the editor(s) disclaim responsibility for any injury to people or property resulting from any ideas, methods, instructions or products referred to in the content.

inventions

MDPI

Article

Hydraulic Drilling Nozzle Design and Research

Przemysław Toczek *, Rafał Wiśniowski, Albert Złotkowski and Wojciech Teper

Drilling and Geoengineering Department, Oil and Gas Faculty, AGH University of Krakow, 30-059 Krakow, Poland; wisniows@agh.edu.pl (R.W.); azlot@agh.edu.pl (A.Z.)
* Correspondence: toczek@agh.edu.pl; Tel.: +48-79-8744473

Abstract: In light of the European Union's zero-emissions policy and the growing demand for energy associated with technological advances, it is necessary to consider adopting technologies and innovative solutions that simultaneously reduce greenhouse gas emissions while increasing potential extraction from existing hydrocarbon deposits, for example. This can result in increased production from deposits with low reservoir energy values or those in which the energy value does not allow the resource to be exploited on its own. By using a hydraulic drilling nozzle that harnesses the hydraulic energy of the fluid stream for workover, the possibility of increasing the contact between the reservoir layer and the producing well increases in direct proportion to the number of small-diameter radial wells drilled with a hydraulic rotary head from a horizontal well toward the reservoir layer. The main aspect of this paper is to outline an algorithm for the design of rotary drilling heads to maximize the use of the hydraulic energy from fluid streams flowing from the face of innovative drilling tools. The presented design algorithm allows changing the mutual position between the holes in the face section and the angle of the holes with respect to the longitudinal axis of the designed hydraulic rotary nozzle, simplifying the design work. The use of the rotary head developed using this algorithm enables seamless drilling in rocks with compressive strength R_c = 50 MPa, considering the drilling progress at ROP = 4 mm/s.

Keywords: hydraulic radial drilling; drilling nozzle; nozzle designs; radial jet drilling; small diameter borehole; hydraulic energy

1. Hydraulic Radial Jet Drilling System

At present, jet nozzle drilling technology is widely utilized for cutting, hydraulic jet drilling, or pipeline cleaning due to its effective energy concentration in the jet. The general equipment and tool arrangement for creating radial holes using a high-energy liquid jet flowing through the openings of the nozzle at high pressure includes some necessary pieces such as a coiled tubing unit, a casing windows milling kit, positioning kit, high-pressure elastic hose, deflector, anchors, packers, and at the end of the high-pressure hose, an installed hydraulic drilling nozzle with openings on its tool face (Figure 1) [1–3], (Figure 2) [4]. This approach is commonly found in various configurations and is extensively documented in numerous publications and patents [5–10]. While specific solutions may differ in technical specifics, the basic method for drilling radial boreholes remains grounded in hydraulic jet drilling techniques. Most equipment for drilling lateral boreholes from a parent well requires the creation of a hole in the casing wall using a tool head, typically in the form of a mill. Before drilling into the rock formation, it's often necessary to mill through the casing and cement sheath. This is done using either a tungsten carbide mill (which needs to be retrieved to the surface) or a jet nozzle (like the mill), which is used to bore through the rock. The drive for the milling head/mill is provided by a motor suspended on coiled tubing (CT) wound on a drum. A downhole hydraulic or electric motor may require a gearbox to achieve the appropriate rotational speed for the milling bit cutting through the casing wall. The motor needs to be anchored in the production or casing tubing to transfer the resistance torque from the mill. Then, to pass through the

hole in the casing, a hose with a jetting head is used to erode a lateral hole in the rock formation. As the drilling progresses, the coiled tubing is usually lowered, to which the flexible hose is attached. The differences generally lie in the method of creating holes in the casing. For each subsequent lateral borehole, the milling head, drive assembly, and coiled tubing must either be retrieved from the deflector and replaced with a drilling tool, such as a jetting nozzle, or the jetting head bores through the casing, continuing to drill the hole to a specified length.

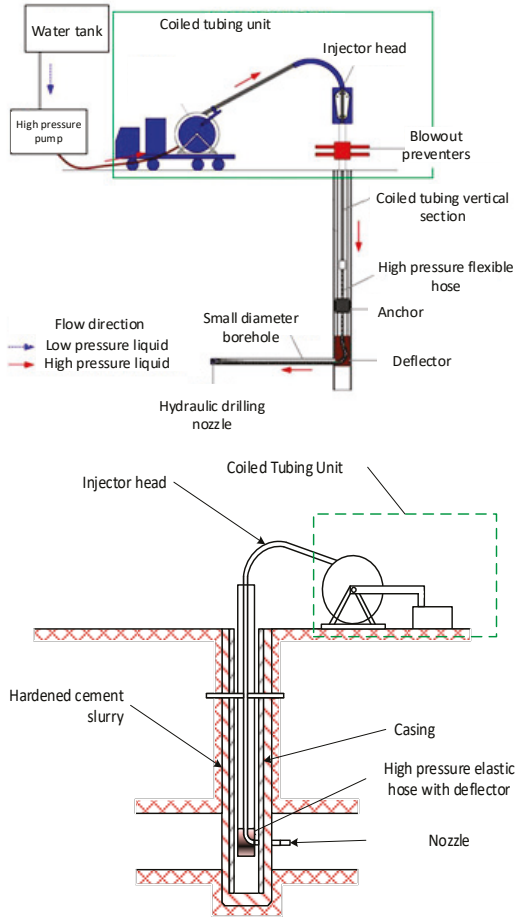


Figure 1. Ultrashort radius radial system (URRS) scheme [1,2].

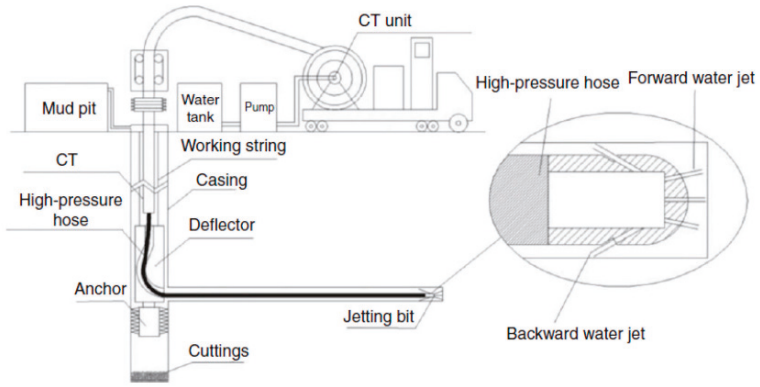


Figure 2. Ultrashort radius radial system (URRS) scheme with indication of hydraulic nozzle [4].

During the drilling of such radial boreholes, the sections are typically horizontal, varying in length from 100 to 300 m, with the diameters ranging between 20 and 60 mm. The significant variability in horizontal section lengths is due to specific requirements for

the length of the drainage zone. The absence of a fixed borehole diameter results from the nature of nozzle hydroprobing, the structure of the wellbore medium, and various technological factors and parameters associated with the reservoir rock.

In radial drilling systems, achieving the desired objective is crucial: to create a horizontal borehole with a diameter ranging from 20 to 60 mm and a length of up to 200 m using hydroabrasion techniques in rocks of specified strength, porosity, and permeability, containing specific reservoir fluids, and located at a certain depth. When considering the entire system from the beginning, which includes the Coiled Tubing Unit with the tubing wound on the drum and the working fluid tanks, parameters such as the tensile strength of the flexible tubing, the density and viscosity of the working fluid, the resistance between the flexible tubing and the injector head of the CT unit, and then the tensile strength of the flexible tubing after passing through the blowout preventer system should be taken into account. Pressure losses will occur along the entire length of the tubing wound on the drum during the flow of the working fluid, which will depend on the parameters of the fluids used, such as the aforementioned density and dynamic viscosity. The total pressure losses during the flow of the working fluids must also consider losses at the point where the tubing passes through the deflector of the hydraulic head, the rotary nozzle of the hydraulic head, and all pressure losses in the straight sections of the conduit delivering the fluid to the bottom of the well. Increasing the length of the borehole hydraulically drilled will be important from the perspective of hydroabrasion. There are, therefore, a number of different types of relationships, mainly hydrodynamic, mechanical, and strength-related, between the individual elements of the system. Each element of the system has a greater or lesser impact, not only on the other elements but also on the entire system. The effect of the system on the surrounding medium (reservoir rock) causes a response from this medium (borehole diameter, length of the borehole, borehole wall roughness, curvature, and inclination of the borehole), which in turn affects the system and its elements. For example, certain technological parameters of the drilling process will create, among other things, a certain roughness of the borehole wall, which in turn will affect its length and, consequently, the range of such a borehole, resulting from the frictional force between the borehole wall and the pressure tubing. After the development of the rotary drilling nozzle, the first stage of the research program is to start drilling with the designed nozzle on the surface under atmospheric pressure. This will provide data directly related to the drilling capabilities of the rotary drilling nozzle. The distance between the nozzle and the rock helps calculate the hydraulic pressure of the jet, the power of the jet, and the diameter of the jet to enable drilling. In addition, it helps to design the diameter and location of the discharge holes on the face and back of the rotary drilling nozzle. Tests carried out in an atmospheric pressure environment will allow the creation and planning of laboratory tests in the environment of a nozzle immersed in liquid and ambient pressure in the range of 2–12 MPa in a pressure chamber. All laboratory tests are closely related to each other. Ultimately, after the tests are completed, it is possible to infer from the drilled holes the final diameter of the holes and their mutual arrangement in the rotary drilling nozzle. Therefore, the design of each component of the system must take into account a number of relationships between them. These, in turn, form the basis for selecting pumps, nozzles, and conduits for specific reservoir conditions.

2. Basics of Radial Jet Drilling

Drilling techniques for small-diameter boreholes using hydroabrasion require a departure from traditional methods of transferring mechanical energy to the drill bit through a rotating drill string, torque from a downhole motor, mechanically generated impact energy, or indirectly through a hydraulic medium. Utilizing the energy from the jet stream exiting the drill bit nozzles allows for the utilization of previously unused hydraulic energy for hydroabrasion of hard rocks. A similar case arises when abrasive particles are added to the drilling fluid, directly increasing the impact force on the hydro-abraded rock surface. Maurer presented an example of the development of drilling head solutions utilizing rock

hydroabrasion methods [11]. The measure of energy required to drill a unit volume of rock during the drilling process is the specific drilling energy. In the case of hydroabrasion, the focus is often on the energy consumed to create a fissure in the rock [11], expressed as the ratio of energy to the product of the depth and width of the fissure and the velocity during the fissure cutting process. In classical drilling, we refer to the total drilling energy TSE (total specific energy), expressed as the sum of the energy rotational motion, the movement of the drill string, and the hydraulic energy required to drill a unit volume of rock during the drilling process [12–15]. In the 1960s, a patent [16] was already granted for a drill utilizing the hydraulic energy of a liquid jet combined with the addition of abrasive material. Steel shot with a diameter of 1.6–3.3 mm and a concentration of 890 N/158.99 L of drilling fluid was commonly used, or alternatively, rounded Ottawa sand grains with a diameter of 0.8–3.2 mm and a concentration of 445 N/158.99 L of drilling fluid. Patents reveal numerous solutions regarding the implementation of hydraulic drilling with a liquid jet, considering various factors.

Requirements for Developing Radial Drilling Technology

When designing hydraulic parameters for radial drilling, the selection of parameters is based on ensuring:

- The ability to drill the rock structure using a high-pressure and high-velocity fluid jet from the nozzle through the front openings,
- The ability to pull the pressure hose directly to the bottom of the borehole that is radially drilled due to the openings directed in the opposite direction to the front nozzles, creating a radial opening.

When selecting hydraulic parameters, it is also important to consider the allowable operating pressure of the system and the length and diameter of the horizontal section. Worldwide, various research is being conducted to determine the hydraulic parameters for radial drilling equipment. The technique of drilling small-diameter holes using hydraulic fracturing requires a departure from traditional methods of transferring mechanical energy to the drill bit, such as rotating the drill pipe, torque from the downhole motor, or mechanical impact energy generated directly or indirectly by hydraulic means. Utilizing the energy of the fluid jet from the drill nozzles allows for the utilization of hydraulic energy, which was previously not directly utilized, to fracture hard rocks.

3. Construction of a Rotary Drilling Head

The process of rock breaking using the energy of a liquid jet requires the use of a suitable device to convert the potential energy of the liquid jet into kinetic energy. For this purpose, a breaking head is used, which is designed to change the static pressure of the fluid into dynamic pressure. This change is achieved by altering the cross-section of the outlet channel through which the pumped fluid is released outside the openings of the drilling rotary nozzle.

Hydraulic drilling nozzles can be divided into:

- Static ones—where the liquid jets and head elements do not rotate,
- Rotating ones—if the rotating element generates a field of rotating jets or internal jet guidance causes swirling, resulting in a swirling motion after leaving the breaking head.

In addition, the hydraulic drilling nozzle may have an option for mechanical rock cutting (if it is designed as a rotating structure and equipped with cutting blades on its rotating element). In this case, the outlet hole arrangement should be designed to serve as a driving mechanism adapted to generate the torque required for rock cutting through slicing.

Custom hydraulic rotary drilling nozzles were fabricated based on the authors' own concept. The heads were subjected to tests of thrust force in atmospheric air and in conditions of a jet submerged in liquid, as well as to investigate their interaction with

the drilled rock formation in the form of blocks measuring 300 × 300 × 500 mm. The tool designs proposed below stem from an analysis of available literature solutions of patented inventions. Patents reveal static nozzle solutions and solutions with rotating parts equipped with outlet openings [17,18]. In many solutions, multiple outlet openings are positioned at appropriate angles relative to the head axis. This results in improved coverage of the borehole bottom surface during hydraulic fracturing [8,9,19,20]. Rotating nozzle tools composed of a bearing assembly with dynamic sealing provide more efficient and effective drilling compared to static heads. The bearing assembly, with a static outer body, transfers mechanical and hydraulic loads to the rotating shaft [21]. In some solutions, abrasive material was utilized to enhance the impact force on the bottom of the drilled hole [22]. For the implementation of the planned testing procedure, a research head was fabricated in several variants. The openings in the interchangeable tips were made cylindrical with diameters of 0.4, 0.5, 0.6, 0.7, 0.8, 1.0 and 1.2 mm. The range of jets flowing out of the openings with different diameters was determined during the tests of the hydraulic fracturing efficiency of the test head equipped with one central front opening and six openings made on the side of the cylinder, into which tips with appropriately calibrated diameters of outlet openings were screwed [15]. Given the jet range obtained during the tests of the jet flow from openings of varying diameters, the maximum point is determined along the red line, where the energy of the jet flowing out of the opening allows for volumetric rock hydraulic fracturing, as shown in Figure 3. Projecting this point onto a plane parallel to the cross-section of the rotating head in a direction perpendicular to the axis of the head will allow for the determination of the exit point of the second breaking hole with a designed outlet diameter d. Re-determining the maximum range of the jet flowing out of the opening with the designed diameter and its projection onto a plane parallel to the cross-section perpendicular to the axis of the rotating head will allow for the determination of the exit point of the third outlet hole of the designed rotating drilling nozzle.

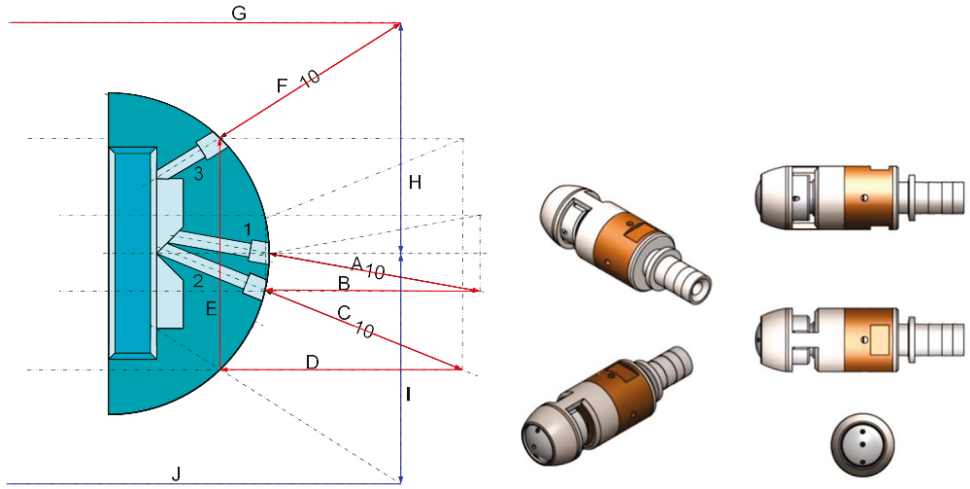


Figure 3. Angle of openings, hydraulic radial drilling hole diameter determination scheme, and an external view of the designed rotary drilling nozzle with its tool face.

The maximum range of the jet flowing out of the designed opening and its projection onto a plane parallel to the cross-section in a direction perpendicular to the axis of the rotating head allow for the determination of the effective range of the jet and the radius from the axis of the rotating head to the diameter of the propagated hole. The design of the rotary head begins by assuming an angle of inclination of the outlet hole 1 with respect to the axis of the rotary head and along line A at the chosen angle plotting a line with the length of the stream reach allowing volumetric mining of the rock equal to 10 cm for a given diameter of the outlet hole (in our case it is a 0.8 mm diameter hole at a discharge pressure P = 40 MPa [15]). Then, from a point 10 cm away on line A from the head face, line B is plotted to the head face parallel to the head axis, determining the location of hole

2. Assuming the same diameter of the outlet holes, line C is plotted again, coming out of outlet hole 2 with a length of 10 cm as before. By dropping a point on straight line C with a length of 10 cm from the head of the rotary head by line D and transferring to the other side of the head by line E, it is possible to determine the outlet of hole 3 on the head of the rotary head. Analogously, as before, assuming the diameter of outlet hole 3 is equal to 0.8 mm, a straight line 10 cm long from the face of the head along line F is determined. From that point on line F, a line G is plotted, which determines, together with line J by plotting lines H and I perpendicular to the head axis, the diameter of the borehole made by the hydraulic rotary head. Considering the above methodology, various rotary tip threads installed at the end of the rotary drilling nozzle, as shown in Figure 4, were prepared in order to study the possibility of propagating a hole of sufficient diameter that will allow the rotary drilling nozzle to move freely into the depths of the hydraulic borehole being drilled.



Figure 4. The beginning of hydraulic radial drilling using the rotary drilling nozzle (the visible rings are caused by the rotational movement of the liquid jets flowing from the outlet openings at various distances between the face tool and the rock).

The geometry of the three cones formed during the initial operation of the test nozzle is shown in Figure 5 below, where successive cones are visible, overlapping as hydraulic fracturing progresses.



Figure 5. Designed rotary drilling nozzle during laboratory research tests.

4. Filed Research Tests

To confirm the feasibility of hydraulic drilling with the designed hydraulic rotary head as shown in Figure 6, a series of laboratory tests were planned, both in atmospheric pressure conditions and in an environment with a submerged jet in fluid. Additionally, tests under surrounding pressure conditions ranging from 2 to 12 MPa were also scheduled. The liquid used in the study was water. Tests were conducted under various temperature conditions ranging from 1–28 degrees Celsius.

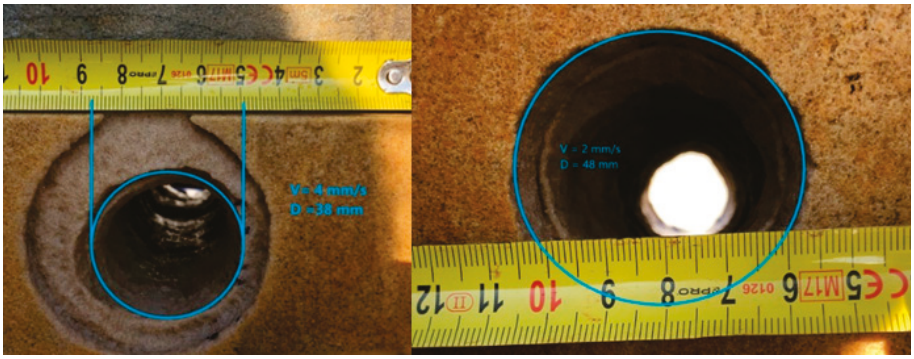


Figure 6. Diameter of boreholes drilled with a hydraulic rotary head at different rates of penetration for sample B1 under atmospheric pressure conditions.

Due to the broad scope of the tests conducted, only fragmented results are presented in this article. The main purpose of the conducted research was to confirm the hydraulic drilling of rock samples using the designed hydraulic rotary head. Two sandstone blocks with compressive strengths of B1 = 24.07 MPa and B2 = 49.64 MPa, respectively, and porosities of 22.41 and 22.21% were subjected to the study. Grain thickness was observed at the level of 0.2–0.3 mm for sample B1 and 0.05–0.1 mm for sample B2. The research tests were conducted at a jet pressure of 50 MPa in atmospheric pressure conditions.

Below are shown the inlet holes made in the B2 rock blocks (Figure 7). The measurement of the diameter of the drilled holes in the tested rock blocks involved overlaying dimensioned photographs with circles closely matching the outlet holes.



Figure 7. Diameter of boreholes drilled with a hydraulic rotary head at different rates of penetration for sample B2 under atmospheric pressure conditions.

The comparison of the diameters of the drilled holes in sandstone B2 (Figure 7) using a rotary drilling head confirms that a decrease in drilling speed results in an increase in the diameter of the entire drilled hole. This is due to the effective flow time of the fluid jet working with the rock block. The percentage increase in the penetration rate used in the tests for the gray sandstone is 12.9%, benefiting drilling at a speed of V = 2 mm/s. This is, of course, dictated by the extended contact time of the fluid jet with the rock formation being drilled. For sandstone B1 (Figure 6), the increase in the penetration rate when reducing the drilling speed to V = 2 mm/s is comparable and amounts to 14.3%. The recording of the parameters during the tests conducted with the developed nozzle at different rates of penetration is shown in Figure 8 below. As mentioned earlier, the designed hydraulic radial nozzle will allow for drilling with the use of jet stream energy. The possibility of rock cutting depends on various parameters. The penetrability of rock samples is directly proportional to physical and mechanical parameters such as porosity, permeability, and compressive strength, as well as the type and size of the mutual arrangement of rock grain.

If a situation arises where the hydraulic drilling nozzle gets stuck at the bottom of the hole during the drilling process, changing the diameter and angle of the openings on the tool face of the nozzle, according to Figure 3, will allow a deeper borehole to be drilled. Before starting the drilling process with a newly designed tool face, it must be preceded by laboratory tests with a newly developed rotary drilling nozzle.

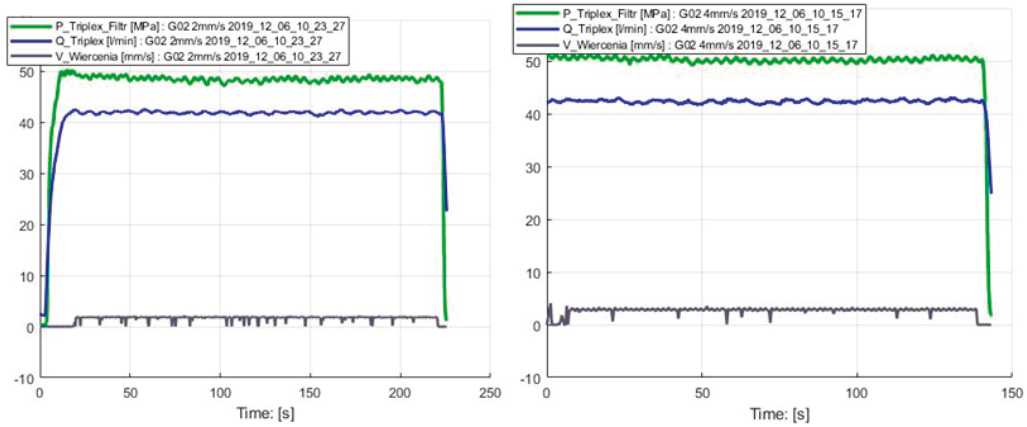


Figure 8. The recording of the parameters during the conducted tests at drilling speeds V = 2 mm/s and V = 4 mm/s.

5. Conclusions

The liquid jet, which has been given significant velocity as it flows out of the outlet holes, is directed towards the rock. If the liquid jet, upon contact with the rock, has sufficiently high energy and creates stress on the rock surface exceeding its breaking strength, a crater is formed. By multiplying the number of jets exiting the head and directing them appropriately, a field of craters is created, forming the bottom of a small-to-medium-sized borehole drilled using the hydraulic fracturing technique. The propagation of the borehole is possible if the movement of the head leads to the deepening of the craters formed. This propagation occurs when the reverse openings of the breaking head generate a thrust force greater than the force pushing the head through the front openings. The force pushing the head towards the bottom of the hole depends on the perpendicular projections of the forces on the surface normal to the main axis of the head. The component forces, however, depend on the jet velocities, fluid density, and cross-sectional areas of the openings. Drilling operations carried out with a hydraulic rotary drilling nozzle under atmospheric pressure conditions at drilling speeds of V = 2 mm/s and V = 4 mm/s have shown that drilling proceeds smoothly, as indicated in Figure 8. There was no jamming of the drilling head during the conducted tests. This indicates a properly designed rotary drilling head, along with the outlet holes, their diameters, and their inclination relative to the axis of the designed rotary drilling head.

Taking the above into consideration, it is also necessary to confirm the proposed methodology for designing the diameter of the outlet holes in the rotary head, as well as their angle of inclination relative to the axis of the designed rotary heads. The methodology presented in Figure 3 allows for determining the maximum diameter of the propagated hole. However, knowledge of the maximum ranges of the fluid jets at the appropriate injection pressure emanating from the outlet holes of the rotary head with different hole diameters is essential. The method for determining the range of the fluid jet at which volumetric hydraulic fracturing of the tested rock formation still occurs is presented in the study [15]. The developed rotary hydraulic nozzle has been thoroughly investigated. Studies in the environment of a submerged fluid jet and under surrounding pressure conditions have been described in another forthcoming publication. The future scope of research will focus on conducting laboratory tests in an environment ranging from 2–12 MPa in a pressure chamber. The study will demonstrate the correctness of the drill head design used and identify possible directions for improvement of the designed rotary device.

Author Contributions: Conceptualization, P.T. and R.W.; methodology, P.T., R.W., A.Z. and W.T.; software, P.T.; validation, P.T., A.Z. and W.T.; formal analysis, P.T.; investigation, P.T.; resources, P.T., A.Z. and W.T.; data curation, P.T., A.Z. and W.T.; writing—original draft preparation, P.T.; writing—review and editing, P.T.; visualization, P.T.; supervision, P.T. and R.W. All authors have read and agreed to the published version of the manuscript.

Funding: This research received no external funding.

Data Availability Statement: The raw data supporting the conclusions of this article will be made available by the authors on request.

Conflicts of Interest: The authors declare no conflict of interest.

References

1. Chi, H.; Li, G.; Huang, Z.; Tian, S.; Song, X. Maximum Drillable Length of the Radial Horizontal Micro—Hole Drilled with Multiple High–Pressure Water Jets. *J. Nat. Gas Sci. Eng.* **2015**, *26*, 1042–1049. [CrossRef]
2. Toczek, P.; Wiśniowski, R. Enhancing Deposit Exploitation Efficiency Utilizing Small-Diameter Radial Boreholes via Hydraulic Drilling Nozzles for Optimal Resource Recovery. *Appl. Sci.* **2024**, *14*, 3552. [CrossRef]
3. Bi, G.; Li, G.; Shen, Z.; Huang, Z.; Ma, D.; Dou, L. Experimental Research on the Technology of Hydra–Jet Sidetracking of Radial Micro–borehole. *J. Eng. Sci. Technol. Rev.* **2013**, *6*, 137–142. [CrossRef]
4. Wiechman, A.; Ahmed, R. A Generalized Hydraulic Model for Propulsion Force Calculations in Radial Jet Drilling. *SPE Drill. Complet.* **2023**, *38*, 289–305. [CrossRef]
5. Toma, P.; Reitman, V.; Coffin, P.; Dickinson, W. Long and Ultrashort Turning Radius of Horizontal Wells Predictions of Future Production Based on Today's Experience. In Proceedings of the 13th World Petroleum Congress, Buenos Aires, Argentina, 20–25 October 1991.
6. Salem Ragab, A.M. Improving well Productivity in an Egyptian Oil Feld Using Radial Drilling Technique. *J. Pet. Gas Eng.* **2013**, *4*, 103–117.
7. Kamel, A.H. A Cost Effective Frackless Solution for Production Enhancement in Marginal Fields. In Proceedings of the SPE Eastern Regional Meeting, Canton, OH, USA, 13–15 September 2016. [CrossRef]
8. Landers, C. Method of and Apparatus for Horizontal Well Drilling. Patent US6125949A, 3 October 2000.
9. McLeod, R.D.; Dwight, N.L. Lateral Jet Drilling System. Patent US6125949B1, 20 February 2001.
10. Peters, J.N. Method and Apparatus for Lateral Well Drilling Utilizing an Abrasive Fluid Stream Discharged from Rotating Nozzle. Patent US0173544A1, 9 July 2009.
11. Maurer, W.C. *Advanced Drilling Techniques*; Petroleum Publishing Co.: Tulsa, OK, USA, 1980.
12. Jeffryes, B.P. Schlumberger Oilfield Research, Novel Drilling Techniques, Chapter 9.5. In *Advanced Drilling and Well Technology*; SPE: Willis, TX, USA, 2009.
13. Wiśniowski, R.; Knez, D.; Hytroś, Ł. Drillability and Mechanical Specific Energy Analysis on The Example of Drilling in The Pomeranian Basin. *AGH Drill. Oil Gas* **2015**, *32*, 201. [CrossRef]
14. Toczek, P.; Wisniowski, R.; Stryczek, S.; Ziaja, J.; Mazur, C. Total Specific Energy (TSE) As a New Indicator of Drilling Efficiency. *AGH Drill. Oil Gas* **2017**, *34*, 715–729. [CrossRef]
15. Toczek, P.; Wisniowski, R.; Zlotkowski, A.; Teper, W. Hydraulic Radial Drilling Using a Rotary Hydraulic Nozzle Aimed at Increasing the Exploitation of Deposits. *Energies* **2023**, *16*, 7867. [CrossRef]
16. Bobo, R.A. Method of Drilling with High Velocity Jet Cutter Roller Bit. Patent 3112800, 3 December 1969.
17. Buckman, G.W. Method and Apparatus for Jet Drilling Drainholes from Wells. Patent US6263984, 24 July 2001.
18. Buckman, G.W. Nozzle for Jet Drilling and Associated Method. Patent US6668948, 30 December 2003.
19. Landers, C. Method of and Apparatus for Horizontal Drilling. Patent US5413184, 9 May 1995.
20. Landers, C. Method of and Apparatus for Horizontal Well Drilling. Patent US5853056, 29 December 1998.
21. Buckman, G.W. Rotary Jet Bit for Jet Drilling and Cleaning. Patent US0054092A1, 27 February 2014.
22. Ben, W.O.D.; Dickinson, R.W.; Jensen, R.; May, S.C.; Mackey, C.S.; Wilkes, R.D. Hydraulic Drilling Apparatus and Method. 29 November 1988.

Disclaimer/Publisher's Note: The statements, opinions and data contained in all publications are solely those of the individual author(s) and contributor(s) and not of MDPI and/or the editor(s). MDPI and/or the editor(s) disclaim responsibility for any injury to people or property resulting from any ideas, methods, instructions or products referred to in the content.

inventions

MDPI

Article

Improving the Hydrodynamic Performance of Underwater Tags for Blue Shark Monitoring

José Azevedo [1], Violeta Carvalho [1,2,3,4], Tiago Bartolomeu [5], Ana Arieira [2], Senhorinha F. Teixeira [3,*] and José C. Teixeira [1]

[1] MEtRICs Research Centre, University of Minho, 4800-058 Guimarães, Portugal; guilherme_azevedo94@hotmail.com (J.A.); violeta.carvalho@dps.uminho.pt (V.C.); jt@dem.uminho.pt (J.C.T.)
[2] CMEMS Research Centre, University of Minho, 4800-058 Guimarães, Portugal; ana.a.arieira@gmail.com
[3] ALGORITMI Research Centre, University of Minho, 4800-058 Guimarães, Portugal
[4] LABELS—Associate Laboratory, 4800-058 Guimarães, Portugal
[5] CEiiA, Av. D. Afonso Henriques, 1825, 4450-017 Matosinhos, Portugal; tiago.bartolomeu@ceiia.com
* Correspondence: st@dps.uminho.pt

Abstract: The use of tag devices in marine environments has become indispensable in attaining a better understanding of marine life and contributing to conservation efforts. However, the successful deployment and operation of underwater tags both depend significantly on their hydrodynamic characteristics, particularly their resistance to motion and stability in various environmental conditions. Herein, a comprehensive study on the hydrodynamic characteristics and optimization of an underwater tag designed for monitoring blue sharks is presented. Firstly, a validation process is conducted by comparing the computational fluid dynamics (CFD) results with the experimental data from Myring's study, focusing on the resistance characteristics of the tag's body and the impact of various operational conditions. Subsequently, the validated CFD model is applied to assess the hydrodynamic performance of the tag under different flow conditions, velocities, and angles of attack. Through iterative simulations, including mesh independence studies and boundary condition adjustments, the study identifies key parameters influencing the tag's resistance and stability. Furthermore, the paper proposes and implements design modifications, including the incorporation of stabilizing fins, aimed at minimizing resistance and improving the tag's equilibrium position. The effectiveness of these design enhancements is demonstrated through a comparative analysis of resistance and pitching moments for both preliminary and optimized tag configurations. Overall, the study provides valuable insights into the hydrodynamic behavior of underwater tags and offers practical recommendations for optimizing their design to minimize interference with the movement of tagged marine animals.

Keywords: tag devices; sharks; CFD; validation; design improvement; hydrodynamic

1. Introduction

Underwater tagging technology plays a crucial role in understanding the behavior and ecology of marine animals [1–4]. These devices provide researchers with valuable data on migration patterns, behavior, and ecological interactions [5–8]. Moreover, the data collected from tag devices contribute to the development of evidence-based conservation policies and protected marine areas [9–12]. However, their use in marine environments comes with challenges [13]. Ensuring the welfare of tagged animals, minimizing the environmental impact of the tags, and addressing data accuracy issues are ongoing considerations in marine research. To ensure that the acquired data accurately reflect the typical behavior of the animal and can be generalized for the entire species, it is imperative to guarantee that the tagging process does not disrupt the animal carrying the tag [14,15]. For this reason, researchers have dedicated considerable efforts to advancing hydrodynamic tags tailored for specific applications [16,17].

Computational fluid dynamics (CFD) offers researchers the ability to analyze complex flow problems with precision in several engineering areas, including aquatic research [18–20]. Nevertheless, it is of great importance to validate the numerical model. Pan et al. [21] were able to predict within a 5% discrepancy margin, when compared with experimental results, the force and moment coefficients for a submarine shape inspired in Myring's design [22]. Another example was presented by Bartolomeu et al. [23], who correlated simulated data through CFD with the experimental data gathered in Myring's work, towing a torpedo-shaped body through a water tank. Although the presented cases refer to large-scale bodies when compared to the ones typical of a tagging device and not necessarily operating in the same range of Reynolds number, one particular paper presented the results of a laminar flow across a micro autonomous underwater vehicle, which was 200 mm in length [17]. The authors could find some correlation between the few experimental data and simulated results. On the other hand, Wang and co-workers [24] proposed a micro hydropower system to enhance the energy supply for marine animal telemetry tags, allowing them to collect environmental and biological behavior data during migrations and dives. The researchers developed a mathematical model for the power system and validated it through experimental tests. The results showed that the energy efficiency is minimally influenced by the dive depth and showed to be a highly efficient method for ultra-high head hydropower generation in marine environments.

Artificial intelligence is another tool that that can help us to have a deeper understanding of the underwater world in regard to topics such as species conservation, pollution monitoring, and sustainable fisheries management [25,26]. This synergy can greatly improve aquatic monitoring and the exploration of the ocean depths. Furthermore, AI-powered robots, such as the CUREE robot [25], are an example of that, as they can operate autonomously, minimizing human interference with marine life.

Despite the efforts made so far, as technology continues to advance, researchers are exploring innovative solutions to enhance the capabilities of tag devices, while mitigating potential drawbacks. For instance, blue sharks are one of the most widely spread species of sharks and also one of the most fished [6]. Although there are a lot of unknowns about their existence, distribution, and habits, they are considered to be "near threatened" [27–29] according to the extinction scale. Bearing this in mind, a non-intrusive shark tagging-device conceptualization was previously developed [30], aiming to not harm the animals and not disrupt their natural behavior. In the present work, the optimization of this shark tagging device is presented, highlighting the integration of stabilizing elements such as fins. CFD simulations were conducted by using Ansys Fluent software, and their validation was conducted.

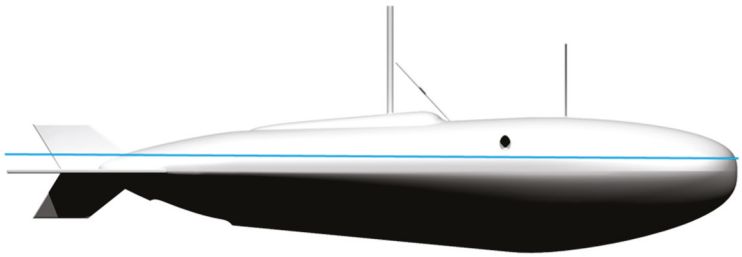
2. Materials and Methods

2.1. Geometry and Mesh

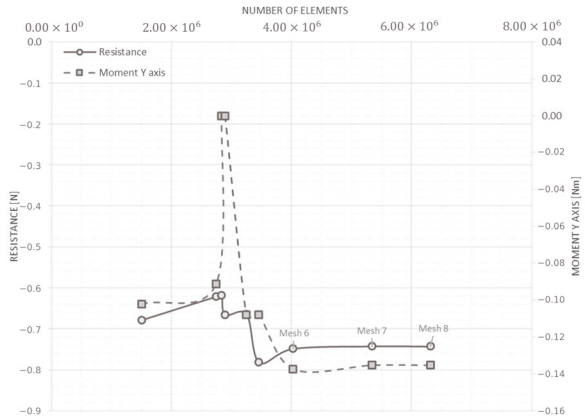
The conceptual shape of the tag's body device is simulated in order to study the effects of the flow conditions (Figure 1a) [28]. In this way, the flow domain around the tag was also modelled. To ensure that the full development of the wake would be well captured, a length downstream of the body of three times its length was kept [23,31]. The domain was designed with a curved inlet region, allowing for the flexibility of inlet directions.

The next step consisted of discretizing the domain into small elements, forming the mesh to perform the CFD simulation. In the first stage, the elements forming the faces of the body were downsized, assuring shape fidelity. Subsequently, the first layers of elements around the body were refined so that they gradually grow from the body until the free stream region. This refined region, also known as the inflation layer, allows us to capture the viscous phenomena inside the boundary layer of the flow. Furthermore, the first layer's height is a determinant factor for the y+ mesh value, which is the non-dimensional distance of this height based on the local fluid velocity. Lastly, the wake region also needs to be more refined compared to the undisturbed region of the flow, which may be achieved by implementing a control volume—in this case, a cylinder. These regions are prone to

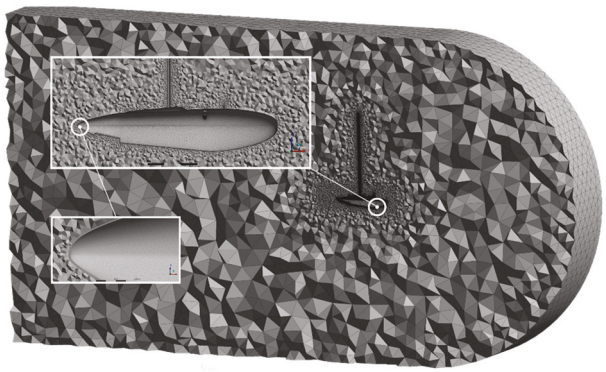
the formation of vortices and reverse flow, hence affecting the overall resistance. A mesh independence study was necessary in order to choose the best domain discretization (Figure 1b).



(**a**)



(**b**)



(**c**)

Figure 1. (**a**) Validated concept. (**b**) Mesh independency study for the tag concept design. (**c**) Validated concept's mesh.

Figure 1b shows the results obtained with the different meshes, in which it is visible that mesh 6 yields basically the same results as meshes 7 and 8, having 2 million elements less than the latter. For this reason, mesh 6 was selected for simulating the different operational cases. Figure 1c depicts the mesh size along a longitudinal plane, including the regions of refined mesh (as inserts).

2.2. Governing Equations

The fluid flow around the tag was simulated utilizing a finite volume-based simulation approach implemented into the Ansys FLUENT R19 software. This solves the three-dimensional equations for mass (Equation (1)) and momentum (Equation (2)), assuming conservation for each variable:

$$\nabla \vec{v} = 0 \tag{1}$$

$$\nabla \cdot \left(\rho \vec{v} \vec{v} \right) = -\nabla p + \nabla \cdot (\overline{\overline{\tau}}) \tag{2}$$

The fluid was assumed incompressible and turbulent. In turbulent flows, such as those expected around the tag, chaotic fluctuations in velocity and pressure are verified [32]. In the present work, the $k - \omega$ SST model was chosen since it not only reveals a better agreement with the experimental [20] results but is also able to capture the viscous effects inside the boundary layer opposite to the $k - \epsilon$ model [32].

This is an empirical model based on modelled transport equations for the turbulent kinetic energy, k, and the specific dissipation rate, ω (Equations (3) and (4)):

$$\frac{\partial}{\partial x_i}(\rho k u_i) = \frac{\partial}{\partial x_j}\left(\Gamma_k \frac{\partial_k}{\partial x_j}\right) + G_k - Y_k + S_k \tag{3}$$

$$\frac{\partial}{\partial x_i}(\rho \omega u_i) = \frac{\partial}{\partial x_j}\left(\Gamma_\omega \frac{\partial_\omega}{\partial x_j}\right) + G_\omega - Y_\omega + D_\omega + S_\omega \tag{4}$$

where G_k represents the generation of turbulence kinetic energy due to mean velocity gradients; G_ω represents the generation of ω; Γ_ω and Γ_k represent the effective diffusivity of k and ω, respectively; Y_k and Y_ω represent the dissipation of k and ω due to turbulence; D_ω represents the cross-diffusion term; and, finally, S_k and S_ω are user-defined source terms.

2.3. Boundary Conditions and Fluid Properties

The selected fluid for the simulations was liquid water. However, its density was adjusted to 1025 kg m^{-3}, and its dynamic viscosity was defined as 0.001518 kg m^{-1} s^{-1} to better reflect seawater at a 1000 m depth [33].

To close the differential equations (Equations (1) and (2)), an inlet velocity was assumed based on the flow direction and magnitude, as well as a pressure outlet on the opposite wall. Also, the wet surfaces of the tag were defined as walls, and the lateral boundaries were defined as walls with a free-slip condition to avoid the influence of its viscous effects on the remaining flow.

The turbulence intensity was set to 0.05%, as recommended by Ansys for free stream flows. As for the turbulence length scale, it was set to 7% of the bodies' length, which is an appropriate approximation for a flow across an obstacle [34]. Nonetheless, the turbulence generated in the shear layers makes the result insensitive to this value.

3. Numerical Model Validation

Before proceeding with the various tests and obtaining the results, a validation of the numerical model is important. The model was applied to a known geometry whose accurate experimental results are available in the literature.

3.1. Geometry and Mesh

Amongst all the reviewed works, Myring's study [22] emerges as a reference for many designs of underwater vehicles. Moreover, this work is the most detailed in terms of resistance characterization. As such, the intended flow conditions ought to be implemented, based on one of his designs, and the model validated through comparison with his results. The geometry studied by Myring is defined by equations that provide the radius (r) at a given axial location (x), as described in Equations (5)–(7):

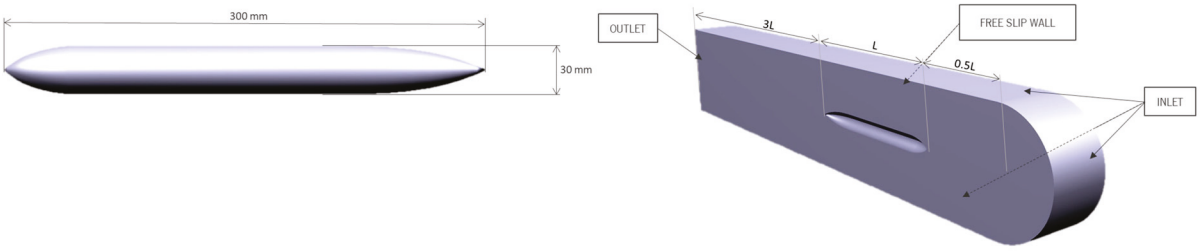
$$\text{Nose section :} \qquad r = \frac{1}{2}D\left[1 - \left(\frac{x-a}{a}\right)^2\right]^{\frac{1}{n}} \tag{5}$$

$$\text{Mid-section :} \qquad r = \frac{1}{2}D \tag{6}$$

$$\text{Tail section :} \qquad r = \frac{1}{2}D - \left[\frac{3D}{2(100-a-b)^2} - \frac{\tan\alpha}{100-a-b}\right](x-a-b)^2 + \left[\frac{D}{(100-a-b)^3} - \frac{\tan\alpha}{(100-a-b)^2}\right](x-a-b)^3 \tag{7}$$

where a and b are the nose and mid-section lengths, n represents the nose index, and α represents the tail semi-angle. Although these equations are based on percentage values,

the output was scaled to match the tag's desired 300 mm maximum length, assuring, by this manner, similitude between this case and the tag's studies. Figure 2a displays the resultant body, which is based on Myring's model B.



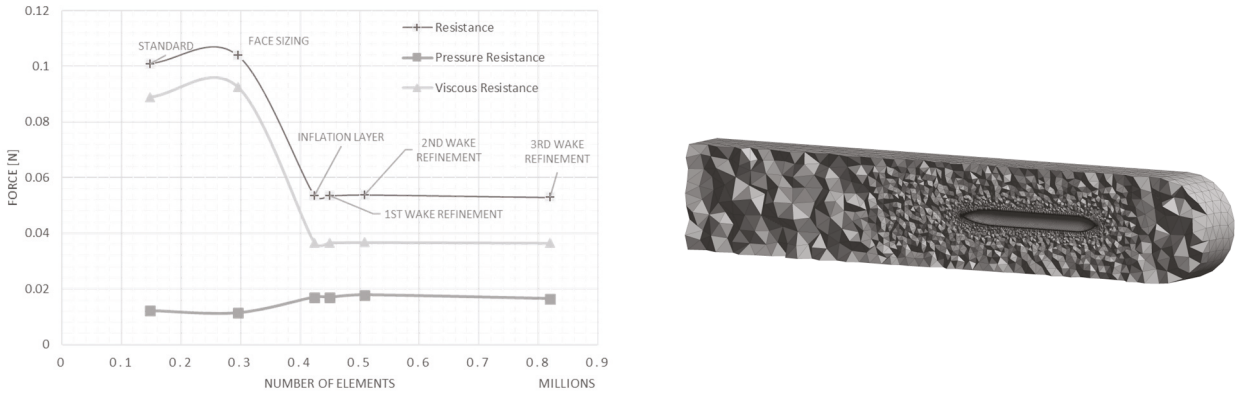
(**a**) (**b**)

Figure 2. (**a**) Myring's model B scaled to a length of 300 mm. (**b**) Section view of the flow domain used for validation of the model.

As mentioned before in the tag case, the flow domain was also modelled. Figure 2b represents a longitudinal cross-section view the flow domain used, and the same boundary conditions are illustrated.

Although the flow conditions are the same as in the tag case, since the geometry changed, it was required to perform a new mesh independency study to find the ideal compromise between the number of elements—hence, the computational time—and the accuracy in resistance prediction. The rationale behind the process remained the same, and convergence, based on the number of cells, was searched for the resistance and pitching moment.

Figure 3a represents the mesh independency in the study of the drag force performed for the Myring's shape at 1 m s^{-1} and an angle of attack of zero degrees. Studying this diagram, it is possible to conclude that the last three meshes provide approximately the same results. As such, it was decided, for computational economic purposes, to use the one with fewer elements to proceed with the validation study. In Figure 3b, it is possible to visualize the selected mesh.



(**a**) (**b**)

Figure 3. (**a**) Mesh independency study and (**b**) final mesh for Myring's shape case study.

3.2. Validation Results

Once the mesh was defined, a set of computations were run. For each one, the flow velocity was varied—consequently, the flow Reynolds number. To enable comparability of the results, the tested range comprehends the expected real-world conditions of the tag.

The output results were the forces acting on the body. For all simulated scenarios, a major contribution of the skin friction resistance was verified, which always represented

more than 90% of the total resistance. As such, the resistance coefficient was plotted against Myring's own results [22] based on the wet surface area, displayed in Figure 4a.

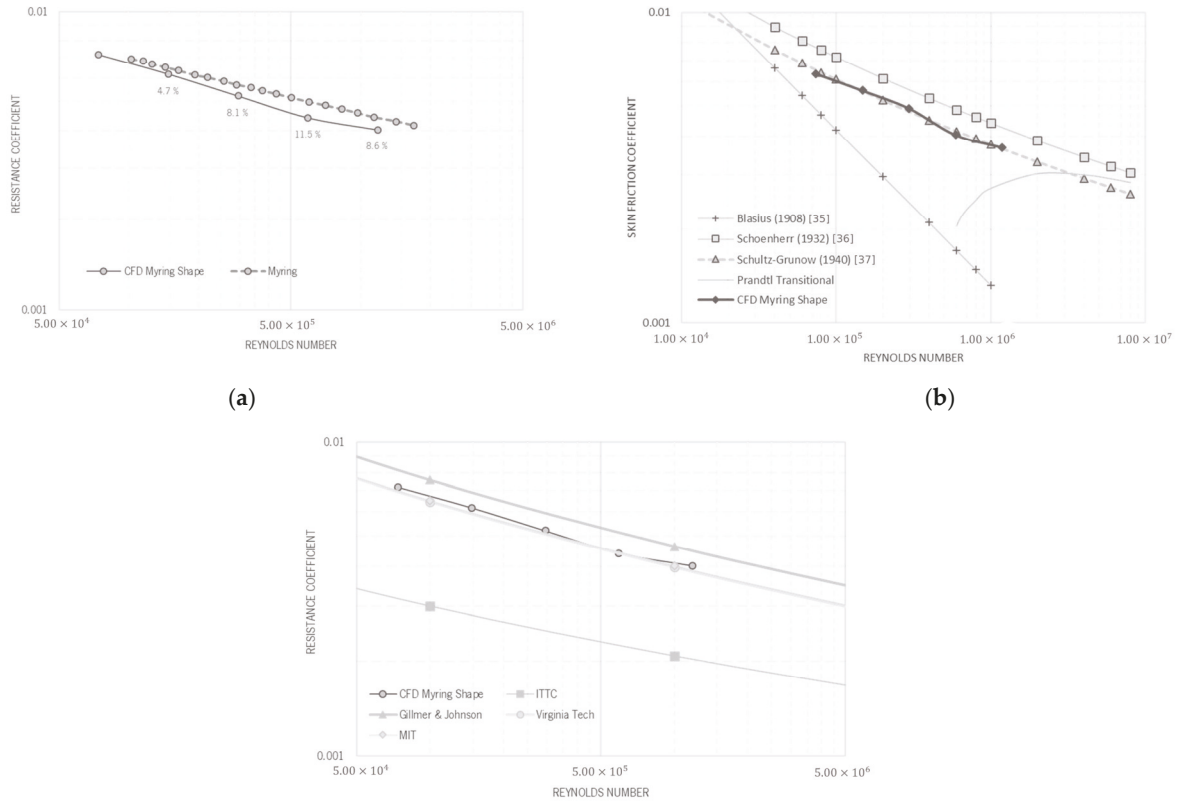


Figure 4. (**a**) Comparison of CFD resistance coefficient results with Myring's results. (**b**) Comparison of CFD skin-friction coefficients with analytical models [35–37]. (**c**) Comparison of CFD results with viscous resistance models.

A good agreement may be found with the experimental data obtained by Myring across all the Reynolds numbers. Figure 4b depicts this comparison, and good agreement with the Schultz-Grunow model was observed. This is of great significance for the present study since this is the only model that is suitable for the given range of Reynolds numbers.

To close the validation process, based on the Schultz-Grunow model, the three analytical models of total resistance and the ITTC line were also compared with the CFD results, as displayed in Figure 4c.

The computational results are in good agreement with the viscous models (from the Massachusetts Institute of Technology—MIT and Virginia Tech, Blacksburg, VA, USA), except for the ITTC (International Towing Tank Conference) line, which revealed poor agreement. This fact may result from the verified transitional Reynolds, for which this line tends to emulate laminar flow. As such, the model was successfully validated; consequently, the same process ought to be applied to the designed tag.

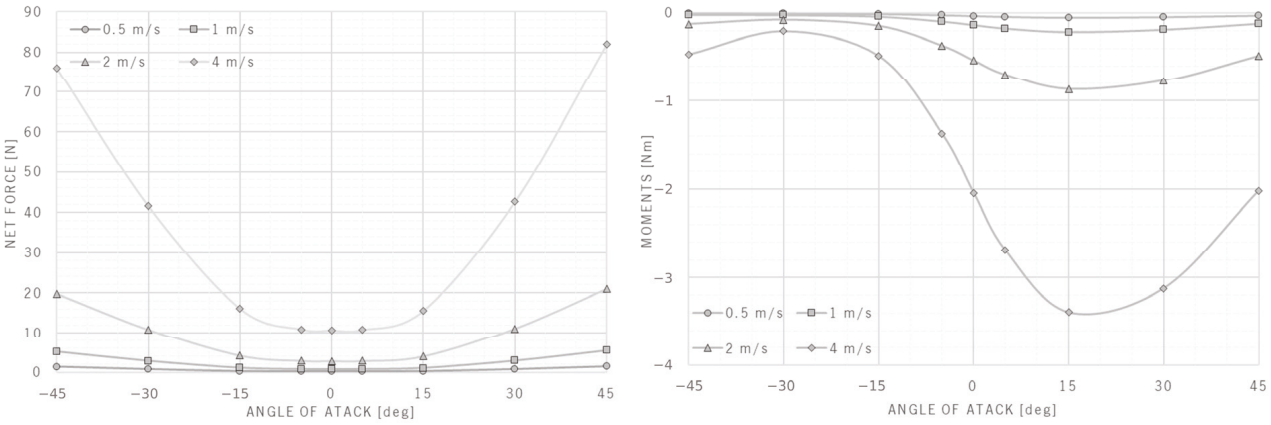
4. Results and Discussion

4.1. Motion and Drag

As the present study intended to evaluate the effect of the attached tag on the shark, it was important to predict and minimize the resulting forces on the animal for several operative scenarios. These, ought to represent the common and critical volitional behaviors of blue sharks and, consequently, the conditions in which the tag will operate during its active periods. Simulations were run for 36 different scenarios, with velocities ranging

between 0.5 and 4 m s^{-1}; and angles of attack of 0, ±5, ±15, ±30, and ±45 degrees, aiming to generate enough data to interpolate most situations that the tag would face.

Every case ran through one thousand iterations, and this decision was found to be sufficient for convergence (residuals were below 10^{-4}) of every case tested. In all scenarios, the forces and moments in the three-orthogonal axis, exerted exclusively by the flow on the tag, were obtained. The results are summarized in Figure 5a,b, and their careful analysis allows us to form some preliminary conclusions.



(**a**) (**b**)

Figure 5. (**a**) Forces imposed on the concept's body by the flow. (**b**) Moments imposed on the concept's body by the flow.

In the present state of concept maturation, it is noticeable that the tag's body was hydrodynamically unstable. In fact, as the moments for any of the given angles are negative, the tag always tends to pitch up. Although no cases where the angle of attack exceeds 45 degrees were simulated, it is predictable that the tag's equilibrium in pitch would reside at higher angles of attack. This, in turn, would reflect in higher drag and consequently stronger pulling forces for the shark towing it. It is also possible to note that the resistance imposed on the motion is highly dependent on the angle of attack, being smaller at lower angles of attack.

To better understand the origin of the resistance, it was important to identify which are its main contributors. The calculated resistance was decomposed by the contributions of the different sections of the domain. These results for the simulation of 4 m s^{-1} at a 0° angle of attack are illustrated by the diagram in Figure 6, which also shows the flow's velocity around the profile of the concept.

Evident on the pie chart displayed is the preponderance of the resistance induced by the shark's body. However, it is important to note that this simulation does not account for the interaction flow-solid. As such, it does not account for the eventual bending of this antenna in the direction of the flow, which would surely decrease its resistance. Consequently, one may assume that these results represent very conservative estimates for resistance.

Nevertheless, a comparison between these results and those obtained for the resistance of a blue shark swimming at zero-degree angle of attack was performed. This comparison was performed while assuming the concept will be eventually stable for angles of attack between −15 and 15 degrees. Table 1 presents this comparison. (The resistance values for the shark were granted by CEiiA. A second-degree interpolation to these results was used to extrapolate the values of resistance for the same velocities at which the concept was tested.)

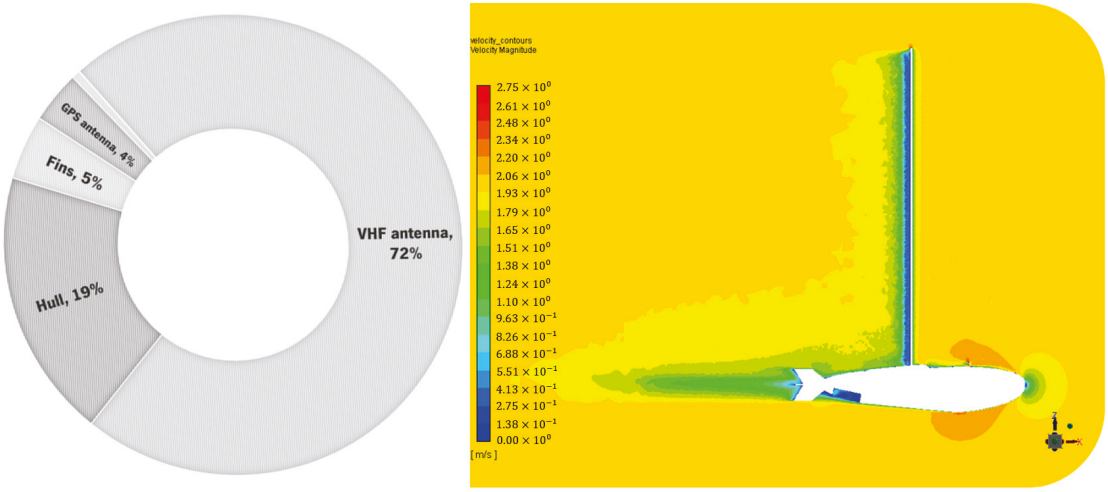


Figure 6. Resistance breakdown and velocity contours of final concept at 2 m s^{-1} and 0° angle.

Table 1. Influence of concept's body on shark's resistance.

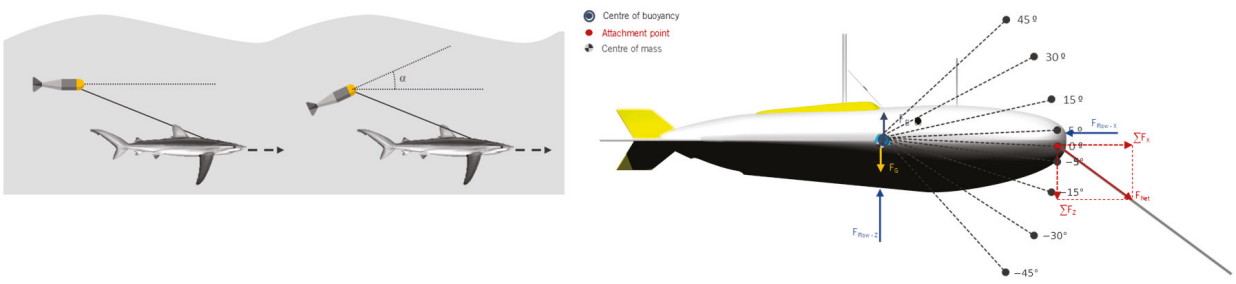
Velocity	Shark Resistance	−15° Angle of Attack		−5° Angle of Attack		0° Angle of Attack		5° Angle of Attack		15° Angle of Attack	
		Resistance	Variation	Resistance	Variation	Resistance	Variation	Resistance	Variation	Resistance	Variation
m s^{-1}	N	N	%	N	%	N	%	N	%	N	%
0.5	0.8	0.3	36	0.2	25	0.2	25	0.2	25	0.3	36
1.0	5.3	1.1	21	0.8	14	0.7	14	0.8	14	1.1	20
2.0	23.2	4.2	18	2.9	13	2.8	12	2.9	12	4.0	17
4.0	98.4	16.1	17	11.0	12	10.7	11	10.8	11	15.6	16

It was important to note that, at high velocities, the impact of the concept's resistance represents less than 20% of the shark's own resistance. Despite the simplifications imposed on the simulations, these are very good indicative values, within the range reported by other researchers Hazekamp et al. [15], highlighting the potential of this design.

4.2. Assessment of the Operation Attitude

As mentioned, for each one of the scenarios simulated, the forces in the x, y, and z directions, exerted by the flow on the tag, were derived, as well as the moments with respect to its center of mass. These data were then used to determine the static load conditions that the tag was subject to in each one of the situations by balances of force and moment.

These static conditions were all built in a spreadsheet based on variable coordinates for the attachment point relative to the tags referential. These coordinates, together with the ones of the buoyancy center, were rotated according to the tag's angle of attack. This condition tries to duplicate the situation where the shark moves at constant speed and depth in an approximately straight line, as shown in Figure 7.



(**a**) (**b**)

Figure 7. (**a**) Simulated phenomenon. (**b**) Forces applied to the tag at a 15° angle of attack (not to scale).

Figure 7b displays, in the grey color, the relative positions of these points for all scenarios simulated, as well as the schematics of forces acting on the body. The net force on the x-axis may be estimated by Equation (8):

$$\sum \vec{F_x} = \vec{F}_{Flow\_X}(\vec{U}; \alpha) \tag{8}$$

The resultant force on the z-axis is given by Equation (9):

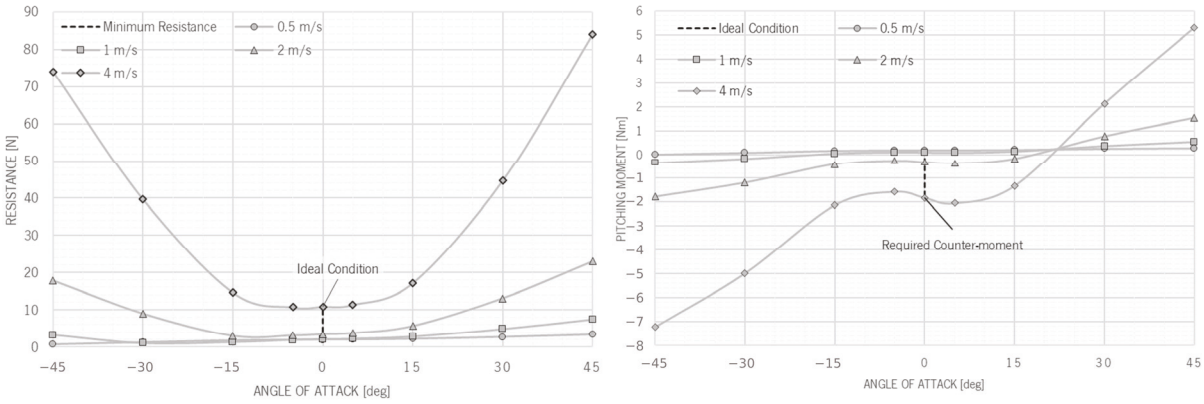
$$\sum \vec{F_z} = \vec{F}_G + \vec{F}_B + \vec{F}_{Flow\_Z}(\vec{U}; \alpha) \tag{9}$$

And the resultant pitching moment around the CG is determined by Equation (10):

$$\begin{aligned} \sum M_y &= M_{Flow-y}(\vec{U}; \alpha) + \vec{F}_B(x_{CB}(\alpha) - x_{CG}) \\ &+ \sum \vec{F_z}(x_{Attachment} - x_{CG}) + \sum \vec{F_x}\,(z_{Attachment} - z_{CG}) \end{aligned} \tag{10}$$

where x_{CB}, x_{CG}, and $x_{Attachment}$ represent the x coordinates of the center of buoyancy, center of mass, and attachment point; similarly, $z_{Attachment}$ refers to the z coordinate of the attachment point.

Interpolating these results allowed us to determine the natural attitude of this tag configuration by finding the angle at which the pitch moment is null. The direction and magnitude of the force affecting the shark were also determined by the net force on the tag's attachment point. The resultant force and pitch moments based on the angle of attack and velocity are plotted, respectively, in Figure 8a,b.



(**a**) (**b**)

Figure 8. (**a**) Resistance on validated concept based on flow velocity and angle of attack. (**b**) Pitching moments verified on validated concept based on flow velocity and angle of attack.

A detailed understanding of the computational data is of the highest importance when taking the design optimization process to a higher level. We observed that minimum resistance occurs at zero degrees of pitch angle, and one may conclude that this is the ideal operative condition. As such, consulting the pitch-moment diagram at a zero-degree attack angle allows us to determine the necessary counter-moment on the tag's shape to make this its natural position.

It is also possible to make use of the resultant force angle to adjust the tether's length to avoid contact with the shark's body and maximize surfacing opportunities at a given depth.

5. Improved Design

5.1. Design of Stabilizing Elements

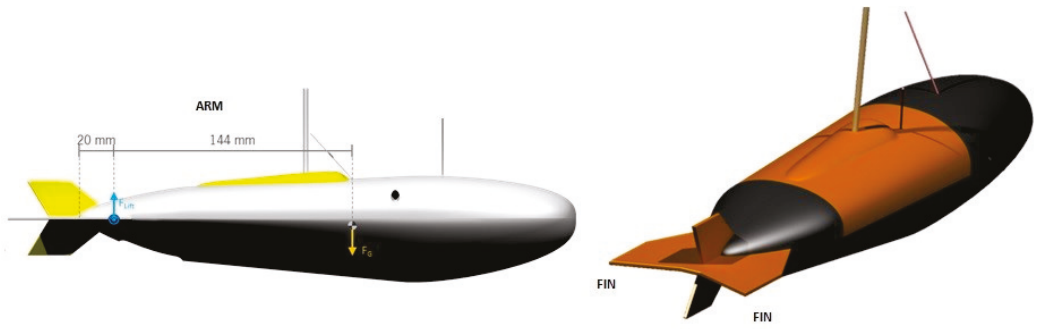
As determined in the previous section, the angle of attack that offers less resistance to the motion of the tag is at zero degrees. As such, to ensure minimal effort variation from the shark carrying the tag, it is important to pursue ways of making this angle of attack coincide with its equilibrium position.

Several approaches could have been taken, for instance, at a high velocity. Since the natural tendency of the tag is to pitch up at about twenty degrees, one could have increased or moved weight forward. However, this would disturb the static stability. Another alternative would be adjusting the attachment point in search of a better suiting equilibrium moment. This method is simple and convenient, and it may result in some improvements depending on the body's shape. For the present work, shifting the attachment point 25 mm forward in the longitudinal axis allowed a correction of roughly five degrees. However, it would hardly be enough to ensure the ideal condition of a zero-degree angle of attack.

Hence, the need arises for the use of stabilizing elements such as fins. The physical principle behind these elements is based on the use of surface areas, in strategic points and orientations, so that the forces acting on them due to the external flow balance, in a swift manner, the moments of the body.

As aforementioned, fins generate corrective moments on the tag's body through the lift forces exerted by incoming flows. The degree of complexity of these elements may vary depending on their purpose. However, for the present application, simplicity and ease of manufacture were the guidelines for their design. As such, the design would consist of flat plates with the required surface area to generate the counter moment needed.

Analyzing the simulated results, it is possible to conclude that for the worst-case scenario, at 4 m s^{-1}, the desired counter-moment was approximately 1.8 Nm. To generate the desired lift, the fins had to be placed in the rear of the tag. Taking a conservative approach, the generated forces were considered to act at the minimum distance between the center of mass and the fins. This distance was calculated while assuming that a 20 mm length of the fin was inserted in the tag's body to provide proper support, resulting in a 144 mm arm. Figure 9a illustrates this concept.



(**a**) (**b**)

Figure 9. (**a**) Acting point of the lift force generated by the stabilizing elements. (**b**) Stabilizing elements of the tag.

Knowing the desired moment, M_{Fins}, and the arm, Δx, of the lift force, it is possible to determine the required magnitude of the lift force, $\vec{F}_{Lift}$, by Equation (11):

$$M_{Fins} = \vec{F}_{Lift} \Delta x \Leftrightarrow \vec{F}_{Lift} = 12.5 \text{ N} \quad (11)$$

Since the design is based on a flat plate, which only produces lift at a non-null angle of attack, α, a maximum desirable angle of pitch between ± 4 degrees was established. Within

this range, according to [38], the lift coefficient, C_{Lift}, for a flat plate may be estimated by Equation (12):

$$C_{Lift} = 2\pi \sin(\alpha) \approx 0.44 \tag{12}$$

Inputting this information into the dimensionless lift force equation [39], the required surface area (S) to correct the pitching moment is obtained using Equation (13):

$$C_{Lift} = \frac{\vec{F}_{Lift}}{0.5\,\rho\,\vec{u}^{2}\,S} \Leftrightarrow S = 3.46 \times 10^{-3}\ \mathrm{m}^2 \tag{13}$$

Using this value as a reference, horizontal fins were designed. Their design was inspired by conventional torpedo fins. At this stage, smaller fins were also inserted vertically to make the tag more agile in following the shark's direction changes. Both fins are represented in Figure 9b, assembled with the tag. Once these components were modelled and assembled in the tag, it was important to reiterate across the hydrodynamic assessment process to verify the intended changes.

5.2. Improved Tag Concept

Having designed and sized the stabilizing elements, a new series of simulations was run to verify the tag's hydrodynamic enhancements. The same procedure was used as the one for the preliminary design. The mesh created for the fins' surfaces and its inflation layer was similar to the one of the main sections of the body. Figure 10 displays the flow domain.

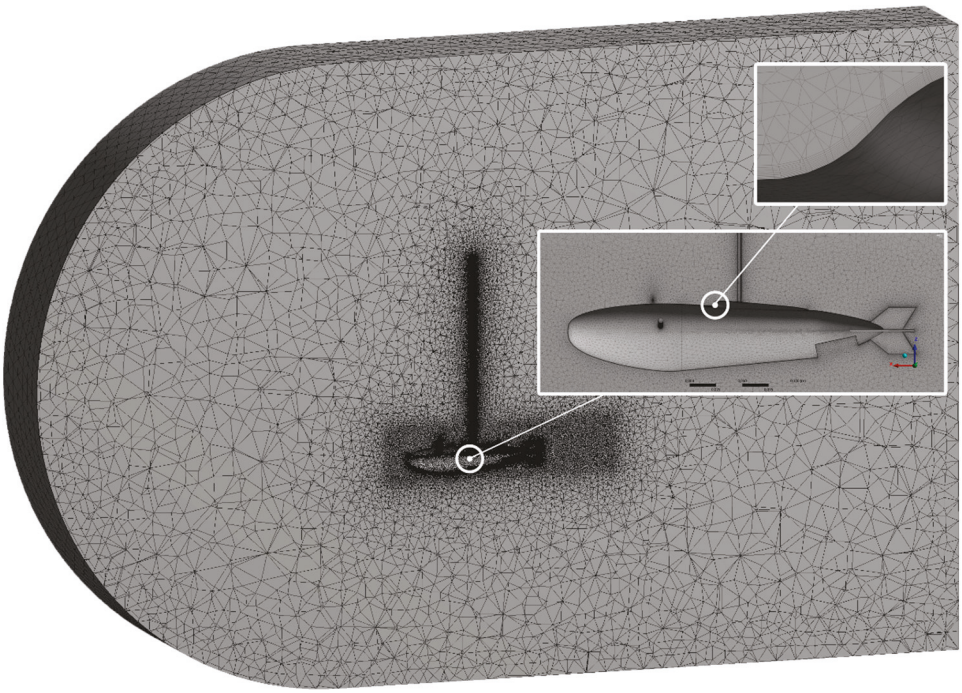


Figure 10. Tag final concept flow domain.

It was found that, as desired, the natural equilibrium position is now at a smaller angle of attack for all the studied velocities. For instance, at 4 m s^{-1}, the worst case considered, this angle decreased from about 20 to only 5 degrees. Figure 11a contains a diagram that compares the resistance and pitch moment on both designs, with and without fins, at 4 m s^{-1}. The results for the drag force show a minimum angle of attack of 0°. Experimental data measured by Bartolomeu [23] shows a similar behavior for axisymmetric shapes with a high length/diameter ratio. As the ratio *L/D* decreases, the U shape (due to the symmetry of the shape) of this relationship becomes less evident. Also, the moment shows

a symmetry in absolute value for negative angles of attack; this corresponds to a nose up, and for positive angles of attack, the reversed is observed.

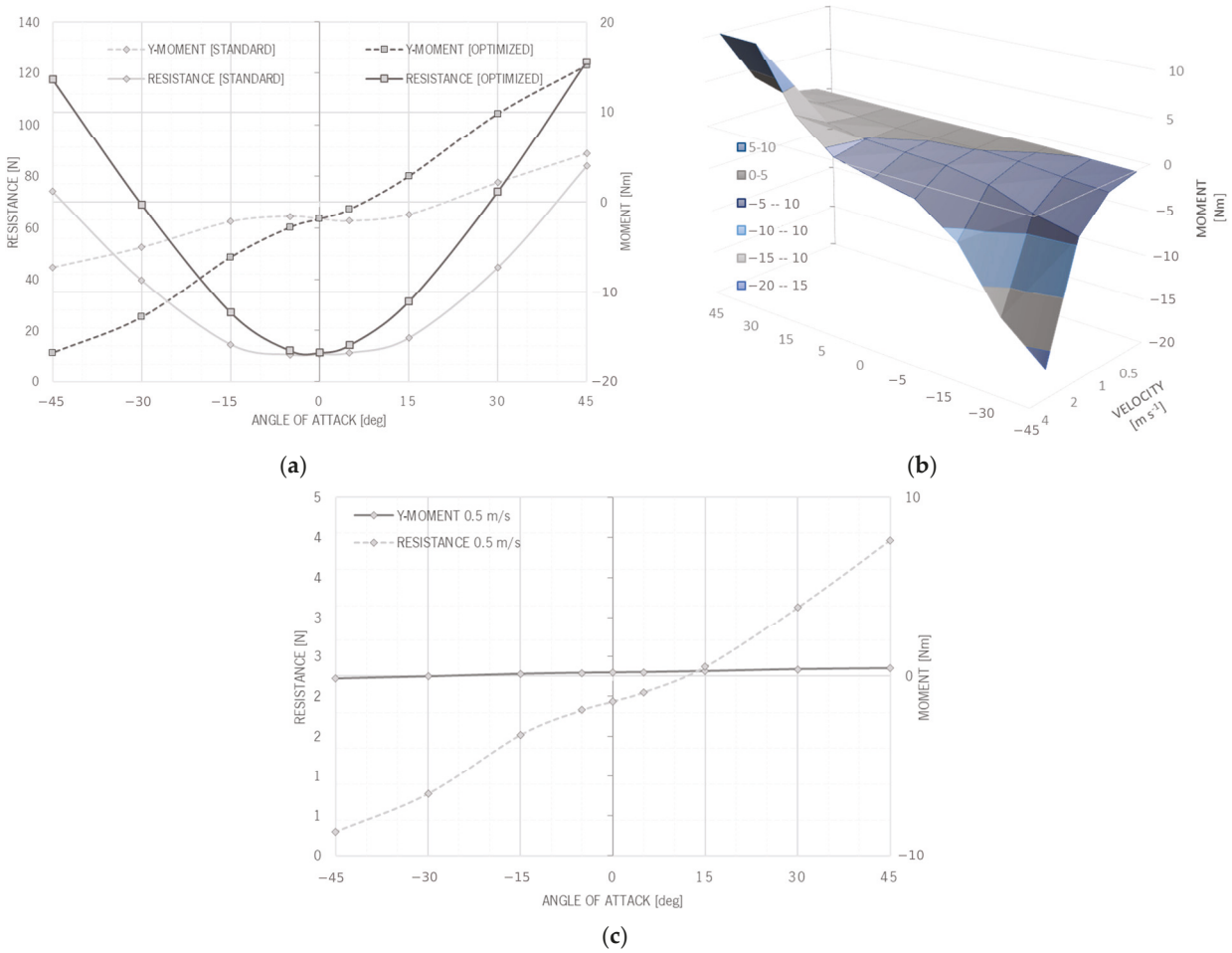


Figure 11. (**a**) Comparison of y-moment and resistance for preliminary and optimized design at 4 m s^{-1}. (**b**) Pitching moment variation with velocity and angle of attack. (**c**) Low-velocity pitch equilibrium and resistance.

As expected, an overall higher resistance was verified in the model equipped with fins, especially for higher attack angles. However, the resistance at the equilibrium position of this model is approximately half of the one verified case in which the fins were not included. By shifting the tendency of the tag to remain at about 5 instead of the original 20 degrees, the associated motion resistance stands to be about 14 N instead of the initial 28 N. Moreover, including the stabilizers, a pitching moment that progresses much more smoothly through the variation of attack angles was obtained. This, in practice, is expected to translate into an easier learning process to adapt the animal's swimming technique to the added effort of carrying the tag. Pan et al. [21] numerically investigated the influence of the angle of attack on the moment acting on the submarine-shaped underwater vehicle. The authors show a nearly linear influence of the angle of attack, as observed in the present study (Figure 11a).

Although ensuring that critical scenarios are optimized, such as high-velocity motion, attention must also be paid to scenarios at the remaining range of expected velocities.

In Figure 11b, a two-variable surface plot allows us to roughly interpolate pitching moments between all studied cases. Careful inspection of this plot shows that the intersection line between the darkest blue and grey areas represents the equilibrium conditions for pitch angle. Through this line, one may see that between 1 and 4 m s^{-1}, the tag will naturally pitch to an angle of attack between ± 5 degrees, assuring in such a way small resistance to its motion.

However, for lower velocities, this does not remain the case. At these smaller velocities, the tag tends to pitch at a very negative angle, as displayed in the diagram Figure 11c for 0.5 m s^{-1}. In the same plot, it is possible to contrast the pitching moment with the respective resistance, which leads to the conclusion that for this velocity a decrease in pitch represents a decrease in resistance.

6. Conclusions

With technological advancement, the continued refinement of tag devices promises to deepen our understanding of marine ecosystems and contribute to the sustainable management of ocean resources. In this regard, CFD has played a pivotal role in understanding and simulating complex fluid flow phenomena.

Herein, the integration of CFD with empirical data and innovative design approaches has allowed for the development of a more efficient and environmentally friendly tagging device. The addition of stabilizing fins has been shown to drastically reduce the tag's resistance and pitching moments, enabling it to maintain equilibrium at shallow angles of attack across a wide range of velocities. This not only enhances the device's performance but also minimizes its impact on the natural behavior of blue sharks during tagging operations.

For the initial design, the VHF transmitter's antenna is the main source of drag, adding up to 20% to the shark's own drag. The skin friction resulted in a negative moment that pitches up the tag, increasing the drag. This phenomenon increases with velocity.

In order to maintain the tag attitude at minimum drag (0°), balancing fins (with a 34.6 cm^2 area) were added to the tag. This feature enables the operation at an equilibrium attitude that reduces the drag.

Author Contributions: Conceptualization, S.F.T. and J.C.T.; methodology, V.C.; software, J.A.; validation, J.A. and V.C.; formal analysis, J.A.; investigation, A.A.; resources, S.F.T.; data curation, V.C.; writing—original draft preparation, V.C.; writing—review and editing, S.F.T.; visualization, A.A.; supervision, J.C.T. and S.F.T.; project administration, T.B.; funding acquisition, J.C.T. All authors have read and agreed to the published version of the manuscript.

Funding: This research received no external funding.

Data Availability Statement: The raw data supporting the conclusions of this article will be made available by the authors upon request.

Acknowledgments: Violeta Carvalho thanks for her Ph.D. grant from FCT with reference UI/BD/151028/2021. This work was supported by FCT—Portuguese Foundation for Science and Technology through the R&D Unit Project Scope UIDB/00319/2020 (ALGORITMI) and R&D Units Project Scope UIDP/04077/2020 (METRICS).

Conflicts of Interest: The authors declare that they have no known competing financial interests or personal relationships that could have appeared to influence the work reported in this paper.

References

1. Hammerschlag, N.; Gallagher, A.J.; Lazarre, D.M. A review of shark satellite tagging studies. *J. Exp. Mar. Biol. Ecol.* **2011**, *398*, 1–8. [CrossRef]
2. Witt, M.J.; Doherty, P.D.; Godley, B.J.; Graham, R.T.; Hawkes, L.A.; Henderson, S.M. *Basking Shark Satellite Tagging Project: Insights into Basking Shark (Cetorhinus maximus) Movement, Distribution and Behaviour Using Satellite Telemetry*; Final Report; Scottish Natural Heritage: Stirling, Scotland, 2016; 72p.
3. Cooke, S.J.; Hinch, S.G.; Wikelski, M.; Andrews, R.D.; Kuchel, L.J.; Wolcott, T.G.; Butler, P.J. Biotelemetry: A mechanistic approach to ecology. *Trends Ecol. Evol.* **2004**, *19*, 334–343. [CrossRef]
4. Cooke, S.J.; Midwood, J.D.; Thiem, J.D.; Klimley, P.; Lucas, M.C.; Thorstad, E.B.; Eiler, J.; Holbrook, C.; Ebner, B.C. Tracking animals in freshwater with electronic tags: Past, present and future. *Anim. Biotelem.* **2013**, *1*, 5. [CrossRef]
5. Pouca, C.P.V. High-Resolution Diving Behaviour of Satellite Tagged Blue Sharks under Different Oceanographic Gradients. Master's Thesis, Universidade do Porto, Porto, Portugal, 2012.
6. Queiroz, N.; Humphries, N.E.; Noble, L.R.; Santos, A.M.; Sims, D.W. Spatial dynamics and expanded vertical niche of blue sharks in oceanographic fronts reveal habitat targets for conservation. *PLoS ONE* **2012**, *7*, e32374. [CrossRef]

7. Nielsen, J.L.; Arrizabalaga, H.; Fragoso, N.; Hobday, A.; Lutcavage, M.; Sibert, J. (Eds.) *Reviews: Methods and Technologies in Fish Biology and Fisheries*; Springer: Berlin/Heidelberg, Germany, 2009. [CrossRef]
8. Ahuekwe, E.F.; Isibor, P.O.; Akinduti, P.A.; Salami, A.O.; Onuselogu, C.C.; Oshamika, O.O.; Oyesola, O.L.; Ichor, T.; Ezekiel, O.M.; Oziegbe, O.; et al. *Application of Nanochitosan in Tagging and Nano-Barcoding of Aquatic and Animal Meats*; Adetunji, C., Hefft, D., Jeevanandam, J., Danquah, M.B.T.-N.G.N., Eds.; Academic Press: New York, NY, USA, 2023; pp. 483–498. [CrossRef]
9. Baeyaert, J.; Graça, G.; Sobral, A.; Prieto, R.; Afonso, P.; Fontes, J. EcoDive Azores—Summer Season—Short Report. 2016. Available online: https://www.researchgate.net/publication/318724014_EcoDive_Azores_-_Summer_Season_2016_Short_Report (accessed on 10 April 2024).
10. Grusha, D.S.; Patterson, M.R. Quantification of drag and lift imposed by pop-up satellite archival tags and estimation of the metabolic cost to cownose rays (*Rhinoptera bonasus*). *Fish. Bull.* **2005**, *103*, 63–70.
11. Arai, N.; Okuyama, J. Biologging. In *Field Informatics*; Springer: Berlin/Heidelberg, Germany, 2012; pp. 21–38. [CrossRef]
12. Domeier, M.L.; Nasby-Lucas, N. Two-year migration of adult female white sharks (*Carcharodon carcharias*) reveals widely separated nursery areas and conservation concerns. *Anim. Biotelem.* **2013**, *1*, 2. [CrossRef]
13. Trotter, A.W.; Rathjens, L.; Schmiegel, S.; Mews, S.; Cowley, P.D.; Gennari, E. Short-term effects of standard procedures associated with surgical transmitter implantation on a benthic shark species requiring anaesthesia. *Fish. Res.* **2024**, *270*, 106880. [CrossRef]
14. Gleiss, A.C.; Norman, B.; Liebsch, N.; Francis, C.; Wilson, R.P. A new prospect for tagging large free-swimming sharks with motion-sensitive data-loggers. *Fish. Res.* **2009**, *97*, 11–16. [CrossRef]
15. Hazekamp, A.A.H.H.; Mayer, R.; Osinga, N. Flow simulation along a seal: The impact of an external device. *Eur. J. Wildl. Res.* **2010**, *56*, 131–140. [CrossRef]
16. Zhang, D.Y.; Luo, Y.H.; Li, X.; Chen, H.W. Numerical simulation and experimental study of drag-reducing surface of a real shark skin. *J. Hydrodyn.* **2011**, *23*, 204–211. [CrossRef]
17. Shaari, M.F. Drag Analysis of Contractile Water Jet Locomoted Micro AUV in Laminar Fluid. *Appl. Mech. Mater.* **2015**, *799*, 1188–1192. [CrossRef]
18. Cheng, B.; Qin, D.; Hu, Z. Research on the propulsion motor cooling by the coupled flow field of unmanned underwater vehicles. *Appl. Therm. Eng.* **2024**, *237*, 121797. [CrossRef]
19. Liu, B.; Xu, X.; Pan, D. Resistance reduction optimization of an amphibious transport vehicle. *Ocean Eng.* **2023**, *280*, 114854. [CrossRef]
20. Karim, M.; Rahman, M.; Alim, A. Numerical computation of viscous drag for axisymmetric underwater vehicles. *J. Mek.* **2018**, *26*, 9–21.
21. Pan, Y.; Zhang, H.; Zhou, Q. Numerical prediction of submarine hydrodynamic coefficients using CFD simulation. *J. Hydrodyn. Ser. B* **2012**, *24*, 840–847. [CrossRef]
22. Myring, D.F. A Theoretical Study of Body Drag in Subcritical Axisymmetric Flow. *Aeronaut. Q.* **1976**, *27*, 186–194. [CrossRef]
23. Bartolomeu, T.C. Hydrodynamic Optimization of a Torpedo-Shaped Hull. Ph.D. Thesis, Universidade da Beira Interior, Covilhã, Portugal, 2016.
24. Wang, J.; Cui, Z. Modeling and experiment validation of a seawater micro hydropower system for marine animal telemetry tag. *Renew. Energy* **2021**, *174*, 73–85. [CrossRef]
25. Wang, G. Machine Learning for Inferring Animal Behavior from Location and Movement Data. *Ecol. Inform.* **2019**, *49*, 69–76. [CrossRef]
26. Thiede, S.; Ghafoorpoor, P.; Sullivan, B.P.; Bienia, S.; Demes, M.; Dröder, K. Potentials and Technical Implications of Tag Based and AI Enabled Optical Real-Time Location Systems (RTLS) for Manufacturing Use Cases. *CIRP Ann.* **2022**, *71*, 401–404. [CrossRef]
27. Szpilman, M. *Tubarões no Brasil: Guia Prático de Identificação*; Mauad Editora Ltd.a: Rio de Janeiro, Brazil, 2004.
28. Stevens, J. Prionace glauca, Blue Shark, IUCN Red List Threat. *Species* **2009**, *11*. [CrossRef]
29. Geng, Z.; Wang, Y.; Kindong, R.; Zhu, J.; Dai, X. Demographic and harvest analysis for blue shark (*Prionace glauca*) in the Indian Ocean. *Reg. Stud. Mar. Sci.* **2021**, *41*, 101583. [CrossRef]
30. Azevedo, J.; Bartolomeu, T.; Teixeira, S.; Teixeira, J.C. Design Concept of a Non-invasive Tagging Device for Blue Sharks José. In *International Conference Innovation in Engineering*; Springer International Publishing: Cham, Switzerland, 2022.
31. Moonesun, M.; Korol, Y.M.; Dalayeli, H. CFD analysis on the bare hull form of submarines for minimizing the resistance. *Int. J. Marit. Technol.* **2015**, *3*, 1–16.
32. ITTC. Recommended Procedures—Fresh water and Seawater Properties. Proc. ITTC—Section 7.5-02-01-03. 2011. Available online: https://www.ittc.info/media/7989/75-02-01-03.pdf (accessed on 10 April 2024).
33. Fluent. *ANSYS Fluent 12.0 User's Guide*; Ansys Inc.: Canonsburg, PA, USA, 2009; Volume 15317, pp. 1–2498. [CrossRef]
34. Versteeg, H.K.; Malalasekera, W. *An Introduction to Computational Fluid Dynamics*; Pearson Education Limited: Edinburgh, UK, 2007. [CrossRef]
35. Blasius, H. Grenzschischten in Flussigkeiten mit Kleiner Reibung, 1908; Translated into NACA Technical Memorandum 1256 as the Boundary Layer in Fluids with Little Friction. 1950. Available online: https://ntrs.nasa.gov/citations/20050028493 (accessed on 10 April 2024).
36. Schoenherr, K.E. Resistance of Flat Surfaces Moving through a Fluid. Ph.D. Thesis, Johns Hopkins University, Baltimore, MD, USA, 1932.
37. Shultz-Grunow, F. *New Frictional Resistance Law for Smooth Plates*; NACA Technical Memorandum 986; National Advisory Commitee for Aeronautics: Washington, DC, USA, 1941.

38. Newman, J.N.; Landweber, L. Marine Hydrodynamics. *J. Appl. Mech.* **1978**, *45*, 457. [CrossRef]
39. White, F.M. *Fluid Mechanics*, 8th ed.; Academic Press: New York, NY, USA, 2016.

Disclaimer/Publisher's Note: The statements, opinions and data contained in all publications are solely those of the individual author(s) and contributor(s) and not of MDPI and/or the editor(s). MDPI and/or the editor(s) disclaim responsibility for any injury to people or property resulting from any ideas, methods, instructions or products referred to in the content.

inventions

MDPI

Article

The Expected Dynamics for the Extreme Wind and Wave Conditions at the Mouths of the Danube River in Connection with the Navigation Hazards

Alina Beatrice Răileanu [1], Liliana Rusu [2], Andra Marcu [3] and Eugen Rusu [1,2,*]

[1] Department of Informatics and Social Assistance, School of Behavioral and Applied Sciences, Danubius University of Galati, 3 Galati Street, 800654 Galati, Romania; alinaraileanu@univ-danubius.ro
[2] Department of Mechanical Engineering, Faculty of Engineering, "Dunarea de Jos" University of Galati, 800008 Galati, Romania; lrusu@ugal.ro
[3] Department of Communication Sciences, School of Communications and International Relations, Danubius University of Galati, 3 Galati Street, 800654 Galati, Romania; andramarcu@univ-danubius.ro
* Correspondence: erusu@ugal.ro

Abstract: The entrance in the Sulina channel in the Black Sea is the target area of this study. This represents the southern gate of the seventh Pan-European transport corridor, and it is usually subjected to high navigation traffic. The main objective of the work is to provide a more comprehensive picture concerning the past and future expected dynamics of the environmental matrix in this coastal area, including especially the extreme wind and wave conditions in connection with the possible navigation risks. The methodology considered assumes analyses performed at three different levels. First, an analysis of some in situ measurements at the zero-kilometer point of the Danube is carried out for the 15-year period of 2009–2023. Together with the maximum wind speed and the maximum value of the wind gusts, the water level variation was analyzed at this point. As a second step, the analysis is based on wind speed data provided by regional climate models. Two periods, each spanning 30 years, are considered. These are the recent past (1976–2005), when comparisons with ERA5 reanalysis data were also performed, and the near future (2041–2070), when two different models and three climate scenarios were considered. The focus was on the extreme wind speed values, performing comparisons between the past and future expected extreme winds. Finally, the third analysis is related to the wave conditions. Thus, using as a forcing factor each of the wind fields that was previously analyzed, simulations employing a spectral wave model were carried out. The wave modeling system was focused using three different computational domains with increasing resolution towards the target area, and the nearshore wave conditions were evaluated. The results show that both the extreme wind and wave conditions are expected to slightly increase in the future. Especially in the wintertime, strong wind fields are often expected in this area, with wind gusts exceeding more than 70% of the hourly average wind velocity. With regard to the waves, due to the complex nearshore phenomena, considerable enhancements in terms of significant wave heights are induced, and there is also an elevated risk of the occurrence of rogue waves. This work is still ongoing, and taking into account the high navigation risks highlighted, the next step would be to elaborate the risk assessment of severe shipping conditions, particularly related to the likelihood or probability of adverse conditions with the potential of generating hazardous situations in this coastal environment.

Keywords: Sulina channel; Danube mouths; Black Sea; navigation hazards; historical data; climate scenarios; atmospheric models; wave model simulations

1. Introduction

The dynamics of the last decades indicate that climate changes affect most natural systems in a significant way, and this especially concerns the global warming phenomena

associated with higher temperature variations [1]. Furthermore, various climate scenarios (see, for example, [2,3]) indicate that a negative impact of climate change is expected in almost all regions of the world, inducing a visible enhancement in the intensity and frequency of the extreme events [4]. Coastal environments are more sensitive to such extreme events [5]. They represent the interface between land and water. On the other hand, the wind is usually stronger in the marine environment [6]. That is why its impact on the land located in the vicinity of the sea is usually higher.

The objective of the present work is to provide a more comprehensive picture concerning the expected dynamics of the extreme wind and wave conditions at the mouths of the Danube River in the Black Sea in connection with the navigation hazards. The focus is on the entrance to the Sulina channel, which represents the main navigation exit from the Danube to the Black Sea [7], being at the same time the southern gate of the seventh Pan-European transportation corridor linking the Black Sea to the North Sea via the Rhine-Main–Danube navigation system (inaugurated in 1992) [8]. The location of the target area in the Black Sea is illustrated in Figure 1. Since this represents the main southern entrance to the largest European inland navigation system, it is subjected to high navigation traffic [9]. Furthermore, for a distance of about 170 km, from Sulina at the Black Sea (considered the zero-kilometer point of the Danube) and up to the Romanian port of Braila (kilometer 170), the so-called Maritime Danube extends. The Danube is also navigable by maritime ships [10], while river ships can navigate upstream to Ulm in Germany [11]. Moreover, since the beginning of the war in Ukraine in February 2022, this traffic was significantly increased [12], with the Danube being an alternative and more secure route for the cereals and other goods exported by Ukraine.

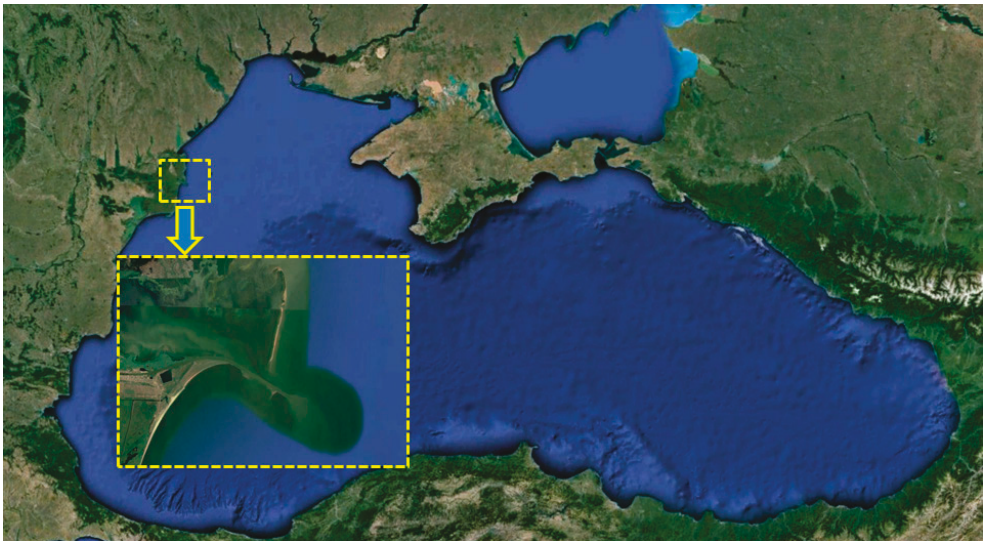


Figure 1. The Black Sea and the main target area (the entrance to the Sulina channel). Figure processed from Google Earth.

The Danube also represents the most important water resource for the Black Sea [13], and the river outflow generates relatively strong currents in the coastal environment neighboring the deltaic zone. The Danube Delta, which is the largest in Europe [14], is delimited by the three principal branches of the river, Chilia, Sulina, and Saint George [15]. In this area, especially in spring, there are often risks of floods [16,17]. The wind and wave climate are characterized by relatively high-energy conditions [18], and extreme storms also occur with a certain frequency in this nearshore [19]. Furthermore, the waves are often increased at the mouths of the Danube by the wave–current interactions that occur between the incoming waves and the coastal currents induced by the river discharge into the sea [20]. Taking into account the complexity of this coastal environment and the associated processes [21], the relatively high frequency of severe weather conditions, the

high navigation traffic, and the proximity of an ongoing war, various studies (see, for example, [22]) indicate that this area is subjected to high risks from the point of view of navigation hazards.

In this context, an analysis of the characteristics of the environmental matrix and its expected dynamics in the coastal area at the mouths of the Danube River, and especially at the entrance to the Sulina channel, is made in the present work. This analysis includes some in situ measurements for the wind and water level, reanalysis of wind data from the European Centre for Medium-Range Weather Forecasts (ECMWF), and projections of the future expected wind fields provided by regional climate models (RCMs) under various RCP (representative concentration pathway) and SSP (shared socioeconomic pathway) scenarios. Furthermore, an analysis of the wave conditions is also made by performing simulations over the entire basin of the sea using the SWAN (acronym from Simulating WAves Nearshore) spectral model [23] and focusing the modeling system with higher-resolution domains on the coastal environment at the mouths of the Danube River.

The present work can be considered as both actual and important because it provides reliable information concerning the navigation conditions and the associated risks in a coastal area with a high strategic and economic importance. At the same time, the proposed work has many elements of novelty. Thus, together with the past wind and wave conditions, the future expected wind and wave climate is assessed considering various climate models and scenarios. Another element of novelty is related to the probabilistic evaluation of the conditions when, due to the wave–current interactions, rogue waves may occur at the mouths of the Danube River.

2. Materials and Methods

2.1. In Situ Measurements

The bathymetric map of the target area considered in the present study is illustrated in Figure 2. Based on the information presented in references [24–26], the average currents generated by the Danube River outflow in the Black Sea are also represented on the map. Two types of data were available for the analysis, which was performed for the 15-year time interval of 2009–2023.

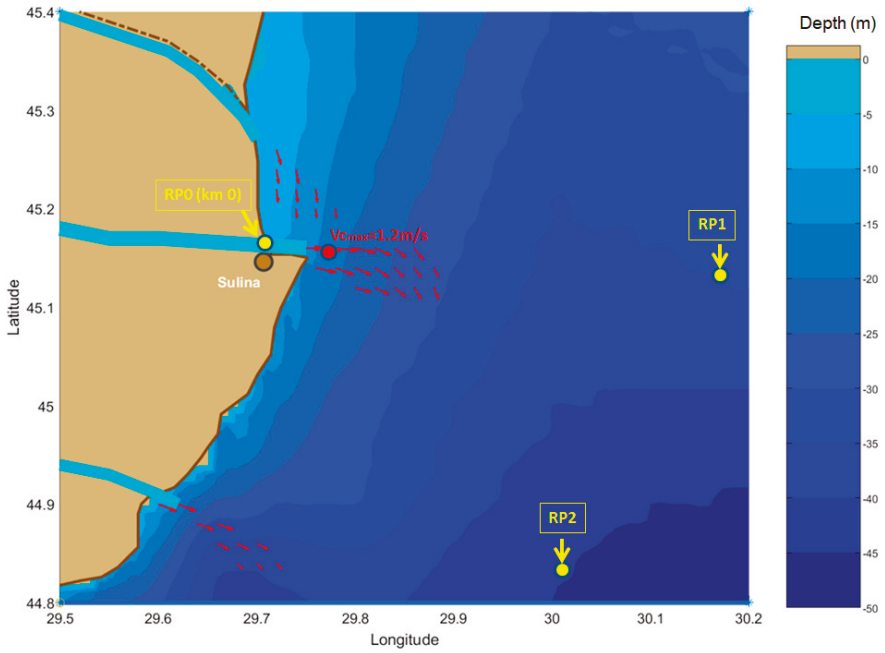


Figure 2. The bathymetric map of the coastal area at the Danube's mouths and the position of the three reference points considered. The coastal currents induced by the river outflow, estimated according to references [24–26], are also represented with red arrows.

The first parameter analyzed is the water level. These values resulted from daily measurements [12] at the entrance to the Sulina channel. The water level is considered as the elevation of the free surface of the Danube relative to a specified vertical datum and refers to the difference in centimeters between the sampling point' vertical datum in reference to a standard Black Sea elevation datum. The wind measurements, with data provided by reference [27], represent the second parameter analyzed. This includes the wind speed provided with a one-hour time step and the corresponding maximum speed of the wind gusts. The average wind direction is also provided by the data analyzed. Both the water level and wind measurements correspond to the zero-kilometer point of the Danube, denoted in Figure 2 as RP0 (reference point zero).

2.2. Wind Model Data Considered

The next analysis is based on the data coming from the wind models. These are carried out in two different locations, reference point 1 (RP1), which is offshore the Sulina channel with the coordinates (30.18° E, 45.12° N), and reference point 2 (RP2), which is offshore the Saint George arm of the Danube with the coordinates (30.01° E, 44.82° N). The first analysis of the wind climate relates to the hindcast period of 30 years (the interval of 1976–2005). The ERA5 database is considered for this analysis. This is a relatively new reanalysis wind product, being an upgrade of the former ERA-Interim [28]. These data start in 1950 and end five days behind the current time. They are provided in the public domain by the European Centre for Medium-Range Weather Forecasts, which is the most recent and one of the most reliable global atmospheric reanalysis databases. The resolution of the ERA5 wind data is $0.25° \times 0.25°$ in the geographical space, and the time step is one hour. For each hour, it gives wind and atmospheric pressure fields that are consistent with the previous evolution of the parameters modelled. In the present work, the wind speed at a 10 m height above the sea level is considered for the analysis, with a 3 h time step.

The second 30-year time period taken into account for analysis considering various climate scenarios (RCP4.5, RCP8.5, and SSP5-8.5) and atmospheric models is 2041–2070. The first wind field considered is that given by the regional climate atmospheric model version 4 (RCA4) provided by the Rossby Centre of the Swedish Meteorological and Hydrological Institute (SMHI) [29]. This regional climate model is driven by the global climate model (GCM), MPI-M-MPI-ESM-LR [30]. MPI-M means the Max Planck Institute for Meteorology, while MPI-ESM indicates the Max-Planck-Institute Earth System Model, and LR is low resolution. These data are made available in the public domain via the COPERNICUS database [31]. A second RCM considered is ALADIN (versions 6 for RCPs and 6x for SSP5-8.5) [32]. ALADIN stands for Aire Limitée Adaptation dynamique Développement International and is a regional climate model forced by the global atmospheric model GCM CNRM-CM5 (Centre National de Recherches Météorologiques), which is an Earth system model that is designed to run climate simulations. This GCM comprises the ARPEGE Climate Model [33]. ARPEGE is run by Météo-France and is the acronym from Action de Recherche Petite Echelle Grande Echelle, with the meaning of a research project on small and large scales. With regard to the SSP climate scenarios, the data considered come from the fully coupled regional climate system model CNRM-RCSM6/ALADIN [34,35] (where RCSM is the acronym for regional climate system model). In addition to the analysis of the data for the 30-year future time period (2041–2070), comparisons were performed with the ERA5 data for the past. Taking into account the availability of the data from the climate wind models, which is different for the SSP scenarios than the data for the RCP scenarios, the 30-year time interval (1979–2008) was considered for SSP, while for RCP (either 4.5 or 8.5) the initial 30-year time interval (1976–2005) was kept.

2.3. Wave Model Simulations

The third-generation phase-averaged model SWAN [23] is considered in the present work to predict the wave conditions. This was implemented and validated against satellite data and in situ measurements in the entire basin of the Black Sea, and further on, it was

focused considering a higher-resolution domain on the coastal area at the mouths of the Danube. This wave model is based on the spectrum concept and solves an advection-type equation in five dimensions (time, geographical, and spectral spaces) [36,37]. As in most of the spectral wave models, the spectrum considered is the action density spectrum (N) and not the energy density spectrum. This is because in the presence of the currents, the action density is conserved while the energy density is not. The action density is equal to the energy density (E) divided by the relative frequency (σ). Although SWAN was initially designed mainly for the nearshore areas, during this time, the model was developed in a significant way, and now it can also be successfully used on sub-oceanic and even oceanic scales, having performances comparable with standard wave models such as WAM (Wave Model) [38] or WW3 (Wave Watch 3) [39], which are designed for large scales. With regard to the sub-oceanic scales, SWAN becomes one of the most appropriate models, since one single model can be focused from large-scale generation to high-resolution domains via various computational levels. From this perspective, SWAN may be considered at this moment to be the most effective and reliable numerical model for predicting wave conditions and climate in an enclosed sea basin such as the Black Sea [40].

The advection-type equation considered in the SWAN model has the following general expression:

$$\frac{\partial N}{\partial t} + \nabla(N) + \frac{\partial}{\partial \sigma}\dot{\sigma}N + \frac{\partial}{\partial \theta}\dot{\theta}N = \frac{S}{\sigma}, \tag{1}$$

For larger-scale applications, the spherical coordinates, longitude (λ), and latitude (φ) are considered, and the operator (∇) has the following expression:

$$\nabla_{\mathrm{Sph}}(N) = \frac{\partial}{\partial \lambda}\dot{\lambda}N + \frac{1}{\cos\varphi}\frac{\partial}{\partial \varphi}\dot{\varphi}N, \tag{2}$$

For coastal applications, the Cartesian coordinates (x) and (y) are more appropriate, and in this case, the operator (∇) becomes:

$$\nabla_{\mathrm{Cart}}(N) = \frac{\partial}{\partial x}\dot{x}N + \frac{\partial}{\partial y}\dot{y}N, \tag{3}$$

The left side of Equation (1) represents the kinematic part, and it indicates the propagation of the wave action in time, geographical, and spectral spaces. Some relevant phenomena such as wave diffraction or refraction are also included. The source *(S)* is expressed on the right hand side as the energy density components. Three components are more relevant in deep water. They correspond to the atmospheric input, dissipation by whitecapping, and nonlinear quadruplet interactions. In shallow and intermediate water, additional terms are included. They correspond especially to the finite depth effects and comprise phenomena such as depth-induced wave breaking, bottom friction, or triad nonlinear wave–wave interactions. Thus, the expression of the source term is as follows:

$$S = S_{in} + S_{nl} + S_{diss} + S_{fd} \tag{4}$$

Such a SWAN-based wave prediction system was previously implemented in the basin of the Black Sea and focused on its western coast, considering various computational levels [41,42]. Table 1 presents the characteristics of the three computational domains considered in the present work. The first domain, defined in spherical coordinates (longitude and latitude, $\Delta\lambda$ and $\Delta\varphi$), corresponds to the entire basin of the Black Sea (illustrated in Figures 1 and 2). The second computational domain, defined also in spherical coordinates, is focused on the coastal area at the mouths of the Danube River and the corresponding geographical space. This is illustrated in Figure 2. Finally, a higher-resolution domain focused only on the Sulina channel was defined in Cartesian coordinates. The corresponding geographical space is illustrated in Figure 1.

Table 1 indicates the resolution in the geographical space ($\Delta\lambda$ and $\Delta\varphi$, measured in degrees for spherical coordinates and Δx and Δy, measured in meters for Cartesian

coordinates), where Δt is the time resolution in minutes, *nf* is the number of frequencies considered in the spectral space, $n\theta$ is number of directions, $ng\lambda$ (or *ngx*) is the number of grid points along the longitude (or x-axis), $ng\varphi$ (or *ngy*) is the number of grid points along the latitude (or y-axis, respectively), and *np* is total number of grid points. As it is known, in the case of the structured grids, the computational domain corresponding to the geographical space is discretized with a constant spatial step. This may, however, be different between the x and y axes, or between the longitude and latitude for the case of the spherical coordinates. On the other hand, the spectral space is defined by the number of frequencies (*nf*) having a logarithmic distribution and the number of directions ($n\theta$) that are equally distributed. This means that the directional step considered in these simulations is constant ($\Delta\theta = 10^\circ$), while the step in the frequency space (Δf) is variable. It must also be highlighted at this point that, in the case of the larger geographical spaces, the spherical coordinates and the non-stationary mode are more reliable, while for the high-resolution computational domains, the Cartesian coordinates and stationary mode are usually considered to be more effective.

Table 1. Characteristics of the computational domains defined for the SWAN model simulations focused on the coastal area at the mouths of the Danube in the Black Sea.

Spherical Domains	$\Delta\lambda \times \Delta\varphi$	Δt **(min)**	*nf*	$n\theta$	$ng\lambda \times ng\varphi = np$
Sph1—Black Sea	$0.08^\circ \times 0.08^\circ$	10 non-stat	24	36	$176 \times 76 = 13{,}376$
Sph2—Danube mouths	$0.01^\circ \times 0.01^\circ$	10 non-stat	24	36	$71 \times 61 = 4331$
Cartesian Domain	$\Delta x \times \Delta y$ **(m)**	Δt **(min)**	*nf*	$n\theta$	$ngx \times ngy = np$
Cart—Sulina	50×50	60 stat	30	36	$135 \times 216 = 29{,}160$

The physical processes activated in the SWAN simulations, corresponding to each of the three computational domains considered in the present work are presented in Table 2. In this table, Wave indicates the wave forcing, Wind indicates the wind forcing, Td indicates the tide forcing, Curr indicates the current field input, Gen indicates generation by wind, Wcap indicates the whitecapping process, Quad is the quadruplet nonlinear interactions (interactions between four waves that usually occur in deep water), Tri is the triad nonlinear interactions (reflecting the interactions between three waves, which are usually characteristic to intermediate and shallow water), *Dif* is the diffraction process, Bfr is the bottom friction, Set u*p* is the wave-induced set up, and Br is the depth-induced wave breaking.

Table 2. Physical processes activated in the SWAN simulations, corresponding to the eight defined computational domains. X—process activated, 0—process inactivated.

Input/Process / **Domains**	**Wave**	**Wind**	**Tide**	**Curr**	**Gen**	**Wcap**	**Quad**	**Triad**	**Diffr**	**Bfric**	**Set Up**	**Br**
Sph1	0	X	0	0	X	X	X	0	0	X	0	X
Sph2	X	X	0	X	X	X	X	X	0	X	0	X
Cart	X	X	0	X	X	X	X	X	X	X	X	X

Previous calibrations and validations were carried out to assess the reliability and performance of this wave prediction system in the Black Sea, indicating that the SWAN results are in general reliable for both average energy and storm conditions. For example, in reference [43], comparisons against satellite data were performed for the 20-year period of 1997–2016. In terms of significant wave heights (*Hs*), the following values resulted for the main statistical parameters: *Bias* = 0.05 m, *RMSE* = 0.38 m, *SI* = 0.36, *R* = 0.87, and *S* = 0.99. The parameters above presented are *Bias*, root mean square error (*RMSE*), scatter index (*SI*), correlation coefficient (*R*), and the regression slope (*S*), all of them being computed

according to their standard definitions, as given below, where X_i represents the measured value, Y_i is the simulated value, and n is the number of observations:

$$X_{med} = \widetilde{X} = \frac{\sum_{i=1}^{n} X_i}{n},\ Bias = \frac{\sum_{i=1}^{n}(X_i - Y_i)}{n},\ RMSE = \sqrt{\frac{\sum_{i=1}^{n}(X_i - Y_i)^2}{n}} \quad (5)$$

$$SI = \frac{RMSE}{\widetilde{X}},\ r = \frac{\sum_{i=1}^{n}(X_i - \widetilde{X})(Y_i - \widetilde{Y})}{(\sum_{i=1}^{n}(X_i - \widetilde{X})^2 \sum_{i=1}^{n}(Y_i - \widetilde{Y})^2)^{\frac{1}{2}}},\ S = \sqrt{\frac{\sum_{i=1}^{n} Y_i{}^2}{\sum_{i=1}^{n} X_i{}^2}} \quad (6)$$

It has to be highlighted at this point that the values of the statistical parameters *Bias*, *RMSE*, and *SI* are better when they are smaller, while the correlation coefficient and the regression slope are considered to be better when they are closer to the unity. In the case of the waves with significant wave heights higher than 3 m (associated with the storm conditions), for the 20-year time interval considered, the following values resulted for the main statistical parameters: *Bias* = −0.07 m, *RMSE* = 0.47 m, *SI* = 0.21, *R* = 0.78, and *S* = 1.05. Furthermore, the simulation results also indicate that, in the Black Sea basin, the storm waves represent about 2% of the total. These statistical results can be considered as reasonably accurate, and they give a good degree of credibility to the analyses related to the past and future storm conditions in the Black Sea, which are presented next. Furthermore, an assimilation scheme of the satellite data, based on an optimal interpolation approach, has been implemented [44], improving the statistical results in relative terms (*Bias* 57%, *RMSE* 17%, *SI* 20%, *R* 3%, and *S* 1%). It should also be highlighted that the above results were performed when the wave modeling system was forced with ERA5 reanalysis data, while for the future wave projections, RCM wind data have been used [45], considering SWAN version 41.31AB.

3. Results

3.1. Analysis of the In Situ Measurements

An analysis of some in situ measurements performed at the entrance to the Sulina channel (denoted in Figure 1 as RP0) is performed next for the 15-year time interval of 2009–2023. The first parameter considered is the water level. Figure 3 illustrates the variations in the water level at the entrance to the Sulina channel (RP0). The data processed present the results of the daily measurements carried out for the 15-year time interval of 2009–2023. The results show that the maximum value of the water level measured during this time interval was 125 cm, the minimum was 13 cm, and the average value was 71.6 cm.

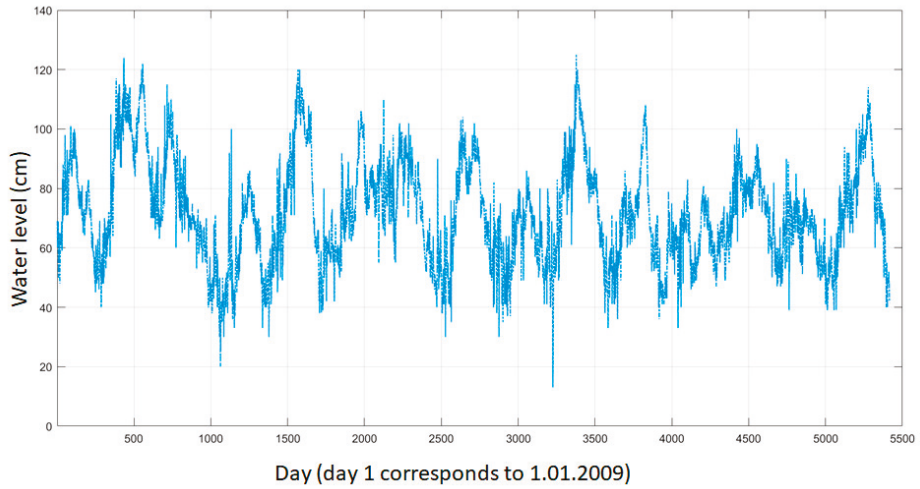


Figure 3. Variations in the water level at the entrance to the Sulina channel (RP0). Results of the daily measurements carried out for the 15-year time interval of 2009–2023.

The next analysis relates the wind speed measured at the same reference point (RP0). The data processed provides the hourly values of the wind speed (*Uw*), the maximum value of the wind gust (*Uwg*) registered in the respective hour, and the mean wind direction. Thus, Figure 4 presents the wind roses for the two parameters, *Uw* and *Uwg*. Figure 5 illustrates the annual maximum series (bars) for both wind parameters considered (*Uw* and *Uwg*), corresponding to the 15-year time interval considered. In this figure, the linear regression (indicating the trend) is also illustrated. A trend line, or the line of best fit [46], is given by the following relationship:

$$y = sx + m, \tag{7}$$

where x is the independent variable, y is the dependent variable, s is the slope of the line, and m is the y-intercept. The regression parameters (s and m) are computed based on the following relationships:

$$s = \frac{\sum_{i=n}^{n} (x_i - \overline{x})(y_i - \overline{y})}{\sum_{i=1}^{n} (x_i - \overline{x})^2} \tag{8}$$

$$m = \overline{y} - s\overline{x} \tag{9}$$

whith n the number of years for which the maximum annual values were calculated (in the present case, 15 years), x is the independent variable represented by each year and y is the dependent variable indicating the maximum value corresponding to each year.

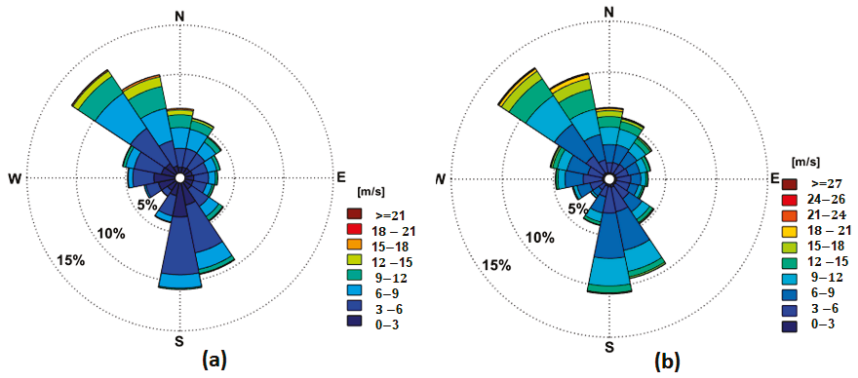


Figure 4. Wind roses corresponding to the 15-year time interval of 2009–2023. (**a**) *Uw*—hourly averaged values of the wind speed; (**b**) *Uwg*—maximum value of the wind gust.

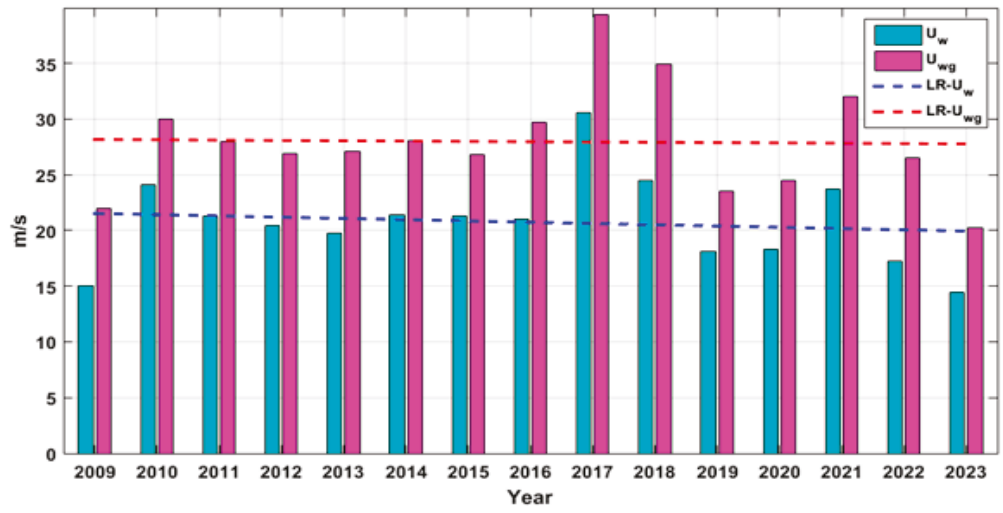


Figure 5. *Uw* and *Uwg* represent annual maxim series measured at the entrance to the Sulina channel (RP0), corresponding to 15-year time interval of 2009–2023.

Table 3 presents the maximum values of the wind speed and wind gust, corresponding to each month for the 15-year period of 2009–2023. The values of the ratio between *Uwg* and *Uw* are also presented in this table. As can be seen in Table 3, the maximum value of this ratio is 1.44. However, it can be noticed that this value is mainly characteristic to the high winds, because the average value of the same ratio for the entire data set is 1.73. This means that under normal conditions, we can very often expect wind gusts with an intensity that is almost double than the hourly registered value of the wind speed at the entrance to the Sulina channel.

Table 3. Maximum values for the wind speed (*Uw*) and wind gust (*Uwg*) corresponding to each month for the 15-year period of 2009–2023.

Month	Jan	Feb	Mar	Apr	May	Jun	Jul	Aug	Sep	Oct	Nov	Dec
Uw (m/s)	30.6	24.1	17.2	21.0	16.9	16.7	20.7	17.6	18.3	18.4	18.2	21.4
Uwg (m/s)	39.4	32.0	22.4	27.3	21.2	24.0	23.9	23.0	23.3	25.6	24.2	30.0
Uwg/Uw	1.29	1.33	1.30	1.30	1.25	1.44	1.16	1.31	1.27	1.39	1.33	1.40

3.2. Analysis of Wind Data Offshore the Danube's Mouths: Recent Past vs. near Future

The next analysis is made considering model wind data for the reference points RP1 (offshore Sulina) and RP2 (offshore Saint George). The analysis is made first for the past by processing the ERA5 data. The regional climate wind models, considered to evaluate the future expected wind conditions for the near future period of 2041–2071, are RCA4 and ALADIN6, both for RCP4.5 and RCP8.5, and ALADIN6x for SSP5-8.5. Since the historical data provided by the climate models are available for the 30-year time interval of 1976–2005, this period is considered for comparison with the ERA5 reanalysis data to assess the convergence and differences between the hindcast and historical data of the wind models. On the other hand, the SSP data are provided starting with 1979. In this case, the comparison with ERA5 is made for the 30-year period of 1979–2008. The wind roses corresponding to the reference points RP1 and RP2 (Sulina and Saint George, respectively) are illustrated in Figures 6 and 7. In order to cover the entire period of 1976–2008, Figures 6a and 7a were designed for this 33-year period, Figure 6b,c and Figure 7b,c for the 30-year period of 1976–2005, and Figures 6d and 7d for the 30-year time interval of 1979–2008. First, it can be noticed from these figures that the wind conditions in the two locations (RP1 and RP2) are generally similar. With regard to the values of the maximum wind speed, for Sulina, they are U_{10ERA} = 20.94 m/s, U_{10RCA} = 27.49 m/s, U_{10AL6} = 26.16 m/s, and U_{10AL6x} = 24.2 m/s, while for Saint George, they are U_{10ERA} = 21.55 m/s, U_{10RCA} = 22.01 m/s, U_{10AL6} = 25.77 m/s, and U_{10AL6x} = 25.4 m/s. According to the results presented, the highest value of the maximum wind speed (27.49 m/s) between the two reference points considered corresponds to RP1 (Sulina). This was provided by the RCA4 climate wind model.

The annual maximum series corresponding to the same time intervals form the recent past considered before are presented in Figure 8 (for RP1) and Figure 9 (for RP2). At this point, it should be also highlighted that the time step of all the wind model data considered and processed is of 3 h, so considerably higher wind speed values can occur in this time window. It should be also noticed that there is an acceptable concordance between the models and the RCMs (especially ALADIN), providing generally higher wind speed values than ERA5.

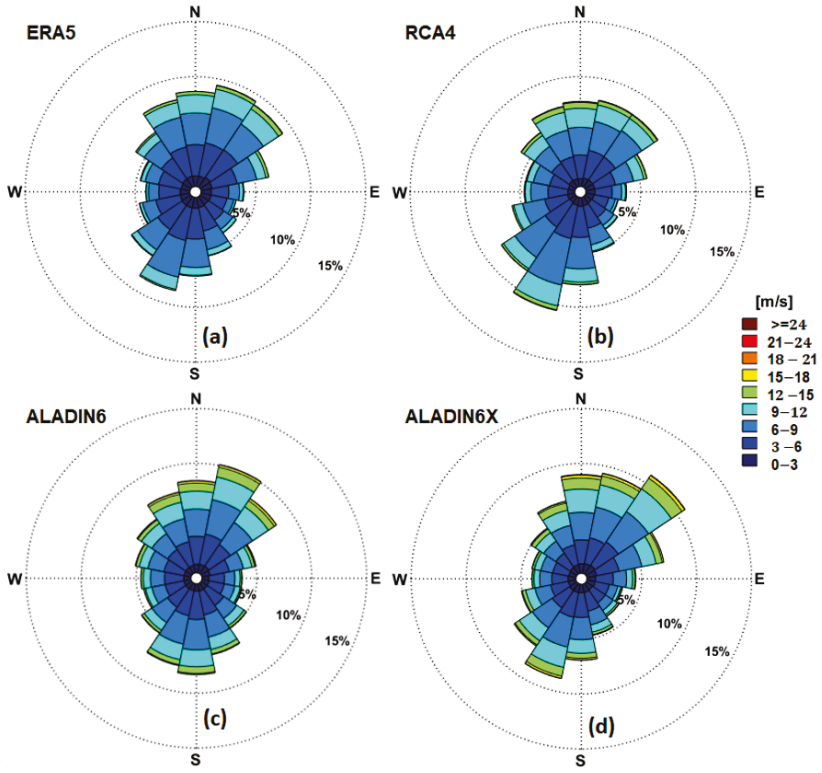


Figure 6. Wind roses offshore the Sulina channel (RP1) for the recent past period based on an analysis of the hindcast and climate model data. (**a**) ERA5 (1976–2008); (**b**) RCA4 for the RCP scenarios (1976–2005); (**c**) ALADIN6 for the RCP scenarios (1976–2005); (**d**) ALADIN6x for the SSP scenario (1979–2008).

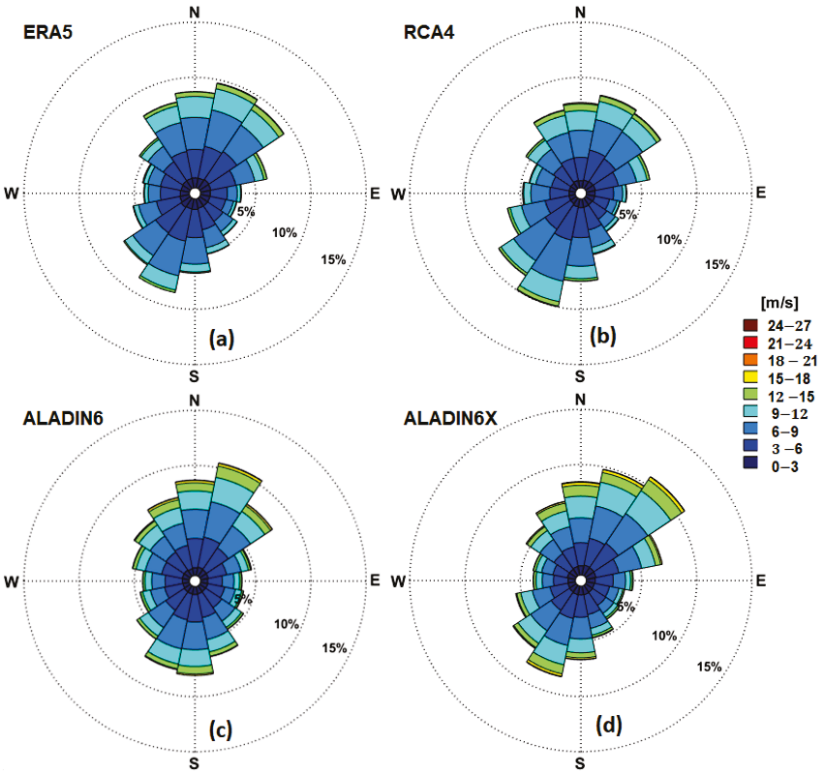


Figure 7. Wind roses offshore the Saint George arm of the Danube (RP2) for the recent past period based on an analysis of the hindcast and climate model data. (**a**) ERA5 (1976–2008); (**b**) RCA4 for the RCP scenarios (1976–2005); (**c**) ALADIN6 for the RCP scenarios (1976–2005); (**d**) ALADIN6x for the SSP scenario (1979–2008).

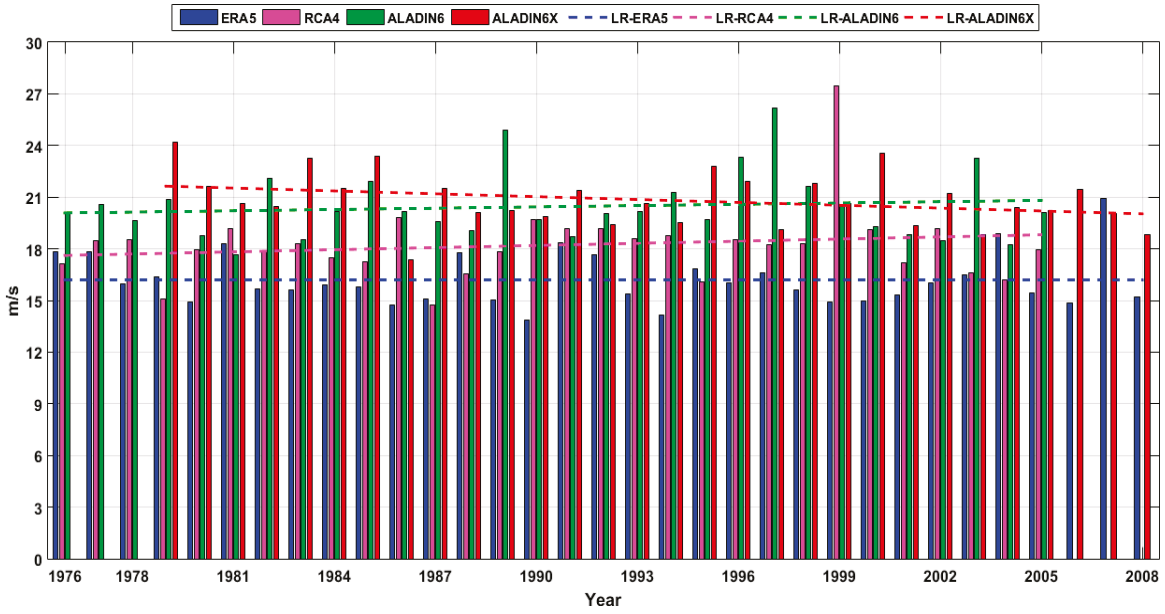


Figure 8. Wind speed (U_{10}) annual maximum series and linear trends for the recent past period offshore Sulina (RP1). ERA5 (1976–2008), RCA4 and ALADIN6 (1976–2005), and ALADIN6x (1979–2008).

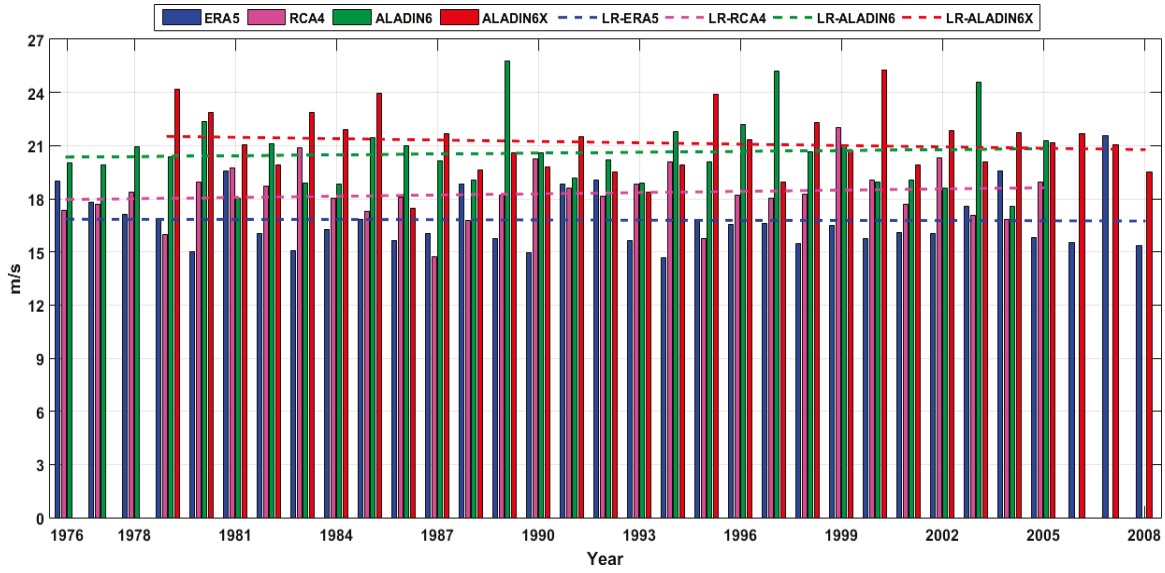


Figure 9. Wind speed (U_{10}) annual maximum series and linear trends for the recent past period offshore Saint George (RP2). ERA5 (1976–2008), RCA4 and ALADIN6 (1976–2005), and ALADIN6x (1979–2008).

The wind roses expected for the near future period (2041–2070) are illustrated in Figures 10 and 11 for RP1 and RP2, respectively. The results presented indicate similarity with the recent past, with the observation that a higher percentage of the wind coming from the Northeast direction is expected in the future.

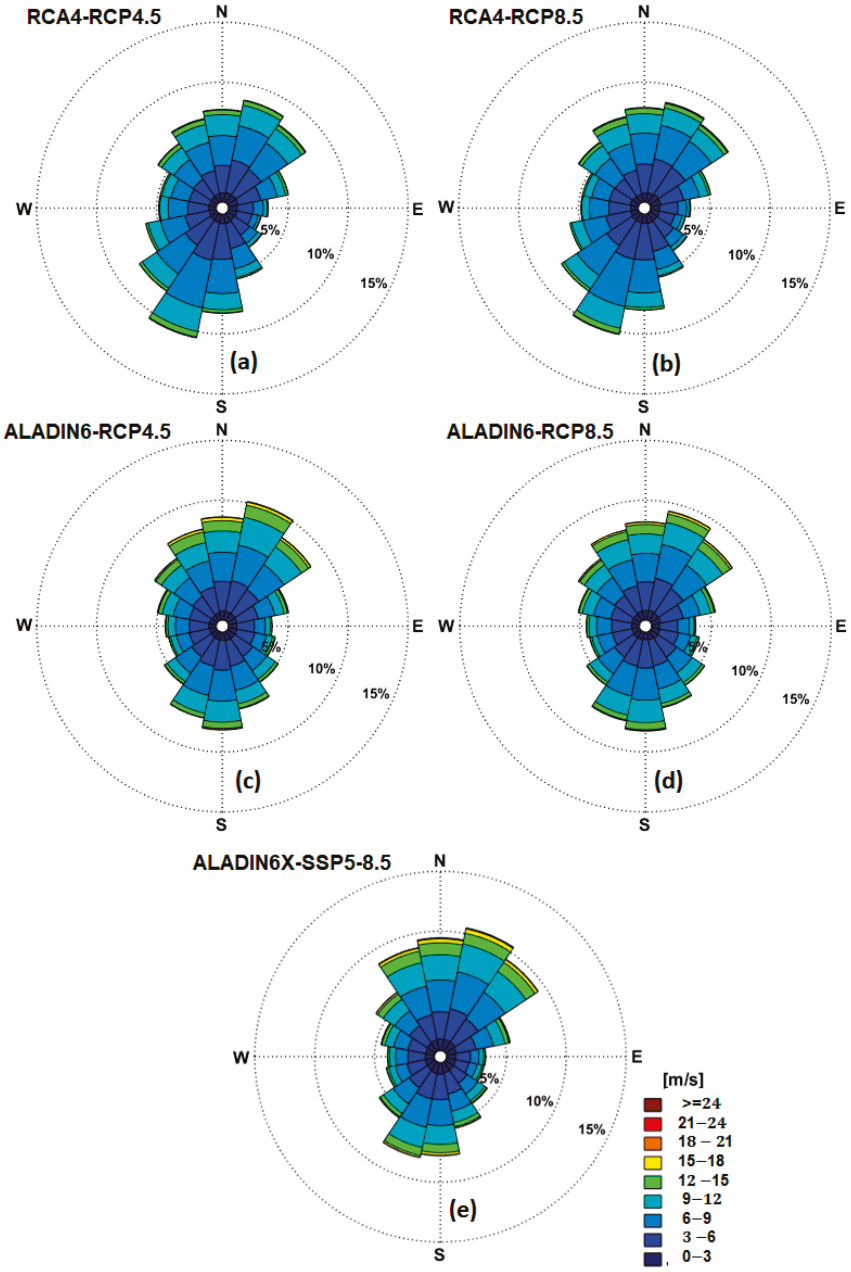


Figure 10. Wind roses offshore the Sulina channel (RP1) for the near future period (2041–2070) based on an analysis of the climate model data. (**a**) RCA4-RCP4.5; (**b**) RCA4-RCP8.5; (**c**) ALADIN6-RCP4.5; (**d**) ALADIN6-RCP8.5; (**e**) ALADIN6x-SSP5-8.5.

The corresponding annual maximum series and linear trends are presented in Figures 12 and 13, respectively. For Sulina, the maximum values of the wind speed evaluated using the climatic models are $U_{10RCA4.5}$ = 26.11 m/s, $U_{10RCA8.5}$ = 23.96 m/s, $U_{10AL4.5}$ = 24.65 m/s, $U_{10AL8.5}$ = 24.48 m/s, and $U_{10AL5\text{-}8.5}$ = 29.85 m/s, while for Saint George, they are $U_{10RCA4.5}$ = 25.35 m/s, $U_{10RCA8.5}$ = 22.16m/s, $U_{10AL4.5}$ = 25.02 m/s, $U_{10AL8.5}$ = 22.83 m/s, and $U_{10AL5\text{-}8.5}$ = 28.32 m/s.

As for the recent past period, the results show that in the near future time interval considered, the highest wind speed is also expected in Sulina (29.85 m/s). However, this time, the highest wind conditions are provided by the SSP5-8.5 climate scenario.

It can also be noticed that, for the near future period analyzed, the SSP5-8.5 data provide systematically higher wind speed values than all the other climate scenarios. On the other hand, the SSP data indicate higher wind speeds than in the past, a relative increase of about 22% in RP1 and of 11.5% in RP2. From this perspective, the results indicate a slight tendency of enhancement of the extreme winds in the coastal environment at the mouths of the Danube River. This tendency has also been reported in other works (for example, reference [47]).

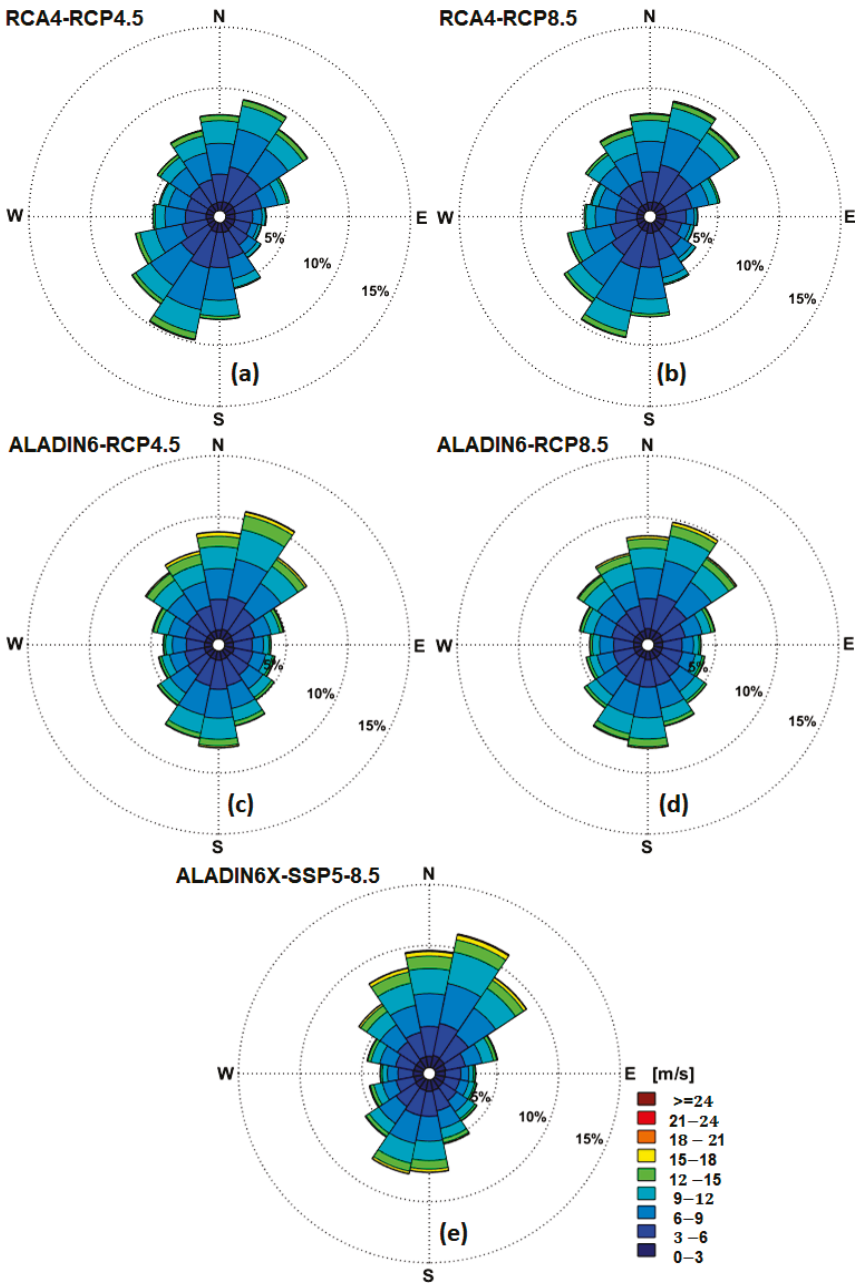


Figure 11. Wind roses offshore Saint George (RP2) for the near future period (2041–2070) based on an analysis of the climate model data. (**a**) RCA4-RCP4.5; (**b**) RCA4-RCP8.5; (**c**) ALADIN6-RCP4.5; (**d**) ALADIN6-RCP8.5; (**e**) ALADIN6x-SSP5-8.5.

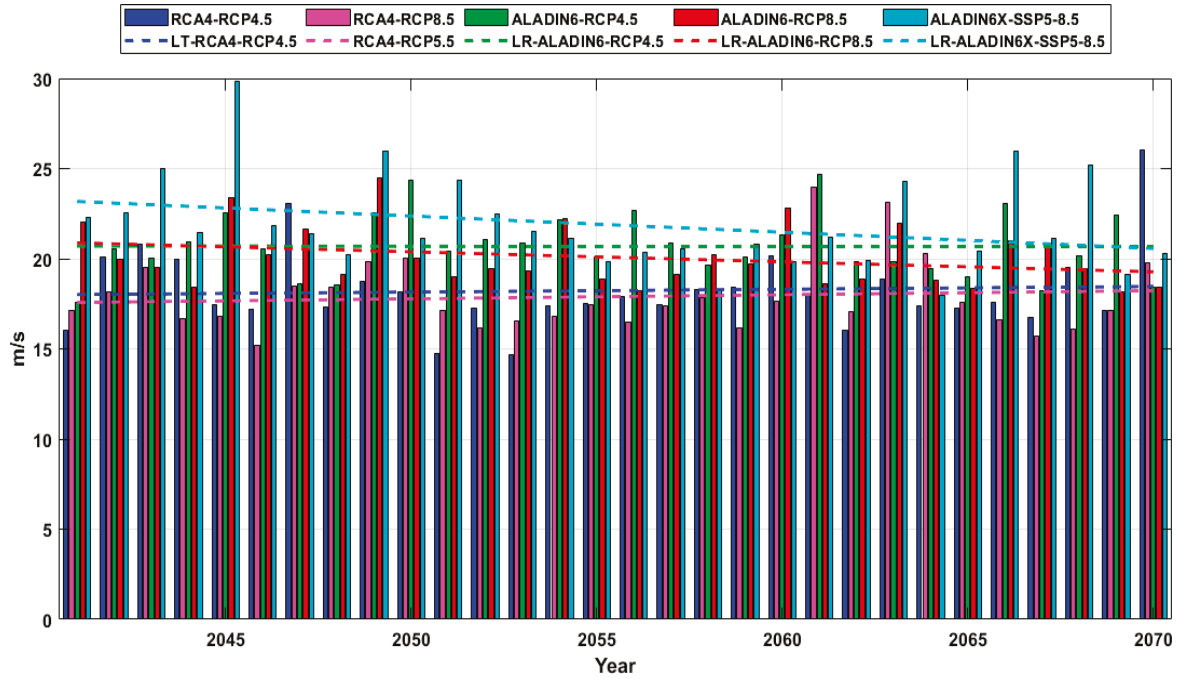


Figure 12. Wind speed (U_{10}) annual maximum series and linear trends, projections for the near future period (2041–2070) offshore Sulina (RP1). RCA4 (RCP4.5 and RCP8.5), ALADIN6 (RCP4.5 and RCP8.5), and ALADIN6x SSP5-8.5.

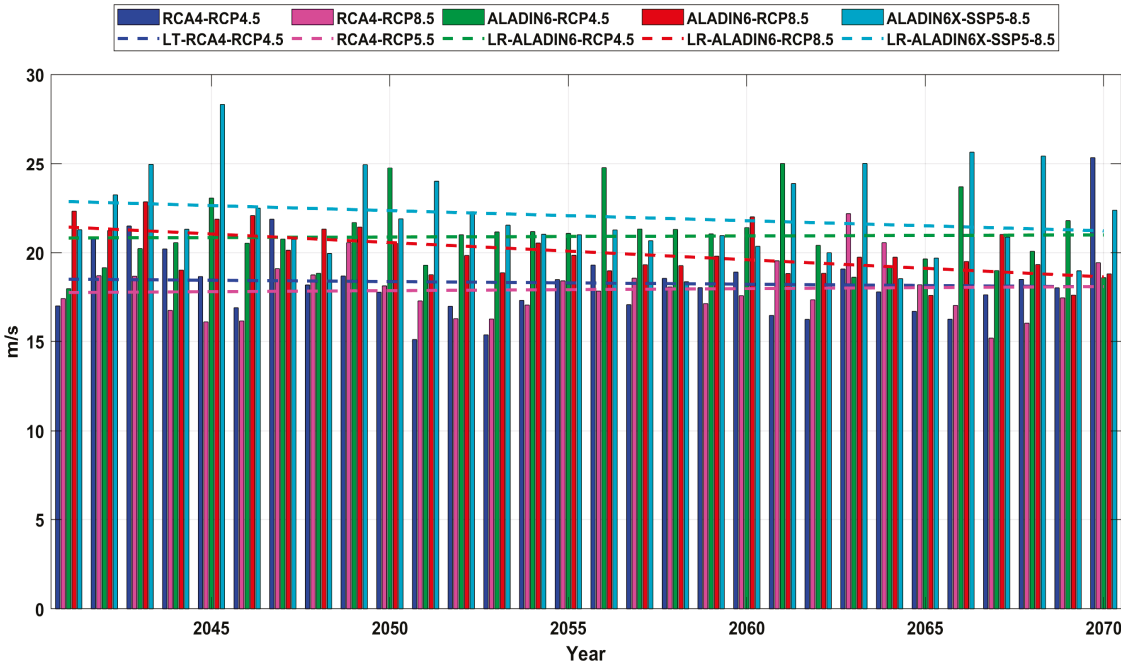


Figure 13. Wind speed (U_{10}) annual maximum series and linear trends, projections for the near future period (2041–2070) offshore Saint George (RP2). RCA4 (RCP4.5 and RCP8.5), ALADIN6 (RCP4.5 and RCP8.5), and ALADIN6x SSP5-8.5.

3.3. Analysis of Wave Data Offshore the Danube's Mouths: Recent Past vs. near Future

Using the wind fields provided by ERA5 for the recent past and those coming from the regional climate models (RCA4 and ALADIN) under the scenarios previously considered (RCP4.5, RCP8.5 and SSP5-8.5), simulations employing the wave modeling system SWAN based were carried out. The focusing of the system towards the target area for a case of a

typical storm in the Black Sea corresponding to the timeframe 21.12.2004h03 is illustrated in Figure 14 in terms of significant wave height scalar fields and wave vectors. The wave vectors indicate the mean wave direction, and their numerical values are represented by the value of the significant associated wave height. The color bar given in this figure associates a different color to each interval value of 0.5 m for the significant wave height. According to the results presented in this figure, for the case of the storms propagating from east to west (which are typical for this region), due to the effects of the wave-current interactions at the mouths of the Danube River, the significant wave height values are very high and very close to the higher value in the entire sea basin. For example, in Figure 14, the maximum *Hs* value in the Black Sea is 7.26 m, while the maximum *Hs* value at the mouths of the Danube is 7.24 m.

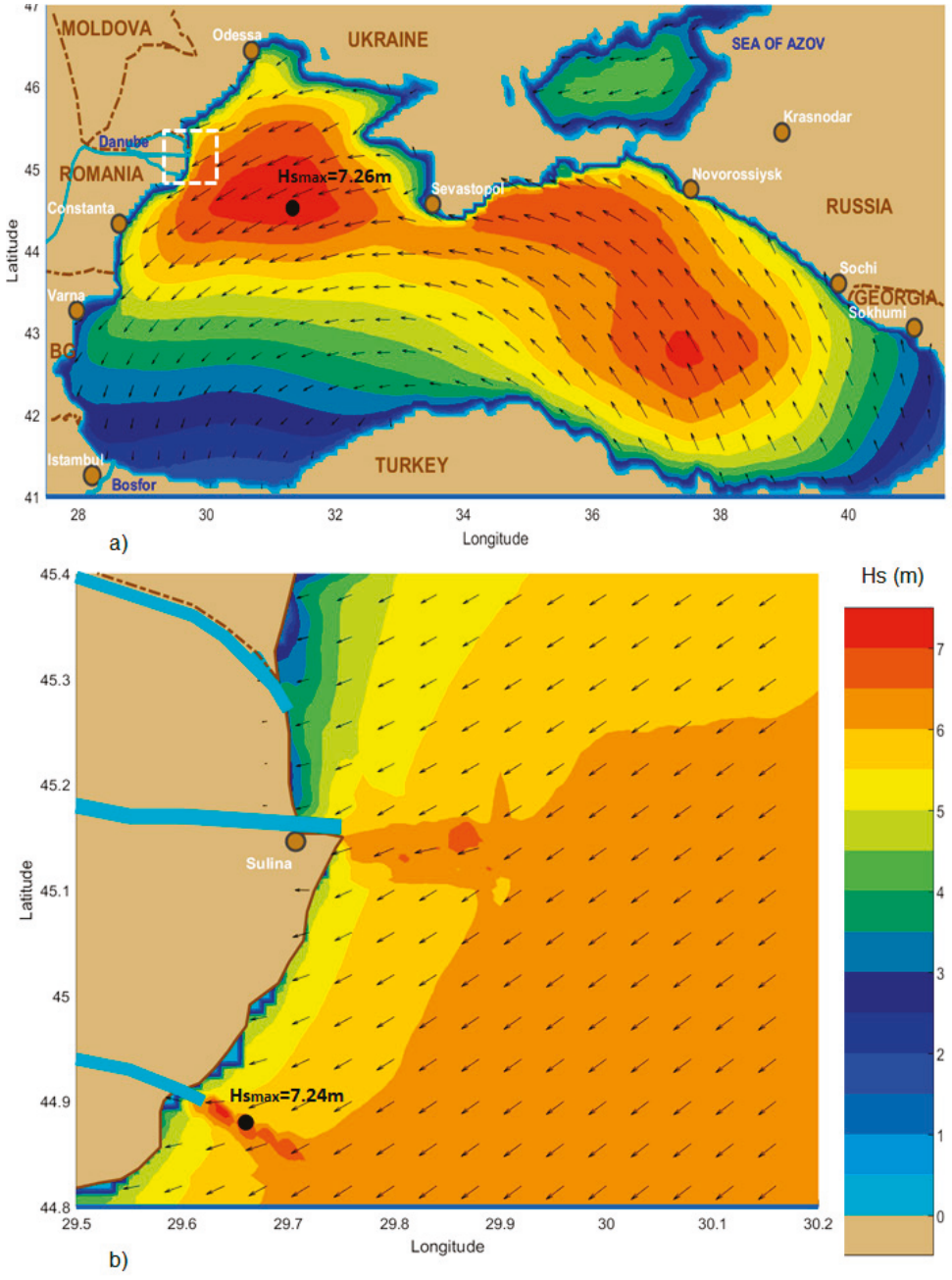


Figure 14. Typical storm in the Black Sea: significant wave height scalar fields and wave vectors. SWAN model simulation corresponding to the timeframe 21.12.2004h03. (**a**) Black Sea basin; (**b**) coastal environment at the mouths of the Danube River.

Based on the results of the wave modeling system in the two reference points defined RP1 and RP2 for the two 30-year time intervals (recent past and near future), and considering as forcing factors the wind fields provided by the models mentioned in the previous section, an analysis of the past and future expected wave climate in the target area is presented next.

The *Hs* wave roses corresponding to the reference points RP1 and RP2 (Sulina and Saint George, respectively) are illustrated in Figures 15 and 16. In order to cover the entire period of 1976–2008, Figures 15a and 16a were designed for this 33-year period, Figure 15b,c and Figure 16b,c for the 30-year period of 1976–2005, and Figures 16d and 17d for the 30-year time interval of 1979–2008. As in the case of the wind, it can be noticed from these figures that the wave conditions in the two locations (RP1 and RP2) are in general similar in terms of both *Hs* and wave directions. With regard to the maximum *Hs* values, for Sulina, they are H_{sERA} = 4.5 m, H_{sRCA} = 5.65 m, H_{sAL6} = 6.27 m/s, and H_{sAL6x} = 7.04 m, while for Saint George, the results are H_{1s0ERA} = 4.91 m, H_{sRCA} = 6.061 m, H_{sAL6} = 6.96 m, and H_{sAL6x} = 7.33 m/s. According to the results presented, the highest value of the significant wave height (7.33 m/s) between the two reference points considered corresponds to RP2. This was provided by the ALADIN6x wind model as the forcing system for SWAN.

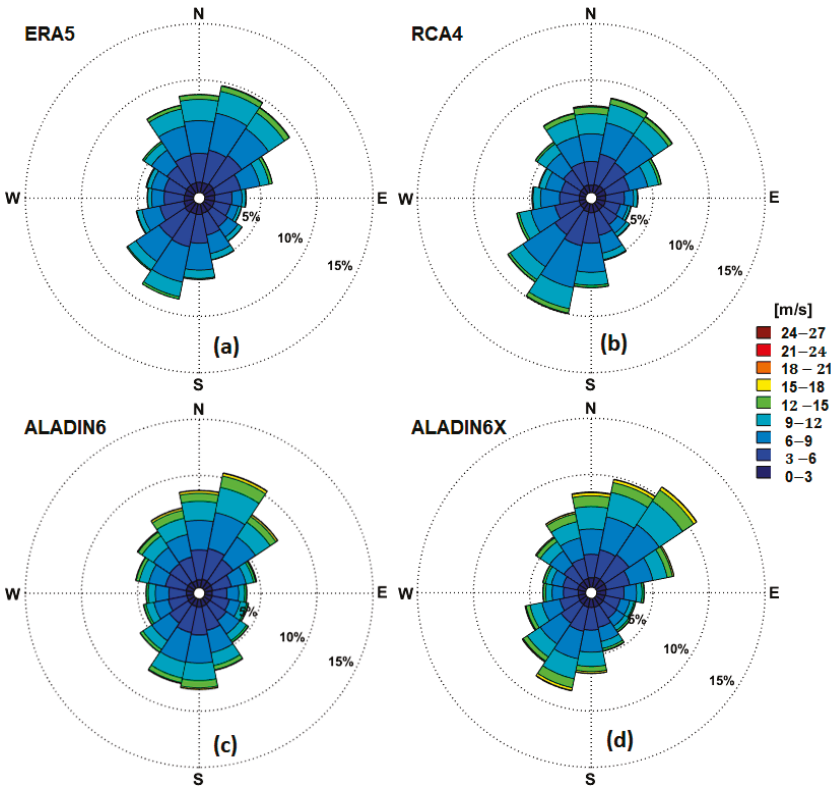


Figure 15. H_s wave roses offshore the Sulina channel (RP1) for the recent past period based on an analysis of the results provided by the wave modeling system forced with reanalysis and climate model data. The forcing wind fields considered are: (**a**) ERA5 (1976–2008); (**b**) RCA4 for the RCP scenarios (1976–2005); (**c**) ALADIN6 for the RCP scenarios (1976–2005); (**d**) ALADIN6x for the SSP scenario (1979–2008).

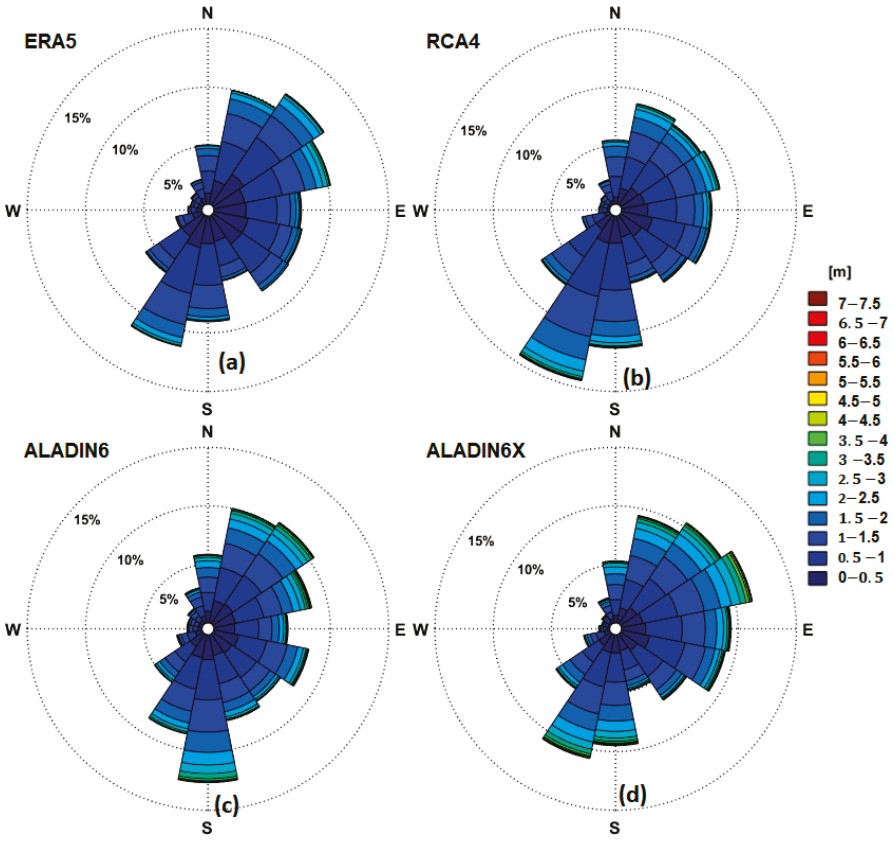


Figure 16. H_s wave roses offshore the Saint George arm of the Danube (RP2) for the recent past period based on the analysis of the results provided by the wave modeling system forced with reanalysis and climate model data. The forcing wind fields considered are: (**a**) ERA5 (1976–2008); (**b**) RCA4 for the RCP scenarios (1976–2005); (**c**) ALADIN6 for the RCP scenarios (1976–2005); (**d**) ALADIN6x for the SSP scenario (1979–2008).

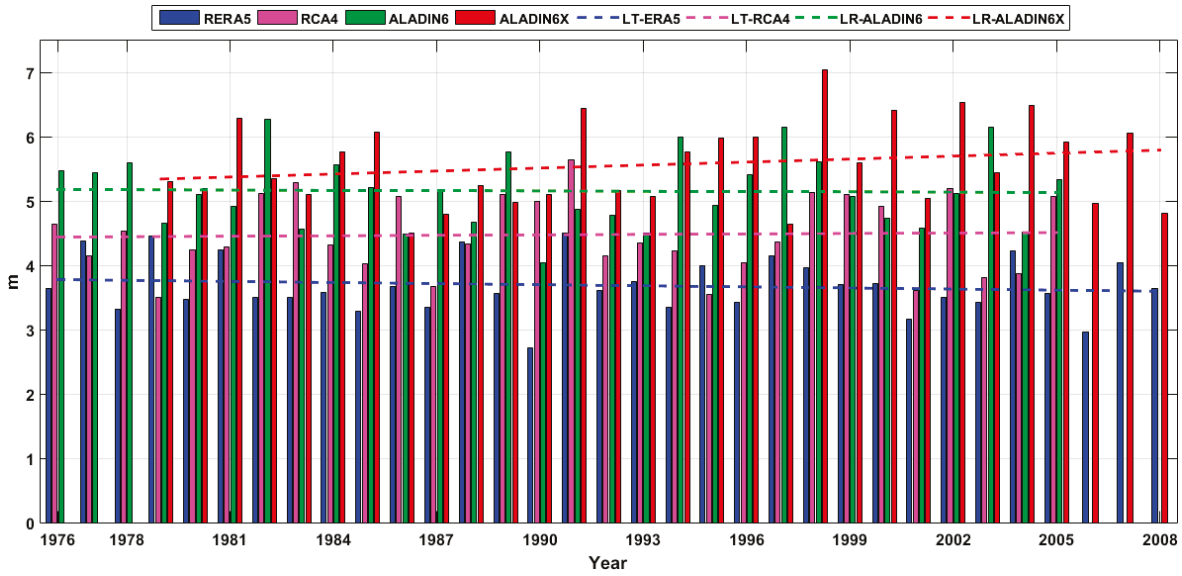


Figure 17. *Hs* annual maximum series and linear trends for the recent past period offshore Sulina (RP1). Results of wave model simulations forced with the following wind fields: ERA5 (1976–2008), RCA4 and ALADIN6 (1976–2005), and ALADIN6x (1979–2008).

The annual maximum series corresponding to the same time intervals from the recent past considered before are presented in Figure 17 (for RP1) and Figure 18 (for RP2). It should be mentioned that, as in the case of the wind, the time step considered for the wave model output is 3 h. It should be also noticed that there is an acceptable concordance between the models. However, it can be observed at this point that when forcing the wave modeling system, the RCMs (and especially ALADIN) generally provide higher *Hs* values than ERA5.

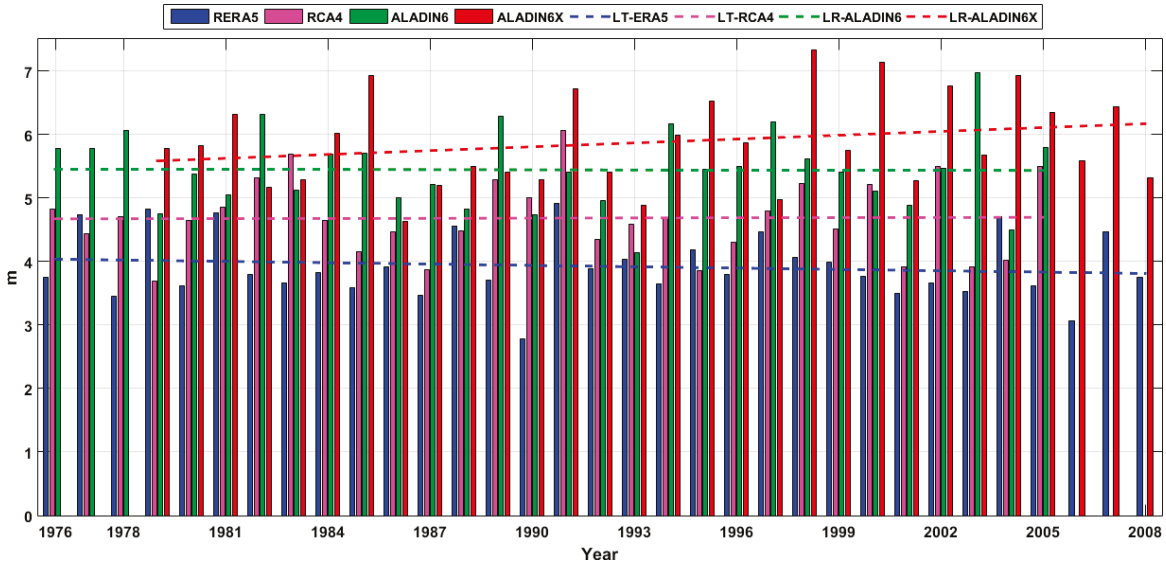


Figure 18. *Hs* annual maximum series and linear trends for the recent past period offshore Saint George (RP2). Results of wave model simulations forced with the following wind fields: ERA5 (1976–2008), RCA4 and ALADIN6 (1976–2005), and ALADIN6x (1979–2008).

The *Hs* wave roses expected for the near future period (2041–2070) are illustrated in Figures 19 and 20 for RP1 and RP2, respectively. The results presented are similar to those from the recent past. The corresponding *Hs* annual maximum series and linear trends are presented in Figures 21 and 22, respectively. For Sulina, the maximum *Hs* values evaluated are $H_{sRCA4.5}$ = 6.19 m, $H_{sRCA8.5}$ = 6.13 m, $H_{sAL4.5}$ = 7.13 m, $H_{1AL8.5}$ = 5.7 m, and $H_{sAL5\text{-}8.5}$ = 7.05 m, while for Saint George, they are $H_{sRCA4.5}$ = 6.86 m, $H_{sRCA8.5}$ = 6.51 m, $H_{sAL4.5}$ = 7.29 m, $H_{1AL8.5}$ = 6.19 m, and $H_{sAL5\text{-}8.5}$ = 7.31 m.

At this point, it can be noticed that, for the near future period analyzed, a similar tendency to the case of the wind fields occurs, in the sense that the ALADIN data provide higher values for the significant wave heights than when the RCA4 model is considered as the forcing wind field for the wave model. However, unlike in the case of the wind analysis, ALADIN6 for the RCP4.5 climate scenario provides higher *Hs* values in the target area than the SSP5-8.5 data. Finally, it can be also underlined that the results provided by the RCMs for the recent past in terms of the maximum values of the significant wave height, which may occur offshore the coastal area at the mouths of the Danube River, appear to be more realistic than the ones provided when ERA5 is considered as the wind driver for the wave model. This is probably because the ERA5 data have a tendency to systematically underestimate the maximum wind speed values. This observation is in line with the findings of various previous works (for example, references [43–45] or [47,48]), but also with some in situ observations.

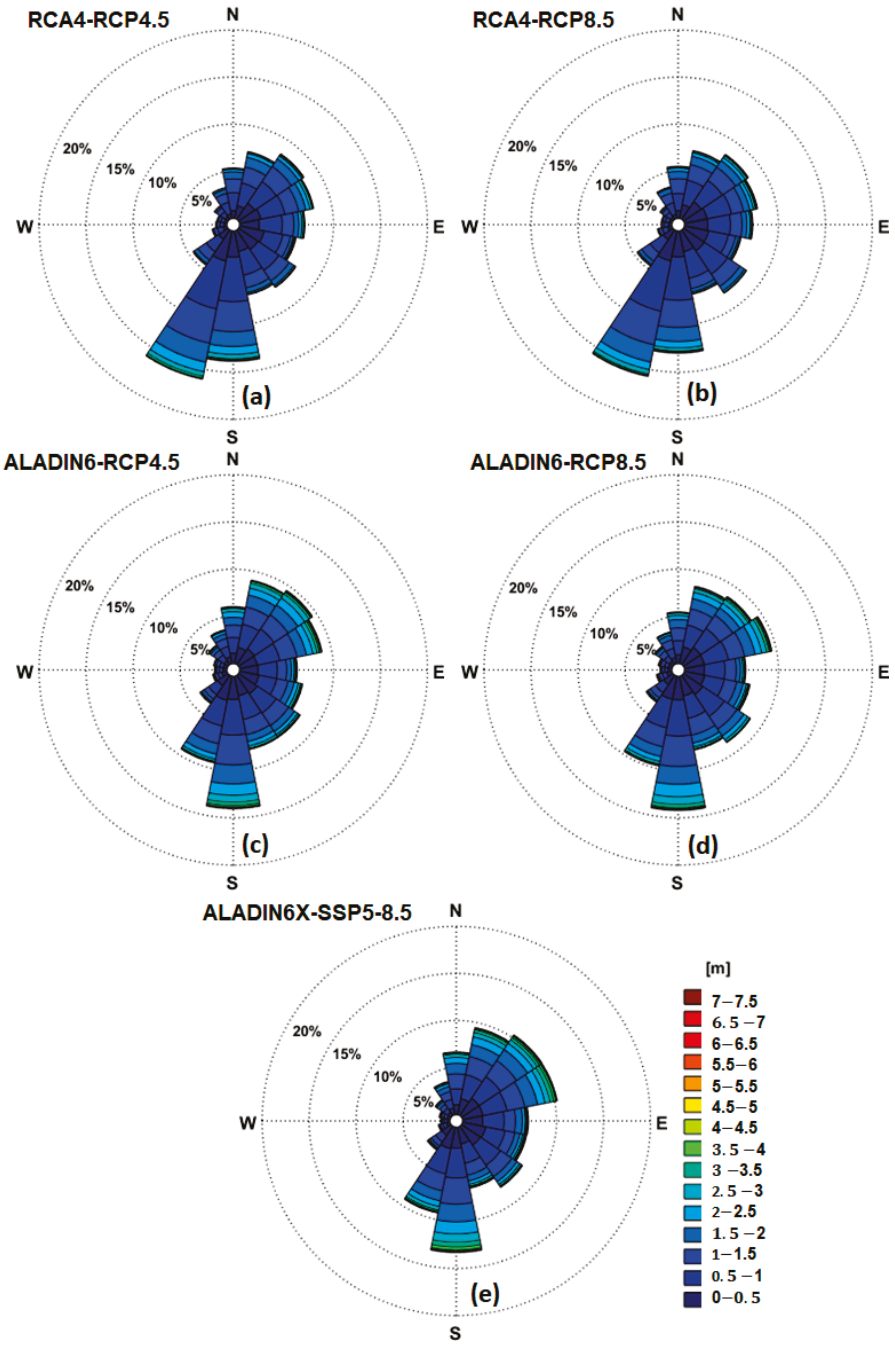


Figure 19. H_s wave roses offshore the Sulina channel (RP1) for the near future period (2041–2070) based on the analysis of the results provided by the wave modeling system forced with the climate model data. The forcing wind fields considered are: (**a**) RCA4-RCP4.5; (**b**) RCA4-RCP8.5; (**c**) ALADIN6-RCP4.5; (**d**) ALADIN6-RCP8.5; (**e**) ALADIN6x-SSP5-8.5.

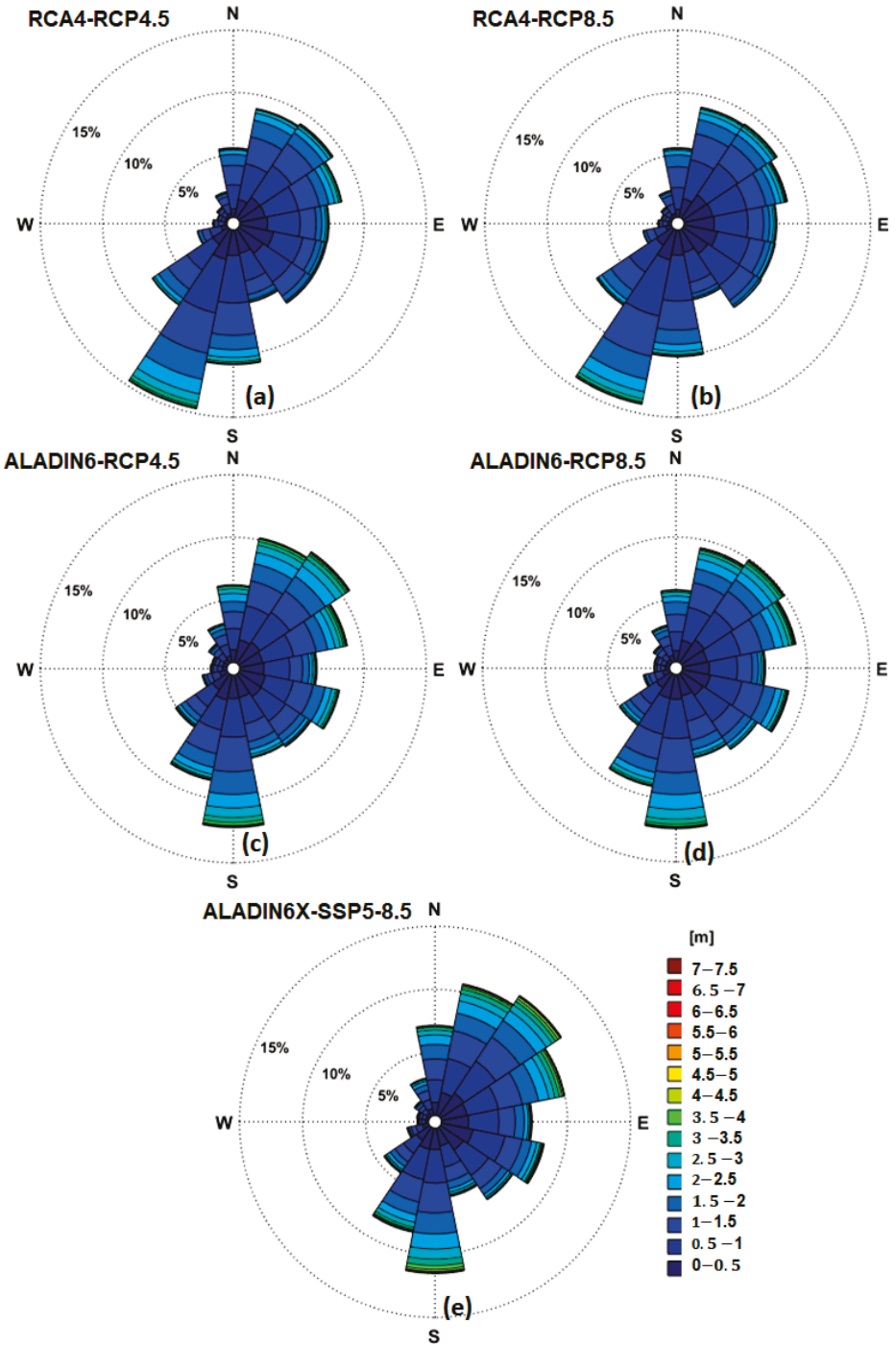


Figure 20. H_s wave roses offshore the Saint George arm of the Danube (RP2) for the near future period (2041–2070) based on the analysis of the results provided by the wave modeling system forced with climate model data. The forcing wind fields considered are: (**a**) RCA4-RCP4.5; (**b**) RCA4-RCP8.5; (**c**) ALADIN6-RCP4.5; (**d**) ALADIN6-RCP8.5; (**e**) ALADIN6x-SSP5-8.5.

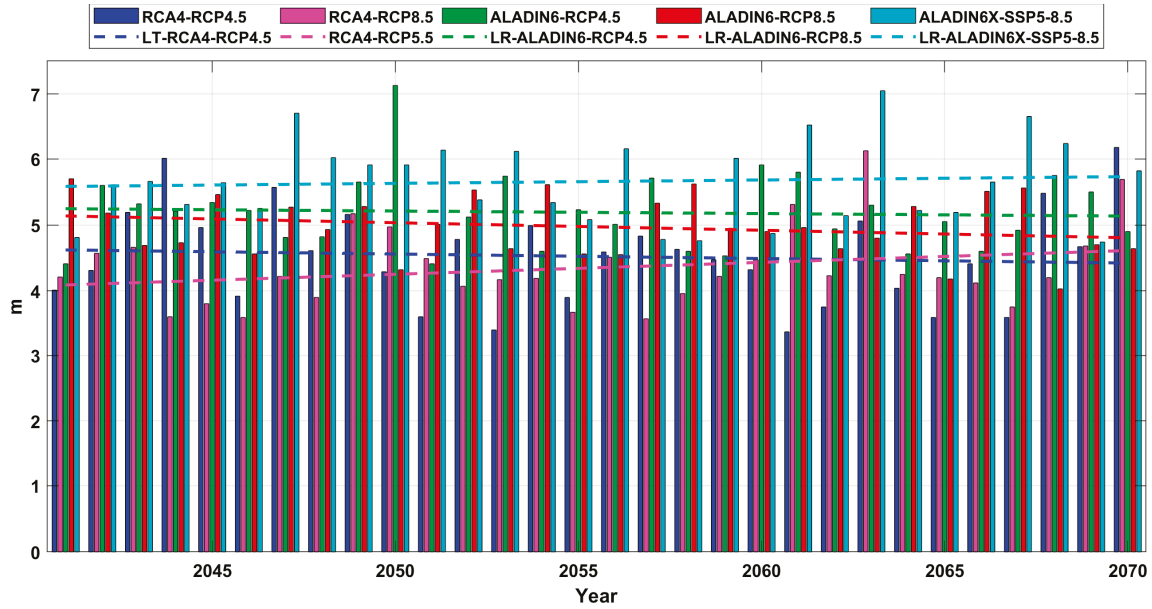


Figure 21. H_s annual maximum series and linear trends, projections for the near future period (2041–2070) offshore Sulina (RP1). Results of wave model simulations forced with the following wind fields: RCA4 (RCP4.5 and RCP8.5), ALADIN6 (RCP4.5 and RCP8.5), and ALADIN6x SSP5-8.5.

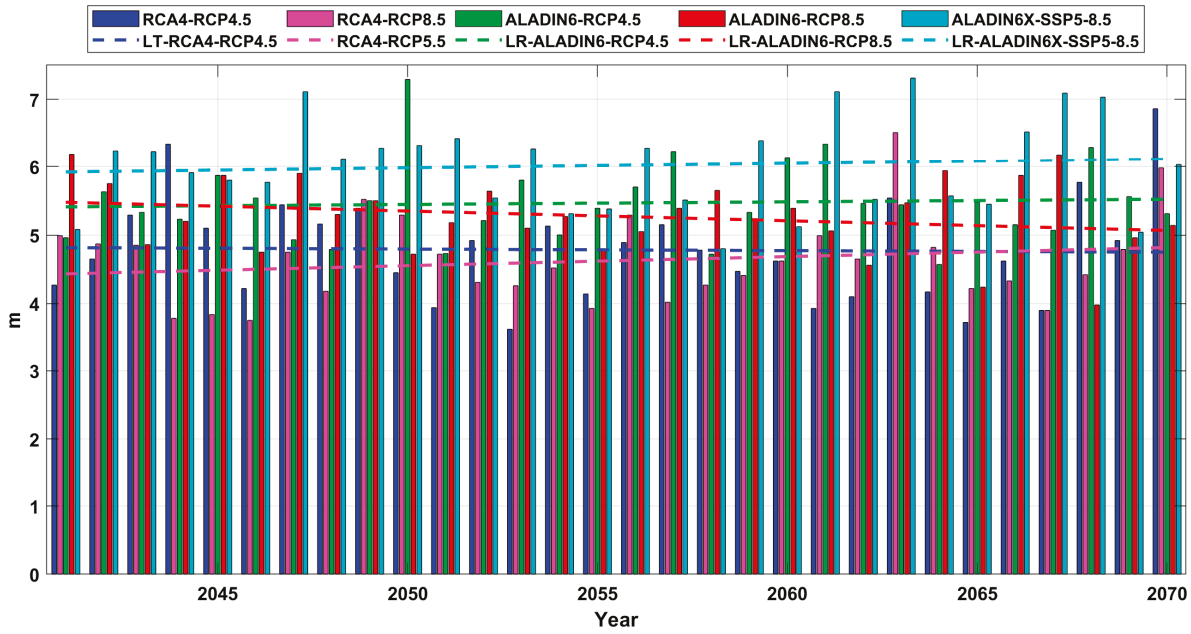


Figure 22. H_s annual maximum series and linear trends, projections for the near future period (2041–2070) offshore Saint George (RP2). Results of wave model simulations forced with the following wind fields: RCA4 (RCP4.5 and RCP8.5), ALADIN6 (RCP4.5 and RCP8.5), and ALADIN6x SSP5-8.5.

4. Discussion

1. The analysis of the wind data shows that there is in general a good match between the measurements and the model results, especially with regard to the intensity of the maximum wind speeds. However, by comparing Figures 4 and 6, we can notice that in RP0, the dominant wind direction is from north to northwest, while in RP1, it is from north to northeast. Furthermore, unlike in RP0, in RP1, significant winds also come from the southeast, while in both cases, significant winds come from the south. The main explanation for these differences is that while RP1 is located 30 km offshore,

RP0 represents the zero-kilometer point of the Danube, where both the influence of the coast and the local wind currents propagating along the river are more consistent.

2. With regard to the waves, the results show that we can expect significant wave heights that are even higher than 7 m in the coastal environment offshore the mouths of the Danube River. Furthermore, as Figure 14 clearly illustrates, the local processes and especially the wave–current interactions and the shallow water effects induce considerable enhancements in the wave height in the nearshore. From this perspective and in order to assess better the influence of the local effects at the entrance to the Sulina channel, wave model simulations were carried out considering the most common wave patterns from the point of view of the significant wave height (*Hso*) and the mean wave direction of the incoming waves on the offshore boundary (*Wdir*), as indicated by Figures 15, 16, 19 and 20. Furthermore, previous results in terms of the wave modeling presented in reference [48] were also considered. Thus, in the high-resolution computational domain described in Table 1, SWAN simulations were performed considering significant wave heights and wave directions in the ranges of [1–5 m] and [30°–150°]. Based on the results of these simulations, an index giving the relative enhancement in the significant wave height at the entrance to the Sulina channel due to the wave–current interactions (RE_{Hs}) was evaluated. The expression of this index is given by the equation below, while the corresponding values are provided in Table 4.

$$RE_{Hs} = (Hs_{max} - Hso)/Hso \quad (10)$$

Table 4. Results of the SWAN model simulations in the presence of currents considering various significant wave heights and mean wave directions incoming on the external boundary of the computational domain.

***Hso* (m)**	**Wdir (°)**									
	30		**60**		**90**		**120**		**150**	
	***RE*$_{Hs}$ (%)**	***BFI***	***RE*$_{Hs}$ (%)**	***BFI***	***RE*$_{Hs}$ (%)**	***BFI***	***RE*$_{Hs}$ (%)**	***BFI***	***RE*$_{Hs}$ (%)**	***BFI***
1	23	0.7	30	0.8	38	0.9	42	0.94	38	0.85
2	17.5	1.2	25	1.5	36.5	1.75	38.5	1.4	27.5	1.3
3	11	1.2	18.6	1.6	32.5	1.9	35	1.7	20.7	1.4
4	8.25	1.1	15	1.5	30	1.8	31.75	1.6	17.75	1.4
5	6	0.9	12.8	1.4	23.4	1.7	24.2	1.5	13.6	1.3

On the other hand, while spectral wave models such as SWAN are used to provide predictions in terms of the significant wave height, which represents four times the area under the spectral density, from the point of view of the navigation hazards, we are more interested in the prediction of the larger wave heights such as the maximum wave height. Usually, this is estimated based on some theoretical probabilistic distributions [49] among which the most common is the Rayleigh distribution [50], according to which waves with a maximum wave height of almost double the significant wave height can be often expected in a wave group. There are, however, situations when the ratio between the maximum and the significant wave height can be higher, or even much higher, than 2. Such kinds of waves are called freak or rogue waves, and they are very dangerous, inducing a high risk of hazards in navigation and many other marine activities. Thus, passing now from a statistical approach to a probabilistic one, we can estimate the higher risks of occurrences for such kinds of waves via the Benjamin–Feir index (*BFI*). The *BFI*, or the steepness-over-randomness ratio, was introduced by Jansen [51] and is defined as follows:

$$BFI = \sqrt{2\pi} St \cdot Q_p \quad (11)$$

where *St* represents the integral wave steepness, representing the ratio between the significant wave height and the wavelength, and Q_p is the peakedness of the wave spectrum, defined as follows:

$$Q_p = 2\frac{\iint \sigma E^2(\sigma,\theta)d\sigma d\theta}{\left(\iint \sigma E(\sigma,\theta)d\sigma d\theta\right)^2} \quad (12)$$

In fact, the *BFI* is a spectral shape parameter that can be related to the kurtosis of the wave height distribution, with the kurtosis depending on the square of the *BFI*. Experimental results indicate that for *BFI* = 0.2, the maximum wave heights are very well described by the Rayleigh distribution, while for *BFI* values greater than 0.9, the ratio of *Hmax/Hs* is substantially underestimated. The values of the *BFI* index corresponding to the most relevant wave propagation patterns are also presented in Table 4. The results indicate that *BFI* values higher than 1.5 occur in this area for waves with significant wave heights between 3 and 4 m and when the mean wave direction on the offshore boundary is between 90 and 120 degrees. From this perspective, two additional simulations were performed, considering the two situations presenting the highest risk from the point of view of the occurrence of rogue waves. The results are illustrated in Figure 23. Thus, Figure 23a presents the bathymetric map of the computational domain and the average current field. Figure 23b illustrates the results of the SWAN simulations in terms of the significant wave height scalar fields and wave vectors, considering offshore wave conditions of *Hs* = 3.5 m and a mean wave direction of 90 degrees. In Figure 23c, the same results are shown, considering offshore wave conditions of *Hs* = 3.5 m and a mean wave direction of 120 degrees. The values of the *BFI* index are indeed higher than those presented in Table 4, being 1.95 (with RE_{Hs} = 28.6%) for the simulations from Figure 23b and 1.9 (with RE_{Hs} = 31.4%) for that illustrated in Figure 23c. The above results indicate that, in addition to the enhancement in terms of *Hs* expressed by the values of the RE_{Hs} index, there is also a high risk of occurrence of abnormal waves for which the ratio between the maximum and the significant wave height is higher than 2.

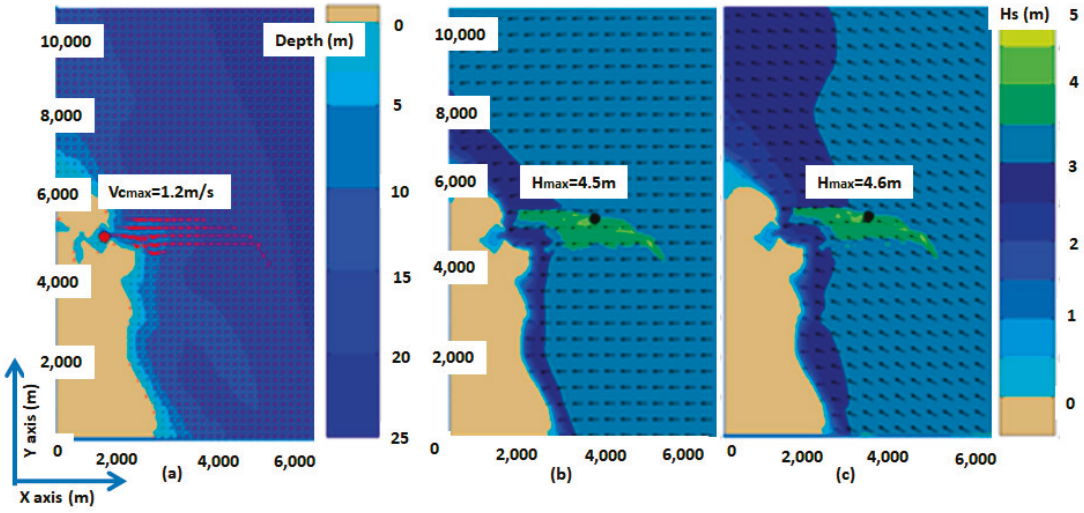


Figure 23. Swan simulations in the high-resolution computational domain focused on the entrance to the Sulina channel. (**a**) Bathymetric map of the computational domain and current field (with red color); (**b**) significant wave height scalar fields and wave vectors considering the offshore wave conditions of *Hs* = 3.5 and a mean wave direction of 90 degrees; (**c**) significant wave height scalar fields and wave vectors considering offshore wave conditions of *Hs* = 3.5 m and a mean wave direction of 120 degrees.

5. Conclusions

The objective of this work was to study the past and future dynamics of the environmental matrix, especially wind and waves, at the entrance to the Sulina channel (the zero-kilometer point of the Danube). This represents the main southern entrance to the

navigation system of Rhine–Main–Danube, the largest inland waterway in Europe linking the Black and the North Seas.

An analysis of 15 years of recent in situ measurements showed that the maximum value of the wind speed registered in this point was almost 31 m/s, while the maximum speed of the wind gust was almost 40 m/s, which was about 30% higher than the hourly value. The results also indicate that, for the entire data set analyzed, the average value of the ratio between the maximum speed of the wind gust and the hourly wind speed value was 1.7. However, in the case of the high wind speeds, the intensity of the wind gusts was relatively lower, and the values of the ratio between the maximum speed of the wind gusts and the hourly wind speed value was generally within the range of [1.3–1.4]. This means that wind gusts with speeds higher than 35 m/s are expected in this coastal area.

A second analysis was performed in two locations (one offshore Sulina and the other offshore Saint George) and was based on data provided by two regional wind climate models (RCA4 and ALADIN) under several scenarios (RCP4.5, RCP8.5, and SSP5-8.5). The analysis was performed for the future 30-year time interval (2041–2070). In order to compare the evolution of the wind climate in relation to the past conditions, a 30-year time interval from the past was also considered. For this period, the ERA5 reanalysis data were processed and analyzed in parallel with the RCM data. The climate model results indicated similar intensities for the past to those provided by the measurements for the maximum wind speed. All the models indicated maximum values of the wind speed that were higher than 25 m/s. It must also be highlighted that the time step considered for all the models was 3 h. The results show that slightly higher values are expected in the future for the wind speed compared to the past, especially in the case of SSP5-8.5.

The last analysis relates to the waves. In this connection, a wave modeling system that was previously validated against both in situ measurements and satellite data was forced successively with each wind data field considered. Simulations were performed for the two 30-year time periods that were previously defined in the case of the wind analysis. The results show that *Hs* values of about 7 m were encountered close to the mouths of the Danube in the past offshore. Such extreme values might be also expected more often in the future. The wave model simulations performed in the high-resolution computational domain that were focused on the Sulina channel also showed that, due to the nearshore effects, an enhancement between 30% and 40% in terms of wave height may be expected at the entrance to the Sulina channel. Furthermore, in addition to the significant wave heights being higher, due to the strong wave–current interaction processes, the probability of rogue waves occurring is very high. From this perspective, the results of the present work indicate that the most dangerous situations, from the point of view of a higher probability of the occurrence of rogue waves, correspond to the incoming waves with directions between 60° and 120° and significant wave heights higher than 2 m. This indicates that waves with heights of 20 m or greater and wind speeds higher than 30 m/s, associated with wind gusts that might exceed 40 m/s, can be expected in extreme storm conditions in this coastal environment.

Finally, based on the summarized three pillars of the above analysis, emphasizing the wind and wave extreme values that may occur as well as the conditions that can generate them, the general conclusion of this work is that the navigation conditions in this sector present a high risk of incidents and accidents, especially in the wintertime. In fact, for this reason, even in the case of moderate storms, the navigation is very often closed at the entrance to the Sulina channel. This work is still ongoing, and a next step would be to elaborate in more detail the risk assessment of severe shipping conditions, particularly focusing on the likelihood or probability of adverse conditions creating hazardous situations in this important navigation area.

Author Contributions: Conceptualization, A.B.R., L.R. and E.R.; methodology, L.R. and E.R.; software, L.R.; validation, E.R. and A.M.; formal analysis A.B.R., L.R. and E.R.; investigation, L.R. and E.R.; resources, A.B.R. and A.M.; data curation, A.B.R., L.R. and E.R.; writing—original draft preparation, E.R.; writing—review and editing, L.R. and E.R.; visualization, L.R. and A.B.R.; supervision, A.B.R.

and E.R.; project administration, A.B.R. and A.M.; funding acquisition, A.B.R. and A.M. All authors have read and agreed to the published version of the manuscript.

Funding: This work is a part of the PLOTO project. This project has received funding from the Horizon Europe innovation actions under grant agreement no. 101069941.

Institutional Review Board Statement: Not applicable.

Informed Consent Statement: Not applicable.

Data Availability Statement: No data except those presented in this paper.

Acknowledgments: The ERA5 data used in this study have been obtained from the ECMWF data server, while the wind fields under the RCP scenarios are from the Copernicus and EURO-CORDEX data servers. The in situ measurements were provided by the Galati Lower Danube River Administration. The authors also acknowledge the Med-CORDEX initiative and Florence Sevault for provision of the SSP data. The authors would also like to express their gratitude to the reviewers for their constructive suggestions and observations that helped in improving the present work.

Conflicts of Interest: The authors declare no conflicts of interest.

Nomenclature

ALADIN	Aire Limitée Adaptation dynamique Développement International
ARPEGE	Action de Recherche Petite Echelle Grande Echelle
BFI	Benjamin–Feir index (or the steepness-over-randomness ratio)
CERFACS	Centre Européen de Recherche et Formation Avancée en Calcul Scientifique
CNRM	Centre National de Recherches Météorologiques
ECMWF	European Centre for Medium-Range Weather Forecasts
ERA	ECMWF re-analysis
LR	Low resolution (and also indicates linear regression in the case of the annual maximum series)
Hs	Significant wave height
Hs_{max}	Maximum value of the significant wave height
Hso	Offshore value of the significant wave height in the high-resolution computational domain
MPI-M	Max Planck Institute for Meteorology
MPI-ESM	Max-Planck-Institute Earth System Model
Qp	Peakedness of the wave spectrum
R	Correlation coefficient
RCA4	Rossby Centre regional atmospheric model, version 4
RCM	Regional climate model
RCP	Representative concentration pathway
RCSM	Regional climate system model
RE_{Hs}	Relative enhancement of the significant wave height due to the wave–current interactions
RMSE	Root mean square error
RP0	Reference point zero (zero-kilometer point of the Danube River)
RP1	Reference point 1 (for wind and wave model data offshore the Sulina channel)
RP2	Reference point 2 (for wind and wave model data offshore the Sain George arm of the Danube)
S	Regression slope
SI	Scatter index
SMHI	Swedish Meteorological and Hydrological Institute
SSP	Shared Socioeconomic Pathway
St	Integral wave steepness
SWAN	Simulating waves nearshore
U_{10}	Wind speed at 10 m above the sea level provided by the model
Uw	Measured wind speed
Uwg	Maximum value of the wind gust

WAM	Wave model
Wdir	Mean wave direction of the incoming waves on the offshore boundary of the computational domain
WW3	Wave Watch 3
λ	Longitude
φ	Latitude

References

1. United Nations. *Report of the Conference of the Parties to the United Nations Framework Convention on Climate Change (21st Session)*; United Nations: Paris, France, 2015; Volume 4, p. 2017.
2. Moss, R.H.; Edmonds, J.A.; Hibbard, K.A.; Manning, M.R.; Rose, S.K.; Van Vuuren, D.P.; Carter, T.R.; Emori, S.; Kainuma, M.; Kram, T.; et al. The next generation of scenarios for climate change research and assessment. *Nature* **2010**, *463*, 747–756. [CrossRef] [PubMed]
3. Schleussner, C.-F. The Paris Agreement—The 1.5 °C Temperature Goal. *Climate Analytics*, January 2022.
4. IPCC. *Managing the Risks of Extreme Events and Disasters to Advance Climate Change Adaptation*; Field, C.B., Ed.; A Special Report of Working Groups I and II of the Intergovernmental Panel on Climate Change; Cambridge University Press: Cambridge, UK; New York, NY, USA, 2012; p. 582.
5. Toimil, A.; Losada, I.J.; Nicholls, R.J.; Dalrymple, R.A.; Stive, M.J.F. Addressing the challenges of climate change risks and adaptation in coastal areas: A review. *Coast. Eng.* **2020**, *156*, 103611. [CrossRef]
6. Rusu, E. A 30-year projection of the future wind energy resources in the coastal environment of the Black Sea. *Renew. Energy* **2019**, *139*, 228–234. [CrossRef]
7. Negm, A.; Zaharia, L.; Toroimac, G.I. *The Lower Danube River Hydro-Environmental Issues and Sustainability*; Springer: Berlin/Heidelberg, Germany, 2022; ISBN 978-3-031-03864-8.
8. Răileanu, A.B.; Rusu, L.; Rusu, E. An Evaluation of the Dynamics of Some Meteorological and Hydrological Processes along the Lower Danube. *Sustainability* **2023**, *15*, 6087. [CrossRef]
9. ShipTraffic.net, River Discharge and Related Historical Data from the European Flood Awareness System. Available online: http://www.shiptraffic.net/2001/04/danube-river-ship-traffic.html?full_screen=yes&map=vf (accessed on 12 February 2024).
10. Stagl, J.C.; Hattermann, F.F. Impacts of Climate Change on Riverine Ecosystems: Alterations of Ecologically Relevant Flow Dynamics in the Danube River and Its Major Tributaries. *Water* **2016**, *8*, 566. [CrossRef]
11. Maternová, A.; Materna, M.; Dávid, A. Revealing Causal Factors Influencing Sustainable and Safe Navigation in Central Europe. *Sustainability* **2022**, *14*, 2231. [CrossRef]
12. Galati Lower Danube River Administration, A.A. Available online: https://www.afdj.ro/en/content/ship-statistics (accessed on 12 February 2024).
13. Rouholahnejad Freund, E.; Abbaspour, K.C.; Lehmann, A. Water Resources of the Black Sea Catchment under Future Climate and Landuse Change Projections. *Water* **2017**, *9*, 598. [CrossRef]
14. Ivan, A.; Gasparotti, C.; Rusu, E. Influence of the interactions between waves and currents on the navigation at the entrance of the Danube delta. Protection and Sustainable Management of the Black Sea Ecosystem, Special Issue. *J. Environ. Prot. Ecol.* **2012**, *13*, 1673–1682.
15. Stanica, A.; Panin, N. Present evolution and future predictions for the deltaic coastal zone between the Sulina and Sf. Gheorghe Danube River mouths. *Geomorphology* **2009**, *107*, 41–46. [CrossRef]
16. Banescu, A.; Arseni, M.; Georgescu, L.P.; Rusu, E.; Iticescu, C. Evaluation of different simulation methods for analyzing flood scenarios in the Danube Delta. *Appl. Sci.* **2020**, *10*, 8327. [CrossRef]
17. Arseni, M.; Roșu, A.; Bocăneală, C.; Constantin, D.-E.; Georgescu, P.L. Flood hazard monitoring using GIS and remote sensing observations. *Carpathian J. Earth Environ. Sci.* **2017**, *12*, 329–334.
18. Onea, F.; Rusu, E. Wind energy assessments along the Black Sea basin. *Meteorol. Appl.* **2014**, *21*, 316–329. [CrossRef]
19. Bernardino, M.; Rusu, L.; Guedes Soares, C. Evaluation of extreme storm waves in the Black Sea. *J. Oper. Oceanogr.* **2021**, *14*, 114–128. [CrossRef]
20. Rusu, E. Modeling of wave-current interactions at the Danube's mouths. *J. Mar. Sci. Technol.* **2010**, *15*, 143–159. [CrossRef]
21. Lazar, L.; Rodino, S.; Pop, R.; Tiller, R.; D'Haese, N.; Viaene, P.; De Kok, J.-L. Sustainable Development Scenarios in the Danube Delta—A Pilot Methodology for Decision Makers. *Water* **2022**, *14*, 3484. [CrossRef]
22. Novac, V.; Stavarache, G.; Rusu, E. Naval accidents causative factors—A Black Sea case study. *Int. Multidiscip. Sci. GeoConference Surv. Geol. Min. Ecol. Manag. SGEM* **2021**, *21*, 551–559.
23. Booij, N.; Ris, R.; Holthuijsen, L. A third generation wave model for coastal regions. Part 1: Model description and validation. *J. Geophys. Res.* **1999**, *104*, 7649–7666. [CrossRef]
24. ICPDR 2004, Danube Basin Analysis, WDF Report 2004. Available online: https://www.icpdr.org/sites/default/files/nodes/documents/danube_basin_analysis_2004.pdf (accessed on 2 December 2023).
25. Poncos, V.; Teleaga, D.; Bondar, C.; Oaie, G. A new insight on the water level dynamics of the Danube Delta using a high spatial density of SAR measurements. *J. Hydrol.* **2013**, *482*, 79–91. [CrossRef]

26. Bajo, M.; Ferrarin, C.; Dinu, I.; Umgiesser, G.; Stanica, A. The water circulation near the Danube Delta and the Romanian coast modelled with finite elements. *Cont. Shelf Res.* **2014**, *78*, 62–74. [CrossRef]
27. Romanian National Authority of Meteorology. 2024. Available online: https://www.meteoromania.ro/servicii/date-meteorologice/ (accessed on 14 September 2023).
28. ERA5/ECMWF. Available online: https://www.ecmwf.int/en/forecasts/datasets/reanalysis-datasets/era5 (accessed on 22 January 2024).
29. Giorgetta, M.A.; Jungclaus, J.; Reick, C.H.; Legutke, S.; Bader, J.; Böttinger, M.; Brovkin, V.; Crueger, T.; Esch, M.; Fieg, K.; et al. Climate and carbon cycle changes from 1850 to 2100 in MPI-ESM simulations for the Coupled Model Intercomparison Project phase 5. *J. Adv. Model. Earth Syst.* **2013**, *5*, 572–597. [CrossRef]
30. Giorgetta, M.; Jungclaus, J.; Reick, C.; Legutke, S.; Brovkin, V.; Crueger, T.; Esch, M.; Fieg, K.; Glushak, K.; Gayler, V.; et al. *CMIP5 Simulations of the Max Planck Institute for Meteorology (MPI-M) Based on the MPI-ESM-LR Model: The piControl Experiment, Served by ESGF. World Data Center for Climate (WDCC) at DKRZ*; PCMDI: San Francisco, CA, USA, 2012. [CrossRef]
31. COPERNICUS Database. Available online: https://cds.climate.copernicus.eu/cdsapp#!/dataset/projections-cordex-domains-single-levels?tab=form (accessed on 12 September 2023).
32. Nabat, P.; Somot, S.; Cassou, C.; Mallet, M.; Michou, M.; Bouniol, D.; Decharme, B.; Drugé, T.; Roehrig, R.; Saint-Martin, D. Modulation of radiative aerosols effects by atmospheric circulation over the Euro-Mediterranean region. *Atmos. Chem. Phys.* **2020**, *20*, 8315–8349. [CrossRef]
33. Roehrig, R.; Beau, I.; Saint-Martin, D.; Alias, A.; Decharme, B.; Guérémy, J.; Voldoire, A.; Abdel-Lathif, A.Y.; Bazile, E.; Belamari, S.; et al. The cnrm globalatmosphere model arpege-climat 6.3: Description and evaluation. *J. Adv. Model. Earth Syst.* **2020**, *12*, e2020MS002075. [CrossRef]
34. Darmaraki, S.; Somot, S.; Sevault, F.; Nabat, P. Past variability of Mediterranean Sea marine heatwaves. *Geophys. Res. Lett.* **2019**, *46*, 9813–9823. [CrossRef]
35. CNRM 2023. Available online: https://www.umr-cnrm.fr/spip.php?article1098&lang=fr (accessed on 14 March 2023).
36. Holthuijsen, H. *Waves in Oceanic and Coastal Waters*; Cambridge University Press: Cambridge, UK, 2007; p. 387.
37. Rusu, E. Strategies in using numerical wave models in ocean/coastal applications. *J. Mar. Sci. Technol.* **2011**, *19*, 58–75. [CrossRef]
38. WAMDI Group. The WAM model—A third generation ocean wave prediction model. *J. Phys. Oceanogr.* **1988**, *18*, 1775–1810. [CrossRef]
39. Tolman, H.L. A third-generation model for wind waves on slowly varying, unsteady and inhomogeneous depths and currents. *J. Phys. Oceanogr.* **1991**, *21*, 782–797. [CrossRef]
40. Rusu, L.; Bernardino, M.; Guedes Soares, C. Wind and wave modelling in the Black Sea. *J. Oper. Oceanogr.* **2014**, *7*, 520. [CrossRef]
41. Rusu, E. Reliability and Applications of the Numerical Wave Predictions in the Black Sea. *Front. Mar. Sci.* **2016**, *3*, 95. [CrossRef]
42. Rusu, E. Study of the Wave Energy Propagation Patterns in the Western Black Sea. *Appl. Sci.* **2018**, *8*, 993. [CrossRef]
43. Rusu, E. An analysis of the storm dynamics in the Black Sea. *Ro. J. Techn. Sci. Appl. Mech.* **2018**, *63*, 127–142.
44. Rusu, L. Assessment of the Wave Energy in the Black Sea Based on a 15-Year Hindcast with Data Assimilation. *Energies* **2015**, *8*, 1037010388. [CrossRef]
45. Rusu, L. A projection of the expected wave power in the Black Sea until the end of the 21st century. *Renew. Energy* **2020**, *160*, 136–147. [CrossRef]
46. Yan, X.; Su, X. *Linear Regression Analysis: Theory and Computing*; World Scientific: Singapore, 2009; pp. 1–2. ISBN 9789812834119.
47. Rusu, L.; Butunoiu, D.; Rusu, E. Analysis of the extreme storm events in the Black Sea considering the results of a ten-year wave hindcast. *J. Environ. Prot. Ecol.* **2014**, *15*, 445–454.
48. Rusu, E.; Soares, C.G. Modelling the effect of wave current interaction at the mouth of the Danube river. In *Developments in Maritime Transportation and Exploitation of Sea Resources*; CRC Press, Taylor & Francis Group: London, UK, 2013; pp. 979–986.
49. Nayaka, S.; Panchangb, V. A Note on Short-term Wave Height Statistics. *Aquat. Procedia* **2015**, *4*, 274–280. [CrossRef]
50. Longuuet-Higgins, M.S. On the Statistical Distribution of the Heights of Sea Waves. *J. Mar. Res.* **1952**, *11*, 245–265.
51. Janssen, P.A.E.M. Nonlinear four-wave interactions and freak waves. *J. Phys. Oceanogr.* **2003**, *33*, 863–883. [CrossRef]

Disclaimer/Publisher's Note: The statements, opinions and data contained in all publications are solely those of the individual author(s) and contributor(s) and not of MDPI and/or the editor(s). MDPI and/or the editor(s) disclaim responsibility for any injury to people or property resulting from any ideas, methods, instructions or products referred to in the content.

inventions

MDPI

Article

The Basic k-ϵ Model and a New Model Based on General Statistical Descriptions of Anisotropic Inhomogeneous Turbulence Compared with DNS of Channel Flow at High Reynolds Number

J. J. H. Brouwers

Romico Hold VBA., 6226 GV Maastricht, The Netherlands; j.j.h.brouwers@gmail.com

Abstract: Predictions are presented of mean values of statistical variables of large-scale turbulent flow of the widely used basic k-ϵ model, and of a new model, which is based on general statistical descriptions of turbulence. The predictions are verified against published results of direct numerical simulations (DNSs) of Navier–Stokes equations. The verification concerns turbulent channel flow at shear Reynolds numbers of 950, 2000, and 10^4. The basic k-ϵ model is largely based on empirical formulations accompanied by calibration constants. This contrasts with the new model, where descriptions of leading statistical quantities are based on the general principles of statistical turbulence at a large Reynolds number and stochastic theory. Predicted values of major output variables such as turbulent viscosity, diffusivity of passive admixture, temperature, and fluid velocities compare well with DNS for the new model. Significant differences are seen for the basic k-ϵ model.

Keywords: turbulent channel flow; k-ϵ model; new fundamentally based model; diffusion representations

1. Introduction

The description of turbulence has been an issue right from the beginning. A solid starting point for analysis is the Navier–Stokes equations, which describe the flow. These can be time-averaged, resulting in equations for mean values of velocity, pressure, and temperature. The problem arises with the average values of the products of fluctuating quantities within the non-linear convection terms in the equations. They describe the effect of fluctuations on mean flow quantities. The proposed representations of average nonlinear convective fluctuations are of a hypothetical nature, drawing analogies with molecular chaos. Boussinesq [1] was the first to follow this line of thinking by introducing the gradient hypothesis: the averaged nonlinear fluxes are proportional to the derivative of the mean flow quantity, preceded by a constant termed the turbulent viscosity or turbulent diffusion coefficient. Several versions and extensions based on the same idea have since been put forward by the pioneers of turbulence theory: Taylor [2], Prandtl [3], and von Karman [4], among others. They also form the basis of many of today's computer models used in engineering and environmental analyses; for example, see the books of Hanjalic and Launder [5] and Bernard and Wallace [6].

An offspring of the aforementioned concept is the basic k-ϵ model, which is widely used in engineering and environmental analyses [5,6]. This model describes the average value of momentum fluxes through the gradient of the mean velocity. Fluctuations are isotropic and the coefficient proceeding the gradient equals $c_\mu \frac{k^2}{\epsilon}$, where k is the mean kinetic energy of fluctuations, ϵ is the mean energy dissipation rate, and c_μ is a calibration constant. The model is completed by equations for k and ϵ. The gradient hypothesis is also applied to several other flux terms in equations with different values of calibration constants.

The problems with gradient-based models include their hypothetical origin and lack of uniqueness. Starting from a sketchy analogy with laminar diffusion, almost limitless forms

of gradient representations and proceeding functional dependencies can be devised. A new development that surpasses these limitations is the statistical description of anisotropic inhomogeneous turbulence; see Brouwers [7–9]. Turbulence at a high Reynolds number is featured by unstable eddies of whirling irregular fluid velocities whose behaviors are governed by the domination of the inertial forces in the momentum balance; see Monin and Yaglom, Vol. II, Ch.8 [10]. The eddies start at sizes of the configuration and then break down to smaller ones until the point where viscous forces come into play at sizes of a few millimeters. Here, Kolmogorov's theory of small viscous scales comes into play [10]. Building on this framework of high Reynolds turbulence and using the methods of the stochastic theory of Van Kampen [11] and Stratonovich [12], explicit statistical descriptions of governing variables are obtained. They are the leading terms of asymptotic expansions based on the small value of the inverse of the universal Lagrangian Kolmogorov constant. The results represent unique descriptions of turbulent flow statistics, subject to deviations due to truncated higher-order terms.

The results of direct numerical simulation (DNS) of the Navier–Stokes equations offer an opportunity for testing the outcomes of turbulence models. With the evolution of modern computing power, it has become possible to generate a wealth of accurate data on turbulent flow at high Reynolds numbers. The recent DNS data of the turbulent channel flow of Hoyas et al. [13,14] and Kuerten et al. [15] are particularly noteworthy. Fluctuating channel velocities are strongly anisotropic and averages of flow quantities vary strongly with distance from the wall. Inhomogeneity and anisotropy are characteristics of turbulence, in practice. The DNS data provide a meaningful test case for models. In this paper, a detailed comparison is presented of the DNS data, along with predictions of the basic k-ϵ model and the new model based on general statistical descriptions, referred to as the fundamental model.

2. The Basic k-ϵ Model and the New Fundamental Model

The turbulent flow of an incompressible or nearly incompressible fluid, e.g., a liquid or gas flowing at speeds where the square of the Mach number is minimal, is considered. The density ρ is assumed to be constant. Turbulent fluctuations measured at a fixed point in space are treated as a statistical process that is stationary or almost stationary in time compared to the time of velocity fluctuations. Statistical averages follow from time-averaging over sufficiently long time intervals. The time-averaged representation of the Navier–Stokes equations is given by the following:

- *Conservation of mass:*

$$\frac{\partial u_i}{\partial x_i} = 0 \tag{1}$$

- *Conservation of momentum:*

$$\frac{\partial u_i}{\partial t} + u_j \frac{\partial u_i}{\partial x_j} + \frac{\partial < u_i' u_j' >}{\partial x_j} = -\frac{\partial p}{\partial x_i} \tag{2}$$

- *Conservation of energy:*

$$\frac{\partial \theta}{\partial t} + u_j \frac{\partial \theta}{\partial x_j} + \frac{\partial < u_j' \theta' >}{\partial x_j} = 0 \tag{3}$$

where angled brackets represent statistical averaging, t and x are time and space coordinates, u, p, and θ are the mean or time-averaged values of fluid velocity, pressure, and temperature, and u' and θ' represent fluctuations of velocity and temperature, referring to velocity and temperature minus their mean value. As we are concerned with the flow at a high Reynolds number, the contributions of the viscous forces and heat conductivity present in the Navier–Stokes equations have been dropped. Their effect can be disregarded when considering the main flow governed by the instability of the inviscid flow outside small boundary layers. The average temperature in energy Equation (3) can also

be used to describe the average distribution of passive or almost passive admixture in the fluid. Restricting the formulation of the conservation equations to an incompressible or almost incompressible fluid implies that the solutions to (1) and (2) are not affected by the value of the conservative scalar temperature. The representation holds as long as the changes in temperature or admixture imposed at external boundary conditions are of limited magnitude.

2.1. Turbulent Diffusion in the Basic k-ϵ Model

The appearance of turbulent fluxes—in the convection terms of the averaged conservation equations—results in an unclosed set of equations for mean flow variables. It is known as the closure problem. To resolve this issue, a diffusion hypothesis has been introduced in the basic *k*-ϵ model. In this hypothesis, turbulent fluxes are treated as isotropic and are described by [5,6].

$$< u_j' u_i' >= \frac{2}{3} k \delta_{ij} - \nu_t (\frac{\partial u_j}{\partial x_i} + \frac{\partial u_i}{\partial x_j}) \tag{4}$$

$$< u_j' \theta' >= -\nu_t \frac{\partial \theta}{\partial x_j} \tag{5}$$

where ν_t is a scalar that represents diffusivity or turbulent viscosity, which is defined by the following:

$$\nu_t = c_\mu \frac{k^2}{\epsilon} \tag{6}$$

where k is the average kinetic energy of fluctuations, $k = \frac{1}{2} < u_i'^2 >$, and $\epsilon = \frac{1}{2}\nu < (\frac{\partial u_i'}{\partial x_j} + \frac{\partial u_j'}{\partial x_i})^2 >$ denotes the average energy dissipation rate, with ν being kinematic viscosity; c_μ in (4) and (5) is a calibration constant whose value is usually taken as 0.09 [5,6]. In Equation (5), correction factors are sometimes added to the diffusion constant, i.e., a turbulent Prandtl number and a turbulent Schmidt number for temperature and admixture, respectively. But these numbers are generally close to unity and are omitted here.

2.2. Turbulent Diffusion in the Fundamental Model

The derivation of the fundamental model starts from a Langevin equation for fluid particle velocity [8–10]. In this equation, the limiting form of Kolmogorov's theory of small scales is implemented, i.e., where the characteristic times for velocity fluctuations are much larger than the times of viscous scales. This is the case when the Reynolds number is large; see Kolmogorov [16]. One further step involves an expansion, in terms of the inverse of the Kolmogorov constant C_0. Matching predictions with measurements and DNS data reveal values of C_0 at around 6–7; in the present analysis, a value of 7 is adopted. Furthermore, the area where the Lagrangian description applies can be reduced to a point in the Eulerian flow description in the limit of small ${C_0}^{-1}$. In this way, Lagrangian-based descriptions are connected to Eulerian ones. The following descriptions for the flux terms are obtained [8,9]

$$< u_j' u_i' >= \frac{2}{3}(k + D_{nk}\frac{\partial u_n}{\partial x_k})\delta_{ij} - D_{ik}\frac{\partial u_j}{\partial x_k} - D_{jk}\frac{\partial u_i}{\partial x_k} \tag{7}$$

$$< u_j' \theta' >= -D_{ik}\frac{\partial \theta}{\partial x_k} \tag{8}$$

where the fundamentally based diffusion tensor, D_{ij}, is described by the following:

$$D_{iJ} = 2C_0^{-1}\epsilon^{-1}\sigma_{in}\sigma_{nj} + 2C_0^{-2}\epsilon^{-2}\sigma_{li}\sigma_{jk}u_n\frac{\partial \sigma_{lk}}{\partial x_n} - 4C_0^{-2}\epsilon^{-1}\sigma_{kj}u_n\frac{\partial}{\partial x_n}(\epsilon^{-1}\sigma_{im}\sigma_{mk}) \tag{9}$$

and

$$\sigma_{in} =< u_i' u_n' > \tag{10}$$

is covariance or Reynolds stress. Relations (8)–(10) are part of the description, which holds in the entire flow configuration (except the thin viscous layers at walls) once they are coupled to conservation Equations (1)–(3). In this way, the turbulent flux change at each point, x, as described by (7) and (8), is connected to the kinetic energy and energy dissipation changes. Although the presence of ν in the expression for energy dissipation $\epsilon = \frac{1}{2}\nu < (\frac{\partial u_i'}{\partial x_j} + \frac{\partial u_j'}{\partial x_i})^2 >$ may suggest otherwise, ϵ is a characteristic of the main inviscid flow outside the boundary layers [10]. The magnitude of velocity gradients in turbulence is governed by the small viscous scales. It scales as $1/\sqrt{\nu}$ and makes the magnitude of ϵ independent of ν. This independence is reflected in the equations for k and ϵ, presented in the next section.

The above expressions for the diffusion of the fundamental model reveal the dependency on mean gradients, which are of a more complex structure than those in the basic k-ϵ model. This reflects the anisotropy of the fluctuating velocity field and reveals a more complex dependency on flow statistics.

The application of the fundamentally based diffusion approximation to a scalar, as conducted in Equation (8), is only justified if the scalar is conservative [8,9]. The value of the conservative scalar is constant when following a fluid particle and fluctuates in value in a fixed coordinate system due to fluid particle fluctuations. This is the case for temperature in an incompressible fluid such as liquids. It is approximately correct if the fluid is almost incompressible, as is the case in gases flowing at speeds where the square of the Mach number is small. The scalar representation can also be applied to passive or almost passive admixtures in fluids, such as aerosols in air [7–9]. It leads to errors when applied to non-conservative scalars such as kinetic energy and pressure; see Section 5.

3. Equations for k and ϵ

Incorporating the expressions for turbulent diffusion from the basic k-ϵ model and the fundamental model into the averaged conservation equations introduces two unknowns: the mean kinetic energy, k, and the mean energy dissipation rate, ϵ. Equations for k and ϵ can be obtained from the Navier–Stokes equations [8,9]. Our aim is to describe flow away from the thin, viscous layers near walls, which are only a few millimeters. In line with this approach, the contributions in the equations for k and ϵ from laminar viscosity will be disregarded (as was conducted in the conservation Equations (1)–(3)). To provide boundary conditions at the wall, the viscous layer is surpassed by applying the solutions of the log layer at $x = 0$: [5,6].

The equation for k reads as follows [5,6]:

$$\frac{\partial k}{\partial t} + u_i \frac{\partial k}{\partial x_i} + \frac{\partial < u_i' k' >}{\partial x_i} + \rho^{-1} \frac{\partial < u_i' p' >}{\partial x_i} = P - \epsilon \tag{11}$$

where P is the mean production of turbulent fluctuations, defined by the following:

$$P = -\sigma_{ij} \frac{\partial u_i}{\partial x_j} \tag{12}$$

and where k' and p' are the fluctuating parts of kinetic energy and pressure, respectively, which are the kinetic energy and dissipation rates minus their time-averaged values. There are two turbulent flux terms in Equation (11), i.e., the third and fourth terms on the LHS of (11), which need to be modeled. In the basic k-ϵ model, both terms are lumped together [5,6] and are described by the following:

- *Basic k-ϵ model*

$$< u_i' k' > + \rho^{-1} < u_i' p' > = -\frac{\nu_t}{\sigma_k} \frac{\partial k}{\partial x_i} \tag{13}$$

where σ_k is a calibration constant, which is usually taken unity: $\sigma_k = 1$ [5,6].

- *Fundamental model*

The theory underlying the fundamental model provides general expressions for turbulent scalar fluxes, which are free from calibration factors. However, these expressions are only valid for conservative scalars and lead to disagreement with DNS results when applied to turbulent fluxes of kinetic energy and pressure [8]. A fallback to empirical construction is needed. It reads as follows:

$$< u_i' k' > + \rho^{-1} < u_i' p' >= -c_k D_{ij} \frac{\partial k}{\partial x_j} \tag{14}$$

where it is noted that if k was a conserved scalar, its diffusion should be described by $D_{ij} \frac{\partial k}{\partial x_j}$. Factor c_k represents correction for non-conservative behavior and includes the relatively small contribution of pressure diffusion [8]. The above relations for the diffusion of kinetic energy and pressure will be compared and calibrated with the DNS results in Section 5.

The equation for ϵ, conventionally applied in CFD models, is largely an empirical construction [5,6]. Its basic form follows from the Navier–Stokes equations. It contains a number of terms that are governed by small viscous scales. These terms are generally replaced by expressions that meet the criteria of matching the results of decaying grid turbulence and the log layer of turbulent channel flow. The equation reads as follows:

- *Basic k-ϵ model*

$$\frac{\partial \epsilon}{\partial t} + \frac{\partial u_i \epsilon}{\partial x_i} = \frac{\partial}{\partial x_i}(\frac{\nu_t}{\sigma_\epsilon} \frac{\partial \epsilon}{\partial x_i}) + (c_{\epsilon 1} P - c_{\epsilon 2} \epsilon) \frac{\epsilon}{k} \tag{15}$$

- *Fundamental model*

$$\frac{\partial \epsilon}{\partial t} + \frac{\partial u_i \epsilon}{\partial x_i} = \frac{\partial}{\partial x_i}(\frac{D_{ij}}{\sigma_\epsilon^*} \frac{\partial \epsilon}{\partial x_j}) + (c_{\epsilon 1} P - c_{\epsilon 2} \epsilon) \frac{\epsilon}{k} \tag{16}$$

The constant $c_{\epsilon 2}$ ensures matching with the case of grid turbulence. Its value is usually taken to be 1.9, which is somewhat less than the theoretical limit value of 2 for the infinite Reynolds number; see George [17]. The von Karman constant κ is equal to 0.4. For the basic k-ϵ model, the calibration constant, σ_ϵ, is usually taken to be around 1.3, and $c_{\epsilon 1}$ is specified by the equation (Equation (8.41) of [16]):

$$\frac{\sqrt{c_\mu} \sigma_\epsilon}{\kappa^2} (c_{\epsilon 2} - c_{\epsilon 1}) = 1 \tag{17}$$

The values appropriate for $c_{\epsilon 1}$ and σ_ϵ^* for the fundamental model are determined in Section 6.

4. Channel Flow

The objective is to compare the results of the basic k-ϵ model and the fundamental model with those of the DNS of the channel flow. The channel consists of parallel planes in between, where the mean velocity, u_1, is unidirectional in the direction, x_1, parallel to the planes. Its magnitude and the value of statistical averages related to velocity fluctuations only change in the direction, x_2, normal to the planes. For channel flow, there is an exact solution for the mean pressure [9], which reads as follows:

$$\frac{p}{\rho} = -u_\tau^2 \frac{x_1}{H} - \sigma_{22} \tag{18}$$

where u_τ is shear velocity and $2H$ is channel height. The shear velocity is determined by the pressure drop in direction x_1 at a given u_1. There are theoretical and experimentally confirmed relations for the relationship determining u_τ. Another exact result for the channel flow is the description of the covariance, σ_{12} or $< u_1' u_2' >$.

$$\sigma_{12} = -u_\tau^2 (1 - \frac{x_2}{H}) \tag{19}$$

which is valid outside the thin viscous layer at the wall, [9].

In the subsequent analysis of channel flow, we shall make use of dimensionless formulations: u_i is made dimensionless by u_τ, σ_{ij} and $\frac{p}{\rho}$ by u_τ^2, x_1 and x_2 by H, and P and ϵ by $\frac{u_\tau^3}{H}$; the subscript $_2$ of x_2 will be dropped. In this new notation, Equations (18) and (19) are as follows:

$$\frac{p}{\rho} = -x_1 - \sigma_{22} \tag{20}$$

which is valid outside the thin viscous layer at the wall.

$$\sigma_{12} = -(1-x) \tag{21}$$

Furthermore, Equation (12) becomes

$$P = (1-x)\frac{du_1}{dx} \tag{22}$$

The above solutions follow from the averaged momentum equations adapted to the case of channel flow [9]. A complete specification of all variables follows from the expressions for turbulent fluxes and the equations for k and ϵ. In the case of channel flow, these reduce to the following:

- *Basic k-ϵ model*

$$\sigma_{11} = \sigma_{22} = \sigma_{33} = \frac{2}{3}k \tag{23a}$$

$$\sigma_{12} = -\nu_t \frac{du_1}{dx} \tag{23b}$$

$$< \theta' u_2' > = -\nu_t \frac{d\theta}{dx} \tag{23c}$$

$$\nu_t = c_\mu \frac{k^2}{\epsilon} \tag{23d}$$

$$\frac{d}{dx}(\frac{\nu_t}{\sigma_k}\frac{dk}{dx}) + P - \epsilon = 0 \tag{23e}$$

$$\frac{d}{dx}(\frac{\nu_t}{\sigma_\epsilon}\frac{d\epsilon}{dx}) + (c_{\epsilon 1}P - c_{\epsilon 2}\epsilon)\frac{\epsilon}{k} = 0 \tag{23f}$$

- *Fundamental model:*

$$\sigma_{22} = \frac{2}{3}(k + D_{12}\frac{du_1}{dx}) \tag{24a}$$

$$\sigma_{33} = \sigma_{22} \tag{24b}$$

$$\sigma_{11} = \frac{2}{3}(k - 2D_{12}\frac{du_1}{dx}) \tag{24c}$$

$$\sigma_{12} = -D_{22}\frac{du_1}{dx} \tag{24d}$$

$$< \theta' u_2' > = -D_{22}\frac{d\theta}{dx} \tag{24e}$$

$$D_{12} = \frac{2}{\epsilon C_0}\sigma_{12}(\sigma_{11} + \sigma_{22}) \tag{24f}$$

$$D_{22} = \frac{2}{\epsilon C_0}(\sigma_{12}^2 + \sigma_{22}^2) \tag{24g}$$

$$c_k \frac{d}{dx}(D_{22}\frac{dk}{dx}) + P - \epsilon = 0 \tag{24h}$$

$$\frac{1}{\sigma_\epsilon^*}\frac{d}{dx}(D_{22}\frac{d\epsilon}{dx}) + (c_{\epsilon 1}P - c_{\epsilon 2}\epsilon)\frac{\epsilon}{k} = 0 \tag{24i}$$

In the subsequent sections, we shall compare the above descriptions with the results of DNS.

5. Testing the Diffusion Representations by DNS

In deriving equations for the mean values of flow quantities, the diffusion representation of mean fluxes has been used, i.e., the mean value of products of fluctuating quantities. Their correctness and accuracy will be assessed by comparing with the DNS results published for friction Reynolds numbers, $Re_\tau = u_\tau \frac{H}{\nu}$ of 950 [15], 2000 [13], and 10^4 [14]. The comparison focuses on the flow in the main region—the region outside the thin boundary layer at the wall. In the main region, flow statistics are governed by unstable large eddies governed by inertia forces, while the effect of viscosity in this region is negligibly small. The presented basic k-ϵ as well as the fundamental model intend to describe these statistics. The boundary layer is governed by viscous forces and is situated in the region $x < \frac{100}{Re_\tau}$; that is, $x < 0.1,\ 0.05$ and 0.01 for $Re_\tau = 950,\ 2000$, and 10^4, respectively. The DNS results of the boundary layer near $x = 0$ are omitted in this analysis.

5.1. Diffusion of Momentum

In the case of channel flow, turbulent momentum transport is apparent in the equation, as follows:

$$< u_1' u_2' >= -v_{DNS} \frac{du_1}{dx} \tag{25}$$

where ν_{DNS} is turbulent viscosity according to the DNS results, which is the value calculated from Equation (25) when substituting the values of $< u_2' u_1' >$ and $\frac{d}{dx} u_1$ obtained from DNS data. The value according to the basic k-ϵ model ν_t is given by Equation (6) and the value according to the fundamental model D_{22} is given by Equation (24g), where the RHSs of these equations are evaluated from the DNS data. The DNS data used are those of $Re_\tau = 10^4$ [14]. The three calculated turbulent viscosities are shown as functions of x in Figure 1. The ratios $\frac{\nu_t}{\nu_{DNS}}$ and $\frac{D_{22}}{\nu_{DNS}}$ versus x are shown in Figure 2. Disregarding the thin viscous layer at the wall, the fundamental model gives satisfactory agreement over the entire x range without the use of calibration factors. Deviations are less than 10% from the DNS results. They can be ascribed to the truncation of higher-order terms in the expansions in powers of C_0^{-1}, which were used in the theory that led to the presented expressions [8,9]. The same conclusion was arrived at when using the DNS data of $Re_\tau = 2000$ [9,13]. The basic k-ϵ model, on the other hand, disagrees quite a lot with DNS. The disagreement is the largest at small x values and gradually becomes smaller when approaching the central axis of the channel: $x = 1$. The dependency on x is apparently not well captured by representation (23d), in contrast with (24g), which shows satisfactory agreement over the entire range.

5.2. Diffusion of Temperature

Temperature is considered a conservative quantity in incompressible flow at high Reynolds numbers, where heat conductivity through molecular vibration is negligibly small outside thin layers at the walls. From the theory underlying the fundamental model, it follows that the thermal diffusion constant equals D_{ik}: cf. Equation (8). In the case of channel flow, it becomes D_{22} and becomes equal to that of turbulent viscosity: cf. Equations (24d) and (24e). This result is confirmed by the Lagrangian-based DNS of channel flow at $Re_\tau = 950$ [15], where the thermal diffusion coefficient, according to DNS, $\frac{< u_2' \theta' >}{\frac{d\theta}{dx}}$ is compared to that of the fundamentally based model, D_{22}. The agreement closely resembles that shown in Figures 1 and 2, c.q., $\frac{< u_2' u_1' >}{\frac{du_1}{dx}}$ and D_{22}. Deviations

of the predictions of the basic k-ϵ model are likely as equally large as those shown in Figures 1 and 2.

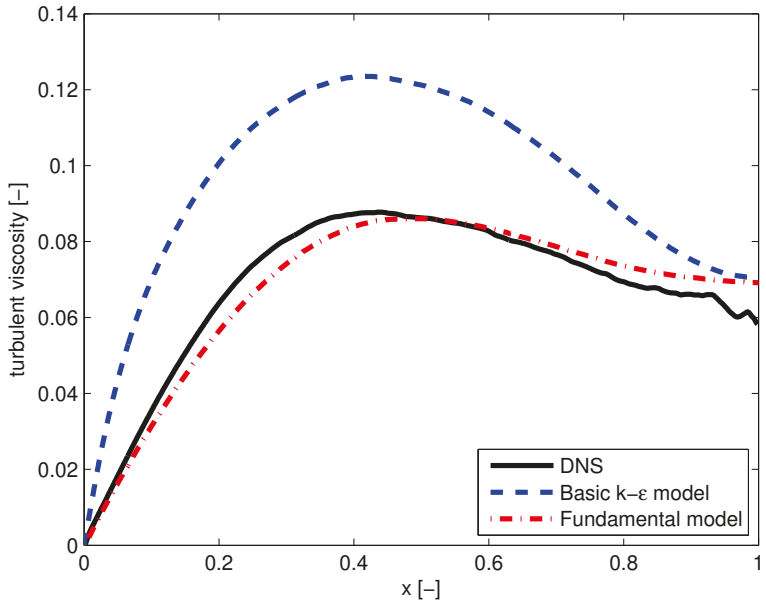


Figure 1. Turbulent viscosities according to ν_{DNS} at $Re_\tau = 10^4$, fundamental model D_{22}, and the basic k-ϵ model ν_t versus the dimensionless distance from the wall, x. Results from DNS are represented by the solid line, results from the fundamental model are represented by a dash–dot line, and results from the basic k-ϵ model are represented by the dashed line.

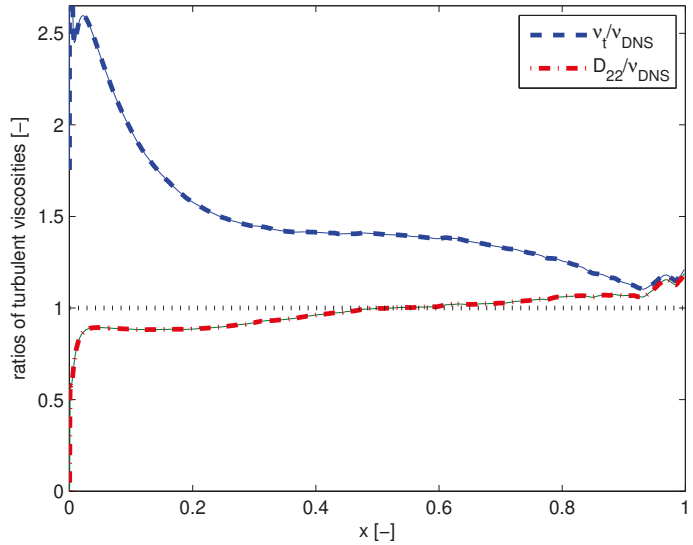


Figure 2. Ratio of turbulent viscosity of the fundamental model to that of DNS at $Re_\tau = 10^4$ $\dfrac{D_{22}}{\nu_{DNS}}$ (lower line) and the ratio of turbulent viscosity of the basic k-ϵ model to that of DNS at $Re_\tau = 10^4$ $\dfrac{\nu_t}{\nu_{DNS}}$ (upper line) versus the dimensionless distance from the wall, x.

5.3. Diffusion of Kinetic Energy and Pressure

In the basic k-ϵ model, fluxes of kinetic energy and pressure are lumped together, as shown in Equation (13). For channel flow, these terms become the following:

$$< k'u_2' > + < p'u_2' >= -\frac{\nu_t}{\sigma_k}\frac{dk}{dx} \tag{26}$$

From Equation (14), we have the following for the fundamental model:

$$< k'u_2' > + < p'u_2' >= -c_k D_{22}\frac{dk}{dx} \tag{27}$$

The description is used in the numerical solution of the equation for k in Section 6.

In Figure 3, we show the sum of both fluxes versus x, when the RHSs of (26) and (27) are evaluated by the DNS data. Values for the calibration constants σ_k and c_k of 1 and 1.3 were taken. Also, the value of the sums is obtained by the direct calculation of their values using the DNS of $Re_\tau = 10^4$. The empirical construction of Equation (27), based on the fundamental model, offers surprisingly good agreement. The agreement extends over the entire x range and is obtained with the calibration constant, $c_k = 1.3$.

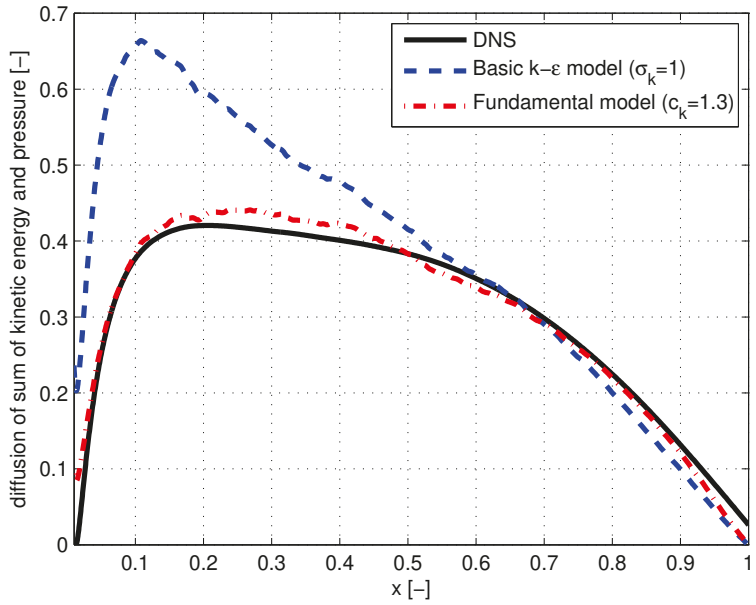


Figure 3. Sum of turbulent fluxes of kinetic energy and pressure versus the dimensionless distance from the wall, x. The solid line is the sum according to DNS at $Re_\tau = 10^4$, the dash–dot line is the empirical construction using the fundamental model, and the dashed line is the empirical construction of the basic k-ϵ model.

5.4. Diffusion of Energy Dissipation

DNS data do not provide information on the average values of products of velocity fluctuations and dissipation fluctuations. Direct verification of the diffusion representation is, thus, not possible. Further, the differential equation for mean energy dissipation in both models is largely an empirical construction. What remains possible is to verify the values of quantities derived from the solutions of the coupled differential equations for mean kinetic energy and mean energy dissipation rate against DNS data. This is the subject of the next section.

6. Solutions of k and ϵ Compared with DNS

In the previous section, predictions of individual components of the models were verified by DNS. Further testing is executed by comparing numerically obtained solutions of the model equations as a whole with DNS.

6.1. Equations and Boundary Conditions

Model equations are given by coupled differential equations for mean kinetic energy and mean energy dissipation. For mean energy dissipation, the variable G is introduced, which is defined by the following:

$$G = \kappa \epsilon x \tag{28}$$

Near the wall, outside the viscous layer, solutions should comply with the solutions of the log layer. Inertial subrange asymptotics [18] reveal that production, P, and dissipation, ϵ, are equal in this region: $P = \epsilon$. Furthermore, $\kappa \frac{du_1}{dx} = 1$, so that $G = 1$. DNS results show values of G in the log layer, which are between 0.9 and 1 [13,14]. In the present analysis, the theoretical value of 1 is taken. Making use of relations (21), (23b), (23d), and (28), differential equations (23e) and (23f) can be transformed into the following coupled equations for k and G, which are appropriate for the basic k-ϵ model.

- *Basic k-ϵ model equations:*

$$\frac{\kappa^2}{\sigma_k} \frac{x}{G} \frac{d}{dx} \left(\frac{Ax}{G} \frac{dk}{dx} \right) + \frac{(1-x)^2}{A} - 1 = 0 \tag{29}$$

$$\frac{\kappa^2}{\sigma_\epsilon} \frac{x^2}{G^2} \frac{d}{dx} \left(\frac{Ax}{G} \frac{d}{dx} \left(\frac{G}{x} \right) \right) + \frac{1}{k} \left(\frac{c_{\epsilon 1}(1-x)^2}{A} - c_{\epsilon 2} \right) = 0 \tag{30}$$

where

$$A = c_\mu k^2 \tag{31}$$

where values of the empirical constants will be taken in agreement with [5,6]: $\kappa = 0.4$, $c_\mu = 0.09$, $\sigma_k = 1$, $\sigma_\epsilon = 1.3$, $c_{\epsilon 1} = 1.49$, $c_{\epsilon 2} = 1.9$. The boundary conditions are as follows:

$$x = 0; \quad k = \frac{1}{\sqrt{c_\mu}}; \quad G = 1 \tag{32}$$

$$x = 1; \quad \frac{dk}{dx} = 0 \; ; \quad \frac{dG}{dx} = G \tag{33}$$

The boundary condition for k at $x = 0$ follows from relations (21), (23b), and (23d), with $\epsilon = \frac{du_1}{dx}$ in the log layer. The boundary condition for G at $x = 1$ corresponds to the zero slope of ϵ at $x = 1$.

The equations appropriate for the fundamental model follow from (24h) and (24i) upon using (28), (21), (24a)–(24g).

- *Fundamental model equations:*

$$\frac{c_k \kappa^2 x}{G} \frac{d}{dx} \left(B \frac{x}{G} \frac{dk}{dx} \right) + \frac{(1-x)^2}{B} - 1 = 0 \tag{34}$$

$$\frac{\kappa^2 x^2 k}{G^2 \sigma_\epsilon^*} \frac{d}{dx} \left(B \frac{x}{G} \frac{d \frac{G}{x}}{dx} \right) + \frac{c_{\epsilon 1}(1-x)^2}{B} - c_{\epsilon 2} = 0 \tag{35}$$

and

$$B = \frac{2}{C_0} (\sigma_{12}^2 + \sigma_{22}^2) = \frac{2}{C_0} ((1-x)^2 + \sigma_{22}^2) \tag{36}$$

In these equations, k and σ_{22} are related to each other by an algebraic relation, which is obtained by the systematic elimination of $\epsilon^{-1}\frac{du_1}{dx}$, σ_{12}, σ_{11}, σ_{33}, D_{12}, D_{22} from Equations (21), (24a), and (24g), as follows:

$$k = \sigma_{22}\frac{3\sigma_{22}^2 + (1-x)^2}{2(\sigma_{22}^2 - (1-x)^2)} \tag{37}$$

The relation can be used to eliminate σ_{22} from (34) and (35), resulting in two differential equations for k and G. However, the analysis of the above relation for k shows that in an area close to $x = 0$, according to (37), σ_{22} can have two values for one value of k. The verification of (37) using the results of DNS confirms the correctness of the equation and the double dependency in this area. The other way around is not the case: For each value of σ_{22}, there is only one value of k possible. The easiest approach is then to substitute the k relation (37) into the two differential equations, i.e., Equations (34) and (35), and solve for σ_{22} and G. The value of k is subsequently obtained from (37). The boundary conditions are as follows:

$$x = 0; \quad G = 1\,; \quad \sigma_{22} = \sqrt{\frac{C_0}{2} - 1} \tag{38}$$

$$x = 1; \quad \frac{d\sigma_{22}}{dx} = 0\,; \quad \frac{dG}{dx} = G \tag{39}$$

where the boundary condition for σ_{22} at $x = 0$ follows from Equations (21), (24d), and (24g), with $\epsilon = \frac{du_1}{dx}$ in the log layer, as in the basic k-ϵ model, $c_{\epsilon 2} = 1.9$. A value of c_k of 1.3 was established in Section 5.3 (Figure 3). A value of σ_ϵ^* of 0.2 is found to lead to the best agreement with DNS.

The value of $c_{\epsilon 1}$ follows from Equation (35) by letting x approach $x = 0$. It yields the following relation:

$$c_{\epsilon 1} = c_{\epsilon 2} - \frac{k_0\kappa^2}{\sigma_\epsilon^*} \tag{40}$$

which is analogous to Equation (17) for the basic k-ϵ model; k_0 is the value of k at $x = 0$ obtained from Equation (37). For $c_{\epsilon 2} = 1.9$, $C_0 = 7$, $\sigma_\epsilon^* = 0.2$ and $k_0 = 4.48$, $c_{\epsilon 1} = -1.68$. This suggests negative production. However, for the first term on the LHS of Equation (35), one can write the following:

$$x^2\frac{d}{dx}(B\frac{x}{G}\frac{d\frac{G}{x}}{dx}) = x^2\frac{d}{dx}(\frac{B}{G}\frac{dG}{dx}) - x\frac{dB}{dx} + B \tag{41}$$

where the last two terms have the same character as that of production, making the total of production-like terms positive.

6.2. Numerical Solution

Numerical instability is encountered when solving Equations (29), (30), (34), and (35), a feature not uncommon for k-ϵ equations; see Lew et al. [19]. The way out is to convert the equations into a diffusion problem by adding the terms $\frac{dk}{dt}$ and $\frac{dG}{dt}$ on the RHS of (29) and (30), $\frac{d\sigma_{22}}{dt}$ and $\frac{dG}{dt}$ on the RHS of (34) and (35). This requires starting from a suitably chosen initial solution at $t = 0$; see Borse [20]. After sufficient time, the solution converges to the desired stationary result.

Another difficulty encountered in the execution of the numerical calculations concerns the boundary condition for G at $x = 1$: cf. Equations (33) and (39). These are replaced by $(d/dx)G = 0$ at $x = 1$. The effect of this simplification is limited to a small region near $x = 1$.

Figures 4 and 5, respectively, show the distributions of kinetic energy, k, and the energy dissipation rate, G, versus x, according to DNS, the basic k-ϵ model (calculated from Equations (29) and (30)), and the fundamental model (calculated from Equations (34) and (35)).

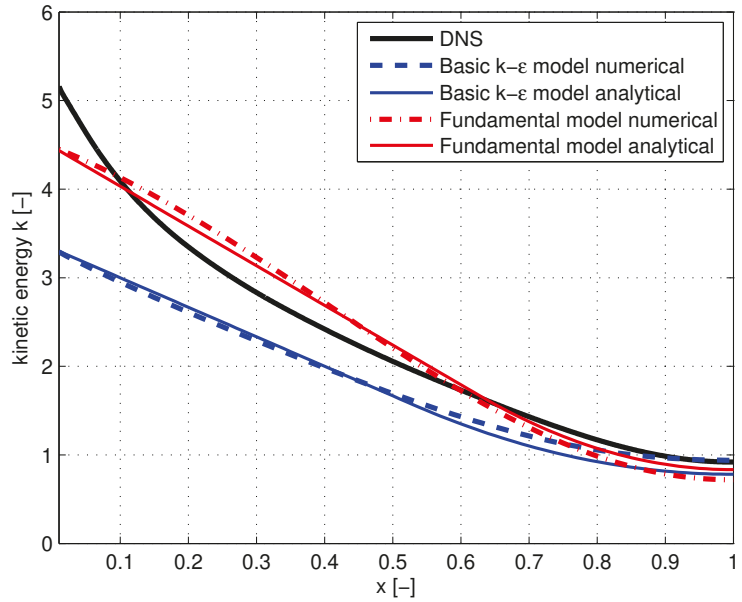


Figure 4. Distribution of kinetic energy, k, versus x, according to DNS (solid line), the numerically and analytically assessed basic k-ϵ model (dashed and full lines, respectively), and the numerically and analytically assessed fundamental model (dash–dot and full lines, respectively).

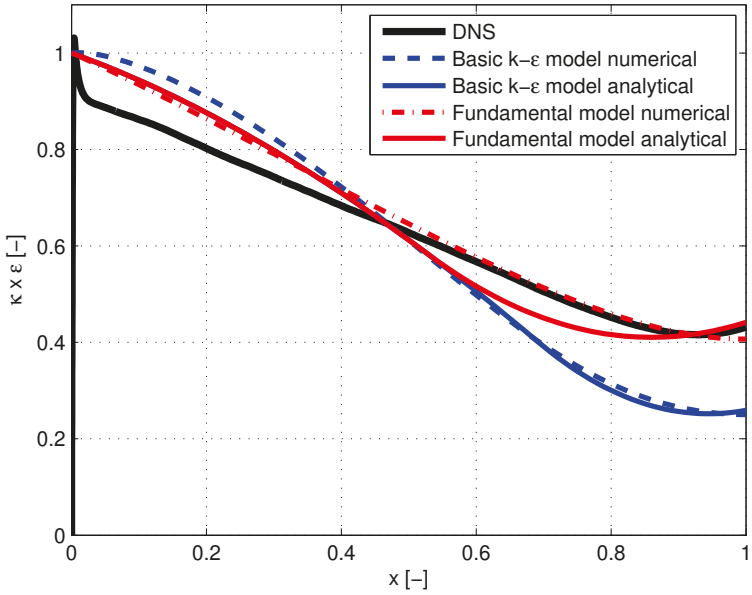


Figure 5. Distribution of kinetic energy, G, versus x, according to DNS (solid line), the numerically and analytically assessed basic k-ϵ model (dashed and full lines, respectively), and the numerically and analytically assessed fundamental model (dash–dot and full lines, respectively).

6.3. Analytical Solution

The distinction is made between the area near the wall referred to as the outer region and the area near the center of the channel referred to as the inner region. The outer region is the area where the production and dissipation of energy are dominant. Turbulent diffusion of kinetic energy and pressure and turbulent diffusion of dissipation are negligibly small. It is the area where the log layer description for mean flow applies and where production equals dissipation [21]. In the inner region, turbulent diffusion of kinetic energy and pressure, as well as turbulent diffusion of dissipation, are important and in balance

with energy dissipation, while production is negligibly small. For each region, analytical solutions can be derived, which are subsequently matched to arrive at a complete solution.

6.3.1. Solutions for k and G in the Outer Region

Solutions valid in the outer region are obtained by retaining the second and third terms in Equations (28) and (33), yielding $A = (1-x)^2$ and $B = (1-x)^2$, or in terms of k and σ_{22}

- *Basic k-ϵ model:*

$$k = \frac{1}{\sqrt{c_\mu}}(1-x) \tag{42}$$

- *Fundamental model:*

$$\sigma_{22} = \sqrt{(\frac{C_0}{2}-1)}(1-x) \tag{43}$$

Using the relation between k and σ_{22}, according to the fundamental model, cf. Equation (37), we have the following:

- *Fundamental model:*

$$k = k_0(1-x) \tag{44}$$

where k_0 is the value of k at $x = 0$,

$$k_0 = \frac{1}{2}\sqrt{(\frac{C_0}{2}-1)}\left(\frac{3C_0-4}{C_0-4}\right) \tag{45}$$

which amounts to $k_0 = 4.48$ for $C_0 = 7$.

To derive the equations for G, which are applicable in the outer region, the second and third terms of Equation (41) need to be taken into account (and replacing B with A in Equation (41), for the basic k-ϵ model). Noting that in the outer region $A = (1-x)^2$ and $B = (1-x)^2$ one obtains for G from Equation (30) using relation (17) and from Equation (35) using relation (40), the result:

- *Basic k-ϵ model and fundamental model:*

$$G = (1-x)\sqrt{(1+x)} \tag{46}$$

The above descriptions for k and G are rather simple. They compare well with the numerical results for values of x, up to about 0.5. At greater distances from the wall, they start to deviate and fail to meet the conditions of the zero slope at $x = 1$. To overcome this deficiency, solutions valid for the inner region are developed.

6.3.2. Solutions for k in the Inner Region

Solutions for k are developed by describing k by a series of successive powers of $\eta = 1 - x$. The linear term in η is omitted in order to satisfy the zero-slope condition at $\eta = 0$. Disregarding terms of $O(\eta^3)$ and higher, we write the following for k:

$$k = k_1 + a\eta^2 \tag{47}$$

where k_1 is the value of k at $x = 1$; and k_1 and a are to be determined. Substituting expression (47) in Equations (29) and (34), and equating the leading terms of $O(\eta^0)$ for a in the basic k-ϵ and fundamental models, respectively, we obtain the following relations:

$$2a\frac{c_\mu \kappa^2 k_1^2}{\sigma_k} = G_1^2 \tag{48}$$

and

$$\frac{16ac_k\kappa^2k_1^2}{9C_0} = G_1^2 \tag{49}$$

where G_1 is the value of G at $\eta = 0$. In deriving result (49), we take for σ_{22} at $\eta = 0$ the value $\frac{2}{3}k_1$ in accordance with Equation (37). The boundary between the inner and outer region is defined by $\eta_0 = 1 - x_0$. At this boundary, the value of k and its slope should match the values of the outer region. This yields the following relations:

$$k_1 + a\eta_0^2 = \frac{\eta_0}{\sqrt{c_\mu}};\ \ k_1 + a\eta_0^2 = \eta_0 k_0 \tag{50}$$

$$2a\eta_0 = \frac{1}{\sqrt{c_\mu}};\ \ 2a\eta_0 = k_0 \tag{51}$$

for basic k-ϵ and the fundamental model, respectively. From Equations (47)–(51), the following solutions are obtained:

- For the basic k-ϵ model:

$$\eta_0 = 4\sigma_k G_1^2 \frac{\sqrt{c_\mu}}{\kappa^2};\ \ k_1 = \frac{\eta_0}{2\sqrt{c_\mu}};\ \ a = \frac{1}{2\sqrt{c_\mu}\eta_0} \tag{52}$$

- and for the fundamental model:

$$\eta_0 = \frac{9G_1^2C_0}{2\kappa^2k_0^3c_k};\ \ k_1 = \frac{k_0\eta_0}{2};\ \ a = \frac{k_0}{2\eta_0} \tag{53}$$

The above solution parameters can be determined by implementing the values of the system parameters, $\sigma_k, c_\mu, \kappa, C_0, k_0$, and c_k. The value of G_1 is taken from the numerical results: $G_1 = 0.25$ in the case of the basic k-ϵ model and $G_1 = 0.44$ in the case of the fundamental model. An alternative approach to determine G_1 is to couple the above analytical solution of k to that of G presented in Section 6.3.3 below. It yields values for G_1 without recourse to the numerical results. The values are practically equal to those of the numerical results.

A complete analytical description of k for the outer and inner regions is obtained from Equations (41) and (44) when $x \leq x_0$, and Equations (47) and (52) when $x \geq x_0$, where $x_0 = 0.47$ in the basic k-ϵ model, and $x_0 = 0.33$ in the fundamental model. The results are shown in Figure 4 with solid blue and red lines.

6.3.3. Solutions for G in the Inner Region

For G in the inner region, the following expansion is used:

$$G = G_1(1 - \eta) + a\eta^2. \tag{54}$$

where the linear term, $G_1\eta$, is introduced to satisfy the boundary condition at $x = 1$: cf. Equations (33) and (39). The values of G_1 and a are to be determined. Substituting description (54) into Equations (30) and (35) and equating the leading terms of $O(\eta^0)$ yield the following:

$$a = \alpha G_1^3 \tag{55}$$

where

$$\alpha = \frac{\sigma_\epsilon c_{\epsilon 2}}{2\kappa^2 c_\mu k_1^3} \tag{56}$$

and

$$\alpha = \frac{9C_0\sigma_\epsilon^* c_{\epsilon 2}}{16\kappa^2 k_1^3} \tag{57}$$

for the basic k-ϵ model and fundamental model, respectively. At the boundary of the inner and outer regions, $\eta = \eta_1$, the values of G and its slope, according to the outer and inner regions, should become equal. This yields the following relations:

$$\eta_1\sqrt{(2-\eta_1)} = (1-\eta_1)G_1 + \alpha G_1^2\eta_1^2 \tag{58}$$

$$\frac{(2-\frac{3}{2}\eta_1)}{\sqrt{2-\eta_1}} = -G_1 + 2\alpha G_1^2\eta_1 \tag{59}$$

Eliminating G_1 from the above equations yields the following irreducible equation for η_1:

$$\alpha = \frac{2}{\eta_1^4}\frac{(1-\frac{\eta_1}{2})^3}{(1-\frac{\eta_1}{4})^3}(1-\frac{3\eta_1}{4}+\frac{\eta_1^2}{4}) \tag{60}$$

The value of α follows from Equation (56) by using the system's values for the various parameters and taking for k_1 the value of the numerical calculations, i.e., $k_1 = 0.8$. Consequently, $\alpha = 134$ and $\alpha = 18$ for the basic k-ϵ model and the fundamental model, respectively. Iteratively, one finds from Equation (60) that for the basic k-ϵ model $\eta_1 = 0.31$ $(x_1 = 0.69)$ and the fundamental model, $\eta_1 = 0.47$ $(x_1 = 0.53)$. A complete analytical description of G for the outer and inner regions is obtained from Equation (46) when $x \leq x_1$ and Equations (54)–(56) when $x \geq x_1$. The results are shown in Figure 5 with solid blue and red lines.

6.4. Discussion of Results

Numerical and analytical solutions for kinetic energy, k, and energy dissipation, ϵ, with the latter in terms of $G = \kappa x\epsilon$, have been developed for the basic k-ϵ model and a new fundamental model. The solutions are compared with DNS results and are shown in Figures 4 and 5. Our conclusions are as follows:

1. Analytical solutions agree in a satisfactory manner with numerical solutions. The analytical solutions reveal the relative contributions of turbulent diffusion, energy production, and energy dissipation in the outer and inner regions of the channel. They show to what extent the descriptions are empirically or fundamentally based and depend on calibration factors.
2. Solutions for k in the outer region $(x \leq 0.33)$ according to the fundamental model do not depend on calibration constants. They have a fundamental basis. The differences with DNS can be ascribed to errors as a result of truncation in the expansion with respect to C_0^{-1}, which underlies the fundamental model.
3. Solutions for k in the inner region $(x \geq 0.33)$ according to the fundamental model depend on the calibration factor, c_k.
4. Solutions for k in both the outer and inner regions, according to the basic k-ϵ model, depend on the calibration factors c_μ and σ_k.
5. Solutions for G in the outer region, according to the fundamental model and the basic k-ϵ model, $(x \leq 0.53)$ and $(x \leq 0.69)$, do not depend on calibration factors. Differences with DNS are due to some deviation between the value of production and dissipation in this area.
6. Solutions for G in the inner region, according to the fundamental model and the basic k-ϵ model, $(x \geq 0.69)$ and $(x \geq 0.53)$, respectively, depend on the calibration factors σ_ϵ^* and σ_ϵ.
7. Using standard calibration constants in the solutions of the basic k-ϵ model results in notable deviations compared to DNS data. The deviations can be reduced by recalibrating σ_ϵ, c_μ and σ_k. Deviations between diffusion constants remain significant because of different functional dependencies; see Figures 1–3.

7. Velocity Distributions

The basic k-ϵ model is based on the assumption of an isotropic turbulence field. It cannot predict the anisotropic behavior of covariances or turbulent stresses. For the fundamental model, the distribution of σ_{22} follows from the solution of Equation (34). According to Equation (24b) $\sigma_{33} = \sigma_{22}$, while $\sigma_{11} = \frac{1}{2}k - \sigma_{22}$, where k is given by Equation (37). In Figure 6, the distribution, versus x, of the calculated values of the standard deviations of the fluctuations $\sqrt{\sigma_{11}}$, $\sqrt{\sigma_{22}}$, and $\sqrt{\sigma_{33}}$, is shown, according to the fundamental model and the results of DNS. Deviations are similar to those shown in [9] and are ascribed to the truncation of the expansions of C_0^{-1}, underlying the theory of the fundamental model. Deviations of the three variances, $\sigma_{11}, \sigma_{22}, \sigma_{33}$ from k, which describe anisotropy, are next to the leading order in the C_0^{-1} expansion (cf. Equations (24a)–(24c)), and are, therefore, more sensitive to the truncation error.

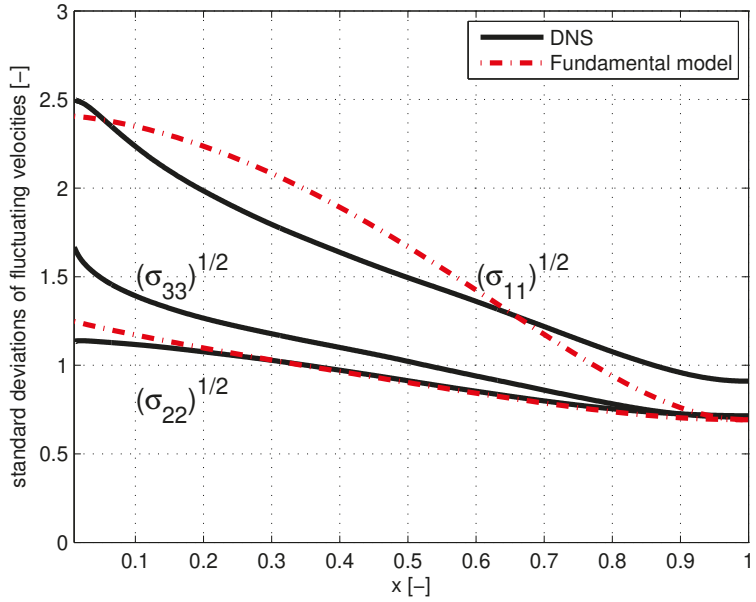


Figure 6. Distribution of the standard deviations of fluctuating velocities $\sqrt{\sigma_{11}}$, $\sqrt{\sigma_{22}}$, and $\sqrt{\sigma_{33}}$, versus x, according to DNS (solid line) and the fundamental model (dash–dot line).

For the gradient of the mean flow, the following relations can be derived. For the basic k-ϵ model from Equations (21) and (23b), we have the following:

$$\frac{du_1}{dx} = \frac{1-x}{\nu_t} \tag{61}$$

For the fundamental model from Equations (21) and (24d), we have the following:

$$\frac{du_1}{dx} = \frac{1-x}{D_{22}} \tag{62}$$

In Figure 7, the distributions are shown of $\kappa x \frac{du_1}{dx}$ versus x, according to DNS, the basic k-ϵ model, and the fundamental model. The deviations between DNS and the basic k-ϵ model are similar to those shown for ν_{DNS} and ν_t in Figures 1 and 2. Similarly, the agreement between ν_{DNS} and D_{22} is shown in Figures 1 and 2. According to (21), $P = (1-x)\frac{du_1}{dx}$, indicating that the disagreement of production with DNS in the case of the basic k-ϵ model is similar to that shown in Figure 7, and that the agreement of production with DNS for the fundamental model is similar to that shown in Figure 7.

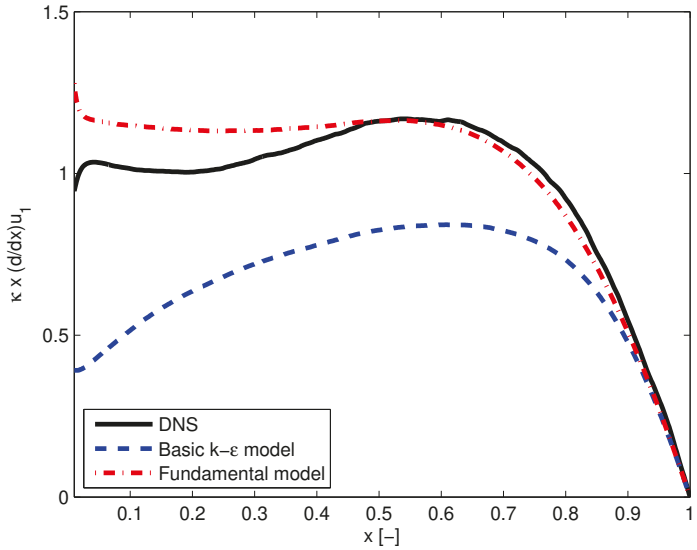


Figure 7. Distribution of $\kappa x \frac{du_1}{dx}$, versus x, according to DNS (solid line), the basic k-ϵ model (dash–dot line), and the fundamental model (dashed line).

The distribution of mean velocity u_1 predicted by the basic k-ϵ model and the fundamental model is obtained by integrating the RHSs of Equations (61) and (62). Because the models do not describe the velocity in the viscous layer at the wall, the integration starts at some distance from the wall for which the position $x = \dfrac{100}{Re_\tau}$ is taken. The value of u_1 at this point, according to the DNS results of $Re_\tau = 10^4$, is 17.2, which agrees with the values obtained from the measurements; see Monin and Yaglom, Vol. I, Figure 25 [21]. The results of the integration are shown in Figure 8, where the distributions of the mean velocity of the two models and DNS are presented. It is seen that for equal shear velocity (i.e., for equal longitudinal pressure gradient in the channel), the fundamental model somewhat overestimates mean velocity (by 5%), while the basic k-ϵ model underestimates it by 18%.

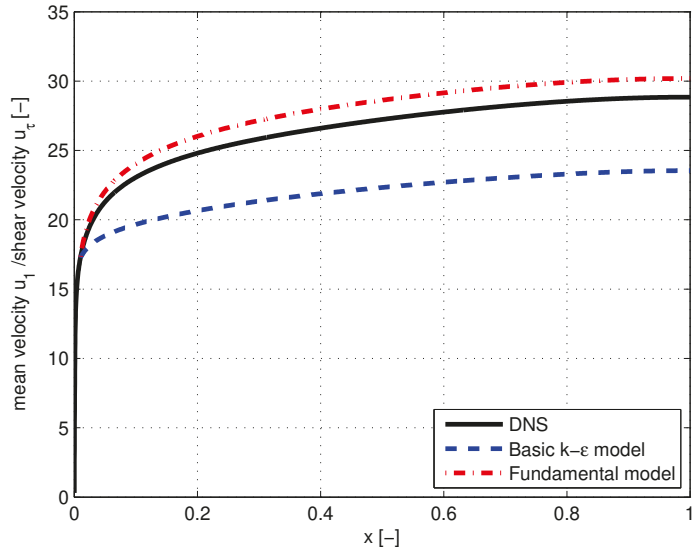


Figure 8. Distribution of mean velocity divided by shear velocity, versus x, according to DNS (solid line), the basic k-ϵ model (dash–dot line), and the fundamental model (dashed line).

8. Discussion

An analysis is presented of two models to determine the mean values of turbulent flow variables, i.e., velocity, u_i, pressure, p, turbulent diffusion, D_{ij}, kinetic energy, k, and energy dissipation, ϵ. The two models are the basic k-ϵ model widely used in engineering applications and environmental analysis [5,6], as well as a new fundamentally based model, which is derived from recently published statistical descriptions of inhomogeneous anisotropic turbulence [7–9]. The analysis focused on turbulent channel flow, which is highly anisotropic and inhomogeneous. It is of direct relevance to duct flow applications, turbulent boundary layers around bodies, and the atmospheric surface layer around the earth. Model predictions were verified against the published results of direct numerical simulations (DNS) for shear Reynolds numbers of 950 [15], 2000 [13], and 10^4 [14]. The comparison focused on the regions outside the thin viscous boundary layers, which are a few millimeters at the wall. The development status of DNS is mature; its results can serve as a reliable source for verifying model predictions.

The basic k-ϵ model is built on an empirical isentropic representation of the turbulence field. It contains a gradient hypothesis for turbulent diffusion, which is supplemented by calibration constants. Using conventionally proposed values for the calibration constants [5,6], model predictions of several variables are found to deviate remarkably from the results of DNS. A summary is presented in Table 1.

Table 1. The predictions of the basic k-ϵ model and the new fundamental model, compared with the DNS of turbulent channel flow.

Variable	Basic k-ϵ Model	New Fundamental Model
Turbulent viscosity	Empirical Equation (23d). Significant deviations: Figures 1 and 2	Fundamentally based Equation (24d). Satisfactory agreement: Figures 1 and 2
Turbulent diffusion of temperature, smoke, aerosol	Empirical Equation (23c). Significant deviations similar to Figures 1 and 2	Fundamentally based Equation (24e). Satisfactory agreement similar to Figures 1 and 2
Turbulent diffusion of kinetic energy and pressure	Empirical Equation (26). Deviation: Figure 3	Empirical Equation (27). Satisfactory agreement Figure 3
Mean value of kinetic energy	Empirical Equation (29). Deviation: Figure 4	In the outer half of the channel: Fundamentally based Equation (55). In the inner half: Empirical Equation (55). Satisfactory agreement Figure 4
Mean value of energy dissipation rate	In the outer half of the channel: fundamentally based Equation (46). In the inner half: empirical Equation (55). Deviation: Figure 5	In the outer half of the channel: fundamentally based Equation (46). In the inner half: Empirical Equation (55). Satisfactory agreement: Figure 5
RMS values of fluctuations	No prediction	Qualitative agreement: Figure 6
Mean value of velocity	Empirical Equation (61). Deviations: Figures 7 and 8	Fundamentally based Equation (62). Satisfactory agreement Figures 7 and 8

The fundamental model is derived from a theory that has a theoretical basis [7–9]. Expressions for the turbulent diffusion of momentum and of conservative scalars, such as temperature and passive admixture (smoke, aerosols), are of a general nature. They are free from calibration constants. They are found to agree in a satisfactory manner with DNS results at all distances, x, from the wall (outside the thin boundary layer at the wall). The theory underlying the fundamental model does not provide generally valid expressions for the turbulent diffusion of non-conservative scalar kinetic energy, pressure, and energy dissipation. The non-conservative diffusion terms are only important for the determination of k and ϵ in the inner half of the channel. Here, non-conservative behavior has been modeled by using the diffusion expressions of conservative scalars provided with calibration factors. A summary is presented in Table 1.

9. Conclusions

CFD codes are generally based on empirical propositions for diffusion by turbulent fluctuations. This includes the basic k-ϵ model widely used in engineering and environmental analyses. The limitation of these models is that they lack generality. It is uncertain whether the constituting variables are truly and accurately represented by the proposed expressions, both in magnitude and spatial dependency. The addition of calibration factors tempers the prediction inaccuracies to some extent. At the same time, they need to be specified for each new case. However, calibration predictions can still deviate markedly from the correct results at different positions in the flow field.

Models that are derived from generally valid principles do not suffer from these limitations. The presented new model contains descriptions of important diffusion terms, which satisfy this criterion. Calibration factors are absent, and because of their generality, applicability exceeds that of channel flow. Points for improvement of the new model are as follows:

(i) The agreements between the new model and DNS are satisfactory but not perfect, due to the truncation of the expansion in powers of the inverse of the universal Kolmogorov constant that underpins the theoretical foundation of the model. Extending the expansion will reduce the truncation error significantly.
(ii) What is missing is a general description of the turbulent dispersion of non-conservative scalars. Their impact is limited to the description of k and ϵ in the interior part of the channel, or more generally, substantially away from walls where shear is imposed. The development of well-based descriptions for the diffusion of k and ϵ will eliminate the remaining empiricism of the model.

Funding: This research received no external funding.

Data Availability Statement: Data are contained within the article.

Acknowledgments: B.G.J. Ruis and H.S. Janssen are acknowledged for performing numerical calculations; G.M. Janssen is acknowledged for preparing the manuscript.

Conflicts of Interest: The author declares no conflicts of interest.

References

1. Boussinesq, J. Mem.pres.par.div. savantis a l'acad. *Sci. de Paris* **1877**, *24*, 726–736.
2. Taylor, G.I. Eddy Motion in the Atmosphere. *Phil. Trans. R. Soc. Lond. A* **1915**, *215*, 1–26. [CrossRef]
3. Prandtl, L. 7. Bericht über Untersuchungen zur ausgebildeten Turbulenz. *ZAMM* **1925**, *5*, 136–139. [CrossRef]
4. Von Kármán, T. *Mechanische Ähnlichkeit und Turbulenz*; Weidmannsche Buchh.: Berlin, Germany, 1930; pp. 58–76.
5. Hanjalić, K.; Launder, B. *Modelling Turbulence in Engineering and the Environment: Second-Moment Routes to Closure*; Cambridge University Press: Cambridge, UK, 2011.
6. Bernard, P.S.; Wallace, J.K. *Turbulent Flow: Analysis, Measurement and Prediction*; Wiley: Hoboken, NJ, USA, 2002.
7. Brouwers, J.J.H. Statistical description of turbulent dispersion. *Phys. Rev. E Stat. Nonlinear Soft Matter Phys.* **2012**, *86*, 066309. [CrossRef] [PubMed]
8. Brouwers, J.J.H. Statistical Models of Large Scale Turbulent Flow. *Flow Turbul. Combust.* **2016**, *97*, 369–399. [CrossRef]
9. Brouwers, J.J.H. Statistical Descriptions of Inhomogeneous fundamentally based Turbulence. *Mathematics* **2022**, *10*, 4619. [CrossRef]
10. Monin, A.S.; Yaglom, A.M. *Statistical Fluid Mechanics, Vol. II, Ch 8*; Dover: New York, NY, USA, 2007.
11. van Kampen, N.G. *Stochastic Processes in Physics and Chemistry*, 3rd ed.; Elsevier: New York, NY, USA, 2007.
12. Stratonovich, R.L. *Topics in the Theory of Random Noise*; Gordon and Breach: New York, NY, USA, 1967; Volume 1.
13. Hoyas, S.; Jiménez, J. Scaling of the velocity fluctuations in turbulent channels up to $Re\_\tau = 2003$. *Phys. Fluids* **2006**, *18*, 011702. [CrossRef]
14. Hoyas, S.; Oberlack, M.; Alcántara-Ávila, F.; Kraheberger, S.V.; Laux, J. Wall turbulence at high friction Reynolds numbers. *Phys. Rev. Fluids* **2022**, *7*, 014602. [CrossRef]
15. Kuerten, J.; Brouwers, J.J.H. Lagrangian statistics of turbulent channel flow at $Re\_\tau = 950$ calculated with direct numerical simulation and Langevin models. *Phys. Fluids* **2013**, *25*, 105108. [CrossRef]
16. Kolmogorov, A. The Local Structure of Turbulence in Incompressible Viscous Fluid for Very Large Reynolds' Numbers. *Akad. Nauk. Sssr Dokl.* **1941**, *30*, 301–305.
17. George, W.K. The Decay of Homogeneous Isotropic Turbulence. *Phys. Fluids A* **1992**, *4*, 1492–1509. [CrossRef]

18. Brouwers, J.J.H. Dissipation equals Production in the Log Layer of Wall Induced Turbulence. *Phys. Fluids* **2007**, *19*, 101702. [CrossRef]
19. Lew, A.J.; Gustavo, C.; Carrica, B.; Carrida, P.M. A Note on the Numerical Treatment of the k-epsilon Turbulence Model*. *Int. J. Comput. Fluid Dyn.* **2001**, *14*, 201–209. [CrossRef]
20. Borse, G.J. *Numerical Methods with Matlab*; Chapter 22; PWS Publishing: Boston, MA, USA, 1997; ISBN 0534938221
21. Monin, A.S.; Yaglom, A.M. *Statistical Fluid Mechanics, Vol. I*; Dover: New York, NY, USA, 2007.

Disclaimer/Publisher's Note: The statements, opinions and data contained in all publications are solely those of the individual author(s) and contributor(s) and not of MDPI and/or the editor(s). MDPI and/or the editor(s) disclaim responsibility for any injury to people or property resulting from any ideas, methods, instructions or products referred to in the content.

inventions

MDPI

Article

Numerical Study of the Gas–Solid Separation Performance of Axial Flow Cyclone Separators

Yanqin Mao [1,2], Roman Chertovskih [1,*] and Liang Cai [2]

[1] SYSTEC, ARISE, Faculty of Engineering, University of Porto, 4200-465 Porto, Portugal; 18753364521@163.com
[2] School of Energy and Environment, Southeast University, Nanjing 211102, China; 101008806@seu.edu.cn
* Correspondence: roman@fe.up.pt

Abstract: Cyclone separators, which have a high separation performance, play a crucial role in mitigating the occurrence of dust explosion incidents. This study aims to improve the performance of an axial cyclone separator using the results of simulations employing the RNG $k-\varepsilon$ model together with a user-defined function to simulate the wall collision process. The effectiveness of various structural modifications to the vortex tube has been addressed. Specifically, we found that increasing the number of blades, reducing the blade exit angle, and adopting L-shaped blades increase separation efficiency. Additionally, enlarging the guide vane and exhaust pipe diameters, as well as increasing the exhaust pipe inclination angle, contribute to an improved separation performance due to the developed tangential velocity and vortex cores. However, it also increases the pressure drop losses due to the increase in the turbulence pulsation entropy and the wall entropy, while the time-averaged entropy is found to be less significant. As a result, our study sheds light on the flow characteristics, the gas–solid separation process, and the energy loss mechanism in the cyclone separator.

Keywords: separation efficiency; pressure drop; structure parameter; entropy production

1. Introduction

Dust explosions pose a significant, persistent risk in various industries where flammable particulates are processed [1–3]. Such incidents can cause severe harm to people and substantial property damage. For instance, an explosion in an aluminum powder plant in Kunshan, Jiangsu, China, in August 2014, initiated by an open flame, resulted in 75 deaths. More recently, a starch dust explosion in Qinhuangdao, Hebei, in 2021, led to 21 deaths and 47 injured persons, and a dust explosion in a Changzhou, Jiangsu, metalworking facility in January 2024 caused 8 deaths and as many injuries. These events highlight the critical importance of effective dust management strategies in industrial environments. Minimizing airborne combustible dust concentrations is essential for preventing such catastrophic events. This necessitates a concerted effort toward implementing stringent dust control measures, enhancing safety protocols, and fostering a culture of safety awareness across sectors susceptible to dust explosion hazards.

Dust removal technologies are pivotal in mitigating the risks associated with combustible dust in industrial settings [4]. Many dust removal technologies can be used to improve air quality, such as mechanical dedusting, filtering technology, electrostatic precipitation, ultrasonic dedusting, pulse injection technology [5], corona dust removal technology [6], and Fischer–Tropsch synthesis [7]. Among these, mechanical dedusting stands out for its widespread application, offering advantages such as minimal spatial requirements, low construction costs, simplicity in operation, and the absence of moving parts. Specifically, cyclone separators, a subset of mechanical dedusting methods, play a crucial role in industries ranging from petrochemicals to agriculture. These devices leverage centrifugal force, generated through a rotating airflow, to segregate particles from air streams. Predominantly, cyclone separators are differentiated into two main types: conventional reverse flow cyclones and straight flow (axial) cyclones. Reverse flow cyclones utilize a tangential inlet to generate centrifugal forces [8], with purified air exiting upwards through the outlet [9]. Conversely,

axial cyclone separators, employing a swirl generator, maintain the air flow's initial direction, resulting in a lower pressure drop [10]. This characteristic, alongside a higher throughput and enhanced flexibility in the separation process, makes axial cyclones particularly effective in controlling combustible dust accumulation and reducing explosion risks.

The evaluation of axial cyclone separators predominantly hinges on two critical metrics—separation efficiency and pressure drop—that serve as benchmarks for assessing technological performance. The genesis of axial cyclone design traces back to 1948 with Umney's pioneering model [11]. Initially, the axial cyclone's lower separation efficiency restricted its application range compared to its reverse-flow counterparts. Nevertheless, ensuing research endeavors have substantially focused on augmenting the efficacy of axial separators. It has been established that the geometrical dimensions of an axial separator profoundly influence its filtration capabilities. Notably, the design of swirl vanes emerges as a pivotal factor, accounting for a significant portion of total pressure loss while crucially impacting centrifugal force generation and, consequently, separation efficiency. Innovations aimed at enhancing axial cyclone performance have been noteworthy [12–14]. Andreussi's [15] introduction of an adjustable guide vane, tailored to inlet velocity, dust concentration, and particle characteristics, marks a significant advancement. Similarly, Trow's exploration [16] into the impact of tube diameter on separator efficiency identified optimal long-length ratios, highlighting the nuanced relationship between structural dimensions and performance. Dirkzwager's research [17] further elucidated that a heightened centrifugal force field could be achieved through reduced diameter designs, offering insights into optimizing the balance between efficiency and pressure management.

Experimental investigations stand as a cornerstone in the advancement of cyclone separator technology, offering unparalleled precision and reliability in outcomes. Hsiao and Chen's exploration into multi-stage cyclones underscored the critical role of Reynolds and Stokes numbers on particle separation efficiency, pinpointing the fluid dynamics and particle behavior as fundamental to optimizing cyclone design [18]. Similarly, Koffman's study on the parallel use of 14 cyclone separators revealed a decline in collective efficiency from 96% to 92.2%, with this reduction being attributed to variations in inlet velocity, thereby highlighting the importance of uniform airflow for maximal performance [19]. Further, Akiyama's research on the impact of outlet structural variations on particle separation illuminated the intricate relationship between design elements and functional efficacy. These studies not only deepen our understanding of cyclone separator mechanics, but also guide the development of more efficient, reliable systems through focused modifications in design parameters [20].

Many scientists have carried out studies aiming to improve the performance of vortex tube separators. However, the existing methods can lead to an increase in pressure loss and reduce the aerodynamic performance and the energy efficiency. Therefore, analyzing the separation efficiency and pressure loss of the cyclone separator through numerical simulation methods can help the design process. To deepen the understanding of internal gas–solid flow, the complex dynamics in the cyclone tubes, as well as the influence of various structural and operational variables on the performance, need further exploration. This study uses Computational Fluid Dynamics (CFD), enriched by particle–wall collision and entropy generation models, to dissect the impact of modifications in blade count, morphology, outlet angles, guide cone, and exhaust pipe dimensions, as well as exhaust pipe configuration, on the vortex tube's energy dissipation, separation efficiency, and entropy generation. Our findings offer some insights into the internal gas–solid two-phase flow structure, which can contribute to a better understanding of the energy loss mechanism and influence the performance of the separator.

2. Materials and Methods

2.1. Grid Generation Methods

The cyclone separator in Figure 1 mainly includes the blade, guide vane, straight pipe, and exhaust tube. The parameters are given in Table 1, with a 50 mm outer diameter and 35° blade outlet angle.

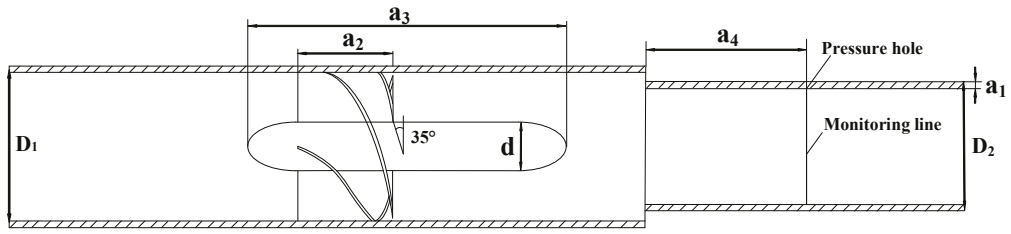
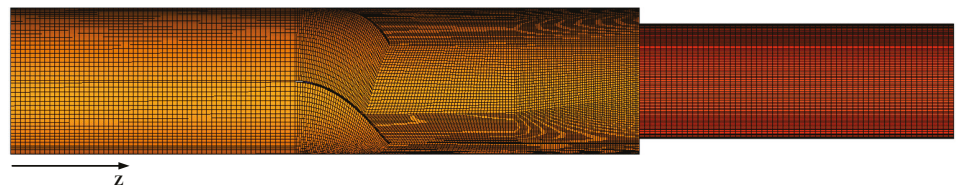


Figure 1. The structure of an axial cyclone separator.

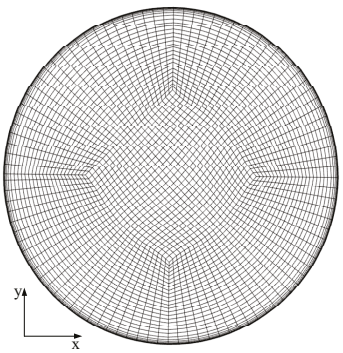
Table 1. The dimensions of the swirl generator.

Variable	Project	Value/mm
D1	outer diameter	50
D2	inner diameter	46
d	diameter of guiding cone	
a1	wall thickness	2
a2	guide vane length	30
a3	guiding cone length	100
a4	distance between the pressure hole and dust outlet	50

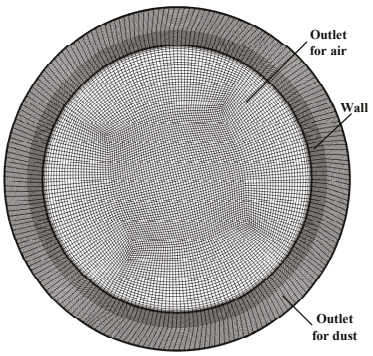
Figure 2 shows the mesh distribution generated by the ICEM 2020 R2 software with 2,991,661 grid cells. The inlet air is regarded as having incompressible turbulent flow and the RNG $k-\varepsilon$ model is used as the turbulence model since it has been proved useful in simulations of rotation flows [21,22]. The discrete phase model (DPM) is used to track the particle separation efficiency coupling with the continuous phase in ANSYS FLUENT. The results in Figure 3 shows that the simulation of the pressure drop corresponds to the experiment data, ensuring the calculation accuracy of the continuous phase. For the discrete phase model, the simulated 167 μm and 296 μm particles are found to be 91.64% and 82.17%, respectively; these values are close to the experimental ones: 87.00% and 79.13% (see [23]). Overall, the maximum error of 5.3%, and the efficiency and pressure drop, in our view, let us conclude that the simulations were performed with satisfactory computational accuracy.



(**a**) Global grid distribution



(**b**) Inlet



(**c**) Outlet

Figure 2. The grid distribution.

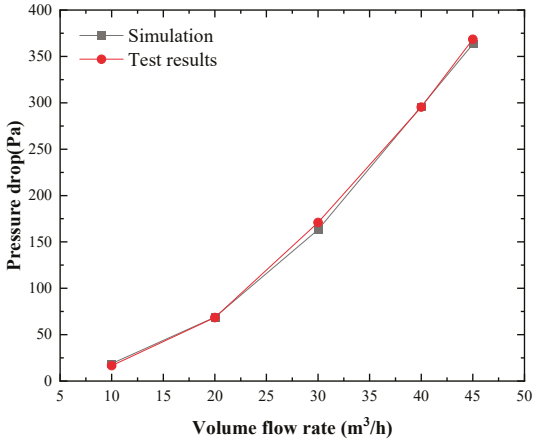


Figure 3. The pressure drops of the simulation and test values.

2.2. Governing Equations

The flow field in an axial cyclone separator is simulated using the following governing equations [24]:

The continuity equation of a fluid flow:

$$\frac{\partial u_i}{\partial x_i} = 0 \tag{1}$$

The equation of momentum balance:

$$\frac{\partial u_i}{\partial t} + \frac{\partial u_i u_j}{\partial x_j} = -\frac{\partial P}{\partial x_i} + \frac{\partial}{\partial x_j}\left[\mu\left(\frac{\partial u_i}{\partial x_j} + \frac{\partial u_j}{\partial x_i}\right)\right], \tag{2}$$

where u_i and u_j are the velocity components, ρ is the air density, P is the air pressure, μ is the dynamic viscosity, and t is time.

The equations of the RNG $k-\varepsilon$ turbulence model are [25]:

$$\frac{\partial}{\partial t}(\rho k) + \frac{\partial}{\partial x_i}(\rho k u_i) = \frac{\partial}{\partial x_j}\left[\alpha_k \mu_{eff}\frac{\partial k}{\partial x_j}\right] + G_k - \rho\varepsilon \tag{3}$$

$$\frac{\partial}{\partial t}(\rho \varepsilon) + \frac{\partial}{\partial x_i}(\rho \varepsilon u_i) = \frac{\partial}{\partial x_j}\left[\alpha_\varepsilon \mu_{eff}\frac{\partial \varepsilon}{\partial x_j}\right] + \frac{\varepsilon}{k}(C_{1\varepsilon}G_k - C^*_{2\varepsilon})\rho\varepsilon \tag{4}$$

where k is the turbulence kinetic energy, ε is the turbulence dissipation rate, G_k is the turbulence kinetic energy generation rate, α_ε is the effective reverse Prandtl number, μ_{eff} is the effective viscosity coefficient, and C is a constant.

The equation of the DPM force balance model can be written as [26]:

$$m_p\left(\frac{du_p}{dt}\right) = m_p F_D(u-u_p) + m_f\left(\frac{D_u}{D_t}\right) + \frac{1}{2}m_f\left(\frac{D_u}{D_t} - \frac{du_p}{d_t}\right) + (m_p - m_f)g + \frac{1}{2}(\pi\rho_p r^2)C_L L V^2 \tag{5}$$

where u_p is the particle velocity, u is the air velocity, m_p is the mass of the particle, m_f is the fluid mass, g is the gravity acceleration, r is the particle radius, ρ_p is the particle density, C_L is the Saffman lift coefficient, L is the directional cosine, V is the relative velocity magnitude, and $F_D(u-u_p)$ is the drag force computed as:

$$F_D = \frac{18\mu}{\rho_p d_p^2}\frac{C_D \mathrm{Re}}{24}, \tag{6}$$

where d_p is the particle diameter, μ is the air dynamic viscosity, $C_D = \varphi(\mathrm{Re})$ is the drag coefficient, and Re is the relative Reynolds number:

$$\mathrm{Re} = \frac{\rho d_p |u_p - u|}{\mu}. \tag{7}$$

To investigate the energy loss in a cyclone separator, in our study we employed the entropy production theory to analyze the energy dissipation, i.e., considering the direct viscous entropy production, turbulent entropy production, and wall entropy production based on the Reynolds-averaged method. Herwig et al. provided the function for obtaining the rate of entropy production per unit volume [27]:

(1) Rate of the time-averaged entropy production caused by viscous dissipations in the average flow field:

$$S'''_{\overline{D}} = \frac{\mu}{\overline{T}}\left\{2\left[\left(\frac{\partial \overline{u}}{\partial x}\right)^2 + \left(\frac{\partial \overline{v}}{\partial y}\right)^2 + \left(\frac{\partial \overline{w}}{\partial z}\right)^2\right] + \left(\frac{\partial \overline{u}}{\partial y} + \frac{\partial \overline{v}}{\partial x}\right)^2 + \left(\frac{\partial \overline{u}}{\partial z} + \frac{\partial \overline{w}}{\partial x}\right) + \left(\frac{\partial \overline{v}}{\partial z} + \frac{\partial \overline{w}}{\partial y}\right)\right\} \tag{8}$$

(2) Since the Reynolds-averaged approach cannot explicitly provide the turbulent velocity, Herwig et al. correlated the 'ε' variable in the RANS simulation model with the entropy production rate. This correlation yields the turbulent dissipation entropy production rate resulting from the flow field fluctuations:

$$S'''_{D'} = \frac{\rho \varepsilon}{\overline{T}}. \tag{9}$$

The entropy production induced by the time-averaged velocity and fluctuating velocity can be obtained by integration, i.e.,

$$S_{\overline{D}} = \int_V S'''_{\overline{D}} \mathrm{dV} \tag{10}$$

$$S_{D'} = \int_V S'''_{D'} \mathrm{dV} \tag{11}$$

In these expressions, $S_{\overline{D}}$ is the direct dissipation entropy production caused by time-averaged velocity, W/K, $S_{D'}$ is the turbulent dissipation entropy production induced by fluctuating velocity, W/K, and 'V' represents the volume of the computational domain, m^3.

(3) The entropy production generated at the wall due to velocity gradients is calculated by the following expression [28]:

$$S_W = \int_A \frac{\tau_w \cdot u_w}{\overline{T}} dA. \tag{12}$$

Here, τ_w is the wall shear stress, Pa, u_w is the velocity at the center of the first layer of the grid near the wall, m/s, and 'A' is the area, m^2. The total entropy production 'S' within the computational domain is:

$$S = S_{\overline{D}} + S_{D'} + S_W \tag{13}$$

2.3. Boundary Condition and Solver Settings

The inlet boundary condition is velocity inlet, and the DEFINE_PROFILE macro was used to calculate the fully developed turbulent flow as:

$$u_{ave} = u_{\max}(1 - r/r_0)^{1/7}, \tag{14}$$

where r represents the radial position, r_0 is the radius of the cyclone, u_{ave} is the average velocity, and $u_{\max}$ is the maximum velocity:

$$u_{ave} = \frac{49}{60} u_{\max} \tag{15}$$

The discrete phase boundary condition for particles is trap with 0.9 flow rate weighting, and, for cleaned air, it is defined as escape with 0.1 flow rate weighting. The separation efficiency is calculated by the ratio of the escaped particles and the released particles:

$$\eta = \frac{N_{\text{trap}}}{N_{\text{track}}} \tag{16}$$

where η is the separation efficiency, N_{trap} is the number of trapped particles at the outlet, and N_{track} is the number of tracked particles.

Figure 4 shows the particle size distribution measured by the Microtrac S3500 particle size distribution analyzer [23]. The median diameter is 167 μm, the maximum diameter is 296 μm, and the particle concentration is 20 g/min. To simplify the calculation, the efficiencies of 167 μm and 296 μm particles are considered with 2650 kg/m^3 particle density.

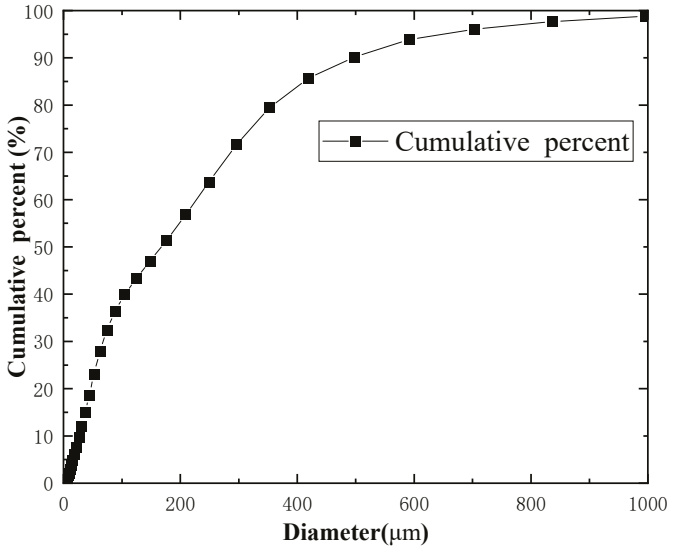


Figure 4. Particle diameter distribution [23].

The solution method for the cyclone separator is pressure-based with a steady state using the RNG $k-\varepsilon$ turbulence model. The standard wall function is adopted for the near-wall, which is assumed to be a no slip wall. The Navier–Stokes equation is solved by the SIMPLE method, and approximations for the gradients are computed by the least squares cell-based method. The governing equations for the turbulent kinetic energy and turbulent dissipation rate are solved by the second order upwind method.

2.4. Particle–Wall Collision Model

In order to improve accuracy of the separation efficiency, the 410 stainless steel collision model is adopted to characterize the particle–wall collision effects considering the particle velocity after impact to the particle velocity before impact. The DEFINE_DPM_BC macro is used to simulate the particle–wall interaction process considering the tangential velocity restitution ratio and the normal velocity restitution ratio component. The 410 stainless steel collision model is [29]:

$$\begin{aligned} e_N &= V_{N2}/V_{N1} = 1-0.4159\beta_1 - 0.4994\beta_1^2 + 0.292\beta_1^3, \\ e_T &= V_{T2}/V_{T1} = 1 - 2.12\beta_1 + 3.0775\beta_1^2 - 1.1\beta_1^3, \end{aligned} \tag{17}$$

where e_N represents the normal velocity restitution ratio, e_T is the tangential velocity restitution ratio, V_{N1} is the normal particles' velocity before collision, V_{N2} is the normal particles' velocity after collision, V_{T1} is the tangential particles' velocity before collision, and V_{T2} is the tangential particles' velocity after collision.

2.5. Calculation Steps

Step 1. The single-phase gas flow is simulated.

Step 2. For the flow computed at the previous step, the particle separation efficiency is calculated using the DPM model based on the particle wall collision process governed by the user-defined function.

Step 3. The energy loss process is analyzed by the entropy production model and using the CFD-Post 2020 R2 software. The direct viscous and turbulent entropy production, as well as the wall entropy production, are computed from the simulation results obtained at the previous step.

3. Results and Discussion

3.1. Effect of Blade Number

The blade structure has a significant impact on the separation efficiency and pressure drop. Figure 5 shows the separation performance in the axial cyclone separator at 5 m/s inlet average velocity as a function of the blade number. These results indicate that more blades can result in the increase in energy loss, and improve the separation efficiency of the 167 μm particle. The 296 μm particle has a higher efficiency when the blade number is 4. With the blade number changing from 2 to 8, the pressure drop is gradually increased from 75.83 Pa to 244.62 Pa. For 167 μm for 296 μm particles, the separation efficiencies are increased from 78.32%, and 62.96% to 94.85%, and 79.53%, respectively. This indicates that the reasonable blade number is 4, and, although increasing the number of blades also contributes to efficiency, this causes more energy loss.

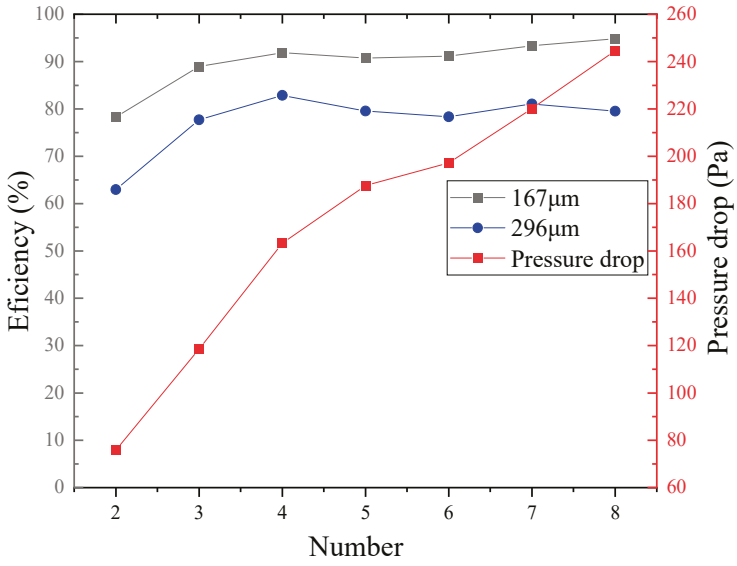
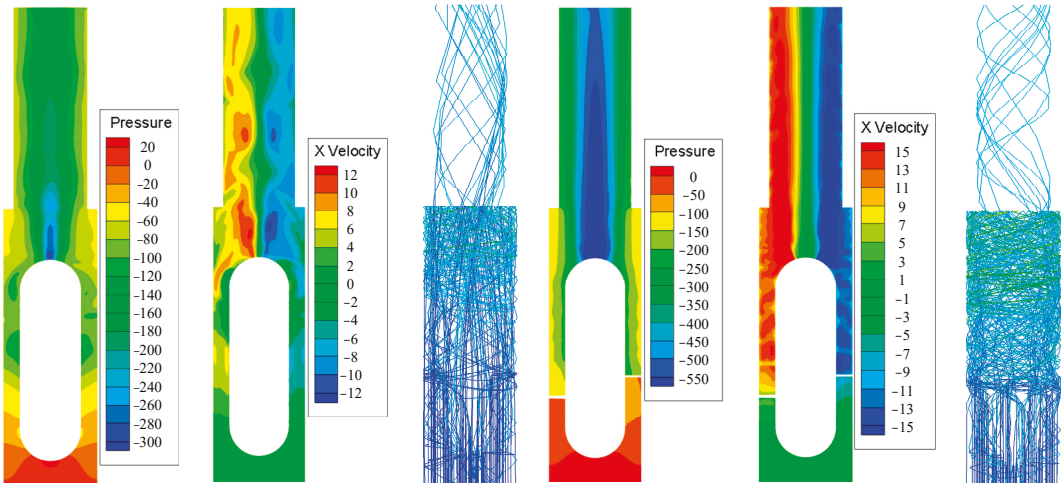


Figure 5. Separation efficiency and pressure drop varies with blade numbers.

Figure 6 shows the flow field and pressure distribution in the cyclone separator, and the X velocity represents the tangential velocity which is related to the separation process. The units for pressure and velocity are Pa and m/s, correspondingly. The flow field has visible differences—the seven-blade cyclone has a negative pressure region at the rear of guide vanes, with a more uniform and fully developed tangential velocity. The 167 μm particles have more spiral rotation in the seven-blade cyclone separator. This indicates that a stronger rotating field is generated in the cyclone with a greater number of blades.



(**a**) Two-blade cyclone (**b**) Seven-blade cyclone

Figure 6. Flow field in the cyclone.

Figure 7 shows the vortex core region in the cyclone at the condition of 0.06 swirling strength. When the blade number is 2, the vortex core region is unstable. By increasing the blade number, the rotation flow is gradually developed; the vortex core is close to a steady state when the blade number is 4.

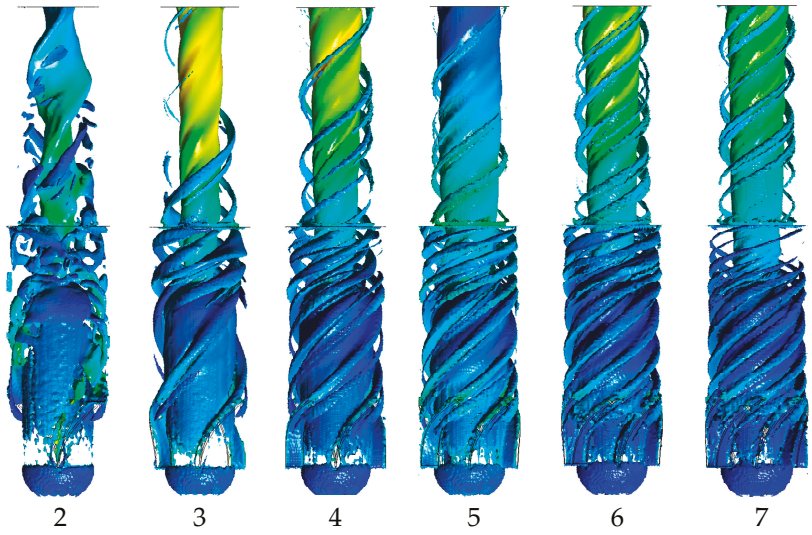
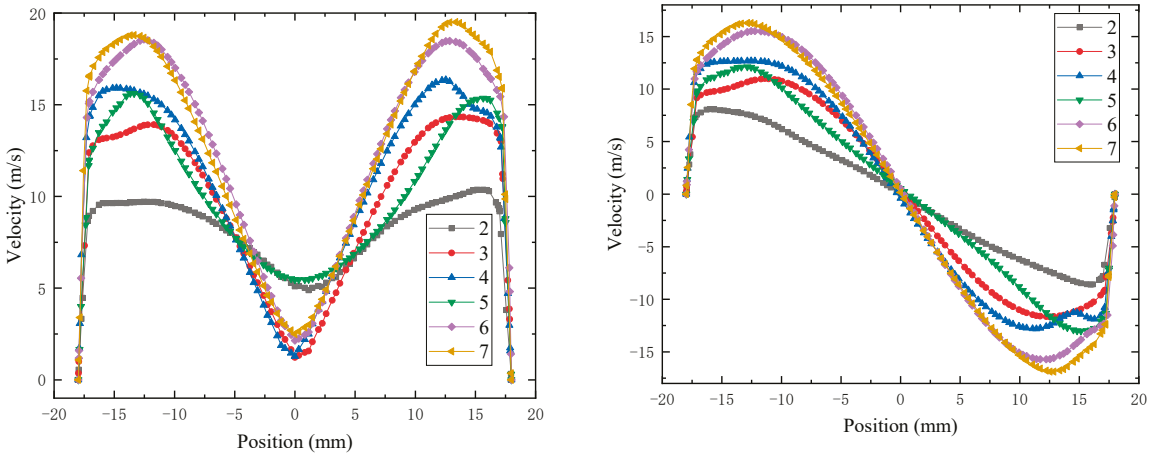


Figure 7. Vortex core region (swirling strength = 0.06).

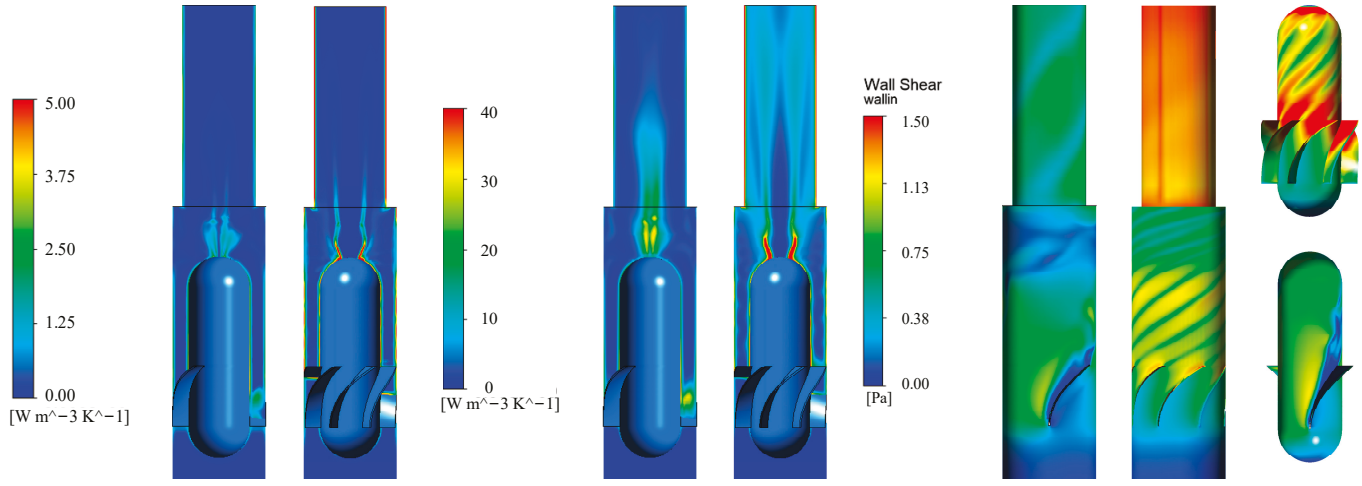
Figure 8 compares the velocity distributions at the center of the discharge pipe at the monitoring line (in Figure 1). The flow velocity is zero at the discharge wall because of the non-slip condition. Due to the presence of the centrifugal force, the velocity at the center of the tube is relatively low. Total and tangential velocity decrease significantly at the distance of 0.1 *D*–0.2 *D* from the out wall. When the number of blades increases, the maximum total velocity increases from 9.7 m/s to 19.5 m/s, and the maximum tangential velocity increases from 8.6 to 16.9 m/s, reflecting the improvement in the separation efficiency for a higher number of blades.



(**a**) Total velocity (**b**) Tangential velocity

Figure 8. The outlet velocity distribution in various blades.

Figure 9 depicts the entropy production and wall shear stress distributions through cloud diagrams, focusing on viscous, turbulent entropy production, and wall shear stress across the system. The analysis reveals a concentration of both average and fluctuating entropy production near the guide vanes, at the draft tube cone's wall surface, and within the exhaust pipe. Notably, wall shear stress predominantly occurs at the guide vanes' exit and along the exhaust pipe's walls. With an increase in blade count from 2 to 7, there is a marked enhancement in the mixing dynamics between the high-velocity airflow at the draft cone's tail and the slower-moving flow within the recirculation zone. This interaction boosts the time-averaged and turbulent entropy production values. The acceleration of airflow at the guide vanes' exit further amplifies, intensifying the vortex tube wall shear stress. As a result, the measurements of time-averaged entropy production, turbulent entropy production, and wall entropy production escalate significantly from 8.0×10^{-5} W/K, 6.9×10^{-4} W/K, and 6.5×10^{-4} W/K to 2.1×10^{-4} W/K, 1.9×10^{-3} W/K, and 1.6×10^{-3} W/K, respectively, indicating an increase in energy dissipation. Extended analysis reveals that the time-averaged entropy production constitutes around 5.7% of the total, significantly less than the contributions from the turbulent (50.3%) and wall entropy production (44.0%). This delineates the latter two as the primary mechanisms driving energy losses within the vortex tube, highlighting the importance of optimizing design and operational parameters to mitigate these losses.



(**a**) Average velocity entropy (**b**) Turbulent dissipation entropy (**c**) Wall shear

Figure 9. Entropy production rates and wall shear distribution.

3.2. Effect of Blade Outlet Angle

The effect of the blade outlet angle on the separation capacity is shown in Figure 10. When the blade outlet angle changes from 20°to 50°, the separation efficiency of the 167 µm particle decreases from 97.27% to 87.50%, the efficiency of the 296 µm particle decreases from 88.70% to 73.65%, and the pressure drop decreases from 297.35 Pa to 82.57 Pa. This shows that a smaller blade outlet angle has a higher efficiency and pressure dissipation.

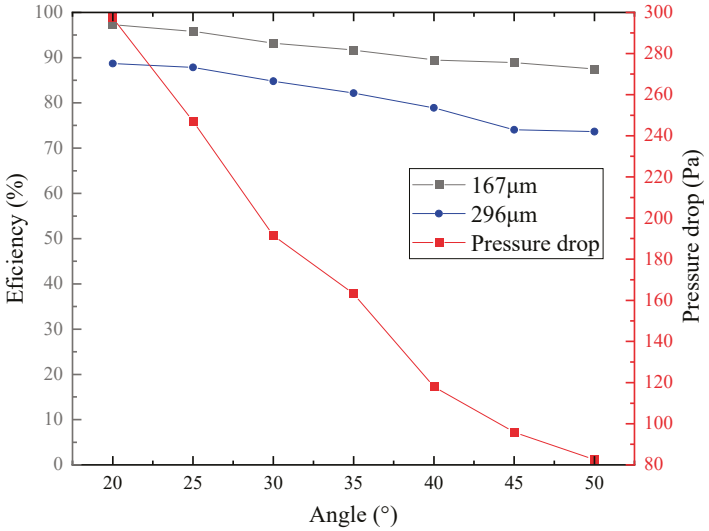
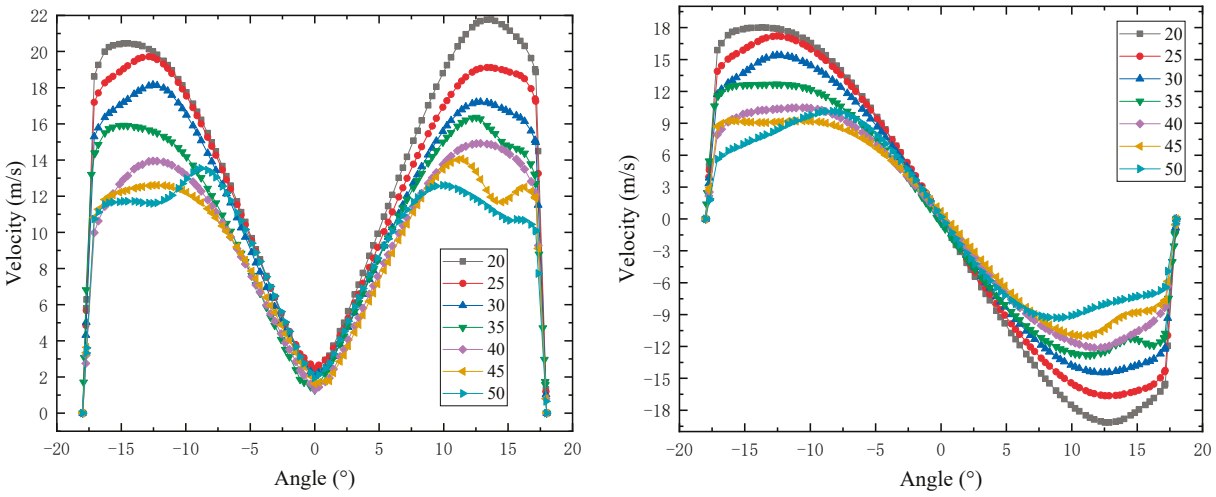


Figure 10. The separation performance under different blade outlet angle.

Figure 11 shows the velocity variation with the blade outlet angle along the monitoring line (see Figure 1). There is no large difference between the flow distribution characteristics for the total and tangential velocity. The only visible difference is that the total velocity decreases from 21.78 m/s to 12.60 m/s and the tangential velocity decreases from 19.16 m/s to 10.13 m/s when the blade outlet angle changed from 20° to 50°. This reveals that a smaller angle creates a stronger centrifugal field, which helps to increase the efficiency.

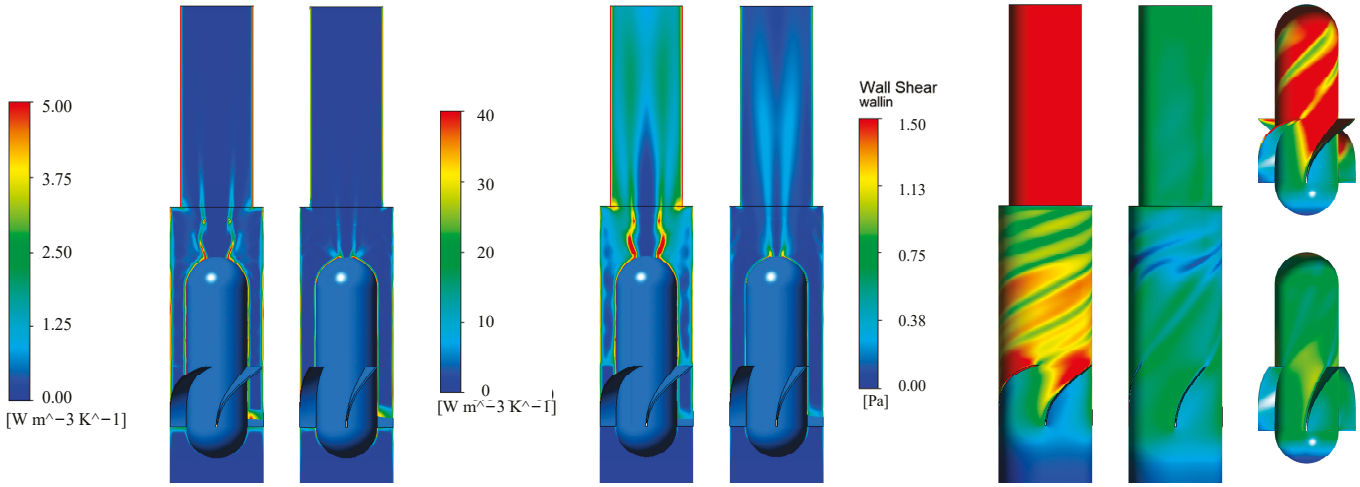


(**a**) Total velocity (**b**) Tangential velocity

Figure 11. The velocity distribution at different outlet angle.

Figure 12 demonstrates the entropy production at different blade outlet angles. When it changes from 20° to 50°, the production of time-averaged entropy, turbulent entropy, and wall entropy decrease from 2.8×10^{-4} W/K, 3.0×10^{-3} W/K, and 2.4×10^{-3} W/K

to 1.4×10^{-4} W/K, 8.5×10^{-4} W/K, and 5.8×10^{-4} W/K, respectively. This is due to a decrease in the total velocity, leading to a decrease in the mixing effect at the rear end of the guide vane and the exhaust pipe. Furthermore, the decreasing relative speed between the rotating air and the wall may also cause a smaller energy loss.

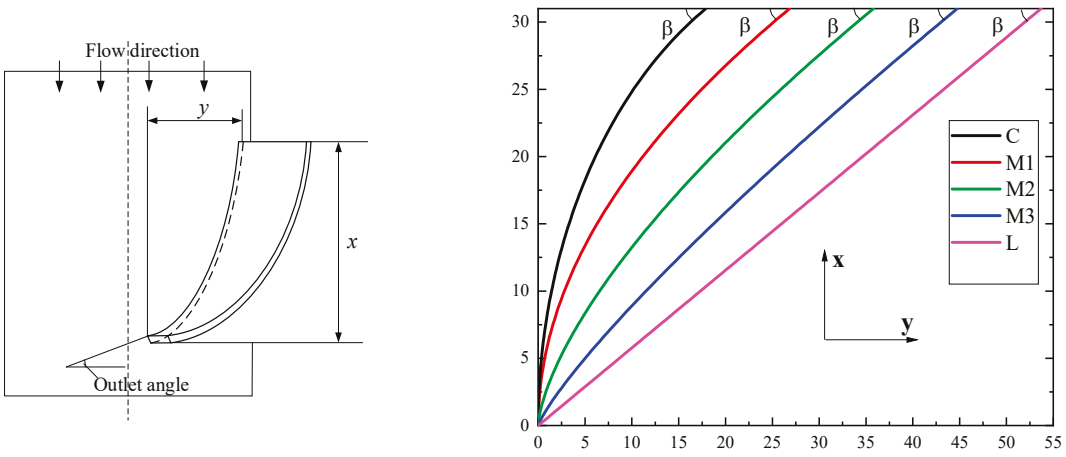


(**a**) Average velocity entropy (**b**) Turbulent dissipation entropy (**c**) Wall shear

Figure 12. The influence of blade outlet angle on entropy production rates.

3.3. Influence of the Blade Shape

Figure 13 demonstrates the structure parameter of the blade. In Figure 13a, x represents the blade length alone the flow direction, y represented the circumferential length of the blade, and the functions between x and y relating to the different blade curves are shown in Table 2. Figure 13b is the blade control line along the circumferential direction, the control line of the C blade is an arc line, the lines of M1, M2, and M3 are power functions, and the line of L is a straight line.



(**a**) Blade structure (**b**) Expansion graph for blade line

Figure 13. The detailed parameters of the blade.

Table 2. The function relationships and parameters of different blades.

Blade Shape	Function	Parameter
C	$y = r - \sqrt{r^2 - x^2}$	$r = 37.84$
M_1	$y = Ax^B$	$A = 0.0328$ $B = 1.9107$
M_2		$A = 0.1969$ $B = 1.4657$
M_3		$A = 0.6280$ $B = 1.1889$
L	$y = x/\tan(\beta)$	$\beta = 35°$

The dust removal performance at different blade shapes is shown in Figure 14. As the blade shape changes from C to L, the calculated efficiency of the 167 μm particles increases from 91.65% to 98.76%, the efficiency of the 296 μm particles increases from 82.17% to 93.37%, and the pressure drop is drastically changed from 163.19 Pa to 595.28 Pa. These results demonstrate that a long circumferential length can improve the separation capability; however, it introduces more pressure loss.

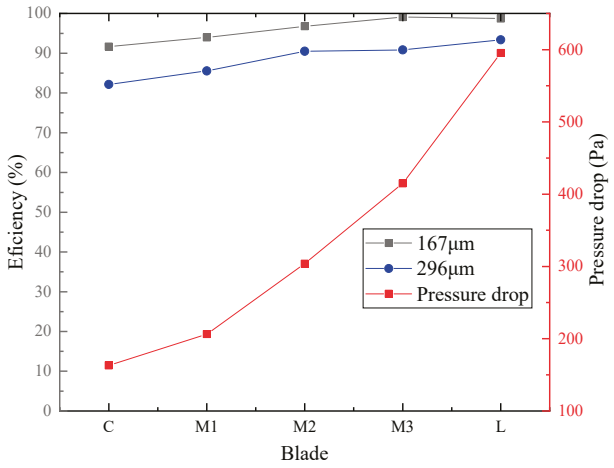


Figure 14. The separation performance varies with blade shape.

The influence of the blade structure on the flow field is shown in Figure 15. When the blade shape is changed from C to L, the flow path gradually increases, and smaller vortex regions are generated. This indicates that the L blade can produce a stronger induced action.

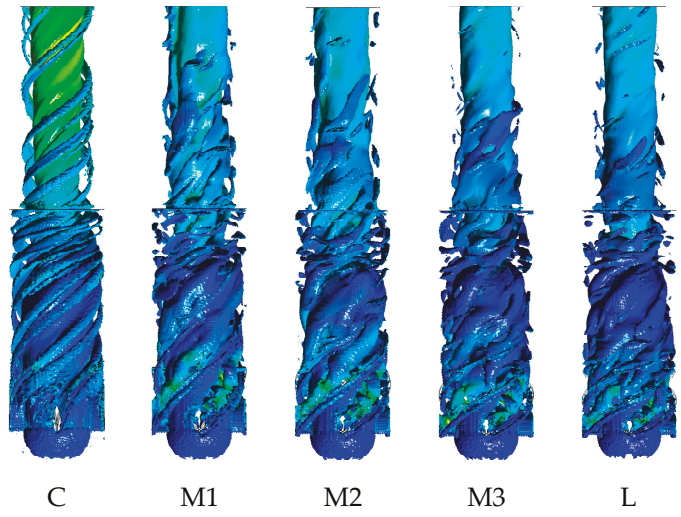
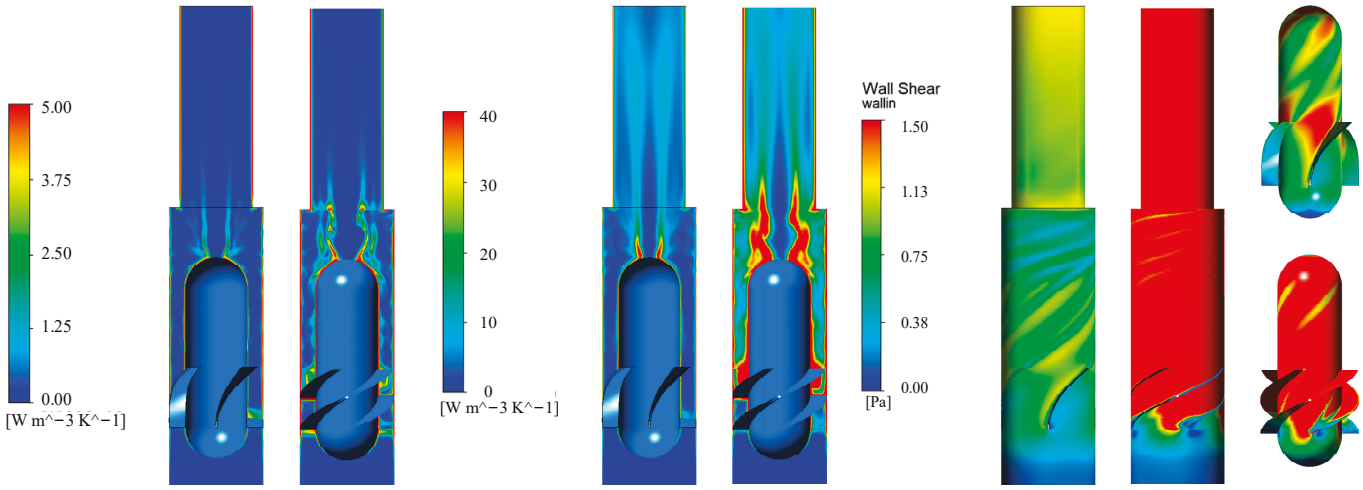


Figure 15. Vortex structures of different blades in the cyclone.

According to Figure 16, when the blade shape changes from C to L, the production of time-averaged entropy, turbulent entropy, and wall entropy change from 2.1×10^{-4} W/K, 1.5×10^{-3} W/K, and 1.1×10^{-3} W/K to 6.0×10^{-4} W/K, and 5.7×10^{-3} W/K, 5.4×10^{-3} W/K, respectively. The flow becomes more turbulent in a long flow-guiding passage, leading to the increase in entropy production and wall shear at the position of the blade and the guide vane, resulting in a higher energy loss.



(**a**) Average velocity entropy (**b**) Turbulent dissipation entropy (**c**) Wall shear

Figure 16. Effect of blade structure on entropy production rates and wall shear.

3.4. Guide Cone Diameter

The influence of the cyclone guide cone diameter on the separation efficiency and the pressure drop can be seen in Figure 17. When the guide cone diameter is changed from 10 mm to 40 mm (0.2 *D* to 0.8 *D*), the separation efficiency of the 167 μm particles is increased from 59.10% to 100%, the separation efficiency of the 296 μm particles is increased from 48.16% to 98.98%, and the pressure drop is increased from 43.02 Pa to 977.76 Pa. Comparing the numerical results, we conclude that the 30 mm and 35 mm guide cones (0.6 *D* and 0.7 *D*) have satisfactory properties and the separation efficiencies for the 167 μm particles are 91.87% and 98.83% with 163.19 Pa and 303.81 Pa pressure drops, respectively.

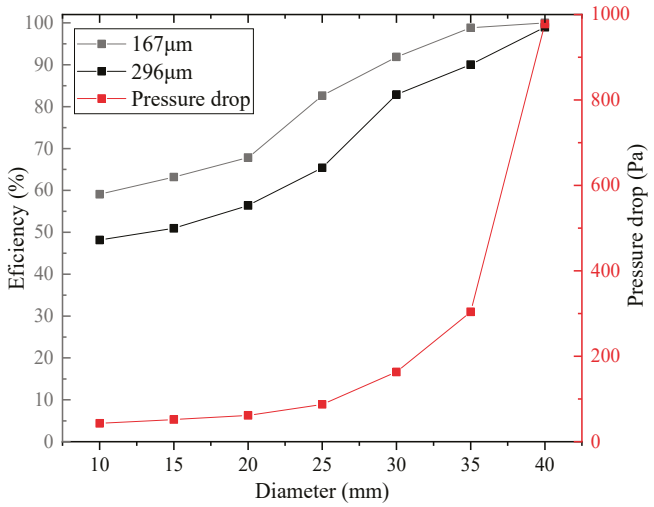
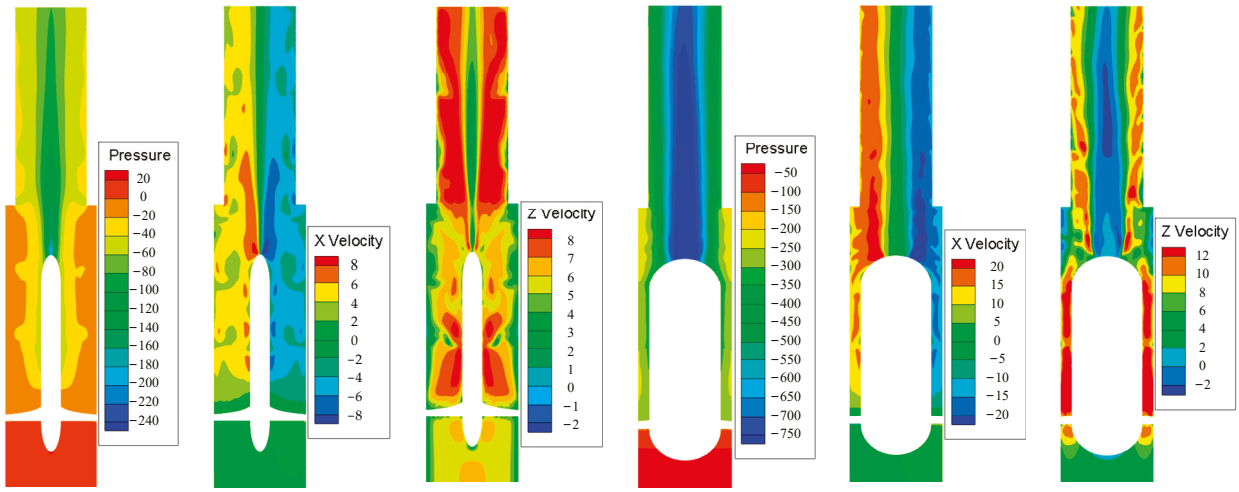


Figure 17. Influence of guide vane diameter on performance.

The flow fields between the 10 mm and 35 mm guide cones are given in Figure 18 (the units for the pressure and velocity fields are Pa and m/s, respectively). For the 35 mm

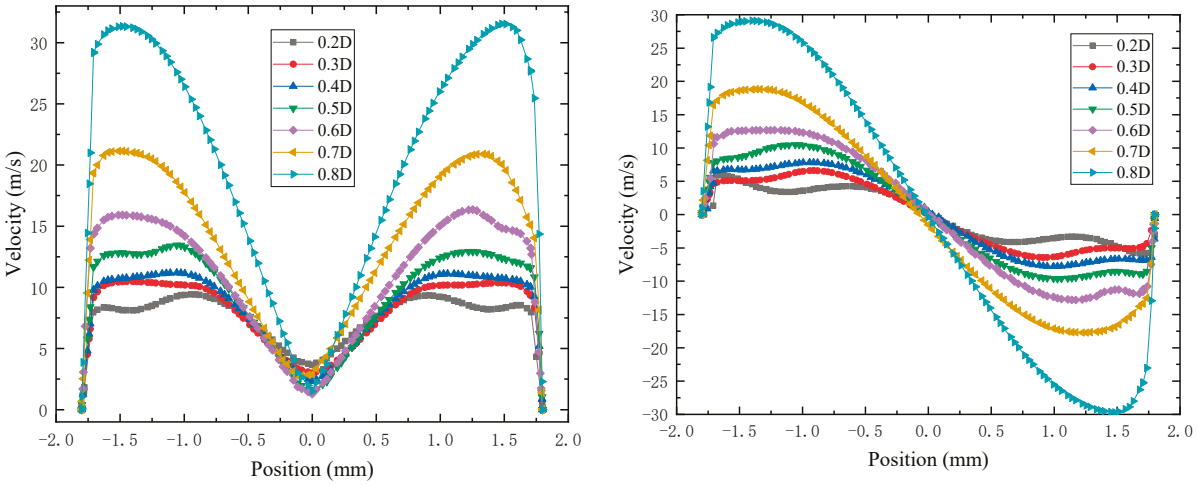
guide vane, the flow has a larger pressure gradient, a higher tangential velocity, and a larger reflow region than that of the 10 mm guide cone. The maximum tangential velocity in the 10 mm guide cone cyclone is mainly distributed at the rear of guide cone. By comparison, the tangential velocity in the 35 mm guide vane tube is increased significantly near the particle outlet.



(**a**) 10 mm guide vane (0.2 *D*) (**b**) 35 mm guide vane (0.7 *D*)

Figure 18. Details of the flow field in the cyclone.

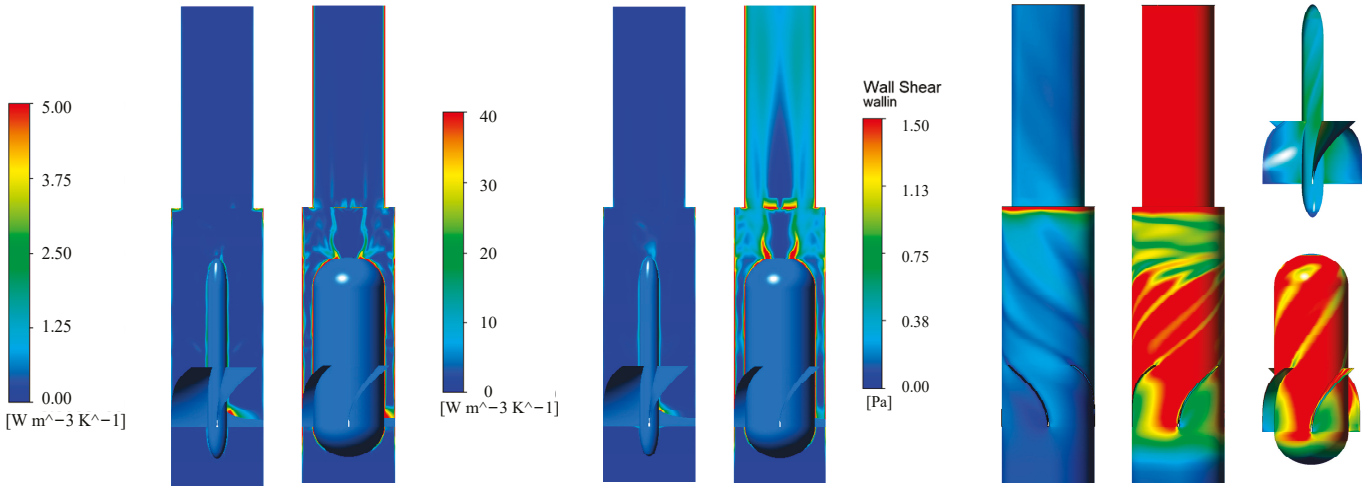
When the diameter of guide vane is changed from 0.2 *D* to 0.8 *D* (see Figure 19), the maximum outlet velocity is increased from 9.48 m/s to 31.54 m/s and the maximum tangential velocity is changed from 6.61 m/s to 29.09 m/s. This can be explained by the fact that the cross-sectional area is changed by the guide vane, creating a higher diameter of the guide vane and enabling a higher tangential velocity; hence, the particles are separated more efficiently.



(**a**) Total velocity (**b**) Tangential component velocity

Figure 19. The velocity under different diameters of guide vanes.

Figure 20 presents the entropy production at different diameters of the guide vane. When the diameter of the guide vane is increased from 0.2 *D* to 0.7 *D*, the time-averaged entropy, turbulent entropy, and wall entropy are gradually increased from 4.3×10^{-5} W/K, 2.2×10^{-4} W/K, and 2.0×10^{-4} W/K to 4.6×10^{-4} W/K, 3.1×10^{-3} W/K, and 2.7×10^{-3} W/K due to the higher velocity and turbulence intensity.



(**a**) Average velocity entropy (**b**) Turbulent dissipation entropy (**c**) Wall shear

Figure 20. Entropy dissipation rates and wall shear at different guide vanes.

3.5. Exhaust Pipe Diameter

Figure 21 illustrates the separation performance for different exhaust pipe diameters. By increasing the exhaust pipe diameter from 36 mm to 44 mm, the efficiency of the 167 μm particles is decreased from 96.52% to 67.82%, that of the 296 μm particles is decreased from 90.03% to 49.09%, and pressure drop is decreased from 195.11 Pa to 116.83 Pa. A smaller diameter of the exhaust tube can increase the particle separation efficiency. Similarly, it also leads to an increase in the pressure drop.

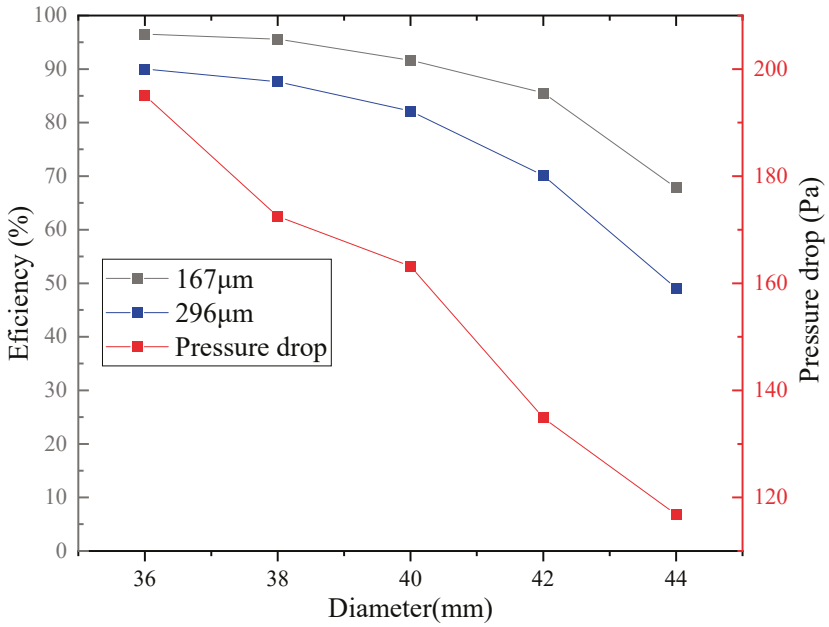
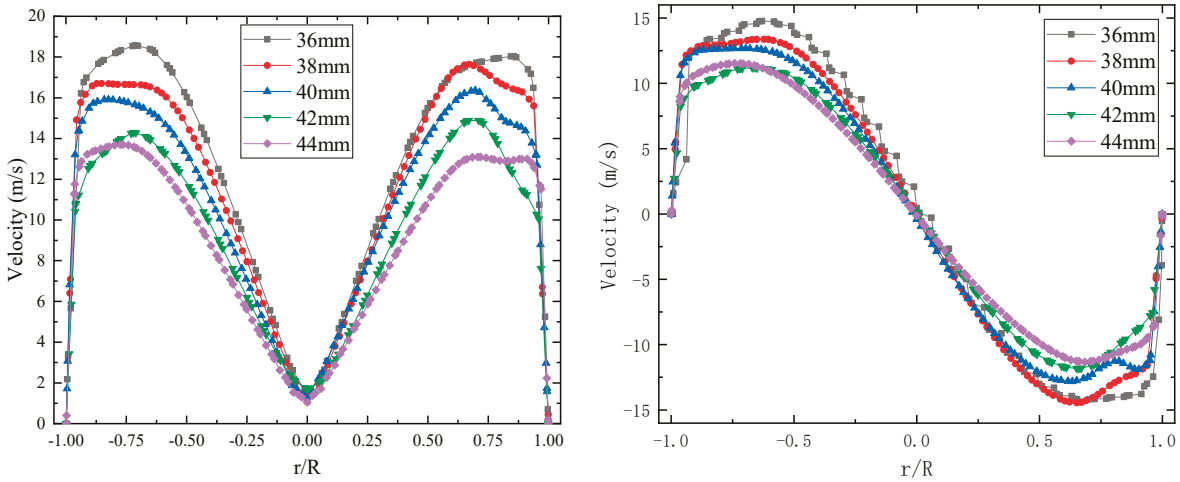


Figure 21. Influence of exhaust pipe diameter on performance.

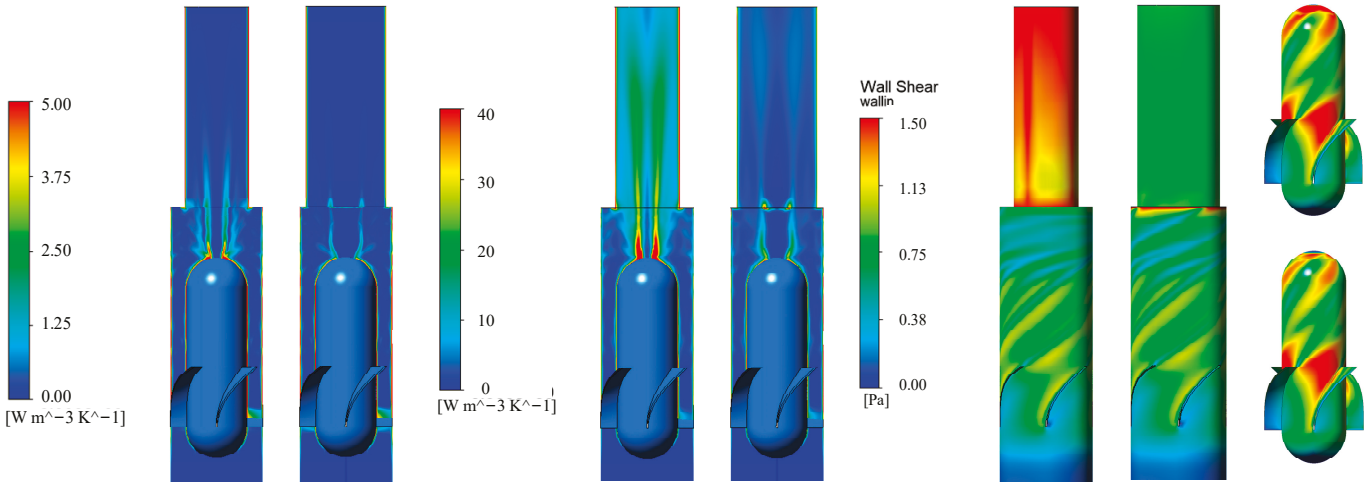
The cyclone exhaust pipe diameter has a notable influence on the velocity distribution, as shown in Figure 22. With the exhaust pipe changing from 44 mm to 36 mm, the distribution of internal velocity showed no significant difference, except for the variation in the velocity value. Correspondingly, the maximum total velocity changed from 13.70 m/s to 18.04 m/s and the maximum tangential velocity changed from 11.53 m/s to 14.17 m/s.



(**a**) Total velocity (**b**) X velocity

Figure 22. Effect of the exhaust pipe diameter on the outlet velocity.

Figure 23 shows the entropy production for different outer diameters of the exhaust pipe changing from 36 mm to 44 mm. The entropy production rate at the rear end of the guide vane and exhaust pipe caused by the cross-section area gradually decreases, which results in a decrease in the time-averaged entropy, turbulent entropy, and wall entropy from 2.5×10^{-4} W/K, 2.0×10^{-3} W/K, 1.3×10^{-3} W/K to 1.8×10^{-4} W/K, 1.1×10^{-3} W/K, 1.0×10^{-3} W/K.



(**a**) Average velocity entropy (**b**) Turbulent dissipation entropy (**c**) Wall shear

Figure 23. Entropy dissipation rates and wall shear for different exhaust pipe diameters.

3.6. Exhaust Pipe Shape

The cyclone performances of different exhaust pipe shapes are shown in Figure 24. When the inclination angle is changed from 2° to 10°, the efficiencies of 167 μm particles and 296 μm particles are increased from 95.44% and 88.30% to 100% and 96.36%. Correspondingly, the pressure drop is increased from 166.33 Pa to 968.38 Pa. This indicates that a larger inclination angle can improve the dust removal efficiency and increase the pressure consumption.

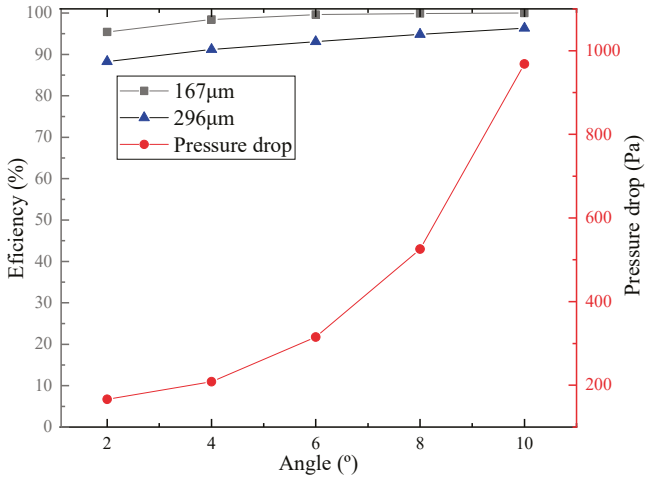


Figure 24. Effects of outlet pipe shape on performance.

Figure 25 shows the axial flow velocity distribution measured in m/s. The downstream flow field of the guide cone is significantly affected by the shape of the exhaust pipe. A higher inclination angle can increase the velocity at the inlet of the exhaust pipe, causing more zones to be affected by the back flow at the inlet of exhaust pipe.

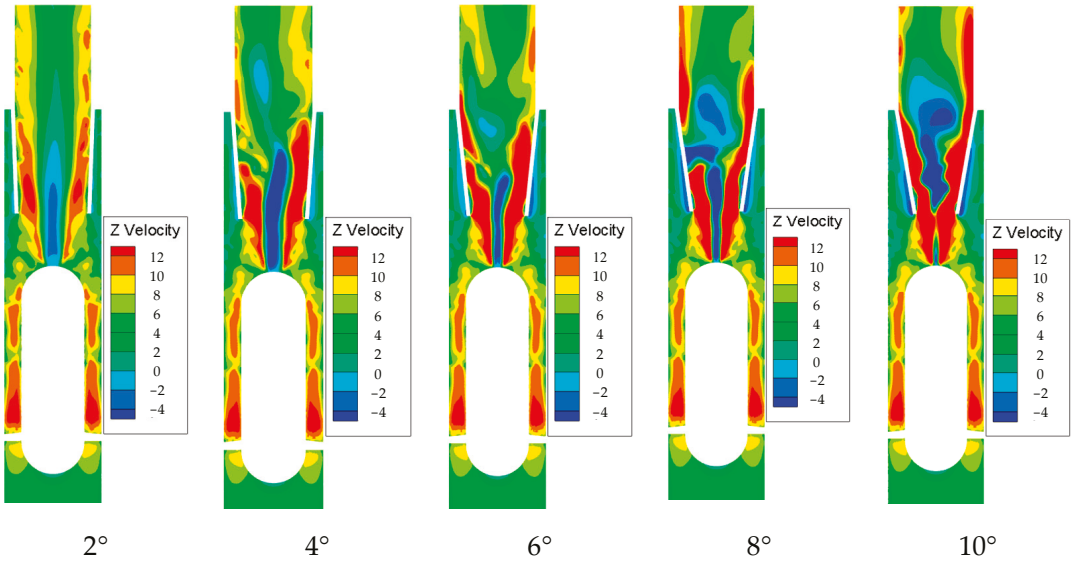
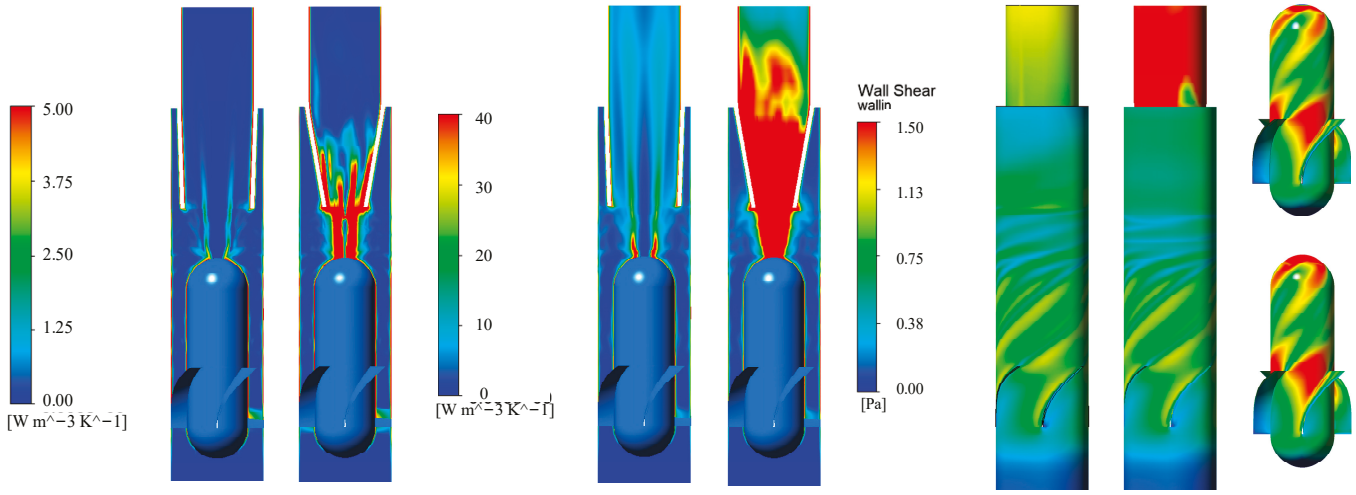


Figure 25. The axial velocity distribution with different outlet shape.

From Figure 26, one sees that as the exhaust pipe inclination angle increases, the fluid distribution at the blade and guide vane has little variation. However, an obvious acceleration zone and a recirculation zone appears at the rear end of the guide vane and exhaust pipe, leading to higher energy loss at this position. Correspondingly, the time-averaged entropy production, turbulent entropy production, and wall entropy production are increased from 2.4×10^{-4} W/K, 1.7×10^{-3} W/K, and 1.2×10^{-3} W/K to 3.9×10^{-4} W/K, 7.5×10^{-3} W/K, and 1.9×10^{-3} W/K.



(**a**) Average velocity entropy (**b**) Turbulent dissipation entropy (**c**) Wall shear

Figure 26. Entropy dissipation rates and wall shear at different exhaust pipe angles.

4. Conclusions

A study of the separation performance of the axial cyclone separator was performed using the RNG $k-\varepsilon$ model based on the entropy production model. The effects of blade number, blade outlet angle, and blade shape on the separation performance are considered. In addition, the influence of guide cone diameter, exhaust pipe diameter, and exhaust pipe shape are investigated.

Numerical simulation shows that a higher performance of an axial cyclone separator can be achieved by an appropriate structure design. Increasing blade number, decreasing blade outlet angle, and choosing the L blade form increase the separation efficiency. Furthermore, a larger guide cone diameter, a smaller exhaust pipe diameter, and a large exhaust pipe inclination angle can also improve the separation efficiency. All of these methods can lead to a larger pressure drop and entropy production due to a higher turbulence dissipation entropy and wall entropy, which is a main reason for energy loss. Our results provide new insights into the particle separation processes and give practical recommendations for improving the dust removal performance of industrial axial flow cyclone separators.

Author Contributions: Investigation and Writing the original version of the manuscript: Y.M.; Project administration, Supervision and Editing the manuscript: R.C. and L.C. All authors have read and agreed to the published version of the manuscript.

Funding: This research was funded by Fundação para a Ciência e Tecnologia grant number UIDB/00147/2020, UIDP/00147/2020, LA/P/0112/2020, PTDC/EEI-AUT/3522/2020, DSAIPA/CS/0086/2020.

Data Availability Statement: Data are unavailable due to privacy or ethical restrictions.

Acknowledgments: RC acknowledges the funding sources including the Base (UIDB/00147/2020) and Programmatic funding (UIDP/00147/2020) of the SYSTEC (Center for Systems and Technologies) and ARISE (Associate Laboratory for Advanced Production and Intelligent Systems, LA/P/0112/2020); as well as the projects RELIABLE (ref. PTDC/EEI-AUT/3522/2020) and MLDL-COV projects (ref. DSAIPA/CS/0086/2020) all funded by the Foundation for Science and Technology (FCT, Portugal). YL has been supported by the China Scholarship Council.

Conflicts of Interest: The authors declare no conflicts of interest.

References

1. Eckhoff, R.K.; Li, G. Industrial dust explosions. A brief review. *Appl. Sci.* **2021**, *11*, 1669. [CrossRef]
2. Zhou, X.; Li, X.; Cui, Z.; Wu, L.; Zhou, H.; Lu, X. Combustible wood dust explosions and impacts on environments and health-A review. *Environ. Res.* **2023**, *216*, 114658. [CrossRef] [PubMed]

3. Ray, S.K.; Khan, A.M.; Mohalik, N.K.; Mishra, D.; Mandal, S.; Pandey, J.K. Review of preventive and constructive measures for coal mine explosions: An Indian perspective. *Int. J. Min. Sci. Technol.* **2022**, *32*, 471–485. [CrossRef]
4. Afshar-Mohajer, N.; Wu, C.-Y.; Curtis, J.S.; Gaier, J.R. Review of dust transport and mitigation technologies in lunar and Martian atmospheres. *Adv. Space Res.* **2015**, *56*, 1222–1241. [CrossRef]
5. Shim, J.; Joe, Y.-H.; Park, H.-S. Influence of air injection nozzles on filter cleaning performance of pulse-jet bag filter. *Powder Technol.* **2017**, *322*, 250–257. [CrossRef]
6. Gu, Y.; Tian, E.; Xia, F.; Yu, T.; Afshari, A.; Mo, J. A new pin-to-plate corona discharger with clean air protection for particulate matter removal. *Energy Built Environ.* **2020**, *1*, 87–92. [CrossRef]
7. Han, N.; Wang, Y.; Su, B.-L. Unveiling oscillatory nature for sustainable fuel production. *Natl. Sci. Rev.* **2024**, nwae068. [CrossRef]
8. Liu, Y.; Cheng, Q.; Zhang, B.; Tian, F. Three-phase hydrocyclone separator–A review. *Chem. Eng. Res. Des.* **2015**, *100*, 554–560. [CrossRef]
9. Nassaj, O.R.; Toghraie, D.; Afrand, M. Effects of multi inlet guide channels on the performance of a cyclone separator. *Powder Technol.* **2019**, *356*, 353–372. [CrossRef]
10. Sakin, A.; Karagoz, I.; Avci, A. Performance analysis of axial and reverse flow cyclone separators. *Chem. Eng. Process. Process. Intensif.* **2019**, *144*, 107630. [CrossRef]
11. Wang, Z.; Zhang, X.; Liao, R.; Lei, Y.; Fang, Z. Study on Pressure Drop Characteristics of a Two-Stage Swirler Separator. *SPE Prod. Oper.* **2022**, *37*, 107–119. [CrossRef]
12. Liu, L.; Bai, B. Numerical study on swirling flow and separation performance of swirl vane separator. *Interfacial Phenom. Heat Transf.* **2017**, *5*, 9–21. [CrossRef]
13. Liu, L.; Bai, B. Scaling laws for gas–liquid flow in swirl vane separators. *Nucl. Eng. Des.* **2016**, *298*, 229–239. [CrossRef]
14. Matsubayashi, T.; Katono, K.; Hayashi, K.; Tomiyama, A. Effects of swirler shape on swirling annular flow in a gas–liquid separator. *Nucl. Eng. Des.* **2012**, *249*, 63–70. [CrossRef]
15. Huard, M.; Briens, C.; Berruti, F.; Gauthier, T.A. A review of rapid gas-solid separation techniques. *Int. J. Chem. React. Eng.* **2010**, *8*. [CrossRef]
16. Gao, S.; Liu, Y.; Fan, Y.; Lu, C. Experimental assessment on an integral two-stage demister of coupling cyclonic separation and granular bed filtration. *Powder Technol.* **2023**, *416*, 118178. [CrossRef]
17. Rocha, A.D.; Bannwart, A.C.; Ganzarolli, M.M. Numerical and experimental study of an axially induced swirling pipe flow. *Int. J. Heat Fluid Flow* **2015**, *53*, 81–90. [CrossRef]
18. Hsiao, T.-C.; Chen, D.-R.; Li, L.; Greenberg, P.; Street, K.W. Development of a multi-stage axial flow cyclone. *Aerosol Sci. Technol.* **2010**, *44*, 253–261. [CrossRef]
19. Mo, X.; Cai, R.; Huang, X.; Zhang, M.; Yang, H. The effects of wall friction and solid acceleration on the mal-distribution of gas–solid flow in double identical parallel cyclones. *Powder Technol.* **2015**, *286*, 471–477. [CrossRef]
20. Ali, H.; Plaza, F.; Mann, A. Flow visualization and modelling of scrubbing liquid flow patterns inside a centrifugal wet scrubber for improved design. *Chem. Eng. Sci.* **2017**, *173*, 98–109. [CrossRef]
21. Azadi, M.; Azadi, M.; Mohebbi, A. A CFD study of the effect of cyclone size on its performance parameters. *J. Hazard. Mater.* **2010**, *182*, 835–841. [CrossRef] [PubMed]
22. Li, Y.-J.; Wang, F-J. Numerical investigation of performance of an axial-flow pump with inducer. *J. Hydrodyn.* **2007**, *19*, 705–711. [CrossRef]
23. Mao, Y.; Pu, W.; Zhang, H.; Zhang, Q.; Song, Z.; Chen, K.; Han, D. Orthogonal experimental design of an axial flow cyclone separator. *Chem. Eng. Process. Process. Intensif.* **2019**, *144*, 107645. [CrossRef]
24. Kwak, D.; Kiris, C.; Kim, C.S. Computational challenges of viscous incompressible flows. *Comput. Fluids* **2005**, *34*, 283–299. [CrossRef]
25. Sung, G.; Kim, H.-U.; Shin, D.; Shin, W.G.; Kim, T. High efficiency axial wet cyclone air sampler. *Aerosol Air Qual. Res.* **2018**, *18*, 2529–2537. [CrossRef]
26. Tarpagkou, R.; Pantokratoras, A. CFD methodology for sedimentation tanks: The effect of secondary phase on fluid phase using DPM coupled calculations. *Appl. Math. Model.* **2013**, *37*, 3478–3494. [CrossRef]
27. Kock, F.; Herwig, H. Local entropy production in turbulent shear flows: A high-Reynolds number model with wall functions. *Int. J. Heat Mass Transf.* **2004**, *47*, 2205–2215. [CrossRef]
28. Hou, H.; Zhang, Y.; Li, Z.; Jiang, T.; Zhang, J.; Xu, C. Numerical analysis of entropy production on a LNG cryogenic submerged pump. *J. Nat. Gas Sci. Eng.* **2016**, *36*, 87–96. [CrossRef]
29. Delimont, J.M.; Murdock, M.K.; Ng, W.F.; Ekkad, S.V. Effect of Temperature on Microparticle Rebound Characteristics at Constant Impact Velocity—Part I. *J. Eng. Gas Turbines Power* **2015**, *137*, 112603. [CrossRef]

Disclaimer/Publisher's Note: The statements, opinions and data contained in all publications are solely those of the individual author(s) and contributor(s) and not of MDPI and/or the editor(s). MDPI and/or the editor(s) disclaim responsibility for any injury to people or property resulting from any ideas, methods, instructions or products referred to in the content.

inventions

MDPI

Article

Modeling and Optimization of Interior Ballistics within Pneumatic Underwater Launchers

Haixia Gong *, Zhuoran Ping, Fance Meng and Shuping Hou

College of Mechanical and Electrical Engineering, Harbin Engineering University, No. 145 Nantong Street, Nangang District, Harbin 150001, China; pingzhuoran@hrbeu.edu.cn (Z.P.); roymeng@hrbeu.edu.cn (F.M.); houshuping@hrbeu.edu.cn (S.H.)

* Correspondence: gonghaixia@hrbeu.edu.cn

Abstract: A new area of underwater equipment research focus is the use of underwater unmanned vehicles (UUVs) with launch mechanisms to deploy lightweight and small-sized robots for functions including communication, exploration, and detection. The internal ballistic mathematical model of the underwater launch system for small robots is established in this paper. The internal ballistic parameters and the robot displacement and velocity change rule over time are obtained. The optimization calculation of the crucial parameters to be determined by the particle swarm algorithm is completed. Following optimization, the gas cylinder's initial pressure is 2 MPa, its capacity is 30 L, its opening area is 9.683×10^{-5} m^2, and its opening time is 0.02 s. A numerical simulation is performed for the small robot's underwater launch process, based on the mathematical and physical model supplied by Fluent 2020 software. The results yield the robot's motion law and the properties of the flow field during the launch process. The purpose of the underwater launcher experiment is to determine the robot's motion characteristics. The accuracy of the theoretical model is confirmed by comparing and analyzing the numerical simulation results with the actual data.

Keywords: underwater launch; interior ballistic modeling; two-phase flow; dynamic grid; numerical simulation

1. Introductions

Unmanned underwater vehicles (UUVs) have been an increasingly important area of attention for underwater equipment development globally because of their compact size, low weight, extended operating range, and affordable use [1,2]. UUVs with autonomous attack capabilities outperform current underwater combat gear and can be used with an existing underwater assault armament. The challenge of launching a small, light UUV to perform detection and communication duties has emerged as a barrier to the creation of novel UUVs [3], necessitating launcher optimization.

Using a multiphase VOF model and a conventional k-epsilon turbulence model, Liu, HJ et al. [4] examined the gravitational impact of launch velocity on the hydrodynamic properties of a vertically launched underwater vehicle using an air curtain. Numerical simulations were used to examine the link between the undersea vehicle's form and launch velocity. Zhang, JH et al. [5] employed a visual experimental platform and a two-dimensional (2D) transient model to forecast the multiphase flow field during an underwater launch. Researchers studied how the flow field was affected by the muzzle velocity. The findings indicate that while the length of the pressure oscillations shortens, the highest peak pressure of the oscillations rises with increasing muzzle velocity. Gao, S. et al. [6] investigated the vortex structure and trajectory parameters of the wake of an underwater launch vehicle using an enhanced delayed separation vortex simulation, a VOF multiphase flow model, and an overlapping grid approach. A three-dimensional unsteady multiphase flow numerical model was established by Zhang, X. et al. [7] for the sealed firing

of an underwater gun. The VOF multiphase flow model was chosen and integrated with the Schnerr–Sauer cavitation model. The flow field at the muzzle of a 30 mm underwater gun with two tubes fired in parallel was numerically calculated, and the results were compared with those of a single-tube firing. Li, WN et al. [8] created a two-way fluid–structure-linked numerical simulation technique to examine the launch tube's flow properties and dynamic response. There has been additional discussion of the impact of launch depth and lateral flow. Three sample turbulence models—the Reynolds stress model (RSM), the large eddy simulation (LES) model, and the normalized group (RNG) k-epsilon model—were examined by Wang, YN et al. [9] in conjunction with VOF simulations. The volume of fluid (VOF) multiphase model was chosen to investigate bubble flow hydrodynamics in a top-submerged gunboat. In order to study the hydrodynamic characteristics and launch parameters during the whole launch process, Zhang, WQ et al. [10] created a computational fluid dynamics (CFD) model of the AUV launch tube system. The outcomes show how an underwater vehicle launch tube with a turbopump as the power input may operate with great efficiency. A platform for underwater air curtain firing simulation experiments has been built by Zhang, XW et al. [11], a mathematical–physical model of underwater air curtain launching was constructed, and the underwater artillery launching process was anticipated, based on the theory of gas jets in water and internal ballistics. Jayaprakash et al. [12] used a combination of experiments and CFD to study the evolution law of underwater bubble generation, expansion and contraction. For the study of launchers, Wei et al. [13] developed a scalable underwater launching system based on stress wave theory and split Hopkinson pressure rod technology, which can be used to study the cavitation phenomena and hydrodynamic properties of high-speed underwater objects.

As can be seen from the above, a majority of the study of underwater launching by academics has been on heavier weapons, including submarine-launched missiles and torpedoes, with very little research done on the process of micro-robotic underwater launching and associated launch systems. The majority of the present research includes the launch of missiles and torpedoes with dimensions typically between 500 and 2000 mm in diameter, 3500 and 13,000 mm in length, and 160 to 1500 kg in mass. This study's item is 400 mm in length and 100 mm in diameter. In light of the variables influencing internal ballistic performance, this work will create an internal ballistic model of a tiny robotic launcher and optimize the launcher parameters using the particle swarm technique.

2. Materials and Methods

The mini-robot model is displayed in Figure 1 in order to create the ballistic model and optimize the launch parameters within the pneumatic mini-robot launcher. It is around 400 mm in length and 100 mm in diameter.

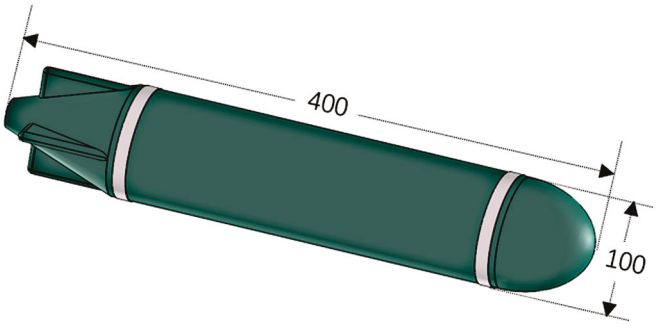


Figure 1. Schematic diagram of the small robot model.

Figure 2 illustrates the components and workings of the pneumatic launcher. The launch tube has a length of 800 mm and a radial clearance of 1 mm between its inner diameter and the robot's outer diameter. High-pressure gas from a gas cylinder is poured into the launch tube of the robot prior to launch. The launch command triggers the program-

controlled launch valve, which opens progressively as soon as the robot is launched. Through the launch valve, compressed gas from the high-pressure gas cylinder enters the launch tube. The gas expands and works to create thrust, which propels the robot and allows it to exit the tube at a fast enough speed.

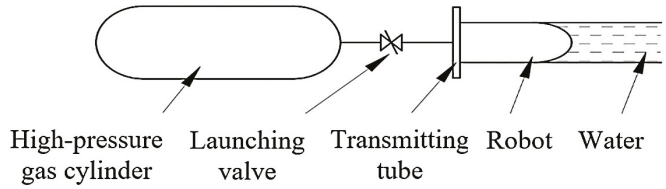


Figure 2. Structure and principle diagram of the pneumatic launcher.

It is assumed that there is no heat exchange between the emission device and the outside world because the physical and chemical properties of the working medium change very little, meaning that the pressure-specific heat capacity is constant. As a result, the emission process can be simplified to an adiabatic process, ignoring the effects of gas leakage, gas viscosity, and the gas potential and kinetic energy.

2.1. Numerical Model Study

2.1.1. High-Pressure Gas Source Deflation Model

The high-pressure cylinder model, based on fundamental assumptions, is comparable to the adiabatic outgassing of a high-pressure cylinder at a constant capacity during the mini-robot's launch. Assume that the high-pressure cylinder's starting values are V_B for the volume, P_B for the pressure, T_B for the temperature, and M_B for the mass of the gas. Since it is believed that the entire launch process is adiabatic, $\mathrm{d}Q = 0$, the launch valve is opened at that point. Since the high-pressure air bottle contains only the exhaust flux, there is no change in the flux entering, so $dm_B = -dm_i$, $\mathrm{d}m_i$ is the mass flow through the release valve [14]. Because the air bottle is in a fixed state, it does not work on the outside, so $\mathrm{d}W_B = 0$. In this case, the first law of thermodynamics can be written as:

$$h_q dm_B = dU. \tag{1}$$

The enthalpy of the gas in the instantaneous high-pressure cylinder is h_q in the equation above. Equation (1) can be expressed for an ideal gas as

$$c_p T_B dm_B = c_v T_B dm_B + c_v m_B dT_B. \tag{2}$$

Rectification leads to the temperature differential equation:

$$\frac{dT_B}{dt} = (\kappa - 1)\frac{T_B}{m_B}\frac{dm_B}{dt}. \tag{3}$$

Differentiating both sides of the equation of state for an ideal gas simultaneously to time yields:

$$\frac{dP_B}{dt}V_B + \frac{dV_B}{dt}P_B = \frac{dm_B}{dt}RT_B + \frac{dT_B}{dt}m_B R. \tag{4}$$

Since the gas cylinder is in a constant volume state, $dV_B/dt = 0$, connected to (1), (3), (4), the differential equation of pressure change can be obtained:

$$\frac{dP_B}{dt} = \kappa\frac{P_B}{m_B}\frac{dm_B}{dt}. \tag{5}$$

2.1.2. Launch Valve Model

According to the gas dynamics theory, the flow rate at the valve port can be expressed as follows [15]:

$$u = \sqrt{\frac{2k}{\kappa - 1}\frac{P_B}{\rho_B}\left[1 - \left(\frac{P_E}{P_B}\right)^{\frac{\kappa-1}{\kappa}}\right]}. \tag{6}$$

where P_B is the upstream pressure of the launch valve, ρ_B is the density of the gas at the launch valve inlet, and P_E is the downstream pressure of the launch valve.

The mass flow rate from the high-pressure gas cylinder through the launch valve can be written as [16]:

$$\frac{dm_i}{dt} = \varphi A_i \rho_i u_i. \tag{7}$$

where φ is the flow coefficient of the launch valve, which can be taken as 0.6~0.65 according to the empirical value, A_i is the instantaneous opening area of the launch valve, ρ_i is the gas density at the exit section of the launch valve, and u_i is the gas flow rate at the exit section of the launch valve.

Since the launching process is isentropic, the mass flows through the launching valve can be obtained from (6) and (7):

$$\frac{dm_i}{dt} = \varphi A_i P_E \sqrt{\frac{2\kappa}{\kappa-1}\frac{1}{RT_B}\left[\left(\frac{P_E}{P_B}\right)^{\frac{2}{\kappa}} - \left(\frac{P_E}{P_B}\right)^{\frac{\kappa+1}{\kappa}}\right]}. \tag{8}$$

where T_B represents the absolute temperature of the gas at the inlet of the launch valve.

According to the energy equation of an ideal gas adiabatic process, the critical pressure ratio can be obtained:

$$\beta = \frac{P_E}{P_B} = \left(\frac{2}{\kappa+1}\right)^{\frac{\kappa}{\kappa-1}} = 0.5283. \tag{9}$$

Bringing Equation (9) into (8), the mass flow rate of the sound velocity flow can be obtained as:

$$\frac{dm_i}{dt} = \varphi A_i P_E \sqrt{\frac{\kappa}{RT_B}\left(\frac{\kappa}{\kappa+1}\right)^{\frac{\kappa+1}{\kappa-1}}}. \tag{10}$$

2.1.3. Launching Tube Model

The robot is propelled to move when the launch valve is opened, allowing high-pressure gas to enter the launch tube. The thermal process of the gas in the launch tube can be represented by the first law of thermodynamics in the following way, assuming that there is no heat exchange between the gas and the tube during the launch process:

$$U_E = U_{E0} + H_i - W - W_h. \tag{11}$$

where U_E represents the internal energy of the gas in the launch tube of the launch process species, U_{E0} represents the internal energy of the gas in the launch tube before launch, H_i represents the enthalpy of the gas flowing into the launch tube through the launch valve, W represents the work done to propel the robot motion and W_h represents the work done to push the seawater between the launch tubes of the robot.

The temperature equation and pressure equation for the gas in the launch tube are:

$$T_E = \frac{U_E}{m_E c_v}, \tag{12}$$

$$P_E = \frac{m_E R T_E}{V_E}. \tag{13}$$

where m_E represents the mass of the gas in the launch tube; V_E represents the instantaneous volume of gas in the launch tube.

The enthalpy equation of the gas entering the tube through the launch valve is

$$\frac{dH_i}{dt} = c_p T_B \frac{dm_i}{dt}. \tag{14}$$

The rate of change of the gas mass in the launch tube is

$$\frac{dm_E}{dt} = \frac{dm_i}{dt}. \tag{15}$$

The volume flow rate of seawater out of the annular gap between the robot and the wall of the launch tube is

$$V_h = \varphi_j S_h \sqrt{\frac{2}{\rho_w}(P_E - P_h)}. \tag{16}$$

where φ_j represents the flow coefficient of seawater through the annular gap; S_h represents the annular clearance area between the launching tube and the robot; ρ_w stands for seawater density; P_h stands for seawater pressure at the launch tube port.

To propel the robot forward, the launch valve is opened, allowing gas to flow through it and into the launch tube. The launch tube's gas volume is continuously growing, and the rate at which this volume changes is as follows:

$$\frac{dV_E}{dt} = \varphi_j S_h \sqrt{\frac{2}{\rho_w}(P_E - P_h)} + Sv_d. \tag{17}$$

where S represents the cross-section area of the robot; v_d represents the motion speed of the robot.

2.1.4. Robot Motion Model in the Launch Tube

Five forces act on the mini-robot during the ejection process: the mini-robot's own gravity, the thrust of the gas inside the launch tube, the resistance of the water to the mini-robot's motion, the friction between the mini-robot and the launch tube, and the static pressure of the surrounding water environment. When the seawater flowing within the launch tube and the robot are examined collectively in accordance with Newton's second rule, the robot's equation of motion may be written as follows:

$$m_d \frac{dv_d}{dt} = S_i P_E - R_X, \tag{18}$$

$$R_X = \tfrac{1}{2} C_D \rho_W S {v_d}^2 + m(m_d g - F_d) + SP_h. \tag{19}$$

where m_d represents the total mass of the robot and the seawater moving in the tube; S_i represents the cross-sectional area of the inner diameter of the launching tube; R_X represents the resistance of the robot; C_D represents the resistance coefficient of the underwater movement of the robot; μ represents the friction coefficient between the robot and the launching tube; F_d stands for the buoyancy force on the robot.

During the motion, the power of the work done by the gas thrust on the robot is

$$\frac{dW}{dt} = SP_E v_d. \tag{20}$$

During the motion, the work done by extruding the seawater in the annular gap between the robot and the tube wall is

$$dW_h = \varphi_j S_h \sqrt{\frac{2}{\rho_w}} (P_E - P_h)^{\frac{3}{2}}. \tag{21}$$

2.2. Optimization Design

2.2.1. Optimization Objective Determination

The performance of the ejection system is mainly determined by the cylinder's initial pressure, volume, opening time, and opening area for a small robotic underwater launch system where the robot dimensions, the diameter of the launch cylinder, and the depth of the launch water are all essentially known. Consequently, the four aforementioned parameters have been selected for optimization.

2.2.2. Optimization Parameters' Determination

The chosen range of the optimization parameters will have a greater influence on the optimization process. A selection range that is too short may restrict the local optimum and yield less than ideal outcomes. A selection range that is too big can readily create an excessive number of incorrect solutions, leading to a low optimization efficiency. The range of parameters that need to be optimized for this inquiry is shown in Table 1.

Table 1. Value ranges of parameters to be optimized.

Parameter to Be Optimized	Value Rang
Initial cylinder pressure P_B	1.5–3 MPa
Cylinder volume V_B	20–50 L
Launch valve opening time t_i	0.02–0.05 s
Launch valve opening area A_i	1.96625×10^{-5}–1.76625×10^{-4} m^2

2.2.3. Objective Function Determination

To maximize the ballistic parameters in this research, the little robot has to escape the launch tube at a high exit velocity with the least amount of acceleration possible. As a result, the objective function is as follows:

$$minf(x_i) = v_d - \alpha \frac{dv_d}{dt}. \tag{22}$$

where v_d represents the robot's moving speed; α represents the correction coefficient, which is set to 0.1.

2.2.4. Optimization Process

The particles in the particle swarm algorithm are influenced by themselves and other particles in the population in the optimization process to complete the search for the optimal solution, and the specific steps can be carried out as follows:

1. Initialize the particle swarm, and the parameters to be set are the learning factors c_1 and c_2, the maximum evolutionary generation G and the current evolutionary generation g. Randomly generate *size* particles, the initial population position and motion speed; in the solution space, the population size is denoted by *size*, each particle is a solution in the space, the position of the i-th $(1 \le i \le size)$ particle in the space is denoted by x_i, and the velocity of the particle is denoted by v_i. The individual extreme value of the i-th particle from the beginning to the current iteration search is denoted by p_i, and the optimal solution of the whole population is denoted by *bests*;
2. The initial position of each particle in the population is treated as an individual extreme value, and the fitness value $f(x_i)$ of each particle is calculated according to the objective function, in which the current optimal position of the population is found;
3. To prevent the particles from falling into a local optimum, the velocity and position of the particles are updated using the equation

$$v_i^k = wv_i^{k-1} + c_1 r_1 (p_i^{k-1} - x_i^{k-1}) + c_2 r_2 (bests_i^{k-1} - x_i^{k-1}), \tag{23}$$

$$x_i^k = x_i^{k-1} + v_i^{k-1}. \tag{24}$$

The inertia weight w, which is non-negative in the equation, is primarily responsible for modifying the query range of the solution space; for the two stochastic functions r_1 and r_2, the range of values is [0,1], $k = 1, 2, \ldots, G$, $i = 1, 2, \ldots, size$, and the learning factor is c_1 and c_2.

4. Compare the fitness value $f(x_i)$ of the particle at this moment with the previous extreme value p_i of the particle, and if $f(x_i)$ is better than p_i, replace p_i with the current value $f(x_i)$ as the new individual extreme value and update the position of the particle. Compare the fitness value $f(x_i)$ of the particle at this moment with the optimal value *bests* of the population, and if $f(x_i)$ is better than *bests*, then replace the current *bests* with the optimal value $f(x_i)$ of the population to become the new fitness value and update the global optimal solution of the population;
5. To judge whether the algorithm satisfies the termination condition, if it does, it stops running and also outputs the optimal result; if it does not satisfy the termination condition, it takes $k = k + 1$ and returns to step (3) to continue its iteration; the

final termination condition of the algorithm is to reach the set maximum number of evolutionary generations or the result of the evaluation is lower than the set accuracy.

The computational flow of the particle swarm algorithm is shown in Figure 3.

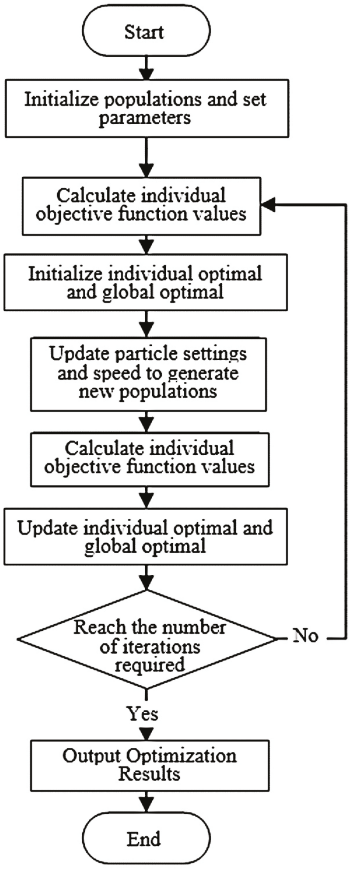


Figure 3. Flow chart of particle swarm optimization.

2.3. Simulation and Experimentation

2.3.1. VOF Method

A two-dimensional axisymmetric internal ballistic model was developed in order to precisely ascertain the changes in the flow field and velocity of the tiny robotic underwater launcher during horizontal launching. The computational fluid dynamics (CFD) analysis software Fluent 2020 was utilized to simulate the robot's exit from the cylinder. Due to the combined flow of high-pressure gas and water during the underwater launch process, there is a significant interaction between both phases, resulting in a strongly coupled nonlinear process. This work chooses the realizable turbulence model and the VOF multiphase flow model to represent the relative motion and development of the free interface between the gas and water phases, taking into account the flow characteristics in underwater launches. Furthermore, a six-degrees-of-freedom model and dynamic grid technology are used to characterize the different types of motion displayed by tiny robots.

The VOF approach tracks the interface in the simplified tiny robot underwater launch issue, which is a gas–liquid two-phase flow problem. The following is the governing volume fraction equation:

$$\frac{\partial \alpha_l}{\partial t} + \vec{v} \cdot \nabla \alpha_l = 0. \tag{25}$$

The VOF model tracks the interface between the gas–liquid phase by solving the continuous equation of the volume fraction of the liquid phase. Without considering the phase transition, there is no mass source term in the liquid phase, the right end of the

equation is zero, and the calculation of the volume fraction should follow the following restrictions:

$$\alpha_g + \alpha_l = 1. \tag{26}$$

where α_g is the gas phase volume fraction; α_l is the liquid phase volume fraction.

The continuity equation is

$$\frac{\partial \rho}{\partial t} + \frac{\partial}{\partial x_i}(\rho u_i) = 0. \tag{27}$$

Regarding the momentum equation, the VOF model computes a single momentum equation for the entire basin, the results of which are shared by the phases:

$$\frac{\partial}{\partial t}(\rho u_i) + \frac{\partial}{\partial x_j}(\rho u_i u_j) = \frac{\partial p}{\partial x_i} + \frac{\partial}{\partial x_j}\left[\mu\left(\frac{\partial u_i}{\partial x_j} + \frac{\partial u_j}{\partial x_i}\right)\right] + \frac{\partial}{\partial x_i}\left(-\frac{2}{3}\mu\nabla \cdot V\right). \tag{28}$$

where ρ is the density of the mixed phase; ϕ is the material parameter, and $\phi = \alpha_g\phi_g + \alpha_l\phi_l$ is obtained by the weighted average of the volume fraction (ϕ can be ρ, μ, etc.)

The energy equation is as follows:

$$\frac{\partial}{\partial t}(\rho E) + \frac{\partial}{\partial x_j}\left[u_j(\rho E + p)\right] = \frac{\partial}{\partial x_j}\left(k_{eff}\frac{\partial T}{\partial x_j}\right). \tag{29}$$

where: E is the mass average energy of each phase; T is the mass average temperature of each phase, $\varphi = \frac{\alpha_l\rho_l\varphi_l + \alpha_g\rho_g\varphi_g}{\alpha_l\rho_l + \alpha_g\rho_g}$ (φ is E or T); k_{eff} is the mass average energy effective thermal conductivity of each phase ($k + k_t$); k_t is the turbulence thermal conductivity, defined by the turbulence model used.

The equation of state can be shown as

$$\rho_q = \begin{cases} p/RT, & q = g \\ \text{const} & q = l \end{cases}. \tag{30}$$

The VOF model allows only one phase to be defined as compressible: the gas phase as compressible, and the liquid phase as incompressible.

Regarding interpolation near the interface: By calculating the relative flow and diffusion flux of the flow over the control volume's surface, the fluid software balances the source term of the control volume itself. In the VOF model, the surface flow may be computed using four different methods: geometric reconstruction, material acceptance, the Euler explicit, and the Euler implicit. The first two approaches employ distinct techniques to address the interpolation problem of elements surrounding various intersecting interfaces, whereas the remaining two approaches handle the same interpolation method for single-phase or polyphase elements, i.e., by utilizing the conventional first-order upwind, second-order upwind, or QUICK format. The most precise geo-metric reconstruction technique, appropriate for any unstructured mesh, is used in this research.

Regarding surface tension and avoid adhesion: The interphase surface tension may be reproduced when utilizing the VOF model to simulate multiphase flow problems by adjusting the contact angle that the fluid and the wall generate. It is caused by the surface-only gravitational force between the fluid microclusters, which reduces free energy by shrinking the interface's area. The source term in the momentum equation of the continuum surface force (CSF) model is produced by the extra surface tension encountered during the VOF model's simulation. This equation is as follows:

$$F_{vol} = \sum_{i<j}\sigma_{i,j}\frac{\alpha_i\rho_i\kappa_j\nabla\alpha_j + \alpha_j\rho_j\kappa_i\nabla\alpha_i}{\frac{1}{2}(\rho_i + \rho_j)}. \tag{31}$$

where: κ is the surface curvature.

$$\kappa = \nabla \cdot \frac{\nabla \alpha_i}{|\nabla \alpha_i|}. \tag{32}$$

The effect of surface tension is determined by Reynolds number Re and capillary number Ca or Weber number We. The use of the capillary number and the Weber number depends on the size of the Reynolds number, when $Re << 1$, the capillary number needs to be used, and vice versa. The two are defined as follows:

$$Ca = \frac{\mu U}{\sigma}, \tag{33}$$

$$We = \frac{\sigma}{\rho L U^2}. \tag{34}$$

where U is the free flow speed, when $Ca << 1$ or $We >> 1$, the surface tension can be ignored.

The VOF model is limited by the boundary condition of the wall itself, and the normal direction of the unit near the wall can be adjusted by setting the proper contact angle of the wall, so as to reduce the boundary limit. The surface normal of the actual element near the wall is:

$$n = n_w \cos\theta_w + \hat{t}_w \sin\theta_w. \tag{35}$$

where: θ_w is the wall contact angle; n_w is the unit normal vector of the wall surface; $\hat{t}_w$ is the unit tangent vector of the wall.

2.3.2. Turbulence Model

There is a lot of turbulent flow when a little robot is being launched underwater out of the tube. Currently, direct numerical simulation (DNS), large eddy simulation (LES), and Reynolds time mean numerical simulation (RANS) are the three most widely utilized numerical simulation techniques for turbulence.

By referring to the relevant literature in the field of underwater launching and combining with previous calculation experience, this paper adopts the realizable $k-\varepsilon$ model of the vortex viscosity model in the RANS method for numerical calculation. The two transport equations that constitute the realizable $k-\varepsilon$ model are as follows:

$$\frac{\partial(\rho k)}{\partial t} + \frac{\partial(\rho u_j k)}{\partial x_j} = \frac{\partial}{\partial x_j}\left[\left(\mu + \frac{\mu_t}{\sigma_k}\right)\frac{\partial k}{\partial x_j}\right] + G_k + G_b - \rho\varepsilon - Y_M + S_k, \tag{36}$$

$$\frac{\partial(\rho \varepsilon)}{\partial t} + \frac{\partial(\rho \varepsilon u_j)}{\partial x_j} = \frac{\partial}{\partial x_j}\left[\left(\mu + \frac{\mu_t}{\sigma_\varepsilon}\right)\frac{\partial \varepsilon}{\partial x_j}\right] + \rho C_1 S\varepsilon - \rho C_2 \frac{\varepsilon^2}{k + \sqrt{v\varepsilon}} + C_{1\varepsilon}\frac{\varepsilon}{k} C_{3\varepsilon} G_b + S_\varepsilon. \tag{37}$$

where: G_k is the turbulence's kinetic energy generated by the laminar flow velocity gradient; G_b is the turbulence's kinetic energy caused by buoyancy; Y_M is the fluctuation caused by turbulent pulsation; σ_k is the turbulent Prandtl number of the equation; σ_ε is the turbulent Prandtl number of the equation; S_k and S_ε are the source items.

$C_1 = \max[0.43, \frac{\eta}{\eta+5}]$, $\eta = \frac{S_k}{\varepsilon}$, and usually $C_{1\varepsilon} = 1.44$, $C_2 = 1.9$, $\sigma_k = 1.0$, and $\sigma_\varepsilon = 1.2$.

The turbulent viscosity is expressed as follows:

$$\mu_t = \rho C_\mu \frac{k^2}{\varepsilon}, \tag{38}$$

$$C_\mu = \frac{1}{A_0 + A_S k U^*/\varepsilon}. \tag{39}$$

In the formula, $A_0 = 4.04$, $A_s = \sqrt{6}\cos\phi$, $\phi = \frac{1}{3}\arccos(\sqrt{6}W)$, $W = \frac{S_{i,j}S_{j,k}S_{k,j}}{\left(S_{i,j}S_{i,j}\right)^{3/2}}$, and $S_{i,j} = \frac{1}{2}\left(\frac{\partial u_j}{\partial x_i} + \frac{\partial u_i}{\partial x_j}\right)$, $U^* = \sqrt{S_{i,j}S_{i,j}}$.

2.3.3. Dynamic Grid Technology

In this research, we examine a tiny robot's underwater launch procedure. For the purpose of computation, a simple static grid technique is not appropriate since the grid form in the model calculation domain varies as the robot moves. We can opt to employ the moving grid approach to solve this type of flow problem since the geometry of the grid in the computational domain varies as the boundary moves. In order to use the dynamic grid model, we must first define the moving boundary's motion mode and the grid area that it is connected to. The boundary function and UDF are included in the definition of the boundary's motion mode. The motion mode of the boundary is determined by the Fluent program based on the robot's motion law in the flow field and the size of the selected time step; therefore, the model used in this work does not need to specify it beforehand. Based on the computation, Fluent anticipates where the motion boundary will be at the next instant and checks to see if the grid height barrier has been met. The mesh close to the moving border is either merged or divided based on the decision conditions.

For dynamic mesh models, Fluent offers three mesh-updating techniques: local remeshing, dynamic layering, and spring-based smoothing. Only the axial motion of the robot—which can be thought of as the impact of the grid boundary change on the flow field of the multiphase flow—is taken into account for the modeling of the unsteady flow field of the tiny robot in the underwater extraction process covered in this work. Thus, in order to achieve the robot movement, the dynamic stratification approach and the local reconstruction method are used.

Regarding the dynamic stratification method: The dynamic layering method is used to merge or split the grid layers according to the change in the height of the grid layers near the moving boundary. The relationship between stretching and compression is as follows:

$$h_{\max} > (1 + \alpha_s)h_0, \tag{40}$$

$$h_{\min} < \alpha_c h_0. \tag{41}$$

where: h_0 is the height of the ideal mesh cell; α_s is the splitting factor; α_c is the merge factor.

Regarding the local reconstruction method: The fairing approach may be used to update unstructured mesh. The fairing approach may lower the mesh quality and cause a negative volume and simulation error termination if the moving boundary advances too far during the mesh updating procedure. A mesh reconstruction method is created to increase the dynamic mesh's application span. When the dynamic mesh's moving border extends beyond a certain point, causing significant distortion to the mesh, Fluent 2020 software will regenerate both the highly deformed and the surrounding mesh. The freshly produced mesh will be utilized if the regenerated mesh can satisfy the calculation's quality and size criteria. The freshly created grid is abandoned if it does not match the specifications.

2.3.4. Multiphase Flow Field Modeling

The model has to be suitably streamlined in order to account for the computation time while still guaranteeing calculation accuracy. Figure 4 depicts the simplified calculation model.

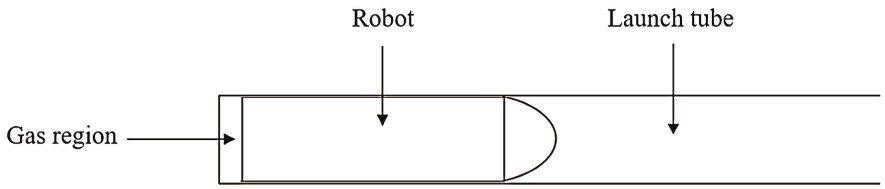


Figure 4. Simplified calculation model.

The independence of the meshes must be investigated to eliminate the meshes' impact on the simulation results and minimize the mistakes brought about by meshes in numerical simulations. Three grid numbers—Grid A (270,000), Grid B (390,000), and Grid C

(550,000)—have their respective outcomes chosen for comparative study in this work. The findings displayed in Figure 5a,b are the consequence of choosing the first three outcomes for simulation till convergence and post-processing analysis. The data demonstrate the significant discrepancy of around 8% between the computed outcomes of Grid A and Grid B. Between Grid B and Grid C, the highest error is negligible—it is not greater than 3%. Grid B can be used in the final numerical computation to increase the calculation speed and produce numerical results that are precise enough.

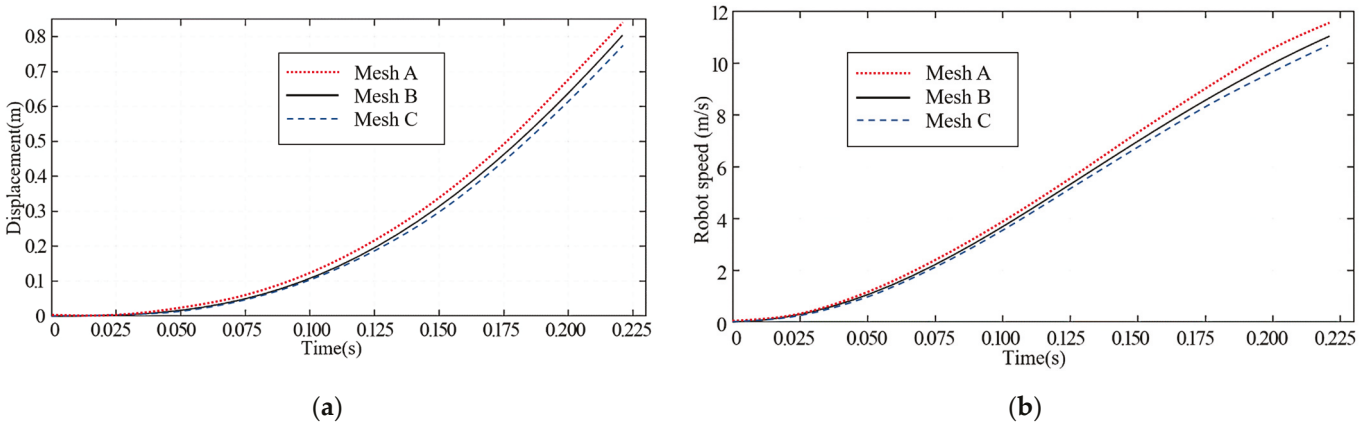


Figure 5. Grid independence verification. (**a**) Displacement–time curves for the different meshes; (**b**) Velocity–time curves for the meshes.

Both the robot and the launch tube exhibit symmetry, as shown by the simplified computational model in Figure 4. A two-dimensional axisymmetric model may be utilized to decrease the amount of computation and increase computational efficiency. The simulation in this study disregards gravity, and the robot's head, tail, and the launch tube wall are all set as wall boundaries, with the walls being adopted as adiabatic and non-slip walls; the external boundary of the launch tube and the boundary of the water area are all set as pressure outlets; the head and tail of the robot are designated as the motion limits, and the software's 6DOF model is used to determine the robot's axis' direction. Since this study uses the sub-regional grid division approach, in order to achieve data exchange between the nodes, the boundaries of the moving and stationary waters must be specified as interface pairs. Figure 6 illustrates the specific boundary conditions that are specified.

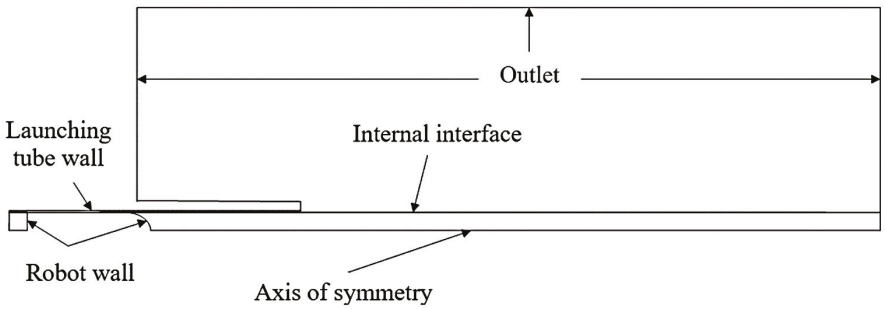


Figure 6. Boundary condition setting.

2.3.5. Experimental System

A robot, a gas supply system, a launch support system, a valve control system, and a high-speed camera image capture system make up the robotic underwater ejection experiment system. Figure 7 displays the schematic diagram of the launch's experimental setup.

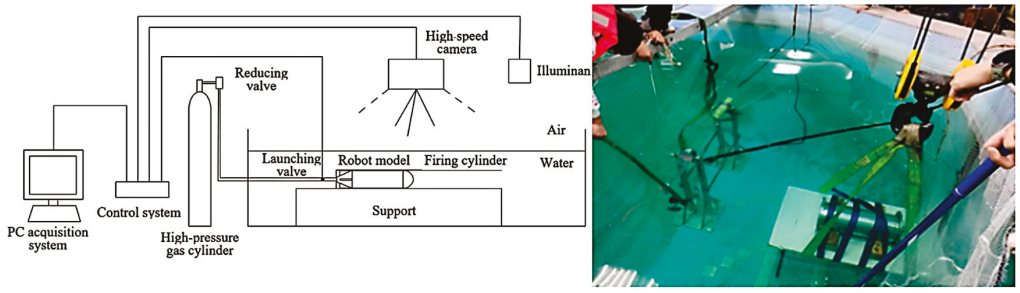


Figure 7. Schematic layout of the launcher experiment.

3. Results and Discussion

3.1. Optimization Results and Analysis

Numerical solution software is used to program the particle swarm method's mathematical model and the goal function. In order to determine the ideal settings for the robot ejection mechanism, the particle swarm method is applied, setting the primary parameters of the algorithm. Examples include the particle population size N, the inertia weight w, the maximum velocity v_{max}, learning factors c_1 and c_2, and the maximum number of evolutionary generations G. While N often is a number between 20 and 100, this study uses N = 50. The inertia weight w in the particle swarm algorithm primarily regulates the algorithm's development and exploration; its value's magnitude signifies the extent to which the speed of the preceding particle generation influenced the current speed; thus, the inertia weight's magnitude should be selected judiciously. The method may enter a local optimum during runtime if the numbers are irrational, which would impair the search function. This study uses w = 0.8 as the inertia weight. The method's search capabilities may be impacted if the value is not acceptable and causes the algorithm to run into a local optimum. The particle's step duration is primarily restricted to an individual optimum search by the learning factor c_1, and to a global optimal search by the learning factor c_2, both of which typically take values between 0 and 4. In this investigation, $c_1 = c_2 = 2$ is used. The value of the particle's moving velocity spans between -v_{max} and v_{max}, and the maximum velocity v_{max} = 0.2 is used in this study. v_{max} shows the maximum velocity of the particles in the population traveling in space. The program is said to finish after a certain number of iterations, denoted by the maximum number of iterations G, and the optimal answer in the final computation result is produced. The particle swarm optimization algorithm's maximum evolutionary algebra, G = 500, is chosen for this work. Table 2 displays the optimum parameters that were determined by applying the particle swarm technique.

Table 2. Parameter values after optimization.

Parameter to Be Optimized	Numerical Value
Initial cylinder pressure P_B	2 MPa
Gas cylinder volume V_B	30 L
Launch valve opening time t_i	0.02 s
Launch valve opening area A_i	9.683×10^{-5} m^2

The robot ejection system's mathematical model of ballistic trajectory is fitted with the parameters optimized by the particle swarm algorithm, as illustrated in Figure 8. The optimized initial pressure of the gas cylinder is altered from the initial assumption of 2.5 MPa to 2 MPa, and the cylinder's residual pressures at the conclusion of the launch are 2.36 MPa and 1.80 MPa, respectively. Following optimization, the launch time is down to 0.2 s, which is a little faster than the pre-optimization of 0.202 s. The pre-optimization of 0.202 s is somewhat longer than the launching time of 0.2 s, which is also significantly shorter. The launch time is 0.2 s after optimization, which is somewhat less than the 0.202 s before optimization. Simultaneously, the pressure change curve of the cylinder experiences a numerical decline sooner than before the optimization due to the launch valve's opening

time being 0.02 s after optimization. Due to the shortened launch valve opening time, the optimized launch cylinder chamber pressure curve is higher than the pre-optimization one in the early stage and reaches the peak value more quickly. The peak launch tube chamber pressure after optimization has a slight decrease, with the peak value changing from 0.5 MPa to 0.48 MPa, the decrease being 4%. Because of the launch valve's quicker opening after optimization, the optimized robot starts up earlier than the pre-optimized robot did. The improved robot's exit velocity marginally drops from 12.33 m/s before optimization to 12 m/s as a result of the gas cylinder's starting pressure being reduced, and its internal ballistic performance improves when compared to the pre-optimization.

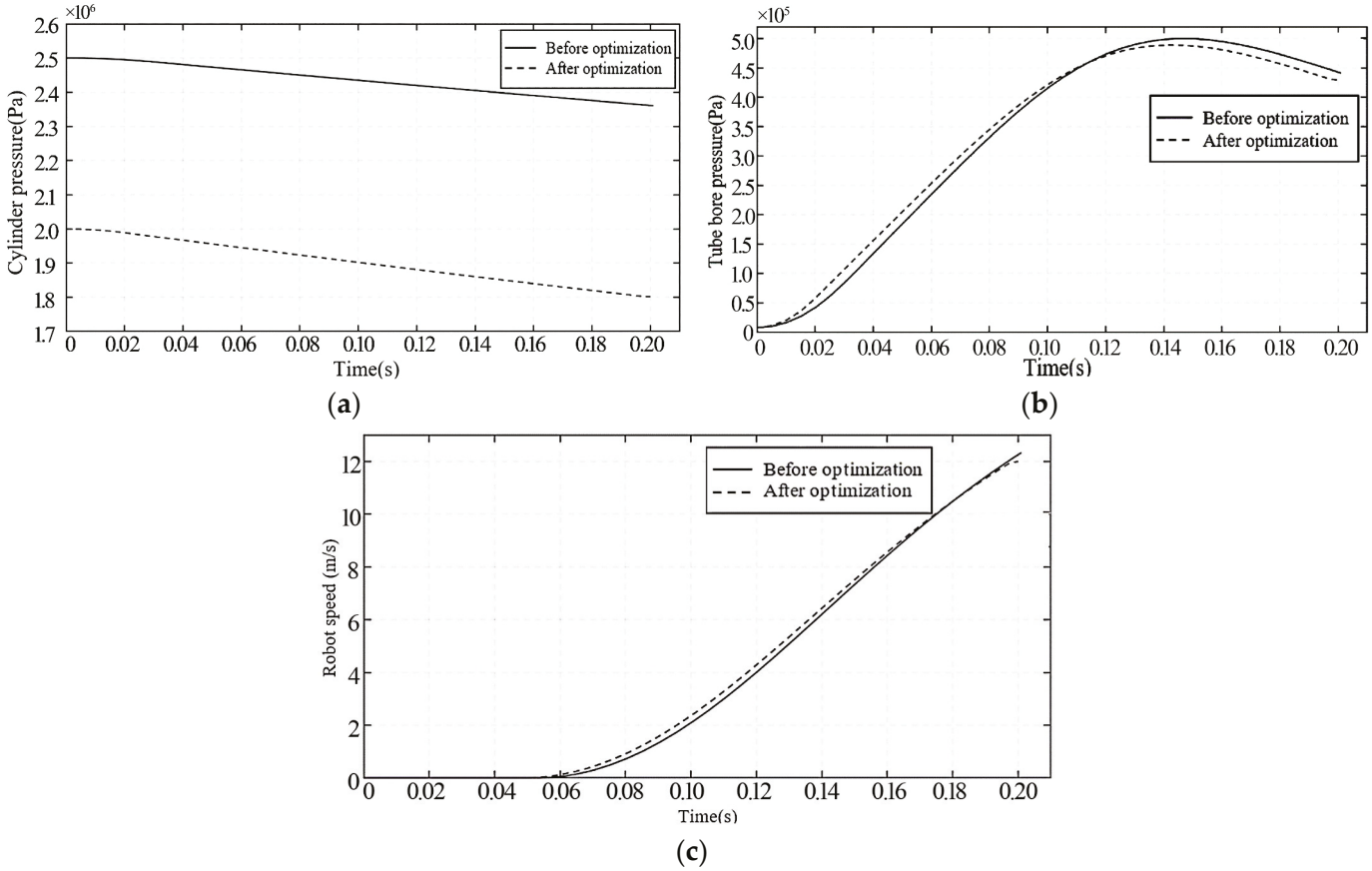


Figure 8. Simulation curve. (**a**) Pressure curve of high pressure cylinder with time; (**b**) Pressure curve of firing tube chamber with time; (**c**) Robot velocity curve with time.

3.2. Simulation Analysis

3.2.1. Flow Field Characteristic Analysis

The gas–water phase diagram of the robot exit tube section is shown in Figure 9, and the flow field parameters for the robot's underwater horizontal launch were obtained using numerical simulation.

As the robot emerges from the tube underwater, the sealing ring at its tail limits the flow of high-pressure gas at the rear of the launch tube. In order to accomplish its task, the high-pressure gas expands, applying a propulsive force to the robot and forcing it to exit the tube. The high-pressure gas at the bottom flows out of the gap between the robot and the launch tube before the robot does because of the gap, and because the high-pressure gas is moving faster than the robot, it exits the launch tube before the robot does, creating the gas jet phenomenon at the mouth of the launch tube barrel. As seen in Figure 9, from (a) to (c), the jets are expelled in two distinct gas stream forms rather than being collected together as would be expected for a three-dimensional structure, which would be ejected in the shape of a ring. The annular jet that first emerges from the launch tube progressively separates

from the rear gas as time goes on due to the combined effects of the robot's motion and the external water pressure. The robot squeezes the gas passing through the gap just before it leaves the tube, creating vortices to the sides and back of the launch tube mouth, as shown in Figure 9d–f. The gas mass has symmetry since the simulation is predicated based on the robot being in an environment with a uniform flow field. As seen in Figure 9g,h, when the robot emerges fully from the tube, high-pressure gas pours out of the tube, causing the gas mass to rapidly expand and be stretched by the robot. The gas mass also wraps around the robot together to the front during the robot's escape from the tube.

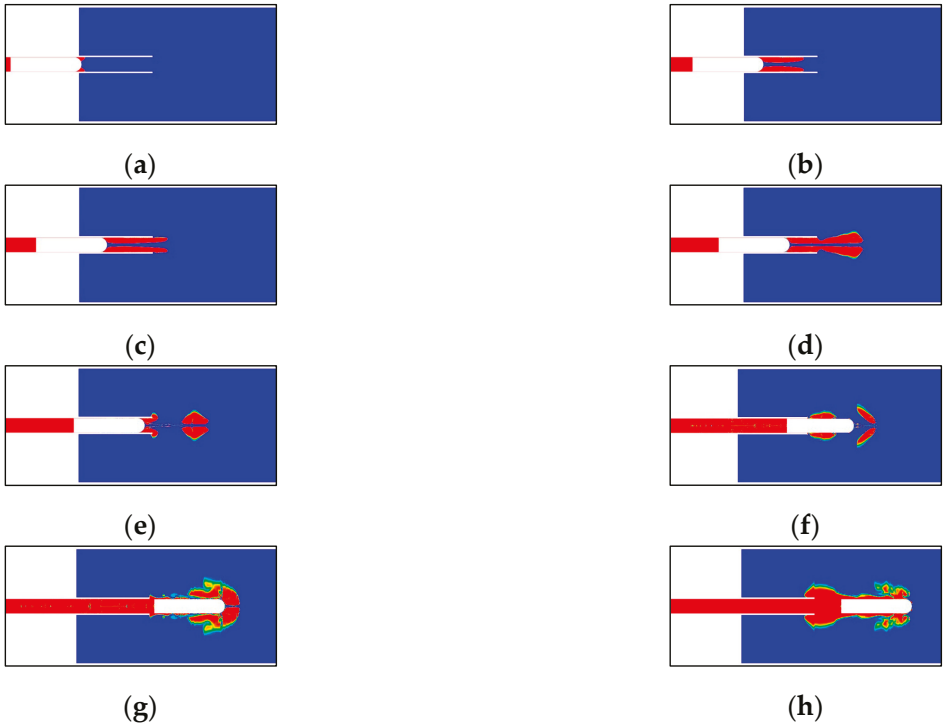


Figure 9. Phase diagram of the robot-piping process. (**a**) Pre-launch period; (**b**) Pre-launch period; (**c**) Pre-launch period; (**d**) Mid-launch period; (**e**) Mid-launch period; (**f**) Mid-launch period; (**g**) Post-launch period; (**h**) Post-launch period.

3.2.2. Internal Ballistic Characteristics Analysis

The software was used to organize and analyze the two-dimensional axisymmetric numerical simulation data of the robot's underwater launch. The values of the robot's motion displacement and velocity at each moment were then derived using UDF, and the aforementioned values were plotted against time.

It is evident from the robot displacement graphs in Figure 10 that the robot's displacement with respect to time is roughly quadratic. The robot's displacement increases more slowly in the beginning and faster in the later stages. This is because the robot moves more slowly in the first stage and faster in the later stages, which causes the displacement to increase more largely. It takes the robot 0.22 s to exit the launch tube. When the robot initially starts moving, its velocity is almost linear. After an acceleration duration of 0.22 s, the robot may emerge from the tube at 11 m/s. The robot may smoothly leave the tube under these operating conditions since the velocity value is somewhat less than that found by solving the internal ballistic equation but still larger than the design velocity.

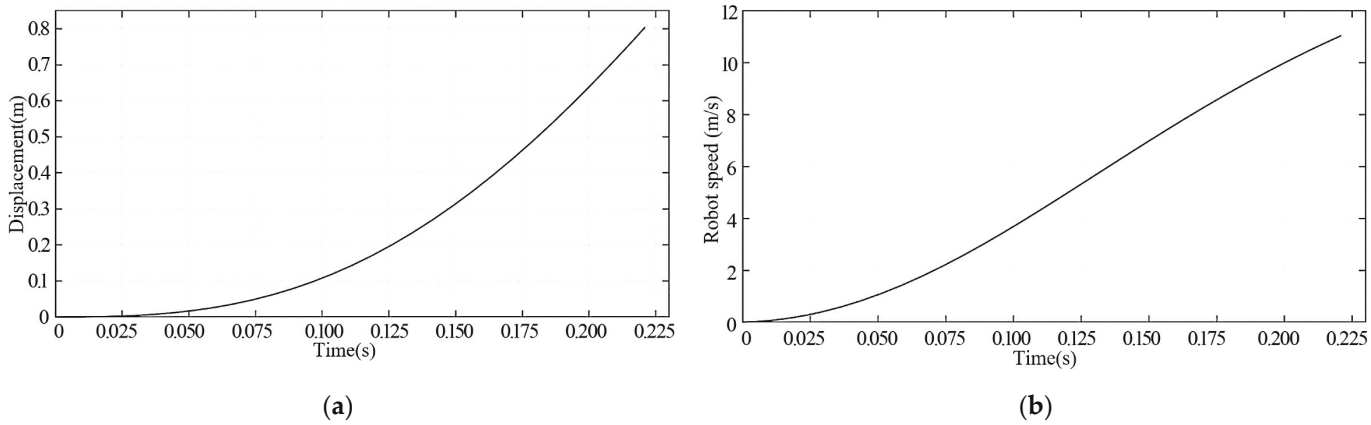


Figure 10. Simulation curve. (**a**) Robot displacement curve; (**b**) Robot velocity curve.

3.3. Experimental Analysis

3.3.1. Multi-Phase Flow Field Characterization Analysis

This experiment primarily aims to investigate the properties of the robot after it emerges from the tube during the horizontal launch process. Two robots are launched for the test, and each robot is subjected to a different gas source pressure. The high-speed camera used in this experiment is the VE0710L. The full frame is 1280 × 800 pixels with 1500 frames. Figure 11 shows the flow field change characteristics of the robot's out-of-the-tube process taken by the high-speed camera. The pressure of the cylinder outlet is set to 2 MPa by utilizing the pressure reducer.

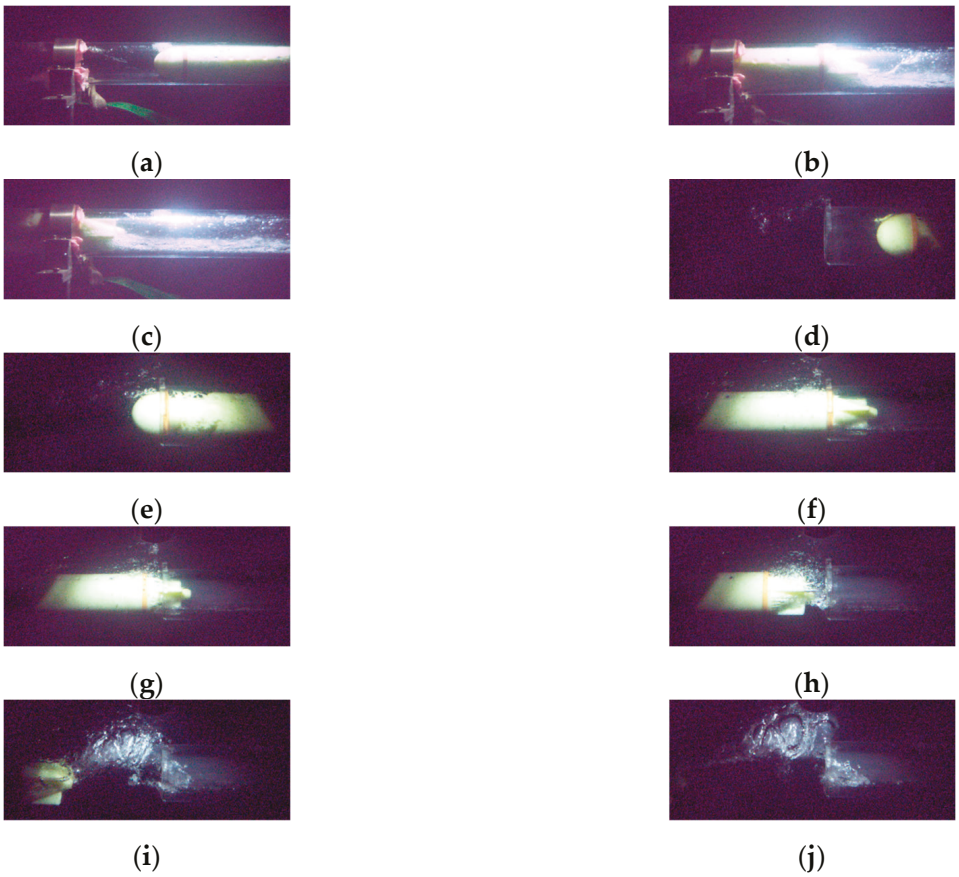


Figure 11. Phase diagram of the robot-piping process. (**a**) Pre-launch period; (**b**) Pre-launch period; (**c**) Pre-launch period; (**d**) Mid-launch period; (**e**) Mid-launch period; (**f**) Mid-launch period; (**g**) Mid-launch period; (**h**) Post-launch period; (**i**) Post-launch period; (**j**) Post-launch period.

When the launch valve is opened, high-pressure gas from the cylinder enters the launch tube through the gas tube and propels the robot into the water. At the start of the launch, as shown in Figure 11, from (a) to (c), the robot and the water in front of its head work together to push forward in the wake of the gas. Figure 11d,e show how the gas exits the launch tube before the robot and forms bubbles at the barrel's mouth location. Because there is not much jet flow at this time, the bubbles are mostly small and their morphology is changing very little; the early bubbles are primarily axial in development; as time goes on, the rear gas continues to flow out, and the bubbles start to develop radially due to the influence of buoyancy and the blocking effect of the water. The robot's initial seal ring movement out of the launch tube is shown in Figure 11e,f, where the number of bubbles greatly increased and a portion of the bubbles moved with the robot ahead; the robot's second seal ring movement is shown in Figure 11g–j. The robot's second seal ring moves out of the launch tube, causing a massive amount of gas to shoot out in the form of a cylindrical jet. The bubbles continue to expand and increase in volume, and the buoyancy force causes the bubbles' position to rise. At the same time, the water flow disturbs the bubbles and deflects them. The robot's forward speed causes the bubble to constantly elongate, drastically alter its shape, and cause the phenomena known as neck shrinkage. It is also evident in Figure 11j that when the launch valve is closed and the gas in the launch tube exits, a tiny quantity of water rushes backward into the launch tube.

3.3.2. Robot Motion Characteristic Analysis

The high-resolution picture acquisition system's data is processed by numerical computation software to ascertain the hydrodynamic characteristics of the robot's horizontal launch.

Figure 12 shows that when the launch valve is opened, the robot initially stays motionless. After that, its velocity progressively increases from 0 to a peak that is reached when it exits the launch tube. In the first phase, the pressure within the launch tube is low, and the velocity grows more slowly. In the second phase, the pressure inside the launch tube is steady, and the velocity increases almost linearly, peaking at 7.3 m/s in 0.305 s. The robot displacement is parabolic when the launch valve is opened; it first stays constant, increases gradually, and then steadily increases after a certain amount of time. This is due to the launch tube's initially low and unstable pressure, which causes the robot to move as soon as it overcomes its resistance and accelerate as the pressure inside the tube rises.

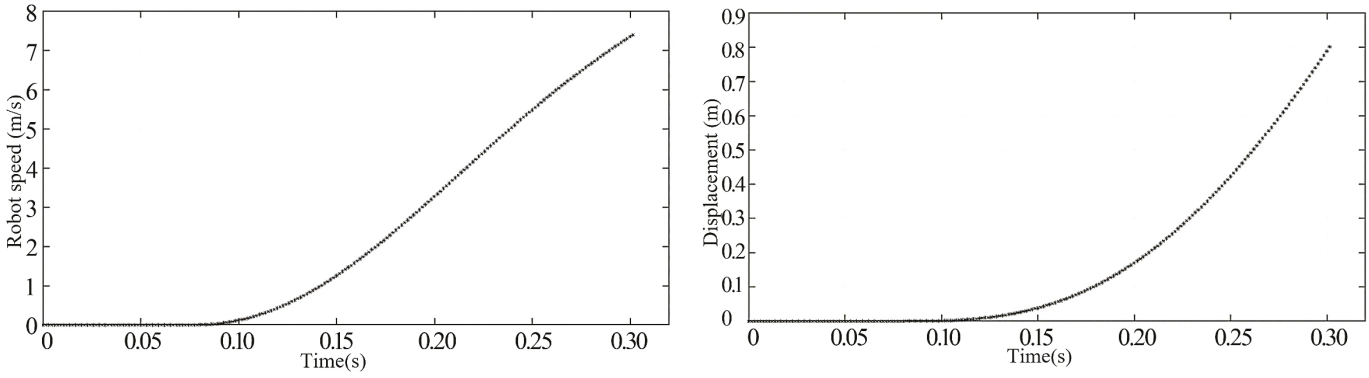


Figure 12. Experimental curve. (**a**) Robot speed-time graph; (**b**) Robot displacement-time graph.

3.4. Comparative Analysis of Numerical Simulation Results and Experimental Results

The underwater horizontal robot launching process is numerically simulated and compared to the experimental launching procedure. While the actual annular bubbles occur together with some tiny bubbles, the numerical simulation displays the appearance of annular bubbles sooner than the experiment and with a consistent form. The annular

bubbles all separate from the back gas when the robot head is ready to depart the tube; however, the axial movement of the annular bubbles predicted by the numerical simulation is significantly more than that of the actual data, and the bubble scale is bigger. The high-pressure gas inside the tube all forms a columnar jet at the tube's mouth after the robot's tail exits it. Bubbles form in both axial and radial directions, and the gas cloud expands and necks. However, the radial scale of the gas cloud that forms during the experimental process is larger than the results of the numerical simulation.

The underwater horizontal launch of the robot out of the tube procedure was compared in terms of its hydrodynamic properties. The results are compared as shown in Figure 13. When the launch valve is opened, it takes some time to build up the launch tube's chamber pressure. The robot begins to move when the chamber pressure inside the tube is greater than its resistance. These are the hydrodynamic characteristics of the robot during the underwater horizontal launch out of the tube. There are some discrepancies between the two hydrodynamic data because the experimental launch procedure is more complicated than the numerical simulation, which is configured for perfect launch circumstances.

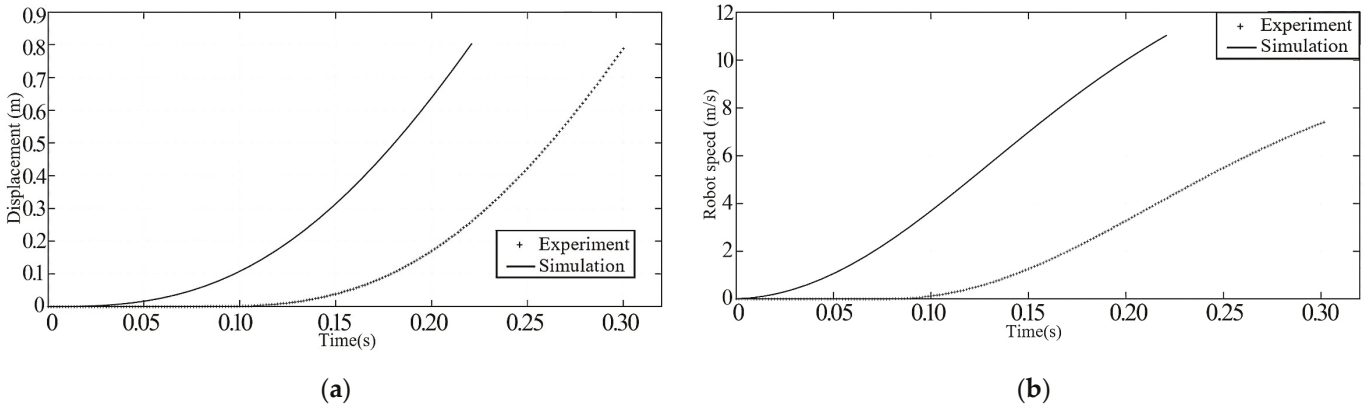


Figure 13. Comparative curves. (**a**) Comparison of displacement between experimental and numerical simulation; (**b**) Comparison of experimental and numerical simulation speeds.

The displacement–time and velocity–time change laws of the numerical simulation results and the experimental findings are essentially the same, as can be inferred from Figure 13. The primary variations between the two are the robot's speed as it exits the tube and the duration of time that each uses. The robot emerges from the launching tube in 0.305 s in the experiment, but it takes 0.22 s in the simulation—a 39% mistake. Moreover, the robot's exit velocity from the tube is 7.3 m/s in the experiment, but it exits the tube at 11 m/s in the simulation—a 34% inaccuracy. The high-pressure gas in the robot's tail in the simulation can fully act on the robotic tail, despite the fact that the simulation model and the actual model have the same cross-sectional area and a flat tail, respectively. However, the real model experiences a phenomenon known as partial push compensation, which causes the numerical simulation emission pipe to rise more quickly, resulting in a robot that operates in less time and at a higher output speed.

4. Conclusions

This paper optimizes the cylinder pressure, cylinder volume, launch valve opening area, and launch valve opening time using the particle swarm approach. Establishing a complex two-phase flow field computational model of a small robot's underwater horizontal launch-out-of-the-tube process, setting up an underwater launch experiment system, and conducting underwater launch experiments are all accomplished with the use of Fluent 2020 software, which is based on the VOF model, realizable turbulence model, and dynamic mesh technology. This research can serve as a guide for the development of underwater launching systems for these robots, enabling the more accurate and convenient

performance of tasks including detection, exploration, and communication underwater by small, lightweight robots.

1. Following optimization, the gas cylinder's initial pressure is 2 MPa, its capacity is 30 L, its opening area is 9.683, its opening time is 0.02 s, and its opening time is 0.02 s. Following optimization, there is a modest reduction in the launching time, a peak pressure decrease in the launching tube rifling, and a slight decrease in the robot's exit velocity from the tube.
2. The analysis of the evolution of bubble expansion and contraction at the cylinder's mouth during the robot-launching process yielded the following results: the robot moved out of the launching tube in 0.22 s, and its top speed was 11 m/s. These results confirmed the viability of the optimized launching device.
3. The robot's underwater launching bubbles' evolution process is identified. The robot needs 0.305 s to travel out of the launching tube, and its exit velocity from the tube may reach 7.3 m/s. The robot's launch time results in an error of 39%, and the tube's exit velocity results in an error of 34%, according to a comparison and analysis of the simulation and experimental data. This is because the experimental model's tail is conical and has a tail, but the simulation model's tail is flat. There is a situation in the real model where certain thrusts cancel each other out.

Author Contributions: Conceptualization, H.G. and Z.P.; methodology, F.M.; software, F.M.; validation, H.G. and S.H.; formal analysis, Z.P.; investigation, H.G.; resources, S.H.; data curation, F.M.; writing—original draft preparation, H.G. and Z.P.; writing—review and editing, F.M. and S.H.; visualization, Z.P.; supervision, S.H.; project administration, F.M.; funding acquisition, H.G. All authors have read and agreed to the published version of the manuscript.

Funding: This research was funded by the Key R&D Program of Shandong Province of China, grant number 2021JMR0302, and the National Natural Science Foundation of China, grant number 5207110396.

Data Availability Statement: The data used to support the findings of this study are available from the corresponding author upon request.

Acknowledgments: The authors gratefully acknowledge the financial support from the Key R&D Program of Shandong Province of China, and the National Natural Science Foundation of China.

Conflicts of Interest: The authors declare no conflicts of interest.

Nomenclature

V_B	The volume of high-pressure cylinders
P_B	The pressure of the gas in a high-pressure cylinder
T_B	Temperature
M_B	Quality of gas in high-pressure cylinders
Q	Heat
W_B	Work
$\mathrm{d}m_i$	Energy input
$\mathrm{d}m_B$	Energy output
h_q	The enthalpy value of the gas in a transient high-pressure cylinder
c_p	The specific heat capacity at a constant volume
c_v	The specific heat capacity at a constant pressure
t	Time
κ	Specific heat capacity ratio
R	Universal constant
P_B	Upstream pressure of the launch valve
ρ_B	Density of gas at the inlet of the launch valve
P_E	Downstream pressure of the launch valve
φ	Flow coefficient of the launch valve
A_i	Instantaneous opening area of the launch valve

ρ_i	Gas density at the exit section of the launch valve
u_i	Gas flow rate at the exit section of the launch valve
β	Critical pressure ratio
U_E	The internal energy of the gas in the tube during emission
U_{E0}	The internal energy of the gas in the tube before launch
H_i	The enthalpy of the gas flowing through the launch valve into the launch tube
W	The work done to move the robot
W_h	The work that pushes the water between the robot's launch tubes
m_E	The mass of the gas in the tube
V_E	The instantaneous gas volume in the launch tube
φ_j	The flow coefficient of seawater through an annular gap
S_h	Area of annular clearance between the launch tube and the robot
ρ_w	Seawater density
P_h	Seawater pressure at the launch tube's mouth
S	The cross-sectional area of the robot
v_d	The speed of the robot
m_d	The robot and the total mass of the moving seawater in the tube
S_i	Tube diameter of a cross-sectional area
R_X	The resistance of the robot
C_D	The resistance coefficient of the robot's underwater movement
μ	The friction coefficient between the robot and the launching tube
F_d	The buoyancy of the robot
α	Correction factor
α_g	Gas phase's volume fraction
α_l	Liquid phase's volume fraction
ρ	Density of the mixed phase
ϕ	Material parameter
E	The mass average energy of each phase
T	Mass mean temperature of each phase
k_{eff}	Mass average energy effective thermal conductivity of each phase's conductivity
k_t	Turbulent heat conductivity
κ	Surface curvature
U	Free flow velocity
θ_w	Wall contact angle
n_w	Unit normal vector of the wall
$\hat{t}_w$	Unit tangent vector of the wall
k	Turbulent kinetic energy
ε	Turbulent energy dissipation rate
G_k	Turbulent kinetic energy generated by the laminar velocity gradient
G_b	Turbulent kinetic energy caused by buoyancy
Y_M	Turbulence caused by pulsation
σ_k	Equation k turbulence Prandtl number
σ_ε	Equation ε turbulence Prandtl number
S_k, S_ε	Source item
μ_t	Turbulent viscosity
h_0	Ideal height of grid cells
α_s	Fission factor
α_c	Merge factor

References

1. Chen, Y.L.; Wang, J.T.; Zhu, S.T.; Gu, Y.; Dai, H.Y.; Xu, J.Y.; Zhu, Y.P.; Wu, T.X. Knowledge Graph Construction for Foreign Military Unmanned Systems. In Proceedings of the 7th China Conference on Knowledge Graph and Semantic Computing (CCKS), Qinhuangdao, China, 24–27 August 2022; pp. 127–137.
2. He, Y.; Wang, D.B.; Ali, Z.A. A review of different designs and control models of remotely operated underwater vehicle. *Meas. Control* **2020**, *53*, 1561–1570. [CrossRef]
3. Huang, M.; Jiang, Y.; Wang, B. Research on Interior Ballistic of a Gas Multi-stage Cylinder Ejection. *MATEC Web Conf.* **2018**, *179*, 03005. [CrossRef]

4. Liu, H.J.; Peng, X.Z.; Zou, Z.Z. Effects of the launch speed on hydrodynamic force of the underwater vehicle vertical launch with the gas curtain. In Proceedings of the International Conference on Mechanics, Dynamic Systems and Materials Engineering (MDSME 2012), Guangzhou, China, 24–25 November 2012; pp. 84–87.
5. Zhang, J.H.; Yu, Y.G.; Zhang, X.W. Numerical investigation on the multiphase flow field at various muzzle velocities. *J. Mech. Sci. Technol.* **2022**, *36*, 4021–4032. [CrossRef]
6. Gao, S.; Shi, Y.; Pan, G.; Quan, X.B.; Yu, Y.L. An investigation on the wake vortex structure and trajectory characteristics of the vehicle launched underwater. *Ships Offshore Struct.* **2023**. [CrossRef]
7. Zhang, X.; Yu, Y.G.; Zhang, X.W. Research on multiphase flow field characteristics of underwater gun double-tube parallel firing. *Propellants Explos. Pyrotech.* **2023**, *48*, e202300068. [CrossRef]
8. Li, W.N.; Zhang, Z.Y.; Lu, J.X.; Li, Z.S.; Wang, C. Investigations on the flow characteristics and the structural response of the launch tube during the underwater launching process. *Ocean. Eng.* **2023**, *279*, 114603. [CrossRef]
9. Wang, Y.N.; Vanierschot, M.; Cao, L.L.; Cheng, Z.F.; Blanpain, B.; Guo, M.X. Hydrodynamics study of bubbly flow in a top-submerged lance vessel. *Chem. Eng. Sci.* **2018**, *192*, 1091–1104. [CrossRef]
10. Zhang, W.Q.; Jia, G.T.; Wu, P.; Yang, S.; Huang, B.; Wu, D.Z. Study on hydrodynamic characteristics of AUV launch process from a launch tube. *Ocean. Eng.* **2021**, *232*, 109171. [CrossRef]
11. Zhang, X.W.; Yu, Y.G.; Zhou, L.L. Numerical study on the multiphase flow characteristics of gas curtain launch for underwater gun. *Int. J. Heat Mass Transf.* **2019**, *134*, 250–261. [CrossRef]
12. Jayaprakash, A.; Singh, S.; Chahine, G. Experimental and Numerical Investigation of Single Bubble Dynamics in a Two-Phase Bubbly Medium. *J. Fluids Eng.-Trans. ASME* **2011**, *133*, 121305. [CrossRef]
13. Wei, Y.P.; Wang, Y.W.; Fang, X.; Huang, C.G.; Duan, Z.P. A Scaled Underwater Launch System Accomplished by Stress Wave Propagation Technique. *Chin. Phys. Lett.* **2011**, *28*, 024601. [CrossRef]
14. Lu, H.T.; Li, W.B.; Cui, B. The Performance of Pneumatic Gun Launching Spherical Projectile. In Proceedings of the 32nd International Symposium on Ballistics, Reno, NV, USA, 8–13 May 2022.
15. Yuan, R.B.; Sun, C.G.; Lee, Q.; Yang, H.F. Dynamic Simulation of Position Servo System of Pneumatic Manipulator Based on AMESim and Simulink. In Proceedings of the International Conference on Manufacturing Science and Engineering (ICMSE 2009), Zhuhai, China, 26–28 December 2009; pp. 2580–2584.
16. Bing, T. Optimization of Structure Parameters for Hydraulic Energy Accumulated Torpedo Launching Device. *Mater. Sci. Forum* **2011**, *704–705*, 612–618.

Disclaimer/Publisher's Note: The statements, opinions and data contained in all publications are solely those of the individual author(s) and contributor(s) and not of MDPI and/or the editor(s). MDPI and/or the editor(s) disclaim responsibility for any injury to people or property resulting from any ideas, methods, instructions or products referred to in the content.

inventions

MDPI

Article

From Sparse to Dense Representations in Open Channel Flow Images with Convolutional Neural Networks

Filippos Sofos [1,*], George Sofiadis [2], Efstathios Chatzoglou [2], Apostolos Palasis [1,2], Theodoros E. Karakasidis [1] and Antonios Liakopoulos [2]

[1] Condensed Matter Physics Laboratory, Department of Physics, University of Thessaly, 35100 Lamia, Greece; appalasis@uth.gr (A.P.); thkarak@uth.gr (T.E.K.)
[2] Hydromechanics and Environmental Engineering Laboratory, Department of Civil Engineering, University of Thessaly, Pedion Areos, 38334 Volos, Greece; sofiadis@uth.gr (G.S.); efchatzoglou@uth.gr (E.C.); aliakop@uth.gr (A.L.)
* Correspondence: fsofos@uth.gr

Abstract: Convolutional neural networks (CNN) have been widely adopted in fluid dynamics investigations over the past few years due to their ability to extract and process fluid flow field characteristics. Both in sparse-grid simulations and sensor-based experimental data, the establishment of a dense flow field that embeds all spatial and temporal flow information is an open question, especially in the case of turbulent flows. In this paper, a deep learning (DL) method based on computational CNN layers is presented, focusing on reconstructing turbulent open channel flow fields of various resolutions. Starting from couples of images with low/high resolution, we train our DL model to efficiently reconstruct the velocity field of consecutive low-resolution data, which comes from a sparse-grid Direct Numerical Simulation (DNS), and focus on obtaining the accuracy of a respective dense-grid DNS. The reconstruction is assessed on the peak signal-to-noise ratio (PSNR), which is found to be high even in cases where the ground truth input is scaled down to 25 times.

Keywords: convolutional neural networks; flow reconstruction; super resolution; deep learning; open channel flows

1. Introduction

The term open channel flow describes a free surface flow where a liquid–air contact surface exists and atmospheric pressure is applied. Therefore, free-surface flows include all flows in natural and man-made ducts, and most of the time, these are turbulent flows. The exceptions are few and concern very low-depth flows [1,2]. Turbulence causes the occurrence of vortices within a wide range of length and time scales that interact in a dynamically complex way. In general, in engineering applications, the investigation focuses either on experiments or numerical simulations (or both). Additional problems may arise, though, and experiments may end up with limited or noisy measurements, while numerical simulations for complex and large systems oftentimes demand high computational times and computer power [3].

Experiments on open channel flows have reported inherent difficulties in measurements very close to the free surface, where fluctuations of the root-mean-square (rms) velocity in the vertical direction are observed [4–7]. Moreover, it was found that the fluctuations in the vertical direction were damped in contrast to those in the tangential direction, which were amplified close to the free surface. It is therefore not surprising that a significant part of the scientific community has devoted itself to the development of numerical models to study the effects of turbulence, since its inclusion in engineering applications is significant. The methods, depending on the level of precision they offer, are classified in the following categories: (a) RANS (Reynolds Averaged Navier–Stokes), (b) LES (Large Eddy Simulations), and (c) DNS (Direct Numerical Simulations) [8–10].

More specifically, in the turbulence models for RANS equations, the objective is focused on the mean flow and the way the turbulence affects its properties. Before applying any numerical method, the Navier–Stokes (N-S) equations are written in the form of time-averages. In the RANS flow equations, additional terms appear due to the interactions between the turbulent fluctuations, so these terms have to be modeled in turn with turbulence models. It is worth noticing that the computational resources required for reasonably accurate results related to the flow field are relatively simple, which is why RANS ranks at the bottom of the hierarchy in terms of computational power requirements for common engineering problems [11]. The principal concept of the LES method is based on the detection of the behavior and development of Large Eddies. The method involves spatial filtering of the unsteady N-S before the calculations, which aims to keep the largest scales and discard the smallest ones. The equations of non-steady flow have to be solved, where the computational cost requirements in terms of storage and volume of calculations are higher compared to the RANS method, and, for this reason, LES is an intermediate computation form for turbulent flows [12,13].

On the other hand, DNS has been the method of choice when accuracy is the question and has contributed remarkably to turbulence research in the last decades [14]. The continuity and the N-S equations for incompressible constant viscosity turbulent flow constitute a closed system of four equations with the following four unknown variables: velocity components u, v, and w (in x-, y-, and z-directions, respectively), and pressure, p. This set of equations is taken as the starting point in DNS, and a transition solution is developed in a sufficiently dense spatial mesh (in order to resolve the Kolmogorov length scales in which the energy dissipation takes place) with sufficiently short time steps to capture even the smallest eddies and the "fastest" fluctuations. The advantages of DNS include the fact that no empirical turbulence model is required, whereas one of the main disadvantages of the method, which makes it not widely used in industry, is that the calculations are very demanding in terms of computational resources [15].

Nevertheless, the increased computational effort inherent in DNS and other numerical formulations, both in terms of time and hardware needs, has opened the way to adopt novel computational techniques stemming from machine learning (ML) [16]. Aerodynamic coefficient prediction, turbulence modeling, transitional flow modeling, and flow reconstruction are just a few fields of application [17,18]. More specifically, deep learning (DL) techniques have attracted a lot of interest, especially for their use as surrogate models in computational fluid dynamics (CFD). DL models can deal with complex mathematical concepts through a layered network of interconnected nodes, and they can be easily applied to applications involving data in 2D and 3D dimensions, where the computational domain is discretized using meshes. In CFD, a dense grid leads to higher accuracy, and this corresponds to a deeper network in the DL method. Therefore, the alternative solution of employing DL methods can improve flow estimation and diminish computational time.

A constantly evolving field of research lately with ever-increasing accuracy, super resolution (SR), utilizes high-resolution (HR) data reconstruction using sparse measurements with DL approaches [19,20]. To achieve this, convolutional neural networks (CNNs), Variational Autoencoders (VAEs), and generative adversarial networks (GANs) [21–24] are among the most common architectures utilized. A relevant example has utilized a U-Net type architecture with CNN layers achieving satisfying results in flow image reconstruction [25]. Even with lightweight networks, performance is fine, suggesting a fast and practical solution for handling turbulent flow data. Real-time reconstruction has also been achieved within a spatio-temporal high-resolution (HR) flow field from low-resolution (LR) data using CNNs and MST-UNet [26]. In this model, the HR images of the previous frame and the LR images of the current frame pose as the model input in a multi-scale manner. The U-Net architecture has been widely employed in image segmentation tasks [27]. Another successful implementation, ResNet, has been introduced to address the vanishing gradient problem [28]. The NuNet architecture has also achieved remarkable

performance when compared with the OpenFoam AMR solver [29], presenting impressive discriminative capabilities.

A comparison of SR model performance is usually made based on the value of the peak signal-to-noise ratio (PSNR). Common values for successful models range between PSNR = 30–40 dB. Nevertheless, higher values have been reported by the multiple path super-resolution convolutional neural network (MPSRC) [30], which has given a value of PSNR > 50.0 dB, while the recent deep learning flow image (DELFI) has also achieved high accuracy and architecture simplicity, with PSNR $\cong$ 39 dB [31].

In the present paper, open channel flow image data derived from DNS simulations are employed to train a super-resolution model, the Upscaling CNN (UpCNN), making it capable of upscaling sparse/coarse data onto a high-resolution (HR) field. The architecture of UpCNN is based on consecutive CNN layers in an encoding/decoding manner, with residual connections to ensure proper information exchange. The proposed architecture achieves high performance on fluid image reconstruction tasks, with PSNR = 51.5 dB, in short training time, without the need to occupy complex computer architectures and memory, as it can just run on common computer hardware. To achieve efficient network training, HR images are first scaled down to a factor of 5–25 and enter the network along with their respective HR images in pairs, so as to create an upscaling mechanism able to reconstruct coarse fields into their fine analog. The reconstruction results on our open channel flow DNS data are very close to the HR images, suggesting that the method can be employed in relevant fluid mechanics applications as a complimentary method to time- and resource-intensive DNS simulations.

2. Materials and Methods

2.1. Super-Resolution Components

2.1.1. Convolutional Neural Networks

Convolutional neural networks are the core components of an SR architecture. In a CNN architecture, input data (typically 2D image data) goes through convolutional layers, which transform spatial information into a series of filters to identify local patterns. The network uses a combination of pooling layers, convolutions, and non-linear activation functions to learn hierarchical representations. In order to efficiently deal with big data, spatial dimensions can be reduced through pooling, while global patterns are captured by fully connected layers. Training CNNs involves the minimization of a loss function by modifying network weights through backpropagation [32]. Such architectures are excellent at imaging applications, automatically picking up characteristics and patterns.

2.1.2. Generative Models VAEs-GANs

A type of generative model in the fields of machine learning (ML) and AI are Variational Autoencoders (VAEs). VAEs consist of an encoder, which takes input data and maps it to a probabilistic latent space, and a decoder, which generates output data and reconstructs the input data as accurately as possible [33]. VAEs work on the fundamental premise of acquiring a mapping between a straightforward and constant distribution and the probability distribution of the data [34]. On the other hand, GANs are an alternative class of AI algorithms used in unsupervised learning (UL) and consist of two parts. The first part (the generator) generates new data, and the second part (the discriminator) assesses the generated data, classifying it as real or fake data [35]. Great reconstruction results have also been obtained by an innovative sub-filter modeling method utilizing GANs for reactive turbulent flows [36].

2.1.3. Physics-Informed Neural Networks (PINNs)

To connect ML with physics principles by means of partial differential equations (PDEs), the Physics-Informed Neural Networks (PINNS) have emerged. They are a class of ML that incorporates knowledge from physics equations into the ML training process [37]. They include an additional physics-informed loss term in addition to the standard loss

function used for training, adhering to physical laws [38]. Therefore, during the training process, the NN learns from both the input/output data and the physics-informed loss term [39]. A new method of scaling up PINNs to solve arbitrary high-dimensional PDEs is presented in [40]. The performance of the PINN/Resnet block has been investigated by employing Burger's equation with a discontinuous solution and the Navier–Stokes (N-S) equation with a continuous solution [41]. The findings have clearly shown that Res-PINN exhibits greater predictive power when compared to traditional DL methods.

2.1.4. LSTM Networks

In scientific and engineering practice, there are often scenarios where modeling temporal dependencies, handling sequential data, and capturing long-term information need to be confronted at the same time. To this end, Long Short-Term Memory (LSTM) networks are suggested [42]. These networks are a special type of recurrent neural network (RNN), containing memory cells to store information over a long period of time. These cells have an internal structure that allows them to decide whether to forget, keep, or write the information. The flow of information is controlled through gates, which dynamically adjust [43].

2.2. Simulation and Data Augmentation

2.2.1. Open Channel Flow Data

In order to obtain accurate data for training and validation of an SR imaging network, DNS of an open-channel turbulent flow has been conducted. The selection of this geometry has been based on the premise that the open channel serves as a test bed case for many turbulent flow models, due to the interesting flow physics phenomena that arise and its wide application in engineering and environmental space.

The focus of this paper has been on testing an SR algorithm in the turbulent regime, where the bulk Reynolds number is $Re_b = 11,200$. For the numerical modeling of the flow, the OpenFoam finite volume algorithm has been used. OpenFoam is an open-source algorithmic suite that has been previously validated in cases of turbulent open-channel Newtonian and non-Newtonian flows [44,45]. The governing equations that have been solved by the finite volume algorithm are the ones that describe the incompressible turbulent flow and are mathematically expressed in the non-dimensional form of Equations (1) and (2).

$$\nabla \cdot \mathbf{u} = 0 \tag{1}$$

$$\frac{\partial \boldsymbol{u}}{\partial t} + (\boldsymbol{u} \cdot \nabla)\,\boldsymbol{u} = -\nabla P + \frac{1}{Re}\nabla^2 \boldsymbol{u} \tag{2}$$

Equations (1) and (2) represent the continuity and momentum equations for incompressible flow. The variables in these equations represent the non-dimensional velocity vector ($\boldsymbol{u}$) and the non-dimensional pressure (P). Time is denoted by t, while Re stands for the non-dimensional Reynolds number. In order to arrive at the non-dimensional form of Equations (1) and (2), characteristic variables have been chosen. The characteristic length of the channel has been represented by δ, while its total height is set as $h = 2\delta$. Finally, for the characteristic velocity, the symbol U_0 has been used, with the zero-subscript indicating cross-sectional average quantities. Accordingly, the bulk Reynolds number is equal to $Re_b = \frac{\rho U_0 2h}{\mu}$, where ρ and μ represent the fluid density and dynamic viscosity, respectively.

OpenFoam features a large variety of available numerical models that can be utilized for flow modeling. Since the goal of the present research has been to conduct DNS to obtain our dataset, coupling of momentum and pressure through the pressure-implicit split-operator (PISO) method is the choice. The PISO algorithm has already been extensively tested by previous studies and has been proven to require less CPU time [46,47]. At the same time, the algorithm is robust and accurate as well. As far as the numerical schemes are concerned, third-order space-aware and second-order implicit backward-time-aware schemes have been selected.

The flow setup consists of a simple model that incorporates flow between a free surface and a bottom plate with slip and no-slip boundary conditions, respectively. The total height between the free surface and the bottom plate is $h = 2\delta$, while the size in the other two directions has been set to $3\pi\delta$ and $2\pi\delta$ (see Figure 1). In the streamwise and spanwise directions, periodic boundary conditions are imposed.

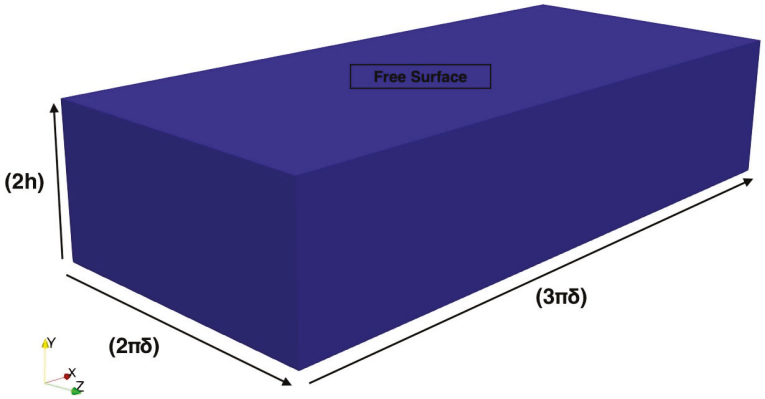


Figure 1. Schematic of the geometry that has been used in the present study.

Finally, regarding the spatial grid resolution of the flow field, two different cases have been studied. The first one (case 2), which serves as the high-resolution grid case, has a grid size of $128 \times 132 \times 128$ elements in the streamwise, wall-normal, and spanwise directions, respectively. Resolution, as well as domain size, have been chosen appropriately in order to ensure that the dynamics and flow physics are captured correctly by the present setup. The chosen values have been previously proven to accurately describe dynamics and flow physics, as early as the original work of Kim et al. [48]. More recently, the implied DNS code has been validated against experimental and well-established DNS results with excellent agreement [44,45]. The second case (case 2), which serves as the coarse grid resolution case, has a grid size of $64 \times 64 \times 64$ elements in the same respective directions. In addition to the difference in result accuracy between the two different spatial grid resolution cases, computational times differ naturally as well. A direct comparison between the two cases could yield approximately double the computational time for the finer grid case to obtain the correct results. An increased burden of computational resources for the finer grid case is also directly connected to the above observation.

After the simulations have reached a statistically steady state, data and results have been exported. For the purpose of the present study, two-dimensional (2D) instantaneous velocity fields have been exported along the x-y plane (mid-vertical plane) for 50 consecutive time steps in both HR and LR.

2.2.2. Data Curation

The DNS-extracted high-resolution (HR) dataset consists of 50 RGB (red, green, and blue) images, 40 of which are fed to the training network and the rest are kept for validation purposes (80–20%, respectively). At first, a data augmentation step is considered [20,49], where the HR images are employed to create a richer dataset to effectively train the model (Figure 2). Images are scaled down by a factor of 5, 10, 15, 20, and 25, which results in blurred instances of the HR, from slight blurring (scale = 5) to extra sparse grids and practically tiny images (scale = 25). Details are given in Table 1.

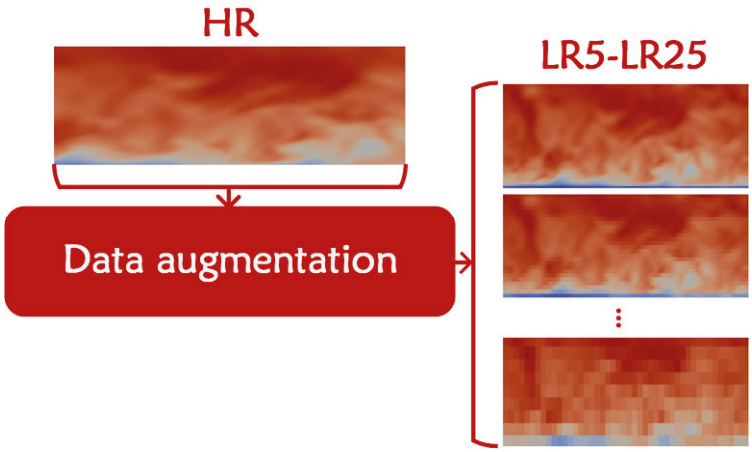


Figure 2. Data augmentation stage, where LR images are created with various resolutions from the HR dataset to create the training set.

Table 1. Input data for model training and validation, with number of training images (N_t), number of validation images (N_v), and image dimensions (height $\times$ width). The total training set contains 200 images, and the validation set contains 50 images.

	N_t	N_v	(H $\times$ W)
HR	40	10	262 $\times$ 1176
LR5	40	10	52 $\times$ 235
LR10	40	10	26 $\times$ 118
LR15	40	10	17 $\times$ 78
LR20	40	10	13 $\times$ 59
LR25	40	10	10 $\times$ 47

The creation of such an artificial training dataset is common practice in the field of super-resolution applications [25,50,51]. The procedure that follows takes an HR image and its LR counterpart, feeds the model with this couple, and finds correlations between them so as to be able to make this upscaling from an unseen LR image in the future. For example, when sparse-grid simulation (e.g., from RANS) images are fed, the model will be able to provide their HR counterpart. This is why it is crucial to effectively train the network in the first place.

A more detailed view of the dataset is given in Figure 3. Figure 3a shows the produced images for all scales considered, while Figure 3b shows the flow at some representative timesteps between 1 and 50. Furthermore, a new coarse dataset, which is the result of another DNS simulation that runs for the same input conditions but with a sparser grid (64^3 elements), is shown in Figure 3c. The sparser grid contains much less information, but it has the advantage of running in substantially shorter times. Thus, even though the resolution of images in both cases is the same, the ones stemming from the coarser grid dataset offer less information. There is no direct correspondence between these images and an HR set, so we will keep them after the model is trained to reconstruct the HR dataset from scratch.

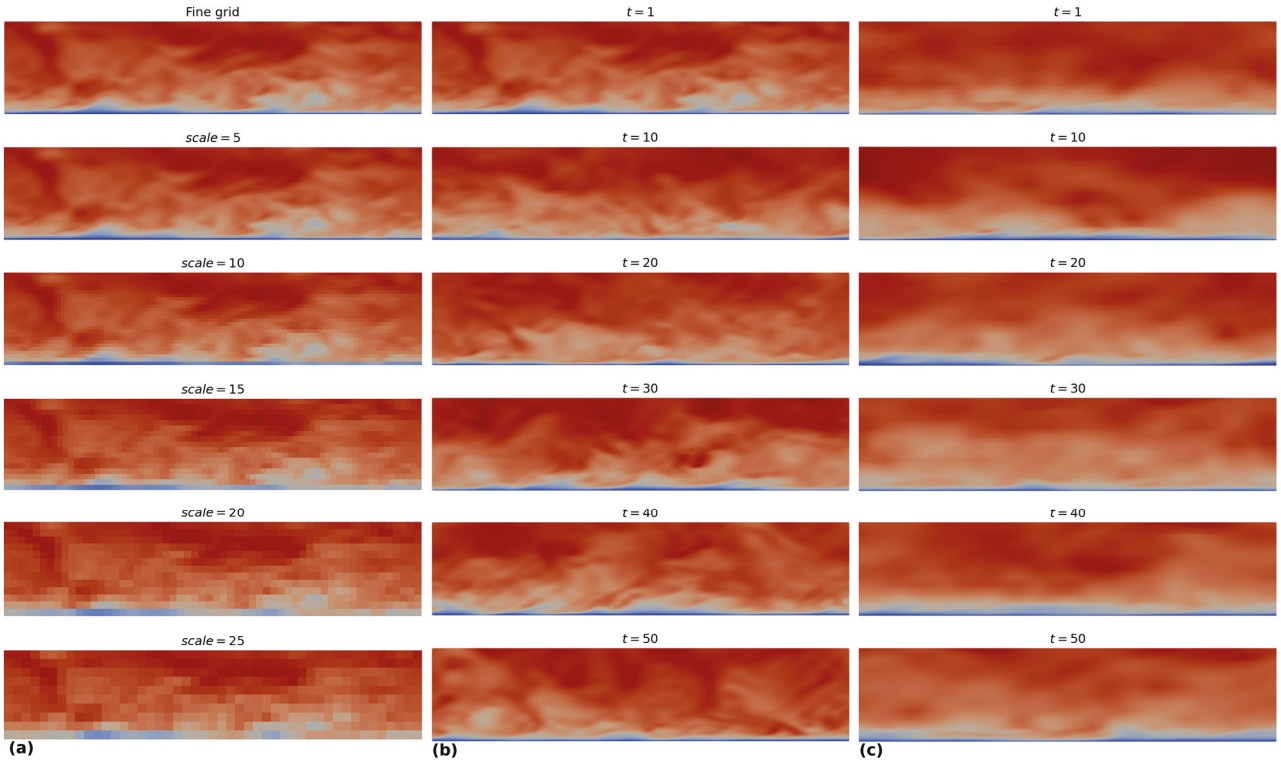


Figure 3. Open channel flow images used for training and validation. (**a**) Fine images (ground truth) and the respective scaled, low-resolution images; (**b**) examples of a sequence of DNS and HR images (case 1) in various timesteps; and (**c**) examples of a sequence of a second set of sparse-grid DNS images (case 2) used for prediction in a post-processing step.

3. Results

3.1. UpCNN Architecture

To implement the super-resolution method for DNS image data, a U-net type [27] up-scaling model (UpCNN) is proposed (Figure 4). In this architecture, an encoder and a decoder branch are created, with several convolutional layers. In the encoder branch, a convolutional kernel, k, applies to an input image, $\boldsymbol{X}$, and outputs a series of images (filters), each one featuring image characteristics that correspond to different frequencies. In UpCNN, image dimensions in internal layers are maintained as the input dimensions, avoiding max- and average-pooling layers that would make the model more complex and might lead to information loss [25]. At each convolution layer, a ReLU activation function applies to induce non-linearity. After a series of convolution operations, information passes onto the decoder branch. Here, an inverse operation is performed (deconvolution), and the filters are joined again in a final RGB image. To minimize information loss, a number of residual connections are formed between opposite encoder/decoder components, transferring input information to the output layers [28].

The output image is the reconstructed version of the input, i.e., the LR image. In such models, it is important to have the HR counterpart available to argue its accuracy. The PSNR is given by the following equation:

$$\mathrm{PSNR_i} = 20 \log\left(\frac{1}{\sqrt{\mathrm{MSE}(\mathrm{HR}_i, \mathrm{RLR}_i)}}\right) \tag{3}$$

where RLR is the reconstructed couple of LR for the ith image and MSE is the mean square error calculated. Typical PSNR values for accurate reconstruction are between 30 and 40 [52], while greater values have also been reported in computer vision applications [53].

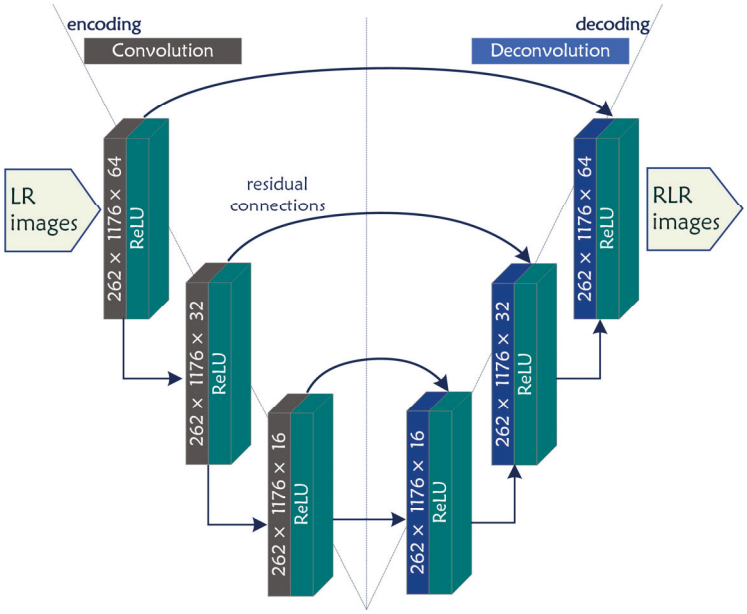


Figure 4. The CNN model constructed, i.e., UpCNN. The left branch is the encoding section, where LR images are fed, with three consecutive convolutional layers, and the right branch is the decoding section, with deconvolutional layers that output the reconstructed images. Residual connections connect information from the encoder to the decoder. Arrows denote the direction of data flow.

The training is performed sequentially, meaning that LR-type images of various scales enter the UpCNN, and full training is achieved after all available scales have been fed.

3.2. Reconstruction Metrics

The next step includes the assessment of the model's accuracy by comparing the HR validation set with the reconstructed result. Figure 5 presents all cases for a random validation image; the images on the left are the LR inputs, and the respective image on the right is the reconstructed (RLR) image. For an LR of scale = 5, where image degradation is only slight, the reconstruction result is excellent, with PSNR = 51.504. Nevertheless, high PSNR is obtained even at greater scales. For scale = 10, there is an obvious effect of image coarsening, and PSNR = 39.052. Of importance is that even in the case of scale = 25, where the image is strongly affected by initial degradation, the PSNR = 33.455 is still satisfactory, and the optical result shows that all main velocity field variations have been recovered. The reconstruction result is worse at the boundary layer (i.e., close to the wall), where velocity values are small.

These first results reveal that UpCNN has the ability to reproduce the velocity field in this type of flow. The question is, however, if one could employ this model to upscale a sparse-grid simulation result. In Figure 6, sparse-grid DNS images are fed to the model, and the reconstruction result is presented. These sparse images are also taken by the same DNS simulation setup, but for a sparser grid. We note that here we do not have the respective HR images to check the accuracy, and the model is asked to predict the output only by accepting a coarse simulation image. The PSNR is calculated between the reconstructed and the respective HR image after averaging all values in all instances. As can be observed, there is a slight improvement from blurred input.

The reconstruction result is better seen in the magnified images of Figure 7, in the region near the boundary layer. The reconstructed results present sharper edges when colors and velocity shapes change and seem to achieve a slight improvement compared to the input image.

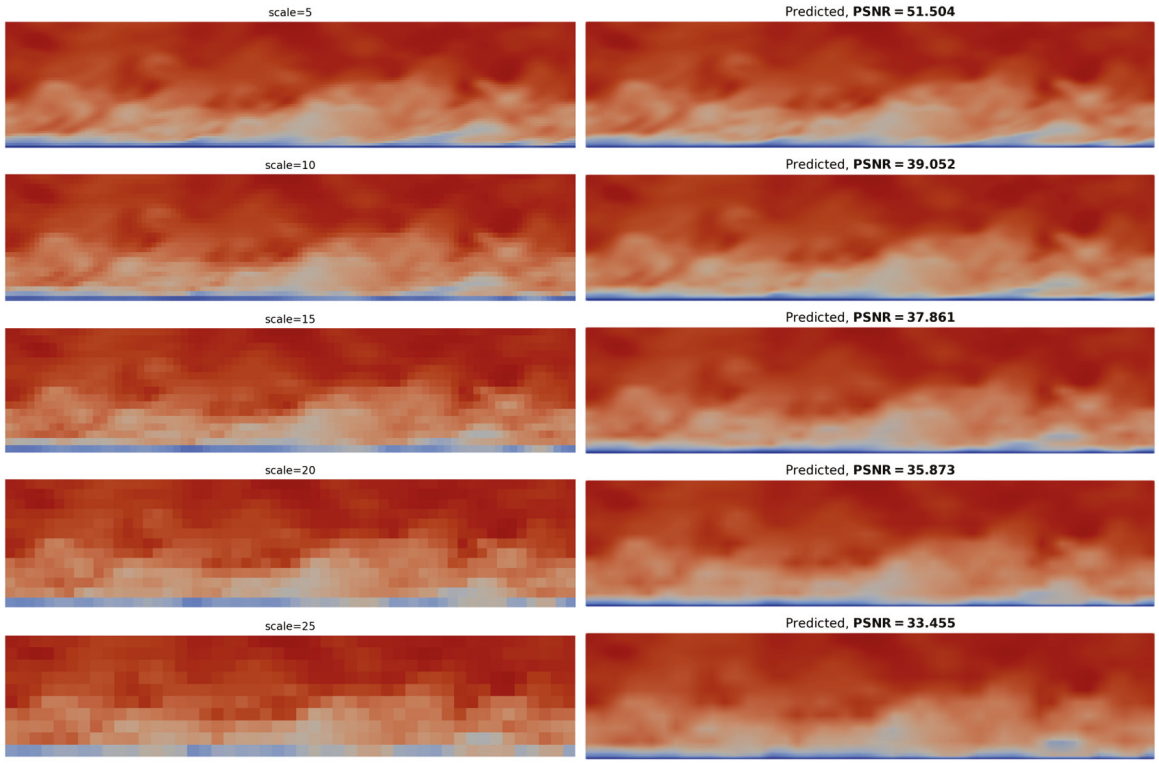


Figure 5. The reconstructed images for each input resolution range from 5 to 25. The obtained PSNR values are also shown.

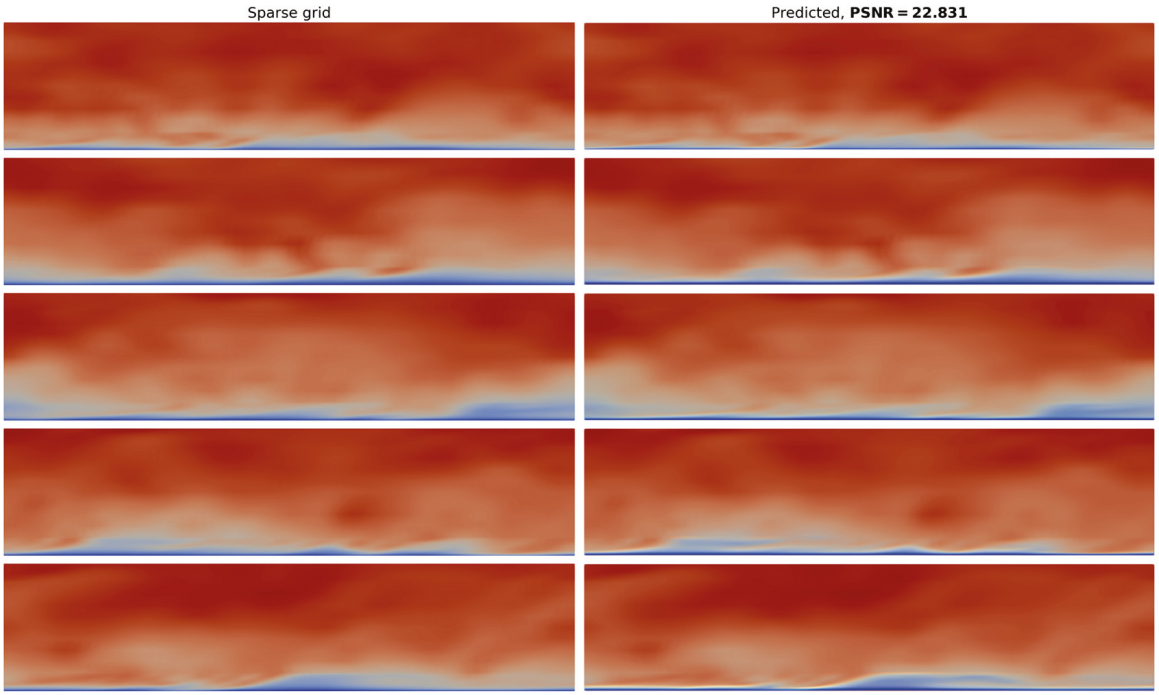


Figure 6. The reconstructed images when the sparse-grid DNS input images are given as inputs. The obtained PSNR value (average) is also shown.

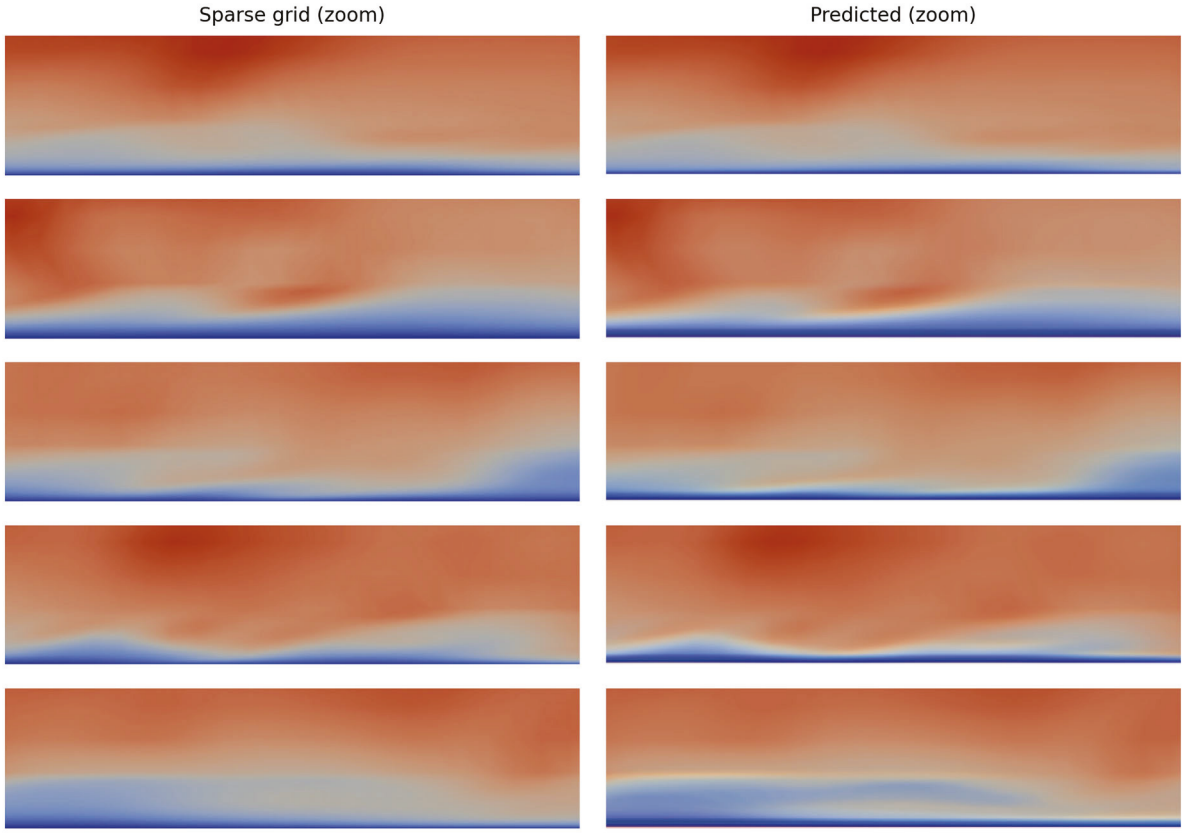


Figure 7. A magnified version of Figure 6. The region shown is close to the fluid–solid boundary.

3.3. Velocity Profiles

One useful and computationally important feature of DL processing is the fact that image pixels represent real values that can be further processed and analyzed. To this end, next we extract velocity profiles across the open channels as average values in time and space (y is the vertical distance from the bottom wall and x is measured along the horizontal). A velocity profile stems from time averaging, followed by a spatial average along the x-direction. Additionally, since a color image consists of three channels (RGB), a final averaging applies to them to end up with one velocity value per pixel. In such a way, the HR velocity profiles refer to all ground truth validation images and the RLR profile to all the predicted (reconstructed) images, which are averaged both in time and space.

A comparison is made between the RLR and the respective HR image sets. Figure 8a presents a close boundary layer view of the velocity profile, where differences are mostly observed. For LR5 reconstruction, no significant differences are observed. This is further verified by the value of the coefficient of determination, $R^2 \to 1$, in the identity plot of Figure 8b.

The reconstructed velocity profile for LR10 is similar to the respective HR in the region outside the boundary layer formed near the bottom wall, while it deviates inside it (Figure 9a). Nevertheless, this happens only for a small region and R^2 is still close to 1 (Figure 9b). Deviations from the respective HR profiles are also observed for LR15 (Figure 10), LR20 (Figure 11), and LR25 (Figure 12).

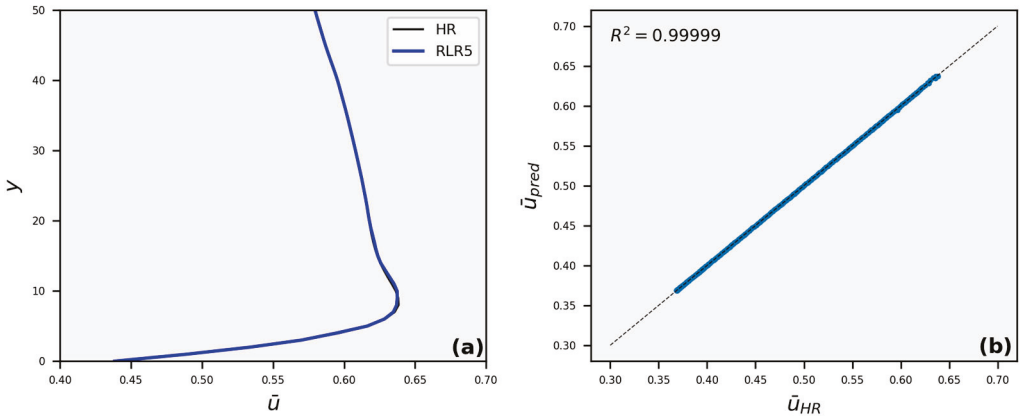


Figure 8. (**a**) Average streamwise velocity ($\overline{u}$), vertical profile, and (**b**) identity scatter plot, where the average velocity of HR images, $\overline{u}_{HR}$, is compared to the average predicted velocity, $\overline{u}_{pred}$, for LR5. Points that lie on the 45° line denote perfect matching.

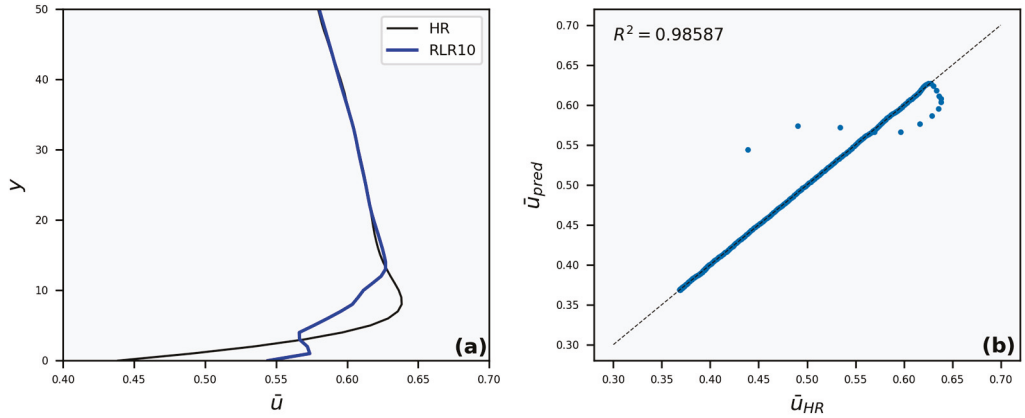


Figure 9. (**a**) Average streamwise velocity ($\overline{u}$), vertical profile, and (**b**) identity scatter plot, where the average velocity of HR images, $\overline{u}_{HR}$, is compared to the average predicted velocity, $\overline{u}_{pred}$, for LR10. Points that lie on the 45° line denote perfect matching.

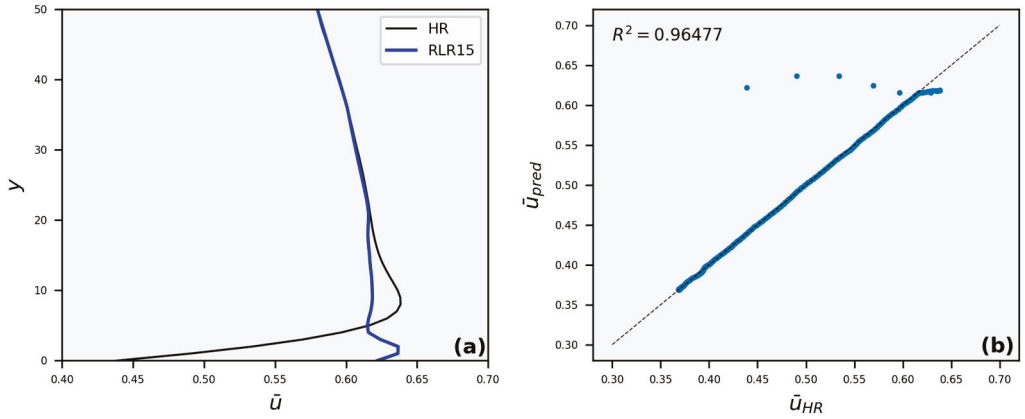


Figure 10. (**a**) Average streamwise velocity ($\overline{u}$), vertical profile, and (**b**) identity scatter plot, where the average velocity of HR images, $\overline{u}_{HR}$, is compared to the average predicted velocity, $\overline{u}_{pred}$, for LR15. Points that lie on the 45° line denote perfect matching.

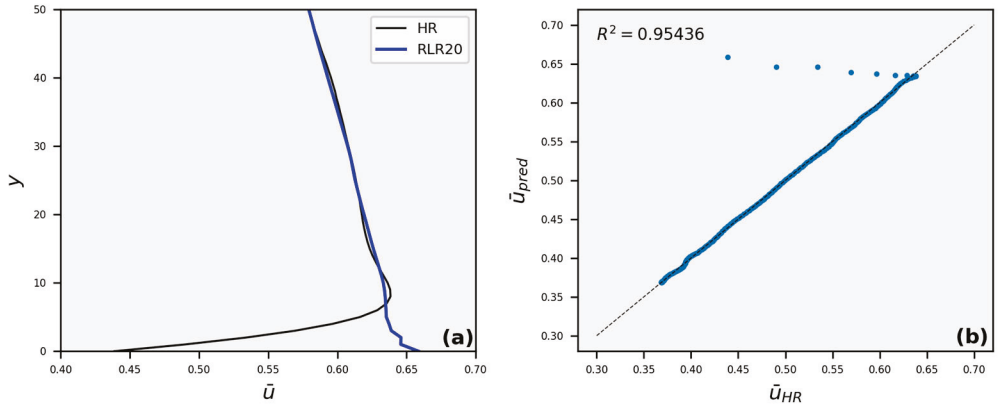


Figure 11. (**a**) Average streamwise velocity ($\overline{u}$), vertical profile, and (**b**) identity scatter plot, where the average velocity of HR images, $\overline{u}_{HR}$, is compared to the average predicted velocity, $\overline{u}_{pred}$, for LR20. Points that lie on the 45° line denote perfect matching.

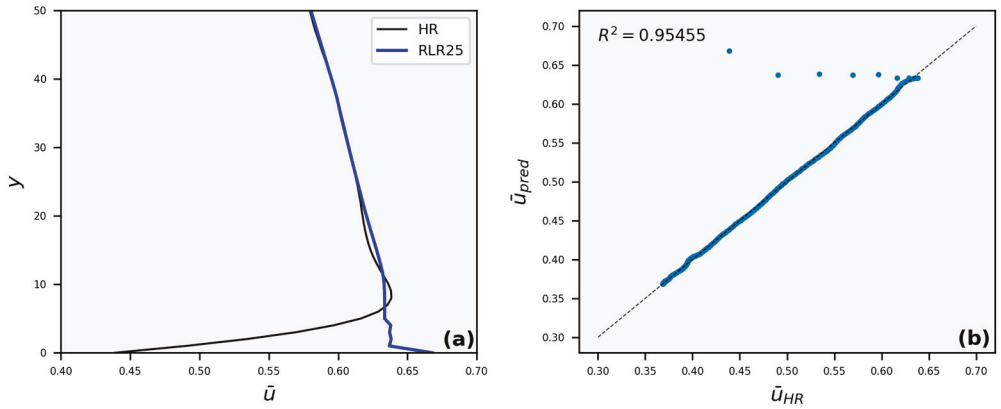


Figure 12. (**a**) Average streamwise velocity ($\overline{u}$), vertical profile, and (**b**) identity scatter plot, where the average velocity of HR images, $\overline{u}_{HR}$, is compared to the average predicted velocity, $\overline{u}_{pred}$, for LR25. Points that lie on the 45° line denote perfect matching.

4. Discussion

The results obtained from image SR have shown a promising potential for enhancing turbulence simulation through DL methods. The case at hand is a turbulent, open channel flow. During training, coarse-grained images taken from their HR and DNS counterparts are fed to the model, building feature correspondence, while, to move on to the prediction process, an unseen set of coarse features is used and the reconstructed result is obtained. It is important to note that the model has to predict features from unseen data accurately. This is the critical point in such methods because image characteristics may depend on new, hidden features that have not been incorporated during the preceding training process. For example, this is the case in RANS simulations, where the employed quantities that extract length and time scales do not present a point-to-point correspondence with the respective DNS quantities [54].

Apart from velocity values, UpCNN can also be incorporated to investigate other flow properties in both internal and external flow applications. An extension of this algorithm could be used to investigate vorticity data or pressure field changes, which are crucial in external aerodynamics. Usually, in this type of flow field simulation, a large spatial grid resolution is required, which in turn translates into a considerable amount of computational resources and time consumption. Thus, the application of UpCNN could provide a fast alternative, producing a sufficiently accurate representation of flow field physics while at the same time cutting down in terms of computational cost. The same applies in the case of internal flow simulations, where complex geometries can lead to extensive computational

costs. The application of the UpCNN algorithm in these cases could produce faster and more accurate results in real-life applications and industrial problems.

To achieve generalizability, consistent training is required. The concept of transfer learning, where a model is trained with a specific dataset and can continue training when new data is fed, could also apply here [29]. Most of the time, DL platforms for transfer learning have been implemented, which are based on rather complex applications that take a long time to run, mostly on high-performance computers (HPCs) [55]. Nevertheless, a practical and fast application, such as UpCNN, could be employed to run independently on small and medium-sized datasets without the need to have been trained on other datasets. For example, in a Mac M2 with an embedded GPU, it takes less than 30 min to train UpCNN with 50 RGB images of (W $\times$ H) = (1176 $\times$ 262). This is important when dealing with scarce datasets, taken either from simulations or experimental measurements. However, complex architectures have been found to be well-suited for demanding applications, and GANs are usually the computational choice for flow reconstruction [56–58].

Therefore, ML and DL techniques should be regarded as computational tools that could aid modeling and diminish processing times in fluid dynamics, especially in demanding turbulence applications. Here we have employed two datasets for two similar but independent DNS simulations. As shown in Section 3 (Results Section), the dense-grid simulation (case 1) that gave images of high resolution has been successfully employed in UpCNN training and validation. The challenge, though, is to ensure that the model works efficiently even when fed with coarse data.

The second DNS run (case 2) involved a sparser grid of 64^3 total grid elements. Comparing the computational time that the two cases require in order to reach a statistically steady state, we observe that this number is approximately doubled for the finer grid case. Of course, this case would provide much more accurate results in terms of flow field physics. Of outmost importance is the fact that a sparse-grid simulation that works synergistically with an UpCNN scheme would improve computational effort by up to 150% with sufficiently accurate results.

Future work should be focused on gradually embedding DL methods in various flow areas previously approached with numerical simulations, such as the flow close to the solid wall where the boundary layers are formed in high Reynolds number flow and require special treatment [59–61]. These would also include applications that require a great deal of computational effort, such as turbulent flows, complex geometries, or external aerodynamics applications. The above-mentioned examples are typically found in many real-life industrial applications, where efficient and accurately produced results are of foremost importance. Moreover, reduced costs will be an additional asset in this case as well.

5. Conclusions

We have performed a two-fold reconstruction process in this paper. First, we have employed high-resolution simulation data and created their lower-resolution counterparts so that a deep learning model can be effectively trained. Towards this direction, convolutional neural networks have been exploited, suggesting a properly tuned U-Net architecture, the UpCNN. The case under investigation is a turbulent open channel flow. The model learns how to make connections between the blurred images and the ground truth images and can function in reconstructing unseen images of the same dataset.

Of interest is examining how the proposed model functions in similar situations for extrapolation tasks. This is one of the main questions in fluid mechanics lately, as successive models that can achieve extrapolation in sparse fields can also be used as direct alternatives to costly simulations. Moreover, these super-resolution methods are employed to create full fields from sparse sensors in various fluid experiments.

Here, we have presented a second reconstruction example, where a coarse fluid velocity grid enters the pre-trained UpCNN model. These coarse images do not have counterparts; they are extracted from a different simulation run on a coarser grid. The

qualitative assessment of the reconstructed result translates to a slight enhancement of the coarse images. Nonetheless, we cannot obtain a quantitative metric to assess the reconstructed result. This approach is based only on the fact that the model performed well in the previous training process, where both high- and low-resolution couples were available.

It is a fact that such computational methods have much to offer; however, they have not matured to the degree necessary to replace fluid mechanics experiments. Interpretable, explainable, and trustworthy artificial intelligence methods must evolve and be directed towards capturing complex fluid behavior without violating physical laws.

Author Contributions: Conceptualization, F.S.; methodology, G.S. and F.S.; software, G.S. and F.S.; investigation, E.C. and A.P.; data curation, G.S.; writing—original draft preparation, A.P., E.C., G.S. and F.S.; writing—review and editing, A.L. and T.E.K.; supervision, F.S., A.L. and T.E.K.; funding acquisition, A.L. All authors have read and agreed to the published version of the manuscript.

Funding: This research project was supported by the Hellenic Foundation for Research and Innovation (H.F.R.I.) under the "2nd Call for H.F.R.I. Research Projects to Support Faculty Members and Researchers" (Project Number: 4584). E.C. was supported by a doctoral candidate scholarship from the Center of Research Innovation and Excellence of the University of Thessaly, funded by the Special Account for Research Grants of the University of Thessaly.

Data Availability Statement: Image data are available on GitHub from the following link: https://github.com/gsof1/From-sparse-to-dense-representations-in-open-channel-flow-images-with-convolutional-neural-networks/tree/main/DNS_Data, accessed on 29 February 2024.

Conflicts of Interest: The authors declare no conflicts of interest.

References

1. Moglen, G.E. *Fundamentals of Open Channel Flow*; CRC Press: Boca Raton, FL, USA, 2022.
2. Nezu, I. Open-Channel Flow Turbulence and Its Research Prospect in the 21st Century. *J. Hydraul. Eng.* **2005**, *131*, 229–246. [CrossRef]
3. Callaham, J.L.; Maeda, K.; Brunton, S.L. Robust Flow Reconstruction from Limited Measurements via Sparse Representation. *Phys. Rev. Fluids* **2019**, *4*, 103907. [CrossRef]
4. Komori, S.; Ueda, H.; Ogino, F.; Mizushina, T. Turbulence Structure in Unstably-Stratified Open-Channel Flow. *Phys. Fluids* **1982**, *25*, 1539–1546. [CrossRef]
5. Nezu, I.; Nakagawa, H. Numerical Calculation of Turbulent Open-Channel Flows in Consideration of Free-Surface Effect. *Mem. Fac. Eng. Kyoto Univ.* **1987**, *49*, 111–145.
6. Rashidi, M.; Banerjee, S. Turbulence Structure in Free-Surface Channel Flows. *Phys. Fluids* **1988**, *31*, 2491–2503. [CrossRef]
7. Komori, S.; Murakami, Y.; Ueda, H. Detection of Coherent Structures Associated with Bursting Events in an Open-Channel Flow by a Two-Point Measuring Technique Using Two Laser-Doppler Velocimeters. *Phys. Fluids A Fluid Dyn.* **1989**, *1*, 339–348. [CrossRef]
8. Zhang, X.-L.; Xiao, H.; He, G.-W.; Wang, S.-Z. Assimilation of Disparate Data for Enhanced Reconstruction of Turbulent Mean Flows. *Comput. Fluids* **2021**, *224*, 104962. [CrossRef]
9. Calzolari, G.; Liu, W. Deep Learning to Replace, Improve, or Aid CFD Analysis in Built Environment Applications: A Review. *Build. Environ.* **2021**, *206*, 108315. [CrossRef]
10. Yousif, M.Z.; Yu, L.; Hoyas, S.; Vinuesa, R.; Lim, H. A Deep-Learning Approach for Reconstructing 3D Turbulent Flows from 2D Observation Data. *Sci. Rep.* **2023**, *13*, 2529. [CrossRef]
11. Xiao, H.; Cinnella, P. Quantification of Model Uncertainty in RANS Simulations: A Review. *Prog. Aerosp. Sci.* **2019**, *108*, 1–31. [CrossRef]
12. Moser, R.D.; Haering, S.W.; Yalla, G.R. Statistical Properties of Subgrid-Scale Turbulence Models. *Annu. Rev. Fluid Mech.* **2021**, *53*, 255–286. [CrossRef]
13. Pope, S.B. Ten Questions Concerning the Large-Eddy Simulation of Turbulent Flows. *New J. Phys.* **2004**, *6*, 35. [CrossRef]
14. Moin, P.; Mahesh, K. Direct Numerical Simulation: A Tool in Turbulence Research. *Annu. Rev. Fluid Mech.* **1998**, *30*, 539–578. [CrossRef]
15. Argyropoulos, C.D.; Markatos, N. Recent Advances on the Numerical Modelling of Turbulent Flows. *Appl. Math. Model.* **2015**, *39*, 693–732. [CrossRef]
16. Drikakis, D.; Sofos, F. Can Artificial Intelligence Accelerate Fluid Mechanics Research? *Fluids* **2023**, *8*, 212. [CrossRef]
17. Chen, J.; Viquerat, J.; Heymes, F.; Hachem, E. A Twin-Decoder Structure for Incompressible Laminar Flow Reconstruction with Uncertainty Estimation around 2D Obstacles. *Neural Comput. Appl.* **2022**, *34*, 6289–6305. [CrossRef]

18. Sahan, R.A.; Koc-Sahan, N.; Albin, D.C.; Liakopoulos, A. Artificial Neural Network-Based Modeling and Intelligent Control of Transitional Flows. In Proceedings of the 1997 IEEE International Conference on Control Applications, Hartford, CT, USA, 5–7 October 1997; pp. 359–364.
19. Anwar, S.; Khan, S.; Barnes, N. A Deep Journey into Super-Resolution: A Survey. *ACM Comput. Surv.* **2020**, *53*, 1–34. [CrossRef]
20. Fukami, K.; Fukagata, K.; Taira, K. Super-Resolution Analysis via Machine Learning: A Survey for Fluid Flows. *Theor. Comput. Fluid Dyn.* **2023**, *37*, 421–4444. [CrossRef]
21. Gao, Q.; Pan, S.; Wang, H.; Wei, R.; Wang, J. Particle Reconstruction of Volumetric Particle Image Velocimetry with the Strategy of Machine Learning. *Adv. Aerodyn.* **2021**, *3*, 1–14. [CrossRef]
22. Wang, Z.; Chen, J.; Hoi, S.C. Deep Learning for Image Super-Resolution: A Survey. *IEEE Trans. Pattern Anal. Mach. Intell.* **2020**, *43*, 3365–3387. [CrossRef]
23. Wang, Z.; Li, X.; Liu, L.; Wu, X.; Hao, P.; Zhang, X.; He, F. Deep-Learning-Based Super-Resolution Reconstruction of High-Speed Imaging in Fluids. *Phys. Fluids* **2022**, *34*, 037107. [CrossRef]
24. Drygala, C.; di Mare, F.; Gottschalk, H. Generalization Capabilities of Conditional GAN for Turbulent Flow under Changes of Geometry. *arXiv* **2023**, arXiv:2302.09945.
25. Sofos, F.; Drikakis, D.; Kokkinakis, I.W.; Spottswood, S.M. Convolutional Neural Networks for Compressible Turbulent Flow Reconstruction. *Phys. Fluids* **2023**, *35*, 116120. [CrossRef]
26. Bao, K.; Zhang, X.; Peng, W.; Yao, W. Deep Learning Method for Super-Resolution Reconstruction of the Spatio-Temporal Flow Field. *Adv. Aerodyn.* **2023**, *5*, 19. [CrossRef]
27. Falk, T.; Mai, D.; Bensch, R.; Çiçek, Ö.; Abdulkadir, A.; Marrakchi, Y.; Böhm, A.; Deubner, J.; Jäckel, Z.; Seiwald, K.; et al. U-Net: Deep Learning for Cell Counting, Detection, and Morphometry. *Nat. Methods* **2019**, *16*, 67–70. [CrossRef] [PubMed]
28. He, K.; Zhang, X.; Ren, S.; Sun, J. Deep Residual Learning for Image Recognition. In Proceedings of the 2016 IEEE Conference on Computer Vision and Pattern Recognition (CVPR), Las Vegas, NV, USA, 27–30 June 2016; pp. 770–778.
29. Obiols-Sales, O.; Vishnu, A.; Malaya, N.P.; Chandramowlishwaran, A. SURFNet: Super-Resolution of Turbulent Flows with Transfer Learning Using Small Datasets. In Proceedings of the 2021 30th International Conference on Parallel Architectures and Compilation Techniques (PACT), Atlanta, GA, USA, 26–29 September 2021; pp. 331–344.
30. Kong, C.; Chang, J.-T.; Li, Y.-F.; Chen, R.-Y. Deep Learning Methods for Super-Resolution Reconstruction of Temperature Fields in a Supersonic Combustor. *AIP Adv.* **2020**, *10*, 115021. [CrossRef]
31. Sofos, F.; Drikakis, D.; Kokkinakis, I.W.; Spottswood, S.M. A Deep Learning Super-Resolution Model for Turbulent Image Upscaling and Its Application to Shock Wave–Boundary Layer Interaction. *Phys. Fluids* **2024**, *36*, 025117. [CrossRef]
32. Li, T.; Buzzicotti, M.; Biferale, L.; Bonaccorso, F. Generative Adversarial Networks to Infer Velocity Components in Rotating Turbulent Flows. *Eur. Phys. J. E* **2023**, *46*, 31. [CrossRef]
33. Beck, A.; Kurz, M. A Perspective on Machine Learning Methods in Turbulence Modeling. *GAMM-Mitteilungen* **2021**, *44*, e202100002. [CrossRef]
34. Buzzicotti, M. Data Reconstruction for Complex Flows Using AI: Recent Progress, Obstacles, and Perspectives. *Europhys. Lett.* **2023**, *142*, 23001. [CrossRef]
35. Kamsu-Foguem, B.; Msouobu Gueuwou, S.L.; Kounta, C.A.K.A. Generative Adversarial Networks Based on Optimal Transport: A Survey. *Artif. Intell. Rev.* **2023**, *56*, 6723–6773. [CrossRef]
36. Bode, M.; Gauding, M.; Lian, Z.; Denker, D.; Davidovic, M.; Kleinheinz, K.; Jitsev, J.; Pitsch, H. Using Physics-Informed Enhanced Super-Resolution Generative Adversarial Networks for Subfilter Modeling in Turbulent Reactive Flows. *Proc. Combust. Inst.* **2021**, *38*, 2617–2625. [CrossRef]
37. Gundersen, K.; Oleynik, A.; Blaser, N.; Alendal, G. Semi-Conditional Variational Auto-Encoder for Flow Reconstruction and Uncertainty Quantification from Limited Observations. *Phys. Fluids* **2021**, *33*, 017119. [CrossRef]
38. Cuomo, S.; Di Cola, V.S.; Giampaolo, F.; Rozza, G.; Raissi, M.; Piccialli, F. Scientific Machine Learning Through Physics–Informed Neural Networks: Where We Are and What's Next. *J. Sci. Comput.* **2022**, *92*, 88. [CrossRef]
39. Shu, D.; Li, Z.; Farimani, A.B. A Physics-Informed Diffusion Model for High-Fidelity Flow Field Reconstruction. *J. Comput. Phys.* **2023**, *478*, 111972. [CrossRef]
40. Hu, Z.; Shukla, K.; Karniadakis, G.E.; Kawaguchi, K. Tackling the Curse of Dimensionality with Physics-Informed Neural Networks. *arXiv* **2023**, arXiv:2307.12306.
41. Cheng, C.; Zhang, G.-T. Deep Learning Method Based on Physics Informed Neural Network with Resnet Block for Solving Fluid Flow Problems. *Water* **2021**, *13*, 423. [CrossRef]
42. Hasegawa, K.; Fukami, K.; Murata, T.; Fukagata, K. CNN-LSTM Based Reduced Order Modeling of Two-Dimensional Unsteady Flows around a Circular Cylinder at Different Reynolds Numbers. *Fluid Dyn. Res.* **2020**, *52*, 065501. [CrossRef]
43. Yousif, M.Z.; Zhang, M.; Yu, L.; Vinuesa, R.; Lim, H. A Transformer-Based Synthetic-Inflow Generator for Spatially Developing Turbulent Boundary Layers. *J. Fluid Mech.* **2023**, *957*, A6. [CrossRef]
44. Sofiadis, G.; Sarris, I. Microrotation Viscosity Effect on Turbulent Micropolar Fluid Channel Flow. *Phys. Fluids* **2021**, *33*, 095126. [CrossRef]
45. Sofiadis, G.; Sarris, I. Reynolds Number Effect of the Turbulent Micropolar Channel Flow. *Phys. Fluids* **2022**, *34*, 075126. [CrossRef]
46. Wanik, A.; Schnell, U. Some Remarks on the PISO and SIMPLE Algorithms for Steady Turbulent Flow Problems. *Comput. Fluids* **1989**, *17*, 555–570. [CrossRef]

47. Barton, I.E. Comparison of SIMPLE-and PISO-Type Algorithms for Transient Flows. *Int. J. Numer. Methods Fluids* **1998**, *26*, 459–483. [CrossRef]
48. Kim, J.; Moin, P.; Moser, R. Turbulence Statistics in Fully Developed Channel Flow at Low Reynolds Number. *J. Fluid Mech.* **1987**, *177*, 133–166. [CrossRef]
49. Yoo, J.; Ahn, N.; Sohn, K.-A. Rethinking Data Augmentation for Image Super-Resolution: A Comprehensive Analysis and a New Strategy. In Proceedings of the IEEE/CVF Conference on Computer Vision and Pattern Recognition (CVPR), Seattle, WA, USA, 13–19 June 2020; pp. 8375–8384.
50. Tai, Y.; Yang, J.; Liu, X. Image Super-Resolution via Deep Recursive Residual Network. In Proceedings of the 2017 IEEE Conference on Computer Vision and Pattern Recognition (CVPR), Honolulu, HI, USA, 21–26 July 2017; pp. 2790–2798.
51. Gu, J.; Sun, X.; Zhang, Y.; Fu, K.; Wang, L. Deep Residual Squeeze and Excitation Network for Remote Sensing Image Super-Resolution. *Remote Sens.* **2019**, *11*, 1817. [CrossRef]
52. Tian, C.; Zhuge, R.; Wu, Z.; Xu, Y.; Zuo, W.; Chen, C.; Lin, C.-W. Lightweight Image Super-Resolution with Enhanced CNN. *Knowl.-Based Syst.* **2020**, *205*, 106235. [CrossRef]
53. Wang, Y.; Su, T.; Li, Y.; Cao, J.; Wang, G.; Liu, X. DDistill-SR: Reparameterized Dynamic Distillation Network for Lightweight Image Super-Resolution. *IEEE Trans. Multimed.* **2023**, *25*, 7222–7234. [CrossRef]
54. Duraisamy, K. Perspectives on Machine Learning-Augmented Reynolds-Averaged and Large Eddy Simulation Models of Turbulence. *Phys. Rev. Fluids* **2021**, *6*, 050504. [CrossRef]
55. Bode, M.; Göbbert, J.H. Acceleration of Complex High-Performance Computing Ensemble Simulations with Super-Resolution-Based Subfilter Models. *Comput. Fluids* **2023**, *271*, 106150. [CrossRef]
56. Nakamura, T.; Fukami, K.; Hasegawa, K.; Nabae, Y.; Fukagata, K. Convolutional Neural Network and Long Short-Term Memory Based Reduced Order Surrogate for Minimal Turbulent Channel Flow. *Phys. Fluids* **2021**, *33*, 025116. [CrossRef]
57. Yu, L.; Yousif, M.Z.; Zhang, M.; Hoyas, S.; Vinuesa, R.; Lim, H.-C. Three-Dimensional ESRGAN for Super-Resolution Reconstruction of Turbulent Flows with Tricubic Interpolation-Based Transfer Learning. *Phys. Fluids* **2022**, *34*, 125126. [CrossRef]
58. Ward, N.J. Physics-Informed Super-Resolution of Turbulent Channel Flows via Three-Dimensional Generative Adversarial Networks. *Fluids* **2023**, *8*, 195. [CrossRef]
59. Liakopoulos, A. Explicit Representations of the Complete Velocity Profile in a Turbulent Boundary Layer. *AIAA J.* **1984**, *22*, 844–846. [CrossRef]
60. Liakopoulos, A. Computation of High Speed Turbulent Boundary-Layer Flows Using the k–ϵ Turbulence Model. *Int. J. Numer. Methods Fluids* **1985**, *5*, 81–97. [CrossRef]
61. Liakopoulos, A.; Palasis, A. On the Composite Velocity Profile in Zero Pressure Gradient Turbulent Boundary Layer: Comparison with DNS Datasets. *Fluids* **2023**, *8*, 260. [CrossRef]

Disclaimer/Publisher's Note: The statements, opinions and data contained in all publications are solely those of the individual author(s) and contributor(s) and not of MDPI and/or the editor(s). MDPI and/or the editor(s) disclaim responsibility for any injury to people or property resulting from any ideas, methods, instructions or products referred to in the content.

MDPI AG
Grosspeteranlage 5
4052 Basel
Switzerland
Tel.: +41 61 683 77 34

Inventions Editorial Office
E-mail: inventions@mdpi.com
www.mdpi.com/journal/inventions



Disclaimer/Publisher's Note: The title and front matter of this reprint are at the discretion of the Guest Editors. The publisher is not responsible for their content or any associated concerns. The statements, opinions and data contained in all individual articles are solely those of the individual Editors and contributors and not of MDPI. MDPI disclaims responsibility for any injury to people or property resulting from any ideas, methods, instructions or products referred to in the content.





Academic Open
Access Publishing

mdpi.com

ISBN 978-3-7258-8718-7